Physics of Atomic Nuclei, Vol. 63, No. 8, 2000, pp. 1305–1314. Translated from Yadernaya Fizika, Vol. 63, No. 8, 2000, pp. 1381–1390.

ON THE 85th ANNIVERSARY OF V.V. VLADIMIRSKY

Neutron Storage in a Magnetic Field

Yu. G. Abov, V. V. Vasiliev, and O. V. Schvedov

Institute of Theoretical and Experimental Physics, Bol'shaya Cheremushkinskaya ul. 25, Moscow, 117259 Russia

Received January 18, 2000

Abstract—The motion of neutrons in magnetic traps is considered for various cases of neutron polarization. The results of implementing such traps in practice and special features of experiments studying magnetic neutron storage are discussed. The problem of neutron losses during injection via magnetic valves can be solved by conjoining a magnetic trap with a converter of cold neutrons into ultracold ones or with a source of ultracold neutrons. Prospects for expanding neutron-storage experiments by invoking a correlation analysis of neutron decay and by using the transport properties of charged particles in a nonuniform magnetic field are analyzed. In such an investigation, the recording of the storage time of neutrons proper can be supplemented with the detection of decay protons and electrons and with a parallel measurement of the asymmetries of proton and electron emission with respect to the magnetic field. A set of relative measurements permits improving the accuracy of an experimental determination of the neutron lifetime and combining this determination with the determination of correlation coefficients. On this basis, it is possible to find directly the ratio of the weak-interaction constants and the constants themselves. The application of the most advanced reactor and accelerator technologies to subcritical electric nuclear devices optimized for generating cold and ultracold neutrons, along with the use of solid deuterium and superfluid helium, creates preconditions for developing a neutron plant and for launching neutron studies at accelerators. Thus, the work that has been done as a development of V.V. Vladimirsky's proposals on magnetic neutron storage is analyzed, and the potential of a further use of ultracold neutrons and magnetic devices for deploying a full-scale precision experiment to study the beta decay of polarized neutrons is demonstrated. © *2000 MAIK "Nauka/Interperiodica".*

1. INTRODUCTION

In 1960, V.V. Vladimirsky showed, for the first time, that a nonuniform magnetic field can be used to transport and confine ultracold neutrons (the corresponding energy range is 10^{-8}–10^{-7} eV) [1]. The energy of neutron interaction with a magnetic field of strength **B** is $U = -(\boldsymbol{\mu} \cdot \mathbf{B})$, where $\mu = -1.91 \times 5.05 \times 10^{-27}$ J/T is the magnetic moment of the neutron. Hence, a neutron of positive polarization (that is, a neutron whose spin is aligned with the magnetic field) is repelled into the region where the field is weaker, while a neutron of negative polarization (a neutron whose spin is antiparallel to the field) is drawn into the region where the field is stronger. This effect is used in many devices for neutron storage. For example, the storage of positively polarized neutrons was implemented in a "magnetic cup" [2]; at the same time, negatively polarized neutrons can be confined in the magnetic field of a straight current [1, 3]. For the neutron spin to follow adiabatically the magnetic-field direction, it is necessary that

$$\omega_m \ll \omega_L = 2\mu B/\hbar, \qquad (1)$$

where ω_m is the frequency of magnetic-field variation in the reference frame comoving with the neutron, while ω_L is the Larmor frequency of neutron-spin precession in the magnetic field B. This means that, in the reference frame associated with the neutron, the magnetic field must not be overly weak and must not change overly fast (or the neutron must move in the field at a sufficiently small velocity). For ultracold neutrons, this condition can be reliably satisfied in magnetic fields of some specific configurations.

For the sake of completeness, we note that the majority of experiments devoted to neutron storage with the aim of measuring the neutron lifetime were performed by using wall traps, where there are specific problems inherent in the method, but these problems have been solved successfully.

This article presents a brief survey of attempts at implementing a magnetic storage of neutrons and an analysis of the potential of magnetic fields for studies of the nature of weak interaction by using ultracold and cold neutrons. It is shown that there exists at least one magnetic-field type that features simultaneously the properties of a neutron trap and the properties of the channel for transporting charged particles. In this case, it is possible to analyze the asymmetry of proton and electron emission with respect to the neutron spin. By combining a measurement of the neutron lifetime with a determination of three correlation coefficients, one can determine directly not only the ratio of the weak-interaction constants but also the constants themselves. As soon as a fairly high precision is achieved, a simultaneous determination of three correlations alone in cold-neutron beams will be sufficient for testing some hypotheses.

All the above facets of neutron investigations originate from Vladimirsky's work on the subject and may

1063-7788/00/6308-1305$20.00

become components of a qualitatively new method for studying weak interaction.

2. MOTION OF A NEUTRON IN A MAGNETIC FIELD

In the following, we assume that the magnetic field in the storage volume is so high that condition (1) is satisfied. It was shown experimentally in [2, 4] that this condition is met in a storage ring and in a magnetic cup. In experiments devoted to neutron storage, neutrons with energies in excess of the critical confinement energy for a given trap die out within the first ten seconds from the beginning of storage. The radial and axial degrees of freedom of a neutron can be mixed in a ring trap of this type, as well as in a cylindrical storage vessel. In a simply connected cylindrical storage vessel, this proceeds, for example, owing to scattering on wall roughnesses, to deviations of the wall shape from an ideal shape, and to deviations of the vessel axis from the vertical direction. At any instant of time after filling the trap, it therefore contains a mixture of a short- and a long-lived component of the neutron gas. In this respect, the situation is independent of the trap type. In order to obtain deeper insights into the aforementioned processes and to assess correctly the contribution of one channel or another to the dynamics of neutron escape from the trap, it is reasonable to perform a mathematical simulation of the neutron trajectory. By changing initial conditions of neutron injection into the trap and by studying the dependence of, say, the number of collisions with the trap walls on the injection angles, one can figure out the role of various structural elements in a model-dependent way and optimize the conditions of injection. Once this has been ensured, only those neutrons are injected into the trap that will have been stored till their beta decay. This will reduce uncertainties in experimental results, and this is especially important when the experiment is aimed at a precision determination of physical quantities like the neutron lifetime and correlation coefficients in neutron decay. For example, a Monte Carlo simulation of the neutron trajectory can become an element of the full model of a given experiment. By combining a code for computing the neutron trajectory with the model of the trajectories of the electron and the proton that are produced in polarized-neutron decay, one can trace the entire process—from the injection of a neutron into the trap to the recording of the neutron or its decay products in detectors.

The force acting on a neutron having the mass m and the magnetic moment μ and occurring in a magnetic field $\mathbf{B}$ has the form

$$\mathbf{F} = -S\mu \cdot d|\mathbf{B}|/d\mathbf{r} + m\mathbf{g}_0, \tag{2}$$

where $\mathbf{g}_0$ is the acceleration due to gravity, while S specifies the orientation of the neutron spin with respect to the magnetic field [$S = +1$ (-1) in the case where the neutron spin is parallel (antiparallel) to the field]. We further go over to dimensionless variables by means of the substitutions

$$r = l_0 l', \quad B = B_0 B', \quad t = t_0 t', \tag{3}$$

where l_0, B_0, and t_0 are the maximal values of length, magnetic induction, and time that are peculiar to a specific problem. We will write equation (2) for the Cartesian coordinates x, y, and z; make the substitution given by (3); and omit the primes after that. Choosing the z-axis direction antiparallel to that of the force of gravity, we arrive at the set of equations

$$\frac{d^2x}{dt^2} = -\frac{S}{2}\frac{\partial B}{\partial x}, \tag{4.1}$$

$$\frac{d^2y}{dt^2} = -\frac{S}{2}\frac{\partial B}{\partial y}, \tag{4.2}$$

$$\frac{d^2z}{dt^2} = -\frac{S}{2}\frac{\partial B}{\partial z} - G, \tag{4.3}$$

where $G = mg_0l_0/(2\mu B_0)$ is a constant that arises in going over to the dimensionless variables. Under the condition $\mu B_0 = mg_0l_0$, where l_0 is the height of the vessel, we obtain $G = 1/2$.

When the above condition is satisfied, equation (4.3) is simplified to become

$$\frac{d^2z}{dt^2} = -\frac{S}{2}\frac{\partial B}{\partial z} - \frac{1}{2}. \tag{4.3a}$$

It is convenient to use the set of equations (4.1), (4.2), and (4.3a) for solving numerical problems, one of which will be formulated below.

3. STORAGE OF NEUTRONS IN A TRAP OF THE CUP TYPE

A long-term storage of neutrons was implemented in magnetic traps of two types. Of these, one belongs to the class of storage rings. The second is referred to as a magnetic cup. There, neutrons are confined within a simply connected region. The hub of such an apparatus is an electromagnet formed by a set of ring concentric coils, each having a rectangular cross section of dimensions 6×8 cm^2. These coils lie between ring iron poles arranged along the bottom and the walls of a cylinder about 1 m in diameter and about 0.4 m in height (see Fig. 1). A thin-wall vacuum chamber is inserted inside the electromagnet and fixed at the surface of the poles. On the lid of the vacuum chamber, there are vacuum-tight inputs for an additional coil and a flange sleeve to which a removable segment of the pipe for oil-free evacuation is connected. The central coil has no core; it embraces the neck of the vacuum chamber and serves as a magnetic valve. Neutrons are delivered to the vacuum chamber through the neck with the aid of the inlet–outlet device (not shown in Fig. 1). The bent neutron-pipe segment, which can be rotated about the cup axis

through an angle of 90°, is the main element of the inlet–outlet device. The lower endface of this segment can be rotated from the inlet position (neutron pipe from the reactor used) to the outlet position (detector of ultracold neutrons) and in the opposite direction from the latter to the former. The removal of the neutrons is performed when the magnetic valve is open to the detector of ultracold neutrons. In the storage mode, the rotatable segment is directed toward the detector, whereby the counting of the neutrons penetrating from the trap through the closed valve is ensured.

The main magnetic field of a cup-type trap can be described qualitatively by the expressions

$$\begin{aligned} B_r &= AI_1(\lambda r)\cos(\lambda z) - BJ_1(kr)\exp(-kz), \\ B_z &= -AI_0(\lambda r)\sin(\lambda z) - BJ_0(kr)\exp(-kz), \end{aligned} \quad (5)$$

where r is the radial coordinate; the coordinate z is measured along the trap axis from the horizontal plane of the bottom poles; λ and k are constants that describe the structures of the bottom and of the wall, respectively; $I_0(\lambda r)$ and $I_1(\lambda r)$ are zero- and first-order modified Bessel functions of the first kind; $J_0(kr)$ and $J_1(kr)$ are zero- and first-order Bessel functions; and the constants A and B depend on the ampere-turns of the coils and on the periods of the structures. By equating both field components to zero, we can easily construct the node lines of the fields. The number of these lines depends on the magnitudes of the periods of the magnetic structures and on the number of these periods. The actual field of the trap [5] differed somewhat from an ideal field as represented by (5). The minimal strength of the field at the lower boundary of the storage region was 2.5 kG.

In order to reduce neutron depolarization at the field nodes, an additional coil was used in the experiment described in [6, 7]. Owing to the superposition of the fields of the main coils and the additional coil, the resulting field configuration was characterized by the presence of node points rather than by the presence of node lines. The coil in question was arranged at an altitude inaccessible to neutrons. By using the results presented in [1], we can show that the probability of depolarization in the vicinity of a node point is estimated by the cross section

$$\sigma = \frac{V\hbar}{\mu}\frac{a^2l^2 + b^2m^2 + c^2n^2}{|abc|},$$

where a, b, and c are the derivatives of the field along the principal coordinate axes, while l, m, and n are the direction cosines of the velocity vector.

It can also be shown that the mean depolarization cross section per unit length of a node line at $H_z = 0$ is

$$\alpha = 0.72\sqrt{\hbar V/\mu b},$$

where V is the mean neutron velocity in the vicinity of a node line, while b is the derivative of the field in the direction from the node line to the point of the closest approach of the neutron trajectory to this line in the plane orthogonal to the node line.

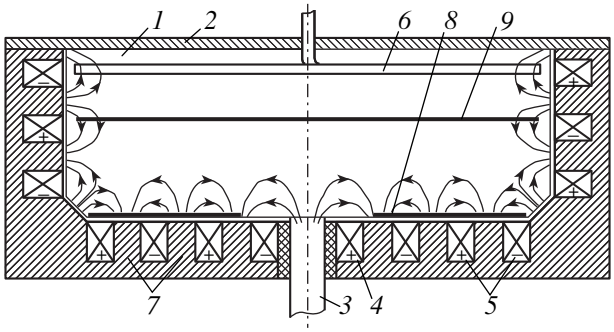

Fig. 1. Magnetic trap for ultracold-neutron storage (magnetic cup): (*1*) vacuum chamber; (*2*) magnetic lid of the chamber; (*3*) injection sleeve; (*4*) central coil; (*5*) main coils; (*6*) additional coil; (*7*) iron ring poles (St3); and (*8*, *9*) absorbers (heaters) of ultracold neutrons.

In order to compare the storage time in the depolarization channel with the neutron lifetime, which is not greater than 900 s, it is necessary to determine the field parameters, the neutron velocities in the vicinities of nodes, etc. In the specific trap shown in Fig. 1, the depolarization time achieved via the above transformation of nodes was estimated at 1.6×10^4 s [8], which makes it possible to study other mechanisms of neutron escape.

The table lists the results that were reported in [7] and which were obtained in an experiment devoted to neutron storage in a cup. The background-counting rate in that experiment was 0.0067 ± 0.0002 s^{-1}. The processing of those data yielded two exponentials. A fast escape of short-lived neutrons occurred within a storage time of 200 s. The storage time in the slow exponential was estimated in [7] at a value greater 700 s (at a 95% C.L.). An analysis of the logarithm of the number of counts at the last four points in terms of the linear form

$$\ln N = (-1.025 \pm 0.20) - (0.0012 \pm 0.0004)t$$

Number of neutrons in a trap versus the time of storage

Time of storage, s	Mean number of neutrons, $\bar{N}$	Uncertainty in the mean number, $S(\bar{N})$	$\ln\bar{N}$	Root-mean-square deviation of $\ln\bar{N}$, $S(\ln\bar{N})$
20	0.724	0.052	–0.32	0.07
80	0.592	0.042	–0.52	0.07
160	0.415	0.048	–0.88	0.12
280	0.276	0.032	–1.29	0.11
400	0.181	0.039	–1.71	0.22
600	0.156	0.027	–1.86	0.17
880	0.15	0.035	–1.9	0.23

yielded the mean neutron-storage time of $\tau = 830$ s. At a 90% C.L., it lies between 625 and 1250 s. It is the value of 830^{+420}_{-205} s that must be treated as the result of the above experiment devoted to neutron storage in a gravitational magnetic trap of the cup type. The upper boundary of the confidence interval was determined there only from the results of the storage experiment without taking into account the known value of the neutron lifetime.

The initial number of long-lived neutrons can be estimated at mean value of 0.3 of a neutron per storage cycle. This value is determined by the reactor power, the efficiency of the source and the neutron pipe, the altitude at which the neutrons are raised in the trap, and the height of the magnetic barrier in the trap. That the accuracy in determining the storage time is not very high in that case is partly due to poor statistics, but the main reason for this is that, in the trap, there are neutrons characterized by a short storage time. The number of such neutrons is about 0.6 per storage cycle, a value that is greater than the number of long-lived neutrons. It follows that it is necessary to take measures to reduce the number of short-lived neutrons and the time of their escape from the region of storage.

4. CONDITIONS OF LONG-TERM STORAGE IN A NONUNIFORM MAGNETIC FIELD

The magnetic field at the bottom and the walls of the cup was too small (at level of 3 kG, on average) for precisely measuring the neutron lifetime. The main objective of the study reported in [7] was to explore the possibility of measuring the lifetime of the free neutron with the aid of magnetic storage and to determine optimal conditions for setting an experiment aimed at this. By generalizing the results of neutron storage in a simply connected trap and in a storage ring, we can draw the following conclusions.

In either type of storage devices, the main factor hindering the improvement of accuracy is the presence of neutrons having an undesirable polarization and higher energies beyond the range of storage. We will refer to such neutrons as short-lived. From the available results, it is clear that, for removing such neutrons from the region of storage within 10 s, it is necessary to meet the following conditions. The storage trap must be equipped with a device that absorbs neutrons of opposite polarization. The volume of the storage region must be known to a high precision. Any short-lived neutrons must be removed from the trap (by means of absorption or heating) upon traversing the boundary of the storage region. For example, the number of short-lived neutrons in the experiment reported in [7] was reduced in relation to that in [6] by deploying an additional absorber; as a result, their storage time was pushed down from 300 to 200 s. If the absorber were positioned precisely at the boundary of the limiting storage volume, the storage time would be determined more accurately. Such an arrangement of the absorber is possible, however, only if the shape of the storage region is sufficiently simple. A further advantage in what is concerned with the accuracy of the result is achieved when the neutron-injection device lets in only long-lived neutrons.

We would like to note that the injectors used were insufficiently adequate both in the case of a storage ring and in the case of a magnetic cup. In the former case, neutrons were injected through a movable segment of the neutron pipe, but this prevented diagnostics during storage. In the magnetic cup, the central, iron-free, injector provided wider possibilities in what is concerned with diagnostics, but it restricted the magnetic field that confined the neutrons in the trap. When the injector was switched on, this gave an accelerating momentum to some of the neutrons, pushing them beyond the interval of long-term storage.

For future experiments, it seems reasonable to combine a trap storing neutrons with a source of ultracold neutrons. For example, a version is possible where the magnetic system is conjoined with a cryogenic detector of ultracold neutrons that is based on liquid helium (^{4}He) [9]. A vessel containing liquid helium can be separated from the high-vacuum storage volume by a valve that ensures filtration of neutrons with required energies. The parts of the device are arranged one above the other and are embraced by the coil creating the magnetic field. The delivery of cold neutrons to the vessel containing liquid helium does not involve difficulties of fundamental nature. The main advantage of such an assembly is that ultracold neutrons are produced directly within the storage volume. Owing to this, one can do without magnetic valves, as well as without switching the current on and off, which is very difficult in superconducting systems. The volume of the vessel containing superfluid helium can be about 10 l. It was shown in [10] that, even under the conditions of a subcritical assembly of power up to 100 kW, it is possible to ensure superfluidity in such volumes of helium. However, only a liquid-helium temperature of 1 K was considered in that study. In respect of neutron-storage times and the cost of cryogenic equipment, a liquid-helium temperature of about 0.6 K can be considered to be optimal. In this case, the time of neutron storage in helium becomes as long as the neutron lifetime [9], whereas the density of neutrons in the trap of the source grows in direct proportion to the storage time. The temperature of 0.6 K is achievable in an extracted cold-neutron beam shielded thoroughly from fast-neutron and gamma-ray background, which is capable of heating cold helium.

It is reasonable to combine the device schematically described in [10] with a target complex of a 200-MeV proton accelerator. If such a complex is equipped with a moderator for neutrons and if the thermal-neutron flux density in it is 10^{16} $(\mathrm{cm}^2\ \mathrm{s})^{-1}$, the production of cold

and ultracold neutrons will be sufficiently efficient for implementing the most ambitious projects.

One such project is considered in Section 7.

5. SIMULATING THE DYNAMICS OF A NEUTRON IN AN ARBITRARY MAGNETIC FIELD

Thus, it was shown experimentally that it would be important to optimize the neutron-storage conditions. In order to ensure fulfillment of these conditions, it is necessary to perform preliminary calculations; that is, we need a mathematical model for describing the motion of neutrons in a trap. Let us consider the possibilities for developing such a model.

From the set of equations (4.1), (4.2), and (4.3a), which describe the motion of a neutron in a magnetic field and the gravitational field of the Earth, we go over to a set of finite-difference equation for determining the neutron velocity and coordinate at the $(i + 1)$th step. We have

$$\begin{aligned} V_x^{i+1} &= V_x^i - \frac{S\partial B}{2\partial x}\Delta t_i, \\ V_y^{i+1} &= V_y^i - \frac{S\partial B}{2\partial y}\Delta t_i, \\ V_z^{i+1} &= V_z^i - \left(\frac{S\partial B}{2\partial z} + \frac{1}{2}\right)\Delta t_i. \end{aligned} \tag{6}$$

We further define new coordinates of the neutron as

$$\begin{aligned} x_{i+1} &= x_i + V_x^{i+1/2}\Delta t_i, \\ y_{i+1} &= y_i + V_y^{i+1/2}\Delta t_i, \\ z_{i+1} &= z_i + V_z^{i+1/2}\Delta t_i, \end{aligned} \tag{7}$$

where

$$\begin{aligned} V_x^{i+1/2} = (V_x^i + V_x^{i+1})/2, \quad V_y^{i+1/2} = (V_y^i + V_y^{i+1})/2, \\ V_z^{i+1/2} = (V_z^i + V_z^{i+1})/2. \end{aligned} \tag{8}$$

The values of $\partial B/\partial x$, $\partial B/\partial y$, and $\partial B/\partial z$ are taken at the intermediate point with the coordinates $x_{i+1/2}$, $y_{i+1/2}$, and $z_{i+1/2}$. By proceeding from the point of neutron generation in the trap, checking the convergence condition at each step, and varying the step length in accordance with the rate of the field variation, we can trace the trajectory of the neutron up to its absorption, heating, or escape to the detector. The finite-difference scheme specified by equations (6)–(8) belongs to the class of implicit schemes of second order in accuracy. Such schemes are widely used to calculate the trajectories of charged particles [11]. By using analytic dependences of the type specified in (5) or interpolation tables describing the magnetic field in the storage region, we can easily determine, on the basis of the above scheme, the trajectory of a neutron for given initial conditions to the required accuracy.

If the finite-difference equations (6)–(8) are supplemented with the set of equations describing the evolution of the spin in an arbitrary magnetic field with allowance for its nodes, we will arrive at a full model that will make it possible to compute many channels of neutron escape and to simulate actual versions of the traps.

6. POTENTIAL FOR A NEUTRON IN THE FIELD OF A STRAIGHT CURRENT

In order to provide the simplest example of the possibilities for storing neutrons of negative polarization and to test the proposed computational code in a way easy to trace, we will consider the motion of a neutron in the field of a straight current [1].

Suppose that a current-carrying conductor (busbar of several conductors) is arranged vertically. We associate with it a system of cylindrical coordinates z, r, and φ and align the z axis with the axis of the current-carrying busbar. In the $z = 0$ plane, we place a horizontal mirror reflecting neutrons. Here, we consider the problem of confining a negatively polarized neutron in the region around the current. We assume that a neutron with an angular momentum M has been generated at a point r in the magnetic field of a straight current. We can then consider the motion of this neutron in the potential

$$U(r) = \frac{M^2}{2mr^2} - \frac{0.2\mu I}{r}, \tag{9}$$

where we have taken into account the magnetic permeability of a vacuum and where the current is measured in megaamperes. In the case of a current flowing in the horizontal plane, it is impossible to confine a neutron since, under the effect of the gravitational force, the neutron leaves the stability region after executing one or two helixes about the current direction. In the following, we will therefore consider only a current flowing in the vertical direction. Any deviation of the current from the vertical direction or any deviation of the mirror from the horizontal plane leads to the mixing of the degrees of freedom and to losses of neutrons because of violation of the storage conditions.

The function in (9) attains a minimum when the neutron-injection radius takes the value

$$r_0 = \mathcal{M}^2/\left(0.2\frac{\mu}{m}I\right), \tag{10}$$

where $\mathcal{M} = M/m$. Since the angular momentum is conserved in a central field, the quantity $\mathcal{M} = V_\varphi r$ is determined by the conditions of injection for a given neutron. By specifying the value of $\mathcal{M}$ at the point where the distance between the neutron in question and the current axis is minimal, $r_{\min}$, we can determine easily

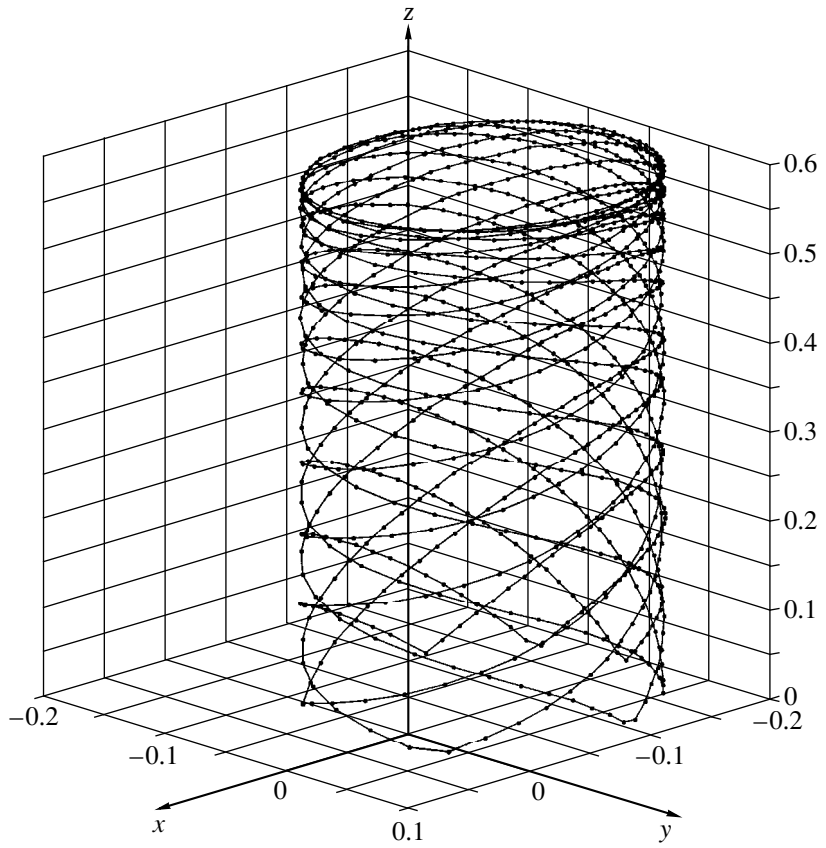

Fig. 2. Trajectory of a negatively polarized neutron in the field of a straight current [the *z* axis is chosen to coincide with the current axis ($x = y = 0$); the coordinates of the neutron-production vertex are $x = 0.52$ m, $y = 0$, and $z = 0.6$ m; $V = V_\varphi = 6.23$ m/s].

the point where this distance is maximal, r_{max}, by means of the relation

$$\mathcal{M}^2 = 0.4\frac{m}{\mu}I\left(\frac{r_{min}r_{max}}{r_{min}+r_{max}}\right). \quad (11)$$

This relation also provides a convenient check upon the codes used to compute the neutron trajectory. Figure 2 exemplifies the calculations of the neutron trajectory in the attractive potential of a straight current. The initial conditions for this specific calculation are formulated in the caption under the figure. The calculated trajectory is in perfect agreement with relation (11). It is obvious that, in the reference frame comoving with the neutron, the magnetic field changes quite slowly; that is, the condition in (1) is satisfied. Figure 3 shows the calculated electron trajectory in the same field. Figure 4 presents an example of a calculated trajectory of a positively polarized neutron in the field of a vertical straight current. The trajectory is bounded in the radial direction by a cylindrical mirror. If this mirror is replaced by a layer of substance absorbing ultracold neutrons, the device in question appears to be a highly efficient polarizer [12].

We note that, by supplementing the above calculations of the trajectories with a solution to spin-evolution equations of the type presented in [1], one would obtain information relevant to experiments measuring the rotation of the neutron-polarization plane due to weak interaction [13]. In a number of experimental studies, this effect was observed for neutrons propagating through a sample situated within a system of magnetic screens in zero field. It seems that no analysis of spurious effects in small fields induced by external sources can yield reliable results without thorough calculations and a numerical simulation of spin rotation in such fields.

7. SPECIAL FEATURES OF NEUTRON STORAGE IN THE FIELD OF A STRAIGHT CURRENT

An apparatus for neutron storage in a magnetic field is too complex to be used to measure neutron lifetime alone. However, the potential of a storage ring or a cup for any other experiment is not very rich. It is therefore advisable to consider alternative magnetic systems—for example, a superconducting system that implements the magnetic field of a straight current in a bounded volume. The nonuniform axisymmetric magnetic field of a straight current is advantageous in that its ability to confine neutrons within a limited region [1] is combined with the appropriate transport proper-

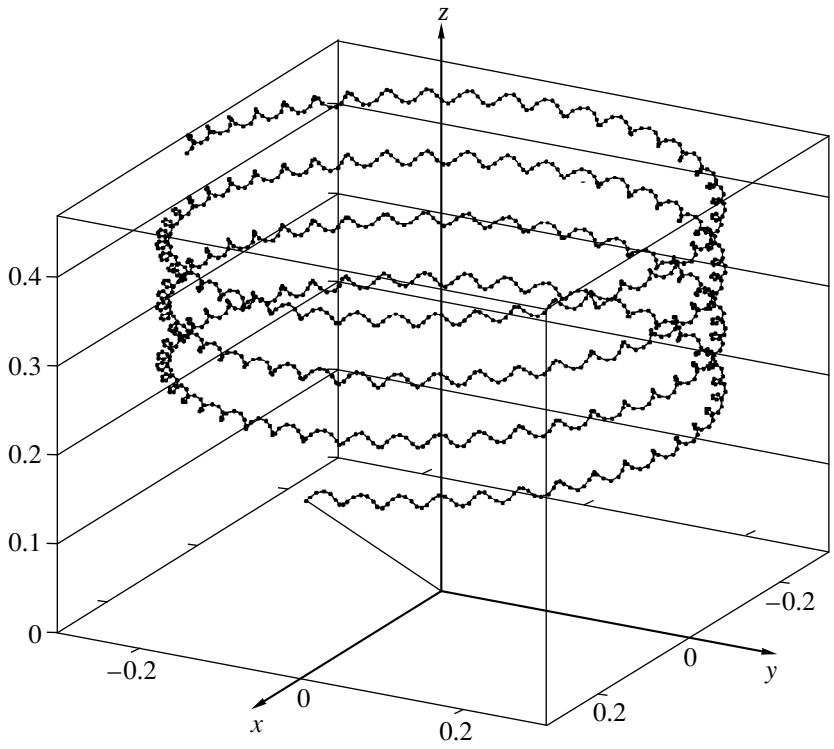

Fig. 3. Trajectory of an electron in the field of a straight current (6×10^5 A). As in Fig. 2, the z axis is chosen to coincide with the current axis.

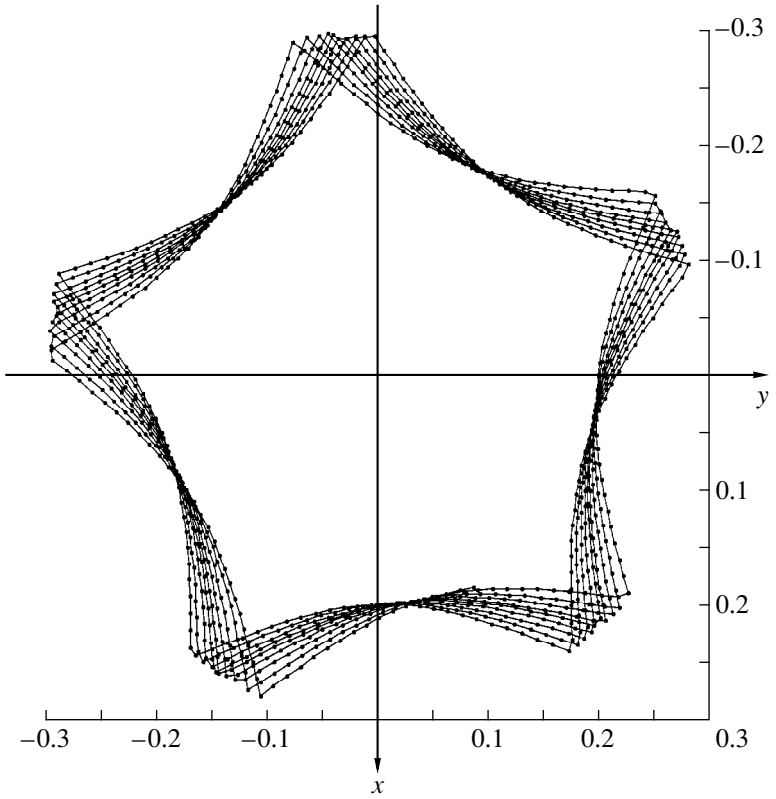

Fig. 4. Trajectory of a positively polarized neutron in the field of a straight current (top view). The motion in the radial direction is bounded by a reflecting mirror (not shown in the figure).

ties of electrons and protons, which are produced in neutron decays, in such a field. Only the transport properties of electrons and positrons were considered previously in fields of the $1/r$ type [14, 15].

We note that the highest values of the momenta of the proton and the electron produced in neutron decay are equal to each other and that, as follows directly from the Lorentz equations, their trajectories are determined by the relevant charge and momentum. It is also obvious that the protons and the electrons drift in opposite directions along the current axis; the direction of this drift is parallel to the current for the protons and is antiparallel to it for the electrons. An example of the electron trajectories is shown in Fig. 3. If the current in the system implementing the field of a straight current is sufficiently high for efficiently confining ultracold neutrons, it follows from the above that, by conjoining the magnetic system with a source of ultracold neutrons, it is possible to ensure the storage of these neutrons and the delivery of the protons and electrons originating from their decays to a detecting system [16].

By measuring the rate of counting for the decay protons and electrons versus the time of storage and by determining the number of neutrons in the storage region—that is, by combining two methods—we can refine the neutron lifetime, which is presently known to within 0.2% [17]. Moreover, the confinement of neutrons in the devices being discussed ensures a high degree of polarization [12]. It also becomes possible to study the asymmetry of the emission of protons and electrons from neutron decays in the storage region. It can easily be shown that the angular momentum is conserved when the motion occurs in a field of the $1/r$ form—in particular, the direction of rotation of a decay particle is conserved, together with the azimuthal momentum component specified by the relevant decay event. For particles originating from neutron decays and moving about the current in the clockwise and counterclockwise directions, the asymmetry of emission can be measured by recording these particles with a radial detector element. Owing to the conditions of the motion, we can record the decay electrons and protons both in spatial and in time coincidences, thereby selecting decay events. It is also possible to record event types corresponding to various orientations of the proton and electron momenta with respect to the neutron spin. All decay events can be classified according to these orientations of the proton and electron momenta and according to the level of the azimuthal momentum component. Without considering here a discrimination in the momentum level, we associate the plus subscript (superscript) with proton (electron) momenta parallel to the neutron spin and the minus subscript (superscript) with proton (electron) momenta antiparallel to the neutron spin—for example, we denote by N^{e+}_{p-} the number of events where the electrons are emitted in the direction of neutron spin and where the protons are emitted in the opposite direction. By using the relative contributions of events of these types, we can find the correlation coefficients A, B, and a in the well-known formula for the probability of polarized-neutron decay [18]. Presented immediately below are equations for determining all these coefficients:

$$
\begin{aligned}
dN^{e+}_{p+} &= 2\pi^2 n_0 \frac{P_\nu}{P_e} \\
&\times\left(+1+\frac{1}{3}A\frac{P_e c}{E_e}\frac{P_\nu}{P_e}-\frac{2}{3}B-\frac{1}{4}a\frac{P_e c}{E_e}\frac{P_\nu}{P_e}\right)dP, \\
dN^{e-}_{p+} &= \left[8\pi^2 n_0\left(1-\frac{1}{2}A\frac{P_e c}{E_e}\right)+2\pi^2 n_0\frac{P_\nu}{P_e}\right. \\
&\left.\times\left(-1+\frac{1}{3}A\frac{P_e c}{E_e}\frac{P_\nu}{P_e}-\frac{2}{3}B+\frac{1}{4}a\frac{P_e c}{E_e}\frac{P_\nu}{P_e}\right)\right]dP, \\
dN^{e+}_{p-} &= \left[8\pi^2 n_0\left(1+\frac{1}{2}A\frac{P_e c}{E_e}\right)+2\pi^2 n_0\frac{P_\nu}{P_e}\right. \\
&\left.\times\left(-1-\frac{1}{3}A\frac{P_e c}{E_e}\frac{P_\nu}{P_e}+\frac{2}{3}B+\frac{1}{4}a\frac{P_e c}{E_e}\frac{P_\nu}{P_e}\right)\right]dP, \\
dN^{e-}_{p-} &= 2\pi^2 n_0\frac{P_\nu}{P_e} \\
&\times\left(+1-\frac{1}{3}A\frac{P_e c}{E_e}\frac{P_\nu}{P_e}+\frac{2}{3}B-\frac{1}{4}a\frac{P_e c}{E_e}\frac{P_\nu}{P_e}\right)dP.
\end{aligned}
\tag{12}
$$

Here, P_ν and P_e are, respectively, the antineutrino and electron momenta; c is the speed of light; E_e is the electron energy; and a, A, and B are correlation coefficients in polarized-neutron decay. For these coefficients, we have

$$
\begin{aligned}
A\frac{P_e c}{E_e} &= 2[(dN^{e+}_{p-}+dN^{e+}_{p+})-(dN^{e-}_{p+}+dN^{e-}_{p-})]/\sum N^i_j, \\
B &= \frac{P_\nu}{P_e}[(dN^{e+}_{p-}+dN^{e+}_{p+})-(dN^{e-}_{p+}+dN^{e-}_{p-})]/\sum N^i_j \\
&\quad -6(dN^{e+}_{p+}-dN^{e-}_{p-})/\sum N^i_j, \\
\frac{1}{8}a\frac{E_\nu}{E_e}\frac{P_\nu}{P_e} &= [(dN^{e+}_{p-}-dN^{e-}_{p-})-(dN^{e+}_{p+}-dN^{e-}_{p+})]/\sum N^i_j \\
&\quad -\left(1-\frac{1}{2}\frac{P_\nu}{P_e}\right),
\end{aligned}
\tag{13}
$$

where

$$\sum N^i_j = (dN^{e+}_{p-}+dN^{e+}_{p+}+dN^{e-}_{p+}+dN^{e-}_{p-}).$$

Measurement of such effects can be used to determine the ratio of the axial-vector constant of weak interaction to the vector constant, $\lambda = G_a/G_V$. If the experiment in question is extended in such a way as to include measurement of the free-neutron lifetime τ_β, it becomes

possible to determine the vector constant G_v and the axial-vector constant G_a separately [19]. It is interesting to note that the parameters describing the contribution to the weak-interaction Hamiltonian from a hypothetical right-handed vector boson are related to the correlation coefficients for polarized-neutron decay by the simple equations [20]

$$\eta = \cos(2\Delta\theta_a) = \frac{B-A}{1-a},$$
$$\omega = \cos(\Delta\theta_a + \Delta\theta_v) = \frac{B+A}{\sqrt{(1-a)(1+3a)}}. \quad (14)$$

By measuring three correlation coefficients in a single experiment, we can set limits on some new physical quantities.

8. CONCLUSION

Thus, Vladimirsky's proposals on the magnetic confinement of neutrons in a simply connected region bounded by a nonuniform magnetic field were implemented with the aid of a gravitational magnetic trap of the cup type. A series of experiments performed from 1983 to 1986 made it possible to ensure a long-term storage of neutrons in the trap. As a result, a storage time of 830^{+420}_{-205} s was achieved. On the basis of these experiments, conditions have been formulated under which the neutron lifetime can be determined by measuring the storage-time dependence of the number of neutrons that remain in the trap after storage.

It has been shown that, for choosing the conditions of injection into the trap that correspond to long-term storage, it is important to perform a numerical simulation of the evolution of a polarized neutron in a magnetic field. A possible algorithm for such a simulation has been described, and the computed trajectories of a neutron in the field of a straight current have been presented. It has been indicated that the known property of the nonuniform field of a straight current to transport charge particles can be applied to electrons and protons from neutron decays and that it is possible to record the asymmetry of proton and electron emission with respect to the neutron spin. The latter will aid in performing a multipurpose experiment where the measurement of the neutron lifetime will be supplemented with a determination of three spatial correlations in neutron decay. The results obtained by calculating the correlation coefficients on the basis of the asymmetries of proton and electron emission from neutron decays in the field of a straight current have been presented. A multipurpose experiment of the above type may result in important refinements of the structure of weak-interaction Hamiltonian describing semileptonic decays.

The most efficient setting for such experiments can be based on a beam of cold neutrons from the target device of an electric nuclear facility. Via the epithermal accumulation of neutrons in superfluid helium by placing the cryostat in a cold-neutron beam of high flux density, a record number of neutron decays will be achieved in a controllable zone of the facility under discussion.

In conclusion, we would like to emphasize that investigations devoted to a magnetic ultracold-neutron storage that were initiated by Vladimirsky also gave rise to correlation studies of polarized-neutron decay. Here, an experiment that measured the asymmetry of electron emission with respect to the neutron spin [21] and which proved to be one of the seminal studies along these lines was performed under his supervision. Possibly, the use of magnetic systems creating a field of the $1/r$ type will make it possible to perform a complete experiment to study polarized-neutron decay. The above arguments prove that, in the program for developing electric nuclear facilities, such an experiment could become a valuable component of fundamental importance. Its practical implementation requires, however, concerted efforts of several research centers and, probably, a collaboration of several countries, since the facility to be used will combine a cryostat containing liquid helium, superconducting magnets, supermirrors for reflecting neutrons, and the most advanced equipment for analyzing correlations during neutron storage under conditions of ultralow background.

REFERENCES

1. V. V. Vladimirskiĭ, Zh. Éksp. Teor. Fiz. **39**, 1062 (1960) [Sov. Phys. JETP **12**, 740 (1960)].
2. Yu. G. Abov, S. P. Borovlev, V. V. Vasil'ev, *et al.*, Yad. Fiz. **38**, 122 (1983) [Sov. J. Nucl. Phys. **38**, 70 (1983)].
3. V. V. Vasil'ev, Preprint No. 38, ITÉF (Institute of Theoretical and Experimental Physics, Moscow, 1990).
4. W, Paul, F. Anton, *et al.*, Z. Phys. C **45**, 2600 (1989).
5. Yu. G. Abov, V. F. Belkin, V. V. Vasil'ev, *et al.*, Preprint No. 44, ITÉF (Institute of Theoretical and Experimental Physics, Moscow, 1976).
6. Yu. G. Abov, S. P. Borovlev, V. V. Vasil'ev, *et al.*, Preprint No. 21, ITÉF (Institute of Theoretical and Experimental Physics, Moscow, 1982).
7. Yu. G. Abov, V. V. Vasil'ev, V. V. Vladimirskiĭ, and I. B. Rozhnin, Pis'ma Zh. Éksp. Teor. Fiz. **44**, 369 (1986) [JETP Lett. **44**, 472 (1986)].
8. Yu. G. Abov, V. V. Vasil'ev, V. V. Vladimirskiĭ, *et al.*, Preprint No. 37, ITÉF (Institute of Theoretical and Experimental Physics, Moscow, 1983).
9. R. Golub, Phys. Lett. A **72**, 387 (1979).
10. V. V. Vasil'ev, O. V. Shvedov, A. A. Dezhurnykh, *et al.*, Preprint No. 9, ITÉF (Institute of Theoretical and Experimental Physics, Moscow, 1995).
11. V. P. Il'in, *Numerical Methods for Solving Electric-Physics Problems* (Nauka, Moscow, 1985).
12. V. V. Vasil'ev, Preprint No. 67, ITÉF (Institute of Theoretical and Experimental Physics, Moscow, 1991).

13. P. A. Krupchitsky, *Fundamental Research with Polarized Slow Neutrons* (Énergoatomizdat, Moscow, 1985; Springer-Verlag, New York, 1987).
14. *Alpha-, Beta-, and Gamma-Ray Spectroscopy*, Ed. by K. Siegbahn (North-Holland, Amsterdam, 1965; Atomizdat, Moscow, 1969).
15. V. V. Apollonov and A. M. Prokhorov, Pis'ma Zh. Tekh. Fiz. **11**, 773 (1985) [Sov. Tech. Phys. Lett. **11**, 321 (1985)].
16. V. V. Vasil'ev, Yad. Fiz. **53**, 1586 (1991) [Sov. J. Nucl. Phys. **53**, 974 (1991)].
17. Particle Data Group, Eur. Phys. J. C **3**, 619 (1998).
18. B. G. Yerozolimsky, in *Collected Works* (Nauka, Leningrad, 1988), p. 3.
19. V. V. Vassiliev, Yad. Fiz. **61**, 2243 (1998) [Phys. At. Nucl. **61**, 2130 (1998)].
20. Yu. V. Gaponov, Usp. Fiz. Nauk **102**, 211 (1970) [Sov. Phys. Usp. **13**, 647 (1970)].
21. V. K. Grigor'ev, A. P. Grishin, V. V. Vladimirskiĭ, *et al.*, Yad. Fiz. **6**, 329 (1967) [Sov. J. Nucl. Phys. **6**, 239 (1967)].

Translated by A. Isaakyan

Physics of Atomic Nuclei, Vol. 63, No. 8, 2000, pp. 1315–1336. Translated from Yadernaya Fizika, Vol. 63, No. 8, 2000, pp. 1391–1412.

ON THE 85th ANNIVERSARY OF V.V. VLADIMIRSKY

Route to Islands of Stability of Superheavy Elements

Yu. Ts. Oganessian

Joint Institute for Nuclear Research, Dubna, Moscow oblast, 141980 Russia

Received January 19, 2000

Abstract—Problems concerning the existence of hypothetical superheavy elements for which theoretical nuclear models predict high stability with respect to various modes of radioactive decay are discussed. The synthesis of superheavy nuclei and the possibilities for performing experiments aimed at detecting rare events of their production and decay in heavy-ion beams are considered. Experimental results suggesting a considerable increase in the lifetime of nuclei as they approach the closed proton and neutron shells determining the islands of stability of superheavy elements are presented. © *2000 MAIK "Nauka/Interperiodica".*

1. PROLEGOMENA

Throughout 60 years since the discovery of the first man-made elements, neptunium and plutonium, investigations into the synthesis of new elements and into their properties have become one of the most important and rapidly developing realms in nuclear physics and chemistry.

A transition from conventional methods for producing man-made elements in continuous and pulsed neutron fluxes to methods employing heavy-ion reactions has made it possible to synthesize 12 elements heavier than fermium ($Z = 100$) to date.

In the mid-1960s, a theoretical description of the masses and fission barriers for new nuclei led to the prediction of islands of stability of heavy and superheavy nuclides near the closed proton and neutron shells. In the present article, experimental data demonstrating higher stability of nuclei near the $Z = 108$ and $N = 162$ deformed shells to various modes of radioactive decay, as well as reactions leading to the synthesis of these nuclei, are discussed from the viewpoint of advancements toward the as-yet-unexplored region of heavier (superheavy) and much more long-lived nuclides occurring near the $Z = 114$ and $N = 184$ spherical shells. The results of the first experiments devoted to the synthesis of superheavy nuclides formed in nuclear reactions induced by ^{48}Ca ions are presented. For various individual nuclei, the observed decay chains consisting of successive events of alpha decay and ending in spontaneous fission, as well as decay energies and times, are consistent with the predictions of theoretical models that describe the structure of heavy nuclei. These data furnish the first indication of the existence of a hypothetical region where superheavy elements are stable.

The experiments in question employed the heavy-ion accelerator installed at the Flerov Laboratory for Nuclear Reactions at the Joint Institute for Nuclear Research (JINR, Dubna, Russia). They were performed in collaboration with physicists from the Lawrence Livermore National Laboratory (Livermore, USA); Gesellschaft für Schwerionenforschungs Institut (GSI, Darmstadt, Germany); Riken (Saitama, Japan); Institute of Physics and Department of Physics, Comenius University (Bratislava, Slovak Republic); and Dipartimento di Fisica, Università di Messina (Messina, Italy).

2. INTRODUCTION

According to QED, the well-known concept of the atom as a system featuring a nucleus, which carries almost entirely the atomic mass, and electron orbits occurring at a large distance from the charge center is valid for very heavy atoms ($Z \leq 170$). In fact, however, the limit of existence of atoms (elements) is achieved much earlier because of instability of the nucleus itself.

Of approximately 2000 nuclear species known at the moment, only 287 nuclides have survived the time interval between the completion of nucleosynthesis and the present instant. It is well known that changes in the relationship between the number of protons and the number of neutrons in these nuclei generates beta decay. An excess of neutrons in a nucleus leads to the reduction of the neutron binding energy; the limit is achieved at $E_n = 0$ (neutron drip line). Similarly, zero proton binding energy, $E_p = 0$ (proton drip line), determines the boundary of existence of proton-excess nuclei.

Another boundary is associated with the maximal possible number of nucleons in the nucleus. Formally, the limiting mass of the nucleus near the boundary of its stability—even at the most favorable value of the proton-to-neutron ratio (nuclei having the highest binding energy and occurring on the beta-stability line)—is determined by the existence of the nucleus as a discrete unit in the case of a high probability of its splitting into parts of smaller mass. For the first time, this type of nuclear transformations, spontaneous fission (SF) of heavy nuclei, was observed for the ^{238}U isotope ($T_{SF} = 10^{16}$ yr) by Flerov and Petrzhak in 1940 [1]. By that

1063-7788/00/6308-1315$20.00

time, Hahn and Strassman had already discovered the induced fission of uranium. In order to describe this phenomenon, N. Bohr and Wheeler proposed the liquid-drop model of nuclear fission [2].

This beautiful theoretical model, which is essentially classical, is based on the assumption that nuclear matter is a macroscopic structureless (amorphous) body similar to a drop of charged liquid. A deformation of the drop due to Coulomb forces—eventually, this deformation leads to the fission of this drop into two parts of approximately identical masses—arises upon overcoming the potential barrier opposing nuclear deformations. For the ^{238}U nucleus, the height of the fission barrier is $B_f \approx 6$ MeV. With increasing Z, the height of the fission barrier decreases fast; as a result, the nucleus becomes absolutely unstable with respect to spontaneous fission ($T_{SF} \sim 10^{-19}$ s) at some critical value of the nuclear charge. According to the estimates of N. Bohr and Wheeler, this critical situation is realized as soon as the charge number reaches values of Z = 104–106. It is interesting to note that, much later, when the first transuranium elements were synthesized with the aid of high-flux reactors, the radioactive properties of the new nuclides confirmed qualitatively the liquid-drop analogy of nuclear matter: the probability of spontaneous fission in the nuclear chain from ^{238}U to ^{257}Fm (Z = 100) increased by more than 13 orders of magnitude.

The discovery of isomers that can undergo spontaneous fission [3] was unexpected insofar as it was at odds with the liquid-drop model. Presently, it has been proven that shape isomerism in 33 nuclei known by that time (isotopes of nuclei occurring between U and Cm) arises owing to a complicated shape of the potential-energy surface of nuclei—in particular, owing to the two-humped shape of their fission barrier. (The reader can find a comprehensive description of this phenomenon in the excellent review article of Bjornholm and Linn [4].) Yet another contradiction to the theory was revealed in considerable variations of partial half-lives with respect to spontaneous fission, which has the highest probabilities in the isotopes of Cf and Fm, as well as in the isotopes of transfermium elements formed in heavy-ion reactions [5]. A more detailed analysis of theoretical and experimental values of nuclear masses has shown that the deviations of the experimental nuclear binding energies from the theoretical ones behave quite regularly: they are maximal (highest binding energy) at specific magic numbers of protons and neutrons in a nucleus.

As a rule, shell effects are described by correction terms in nuclear-mass formulas used in practical calculations. A phenomenological description of shell anomalies in nuclear masses was given in the studies of Swiatecki [6a] and Swiatecki and Myers [6b]. Somewhat later (in 1967), Strutinsky [7] proposed an original and, in my opinion, very physical method for calculating the shell correction to the liquid-drop energy of the nucleus [7]. In his approach, the shell correction is defined as the difference of the sum of single-particle energies for the actual quantum distribution of nucleons and the energy for some uniform distribution of levels in the mean nuclear potential peculiar to a liquid drop. The total energy of the nucleus is represented as the sum $E_{tot} = E_{ld} + \Delta E_{shell}$, where E_{ld} is the macroscopic (liquid-drop) energy, while ΔE_{shell} is the microscopic correction taking into account shell effects and pair correlations of nucleons. Calculations performed within the macroscopic–microscopic model revealed regular shell phenomena in deformed nuclei. This made it possible to improve substantially the accuracy in determining their ground-state masses and shapes. In contrast to the widespread opinion that shell effects disappear with increasing nuclear deformation, it turned out that nucleon states are strongly rearranged in severely deformed nuclei. As the deformation becomes more pronounced, shell effects change, rather than disappear, still considerably correcting the potential energy of the nucleus [8].

Among the phenomena that were explained on the basis of the macroscopic–microscopic model, but which could not be reproduced by the calculations within the classical liquid-drop model, mention can be made of shape isomerism in the actinide nuclei, of the invariability of the heights of their fission barriers, and of sharp changes in the probability of fission near N = 152.

3. NUCLEAR SHELLS AND STABILITY OF HEAVY ELEMENTS

Like any theory, the model being discussed possessed some predictive power—for example, in dealing with very heavy, as-yet-unknown nuclei. Predictions on its basis were made in a number studies. Here, we present the results of Patyk and Sobiczewski [9] and Smolanczuk [10], who computed the masses of even–even nuclei with Z = 104–120 and N = 140–190 and the fission barriers for them.

Let us first dwell at some length on the probabilities of spontaneous fission of superheavy nuclei. The liquid-drop fission barrier is about 1 MeV for the ^{254}102 nucleus, but it is nearly zero for the heavier nucleus ^{270}108. At the same time, it can be seen from Fig. 1*a* that the amplitudes of the shell corrections for these nuclei are 5 and 7 MeV, respectively. Upon the inclusion of the shell correction in the calculation of the nuclear potential energy, the above nuclei develop fission barriers of height about 6–8 MeV. The emergence of the potential barrier upon the deformation of a heavy nucleus is expected to suppress severely spontaneous fission.

Indeed, it follows from the theoretical results displayed in Fig. 1*b* that the partial half-lives with respect to spontaneous fission depend greatly on the amplitude of the shell correction. A considerable growth of $T_{SF}(N)$ for nuclei that recede from the N = 152 shell, which

manifests itself clearly in the radioactive properties of the actinide nuclei, is associated with the effect of another neutron shell, that with $N = 162$. It should be noted that either shell is associated with deformed nuclei to be contrasted against well-known doubly magic nuclei of the ^{208}Pb ($Z = 82$, $N = 126$) type, whose ground-state shape is spherical. The highest stability with respect to spontaneous fission is expected of the ^{270}108 ($N = 162$) nucleus—the T_{SF} value predicted for this nuclide can be as large as a few hours. With increasing number of neutrons, the nuclear deformation becomes less pronounced because, in that case, we move away from the $N = 162$ shell, which is deformed, and because another closed spherical shell, that with $N = 184$, comes into play. For $N > 170$, it is natural to expect a significant growth of $T_{SF}(N)$ persisting up to the ^{292}108 ($N = 184$) nucleus, whose partial half-life with respect to spontaneous fission is $T_{SF} \sim 3 \times 10^4$ yr, an enormous value indeed.

Here, there arises an interesting situation. If superheavy nuclei possess high stability with respect to spontaneous fission, they will decay through other modes, such as alpha decay and, possibly, beta decay. The probabilities of these decay modes and, hence, the corresponding lifetimes will be determined by the ground-state nuclear masses, which can be computed within theoretical models based on various assumptions about the fundamental properties of nuclear matter (nature of nuclear forces). Under such conditions, experimental results are of paramount importance for testing theoretical models. If we follow the calculations of Smolanczuk and Sobiczewski, who relied on the macroscopic–microscopic model, the deformed nucleus ^{268}106 ($N = 162$) will undergo alpha decay with a half-life of $T_\alpha \approx 2$ h (according to the calculations of Möller and Nix [11], this half-life amounts to a few days). For the heavier spherical nucleus ^{294}110 ($N = 184$), T_α becomes as large as a few hundred—or, maybe, a few thousand—years (Fig. 1*b*). Recall that, in the absence of nuclear structure (that is, in the liquid-drop model), this nuclear species would undergo spontaneous fission within a time of $T_{SF} < 10^{-19}$ s. The above two values differ by more than 30 orders of magnitude!

Other calculations of the energy of a nuclear system treated as a many-body ensemble that were performed on the basis of the Hartree–Fock–Bogolyubov model with various options for interparticle forces, as well as relativistic calculations in a self-consistent mean nuclear field, also indicate that the binding energy of a nucleus increases as it approaches the $N = 184$ shell.

Among theorists, there is presently no consensus on what the magic number of protons at $N = 184$ is at which the binding energy of a spherical doubly magic nucleus takes a maximum value. Within the macroscopic–microscopic model, the amplitude of the shell correction is maximal for the ^{298}114 ($N = 184$) nucleus [12, 13], irrespective of the values chosen for the parameters involved. On the contrary, the calculations

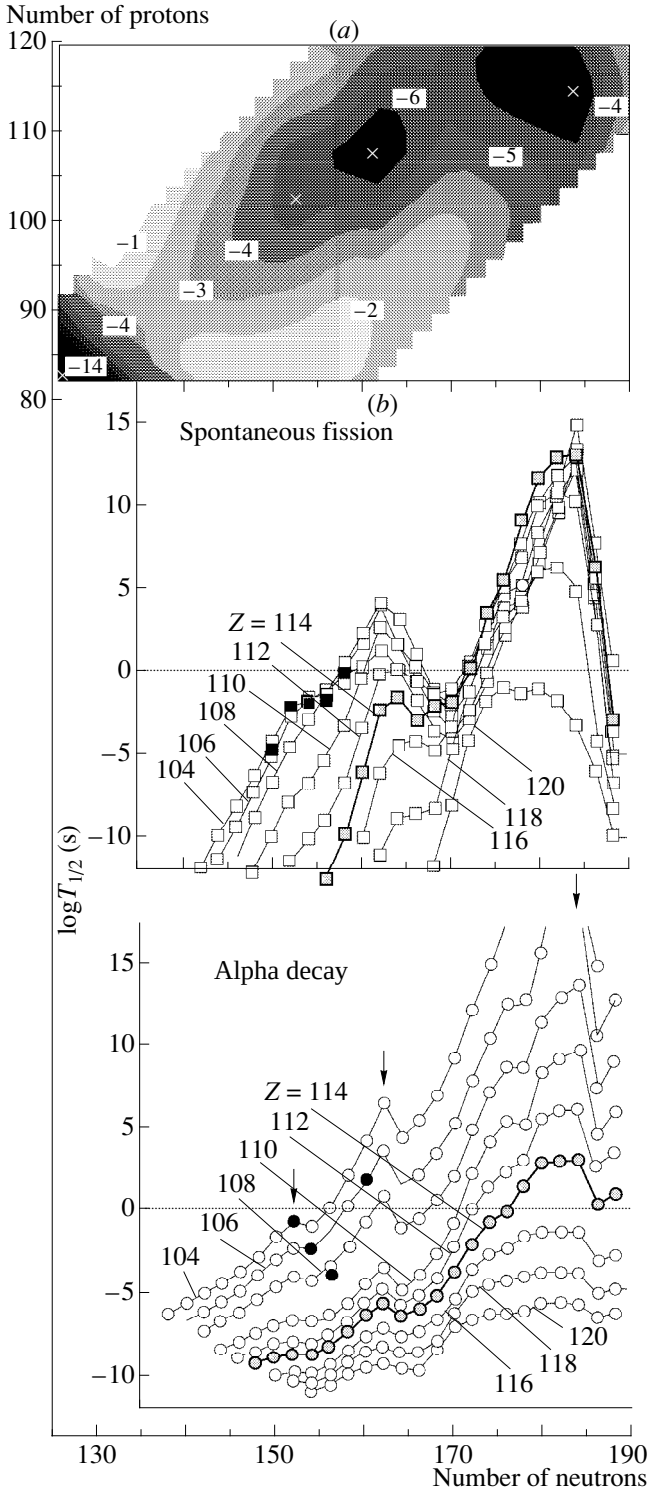

Fig. 1. (*a*) Chart of shell corrections (in MeV) to the liquid-drop nuclear potential energy. (*b*) Partial half-lives (with respect to alpha decay and spontaneous fission) of even–even isotopes containing various numbers of neutrons (the atomic numbers of the elements are indicated on the curves; thick solid curve connects the $Z = 114$ isotopes): (open circles) results of the calculations from [10] and (closed circles) experimental values.

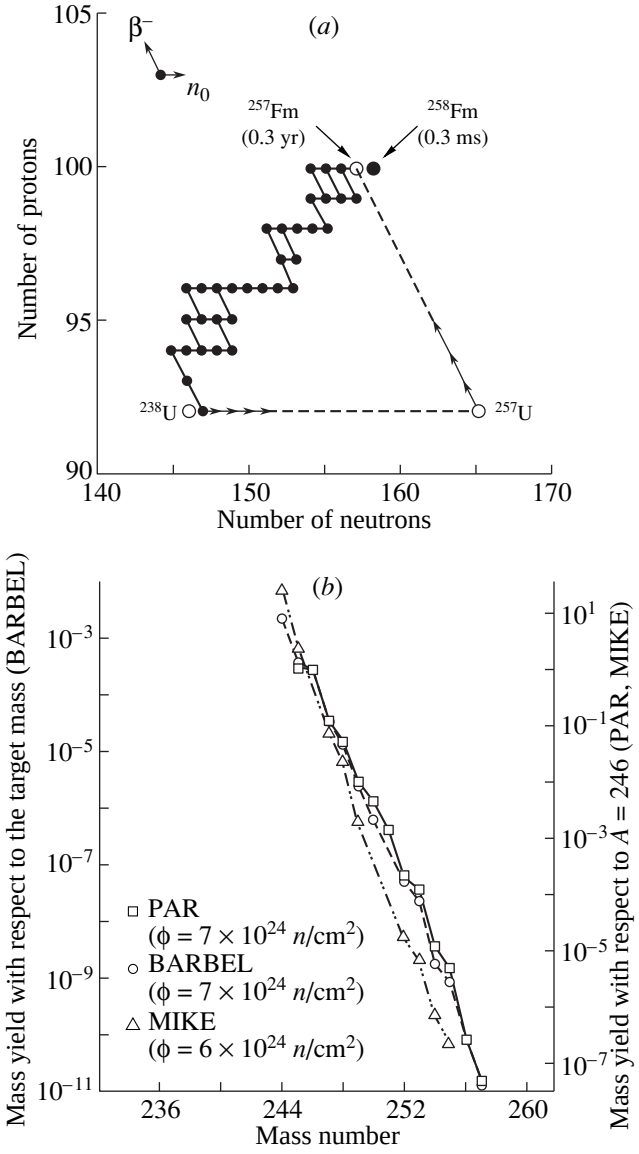

Fig. 2. (*a*) Scheme for producing transuranium elements via successive neutron-capture events in reactors and nuclear explosions. (*b*) Heavy-mass yields in pulsed high-density neutron fluxes from nuclear explosions (the fluences achieved in various experiments are indicated parenthetically).

within the Hartree–Fock–Bogolyubov method indicate, in addition to $Z = 114$, some other possible candidates—$Z = 120$, 122, 126, and even 138—depending on the choice of model parameters [14]. This does not change, however, the basic conclusion that, in the region of very heavy nuclei, there can arise stability islands significantly extending the limits within which superheavy elements may exist.

4. SYNTHESIS REACTIONS

It is well known that the first man-made elements heavier than uranium were synthesized in the reactions of successive neutron captures during long-term exposures at high-flux nuclear reactors. The large lifetimes of new nuclides made it possible to separate and identify them by radiochemical methods followed by the measurements of their radioactive-decay properties. These pioneering studies performed by Professor Seaborg and his colleagues between 1940 and 1953 at the Lawrence Berkeley National Laboratory (for an overview, see, for example, [15]) resulted in the discovery of eight man-made elements with $Z = 93$–100, that of the largest mass being ^{257}Fm ($T_{1/2} \sim 100$ d). A further advancement toward the region of heavier nuclei was hindered by the extremely small lifetime of ^{258}Fm ($T_{SF} = 0.3$ ms). Attempts at overcoming this barrier in pulsed high-intensity neutron fluxes from underground nuclear explosions did not produce anything beyond ^{257}Fm (see Fig. 2).

Transfermium elements with masses $A > 257$ were produced in heavy-ion reactions. In relation to what was achieved within the method based on successive neutron captures, heavy-ion reactions are advantageous in that the entire projectile mass is introduced in the target nucleus in the case of fusion with a heavy particle.

The excitation energy of the compound nucleus is given by

$$E_x = E_P - [M_{CN} - (M_T + M_P)] = E_P - Q,$$

where E_P is the projectile energy, while M_{CN}, M_T, and M_P are the masses of the compound nucleus, the target nucleus, and the projectile ion, respectively. The minimal excitation energy will correspond to the threshold energy for the fusion reaction; for a first approximation, the latter in turn is associated with the Coulomb barrier: $E_x^{min} = B_c - Q$. For heavy target nuclei, we have $B_c \sim$ 5 MeV/nucleon.

In contrast to (n, γ) reactions, where the excitation energy of the nucleus is 6–8 MeV, even a fusion process featuring the extremely light nucleus of ^{4}He is characterized by $E_x^{min} \approx 20$ MeV. With increasing projectile-ion mass, the excitation energy of the compound nucleus will increase owing to the growth of the Coulomb barrier. A deexcitation of a hot nucleus to the ground state ($E_x = 0$) will proceed predominantly through the emission of neutrons and gamma rays. The cross section for product formation upon the evaporation of neutrons can be represented as

$$\sigma_{xn}(E_x) = \sigma_{CN}(E_x) P_{xn} \prod_{i=1}^{x} \left[\frac{\Gamma_n}{\Gamma_{tot}}(E_x)\right]_i,$$

where $\sigma_{CN}(E_x)$ is the cross section for the production of a compound nucleus with energy E_x, P_{xn} is the probability of its deexcitation (cooling) via neutron emission, and Γ_n/Γ_{tot} is the ratio of the width (probability) with respect to neutron emission to the total decay width at each step of successive neutron-emission events.

The ratio Γ_n/Γ_{tot} can be computed within statistical theory under certain assumptions on the thermodynamic properties of a hot nucleus. The quantity $\sigma_{xn}(E_x)$, which characterizes the survival ability of evaporation products decreases fast with increasing E_x (this is equivalent to an increase in the number of neutron-evaporation cascades). The situation is aggravated by the fact that the shell-correction amplitude, which suppresses the fission of a nucleus in the ground state, decreases fast with increasing excitation energy of the nucleus. Both of these factors lead to an extremely small survival probability for heavy compound nuclei.

In relation to (n, γ) reactions that lead to the formation of actinide nuclei and which are characterized by cross sections on the order of 10^1 or 10^2 b, the cross sections for the formation of nuclei in heavy-ion reactions are as small as 10^{-6}–10^{-4} b, exponentially decreasing as we move further into the region of heavier elements (see Fig. 3). Despite so strong a decrease in the yields of required nuclei, heavy-ion fusion reactions are, however, the only efficient way to synthesize transfermium elements ($Z > 100$). Since the relevant cross section is maximal at the lowest value of E_x^{min}, the most asymmetric reactions, which correspond to the lowest Coulomb barrier, are preferable.

This circumstance played a decisive role over the next 25-year period of synthesis of new elements. A great deal of effort went into producing, at high-flux reactors, sizable amounts of heavy isotopes of transuranium elements from Pu to Fm. They were used as a target material for obtaining new elements at heavy-ion accelerators. The work along these lines that was performed at the Lawrence Berkeley National Laboratory and at the Flerov Laboratory for Nuclear Reactions at JINR resulted in the discovery of additional six new elements with $Z = 101$–106. Apart from this, many new isotopes of already known elements with $Z = 92$–100 were synthesized in heavy-ion reactions far away from the beta-stability line.

As was indicated above and as will be explained below in greater detail, the properties of new nuclides changed substantially our ideas of stability of heavy nuclei and contributed substantially to the development of theoretical concepts in determining the boundaries of the existence of elements. Unfortunately, the low survival ability of highly heated heavy nuclei and difficulties associated with the production of a target material in high-flux reactors constrain severely the potential of the above reactions in the synthesis of $Z > 106$ elements.

Below, we consider, however, some special features of the fusion of complex nuclei.

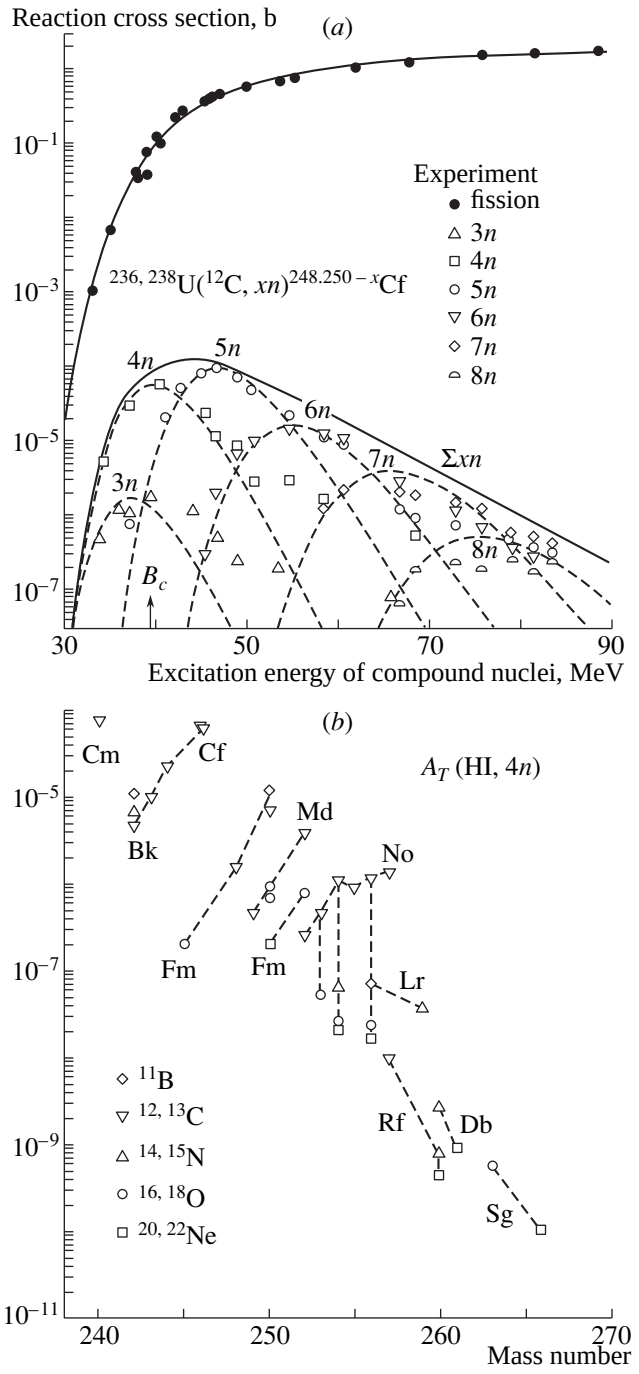

Fig. 3. (*a*) Cross sections for the formation of Cf ($Z = 98$) compound nuclei with various excitation energies in reactions induced by ^{12}C (closed circles) and cross sections for the formation of neutron-evaporation products in the same reactions (open circles). Data from [16] are used in this figure. (*b*) Cross sections for the formation of $Z = 96$–106 isotopes at the peak of the $4n$-evaporation channel of the reactions induced by various heavy ions (HI) whose masses are indicated in the figure.

5. COLD FUSION OF MASSIVE NUCLEI

As the projectile-ion mass is increased, the minimal excitation energy of the compound nucleus, $E_x^{min} = B_c - Q$, grows up to a certain limit (see Fig. 4*a*). A further increase in the projectile-ion mass (and the corresponding decrease in the target nucleus mass) would result in the reduction of the excitation energy E_x because of a

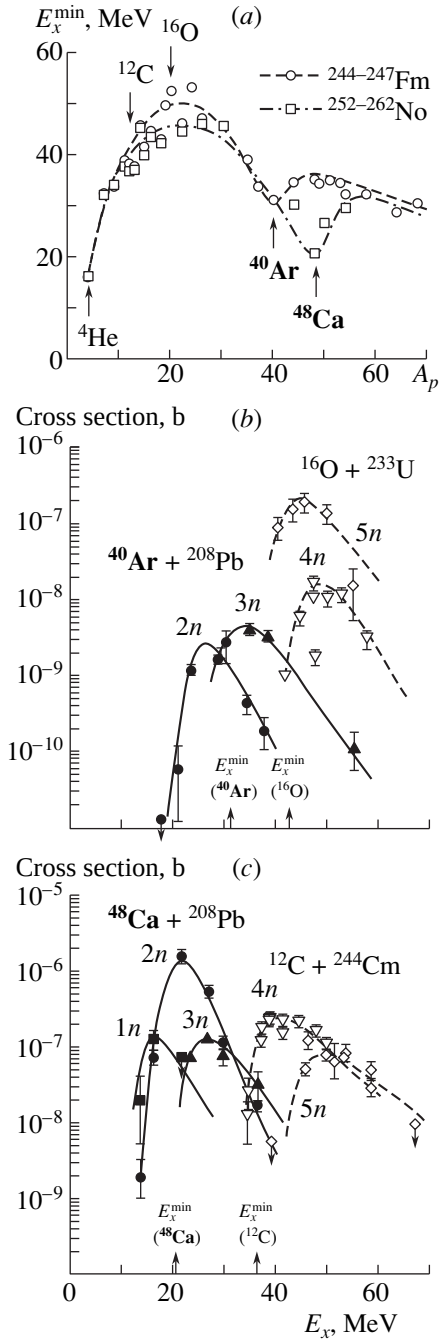

Fig. 4. (*a*) Minimal values of the excitation energies of Fm and No compound nuclei formed in fusion reactions induced by ions of various masses. (*b*) Cross sections for the formation of Fm isotopes versus the excitation energy E_x of compound nuclei originating from reactions induced by ^{16}O and ^{40}Ar ions. (*c*) Cross sections for the formation of No isotopes versus the excitation energy E_x of compound nuclei originating from reactions induced by ^{12}C and ^{48}Ca ions. The arrows indicate the nuclear excitation energies that correspond to the Coulomb barrier.

sizable increase in Q for symmetric reactions. The greatest effect is achieved with targets from doubly magic nuclei ^{208}Pb, for which the mass defect and, hence, the Q value are maximal. A similar effect must be observed in synthesizing Fm isotopes in ^{40}Ar + ^{208}Pb interactions, provided that the fusion of such heavy nuclei is feasible. This reaction was chosen in 1973 by the present author [17] in order to verify the idea being discussed.

The cross sections for the production of Fm isotopes in ^{40}Ar + ^{208}Pb interactions are shown in Fig. 4*b*, along with the experimental results of Nurmia *et al.* [18] for the same product nuclei originating from the more asymmetric interactions between ^{16}O and ^{233}U nuclei. From the displayed data, it follows that the maximum yield of Fm isotopes from ^{40}Ar + ^{208}Pb interactions corresponds to the emission of only two or three neutrons from the compound nucleus ^{248}Fm (E_x^{min} = 30 MeV). As to ^{16}O + ^{233}U interactions, which involve a lighter projectile, final nuclei are formed as the result of the evaporation of four or five neutrons from the compound nucleus ^{249}Fm (E_x^{min} = 45 MeV).

Paradoxical though it may seem, the cross section for the formation of evaporation products in interactions of the HI + ^{208}Pb type must increase with increasing mass of the projectile ion, provided that the reaction mechanism and, in particular, the probability of the fusion of such complex nuclei remain unchanged. The largest cross section (the lowest excitation energy E_x^{min}) corresponds to the case where the target and the projectile are both magic nuclei. Indeed, the cross section for the production of the heavier isotopes of No (Z = 102) in ^{48}Ca + ^{208}Pb interactions (E_x^{min} = 20 MeV) proved to be one order of magnitude larger than the cross section for the production of Fm isotopes [19]. The data in Fig. 4*c* reveal that the channel featuring the emission of only one neutron is realized here with a sizable cross section. In further experiments performed at GSI, it was shown that, when heavier projectiles up to ^{70}Zn are used, the excitation energy of the compound nucleus decreases—as might have been expected—so that the one-neutron-emission channel proves to be dominant in the production of very heavy nuclei [20].

Thus, we can see that, while, in thermal-neutron capture by a ^{235}U nucleus, an excitation energy of $E_x \sim$ 6 MeV is introduced in a compound system, in the fusion of a ^{208}Pb target nucleus with an ion of mass 50–70 amu, the emerging compound nucleus has an excitation energy of only 10–15 MeV! In order to distinguish such reactions from asymmetric hot-fusion reactions that were used previously and which result in the formation of hotter nuclei, the former are referred to as cold-fusion reactions.

Cold-fusion reactions changed substantially the state of affairs in the problem of synthesizing new elements. Since stable isotopes, $^{204–208}$Pb or ^{209}Bi, are used here for a target material, experimental studies in these realms have become accessible to many research

groups. At this stage, it has been advances in accelerator technologies for obtaining intense beams of $A > 40$ ions that have determined the sensitivity of the relevant experiments. At the same time, compound nuclei originating from the fusion of ^{208}Pb nuclei with the nuclei of the heaviest stable isotopes used for projectiles display large neutron deficiency. By virtue of this, eventual evaporation products are offset from the beta-stability line by 10–15 amu; this is the reason why their half-lives decrease considerably.

The two factors underlying the method of cold fusion—the production of intense beams of $A \geq 50$ heavy ions and the need for express procedures to separate and detect new nuclear species ($T_{1/2} \geq 1$ μs)—changed significantly the implementation of experiments devoted to synthesizing new elements.

A successful solution to the problem was found in 1975 at GSI. This solution involved developing the new-generation heavy-ion accelerator UNILAC and the SHIP facility, which permits an in-flight separation ($t \sim 10$ μs) of atoms of new elements from the heavy background of side products from incomplete-fusion reactions. The six heaviest elements with $Z = 107$–112 were synthesized in the cold fusion of ^{208}Pb and ^{209}Bi nuclei with ions from ^{54}Cr to ^{70}Zn. The relevant experiments and analyses of the results deduced from those experiments are comprehensively described in the review articles of Armbruster [21], Münzenberg [22], and Hofmann [23], which cover the 20-year period of work along these lines.

In cold-fusion reactions on targets from the same nuclear species of ^{208}Pb or ^{209}Bi, the increase in the atomic number and the mass of evaporation products of compound nuclei is determined exclusively by the projectile charge and mass. From experimental data, it follows that the cross section for the formation of nuclei of new elements decreases considerably with increasing atomic number of these nuclei (see Fig. 5). As was shown for the first time in [24], similar effects are due to a dynamical suppression of fusion because of an increase in Coulomb repulsive force when more symmetric combinations of the masses and charges of interacting nuclei are used. Here, two factors that determine the cross section for the formation of evaporation products oppose each other: with increasing projectile mass, the survival of compound nuclei increases by virtue of a decrease in $E_x^{\min}$, whereas the probability of compound-nucleus formation decreases fast.

Prior to addressing the problem of synthesizing spherical superheavy nuclei, it is advisable to summarize the above discussion.

Reactions where beta-stable and neutron-excess nuclei are formed via successive slow-neutron captures cannot yield masses in excess of $A = 257$. In heavy-ion reactions, there are no similar limitations at a fundamental level. However, the cross sections for the formation of new elements decrease exponentially with

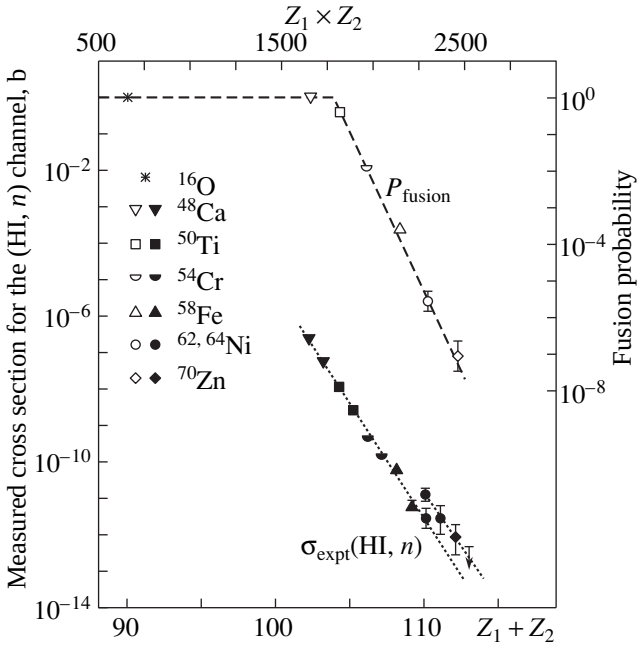

Fig. 5. Cross section for the formation of $Z = 102$–112 isotopes in the cold fusion of ^{208}Pb and ^{209}Bi with ions of various masses (which are indicated in the figure): (closed symbols) experimental values (left scale) for the reaction channel involving the evaporation of one neutron and (open symbols) probabilities of the fusion of various ion species with ^{208}Pb nuclei (right scale) as rescaled from experimental cross sections.

increasing atomic number both in hot-fusion and in cold-fusion reactions. The reasons behind this are different in the two cases: while, in hot-fusion reactions, losses stem from the low survival of evaporation products, in cold-fusion reactions, this is due to the low-probability of compound-nucleus formation.

6. SEARCHES FOR A COMPROMISE

In a similar situation, it is reasonable to seek a compromising solution and impose, in addition, the condition requiring that evaporation products possess a maximal neutron excess. It should be noted that no versions of fusion of stable or even long-lived isotopes can lead to nuclei on top of the stability island with $Z = 114$ and $N = 184$. One may only hope to approach the boundaries of this unknown region so closely as to enter the area affected by the $N = 184$ spherical shell. But even this possibility is highly questionable.

From the data presented in Fig. 1, it follows that, in the transition region between deformed and spherical shells, nuclei become significantly less stable. This is due primarily to changes in the ground-state nuclear masses and shapes and in the structure of the corresponding fission barriers. Only for $N \geq 170$ does there arise a stable spherical configuration—as follows from macroscopic–microscopic calculations, a stabilizing effect of the $N = 184$ spherical shell must already come

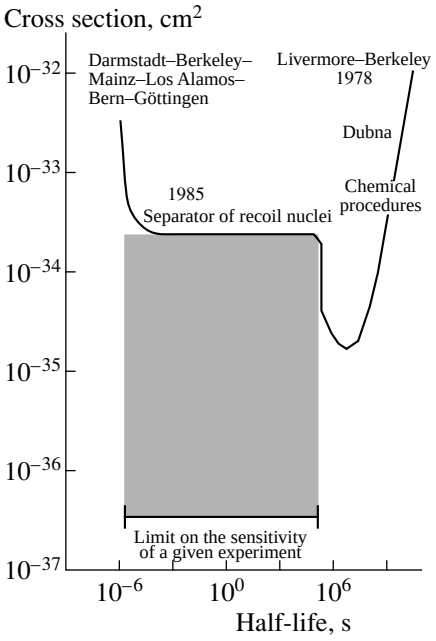

Fig. 6. Limits on the cross sections for the formation of isotopes of the $Z = 116$ element in $^{48}Ca + ^{248}Cm$ interactions according to data from various experiments (solid curve). The lower horizontal curve corresponds to the limiting sensitivity achieved to date.

into play in this region. Nuclides with so high a neutron deficit can in principle be obtained by using heavy actinide isotopes with $Z = 94$–98 for a target material and nuclei of the rare isotope ^{48}Ca for projectiles.

A compromising solution here consists in that, while abandoning the idea of using magic target nuclei upon going over from ^{208}Pb to neutron-excess isotopes of actinide elements, we regain magicity in a projectile ion.

Because of a considerable mass defect in the doubly magic nucleus ^{48}Ca, the excitation energy of the compound nucleus above the Coulomb barrier is about 30 MeV. The cooling of the nucleus occurs via the emission of three neutrons and gamma rays. It can be expected that, at this excitation energy, shell effects are still noticeable in a hot nucleus, in which case the probability of survival of evaporation products must be larger than the analogous probabilities in hot-fusion reactions ($E_x \geq 50$ MeV). At the same time, the asymmetry of nuclear masses in the input channel ($Z_1 \times Z_2 \leq 2000$) must reduce a dynamical suppression of the fusion of the nuclei being considered and, hence, increase the cross section for compound-nucleus formation in relation to that in the case of cold fusion.

Despite these obvious advantages, all the preceding attempts made between 1977 and 1985 at various laboratories [25–27] to synthesize new elements yielded only upper limits on the cross sections for the formation of superheavy elements (see Fig. 6). At the same time, progress in experimental techniques over recent years and the possibility of obtaining intense beams of ^{48}Ca ions at new-generation heavy-ion accelerators make it possible improve the sensitivity of relevant experiments by two orders of magnitude. We have therefore chosen this way to advance toward the region of stability of superheavy elements.

7. STRATEGIES OF EXPERIMENTS AND EXPERIMENTAL EQUIPMENT

The strategy of experiments aimed at the synthesis of superheavy elements is determined to a considerable extent by their radioactive properties and, above all, by the lifetimes of the elements to be synthesized. As was indicated above, these lifetimes can vary within broad limits, their specific values being dependent on whether theoretical predictions concerning the effect of nuclear shells on the stability of heavy nuclides with various values of Z and N are in fact true. Because of this, the operation of the experimental facility to be used must be extremely fast. At the same time, neutron-evaporation products, whose yield is very small, must be separated within a short period of time from a formidable background of reaction by-products whose formation probability is higher by eight to ten orders of magnitude. These conditions can be satisfied in the case of in-flight product separation (within a time interval of duration 10^{-6}–10^{-5} s), allowances for the kinematical features of various reaction channels being required here.

It should be noted that, in a fusion reaction leading to compound-nucleus formation, the projectile momentum is fully transferred to the compound system; as a result, the energy of recoil nuclei and the direction of their motion are well defined. Therefore, the problem amounts to sorting recoil atoms, which are emitted in the narrow angular interval $\theta_L = 0° \pm 2.5°$ with respect to the beam direction, according to their velocities (or energies). This function is performed by Wien velocity filters (SHIP separator at GSI) [28] or by an energy filter (VASSILISSA separator at JINR) [29], where reaction products are separated according to electric rigidities in transverse electric fields (see Fig. 7*a*). As a matter of fact, the same functions are fulfilled by facilities of a different type—gas-filled separators, where recoil nuclei are separated by magnetic rigidities in a hydrogen or a helium gas medium at a pressure of about 1 torr [30] (see Fig. 7*b*).

Upon escaping from the target, recoil and beam nuclei moving in a vacuum have identical momenta and close charges; for this reason, it is impossible to separate them by magnetic rigidities. However, they possess different electric rigidities because of distinctions between their kinetic energies and can therefore be separated while propagating in a transverse electric field. The pattern of motion in a gas medium is totally different. Within N. Bohr's theory, it can be shown that, upon undergoing multiple collisions, an atom moving in such a medium acquires the equilibrium charge [31]

$$\bar{q} \sim (v/v_B)Z^{1/3},$$

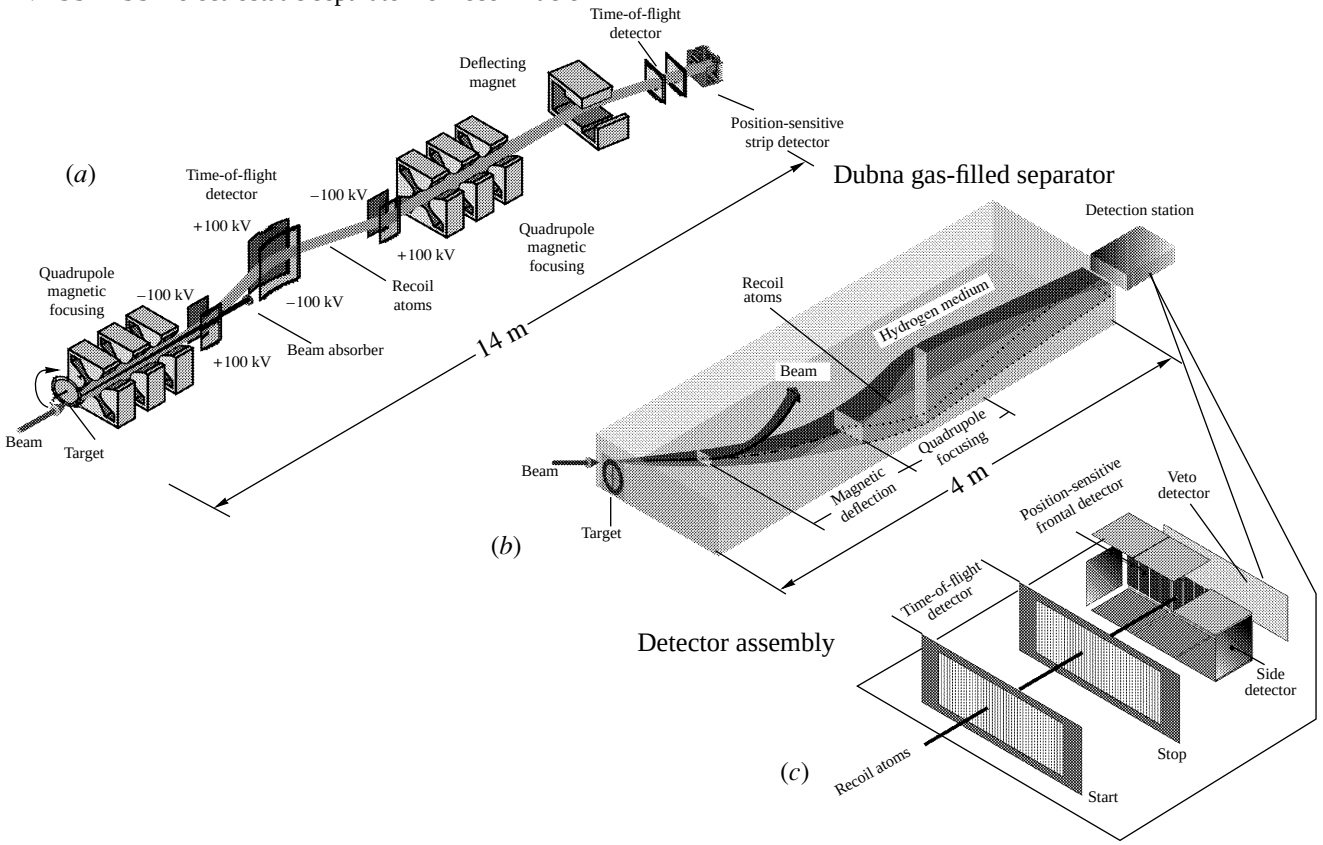

Fig. 7. Layout of kinetic separators used for recoil nuclei in experiments performed at the Flerov Laboratory for Nuclear Reactions to synthesize new elements: (*a*) VASSILISSA separator, (*b*) gas-filled separator, and (*c*) detector region used to record recoil nuclei and their decays.

where Z is the atomic number of the ion being considered.

Since the heavy recoil nucleus and the projectile ion move at different velocities, their equilibrium charges differ significantly from each other. The most pronounced effect is observed at low recoil-atom velocities close to the Bohr velocity ($v_B = 2.19 \times 10^8$ cm/s). In this case, evaporation products can be separated from beam ions and other nuclei owing to a high magnetic rigidity of recoil atoms.

The efficiency of kinematical separators depends on the ratio of the masses of interacting nuclei. This efficiency is only a few percent for fusion reactions featuring relatively light projectile ions ($A_p \leq 20$), but it becomes as high as 30–50% for projectile ions with mass numbers not less than 40. The facilities used also possess a high selectivity: in the focal plane of the separators, the background from the primary ion beam is removed almost completely, and the yield of products from incomplete-fusion reactions is suppressed by four to seven orders of magnitude, specific values of the suppression factor being dependent on the kinematical features of various channels resulting in the formation of these products. This is, however, insufficient for identifying extremely rare cases of the production of atoms of new elements. For this reason, a further selection of sought nuclei is accomplished with the aid of a complicated detecting device that is shown schematically in Fig. 7*c*.

Recoil atoms that have reached a focal plane are implanted into a multistrip semiconducting silicon detector of area about 40–50 cm^2. The length and the width of the strips, as well as their number, are determined by the image of the object in the focal plane of the separator. The facilities displayed in Fig. 7 employ 12 and 16 strips of lengths 40 and 60 mm, respectively. Each strip possesses a longitudinal position sensitivity. The position resolution of each strip is determined experimentally. This is achieved by choosing reactions where known recoil atoms undergo successive alpha decays or spontaneous fission. The position resolution depends on the type of the recorded particle (recoil nuclei, alpha particles, or spontaneous-fission fragments). However, more than 95% of all charged particles accompanying the decay of the implanted object are resolved, as a rule, within the range $\Delta_x \sim 2$ mm.

Thus, the entire area of the frontal detector is effectively partitioned into approximately 500–1000 indi-

vidual cells, each carrying information about the time of arrival of recoil nuclei and about their energies, as well as about the time of subsequent decays accompanied by a change in their spectral properties. The frontal detector is surrounded by side detectors in such a way that the entire apparatus represents a well with an open front wall. This increases the efficiency of detection of particles from the decay of an implanted nucleus (alpha particles or fragments) up to 85–87%. In order to separate signals associated with the recoil nucleus from those that are associated with particles from its decay, a time-of-flight (TOF) detector recording the velocity of implanted nuclei is arranged in front of the frontal detector. The background conditions are substantially improved by an event selection according to the chains of radioactive decay of these nuclei. A parent nucleus implanted in the detector can be reliably identified if the chain of its successive alpha or beta decays leads to nuclides with known properties. This method was used successfully in experiments devoted to the synthesis of the $Z = 107$–112 new elements whose isotopes possess a modest neutron excess ($N - Z \leq 53$). As we advance further into the region of spherical nuclei with a greater neutron excess, the above advantage is lost. Here, the decay of a parent nucleus leads to the formation of unknown isotopes, whose properties can only be predicted within a theoretical accuracy.

At the same time, we can state that, if the basic theoretical prediction that there exists the island of stability of superheavy elements is valid, the daughter nuclei recede ever further from closed shells within any chain of successive alpha or beta decays. This must lead to a considerable increase in the probability of their spontaneous fission in relation to other decay modes. Eventually, the decay chains would end in the formation of spontaneously fissile nuclei. In principle, such a decay pattern is compelling evidence for the formation of a superheavy nucleus. In the methodological aspect, such an event differs substantially from those of other possible correlated decays. Upon the emergence of a signal indicating the arrival of an implanted nucleus at a certain point of the frontal detector, with the time of its flight being measured in the TOF detector, signals from the emission of alpha particles with an amplitude corresponding to their energies of about 8.5–10 MeV will arise, without a TOF attribute, in the same position window in definite time intervals. After that, a large-amplitude signal from spontaneous-fission fragments with total kinetic energy TKE of about 200 MeV will be recorded.

8. STABILIZATION OF DEFORMED NUCLEI NEAR $Z = 108$ AND $N = 162$ CLOSED SHELL

The synthesis of nuclides in this region and investigation of their properties provide a direct test of theoretical ideas of the role of shells in nuclei where there is virtually no liquid-drop fission barrier. Of greatest interest in this respect are isotopes of the element with charge number $Z = 106$.

According to the macroscopic–microscopic calculations of Patyk and Sobiczewski [9], the $Z = 106$ even–even nuclides have commensurate partial half-lives with respect alpha decay and spontaneous fission over a wide mass interval, the corresponding numbers of neutrons at the ends of this interval being $N = 152$ and $N = 164$. Irrespective of the decay type, an increase in the number of neutrons must stabilize nuclei to a considerable extent because of the growth of the shell-correction amplitude (see Fig. 8*b*). At the same time, the calculations of Möller and Nix [32], who considered the same nuclei within the same model, but who used somewhat different parameter values, led to a totally different pattern. It should be noted that either calculation describes well the decay properties of the ^{260}Sg ($Z = 106$, $N = 154$) nucleus, for which experimental data yield $T_\alpha \approx T_{SF}$ [33, 34]. According to [32], however, the half-lives T_α and T_{SF} begin to diverge strongly with increasing number of neutrons in the region $N > 152$: as we approach the $N = 162$ shell, the half-life with respect to alpha decay, T_α, increases, as might have been expected, while the half-life with respect to spontaneous fission, T_{SF}, decreases significantly.

This effect results from a considerable change suffered by the deformation energy of a nucleus as its nascent fission fragments approach the $Z = 50$ and $N = 82$ closed shells. It was shown in [35, 36] that a new fission channel (mode) associated with the shortest path for the collective motion of a nucleus from the ground state to the point of scission into two fragments of approximately equal masses opens up in this case. It can be assumed with a great degree of confidence that, within a short period of time, the hypothetical nucleus ^{264}Fm will undergo strictly symmetric fission into two doubly magic nuclear fragments (^{132}Sn). In the experiments of Hulet *et al.* [37], it was shown that this phenomenon is observed even in the spontaneous fission of the $N = 158$–160 heavy isotopes of Fm, Md, and No. In the probabilities of the spontaneous fission of heavy nuclei, it is in Fm isotopes where this effect manifests itself in the most spectacular way: as we go over from ^{256}Fm ($T_{SF} = 2.9$ h) to ^{258}Fm ($T_{SF} = 0.3$ ms), the half-life changes by a factor of 3×10^7.

For the problem being considered, this circumstance is of paramount importance. If stability with respect to spontaneous fission is expected to be higher near $Z = 108$ and $N = 162$, the ^{266}Sg isotope must have a half-life of a few tens of seconds. Otherwise, this nucleus would undergo spontaneous fission with a half-life of $T_{SF} \sim 10^{-4}$ s; here, the distinction between the T_{SF} values is five orders of magnitude or even greater. In this situation, an experimental determination of the decay properties of heavy isotopes of the $Z = 106$ element could provide a direct criterion for testing various computational procedures, the results that these procedures yield being depicted in Fig. 8*b*.

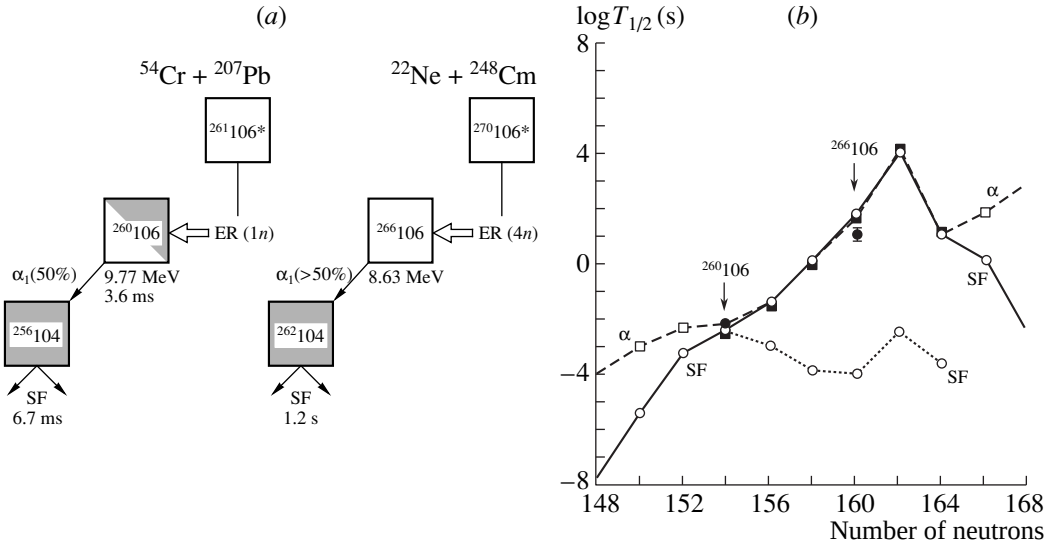

Fig. 8. (*a*) Chains of the successive decays of the $N = 154$ and $N = 160$ isotopes of the $Z = 106$ element that are synthesized in ^{54}Cr + ^{207}Pb and ^{22}Ne + ^{248}Cm interactions. (*b*) Experimental (closed boxes and circles) and calculated half-lives (with respect to alpha decay and spontaneous fission) of Sg isotopes ($Z = 106$). The solid and dashed curves represent the results of the calculations from [9], while the dotted curve depicts the data from [32], which suggest the fast fission mode.

With the aim of synthesizing heavy isotopes with $Z = 106$, we decided to explore ^{22}Ne + ^{248}Cm interactions at a beam energy in the vicinity of the Coulomb barrier, in which case it is natural to expect a maximum cross section for isotope production in reaction channels involving the evaporation of four or five neutrons. In an experiment where a ^{248}Cm target was exposed to a beam of ^{22}Ne ions for 360 h, so that the total dose of irradiation was about 1.6×10^{19}, two isotopes of $Z = 106$ elements with mass numbers 265 and 266 were singled out with the aid of a gas-filled separator [38]. Each of the two nuclear species, ^{265}Sg ($N = 159$) and ^{266}Sg ($N = 160$), undergoes predominantly alpha decay. The energy of the alpha decay of the even–even nuclide ^{266}Sg ($Q_\alpha = 8.76$ MeV) determines its half-life ($T_{1/2} = 20 \pm 10$ s). The chains of the decay of the $N = 152$ and $N = 160$ even–even isotopes of the $Z = 106$ element are displayed in Fig. 8*a*. On the basis of six alpha–SF correlations observed in the decay of the ^{266}Sg nucleus, it was possible to determine the half-life of the daughter nucleus—^{262}Rf ($Z = 104$, $N = 158$) isotope. It undergoes spontaneous fission with a half-life of $T_{SF} \simeq 1.2$ s.

The radioactive properties of the new nuclides indicate that, as these nuclides approach the $Z = 108$ and $N = 162$ closed shells, they become more stable with respect to spontaneous fission (see Fig. 8*b*). Indeed, the quantity T_{SF} grows by more than three orders of magnitude when the number of neutrons in the isotopes of the $Z = 106$ element is changed by six units. At the same time, a transition from ^{258}No ($T_{SF} = 1.2$ ms) through ^{262}Rf to ^{266}Sg (addition of four protons) increases T_{SF} by more than four orders of magnitude. The data obtained in the aforementioned experiments are in qualitative agreement with the results of the macroscopic–microscopic calculations performed by Patyk and Sobiczewski [9]. From the experimental data, it follows that the spontaneous fission of the ^{266}Sg nucleus via the mode that corresponds to a short path of tunneling through the fission barrier is severely suppressed, the suppression factor being greater than 10^4.

On the basis of data obtained for $Z = 106$ nuclei, it can be assumed that, for still heavier nuclides (those with $Z > 106$), fission modes are also unlikely to require revising the optimistic theoretical prediction that there exists a wide region where superheavy nuclei are stable. The $Z = 106$ nuclides are expected to undergo predominantly alpha decay as long as the shell corrections in the deformation energy hinder their spontaneous fission. These conclusions are confirmed by the experiments performed at GSI, where many new alpha-radioactive isotopes with charge numbers up to $Z = 112$ were synthesized and studied. To the same extent, this is true for the heaviest isotopes with $Z = 106$–110 that were obtained in hot-fusion reactions at the Flerov Laboratory for Nuclear Reactions (JINR, Dubna) [38–40].

Changes in the number of neutrons across the $N = 162$ closed neutron shell are expected to produce very specific effects. Here, the energy Q_α must undergo a jump reflecting the strength of the impact that this shell exerts on the properties of the relevant nuclides. Such an effect is observed in the isotopes of the $Z = 110$ element: the difference of the values that Q_α takes for $N = 161$ and $N = 163$ nuclei is about 0.5 MeV, which is in satisfactory quantitative agreement with the theoretical results. This difference is approximately four times as great as the value that ΔQ_α takes when the number of neutrons traverses the $N = 152$ deformed shell in No isotopes, but it is considerably less than the correspond-

ing value for the spherical nucleus ^{210}Po (ΔQ_α = 2.4 MeV).

9. TRANSITION TO THE REGION OF SPHERICAL NUCLEI

The probability of the formation of superheavy nuclei in reactions induced by ^{48}Ca ions is the most uncertain element in the problem being considered. It is very difficult to compute this quantity to an acceptable precision, because describing the dynamics of collective motion of a massive system comprising nearly three hundred nucleons presents a formidable challenge. On the other hand, various extrapolations of known data to the region of superheavy nuclei can hardly be reliable. We made an attempt at determining this probability experimentally by studying the fission of heavy compound nuclei as the main channel of their decay.

The features of the fission of Z = 102 and Z = 112 compound nuclei that are formed in the fusion of ^{48}Ca ions with ^{208}Pb and ^{238}U nuclei, respectively, were measured in series of experiments employing the CORSET facility that recorded the masses, the energies, and the spatial distribution of pair fragments [41].

Figure 9*a* displays the one-dimensional mass distributions of fragments originating from the above interactions. The symmetric mass distribution of fragments that is observed in ^{48}Ca + ^{208}Pb interactions over the entire energy range under study is associated with the fission of ^{256}No compound nuclei. Simultaneously, the cross sections for ^{256}No decay through other channels featuring neutron evaporation were measured by using separators of recoil nuclei [42]. On the basis of these data, it is possible to determine the survival of evaporation products at various values of the excitation energy. This quantity can then be computed on the basis of the statistical model with the parameters fitted in such a way as to ensure the best agreement with the experimental values.

A strongly different pattern is observed in ^{48}Ca + ^{238}U interactions. Here, the yield of pair fragments is primarily due to an asymmetric disintegration of the compound system (quasifission). With the fission of the ^{286}112 compound nucleus, we can associate only a small part of the symmetric mass distribution of fragments. It should be noted that the relative weight of this part decreases sharply at subbarrier energies.

From Fig. 9*b*, it can be seen that the maximum yield of isotopes of the Z = 112 element is expected at energies of the ^{48}Ca ion beam in the vicinity of the Coulomb barrier. The cross section for their production is as small as a few pb (1 pb = 10^{-36} cm^2). Therefore, it comes as no surprise that all preceding attempts at synthesizing superheavy elements in reactions induced by ^{48}Ca ions, where limiting cross sections amount to a few hundred pb, could not lead to positive results. On the same basis, we can conclude, however, that, in order to observe the formation of superheavy nuclei, the sensitivity of the experiments must be improved, in relation to previous experiments, at least by two orders of magnitude.

10. PRODUCING INTENSE BEAMS OF ^{48}Ca IONS

From the above, it follows that producing intense beams of the rare and very expensive isotope ^{48}Ca is a key problem in attempts at synthesizing superheavy elements. In order to achieve this goal, the U-400 heavy-ion accelerator was substantially upgraded. The upgrade included the creation of a new external source of multiply charged ions (ECR-4M) and a channel for injecting a low-energy beam of $^{48}Ca^{5+}$ ions (E_p = 60 keV) at the center of the accelerator chamber.

Neutral atoms of ^{48}Ca were injected into the ionic-source plasma in the form of metal vapors at a controllable crucible temperature. Hot screens whose temperature could be monitored were used in order to avoid the condensation of metal vapors onto the walls of the chamber. The experiments in question employed metal calcium enriched in the required isotope to about 70%. The choice of the optimum operation mode for the ECR source at a minimum consumption of ^{48}Ca, as well as the amount of the substance that remains in the chamber, was monitored by the gamma radiation from the ^{47}Ca isotope ($T_{1/2}$ = 4.5 d). The production of ^{47}Ca was accomplished by activating the original ^{48}Ca sample in the (γ, n) reaction. The procedure developed for regenerating the substance from the chamber of the source after its long-term operation made it possible to increase the efficiency of utilization of the original substance up to 85%. These refinements contributed substantially to producing an internal beam of ^{48}Ca ions that carries more than 10^{13} particles per second at a substance consumption of about 0.3 mg/h.

The extraction of the beam from the chamber of the U-400 accelerator was implemented by means of ion charge exchange on carbon foil of thickness about 40 μg/cm^2. The mean intensity of the beam of ^{48}Ca ions on the target was about 4×10^{12} particles per second. The ion-beam energy could be varied smoothly by shifting the charge-exchange foil in the radial direction. During exposures, this energy was determined and monitored to a precision not poorer than approximately 1 MeV. This was achieved by measuring the energy of scattered ions with the aid of a gold foil 200 μg/cm^2 thick and with the aid of the TOF technique.

11. SEARCHES FOR A NEW ISOTOPE OF THE Z = 112 ELEMENT IN ^{48}Ca + ^{238}U INTERACTIONS

Experiments pursuing this goal were conducted in March 1998 with the VASSILISSA separator [43]. A rotating target from enriched ^{238}U in the form of a layer 0.3 mg/cm^2 thick deposited on an aluminum substrate

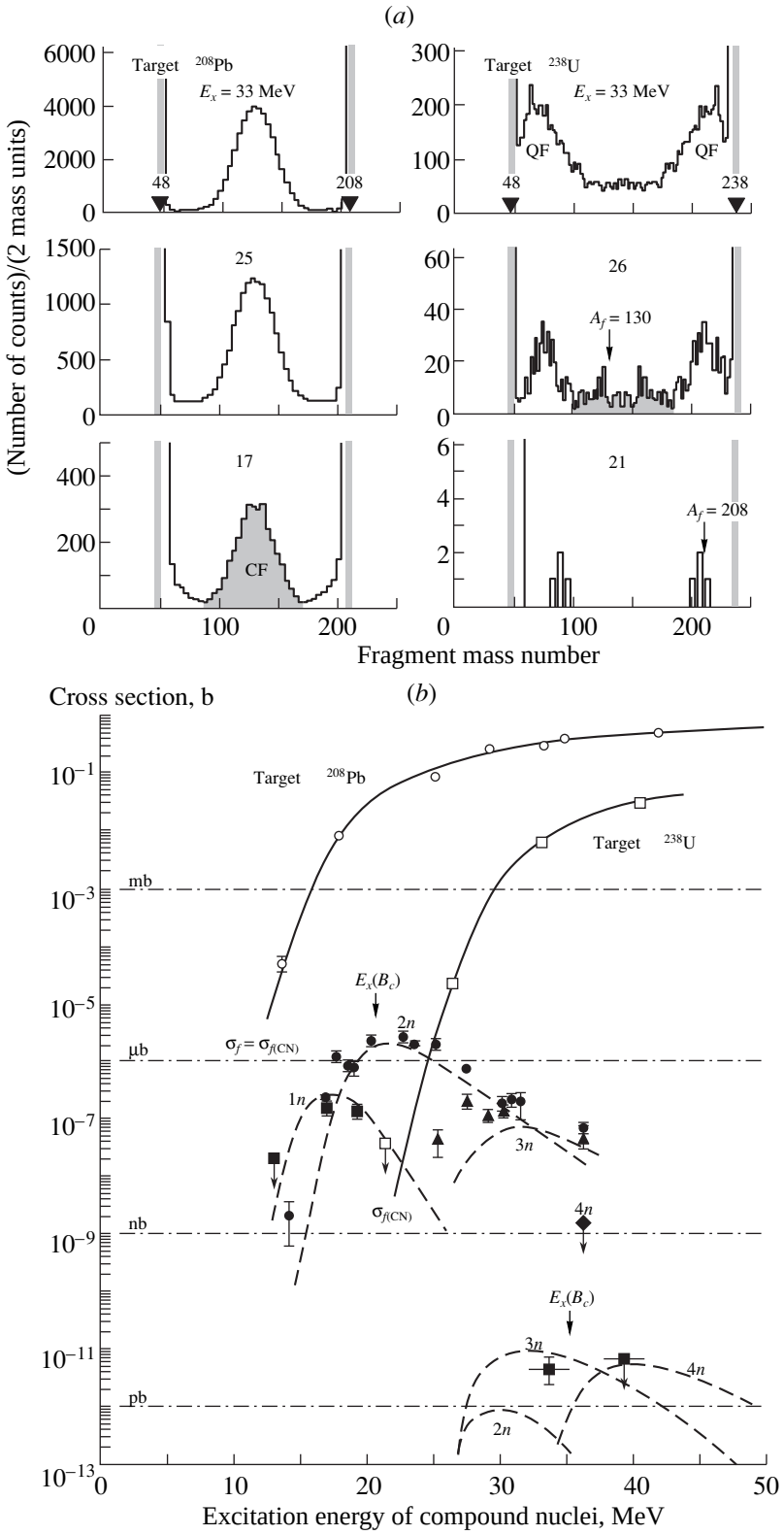

Fig. 9. (*a*) Mass distributions of fragments for the case of the irradiation of ^{208}Pb and ^{238}U nuclei with ^{48}Ca ions of various energies. The excitation energies of $Z = 102$ and $Z = 112$ compound nuclei are indicated in the figures. (*b*) Cross sections for the symmetric fission of $Z = 102$ and $Z = 112$ nuclei as functions of energy. Open circles (boxes) connected by a solid curve represent data for the reactions that occur on ^{208}Pb (^{238}U) nuclei. Closed symbols show the experimental cross sections for the formation of $Z = 102$ evaporation products. Dashed curves depict the results of the calculations within the statistical model. The experimental cross sections for the formation of $Z = 112$ isotopes in ^{48}Ca + ^{238}U interactions are shown by closed boxes.

1.6 mg/cm^2 thick was used to receive an intense ion beam. Two long-term exposures were performed at the ion-beam energies of E_p = 231 and 238 MeV, which corresponded to the compound-nucleus excitation energies of E_x = 33 and 39 MeV. From the data in Fig. 9*b*, it follows that, under these conditions, it is natural to expect a maximum yield of isotopes originating from reactions involving the evaporation of three or four neutrons from the ^{286}112 compound nucleus.

In the first experiment (E_x = 33 MeV), two events of spontaneous fission in the form of two coincident fragments with energies of (162 + 28) MeV and (191 + 21) MeV in the frontal detector and in the side detectors, respectively, were recorded at a total irradiation dose of 3.5×10^{18} ions. So pronounced a distinction between the signal amplitudes was due to a deep implantation of a recoil nucleus with the result that, upon its decay into two fragments, the entire energy of one fragment and part of the energy of second fragment were deposited in the frontal detector. The side detectors recorded only the amount of energy equal to the remaining part of the energy of the second fragment minus the energy loss in the insensitive surface layers of the detectors.

Neither of these events was accompanied by a signal in the TOF detector, whence it follows that the events in question originated from the decays of implanted nuclei. In each case, all signals were analyzed in the corresponding position windows over a broad time interval from 5 μs to 10000 s in order to find the recoil nucleus and to perform a search for alpha particles preceding spontaneous fission. Signals from the implanted ions, with the amplitudes in the frontal detector and the times of flight in the TOF detector that were expected for heavy nuclei, were recorded 52 and 182 s prior to the emergence of the fragments. Within these time intervals, there were no signals from alpha particles preceding spontaneous fission. Other successive-alpha-decay chains that do not end in spontaneous fission and which could be associated with the decay of superheavy nuclei (in the energy range E_α = 8–13 MeV with a half-life of $T_{1/2} \le 1000$ s) were not discovered in the experiment either.

Neither spontaneous fission nor alpha-particle chains that could be associated with the decay of a heavy nucleus were observed in the second exposure (E_x = 39 MeV), where the irradiation dose was 2.2×10^{18} ions.

The half-life determined for the new spontaneously fissile nuclide on the basis of the two aforementioned events is $T_{1/2} = 81^{+200}_{-35}$ s. At the excitation energy of E_x = 33 MeV, it is formed with cross section $\sigma = 5^{+6}_{-3}$ pb; at E_x = 39 MeV, the cross section for its formation was constrained as $\sigma \le 7.5$ pb. For each spontaneous-fission event, the total kinetic energy of the fragments was about 190 and 212 MeV, respectively. It was determined upon calibrating the detectors by using implanted nuclei ^{252}No ($T_{1/2}$ = 2.3 s; SF ≈ 25%) originating from the reaction ^{206}Pb(^{48}Ca, 2*n*).

It should be noted that the properties of nuclei around ^{238}U are well known. Only very heavy isotopes with $Z \ge 96$, which are offset from ^{238}U by 12–16 nucleons, undergo spontaneous fission. The formation of these or still heavier isotopes in ^{48}Ca + ^{238}U interactions is energetically forbidden.

Most probably, the observed spontaneously fissile nuclei are formed in the fusion channel as the result of the decay of a compound system with excitation energy E_x = 33 MeV. Here, there are also only very few possibilities. The evaporation of charged particles from a slightly heated heavy nucleus is strongly suppressed by the Coulomb barrier; fusion-reaction products formed upon the emission of alpha particles and heavier nuclei are additionally suppressed during separation by more than two orders of magnitude. Since the effect was observed at E_x = 33 MeV and since it did not become more pronounced at a higher energy, it is most probable that the observed spontaneous-fission events are associated with the decay of the ^{283}112 (N = 171) even–odd nucleus.

A comparative analysis of the decay properties of the new Z = 112 isotope that are predicted by different theories is performed in [43]. However, the most important conclusion rather follows from the experimental observation that, upon going over from the ^{277}112 isotope ($T_\alpha \sim 0.24$ ms) to the ^{283}112 isotope ($T_{SF} \sim 100$ s), the half-life increases by more than five orders of magnitude.

12. EXPERIMENTS DEVOTED TO THE SYNTHESIS OF SUPERHEAVY NUCLEI IN ^{48}Ca + ^{244}Pu INTERACTIONS

Isotopes of the Z = 114 element, which are the closest ones to the top of the stability island, can be synthesized in the fusion of ^{48}Ca and ^{244}Pu nuclei, which possess the maximum neutron excess. In this reaction, the maximum yield of isotopes formed in the channels involving the emission of three or four neutrons is expected at an energy of ^{48}Ca ions that is close to the Coulomb barrier. According to calculations performed within various theoretical models, the ground-state shapes of the Z = 114 nuclei with N = 174 and N = 175 are expected to be spherical; the stabilizing effect of the strong neutron shell N = 184 must manifest itself in them.

Experiments aimed at synthesizing these isotopes were performed by using a gas-filled separator of recoil nuclei [44].

A thin layer (of thickness about 0.4 mg/cm^2) of a plutonium target material enriched in ^{244}Pu to 98.6% was deposited on a Ti foil 1.5 μm thick. Each of nine targets—it represented a 40° segment of a circle and had an area of about 3.5 cm^2—was mounted on a disk of radius R = 60 mm rotating with a speed of 2000 rpm about an axis orthogonal to the beam direction.

The energy of the ion beam directed at the middle of the target layer was chosen to be 236 MeV. With allow-

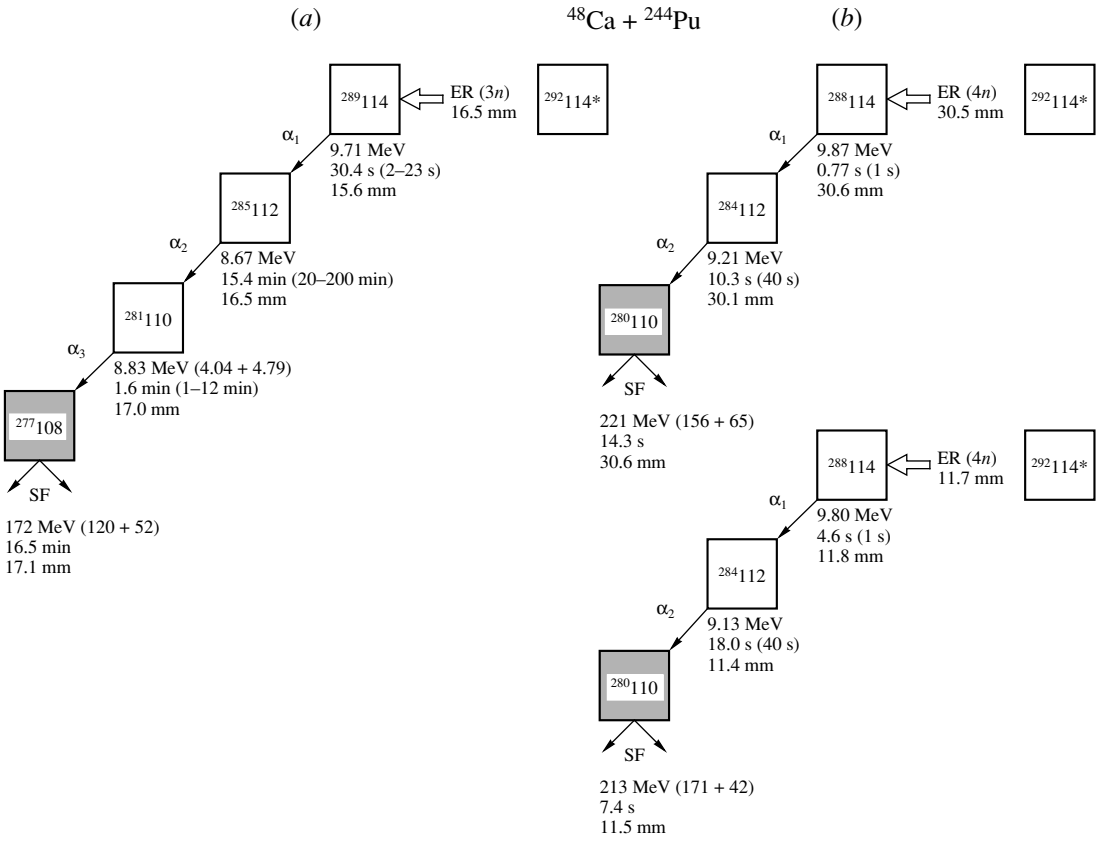

Fig. 10. Chains of successive decays in ^{48}Ca + ^{244}Pu interactions. Energy depositions in the frontal and in the side detector are indicated for spontaneous-fission fragments. The position coordinate is shown for all detected signals.

ance for energy losses in the depth of the target layer and for slight changes in the beam energy during long-term exposures, the excitation energy of ^{292}114 compound nuclei could be estimated to lie between 31.5 and 39 MeV. For each recoil nucleus recorded by the detector assemblage, it was possible to determine, however, a precise (instantaneous) beam-energy value and the target number corresponding to a given event.

Under these conditions, two virtually identical experiments were performed.

In the first experiment, which spanned a two-month period covering November and December 1998, three events of spontaneous fission were observed at a total irradiation dose of 5.2×10^{18} ions.

Two spontaneous-fission events accompanied by the energy depositions of 149 and 153 MeV in the detectors were recorded 1.13 and 1.07 ms after the arrival of recoil nuclei in the corresponding position windows. At the detector counting rate for recoil nuclei about 2 events per hour, the observed short decays must be associated with the known spontaneously fissile isomer ^{244mf}Am (T_{SF} = 0.9 ms), which appears as the product of nucleon exchange with the target nucleus ^{244}Pu. The third event was recorded as two time-coincident signals (two fission fragments) accompanied by the energy release of 172 (120 + 52) MeV. According to detector calibrations on the basis of known information about ^{252}No spontaneous fission, the above energy release corresponds to a fragment TKE of about 190 MeV. By considering the signals that have been found previously and which could be generated by alpha particles with energies $E_\alpha > 8$ MeV at the same positions, we discovered a chain of successive decays that is shown in Fig. 10*a*. Upon the implantation of a heavy nucleus (ER), with residual energy E_r = 6.1 MeV and with a corresponding signal in the TOF detector, an $E_{\alpha 1}$ = 9.71 MeV alpha particle was emitted after a lapse of 30.4 s. After that, a second alpha particle, with energy $E_{\alpha 2}$ = 8.67 MeV, was recorded 15.4 min later. A third alpha particle was emitted after 1.6 min into the backward hemisphere; having deposited an energy of 4.04 MeV in the frontal detector, it is absorbed in the side detector with an energy release of 4.79 MeV ($E_{\alpha 3}$ = 8.83 MeV). Finally, the aforementioned spontaneous-fission event occurred 16.5 min later.

All five signals (ER, α_1, α_2, α_3, SF) lie within a position interval of 1.5 mm, whence it follows that the observed decays are tightly correlated. The total time interval from arrival of the implanted ion to the spontaneous-fission event is 34 min. The probability of random coincidences mimicking such a decay at any point of the detector working surface is below 0.6%. For the

place where the decay event did actually occur (a given position window in a given strip), this probability is much lower (about 10^{-4}).

The basic rule of alpha decay—that which determines a relationship between the decay energy Q_α and the decay probability (corresponding half-life T_α)—is fulfilled for all links of the decay chains. For even–even nuclei, Q_α is directly related to the mass difference between the parent and the daughter nucleus. According to the Geiger–Nutoll rule, the decay energy and half-life then determine the atomic number of the parent nucleus. In the calculations, it is possible to use the Viola–Seaborg formula with constant coefficients [10] that make it possible to describe data on the alpha decays of all known 58 even–even isotopes with $Z > 82$ and $N > 126$ for which the values of Q_α and T_α were measured [10] (see Fig. 11). For odd nuclei, where decays can proceed to low-lying states of the daughter nucleus that are characterized by various spin–parity values, additional selection rules that forbid some transitions may be operative, increasing T_α, on average, by a factor ranging between 3 and 10. Also, the expected half-lives as estimated with allowance for these selection rules at the measured alpha-particle energies in the chain are displayed in Fig. 10 parenthetically.

For the observed alpha transitions, the values of $T_\alpha(Q_\alpha)$ are greater than those for all known alpha-particle emitters, whence we can conclude that we are dealing here with the decay of a heavy nucleus. All events are correlated in time and in position. They are due to the alpha decay of the parent nucleus (E_α = 9.71 MeV) and end in spontaneous fission. It is precisely this scenario that is expected for the decay of superheavy isotopes of the Z = 114 element.

On the basis of the decay features, we can conclude that, under the conditions prevalent in the experiment being discussed, the ^{289}114 isotope, which is formed in the reaction channel involving the evaporation of three neutrons, is the progenitor of the chain. The observed event corresponds to a cross-section value of about 1 pb.

Of course, we cannot rule out the possibility that, in so long a chain of successive decays, one alpha particle has been lost. In this case, the spontaneous-fission event observed at the end of the chain must be associated with the decay of a ^{273}106 nucleus. If we assume that the chain consists of five links (and not of four of them, as was observed experimentally), the probability of losing any alpha particle when the remaining four are recorded is about 34%. The probability of losing the first alpha particle in the chain is about 8.5%. With the probability of 91.5%, the first transition that is characterized by the transition energy of $E_{\alpha 1}$ = 9.71 MeV and which was observed t_1 = 30.4 s after the implantation is therefore associated with the decay of the parent nucleus ^{289}114.

In the second experiment, which spanned the period between June and October 1999, the total irradiation dose was 1.0×10^{19} ions. Yet two identical chains of

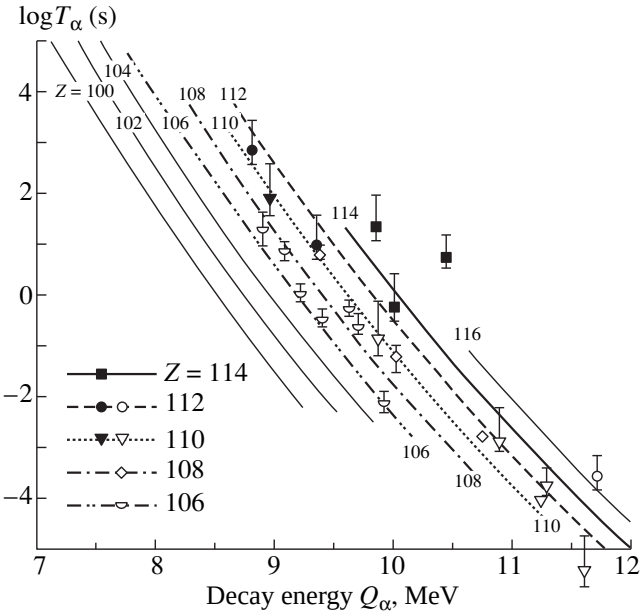

Fig. 11. Experimental values of Q_α and T_α (closed symbols) for all chains of successive alpha decays occurring in ^{48}Ca + $^{242, 244}$Pu interactions and ending in spontaneous fission. The lines represent the dependences $T_\alpha(Q_\alpha)$ computed by the Viola–Seaborg formula with the coefficients from [10]. Open symbols represent experimental values for all known nuclides with $Z \geq 106$.

successive alpha decays, each ending in a spontaneous-fission event (see Fig. 10*b*), were observed here. Below, we consider these chains individually.

Upon the implantation of a E_r = 11.1 MeV nucleus into strip no. 2, an $E_{\alpha 1}$= 9.87 MeV alpha particle was recorded after a lapse of about 0.8 s. A second alpha particle, with energy $E_{\alpha 2}$ = 9.21 MeV, was emitted 10.3 s later. Finally, spontaneous fission into two fragments that deposited the energies of E_{f1} = 156 MeV and E_{f2} = 65 MeV (E_{tot} = 221 MeV) in the frontal and the side detector, respectively, was observed after the next 14.3 s. According to data obtained as the result of calibrations, the above values correspond to TKE ~ 235 MeV. All four signals (ER, α_1, α_2, SF) fall within a position interval of size 0.5 mm, a fact that suggests a tight correlation between the decays being discussed.

In the second chain, an $E_{\alpha 1}$ = 9.80 MeV alpha particle was recorded 4.6 s after the implantation of a 7.8-MeV recoil nucleus into strip no. 8 (as in the first case, the energy of the recoil nucleus and its time of flight in the TOF detector are close to values expected for evaporation products with Z = 114). A second alpha particle, with energy $E_{\alpha 2}$ = 9.13 MeV, was emitted 18 s later. Finally, spontaneous fission into two fragments that deposited the energies of E_{f1} = 171 MeV and E_{f2} = 42 MeV (E_{tot} = 213 MeV) in the frontal and the side detector, respectively, was observed after a lapse of the next 7.4 s. That all four signals (ER, α_1, α_2, SF) were recorded within a position interval of size 0.4 mm again indicates that the observed decays are tightly corre-

lated. Within the detector resolution of $\Delta E \sim 0.05$ MeV and the statistical uncertainty in the decay times, the two events are consistent in all 11 parameters measured experimentally. The probability of random signal coincidences that could mimic recoil nuclei and their correlated decays is estimated at less than 5×10^{-13}. The probability of losing an alpha particle in the observed decays is less than 3%.

It should be noted that only two spontaneous-fission events were recorded in this long-term experiment. They are characterized by large energy depositions from fission fragments and are preceded, in either case, by identical chains of successive alpha decays. The projectile-ion energy measured at the instant when the events in question are detected corresponds to exciting a $^{292}114$ compound nucleus to energies E_x of 36 to 37 MeV. The channel involving the evaporation of four neutrons and leading to the formation of the $^{288}114$ isotope in the ground state is the most probable one at this excitation energy. The parent nucleus $^{288}114$ undergoes alpha decay, the corresponding decay energy and half-life being $Q_\alpha = 9.98 \pm 0.05$ MeV and $T_\alpha = 1.9^{+3.3}_{-0.8}$ s.

It should be recalled that, in the alpha decay of even–even nuclei, the atomic number of the initial nucleus can be determined to a high precision. By using the dependence $T_\alpha(Q_\alpha)$ presented in Fig. 11, it can be found from the measured values that it is the $Z = 114.4^{+1.6}_{-0.8}$ nucleus that decays. Its daughter product, a new even–even isotope of the $Z = 112$ element ($A = 284$), undergoes alpha decay, the decay energy and the half-life being, respectively, $Q_\alpha = 9.30 \pm 0.05$ MeV and $T_\alpha = 9.8^{+17.9}_{-3.8}$ s. From the relationship between T_α and Q_α, the atomic number of this daughter product can be estimated at $Z = 110.2^{+1.5}_{-0.8}$. Finally, the granddaughter nucleus $^{280}110$ undergoes spontaneous decay, the corresponding half-life being $T_{SF} = 7.5^{+13.7}_{-2.9}$ s. For either of the two events, the energy deposited by the fragments in the detectors ($E_{tot} = 217$ MeV) is 40 MeV greater than the value obtained for the known spontaneously fissile nucleus ^{252}No ($Z = 102$). Although the distributions of the fragment TKE are rather broad, the above value also suggests that the granddaughter decay products in the chain are due to the fission of a sufficiently heavy nucleus ($Z > 106$).

According to the calculations presented in [36], the $^{288}114$ ($N = 174$) nucleus is expected to undergo alpha decay rather than spontaneous fission since $T_\alpha = 0.14$ s ($Q_\alpha = 10.3$ MeV), while $T_{SF} = 35$ min. The corresponding partial half-lives of the daughter nucleus $^{284}112$ ($N = 172$) are commensurate ($T_\alpha = 1.1$ s, $T_{SF} = 4$ s); therefore, it could suffer either alpha decay or spontaneous fission with comparable probabilities. However, granddaughter nuclei $^{280}110$ ($N = 170$) should decay via spontaneous fission into two fragments ($T_{SF}/T_\alpha \sim 0.1$).

The observed chain reproduces entirely the predicted decay scenario. The decay properties of the neighboring odd isotope $^{289}114$ comply well with the aforementioned radioactive properties of the even–even nucleus $^{288}114$. As might have been expected, an increase in the half-lives T_α and T_{SF} is observed for the former owing to the presence of an extra odd neutron in the nucleus.

13. EXPERIMENTS WITH ^{242}Pu TARGETS

If the identification of the superheavy nuclei obtained in the previous experiments with ^{238}U and ^{244}Pu targets is valid, we can easily predict the properties of yet another isotope, $^{287}114$ ($N = 173$). It must undergo predominantly alpha decay into the daughter nucleus $^{283}112$, which was previously observed among the products of ^{48}Ca + ^{238}U interactions. In the case being considered, we could expect a short decay chain (α–SF) involving alpha decay characterized by a half-life of a few seconds and followed by spontaneous fission, whose half-life is much longer in the present case (a minute or a few minutes). This isotope of the $Z = 114$ element can be synthesized in the channel of ^{48}Ca + ^{242}Pu interactions that involves the evaporation of three neutrons.

The implementation of the experiment conducted in March and April 1999 [45] was nearly identical to that described above in discussing the synthesis of the $^{283}112$ isotope in ^{48}Ca + ^{238}U interactions.

A rotating target that was made from ^{242}Pu and which had a thickness of about 0.2 mg/cm^2 was exposed to a beam of 235-MeV ^{48}Ca ions; the total irradiation dose was 7.5×10^{18} ions. The most probable channel of deexcitation of the compound nucleus $^{290}114$ ($E_x \simeq 33.5$ MeV) involves the emission of three neutrons and must lead to the formation of the even–odd isotope $^{287}114$ ($N = 173$).

Four events of spontaneous fission were observed in this experiment.

In two cases, spontaneous-fission fragments depositing the energies of $E_{tot} = 144$ and 175 MeV in the detector assembly were recorded 59 and 20 μs after the implantation of recoil atoms into corresponding position windows. These events are associated with the decays of spontaneously fissile isomeric nuclei ^{241mf}Pu ($T_{SF} = 24$ μs) formed upon the ejection of one neutron from the target nucleus ^{242}Pu. Coincident signals from the two fragments were observed for the remaining two events with the energy depositions of $E_{f1} = 130$ MeV and $E_{f2} = 65$ MeV ($E_{tot} = 195$ MeV) in the frontal and the side detector, respectively, in one event and the total energy deposition of $E_{f1} + E_{f2} = 165$ MeV in the other event.

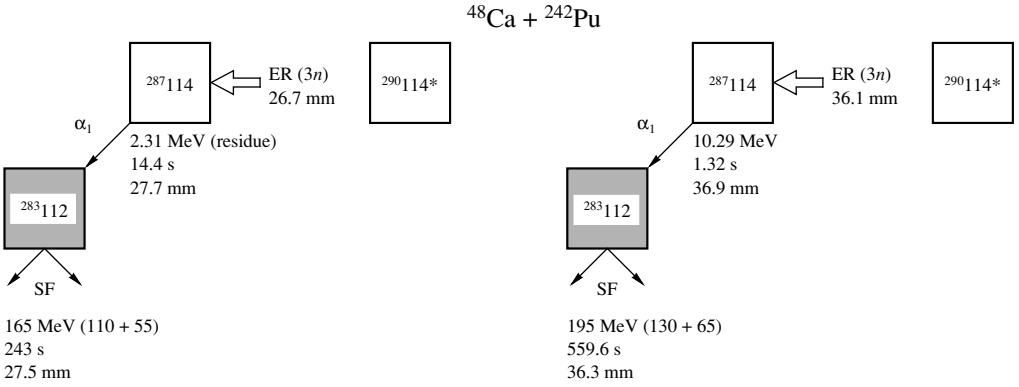

Fig. 12. Chains of successive decays occurring in $^{48}Ca + ^{242}Pu$ interactions.

Searches for alpha decays preceding spontaneous fission resulted in the discovery of two chains shown in Fig. 12.

In one of the chains, only one alpha particle (E_α = 10.29 MeV) was recorded by the frontal detector 1.32 s after the implantation of a heavy recoil atom with energy E_r = 10 MeV. The spontaneous-fission event was observed 559.6 s later. All three signals (ER, α, SF) fall within the position interval of size 0.82 mm, whence we conclude that the observed decays are correlated.

In the second case, spontaneous fission was observed 243 s after the detection of the E_r = 13.5 MeV recoil nucleus. Within this interval, the frontal detector recorded only part of the energy ($E_{\alpha 1}$ = 2.31 MeV) of the alpha particle emitted into the backward hemisphere (open window) after a lapse of 14.4 s from the implantation of the recoil nucleus. That all three signals (ER, α, SF) fall within the position interval of size 1.0 mm again evinces the correlation of the observed decays. The probability that both events are due to a random coincidence of signals that mimic the decay chains (ER, α, SF) in the above position intervals is less than 10^{-9}.

In either event, the parent nucleus undergoes alpha decay. It should be noted that, for these events, the time intervals corresponding to alpha-particle emission differ by a factor of about 10. At such low statistics of events, this comes as no surprise. Since the alpha-particle energy is not defined in the second case and since the daughter nuclei possess identical properties, we have to assume that, in the two cases, alpha decay proceeds from the same state of the parent nucleus. Its half-life as determined on the basis of the two cases in question is $T_\alpha = 5.5^{+10}_{-2}$ s. The daughter nuclei undergo spontaneous fission. Their decay properties are close to those observed previously in $^{48}Ca + ^{238}U$ interactions. All four spontaneous-fission events recorded in the two experiments are described, within the statistical uncertainties, by the same half-life of $T_{SF} = 3.0^{+2.8}_{-1.0}$ min and are associated with the decay of the same nucleus. In $^{48}Ca + ^{238}U$ interactions, this nuclide is formed as the evaporation product in the 3*n* channel, whereas, in $^{48}Ca + ^{242}Pu$ interactions, it appears as the daughter product of the alpha decay of the parent nucleus $^{287}114$ (E_α = 10.29 MeV).

The cross section for the production of the new isotope of the Z = 114 element is about 2 pb. Its half-life is less than that of the heavier isotope $^{289}114$ formed in $^{48}Ca + ^{244}Pu$ interactions, and the chain of the decays that follow it is shorter for the former than that for the latter (Fig. 10*a*). In accordance with theoretical predictions, such a trend is expected as the number of neutrons is decreased—that is, as the nuclear species being studied recedes from the N = 184 closed shell.

14. COMPARISON WITH THEORETICAL PREDICTIONS

Unfortunately, many calculations have not gone beyond searches for the region of the highest stability of superheavy nuclides, paying no attention to a determination of the properties of nuclei that populate this region. Therefore, we consider only those few cases where it is possible to draw a direct comparison with experimental data.

The most consistent quantitative treatment of the properties of superheavy nuclides was given within the macroscopic–microscopic model. The properties of even–even nuclei—in particular, their masses and the alpha-decay and spontaneous-fission energies and probabilities—were calculated by Smolanczuk [10], as well as by the authors of earlier studies (see, for example, [9]). Möller *et al.* [46] obtained data on the alpha-decay properties of odd nuclei, but they did not calculate the partial half-lives with respect to spontaneous fission.

First of all, we note that the heaviest isotopes of Z = 110, 112, and 114 elements from reactions induced by ^{48}Ca projectiles undergo alpha decays. In this region of nuclei, spontaneous fission is observed only for

$(N - Z) \le 61$. For the even–odd nuclei $^{277}108$ ($N = 169$) and $^{283}112$ ($N = 171$), the half-lives with respect to spontaneous fission proved to be, respectively, five and three orders of magnitude larger than the values predicted for the neighboring even–even isotopes. These distinctions may be due to the presence of an odd neutron, which reduces significantly the probability of the spontaneous fission of a heavy nucleus. For the even–even nucleus $^{280}110$ ($N = 170$), the experimental value ($T_{SF} \sim 10$ s) is also approximately three orders of magnitude larger than the value calculated in [36]. Although the calculations of the probability of spontaneous fission, which is associated with tunneling through a potential barrier, involves considerable uncertainties, the above distinctions may suggest a greater contribution of the shell structure to the deformation energy of the nucleus.

Some conclusions can be drawn from an analysis of the ground-state properties of superheavy nuclei.

For all known nuclides with $Z \ge 100$ and $N \ge 148$, Fig. 13 displays the experimental values of the alpha-decay energy. The Q_α values calculated for all even–even isotopes of these elements on the basis of the macroscopic–microscopic model [9, 10] are shown in the same figure. Obviously, the experimental data reflect well the changes in $Q_\alpha(N)$ that are expected in the theory for various values of N and Z, including the region of superheavy elements, where a transition from deformed to spherical shells is predicted. Quantitatively, a small distinction of $\Delta Q_\alpha \le 0.2$ MeV between the calculated and experimental values is observed for nuclei in the transition region between the $N = 152$ and $N = 162$ deformed neutron shells. When we go over to the spherical shell in the region $N = 170$–175, this distinction increases to $\Delta Q_\alpha \le 0.5$ MeV. It should be noted, however, that most of experimental data refers to the decay of even–odd nuclei, for which the calculations take no account of the structure of low-lying states; moreover, the presence of an odd neutron in a nucleus can hinder alpha decay, as was indicated above. For the heaviest nuclides, the measured values of the decay energy Q_α and of the half-lives T_α proved to be less and greater, respectively, than the values predicted by the calculations from [9, 10]. The calculations performed by Möller *et al.* [46] yield deviations in the opposite direction: the computed values of Q_α are less than the measured values by about 0.7 MeV; as a result, the predicted stability of these nuclides is three orders of magnitude higher than that which follows from experimental data.

The calculations of Cwiok, Nazarewicz, and Heenen [48], who relied on the Hartree–Fock–Bogolyubov method, choosing specific forces of interparticle interactions, were performed for the heavy nuclide $^{289}114$ produced in $^{48}Ca + ^{244}Pu$ interactions. In this approach, which can also be extended to other nuclei, it is possible to calculate the ground and low-lying excited states of both even and odd nuclei. This permits

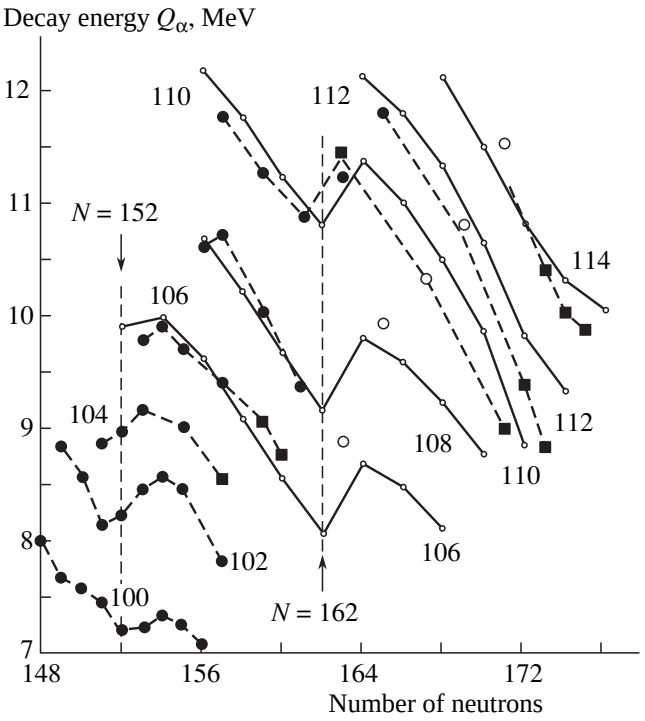

Fig. 13. Experimental values of alpha-decay energies for $Z = 100$–114 isotopes involving various numbers of neutrons. Solid lines depict Q_α values computed on the basis of the macroscopic–microscopic model [9, 10]. Points represent data for (closed boxes) isotopes of the Z = 110, 112, and 114 elements from reactions induced by ^{48}Ca ions and (open circles) $^{86}Kr + ^{208}Pb$ interactions [47]. Dashed lines connecting experimental points are drawn to guide the eye.

determining the most probable transitions and the corresponding Q_α values for the entire chain of successive decays. Fairly good agreement between the results of the calculations and experimental data ($\Delta Q_\alpha \le 0.25$ MeV) for the $^{289}114$–$^{285}112$–$^{281}110$ chain (Fig. 10*a*) seems astonishing at first glance, since the closed proton shell corresponds to $Z = 126$ in the model being discussed.

For heavy nuclei, the alpha-decay energies calculated recently by Bender [49] on the basis of the relativistic self-consistent-mean-field model, which takes into account spin–orbit interaction more precisely (according to the opinion of this author), are displayed in Fig. 14. These results are in excellent agreement with experimental values of Q_α for the $^{288}114$–$^{284}112$ chain of even–even nuclei. For the chain of successive decays of the even–odd nucleus $^{289}114$ ($^{289}114$–$^{285}112$–$^{281}110$), the calculated values of Q_α differ from the experimental values by $\Delta Q_\alpha \le 0.3$ MeV. From the spectra of single-particle proton and neutron levels and from the calculated quadrupole and hexadecapole moments of even–even nuclei, it follows that the small values of Q_α and the corresponding large half-lives of the isotopes of the $Z = 114$ element that are produced in $^{48}Ca + ^{244}Pu$ interactions are due to the formation of local deformed subshells with $Z = 114$ and $N = 174$. This does not rule out,

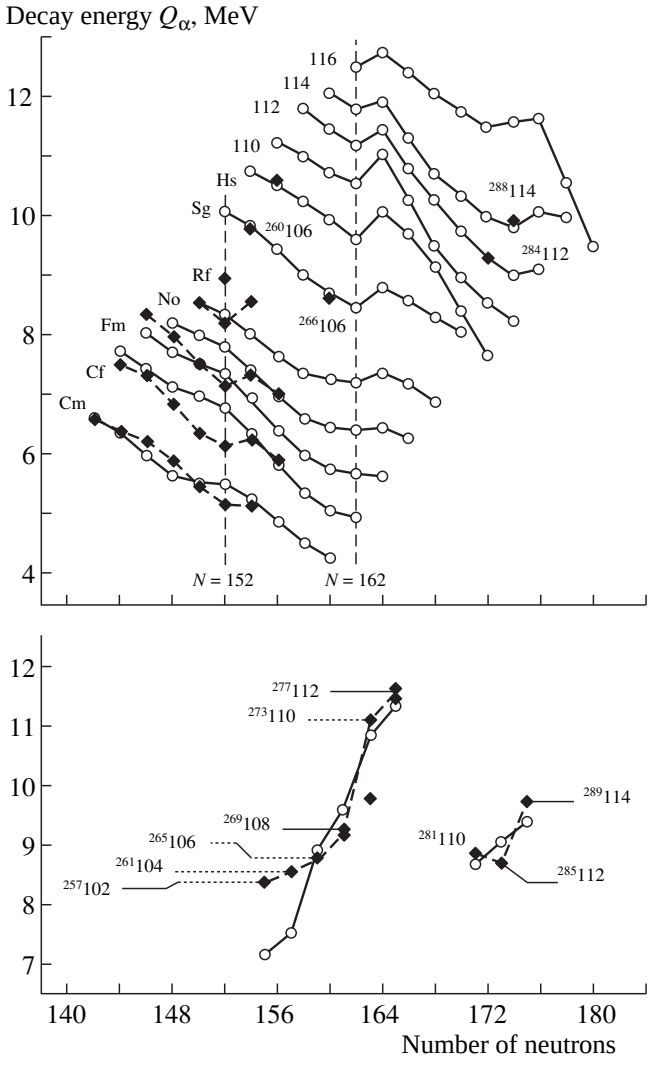

Fig. 14. Alpha-decay energies for Z = 96–116 isotopes containing various numbers of neutrons. In the upper panel, open circles connected by solid lines represent the Q_α values computed for even–even nuclides within the relativistic self-consistent-mean-field approximation, while closed diamonds connected by dashed lines correspond to experimental values. The lower panel displays the (open circles) computed and (closed diamonds) experimental values for the chains of decays of the even–odd nuclides ^{277}112 and ^{289}114.

however, the existence of spherical shells in nuclei with a higher neutron excess.

In all probability, the uncertainties in the predictions of various theoretical models are explained by the fact that the heaviest isotopes with Z = 108–114 that were obtained in the experiments of our group are still at the outliers of the stability island that are far off its top.

Unfortunately, the possibilities for advancements into the region of still heavier isotopes with $Z \geq 114$ and $N > 175$ are very limited. The N = 176, 177 isotopes of the Z = 116 element can in principle be synthesized in the fusion reaction induced by ^{48}Ca + ^{248}Cm interactions. A further increase in the number of neutrons can be achieved by using beams of radioactive nuclei. This way is being presently discussed in connection with the creation of factories of such beams at some large accelerator centers.

15. CONCLUSION AND OUTLOOK

Experiments aimed at producing isotopes of the Z = 108–114 elements in reactions induced by ^{48}Ca ions have been surveyed. That superheavy nuclides synthesized in this way proved to be comparatively long-lived opens the possibilities for studying the chemical properties of these elements. The problem of determining the extent to which they are homologs of the heavy metals from the Os–Pb series and the problem of assessing the extent to which their chemical properties are influenced by the relativistic effect of the electron shells of a heavy atom are among key problems of contemporary chemistry. It should be noted that even–odd and odd–odd isotopes that can be obtained in reactions on ^{237}Np, ^{243}Am, and ^{249}Bk targets may prove to be still more long-lived.

Yet another question that remains open at present is associated with a determination of the proton shell and, hence, with a determination of the half-life of the most unstable nucleus.

On the basis of macroscopic–microscopic calculations, the beta-stable N = 182 isotope of the Z = 110 element is expected to have the longest half-life among all even–even nuclides, its half-life with respect to alpha decay being $T_\alpha \sim 10^2$ yr. For the neighboring even–odd or odd–odd nuclei, the analogous quantity can be greater: $T_{1/2} \sim 10^3$–10^4 yr. At the same time, all experimental values of Q_α that were obtained for the isotopes of the Z = 114 element and for their daughter nuclei are somewhat less than the corresponding calculated values. Possibly, this can be explained by a stronger stabilizing effect of the N = 184 neutron shell even when it is offset by 9–14 atomic masses. The half-life of the superstable nucleus can then be much greater than 10^2 yr.

Since advancements to the region $N > 175$ present considerable difficulties, we can step backward to study the properties of nuclei containing a smaller number of neutrons, thereby filling the region of neutron-deficient superheavy nuclei. This attempt has recently been made in the study of Ninova *et al.* [47], who used, for this purpose, the cold-fusion reaction induced by ^{86}Kr + ^{208}Pb interactions; data from those experiments are also presented in Fig. 13. In reactions induced by ^{48}Ca projectiles, the aforementioned neutron-deficient isotopes can be synthesized by irradiating targets from lighter uranium and plutonium isotopes within the experimental setting described above. By correcting the parameters of the calculations, it would be possible to improve the accuracy of theoretical predictions.

If the half-lives of some superheavy elements prove to be longer than 10^8 yr, it will be impossible to rule out their existence in nature. Skipping the discussion on the mechanism of the formation of superheavy elements in the nucleosynthesis process for the time being—this is a separate problem of interest in itself—we can consider various versions of such investigations.

Experiments that were conducted by Flerov and his colleagues between 1978 and 1988 and which were aimed at searches for spontaneously fissile nuclei in natural samples potentially containing the eka-platinum–eka-bismuth isotopes ($Z \geq 110$) only yielded upper limits on their concentrations at a level of 10^{-14}–10^{-12} g/g (at $T_{1/2} \sim 10^8$ yr) [50]. According to modern concepts, it is more probable that the atomic numbers of the nuclides showing the highest stability do not exceed 110. The choice of experimental strategies and especially the problem of producing enriched samples depends directly on the determination of the chemical properties of superheavy elements.

The above lines of investigations into superheavy nuclides do not exhaust the possibilities for the development of work in these realms. They will obviously become more clear-cut side by side with the accumulation of information in this still poorly explored field of physics.

ACKNOWLEDGMENTS

This article presents results obtained by a large group of researchers. Many of them were among the authors of original studies, and their contribution to my survey is gratefully acknowledged. I am indebted to the JINR directorate—and, in particular, to Profs. V.G. Kadyshevsky, Ts. Vylov, and A.N. Sisakyan—for support of this study and interest in it at all stages of experimenting.

I am grateful to Profs. M.G. Itkis, G. Münzenberg, S. Hofmann, E.K. Hulet, N. Rowley, W. Greiner, V.V. Pashkevich, W. Nazarewicz, A. Sobiczewski, R. Smolanczuk, V.V. Volkov, A.A. Goverdovski, B.I. Pustyl'nik, and D.V. Shirkov for stimulating discussions and enlightening comments.

Most of the efforts were supported by the Ministry for Atomic Energy of the Russian Federation and by the Department of Energy of the United States, as well as by the Russian Foundation for Basic Research and by the International Association for the Promotion of Cooperation with Scientists from the Independent States of the Former Soviet Union.

REFERENCES

1. G. N. Flerov and K. A. Petrzhak, Phys. Rev. **58**, 89 (1940); J. Phys. (Moscow) **3**, 275 (1940).
2. N. Bohr and J. Wheeler, Phys. Rev. **56**, 426 (1939).
3. S. M. Polikanov *et al.*, Zh. Éksp. Teor. Fiz. **42**, 1464 (1962) [Sov. Phys. JETP **15**, 1016 (1962)].
4. S. Bjornholm and J. Linn, Rev. Mod. Phys. **52**, 725 (1980).
5. Yu. Ts. Oganessian *et al.*, Nucl. Phys. A **239**, 157 (1975).
6. (a) W. J. Swiatecki, in *Proceedings of the 2nd International Conference on Nuclear Masses, 1964* (Springer, Vienna, 1964), p. 52; (b) W. D. Myers and W. J. Swiatecki, Nucl. Phys. **81**, 1 (1966).
7. V. M. Strutinsky, Nucl. Phys. A **95**, 420 (1967); **122**, 1 (1968).
8. M. Brack *et al.*, Rev. Mod. Phys. **44**, 320 (1972).
9. Z. Patyk and A. Sobiczewski, Nucl. Phys. A **533**, 132 (1991).
10. R. Smolanczuk, Phys. Rev. C **56**, 812 (1997).
11. P. Möller and J. R. Nix, J. Phys. G **20**, 1681 (1994).
12. A. Sobiczewski, F. A. Gareev, and B. N. Kalinkin, Phys. Lett. **22**, 500 (1966).
13. H. Meldner, Ark. Fys. **36**, 593 (1967).
14. *Heavy Elements and Related New Phenomena*, Ed. by W. Greiner and R. K. Gupta (World Sci., Singapore, 1999), Vol. 1.
15. G. T. Seaborg, *Man-Made Transuranium Elements* (Prentice Hall, New York, 1963).
16. T. Sikkeland, J. Maly, and D. F. Lebeck, Phys. Rev. **169**, 1000 (1968); V. E. Viola and T. Sikkeland, Phys. Rev. **128**, 767 (1962).
17. Yu. Ts. Oganessian, Lect. Notes Phys. **33**, 221 (1974).
18. M. Nurmia, T. Sikkeland, R. Silva, and A. Ghiorso, Phys. Lett. B **26**, 78 (1967).
19. G. N. Flerov *et al.*, Nucl. Phys. A **267**, 359 (1976).
20. F. P. Hessberger *et al.*, Z. Phys. A **321**, 317 (1985).
21. P. Armbruster, Annu. Rev. Nucl. Part. Sci. **35**, 135 (1985).
22. G. Münzenberg, Rep. Prog. Phys. **51**, 57 (1988).
23. S. Hofmann, Rep. Prog. Phys. **61**, 639 (1998).
24. W. J. Swiatecki, Nucl. Phys. A **376**, 275 (1982); J. Blocki, H. Feldmeier, and W. J. Swiatecki, Nucl. Phys. A **459**, 145 (1986).
25. E. K. Hulet *et al.*, Phys. Rev. Lett. **39**, 385 (1977).
26. Yu. Ts. Oganessian *et al.*, Nucl. Phys. A **294**, 213 (1978).
27. P. Armbruster *et al.*, Phys. Rev. Lett. **54**, 406 (1985).
28. G. Münzenberg *et al.*, Nucl. Instrum. Methods **161**, 65 (1979).
29. A. V. Yeremin *et al.*, Nucl. Instrum. Methods Phys. Res. A **274**, 528 (1989).
30. Yu. A. Lazarev *et al.*, in *Proceedings of the International School-Seminar on Heavy Ion Physics, Dubna, Russia, 1993*, JINR Report E7-93-274 (Dubna, 1993),Vol. II, p. 497.
31. N. Bohr, Phys. Rev. **58**, 654 (1940); **59**, 270 (1941).
32. P. Möller and J. R. Nix, Nucl. Phys. A **549**, 84 (1992).
33. A. G. Demin *et al.*, Z. Phys. A **315**, 197 (1984).
34. G. Münzenberg *et al.*, Z. Phys. A **322**, 227 (1985).
35. P. Möller, J. R. Nix, and W. J. Swiatecki, Nucl. Phys. A **469**, 1 (1987); **492**, 349 (1989).
36. R. Smolanczuk, J. Skalski, and A. Sobiczewski, in *Proceedings of the Workshop XXIV on Cross Properties of*

Nuclei and Nuclear Excitations "Extremes of Nuclear Structure," Hirshegg, 1996 (GSI, Darmstadt, 1996), p. 35.
37. E. K. Hulet *et al.*, Phys. Rev. C **40**, 770 (1989).
38. Yu. A. Lazarev *et al.*, Phys. Rev. Lett. **73**, 624 (1994).
39. Yu. A. Lazarev *et al.*, Phys. Rev. Lett. **75**, 1903 (1995).
40. Yu. A. Lazarev *et al.*, Phys. Rev. C **54**, 620 (1996).
41. M. G. Itkis *et al.*, Nuovo Cimento A **111**, 783 (1998).
42. A. V. Yeremin *et al.*, JINR Rapid Commun. 6[92]-98 (1998), p. 21.
43. Yu. Ts. Oganessian *et al.*, Eur. Phys. J. A **5**, 63 (1999).
44. Yu. Ts. Oganessian *et al.*, Phys. Rev. Lett. **83**, 3154 (1999).
45. Yu. Ts. Oganessian *et al.*, Nature **400**, 242 (1999).
46. P. Möller, J. R. Nix, and K.-L. Kratz, At. Data Nucl. Data Tables **66**, 131 (1997).
47. V. Ninov *et al.*, Phys. Rev. Lett. **83**, 1104 (1999).
48. S. Cwiok, W. Nazarewicz, and P. H. Heenen, Phys. Rev. Lett. **83**, 1108 (1999).
49. M. Bender, Phys. Rev. C **61**, 031302 (2000).
50. G. N. Flerov and G. M. Ter-Akopian, Rep. Prog. Phys. **46**, 817 (1983).

Translated by A. Isaakyan

Physics of Atomic Nuclei, Vol. 63, No. 8, 2000, pp. 1337–1340. Translated from Yadernaya Fizika, Vol. 63, No. 8, 2000, pp. 1413–1416.

ON THE 85th ANNIVERSARY OF V.V. VLADIMIRSKY

Angular Correlations in Nuclear Fission

G. V. Danilyan

Institute of Theoretical and Experimental Physics, Bol'shaya Cheremushkinskaya ul. 25, Moscow, 117259 Russia

Received November 25, 1999

Abstract—Interference effects in the angular distributions of products originating from binary and ternary nuclear fission induced by slow neutrons are reviewed. © *2000 MAIK "Nauka/Interperiodica".*

1. INTRODUCTION

Investigation of fission processes, which differ substantially from other nuclear reactions, sometimes furnishes surprising results. That the angular distributions of products originating from nuclear-fission processes induced by photons and fast neutrons proved to be anisotropic was among the first surprises. This phenomenon, which was discovered in the early 1950s, could not be explained within the liquid-drop model of nuclear fission. A satisfactory description of experimental angular distributions was proposed by Strutinsky [1], who relied on A. Bohr's hypothesis [2] on transition quasistationary states of a cold severely deformed nucleus at the saddle point. These states are characterized by the quantum numbers I, K, and π, where I is the total angular momentum of the nucleus, K is its projection onto the axis of nuclear deformation, and π is the parity of a given state. If the total angular momentum of the nucleus is oriented with respect to some quantization axis (in the fission of nonoriented nuclei that is induced by fast particles, the latter introduce their orbital angular momentum in the target nucleus, thereby orienting the nucleus with respect to their momentum), the deformation axis, which coincides with the axis of the emission of the would-be fission fragments, is also oriented with respect to the quantization axis, a specific shape of anisotropy being dependent here on the transition state (fission channel) through which the fission process proceeds. Of course, this scheme is substantially simplified. In fact, several fission channels are open completely or partly at virtually any energy inducing the fission process, so that the angular distributions of fission products have a rather complicated shape. It is common practice to characterize the angular distributions in question by a quantity that is defined as the ratio of the emission probabilities at angles of 0° and 90° with respect to the quantization axis and which is referred to as the degree of anisotropy (or merely anisotropy). Generally, the coincidence of anisotropies does not imply similarity of the corresponding angular distributions. This was demonstrated compellingly in [3], where a strong dependence of the angular distributions of fission fragments on their masses was revealed in subbarrier uranium fission induced by 1-MeV neutrons.

Considerable advances in describing the angular distributions of fragments originating from resonance-neutron-induced fission of oriented nuclei were recently made by Furman *et al.* [4], who relied on the microscopic theory of Barabanov and Furman and who were able to perform a channel analysis of ^{235}U fission in the neutron-energy range from 0.025 to 20 eV. However, a satisfactory fit to data on the anisotropy and partial spin cross sections required invoking 24 adjustable parameters. Among other things, it was established in [4]—and the authors of that study deem that this is an important conclusion—that, in describing the fine structure of the energy dependence of the anisotropy factor, the interference contribution of the $I = J \pm 1/2$ states proves to be sizable.

2. *P*-ODD CORRELATIONS IN BINARY FISSION

Intensive searches for the admixture of weak internucleon potential in nuclear forces were performed in the late 1950s and the early 1960s. In this connection, Vladimirsky and Andreev [6] proposed investigating a *P*-odd correlation in the spontaneous fission of polarized nuclei. They assumed that, owing to nucleons with high angular momenta, the nucleus on the verge of fission has a mirror-asymmetric (pearlike) deformation [7]; because of parity nonconservation, the momentum of either the light or the heavy fragment can be oriented along the spin of the fissile nucleus. That article stimulated experiments aimed at seeking and studying the following *P*-odd correlation in ^{235}U fission induced by polarized thermal neutrons:

$$W(\theta) = \text{const} \cdot (1 + \alpha \mathbf{S} \cdot \mathbf{P}_{\text{LF}}) \longrightarrow 1 + \alpha \cos\theta. \quad (1)$$

Here, $\mathbf{S}$ is a unit vector along the polarization of the neutrons, $\mathbf{P}_{\text{LF}}$ is a unit vector along the momentum of the light fragment, θ is the angle between the above two unit vectors, and α is the correlation coefficient. By that time, Abov *et al.* [8] had already observed a *P*-odd correlation in the radiative capture of polarized thermal neutrons by ^{113}Cd nuclei. In view of the degree of parity nonconservation in the compound nucleus ^{236}U, a still

1063-7788/00/6308-1337$20.00

greater effect was therefore expected in the fission process, provided that there was no suppression factor (for example, a barrier factor [6]) in this process.

Indeed, the effect was discovered [9]. The correlation coefficient α proved to be on the same order of magnitude as that in the radiative capture of polarized thermal neutrons [8, 10]. Before long, similar *P*-odd-correlation effects were discovered in the fission of ^{239}Pu [11] and ^{233}U [12] nuclei. Thus, it turned out that the group of light (or heavy) fragments, which consists of many various nuclei formed in various final states of the fission process (the number of such states is estimated to be on the order of 10^8), behaves in the angular correlations like photons of a certain nuclear transition. According to the theory of angular correlations, the coefficient α includes a factor whose sign and magnitude depends on the quantum numbers of the initial and the final state and on the characteristics of the particle itself. In applying this theory to the fission process, where it is necessary to perform summation over all final states, it is natural to expect a statistical suppression of the effect by a factor on order of $\sqrt{10^8}$. The observed effects could be explained within the unrealistic assumption of a 100% parity violation in the fission process, as this occurs in weak interaction. Upon statistical leveling, effects on the order of 10^{-4} could then be revealed.

However, an investigation of the neutron-energy dependence of the correlation coefficient in ^{239}Pu fission showed [13] that, in the neutron-energy interval as narrow as 0.3 eV, the correlation coefficient changed nearly by a factor of 3. It is clear that so sharp a dependence of the effect on the neutron energy can result only from the weak-interaction-induced mixing of opposite-parity levels in compound nuclei.

The angular asymmetry (1) arises owing to the interference of orbital angular momenta that have opposite parities (in the case of electromagnetic transitions, it is the interference of electric and magnetic multipoles of the same order). This brings about the natural question of how a parity-mixed compound state can lead to the interference of orbital angular momenta of fragments characterized by opposite parities. The answer was provided by Sushkov and Flambaum [14]. In Bohr's concept of transition states in a severely deformed cold nucleus, they replaced the wave function of a symmetric dumbbell by the wave functions of a mirror-asymmetric nucleus (pearlike shape). The rotational levels of such a nucleus are parity-split into doublets, the intrinsic nuclear wave functions in the split states being identical—the only difference is that the nucleus rotates in opposite directions in the doublet components. As a result, the transitions from opposite-parity states into the same final state proceed with equal amplitudes, but the orbital angular momenta of the fragments differ by unity. It is the interference of these amplitudes that leads to the angular asymmetry (1).

3. *P*-EVEN ANGULAR CORRELATIONS IN BINARY FISSION

Obviously, the above semiclassical mechanism of the interference between the orbital angular momenta of the fragments is applicable to the case where the parity-mixed states of a compound nucleus are formed as the result of the interference of *s* and *p* waves in neutron capture. Sushkov and Flambaum considered such correlations as well. In the capture of slow polarized neutrons by unpolarized nuclei, the interference of *s* and *p* waves in the input channel generates the following correlation in the output channel:

$$W = \text{const} \cdot \left\{ 1 + \sum_{j = 1/2,\, 3/2} b(\mathbf{P}_n \cdot \mathbf{P}_{\text{LF}} \cos\varphi - \mathbf{P}_{\text{LF}} \cdot [\mathbf{P}_n \times \mathbf{S}]\beta_j \sin\varphi) \right\}. \quad (2)$$

Here, *b* is a coefficient dependent on the quantum numbers of the levels of the compound nucleus that are involved in the interference, on their energies, on the partial neutron and fission widths, on the full widths, on the *K* value and the spin of the target nucleus, and on the neutron energy; $\mathbf{P}_n$ is a unit vector in the neutron-momentum direction; φ is the relative phase of the amplitudes of the fission processes occurring from the opposite-parity states; and $\beta_j = 1$ for $j = 1/2$ and $\beta_j = -1/2$ for $j = 3/2$. A similar correlation can arise in any other reaction of the $a + A \longrightarrow B + b$ type.

The first term in the summand on the right-hand side of (2) is the forward–backward asymmetry in the angular distribution of the light fragments with respect to the neutron momentum, while the second term is the left–right asymmetry with respect to the plane spanned by the vectors $\mathbf{S}$ and $\mathbf{P}_n$.

The effect of the left–right asymmetry in the angular distribution of particle *b* with respect to the plane spanned by the vector of the polarization of particle *a* and the vector of its momentum is well known in nuclear physics. Even in the first experiments that studied parity violation [8–12], special test measurements of angular correlations of the type (2) were performed to verify that the observed asymmetry is not an instrumental effect determined by such a correlation that is associated with an insufficiently precise symmetry of the facility used. Later on, special experiments performed by a group headed by Lobashev revealed left–right asymmetry in the angular distribution of the light fragments originating from ^{233}U and ^{239}Pu fission induced by polarized thermal neutrons [15]. The asymmetry coefficients proved to be on the order 10^{-4} (2 to 3 units). According to the theoretical estimates from [14], the coefficient *b* is expected to be about *kR*, a quantity equal to 3×10^{-4} for thermal neutrons. Thus, the excellent agreement between the theory and the data validates the Sushkov–Flambaum model. The first mea-

surement of the forward–backward asymmetry was reported in [16].

For the case where only two levels of opposite parities are mixed (two-level approximation), Bunakov and Gudkov [17] explicitly obtained the coefficients for the *P*-even and *P*-odd correlations as functions of the neutron energy. A global analysis of data on the energy dependences of the *P*-odd asymmetry, the left–right asymmetry, and the forward–backward asymmetry makes it possible, in principle, to determine the unknown parameters of participant resonances and the effective matrix element of the weak nucleon–nucleon interaction in the nucleus.

It is worth noting that the forward–backward asymmetry can of course appear in a nuclear-fission processes (or any other $2 \longrightarrow 2$ reaction) not only necessarily induced by thermal neutrons. Attempts at observing this effect (which distinguishes light and heavy fragments, because the coefficients for them must be of opposite signs) in the fission process induced by fast neutrons have been made since the early days of fission physics [18], but they have been futile. This comes as no surprise, because an almost complete set of partial waves interferes in the fission process induced by fast neutrons—the averaging of the effect over a large number of resonances with various spins in the input channel is expected to smooth it out for statistical reasons.

4. *P*-ODD ANGULAR CORRELATIONS IN TERNARY FISSION

By ternary nuclear fission, physicists do not usually imply true fission into three fragments of close masses. According to common consensus, it is a process where disintegration into two fragments is accompanied by the emission of a light charged particle. In 90% of cases, this is a long-range alpha particle, whose angular distribution (Gaussian distribution with a mean angle of 82° with respect to the light-fragment momentum) suggests that it was produced in between the two fragments. The relative probability of ternary fission is about 0.2%. There are many models describing ternary fission, but none of these relates this process to the properties of fission channels—within these models, it is assumed that alpha-particle emission occurs only at the stage of scission of the neck connecting the two would-be fragments. On this basis, it may seem that the Sushkov–Flambaum mechanism governing the formation of the angular distributions of fragments has nothing to do with the angular distributions of alpha particles from ternary fission. Indeed, measurements of the *P*-odd asymmetry in the emission of fragments of ^{233}U and ^{239}Pu ternary fission induced by cold polarized neutrons (see [19] and [20], respectively) showed no distinctions between the correlation coefficients (1) for ternary and binary fission processes. At the same time, measurement of the *P*-odd asymmetry in the angular distributions of alpha particles from ternary fission revealed [21] that such asymmetry, if any, is a few times less than that for the fragments. Since alpha particles are emitted predominantly in the direction of the light-fragment momentum (Coulomb-focusing effect), their angular distribution is expected to feature pseudo-*P*-odd asymmetry, which is kinematically related to the *P*-odd asymmetry of the fragments. Obviously, this asymmetry must be less than the asymmetry of fragment emission by a factor of $(\cos 82^\circ)^{-1}$. The experimental accuracy is still insufficient for observing this effect.

5. *P*-EVEN ANGULAR CORRELATION IN TERNARY FISSION

Quite recently, a search experiment that employed a beam of cold polarized neutrons from the high-flux reactor installed at ILL (Grenoble) revealed a *P*-even, *T*-odd angular correlation in the ternary fission of the ^{233}U nucleus:

$$W = \text{const} \cdot (1 + D\mathbf{S} \cdot [\mathbf{P}_{\text{LF}} \times \mathbf{P}_\alpha]). \qquad (3)$$

Here, D is a correlation coefficient, while $\mathbf{P}_\alpha$ is a unit vector along the direction of the alpha-particle momentum. The measured value of the correlation coefficient is $(2.34 \pm 0.07) \times 10^{-3}$ [22]. It is clear that the experiment has detected left–right asymmetry in the angular distribution of alpha particles with respect to the plane spanned by the vectors $\mathbf{S}$ and $\mathbf{P}_{\text{LF}}$. The theory predicts the emergence of such a correlation owing to final-state interaction—for example, in the decay of a polarized neutron or in the reaction $(n, \gamma_1\gamma_2)$ with the detection of photons belonging to a specific cascade that accompanies the decay of a polarized compound nucleus. In the case of a correlation in ternary fission, however, the correlation coefficient must be summed over all final states; if there were no mechanism prohibiting the alternation of the signs of the correlation coefficients for various final states, the total correlation would vanish for statistical reasons. The data show that this is not the case, and this is a new challenge presented by the fission phenomenon.

6. CONCLUSION

The standard theory of angular correlations [23] has failed to describe the angular correlation of nuclear-fission fragments that is summed over many final states—it is next to impossible to isolate experimentally an individual final state. Bohr's idea that there exist a few transition states at the top of the fission barrier that govern angular correlations appeared to be seminal. This idea was put forth more than forty years ago, but nothing radically new has been invented since that time. Presently, the Bohr–Strutinsky–Sushkov–Flambaum (BSSF) mechanism makes it possible to reproduce almost the entire body of available data on angular correlations in binary fission. Since there must be no contradictions with quantum mechanics, it is mandatory to assume that the BSSF model determines, via some as-yet-unknown mechanism, the quantum numbers of all

final states of binary fission in such a way that the correlation coefficients prove to be of the same sign for all final states of the fragments. As to ternary fission, this process is much more involved than binary fission. Therefore, it is very unlikely that existing theoretical approaches (having to deal with the three-body problem in this case) could clarify, in the near future, the nature of the emergence and "survival" of three-vector correlations in ternary fission.

REFERENCES

1. V. M. Strutinsky, Zh. Éksp. Teor. Fiz. **30**, 606 (1956) [Sov. Phys. JETP **3**, 644 (1956)]; **39**, 781 (1960) [**12**, 546 (1960)].
2. A. Bohr, in *Proceedings of the International Conference on the Peaceful Uses of Atomic Energy, Geneva, 1955* (Academic, New York, 1956; Fizmatgiz, Moscow, 1958), Vol. 2.
3. A. A. Goverdovskii *et al.*, Yad. Fiz. **58**, 230 (1995) [Phys. At. Nucl. **58**, 188 (1995)].
4. W. I. Furman *et al.*, in *Proceedings of the Second International Workshop on Nuclear Fission and Fission Product Spectroscopy, 1998*, Ed. by G. Fioni *et al.*, p. 356.
5. A. L. Barabanov and W. I. Furman, in *Proceedings of the International Conference on Nuclear Data for Science and Technology, Gatlingburg, Tennessee, 1994*, p. 448.
6. V. V. Vladimirskiĭ and V. N. Andreev, Zh. Éksp. Teor. Fiz. **41**, 663 (1961) [Sov. Phys. JETP **14**, 475 (1962)].
7. V. V. Vladimirskiĭ, Zh. Éksp. Teor. Fiz. **32**, 822 (1957) [Sov. Phys. JETP **5**, 673 (1957)].
8. Yu. G. Abov *et al.*, Yad. Fiz. **1**, 479 (1965) [Sov. J. Nucl. Phys. **1**, 341 (1965)].
9. G. V. Danilyan *et al.*, Preprint No. 4, ITÉF (Institute of Theoretical and Experimental Physics, Moscow, 1977).
10. G. V. Danilyan *et al.*, Pis'ma Zh. Éksp. Teor. Fiz. **24**, 380 (1976) [JETP Lett. **24**, 344 (1976)].
11. G. V. Danilyan *et al.*, Pis'ma Zh. Éksp. Teor. Fiz. **26**, 197 (1977) [JETP Lett. **26**, 186 (1977)].
12. B. D. Vodennikov *et al.*, Pis'ma Zh. Éksp. Teor. Fiz. **27**, 68 (1978) [JETP Lett. **27**, 62 (1978)].
13. V. P. Alfimenkov *et al.*, Preprint No. 49, ITÉF (Institute of Theoretical and Experimental Physics, Moscow, 1981).
14. O. P. Sushkov and V. V. Flambaum, Usp. Fiz. Nauk **136**, 3 (1982) [Sov. Phys. Usp. **25**, 1 (1982)].
15. V. A. Vesna *et al.*, Pis'ma Zh. Éksp. Teor. Fiz. **31**, 704 (1980) [JETP Lett. **31**, 663 (1980)].
16. I. S. Guseva *et al.*, in *Proceedings of the International Symposium on Interaction of Neutrons with Nuclei, ISINN-2, Dubna, 1994*, p. 276.
17. V. E. Bunakov and V. P. Gudkov, Nucl. Phys. A **403**, 93 (1983).
18. A. N. Protopopov and V. P. Éĭsmont, At. Énerg. **4**, 194 (1958); **6**, 644 (1959).
19. A. V. Belozerov *et al.*, Pis'ma Zh. Éksp. Teor. Fiz. **51**, 10 (1990) [JETP Lett. **51**, 10 (1990)].
20. A. V. Belozerov *et al.*, Pis'ma Zh. Éksp. Teor. Fiz. **54**, 136 (1991) [JETP Lett. **54**, 132 (1991)].
21. A. Ya. Aleksandrovich *et al.*, Preprint No. 1057, LIYaF (Leningrad Nuclear Physics Institute, Leningrad, 1985).
22. P. Jesinger *et al.*, Yad. Fiz. **62**, 1723 (1999) [Phys. At. Nucl. **62**, 1608 (1999)].
23. S. Devons and L. J. B. Goldfarb, Handb. Phys. **XLII**, 362 (1957).

Translated by M. Kobrinsky

Physics of Atomic Nuclei, Vol. 63, No. 8, 2000, pp. 1341–1355. Translated from Yadernaya Fizika, Vol. 63, No. 8, 2000, pp. 1417–1431.

ON THE 85th ANNIVERSARY OF V.V. VLADIMIRSKY

Double-Beta Decay: Recent Advances in Experimental Studies

I. V. Kirpichnikov

Institute of Theoretical and Experimental Physics, Bol'shaya Cheremushkinskaya ul. 25, Moscow, 117259 Russia

Received January 18, 2000

Abstract—The current situation in experiments studying double-beta decay is surveyed. The amount of experimental information about the two-neutrino mode of the process has grown considerably over the last decade. The two-neutrino double-beta decay of ten nuclei (^{48}Ca, ^{76}Ge, ^{82}Se, ^{96}Zr, ^{100}Mo, ^{116}Cd, ^{128}Te, ^{130}Te, ^{150}Nd, and ^{238}U) was observed in direct and geochemical experiments. However, the main fundamental question—that of neutrinoless double-beta decay, which has not yet been recorded, although the sensitivity of present-day facilities featuring germanium detectors is higher than 10^{25} yr—remains open. The constraint on the effective Majorana mass on the basis of these results is $\langle m_\nu \rangle < (0.4–1.1)$ eV. Further advancements in searches for neutrinoless double-beta decays must rely on developing fundamentally new experimental facilities, since the potential of those that already exist has been exhausted to a considerable extent. © *2000 MAIK "Nauka/Interperiodica".*

1. INTRODUCTION

More than ten years ago, a group from the University of California at Irvine announced [1] a direct observation of two-neutrino double-beta decay—a process where the charge of the decaying nucleus increases by two units as the result of a simultaneous transformation of two neutrons into two protons that is accompanied by the emission of two electrons and two electron antineutrinos ($2\beta2\nu$ decay),

$$A(Z, N) \longrightarrow A(Z + 2, N - 2) + 2e^- + 2\bar{\nu}. \qquad (1)$$

By using an ionization chamber that operated in a magnetic field and which made it possible to observe and measure the main features of the tracks of two electrons emitted simultaneously from one point of a thin solid target [so-called time-projection chamber (TPC)—see Fig. 1], those authors recorded the double-beta decay process $^{82}\text{Se} \longrightarrow {}^{82}\text{Kr} + 2e^- + 2\bar{\nu}$ [1]. The resulting half-life of $T_{1/2} = 1.1 \times 10^{20}$ yr proved to be in good agreement with the value of $T_{1/2} = 1.4 \times 10^{20}$ yr obtained previously [2] from an analysis of the relative abundances of Kr isotopes in selenium-containing ores (geochemical method).

In 1990, a joint group of researchers from the Institute of Theoretical and Experimental Physics (ITEP, Moscow) and Yerevan Physics Institute (YERPHI, Yerevan) discovered the two-neutrino double-beta decay of ^{76}Ge nuclei and found that the corresponding half-life is $T_{1/2} \approx 1 \times 10^{21}$ yr [3]. That experiment employed an apparatus that was based on semiconductor detectors from enriched germanium and which was developed at ITEP for the first time ever (see Fig. 2) [4]. The sensitivity of the detector was improved in this way by two orders of magnitude, and this made it possible to observe the rarest radioactive decay discovered in direct measurements.

The possibility of two-neutrino double-beta decay was substantiated by Göppert-Mayer as far back as the mid-1930s [5]. From the outset, it was clear that the probability of this process is extremely low (Göppert-Mayer estimated the relevant half-life at $T_{1/2} \approx 10^{17}$ yr). According to modern concepts, the decay process in question is described in the second order of the Standard Model of weak interactions, so that the expected values of the relevant half-lives are not less than 10^{19} or 10^{20} yr. Therefore, it comes as no surprise that its discovery required many years of effort from experimental physicists (the first attempt at detecting double-beta decay was made in 1948 [6]).

Were it not for two additional circumstances, the predictions made in [5] could have remained without

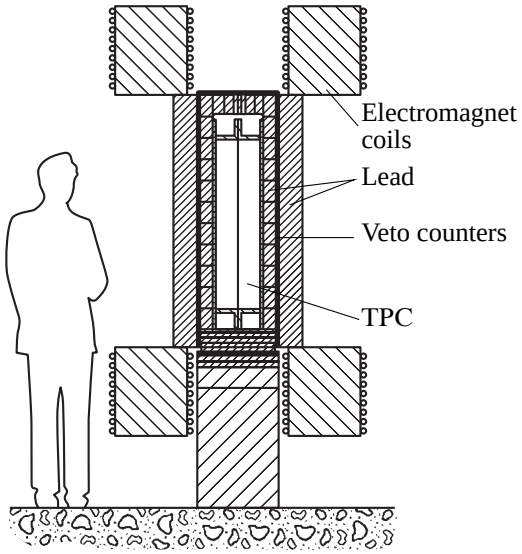

Fig. 1. Facility of the group from the University of California at Irvine [1].

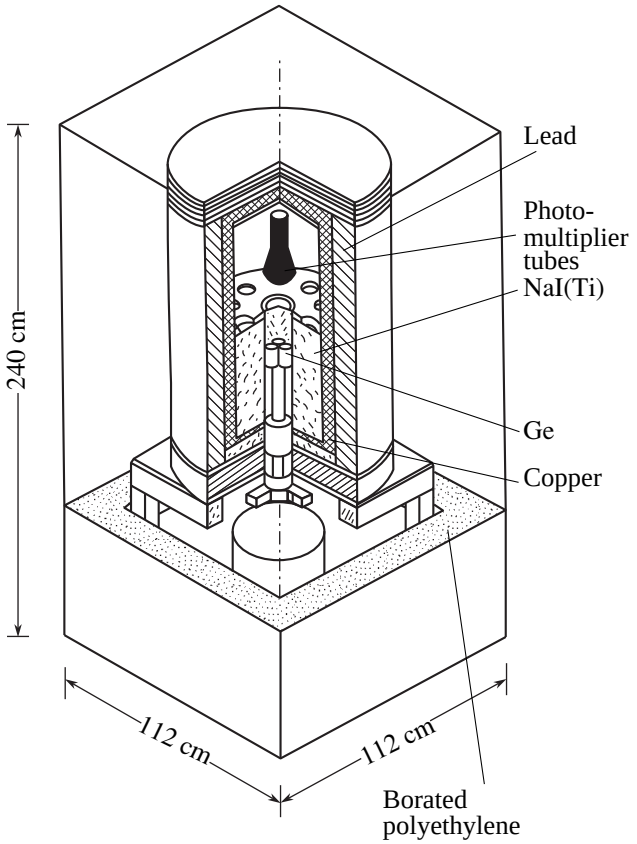

Fig. 2. Facility of the ITEP–YERPHI group.

experimental support so far. In 1939, Furry indicated [7] that, if the neutrino is a Majorana particle (its antiparticle is identical to the particle itself), double-beta decay can occur without neutrino emission:

$$A(Z, N) \longrightarrow A(Z + 2, N - 2) + 2e^{-}. \qquad (2)$$

In this neutrinoless mode, double-beta decay can be visualized as a two-step process: the first neutron that has decayed in a nucleus emits a neutrino, which is absorbed by the second neutron, transforming thereby into a proton. The neutrino here appears to be a virtual particle—only two electrons are produced in the final state; the probability of such a reaction exceeds the probability of reaction (1) by six to seven orders of magnitude.

Experiments did not confirm the above possibility. The first piece of evidence that ^{130}Te may undergo double-beta decay was obtained from an analysis of geochemical data [8], but the corresponding half-life proved to be as great as $T_{1/2} = 1.4 \times 10^{21}$ yr. Investigations along these lines gained additional momentum upon the discovery of maximal parity violation in weak decays [9]. It became clear that the small probability of neutrinoless double-beta decay may be explained by the opposite helicities of the emitted and the absorbed neutrino (a right-handed and a left-handed one, respectively). The discovery of such a process and an inquiry into it would provide physicists with a unique possibility for going beyond the Standard Model of weak interactions. Somewhat later, the hypothesis was put forth [10, 11] that neutrinoless double-beta decay may proceed via yet another mode, that involving a neutral boson (Majoron),

$$A(Z, N) \longrightarrow A(Z + 2, N - 2) + 2e^{-} + \chi^{0}. \qquad (3)$$

The discovery of neutrinoless double-beta decay would imply violation of the law of lepton-number conservation. This would require that the neutrino be a Majorana particle, have a nonzero rest mass, and possibly feature some amount of interaction via right-handed currents. The decay mode involving Majoron emission does not conserve the lepton charge, nor does it respect global $(B - L)$ symmetry (conservation of the difference of the numbers of baryons and leptons).

The possibility of estimating the rest mass of the neutrino as a candidate for particles constituting a significant part of dark matter in the Universe gave a strong incentive to searches for neutrinoless double-beta decay.

From this point on, investigations into double-beta decay—and above all, searches for its neutrinoless mode—have been considered as a potential source of unique physical information. Despite this, virtually no evidence that double-beta decay does indeed occur was obtained beyond geochemical measurements over the following 30 years. Apart from experiments with the aforementioned isotopes ^{82}Se and ^{130}Te, which were subjected to measurements many times [12], the detection of the double-beta decay of ^{128}Te [13–16] is worthy of note in this respect. However, the only positive result from direct measurements with ^{82}Se [17] was in a glaring contradiction with a geochemical analysis: the half-life of about 10^{19} yr found in [17] differed by more than one order of magnitude from the result presented in [2] ($T_{1/2} = 1.4 \times 10^{20}$ yr).

The situation has been changing rapidly since the appearance of the studies reported in [1, 3]. Over a short period of time, direct experiments were able to detect the two-neutrino double-beta decay of ^{48}Ca [18], ^{100}Mo [19, 20], ^{116}Cd [21], ^{150}Nd [22, 23], and ^{238}U [24] (the last isotope was singled out by the radiochemical method). The double-beta decay of ^{96}Zr was discovered by the geochemical method [25] and was then confirmed by laboratory measurements [26]. Barabash *et al.* [27] reported on the observation of the two-neutrino double-beta decay of ^{100}Mo into an excited state of the final nucleus ^{100}Ru. Repeated measurements were performed with ^{76}Ge [28–30], ^{82}Se [31], ^{100}Mo [32, 33], and ^{116}Cd [34]. Presently, there are a few tens of experimental groups studying the problem of double-beta decay.

The accumulation of a vast body of experimental data referring to the two-neutrino mode of double-beta decay is the main outcome of the inquiries into the sub-

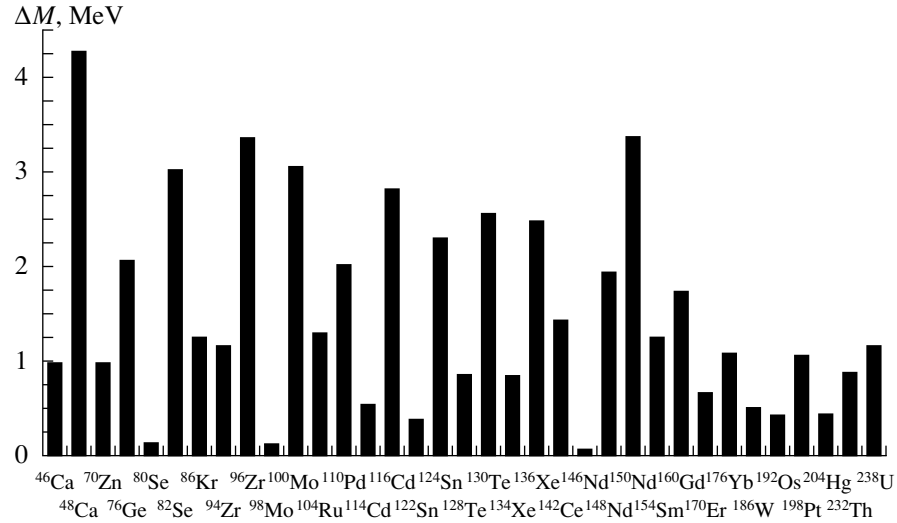

Fig. 3. Nuclei unstable with respect to $2\beta^-$ decay.

ject that have been performed over the last decade. No evidence for the neutrinoless mode has been revealed. An analysis of the results obtained in seeking this mode only yields constraints on constants that determine the probability of the process under various assumptions about its mechanisms—that is, on the Majorana mass of the neutrino, on right-handed admixtures, on the neutrino–Majoron coupling constants, and on some other relevant parameters.

The objective of the present article is to survey a general picture of the development of the problem and to highlight changes that have occurred over the past years in the mainstream lines of investigation in these realms. I am well aware that an unprecedentedly long history of the question, which has been studied over more than 60 years, resulted in the emergence of a number of review articles dealing with the general and particular issues of the theory of double-beta decay or with the current status of relevant experiments. The theoretical aspects of the problem have been repeatedly and thoroughly considered in the literature. There are also comprehensive studies covering almost all aspects of the modern theory on the subject [35–38]. Among the articles devoted to the experimental work in this field, the review article of Zdesenko [39], who provided rich information about the early stages of the development of the problem, and the more recent studies of Moe [40] and O.Ya. Zeldovich [41] are worthy of special note. Tretyak and Zdesenko [12] presented the most comprehensive compilation of tabular data from the studies that had been published by that time. The history of the problem was described in detail by Ya.B. Zeldovich [42] and Lazarenko [43].

Since only $2\beta^-$ decay has been recorded experimentally so far, the present article will deal with questions that are related to this version of the process in one way or another. There is, however, no fundamental difference between $2\beta^-$ and $2\beta^+$ decays. Some special features of the latter and prospects for inquiries into it will be considered separately.

2. GENERAL REGULARITIES

The energy deposited in $2\beta^-$ decay is equal to the atomic-mass difference between the initial and the final nucleus, $\Delta M = M(A, Z) - M(A, Z + 2)$. Two-neutrino double-beta decay is allowed in any version of the theory—the only obvious condition that must be satisfied for such a decay process to occur is $\Delta M > 0$. A second condition is dictated by the extremely small probability of the process: the beta decay of the parent nucleus must be forbidden or severely suppressed.

Thirty-five even–even "stable" isobars meeting the above two conditions are known [44] (see Fig. 3). The competing beta decays of these nuclei are forbidden because the ground states of the $A(Z + 1)$ isobars occur higher on the energy scale. This is not so only for the ^{48}Ca nucleus, but its beta decay is suppressed because of the large difference of the angular momenta between the initial nucleus and the intermediate nucleus ^{48}S ($J^\pi = 6^+$).

Two-neutrino double-beta ($2\beta^-2\nu$) decay. The relevant half-life can be represented as [36]

$$\left(T_{1/2}^{2\nu}\right)^{-1} = F^{2\nu}\left|M^{2\nu}\right|^2 \cong F^{2\nu}\left|M_{\mathrm{GT}}\right|^2,$$

where $F^{2\nu}$ is the reaction phase space, while M_{GT} is the Gamow–Teller matrix element for the transition from the 0^+ state of the $A(Z, N)$ nucleus to one of the final states of the $A(Z + 2)$ nucleus.

Neutrinoless double-beta decay. The most general expression for the probability of the neutrinoless mode of double-beta decay induced by a light neutrino with a

Table 1

Nucleus	Q, keV	$F^{2\nu}\times10^{21}$, $\mathrm{yr}^{-1}\,\mathrm{MeV}^2$	$F^{0\nu}\times10^{13}$, $\mathrm{yr}^{-1}\,\mathrm{fm}^2$	$F^{M}\times10^{15}$, $\mathrm{yr}^{-1}\,\mathrm{fm}^2$
^{48}Ca	4271	10490	49.06	303.1
^{76}Ge	2041	34.70	6.697	12.60
^{82}Se	2995	1151	30.63	108.8
^{100}Mo	3034	2502	57.60	216.1
^{128}Te	868	0.2245	2.701	1.451
^{130}Te	2533	1270	66.40	194.0
^{136}Xe	2479	1275	72.79	207.3
^{150}Nd	3367	31370	345.2	1684

mass of up to a few MeV and by right-handed currents has the form

$$(T_{1/2})^{-1} = C_{mm}(\langle m_\nu\rangle/m_e)^2 + C_{\eta\eta}\langle\eta\rangle^2 + C_{\lambda\lambda}\langle\lambda\rangle^2 + C_{m\eta}(\langle m_\nu\rangle/m_e)\langle\eta\rangle + C_{m\lambda}(\langle m_\nu\rangle/m_e)\langle\lambda\rangle + C_{\eta\lambda}(\langle m_\nu\rangle/m_e)\langle\eta\rangle\langle\lambda\rangle,$$

where $\langle m_\nu\rangle$ is the effective neutrino mass averaged over light neutrino states, $\langle\eta\rangle$ and $\langle\lambda\rangle$ are the effective values obtained by similarly averaging the coupling constants for right-handed currents, and the coefficients C take into account matrix-element and phase-space contributions. In the majority of models that consider neutrinoless double-beta decay, the mass term is dominant. Setting $\langle\eta\rangle = \langle\lambda\rangle = 0$, we obtain

$$(T_{1/2})^{-1} = (\langle m_\nu\rangle/m_e)^2 F^{0\nu}\left|M_{\mathrm{GT}} - M_{\mathrm{F}}\right|^2 = (\langle m_\nu\rangle/m_e)^2 F^{0\nu}\left|M^{0\nu}\right|^2.$$

Neutrinoless double-beta decay involving Majoron emission. The half-life is given by

$$(T_{1/2})^{-1} = \left|\langle g_{\nu\chi}\rangle\right|^2 F^{M}\left|M_{\mathrm{GT}} - M_{\mathrm{F}}\right|^2,$$

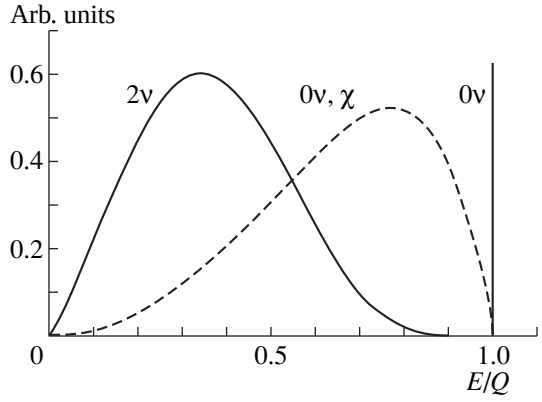

Fig. 4. Total-energy spectrum of electrons from $2\beta^-$ decay for various decay modes.

where $\langle g_{\nu\chi}\rangle$ is the averaged neutrino–Majoron coupling constant and where the matrix element has the same form as in the preceding case, provided that heavy-neutrino exchanges are disregarded.

The simplest (triplet) Majoron model was ruled out by a precise measurement of the Z^0-boson width [45]. In order to sidestep this constraint, Berezhiani *et al.* [46] and Burgess and Cline [47] considered more involved versions. A model featuring the emission of two or more Majorons was proposed by Mohapatra and Takasugi [11].

The phase-space volume can be calculated precisely. Table 1 presents the values of $F^{2\nu}$, $F^{0\nu}$, and F^M from [37] for $0^+ \longrightarrow 0^+$ transitions.

It is worth noting that the different phase-space factors depend differently on the decay energy: $F^{2\nu} \sim Q^{11}$, $F^{0\nu} \sim Q^5$, and $F^M \sim Q^7$.

The spectrum of the total energy E of two product electrons (see Fig. 4) provides the most important criterion for experimentally separating the different modes of double-beta decay. The $A(Z+2)$-isobar yield summed over all decay modes is determined on the basis of the geochemical method.

3. EXPERIMENTAL SITUATION

The two-neutrino double-beta decay of ten nuclei (^{48}Ca, ^{76}Ge, ^{82}Se, ^{96}Zr, ^{100}Mo, ^{116}Cd, ^{128}Te, ^{130}Te, ^{150}Nd, and ^{238}U) was observed in direct and geochemical experiments.

Table 2 displays the results of the most important successful experiments. Information about those experiments that recorded the double-beta decay of a given isotope for the first time is boldfaced. Also presented for geochemical measurements is the maximal scatter of the results obtained by different authors (according to data from [12]).

Among the results coming from direct measurements, the longest half-life was recorded for the ^{76}Ge isotope ($T_{1/2} \approx 10^{21}$ yr). For the other nuclei under discussions, the observed half-life values of $T_{1/2} \approx 10^{19}$–10^{20} yr correspond to the actual sensitivity of the experimental facilities used. The ^{128}Te isotope, whose lifetime was estimated by the geochemical method ($T_{1/2} \approx 10^{24}$ yr), is the most long-lived radioactive source discovered on the Earth.

The scatter of the results obtained by the geochemical method and in direct measurements is quite significant, which is associated both with the extreme smallness of the measured effect and with methodological difficulties peculiar to each of the experimental procedures in use. Special features of these procedures will be described below.

4. GEOCHEMICAL METHOD

The geochemical method consists in determining the abundances of beta-decay products accumulated

Table 2

Nucleus	$T_{1/2}$, yr	Experimental group	Experimental procedure
^{48}Ca	$(4.3^{+2.4+1.4}_{-1.1-1.4}) \times 10^{19}$	**UCI/IAE 1997** [18]	**TPC**
^{76}Ge	$(9^{+1}_{-1}) \times 10^{20}$	**ITEP/YERPHI 1988/1990** [2]	**Semiconductor germanium detector**
	$(9.2^{+0.7}_{-0.5}) \times 10^{20}$	ITEP/PNL/USC/YERPHI 1991 [28]	Semiconductor germanium detector
	$(1.42^{+0.03+0.13}_{-0.03-0.13}) \times 10^{21}$	Heidelberg/Moscow 1995 [29]	Semiconductor germanium detector
	$(1.77^{+0.01+0.12}_{-0.01-0.12}) \times 10^{21}$	Heidelberg/Moscow 1997 [30]	Semiconductor germanium detector
^{82}Se	$(1.4^{+0.2}_{-0.2}) \times 10^{20}$	**1969** [3]	**Geochemistry**
	$(1.0–2.8) \times 10^{20}$	[12]	Geochemistry
	$(1.08^{+0.28}_{-0.06}) \times 10^{20}$	UCI/LLL 1987/1992 [1]	TPC
	$(0.83^{+0.10+0.07}_{-0.10-0.07}) \times 10^{20}$	NEMO 1998 [31]	Counting spectrometer
^{96}Zr	$(3.9^{+0.9}_{-0.9}) \times 10^{19}$	**Tokyo 1993** [25]	**Geochemistry**
	$(2.1^{+0.8}_{-0.4}) \times 10^{19}$	NEMO 1998 [26]	Counting spectrometer
^{100}Mo	$(1.15^{+0.30}_{-0.20}) \times 10^{19}$	**Osaka 1991** [19]	**Counting spectrometer**
	$(1.15^{+0.34}_{-0.08}) \times 10^{19}$	**UCI/LLL 1991** [20]	**TPC**
	$(0.95^{+0.04+0.09}_{-0.04-0.09}) \times 10^{19}$	NEMO 1995 [32]	Counting spectrometer
	$(0.68^{+0.05+0.07}_{-0.05-0.07}) \times 10^{19}$	UCI 1997 [33]	TPC
^{116}Cd	$(2.2^{+0.7}_{-0.4}) \times 10^{19}$	**Osaka 1994** [21]	**Counting spectrometer**
	$(3.75^{+0.35+0.21}_{-0.35-0.21}) \times 10^{19}$	NEMO 1995 [34]	Counting spectrometer
^{128}Te	$(1.5^{+0.2}_{-0.2}) \times 10^{24}$	**1975** [13]	**Geochemistry**
	$(1.4–7.7) \times 10^{24}$	[12]	Geochemistry
^{130}Te	1.4×10^{21}	**1950** [8]	**Geochemistry**
	$(0.6–3.1) \times 10^{21}$	[12]	Geochemistry
^{150}Nd	$(1.9^{+0.66+0.39}_{-0.39-0.39}) \times 10^{19}$	**ITEP/INR 1993/1994** [22]	**TPC**
	$(0.68^{+0.04+0.07}_{-0.04-0.07}) \times 10^{19}$	UCI/LLL 1997 [23]	TPC
^{238}U	$(2.0^{+0.6}_{-0.6}) \times 10^{21}$	**Chicago/SFI/LANL 1991** [24]	**Radiochemistry**

over a geological time in minerals containing potentially 2β-active elements. Basic results were obtained by determining the abundances of inert gases—^{82}Kr, ^{128}Xe, and ^{130}Xe isotopes—originating from the double-beta decay of ^{82}Se, ^{128}Te, and ^{130}Te in minerals containing selenium and tellurium. When such mineral were formed from a melt or from a solution, inert gases were removed almost completely. In this way, there arose necessary preconditions for discovering negligibly small amounts of decay products accumulated over the times of existence of the minerals.

For the first time, the geochemical method was successfully used in 1949 [8] to estimate the half-life of ^{130}Te. The result, $T_{1/2} = 1.4 \times 10^{21}$ yr, appeared to be the first evidence for the occurrence of the process. Many

subsequent measurements [12] did not change this estimate significantly. The $T_{1/2}$ values presented by different authors lie in the range between 6×10^{20} and 3×10^{21} yr. The mean values of the ^{130}Te half-life that were recommended on the basis of an analysis of the entire array of data are $(1.5–2.8) \times 10^{21}$ yr [48] and 0.8×10^{21} yr [49]. The large scatter of the results may be due to an insufficiently accurate determination of poorly controllable parameters, variations in the time of gas accumulation, and the possible reduction of gas abundances in geological rearrangements within periods following mineral formation.

Of particular interest is the investigation of the double-beta decay of ^{128}Te because, in this case, the two-neutrino mode is suppressed in view of a small energy release (868 keV). The recorded half-life values lie in the range $(1.4–7.7) \times 10^{24}$ yr [13–16], so that the decay of ^{128}Te is the rarest process detected so far. The scatter of the results can be attributed to factors inherent in geochemistry and to significant systematic uncertainties that are difficult to take into account because of the extreme smallness of the effect.

The first measurements of the ^{82}Se half-life were performed in 1969 [2]. The resulting half-life value of $T_{1/2} = 1.4 \times 10^{20}$ yr was then confirmed in a number of later experiments [12], although the scatter of the results is great in this case as well [$(1.0–2.8) \times 10^{20}$ yr]. The recommended values of the ^{82}Se half-life are 1.3×10^{20} yr [48] and 1.0×10^{20} yr [49].

In general, the geochemical method is insufficient for establishing the mechanism of double-beta decay, but the two tellurium isotopes in question stand out in this respect owing to noticeably different values of the energy release. The expected ratio of half-lives (^{130}Te/^{128}Te) is $(2–4) \times 10^{-4}$ for the two-neutrino mode and $(4–6) \times 10^{-2}$ for the neutrinoless mode, the phase-space ratios being 1.8×10^{-4} and 4.1×10^{-2}, respectively. By measuring the yields of ^{128}Xe and ^{130}Xe in a single experiment, we can suppress the main uncertainty in the geochemical method, poor knowledge of time of accumulation of decay products and poor knowledge of the rate of gas escape. The most precise value of this ratio, $(3.52 \pm 0.11) \times 10^{-4}$ [15, 50], is virtually coincident with the value computed for the two-neutrino mode. Thus, the observed effect can be associated with the two-neutrino mode of double-beta decay.

The only successful geochemical study that determined the abundance of a solid-state product of double-beta decay (^{96}Mo) was that in which measurements were performed with a ^{96}Zr sample [25]. A high concentration of uranium in the ore used made it possible to determine its age (1.7×10^9 yr) to quite a high precision, but this simultaneously increased the abundance of ^{96}Mo because of spontaneous decay. The contribution of spontaneous fission was determined by means of measurements with a neutron source. The value of $T_{1/2} = (3.9 \pm 0.9) \times 10^{19}$ yr obtained in this way for the ^{96}Zr half-life can be considered as a first approximation.

The discovery of the double-beta decay of ^{238}U, with the relevant half-life being $(2.0 \pm 0.6) \times 10^{21}$ yr [24], demonstrated the potential of the radiochemical method. As in a geochemical analysis, the method consists in determining the abundance of a decay product (^{238}Pu in the case being discussed) accumulated in an ore sample containing a 2β-active isotope. The daughter nucleus ^{238}Pu decays, with a half-life of 88 yr, emitting a 5.6-MeV alpha particle. Owing to this, the number of product nuclei can be measured in the case of comparatively small accumulation times, provided that they are known to a high precision. Unfortunately, the possibilities for repeating an experiment are severely limited because of large amounts of ^{238}Pu in the atmosphere and on the Earth's surface due to atomic-weapon tests. Turkevich *et al.* [24] were able to perform measurements with 8.5 kg of uranyl nitrate that was stored underground for 33 years.

5. DIRECT MEASUREMENTS

Any facility intended for studying double-beta-decay process must ensure extremely low levels of both intrinsic and extrinsic backgrounds. In designing such facilities, use is made of thoroughly selected materials characterized by as low a level of intrinsic radioactivity as possible (contamination with ^{40}K, ^{238}U, and ^{232}Th of no more than 10^{-8}–10^{-10} g/g). The facilities in question are surrounded by a strong passive shielding (10–40 cm of lead) and are equipped with a veto system for suppressing a cosmic background. Some facilities operate in low-background underground laboratories (Baksan, Gran Sasso, Saint Gothard, Cafranc), where the cosmic component of the background is reduced to a minimum.

A simultaneous emission of two electrons from one point of the target is a signature common to all modes of double-beta decay. This is used as a criterion in all the facilities, with the exception of germanium detectors. The total energy of these two electrons is the main measured quantity, the character of the total-energy spectrum being determined by a specific double-beta-decay mode (see Fig. 4). The shape of the spectrum imposes additional constraints on the parameters of the experimental facility chosen to meet the needs of the main problem to be solved.

For example, searches for the two-neutrino decay mode require reducing the background level to the lowest possible extent over a wide energy range, since the total-energy spectrum of electrons represents a wide bell with a maximum at $E \approx Q/3$. For the majority of nuclei whose two-neutrino double-beta decay was detected in direct experiments (^{48}Ca, ^{82}Se, ^{96}Zr, ^{100}Mo, ^{150}Nd), the values of Q lie between 3 and 4 MeV. Hence, it is necessary to perform a thorough analysis of the origin of backgrounds from energies not higher than 0.8–1.0 MeV. In searches for two-neutrino double-beta decays in direct experiments, the greatest success was

achieved by the groups who used tracking detectors of various types.

The first observations of the decays of ^{82}Se [1], ^{48}Ca [18], ^{100}Mo [20], and ^{150}Nd [22, 23] were made with the aid of a TPC (a drift ionization chamber in a magnetic field), which permits a full reconstruction of the geometry and kinematics of each event. For the first time, a TPC was successfully used in the study of UCI–LLL [1] to detect the two-neutrino double-beta decay of ^{82}Se. Later on, the same facility and a TPC that was developed at ITEP [22] were successfully used in searches for the two-neutrino double-beta decay of ^{48}Ca, ^{100}Mo, and ^{150}Nd.

The principle of TPC operation can be illustrated by considering the example of the facility used by the UCI–LLL group (see Fig. 1). The hub of the apparatus is a cylindrical (octagonal) planar ionization chamber of mean diameter 85 cm and height about 25 cm, which operates in a magnetic field of strength 700 G (Fig. 5). The chamber is filled with a mixture of 93% He and 7% C_3H_8 at atmospheric pressure. A film source having a thickness of 7 mg/cm^2 and containing 14 g of Se (97% ^{82}Se) divides the volume of the chamber in height into two equal parts, so that there arise two drift gaps. Over the entire areas of the two endfaces of the chamber, systems of parallelly stretched field wires of diameter 0.075 mm each are arranged at distances 10 cm from the source, the pitch between the wires being 2.5 mm. A voltage of –700 V with respect to this system is applied to the source, ensuring the velocity of ionization-track drift about 5 mm/μs over the entire volume of the chamber. Two planes of a coordinate wire chamber—the anode plane, with a pitch of 5 mm between the wires, and the cathode plane, with a pitch of 2.5 mm—are mounted immediately behind the field wires, the wires of the cathode plane being stretched orthogonally to the anode and field wires. The voltage drop across the anode–cathode gap is 1500 V. Each wire of the anode system has its own amplifier and discriminator; the cathode wires are connected in pairs. The wire chambers determine the coordinates of the tracks in the (X, Y) plane versus time, the accuracy of this determination being 5 mm in each coordinate. For the chosen drift velocity (see above), the total time it takes for the track to travel the distance from the source to the coordinate chamber is 20 μs. This time interval is partitioned into 20 subintervals of duration 1 μs each, and 20 coordinates in the Z axis are fixed for each track to the same accuracy of 5 mm. Thus, the spatial (helical) pattern of each track is fully reconstructed in the chamber to within 5 mm in each of the coordinates. It is worth noting that the term "time projection chamber" (recall that it is abbreviated by convention as TPC) reflects the method for determining the third coordinate of the tracks.

In order to single out the possible cases of double-beta decays, the condition of a simultaneous emission of two electrons from one point of the source was

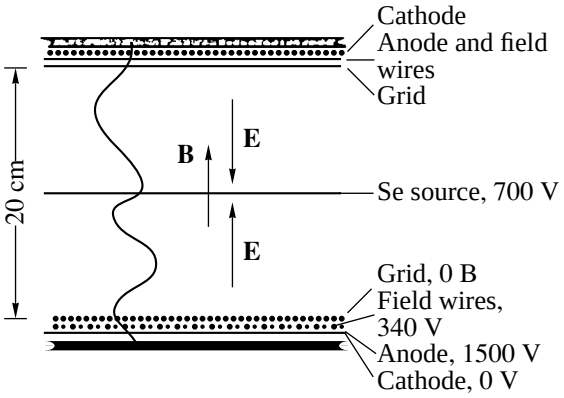

Fig. 5. Schematic view of the TPC from the facility of the experiment reported in [1].

imposed for each of the two drift gaps; after that, a full kinematical analysis of each event was performed. It was shown that the conventional beta decay of nuclei from the uranium and thorium families was the most hazardous source of background mimicking double-beta decay. This background was efficiently suppressed, since the daughter nuclei from the decay of ^{214}Bi and ^{212}Bi isotopes belonging to these families produced beta–alpha chains that could easily be isolated by a TPC.

Owing to the possibility of a thorough event-by-event analysis and to a low level of the intrinsic background in the apparatus, the UCI–LLL group was able to achieve a sensitivity level of 10^{20} yr, which was necessary for disclosing the reasons behind the discrepancy between the results of the geochemical ([2]) and the direct ([17]) determination of the ^{82}Se half-life. A similar sensitivity was achieved with the ITEP facility [22]. This created preconditions for a further successful application of TPCs in experiments that performed searches for the double-beta decays of ^{48}Ca, ^{100}Mo, and ^{150}Nd, whose half-lives proved to be somewhat shorter (10^{19}–4×10^{19} yr).

The counting track detectors ELEGANT-5 and NEMO were successfully used to detect the two-neutrino double-beta decays of ^{100}Mo [19] (this was done simultaneously in [20]) ^{116}Cd [21], and ^{96}Zr [26] in direct measurements.

The operation of the last two detectors was based on the same principles. A thin source under investigation was placed in between two wire volume coordinate chambers, which fixed the tracks of two electrons that were ejected simultaneously from the same point of the source in opposite directions. The energy of each electron was measured by plastic scintillators. The measurements were performed simultaneously with two sources. Of these, one was manufactured from a material highly enriched in the isotope being investigated, while the other had a natural isotope content. The effect of two-neutrino double-beta decay was singled out by comparing the total-energy spectra of electrons for the

two sources. That the intrinsic-background level was low in either source was a crucial circumstance that rendered this procedure quite efficient.

Despite its obvious merits, a TPC facility is disadvantageous in that it is difficult to study large amounts of specific isotopes with such facilities. The same plagues the results of measurements with counting track detectors. A high-pressure TPC used to study the double-beta decay of ^{136}Xe [51] is free from this flaw. As a working gas, this facility employs Xe enriched in ^{136}Xe to 62.5% and pumped at a pressure of 5 atm; 180 l of the chamber useful volume contain 24.2 moles of the active isotope. Double-beta-decay tracks are selected by using their specific shape—namely, the shape that is characterized by a continuous trace with a sharp increase in ionization at both ends because of the moderation of the electrons. The sensitivity of the apparatus to two-neutrino double-beta decay is 4×10^{20} yr, and Luescher *et al.* claim that a significant portion of the experimental spectrum is associated precisely with this process. This gives sufficient ground to believe that the observation of the two-neutrino double-beta decay of ^{136}Xe with a half-life of $T_{1/2} \approx 10^{21}$ yr will be announced in the near future.

The semiconductor germanium detectors that were used in discovering and studying the two-neutrino double-beta decay of ^{76}Ge gave no way to analyze event kinematics. Nonetheless, the highest sensitivity among the results obtained in direct measurements, $T_{1/2} \approx 10^{21}$ yr, was achieved precisely for ^{76}Ge. The use of detectors that had a weight of a few kilograms and which were manufactured from a highly enriched active isotope (87% ^{76}Ge), together with a nearly 100% event-detection efficiency, was the main factor that ensured this advantage. A high purity of semiconducting germanium was also of paramount importance for this.

A group of experimenters from ITEP and YERPHI that was the first to employ detectors from enriched germanium and which discovered in this way the two-neutrino double-beta decay of ^{76}Ge [3] separated the effect by comparing the spectra from detectors manufactured from enriched and natural germanium. Three germanium detectors—two from enriched germanium (of total weight 1.2 kg) and one of natural germanium—were mounted within the same cryostat close to one another, which ensured identical levels of the extrinsic background for them (Fig. 2). This permitted avoiding a computational reconstruction of this background, whose main component in germanium detectors is gamma radiation from the structural materials of the apparatus.

The more recent studies reported in [28–30] relied on a computational procedure, because a considerable reduction of the absolute level of the radiation background rendered this procedure more secure.

To conclude this section, we recall that Barabash *et al.* [27] reported the observation of the $2\beta2\nu$ process $^{100}\mathrm{Mo} \longrightarrow {}^{100}\mathrm{Ru}^*(0_1^+, 1130\ \mathrm{keV})$ followed by the emission of two cascade gamma rays of energies 539 and 591 keV. Those measurements were performed with powder ^{100}Mo by using several gamma-ray detectors made from germanium. A value of $T_{1/2} \approx 10^{21}$ yr (10^{19} yr for the transition to the ground state) was obtained there for the half-life.

The neutrinoless mode of double-beta decay was sought at the same facilities and with the aid of the same methods as those used in studying the processes of two-neutrino double-beta decay. Since the neutrinoless modes of double-beta decay have not yet been discovered, an analysis of the results obtained in seeking them only constrains the values of the parameters that determine the probability of the process in various theoretical models. The level of these constraints depends on the sensitivity of the experiments seeking the decay modes in question and on the accuracy in computing the relevant nuclear matrix elements. Prior to discussing available experimental data, it is therefore reasonable to assess the accuracy of the calculations performed for those matrix elements.

6. CALCULATION OF MATRIX ELEMENTS

The only indirect possibility for estimating the accuracy in computing relevant matrix elements consists in comparing experimental data with the results obtained by calculating the probability of two-neutrino double-beta decay, since the methods used to evaluate $M^{0\nu}$ and $M^{2\nu}$ are quite similar.

Two basic models—the shell model of the nucleus [52–56] and various versions of the quasiparticle random-phase approximation (QRPA) [57–62]—were used in computing nuclear matrix elements. Over the past few years, the shell model has become more appropriate for such calculations owing to evolving codes that make it possible to use vast bases of wave functions and to invoking the Monte Carlo method in the case of heavy nuclei. Nevertheless, it is rather difficult to employ this model for a wide range of nuclei because the relevant calculations are very involved and cumbersome, so that QRPA calculations remain necessary.

The main difficulty in calculating the matrix elements for two-neutrino double-beta decay—both within the shell model and within the QRPA—stems from the fact that the $|M^{2\nu}|$ value extracted from experimental data proved to be one to two orders of magnitude less than the single-particle estimates. The point is that the large components of the wave functions are canceled almost completely; as a result, slight modifications to the nuclear structure lead to considerable changes in the results of the calculations. Within the QRPA, this implies a strong dependence of $M^{2\nu}$ on the quasiparticle coupling constant g_{pp}.

The predictive power of the original model versions [37, 57, 58] proved to be very poor. The matrix elements changed sign (see Fig. 6) at physically signifi-

cant coupling-constant values of $g_{pp} \approx 1$, which resulted in a sharp dependence of the decay probability on the adopted value of g_{pp} ("collapse" effect). Later on, model versions were developed that made it possible to smooth out this dependence to some extent, but the problem has yet to be solved conclusively [61].

The results of the calculations performed within various approximations are presented in Table 3, along with the measured half-lives (the presumed half-life of ^{136}Xe was estimated on the basis of results reported in [51]).

The predictions of the latest versions of the shell model [54, 55] are close to the measured half-life values, but these predictions have been obtained only for a small number of nuclei. Calculations within the QRPA were performed for almost all nuclei that are expected to be 2β-active [58, 59], but the agreement with experimental data is somewhat poorer (within a factor of about 3 for the matrix elements).

There is no direct correlation between the values of $M^{2\nu}$ and $M^{0\nu}$. The matrix element for two-neutrino double-beta decay is calculated by performing summation only over the virtual $J^\pi = 1^+$ states of the intermediate nucleus. In the neutrinoless mode of double-beta decay, summation must also be performed over states with different spin–parity values. Until recently, it was assumed that this smooths out the g_{pp} dependence of $M^{0\nu}$ and that the reliability of the calculation of $M^{0\nu}$ is higher for this reason. It was shown in [63], however, that the inclusion of ground-state proton–neutron correlations is of paramount importance in this case. The problem is still far from being resolved completely, and the most secure criterion of the accuracy in calculating $|M^{0\nu}|$ is provided by the scatter of the resulting half-life values (see Table 4). It should be noted that, for the probability of neutrinoless double-beta decay, the calculations on the basis of the maximally full shell model [55, 56] predict values falling significantly short of the results of the previous studies.

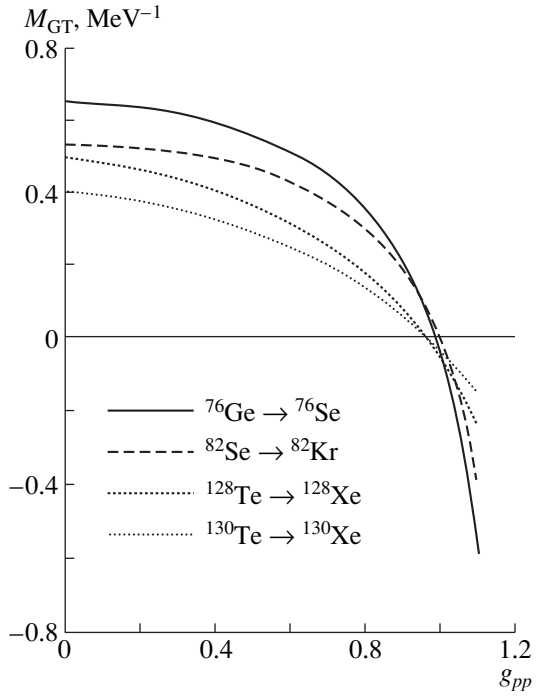

Fig. 6. Gamow–Teller matrix element as a function of the coupling constant g_{pp} [37].

Table 3. Experimental and calculated values of double-beta-decay half-lives ($T_{1/2}$, yr)

Nucleus	Experiment	Shell model		Quasiparticle random-phase approximation	
		[53]	[54, 55]*	[58]	[59]
^{48}Ca	4.3×10^{19}	2.9×10^{19}	5.5×10^{19}		
^{76}Ge	$(0.9–1.8) \times 10^{21}$	4.2×10^{19}	2.2×10^{21}	3.0×10^{21}	0.26×10^{21}
			3.6×10^{21}		
^{82}Se	$(0.8–1.4) \times 10^{20}$	2.6×10^{19}	5.0×10^{19}	1.1×10^{20}	0.85×10^{20}
			8.0×10^{19}		
^{96}Zr	$(2–4) \times 10^{19}$				2.0×10^{20}
^{100}Mo	$(0.7–1.2) \times 10^{19}$			0.13×10^{19}	3.6×10^{19}
^{116}Cd	$(2–4) \times 10^{19}$				1.5×10^{20}
^{128}Te	$(1.4–7.7) \times 10^{24}$	8.8×10^{22}		2.6×10^{24}	2.1×10^{23}
^{130}Te	$(0.8–3.1) \times 10^{21}$	1.7×10^{19}		0.18×10^{21}	7.9×10^{19}
^{136}Xe	$\sim 10^{21}$?		1.7×10^{21}	4.6×10^{21}	1.0×10^{21}
			2.0×10^{21}		
^{150}Nd	$(0.7–1.9) \times 10^{19}$			0.74×10^{19}	1.7×10^{19}
^{238}U	2.0×10^{21}			1.5×10^{23}	0.9×10^{21}

* Two estimates for the expected half-lives $T_{1/2}$ are presented in [55].

Table 4

Nucleus	Shell model		Various versions of the quasiparticle random-phase approximation			
	[52]	[55, 56]	[37]	[58]	[59]	[62]
^{48}Ca	8.8×10^{23}	$\cong 10^{25}$				
^{76}Ge	1.4×10^{24}	1.8×10^{25}	1.9×10^{24}	2.3×10^{24}	2.7×10^{24}	9.5×10^{24}
^{82}Se	2.1×10^{23}	2.4×10^{24}	6.1×10^{23}	6.0×10^{23}	1.9×10^{24}	
^{96}Zr				5.3×10^{23}		
^{100}Mo			2.3×10^{23}	1.3×10^{24}		2.6×10^{23}
^{116}Cd				4.9×10^{23}		6.9×10^{23}
^{128}Te	6.9×10^{24}		4.4×10^{23}	7.8×10^{24}	1.3×10^{25}	1.1×10^{25}
^{130}Te	3.2×10^{23}			4.9×10^{23}	7.2×10^{23}	
^{136}Xe		1.2×10^{25}		2.2×10^{24}	4.3×10^{24}	3.4×10^{24}
^{150}Nd				3.4×10^{22}	5.6×10^{22}	

Neutrinoless double-beta decay. The problem of the Majorana neutrino mass is an intriguing puzzle, and it is in the pursuit of it that attempts at detecting the $2\beta0\nu$ process have been made; therefore, it would be natural to classify various experiments according to the levels of constraints on $\langle m_\nu \rangle$.

Table 5 displays the most significant limits established experimentally for the half-lives in question and the resulting constraints on $\langle m_\nu \rangle$ (no right-handed currents are assumed). Three groups of constraints—one based on the latest version of the shell model [55] and two based on two QRPA versions [58, 62]—are singled out there.

Figure 7 gives a clear idea of the relative accuracy achieved in the measurements with the various nuclei [15, 16, 51, 64–72] and of the prospects for strengthening the constraints on $\langle m_\nu \rangle$ through the improvement of the experimental accuracy. There, the maximal scatter of the results of the calculations from [37, 52–56, 58–62, 72–78] was taken for a measure of the uncertainty in the theoretical estimates of $T_{1/2}^{0\nu}$.

Table 5

Nucleus	$T_{1/2}$, yr (experiment)		Upper limit $\langle m_\nu \rangle$, eV		
			[55]	[58]	[62]
^{76}Ge	$\geq 1.6 \times 10^{25}$	[64, 65]	$\leq\leq 1.07$	≤ 0.38	≤ 0.77
^{82}Se	$\geq 2.7 \times 10^{22}$	[68]	≤ 9.4	≤ 4.7	–
^{100}Mo	$\geq 5.2 \times 10^{22}$	[65]	–	≤ 4.9	≤ 2.2
^{116}Cd	$\geq 3.2 \times 10^{22}$	[66]	–	≤ 3.9	≤ 4.6
^{128}Te	$\geq 2.2 \times 10^{24}$	[16]	–	≤ 1.9	≤ 2.2
	$\geq 7.7 \times 10^{24}$	[15]	–	≤ 1.0	≤ 1.2
^{130}Te	$\geq 5{,}6 \times 10^{22}$	[67]	–	≤ 2.9	–
^{136}Xe	$\geq 4.3 \times 10^{23}$	[51]	≤ 5.2	≤ 2.2	≤ 2.8

The most stringent constraint on $\langle m_\nu \rangle$ from the measurements with germanium detectors is determined by the extremely high limit on the half-life from [64, 65]. The advantage of germanium detectors in searches for neutrinoless double-beta decay becomes obvious if we compare the sensitivities of the different experiments by using the simple relation

$$\lim T_{1/2} \approx k(M\varepsilon t/B\Delta E)^{1/2},$$

where M is the target mass, k is the abundance of the active isotope, ε is the efficiency of the detector, B is the background level [measured in event/(keV kg d)], ΔE is the detector resolution (in keV), and t is the time of measurements.

The high energy resolution of germanium detectors, $\Delta E = 4$ keV (FWHM), even in the case of long-term data accumulation ($\Delta E/E = 0.5\%$ at $E = Q = 2$ MeV) is a circumstance of crucial importance. For the sake of comparison, it can be indicated that the energy resolution of the Xe chamber used in [51] is about 6.5% at $Q \approx 3$ MeV (that is, about 200 keV in absolute units). The possibility of using enriched germanium ($k = 0.85$) in amounts weighing a few kilograms at a 100% efficiency of event detection over an almost entire detector volume is also of importance.

The results of measurements with germanium detectors made it possible to obtain the most stringent constraints on the parameters of right-handed currents: $\langle \eta \rangle \leq 1.3 \times 10^{-8}$ and $\langle \lambda \rangle \leq 1.8 \times 10^{-6}$ (the matrix elements from [58] were used in deducing these estimates).

In conclusion, it is worth noting that the constraint $T_{1/2} \geq 1.6 \times 10^{25}$ yr [64, 65] for ^{76}Ge was obtained by means of a conventional statistical treatment of experimental data. Baudis *et al.* [64] also present the much more stringent constraint $T_{1/2} \geq 5.7 \times 10^{25}$ yr, which was obtained on the basis of a dedicated statistical approach, but the reliability of this result is question-

able [65]. For this reason, we display only the conservative estimate in Table 5.

Neutrinoless double-beta decay involving Majoron emission. Like the dominant neutrinoless mode of double-beta decay, its mode involving Majoron emission has not yet been discovered. In searches for $2\beta0\nu, \chi^0$ decay, the energy resolution of the detector is immaterial, and measurements with germanium detectors do have a crucial advantage. A number of experimental groups (see Table 6) obtained results that made it possible to set virtually identical constraints on the Majoron–neutrino coupling constant $\langle g_{\nu\chi}\rangle$.

The constraints on $\langle g_{\nu\chi}\rangle$ that are listed in Table 6 were obtained by using the matrix elements from [58], since that article presents the most comprehensive results on the subject. Among these results, only limits obtained from geochemical data for ^{128}Te stand out, but it was mentioned above that the probability of large systematic errors is high in that case. As to direct measurements, the accuracy achieved in calculating the relevant matrix elements is insufficiently high for conclusively choosing one of the results displayed here: the upper bounds on $\langle g_{\nu\chi}\rangle$ can change within a factor of 2 to 3 in either direction.

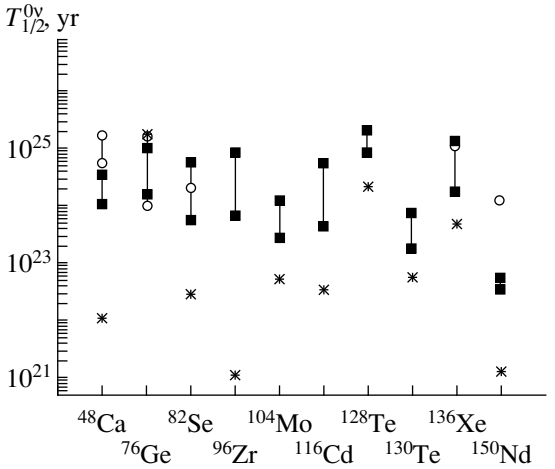

Fig. 7. Calculated values of the half-lives for neutrinoless double-beta decay (in the calculations, it was assumed that $\langle m_\nu\rangle = 1.0$ eV and $\langle\eta\rangle = \langle\lambda\rangle = 0$) and experimental limits on these half-lives: (asterisks) experimental data, (closed boxes) results of the calculations performed within various versions of the quasiparticle random-phase approximation, and (open circles) results of the calculations performed within the shell model of the nucleus.

7. OUTLOOK

Neutrinoless double-beta decay. The nearest prospects for studying neutrinoless double-beta decay are known. The commissioning of a large TPC of volume 13 m^3 filled with Xe at atmospheric pressure, with the abundance of the ^{136}Xe isotope being 7.5 kg, is expected at ITEP in this very year [82]. The calculated sensitivity of the experiment to the neutrinoless mode is $T_{1/2} = (2\text{–}4) \times 10^{24}$ yr, which is an order of magnitude higher than the current level [51]. This will constrain the neutrino mass at the level of 1 eV. In the future, it is planned to use a ^{150}Nd target. At the same sensitivity of the apparatus, this will yield the constraint $\langle m_\nu\rangle \leq 0.2\text{–}0.3$ eV.

The work on constructing the tracking facility NEMO-3 is nearing completion at present [83, 84]. The scales of the facility can be characterized by its following characteristics. The working chamber has a diameter of 2 m and a length of 3 m, the target area being 20 m^2; this makes it possible to perform measurements with 10 kg of the isotope under investigation or with several samples simultaneously. The tracking detector contains 6180 Geiger cells of length 2.7 m each. The weight of plastic scintillators that are used to determine the electron energies and to perform time-of-flight measurements is 7 t. The apparatus employs 1960 photomultiplier tubes. The chamber is placed in a magnetic field of strength 30 G. The energy resolution is about 10% at 3 MeV, while the calculated detection efficiency is 28%. Measurements at this facility will be per-

Table 6

Nucleus	$T_{1/2}$, yr		$\langle g_{\nu\chi}\rangle, \times 10^{-4}$	Experimental procedure
^{76}Ge	$>10^{22}$(68% C. L.)	[2]	<2.2	Semiconductor germanium detector (^{76}Ge)
	$>7.9\times10^{21}$(90% C. L.)	[79]	<2.6	Semiconductor germanium detector (^{76}Ge)
^{82}Se	$>2.4\times10^{21}$(90% C. L.)	[31]	<1.6	Counting tracker detector
^{100}Mo	$>3.1\times10^{21}$(90% C. L.)	[80]	<2.0	Counting tracker detector
^{116}Cd	$>1.2\times10^{21}$(90% C. L.)	[34]	<1.2	Counting tracker detector
^{128}Te	$>2\times10^{24}$	[16]	<0.7	Geochemistry
	$>7.7\times10^{24}$	[15]	<0.3	Geochemistry
^{130}Te	$>8\times10^{20}$	[49]	<2.8	Geochemistry
^{136}Xe	$>7.2\times10^{21}$(90% C. L.)	[81]	<2.0	TPC
^{150}Nd	$>2.8\times10^{20}$(90% C. L.)	[23]	<1.0	TPC

formed, first of all, with molybdenum enriched in ^{100}Mo to 95%. The announced accuracy of the measurements corresponds to a half-life level of $T_{1/2} \approx 10^{25}$ yr under the assumption of zero background (this translates into the constraints $\langle m_\nu \rangle \leq 0.2$–$0.3$ eV on the neutrino mass). It should be borne in mind that irremovable background from the two-neutrino mode of double-beta decay must be taken into account in measurements with molybdenum (this background can impair the sensitivity of the apparatus significantly).

It is planned that the first version of a facility featuring low-temperature bolometric TeO_2 detectors [85, 86] will be put into operation in 2001. The apparatus is designed as a 14-floor tower with four TeO_2 crystals on each floor. Each crystal has dimensions of $5 \times 5 \times 5$ m^3 and a mass of 760 g. The energy resolution of the first four crystals is within 5–10 keV at a background level of 0.5 event/(keV kg yr). The presumed accuracy of the measurements after one year of operation with 56 detectors is $(3\text{–}4) \times 10^{24}$ yr, which corresponds to $\langle m_\nu \rangle \leq 0.3$–$0.4$ eV.

The commissioning of these facilities will make it possible to advance the sensitivity to the Majorana neutrino mass up to a level presently ensured by measurements with germanium detectors. For the purposes of uniformity, all the above estimates are based on the matrix elements as calculated in [58]. If it turns out that the trend toward the reduction of $|M^{0\nu}|$ when more advanced computational models are used is confirmed, the level of constraints on $\langle m_\nu \rangle$ may become lower by a factor of 2 to 3 (a limit of about 0.5–1.0 eV).

In turn, the work with ^{76}Ge detectors will be continued with the aim of achieving a level of $T_{1/2} \approx (5\text{–}10) \times 10^{25}$ yr. Here, however, there may appear the saturation effect associated with the presence of weak background gamma lines near the expected line at $E = 2038.5$ keV from the neutrinoless transition $^{76}\text{Ge} \longrightarrow {}^{76}\text{Se}$.

Further significant advancements can be ensured by evolving new facilities that will make it possible to perform measurements with a few kilograms of an active isotope under much more favorable background conditions. Obviously, this can be possible only when the same unit plays the role of a target and a detector simultaneously. Presently, several versions of such facilities, which are capable of detecting neutrinoless double-beta decay at the Majorana mass of $\langle m_\nu \rangle \approx 10^{-2}$ eV, are being discussed.

The GENIUS project [87] proposes using approximately 1 t of ^{76}Ge (300–400 detectors placed in a common tank filled with liquid nitrogen). It is expected that this will make it possible to reduce the background level by one to two orders of magnitude. The project foresees the possibility for detecting the double-beta-decay transitions to the excited states of the final nucleus ^{76}Se. This will ensure a further reduction of the background level.

The project CUORE [86] is being developed to perform measurements with 1000 bolometric detectors (TeO_2) of total mass about 1 t as well. A facility featuring 56 detectors that is being put into operation at present is considered as the first stage of this project.

Finally, the project of a large liquid-xenon chamber that will simultaneously record electrons and a barium ion appearing as the product of Xe double-beta decay is under discussion now [88, 89]. At the mass of Xe in the chamber up to a few hundred kilograms, the background in such a facility may be nearly zero. However, the limitation associated with the presence of the two-neutrino mode still remains.

A practical implementation of all these projects requires solving a number of technological problems and formidable financial investments.

Two-neutrino double-beta decay. Investigation of this mode will be continued along three lines. At present, the decay of some nuclei with an energy release in excess of 2.5 MeV has been recorded in a number of direct experiments (^{48}Ca, ^{82}Se, ^{96}Zr, ^{100}Mo, ^{116}Cd, and ^{150}Nd; only ^{76}Ge stands out in this respect). Obviously, the search for double-beta-active nuclei will be extended to isotopes with smaller decay energies and, accordingly, with longer half-lives.

Attempts at discovering double-beta-decay transitions to the excited states of final nuclei will be continued. Transitions to 0_1^+ and 0_2^+ levels are suppressed only because of smaller transition energies and, in just the same way as the two-neutrino double-beta decay into the ground state, are allowed by all versions of the theory. Measurements of the probabilities for several such transitions, in addition to the decay process $^{100}\text{Mo} \longrightarrow {}^{100}\text{Ru}^*(0_1^+)$, which has already been discovered, may prove to be useful in discussing the reliability of the calculated matrix elements both for the two-neutrino and for the neutrinoless decay mode [90]. On the other hand, it is important from the experimental point of view that a simultaneous detection of two electrons and a photon will make it possible to reduce the background level considerably, thereby compensating in part a decrease in the decay probability.

Finally, it is natural to expect that more attention will be given to searches for $2\beta^+$-decay processes. In just the same way as the two-neutrino mode of $2\beta^-$ decay, the $2\beta^+$ process accompanied by the emission of two neutrinos is allowed in all versions of the theory. Here, however, the decays via the emission of two positrons do not exhaust all possibilities: the capture of one or two internal electrons is possible (K capture and double K capture, respectively):

$$A(Z, N) \longrightarrow A(Z-2, N+2) + 2e^+ + 2\nu, \quad 2\beta^+2\nu \text{ decay};$$

$$e^- + A(Z, N) \longrightarrow A(Z-2, N+2) + e^+ + 2\nu, \quad K\beta^+2\nu \text{ decay};$$

$$2e^- + A(Z, N) \longrightarrow A(Z-2, N+2) + 2\nu, \quad 2K2\nu \text{ decay}.$$

Table 7

Isotope	Q, MeV	Decay mode	$T^{2\nu}_{1/2}$, yr [91]	$T^{2\nu}_{1/2}$, yr [92]	$T^{0\nu}_{1/2}$, yr [92]
^{78}Kr	0.833	$2\beta^+$	3.7×10^{25}	2.3×10^{26}	1.6×10^{27}
		$K\beta^+$	2.2×10^{23}	5.3×10^{22}	6.5×10^{26}
		$2K$	1.4×10^{23}	3.7×10^{22}	
^{106}Cd	0.734	$2\beta^+$	6.1×10^{26}	4.2×10^{26}	4.8×10^{27}
		$K\beta^+$	5.2×10^{23}	4.1×10^{21}	3.4×10^{26}
		$2K$	7.5×10^{22}	8.7×10^{20}	
^{124}Xe	0.822	$2\beta^+$	1.6×10^{25}	1.4×10^{27}	3.0×10^{27}
		$K\beta^+$	4.3×10^{22}	3.0×10^{22}	1.6×10^{26}
		$2K$	6.4×10^{21}	2.9×10^{21}	

The same versions exist for the neutrinoless mode of $2\beta^+$ decay.

Because of the Coulomb barrier for a positron and because of smaller decay energies, the expected probabilities of all modes of the $2\beta^+$-decay process are much less than the probabilities of all cases of the $2\beta^-$-decay process that have already been detected (with the exception of ^{128}Te $2\beta^-$ decay). In the case of $2\beta^-$ decay, the energy release is equal to the mass difference ΔM between the initial and the final atom. In the case of $2\beta^+$ decay, the transition energy Q is

$$Q = \Delta M - 4m_e \text{ for } 2\beta^+ \text{ decay},$$

$$Q = \Delta M - 2m_e - E_\mathrm{b} \text{ for } K\beta^+ \text{ decay},$$

$$Q = \Delta M - 2E_\mathrm{b} \text{ for } 2K \text{ decay},$$

where E_b is the electron binding energy in the K orbit.

For this reason, isobars with $\Delta M < 2$ MeV cannot decay via the emission of two positrons—only the K- and the $2K$-capture modes are possible in this case; for $\Delta M < 1$ MeV, $2\beta^+$ decay can occur only via $2K$ capture.

In all, 33 isotopes are known for which $2\beta^+$ decay is possible [44]. Of these, only seven nuclear species can decay via the emission of two positrons (^{78}Kr, ^{96}Ru, ^{106}Cd, ^{124}Xe, ^{130}Ba, ^{136}Ce, ^{148}Gd). A direct detection of such processes is impossible at present, since the estimated half-lives of even the most short-lived nuclei (see Table 7) lie in the range $T^{2\nu}_{1/2} \approx 10^{25}$–$10^{26}$ yr.

Prospects for detecting $K\beta^+$ decay are somewhat better ($T_{1/2} \approx 10^{22}$–10^{23} yr). However, the sensitivity of current experiments is at a level of 10^{19}–10^{20} yr [93–96], which is obviously insufficient for recording the process. The observation of the neutrinoless modes of $2\beta^+$ decay is still less probable, since the most optimistic estimates for the corresponding half-lives exceed 10^{26}–10^{27} yr ($\langle m_\nu \rangle = 1$ eV).

8. CONCLUSION

The outcome from the last ten years of investigations into the double-beta-decay process is quite ambiguous. On one hand, there has arisen a new realm in nuclear spectroscopy, the spectroscopy of two-neutrino double-beta decay, and this field of investigation is rapidly developing. The range of activity is virtually unlimited both for theorists and for experimentalists. The periodic table of elements displays 35 pairs of "quasistable" nuclear species for which $2\beta^-2\nu$ decays must occur and 33 nuclear species for which the various versions of $2\beta^+2\nu$ decay are possible (in all, there are more than 60 such nuclei, including those that may decay via K capture and double K capture).

The emergence of a vast array of new experimental data has revealed the poor predictive power of theoretical models that were previously used to calculate the relevant nuclear matrix elements. New models proposed in recent years have made it possible to improve somewhat the situation, but their predictions are still unable to describe experimental data very well.

All the above, refers, however, solely to two-neutrino double-beta decay, which is allowed by all versions of the theory. The main fundamental question remains open—the neutrinoless mode of double beta decay has not yet been observed, although the sensitivity of modern experimental facilities featuring germanium detectors (that of the Heidelberg–Moscow collaboration and IGEX) has increased considerably over the last decade and now exceeds 10^{25} yr. The constraint on the Majorana neutrino mass from this results is $\langle m_\nu \rangle <$ 0.4–1.1 eV.

Further considerable advancements in searches for neutrinoless double-beta decay requires creating radically new experimental facilities, since the potential of the existing devices has been exhausted to a considerable extent.

REFERENCES

1. S. R. Elliott *et al.*, Phys. Rev. Lett. **59**, 2020 (1987); Phys. Rev. C **46**, 1535 (1992).
2. T. Kirsten and H. W. Muller, Earth Planet. Sci. Lett. **6**, 271 (1969).
3. A. A. Vasenko *et al.*, Mod. Phys. Lett. A **5**, 1299 (1990).
4. A. A. Vasenko *et al.*, Prib. Tekh. Éksp., No. 2, 56 (1989).
5. M. Göppert-Mayer, Phys. Rev. **48**, 512 (1935).
6. E. Fireman, Phys. Rev. **74**, 1238 (1948).
7. W. H. Furry, Phys. Rev. **56**, 1184 (1939).
8. M. G. Inghram and J. H. Reynolds, Phys. Rev. **76**, 1265 (1949); **78**, 822 (1950).
9. C. S. Wu *et al.*, Phys. Rev. **105**, 1413 (1957).
10. G. B. Gelmini and M. Roncadelli, Phys. Lett. B **99**, 411 (1981).
11. R. N. Mohapatra and E. Takasugi, Phys. Lett. B **211**, 192 (1988).
12. V. I. Tretyak and Yu. G. Zdesenko, At. Data Nucl. Data Tables **61**, 43 (1995).
13. E. W. Hennecke *et al.*, Phys. Rev. C **11**, 1378 (1975).
14. W. J. Lin *et al.*, Nucl. Phys. A **457**, 285 (1986).
15. T. Bernatowicz *et al.*, Phys. Rev. Lett. **69**, 2341 (1992).
16. N. Takaoka *et al.*, Phys. Rev. C **53**, 1557 (1996).
17. M. K. Moe *et al.*, Phys. Rev. C **22**, 2186 (1980).
18. A. Balysh *et al.*, Phys. Rev. Lett. **77**, 5186 (1996).
19. H. Ejiri *et al.*, Phys. Lett. B **258**, 17 (1991).
20. S. R. Elliott *et al.*, J. Phys. G **17**, S145 (1991).
21. K. Kume *et al.*, Nucl. Phys. A **577**, 405 (1994).
22. V. Artemiev *et al.*, Phys. Lett. B **345**, 564 (1995).
23. A. De Silva *et al.*, Phys. Rev. C **56**, 2451 (1997).
24. A. L. Turkevich *et al.*, Phys. Rev. Lett. **67**, 3211 (1991).
25. A. Kawashima *et al.*, Phys. Rev. C **47**, 2452 (1993).
26. R. Arnold *et al.*, Nucl. Phys. A (2000) (in press).
27. A. S. Barabash *et al.*, Phys. Lett. B **345**, 408 (1995).
28. F. T. Avignone *et al.*, Phys. Lett. B **256**, 559 (1991).
29. A. Balysh *et al.*, Phys. Lett. B **356**, 450 (1995).
30. A. Balysh *et al.*, Phys. Rev. D **55**, 54 (1997).
31. R. Arnold *et al.*, Nucl. Phys. A **636**, 209 (1998).
32. D. Dassie *et al.*, Phys. Rev. D **51**, 2090 (1995).
33. S. R. Elliott *et al.*, Phys. Rev. C **46**, 1535 (1992).
34. R. Arnold *et al.*, Z. Phys. C **72**, 239 (1996).
35. M. G. Shchepkin, Usp. Fiz. Nauk **143**, 513 (1984) [Sov. Phys. Usp. **27**, 555 (1984)].
36. M. Doi *et al.*, Prog. Theor. Phys. Suppl. **83**, 1 (1985).
37. T. Tomoda, Rep. Prog. Phys. **54**, 53 (1991).
38. H. F. Klapdor-Kleingrothaus and A. Schtaudt, *Nonaccelerator Elementary-Paricle Physics* (Nauka, Moscow, 1997).
39. Yu. G. Zdesenko, Fiz. Élem. Chastits At. Yadra **11**, 1369 (1980) [Sov. J. Part. Nucl. **11**, 542 (1980)].
40. M. K. Moe, Int. J. Mod. Phys. E **2**, 507 (1993).
41. O. Ya. Zeldovich, Preprint No. 29-97, ITÉF (Institute of Theoretical and Experimental Physics, Moscow, 1997).
42. Ya. B. Zel'dovich *et al.*, Usp. Fiz. Nauk **54**, 361 (1954).
43. V. R. Lazarenko, Usp. Fiz. Nauk **90**, 601 (1966) [Sov. Phys. Usp. **9**, 860 (1967)].
44. A. H. Wapstra and G. Audi, Nucl. Phys. A **432**, 55 (1985).
45. M. C. Gonzales-Garcia and Y. Nir, Phys. Lett. B **232**, 383 (1989).
46. Z. Berezhiani *et al.*, Phys. Lett. B **291**, 99 (1992).
47. C. P. Burgess and J. M. Cline, Phys. Lett. B **298**, 141 (1993).
48. T. Kirsten *et al.*, in *Proceedings of the International Symposium on Nuclear Beta Decays and Neutrino, Osaka, Japan, 1986*, Ed. by T. Kotani *et al.* (World Sci., Singapore, 1986), p. 81.
49. O. K. Manuel, J. Phys. G **17**, S221 (1991).
50. T. Bernatowicz *et al.*, Phys. Rev. C **47**, 806 (1993).
51. R. Luescher *et al.*, Phys. Lett. B **434**, 407 (1998).
52. M. Doi *et al.*, Phys. Lett. B **103**, 219 (1981).
53. W. C. Haxton and G. J. Stephenson, Jr., Prog. Part. Nucl. Phys. **12**, 409 (1984).
54. E. Caurier *et al.*, Phys. Lett. B **252**, 13 (1990).
55. E. Caurier *et al.*, Phys. Rev. Lett. **77**, 1954 (1996).
56. J. Retamosa *et al.*, Phys. Rev. C **51**, 371 (1995).
57. J. Engel *et al.*, Phys. Rev. C **37**, 731 (1988).
58. A. Staudt *et al.*, Europhys. Lett. **13**, 31 (1990).
59. M. Hirsh *et al.*, Phys. Rep. **242**, 403 (1994).
60. X. R. Wu *et al.*, Phys. Lett. B **272**, 169 (1991); **276**, 272 (1992).
61. F. Šimkovicz *et al.*, Yad. Fiz. **61**, 1318 (1998) [Phys. At. Nucl. **61**, 1218 (1998)].
62. G. Pantis *et al.*, Yad. Fiz. **61**, 1311 (1998) [Phys. At. Nucl. **61**, 1211 (1998)].
63. G. Pantis *et al.*, Phys. Rev. C **53**, 695 (1996).
64. L. Baudis *et al.*, Phys. Rev. Lett. **83**, 41 (1999).
65. C. E. Aalseth *et al.*, Phys. Rev. C **59**, 2108 (1999); Yad. Fiz. **63**, 1299, 1341 (2000) [Phys. At. Nucl. **63**, 1225, 1268 (2000)].
66. N. Kudomi *et al.*, Nucl. Phys. A **629**, 55 (1998).
67. F. A. Danevich *et al.*, Nucl. Phys. B (Proc. Suppl.) **70**, 246 (1999).
68. A. Alessandrello *et al.*, Phys. Lett. B **433**, 156 (1998).
69. S. R. Elliott *et al.*, Phys. Rev. C **46**, 3055 (1996).
70. Ke You *et al.*, Phys. Lett. B **265**, 53 (1991).
71. M. Alston-Garnjost *et al.*, Phys. Rev. Lett. **71**, 831 (1993).
72. M. K. Moe *et al.*, Prog. Part. Nucl. Phys. **32**, 247 (1994).
73. K. Muto *et al.*, Z. Phys. A **334**, 187 (1989).
74. K. Muto *et al.*, Z. Phys. A **339**, 435 (1991).
75. J. Suhonen *et al.*, Nucl. Phys. A **543**, 645 (1992).
76. J. Suhonen *et al.*, Nucl. Phys. A **535**, 509 (1991).
77. J. Suhonen *et al.*, Phys. Rev. C **49**, 3055 (1994).
78. G. Pantis *et al.*, J. Phys. G **18**, S605 (1992).
79. M. Guchtner *et al.*, Phys. Rev. D **55**, 54 (1997).
80. H. Ejiri *et al.*, Nucl. Phys. A **611**, 85 (1996).
81. J.-C. Vuilleumier *et al.*, Phys. Rev. D **48**, 1009 (1993).
82. V. Artemiev *et al.*, Nucl. Instrum. Methods A **303**, 309 (1991).
83. NEMO-3 Proposal, LAL Preprint 94-29 (1994).
84. X. Sarazin *et al.*, Nucl. Phys. B (Proc. Suppl.) **70**, 239 (1999).

85. A. Alessandrello *et al.*, Nucl. Phys. B (Proc. Suppl.) **48**, 238 (1996).
86. A. Alessandrello *et al.*, in *Proceedings of the TAUP99, Paris, 1999*, Nucl. Phys. B (Proc. Suppl.) (2000) (in press).
87. H. V. Klapdor-Kleingrothaus *et al.*, J. Phys. G **24**, S483 (1998).
88. M. K. Moe, Phys. Rev. C **44**, 931 (1991).
89. T. A. Girard *et al.*, Nucl. Instrum. Methods A **316**, 44 (1992).
90. J. Suhonen, Yad. Fiz. **61**, 1286 (1998) [Phys. At. Nucl. **61**, 1186 (1998)].
91. S. K. Balaev *et al.*, Izv. Akad. Nauk SSSR, Ser. Fiz. **53**, 2136 (1989).
92. M. Hirsch *et al.*, Z. Phys. A **347**, 151 (1994).
93. S. I. Vasil'ev *et al.*, Pis'ma Zh. Éksp. Teor. Fiz. **57**, 614 (1993) [JETP Lett. **57**, 631 (1993)].
94. C. Saenz *et al.*, Phys. Rev. C **50**, 1170 (1994).
95. A. Barabash *et al.*, Z. Phys. A **357**, 351 (1997).
96. M. Aunola, J. Suhonen, A. S. Barabash, *et al.*, Pis'ma Zh. Éksp. Teor. Fiz. **62**, 690 (1995) [JETP Lett. **62**, 706 (1995)].

Translated by A. Isaakyan

Physics of Atomic Nuclei, Vol. 63, No. 8, 2000, pp. 1356–1376. Translated from Yadernaya Fizika, Vol. 63, No. 8, 2000, pp. 1432–1453.

ON THE 85th ANNIVERSARY OF V.V. VLADIMIRSKY

Precision Analysis of Experiments Studying the Beta Decay of the Free Neutron: Standard Model and Possibilities of Its Violation

Yu. V. Gaponov* and Yu. A. Mostovoy

Russian Research Centre Kurchatov Institute, pl. Kurchatova 1, Moscow, 123182 Russia

Received February 7, 2000

Abstract—The current status of experimental results on the beta decay of the free neutron is described. An analysis of these data shows that, within the present-day accuracy, the data are fully consistent with the Standard Model of electroweak interaction. At the same time, there exists the possibility of deviations from the Standard Model at a level of 1%. The possible violations due to the contributions of right-handed (W_R) bosons, as well as of leptoquark mechanisms introducing anomalous scalar and tensor terms in the effective weak-interaction Hamiltonian, which include the right-handed neutrinos, are estimated. In the last case, the analysis is performed by an analytic method that makes it possible to take into account, for the first time, the possibility of *CP* violation. © *2000 MAIK "Nauka/Interperiodica".*

1. INTRODUCTION

The approaching 85th anniversary of the birth of V.V. Vladimirsky, an influential scientist of great originality and high creative power, who has been working in the realms of nuclear and elementary-particle physics in Laboratory no. 3 (TTL–ITEP)—presently, Institute of Theoretical and Experimental Physics (ITEP, Moscow)—since the emergence of this institution, furnishes a strong motivation for addressing retrospectively the late 1950s, when he participated actively in laying the fundamentals for the modern standard theory of the beta decay of nuclei. Immediately following the pioneering study of Lee and Yang [1] on parity violation, the physicists from ITEP (known at that time as TTL), who had been completing at that time their investigations into the physics of heavy-water reactors, embarked enthusiastically on new research work, plowing into this nascent realm of fundamental physics [2], proposing experimental methods of their own for studying the beta decay of the free neutron and nuclei [3], and evolving the theory of processes governed by weak interactions [4]. The discovery of parity violation and the creation of new methods of investigations on this basis resulted in a complete rearrangement of the groundwork—the structure of weak interaction—within only two years: the scalar–tensor form of the nucleon–lepton Hamiltonian, a form that was recognized almost universally in the early 1950s, gave way to the modern *V–A* form, which was commonly adopted in the early 1960s. This new turn in elementary-particle theory was stimulated, to a great extent, by experimental studies devoted to measuring the electron–neutrino correlation in free-neutron decay that were performed for the first time ever by an ITEP group with an active participation of Vladimirsky [3, 5, 6]. As a matter of fact, these experiments initiated investigations of correlation parameters in free-neutron decay. Nowadays, such investigations play a key role in studying decays of the lepton–hadron type. The results obtained in this way greatly contributed to establishing, by the mid-1960s, those experimental facts that presently underlie the Standard Model of weak interaction [7], a classical scheme adopted in contemporary physics.

In physics, however—in just the same way as in art—evolution proceeds from classicism to modernism, and the past few years have seen many attempts at going beyond the classical schemes. Although the success of the Standard Model in describing a wide variety of experimental facts has become ever more impressive, the problem of the actual structure of the effective Hamiltonian of weak nucleon–lepton interaction has unceasingly attracted the attention of theorists, both in the period of consolidation of the Standard Model of weak interactions and after its universal recognition. While, in the first period (from the 1960s to the early 1980s), investigations were aimed primarily at seeking facts that support the Standard Model and at refining some of its details, including special features of nuclear processes, in recent years—from the late 1980s—searches for possible effects beyond the Standard Model have gradually come to the fore (for an overview, see [8–11]). On one hand, this proceeds via the development of experimental facilities, which creates preconditions for harnessing new procedures: for example, the technique of ultracold neutrons or precision measurements of angular and polarization features. As a result, the neutron lifetime can be determined more precisely, and the beta-decay spectra and

* e-mail: gaponov@imp.kiae.ru

1063-7788/00/6308-1356$20.00

the correlation parameters of the neutron and nuclei can be refined. On the other hand, the investigation of free-neutron beta decay, a fundamental process of nucleon decay in this respect, as contrasted against the μ–e decay of the purely leptonic type, has ever been gaining in importance. In this special case, where the effect of the nuclear structure is absent, it is possible to compute, to a high precision, radiative corrections of the exchange type [12]. In principle, this would make it possible to probe the W-boson contribution in the region of low energies [13, 14] (usually, this contribution is accessible only in the region of high energies) and to perform searches for nonstandard contributions at a level of extremely high precision.

The use of neutron beta decay for seeking effects beyond the Standard Model is based on the fact that the standard form of the Hamiltonian for the weak hadron–lepton interactions is reduced with respect to the most general Lorentz invariant form. As is well known, the general form of the effective weak-interaction Hamiltonian is [1, 2]

$$H_\beta = (G_{F\beta}/\sqrt{2})\sum_i (\overline{\Psi}_p O_i \Psi_n)(\overline{\Psi}_e O^i (C_i + C_i'\gamma_5)\Psi_{\nu e}), \quad (1)$$

where $G_{F\beta}$ is the universal constant of weak hadron–lepton interaction of the Fermi type (all the remaining constants are usually normalized to it), while the index i labels five possible versions of weak interactions. These are the scalar (S), vector (V), tensor (T), axial-tensor (A), and pseudoscalar (PS) versions. The quantities O_i can be written as

$$O_i = 1\ (S),\ \gamma_\mu\ (V),\ \sigma_{\mu\nu} = 1/(2i)(\gamma_\mu\gamma_\nu - \gamma_\nu\gamma_\mu)\ (T),\ i\gamma_\mu\gamma_5\ (A),\ \gamma_5\ (PS). \quad (2)$$

The PS version does not contribute to allowed beta transitions; hence, the general Hamiltonian (1) describing free-neutron decay can depend on no more than eight complex constants C_i and C_i'. Under the assumption that weak interaction respects CP invariance, these eight constants are real-valued.

In contrast to the general form, the effective Hamiltonian (1) is reduced in the Standard Model, having the form [15]

$$H_{\rm eff} = (G_{V\beta}/\sqrt{2})(\overline{\Psi}_p \gamma_\mu (1 - \lambda\gamma_5)\Psi_n) \times (\overline{\Psi}_e \gamma^\mu (1 + \gamma_5)\Psi_{\nu e}). \quad (3)$$

This reduction stems from the fact that, in relation to the general form, the Standard Model invokes three additional theoretical hypotheses:

(i) It is assumed that CP is not violated in strangeness-conserving decays. This reduces general complex-valued constants C_i and C_i' to a real form.

(ii) The V–A form of weak interaction is treated as a consequence of the assumption that the heavy W boson mediating weak interaction between nucleons (quarks) and leptons is a vector particle. This implies that

$$C_S = C_T = C_S' = C_T' = C_{PS} = C_{PS}' = 0. \quad (4)$$

(iii) The physical neutrinos participating in weak-interaction processes at low energies and, accordingly, the W_L bosons mediating weak interactions are left-handed particles. For the vector and the axial-vector version, this leads to the equalities

$$C_V = C_V', \quad C_A = C_A'. \quad (5)$$

Thus, we can see that, for neutron and nuclear beta decays described by strangeness-conserving hadron–lepton interaction, the general Hamiltonian (1) reduces in the Standard Model to a two-parameter form depending on two fundamental real-valued constants $G_{V\beta}$ and $C_A/C_V = \lambda$, the Fermi constant $G_{F\beta}$ of the general form being coincident with the constant $G_{V\beta}$ of the Standard Model. The currently adopted experimental values of the Standard Model parameters are the following (for details, see below) [16]:

$$G_{V\beta} = 1.4183(18) \times 10^{-62}\ \text{J m}^3, \quad \lambda = -1.2673(10). \quad (6)$$

Below, we will show that all modern neutron experiments are by and large consistent with the Standard Model, but they still leave room for small (at a level of a few percent and below) effects beyond it. From this point of view, the Standard Model dictates the dominant part of the Hamiltonian, whereas observation of experimental deviations from the two-parameter form is interpreted as manifestations of phenomena beyond it. Thus, there arises the problem of seeking nonstandard contributions; here, some versions of the deviations from the standard Hamiltonian can be associated with specific physical mechanisms introduced via additional hypotheses.

Presently, there exist several hypotheses that introduce variations of the standard form of the weak-interaction Hamiltonian and which are widely discussed in the literature and are subjected to various tests in investigations into neutron and nuclei beta decays. Listed below are the most viable of these hypotheses.

A. CP-Violation Hypothesis

Well-known experiments that observed CP violation in K-meson decays naturally raise the question of whether similar violations are possible in strangeness-conserving beta-decay processes. No such violations have been observed so far, but their existence at a level of a few tenths of a percent is not ruled out by experiments; therefore, the introduction of CP violation is admissible. It was indicated above that, if CP violation occurs, the parameters of the Hamiltonian become complex. In the simplest case, it is assumed that the parameter λ is complex (the phase of the constant G_V

does not manifest itself in processes that are due entirely to weak interaction) if we introduce *CP* violation in the Standard Model. In models featuring a more general form of the Hamiltonian, such violations result in that the number of real parameters of the model is nearly doubled (in fact, only the relative phases manifest themselves in purely weak interaction processes—the absolute value of a phase can be determined only in experiments measuring the interference of weak and strong (or electromagnetic) interactions.

B. Hypothesis of Right-Handed Lepton Currents—Right-Handed Neutrinos

In the simplest version of this hypothesis, the right-handed form of neutrinos that is associated with the heavy right-handed W_R boson is introduced along with the left-handed form [17, 18]. This leads to the violation of equality (5). This possibility has been intensively studied in recent years (see, for example, [9, 19–21]). In the beta-decay case, these studies were stimulated to a considerable extent by the experimental neutron anomaly—a mismatch between the results of different-type experiments that measured neutron-decay features (see [20, 22]).

C. Hypothesis of Leptoquark Contribution

According to this hypothesis, weak interaction can be due not only to the standard mechanism associated with the exchange of a color-singlet *W* boson between a lepton and a quark but also to the additional mechanism associated with the exchange of a heavy leptoquark boson (*LQ*) having color and a fractional charge [23–27]. Such bosons can be emitted in the weak transition of a quark into a lepton. In some cases, the latter mechanism can generate small scalar (pseudoscalar) or tensor terms (or both) in the nucleon–lepton Hamiltonian (1). The general form of such terms can be found, for example, in [24]. Dedicated searches for such contributions in the beta decay of nuclei and in muon capture by nuclei have begun in recent years [28–33]. It should be noted that, in such schemes, the leptoquark contributions may involve both standard (left-handed) and nonstandard (right-handed) neutrinos. In the former case, this implies violation of (4), simultaneously requiring fulfillment of the relations

$$C_S = C_S', \quad C_T = C_T'. \tag{7}$$

If the right-handed neutrino is included, the relations

$$C_S = -C_S', \; C_T = -C_T', \; C_V = -C_V', \; C_A = -C_A' \tag{8}$$

will be satisfied for the corresponding additional terms in the Hamiltonian. A mixed case is also possible. Of considerable interest is the version of this hypothesis where left-handed neutrinos are emitted in the vector and axial-vector versions, while right-handed neutrinos are emitted in the additional scalar and tensor versions. For the first time, this version was analyzed in detail phenomenologically in [34]; later, it was considered in [35–40]. This case is characterized by the relations

$$C_V = C_V', \quad C_A = C_A', \quad C_S = -C_S', \quad C_T = -C_T'. \tag{9}$$

The hypothesis being considered leads to some interesting implications whose investigation is still in its infancy [39, 40]. For this reason, we will comprehensively discuss the possibilities of its verification below (Section 4).

Free-neutron beta decay is the simplest elementary process of the hadron–lepton type; therefore, it is especially appealing for analysis (see above). This process is described in terms of the following experimental characteristics: the neutron lifetime; the electron decay spectrum; and correlation and polarization parameters that describe the probabilities of the emission of decay products, including electrons and neutrinos (or recoil nuclei), as functions of the angles and polarizations of these products. In the case of allowed beta transitions of nuclei and the free neutron, the decay probability is given by

$$\begin{aligned} &dW(E_e, Z, \Omega_e, \Omega_\nu) \\ &= G_{F\beta}^2/(2\pi)^5 F(\pm Z, E_e)(E_e - E_{e0})^2 E_e p_e dE_e d\Omega_e d\Omega_\nu \\ &\quad \times (1 + (bm_e/E_e)\sqrt{1-\alpha Z^2} + a(\mathbf{p}_e \cdot \mathbf{p}_\nu)/(E_e E_\nu) \\ &\quad + A(\mathbf{J} \cdot \mathbf{p}_e)/E_e + B(\mathbf{J} \cdot \mathbf{p}_\nu)/E_\nu + D(\mathbf{J} \cdot [\mathbf{p}_e \times \mathbf{p}_\nu])/(E_e E_\nu)), \end{aligned} \tag{10}$$

where $\mathbf{J}$ is the polarization of the decaying nucleus; E_e and $\mathbf{p}_e$ are the electron energy and momentum, respectively; E_ν and $\mathbf{p}_\nu$ are the neutrino energy and momentum, respectively; and $F(\pm Z, E_e)$ is the Coulomb Fermi function. The quantities a, A, B, and D are the correlation characteristics of the decay process being considered, while b is a parameter that describes the energy dependence that deviates from the standard Fermi form. Free-neutron beta decay can be investigated in experiments of various types. Of these, five have already been implemented. These are (i) measurement of the neutron lifetime; (ii) measurement of the angular electron–neutrino correlation; (iii) measurement of the correlation between the spin of a polarized decaying neutron and the electron momentum; (iv) measurement of the correlation between the neutron spin and the neutrino momentum; and (v) measurement of the triple correlation between the polarized-neutron spin, the electron momentum, and the neutrino momentum. The parameters that are determined in experiments of these types are (i) $(f\tau)_n$, (ii) a, (iii) A, (iv) B, and (v) D.

In standard analyses of data on neutron decay, it is usually assumed in addition (often without any discussion) that the spectrum of decay electrons features no contributions inversely proportional to the electron energy—so-called Fierz terms that are determined in the Fermi and Gamow–Teller components by the parameters b_F and b_{GT}, respectively.

Apart from experiments studying neutron beta decay, there are also complementary experiments dealing with nuclear beta decays and playing an important role in determining the basic properties of weak interaction. These are first of all experiments studying 0^+–0^+ nuclear beta transitions between different components of isotriplets, where there occurs a Fermi-type transition conserving the total nuclear spin equal to unity. According to modern concepts, the vector current—an isotopic analog of the electromagnetic current—must be conserved in such beta transitions (conservation of the vector current, also known as the CVC hypothesis). This conservation law is violated by Coulomb corrections, and this makes it possible to estimate the matrix elements of this transition to a high precision [41–43]. At the same time, the main characteristic of such a transition in the Standard Model—the coupling constant $G_{V\beta}$—together with the constant $G_{\mu e}$ for leptonic (μ–e) decay, determines one of the important characteristics of particle physics, the cosine of the Cabibbo angle ($\cos\theta_C$); further, this makes it possible to estimate the element V_{ud} of the Kobayashi–Maskawa matrix without radiative corrections [43]. The latter in turn is related to other elements of this matrix, which are determined on the basis of data on strange- and beauty-particle decays by using the unitarity condition

$$V_{ud}^2 + V_{us}^2 + V_{ub}^2 = 1, \quad V_{ud} = \cos\theta_C. \qquad (11)$$

This enables one to check the value of the neutron constant $G_{V\beta}$ by invoking independent experimental data from particle physics.

For purely technical reasons, other experiments used in a detailed analysis of data on beta decay have been implemented only for nuclei. These are experiments measuring the electron and neutrino polarizations and correlation experiments dealing with these quantities. One has to use the data from these experiments because an implementation of analogous experiments with neutrons is questionable at present for one reason or another.

From the above listing alone, it can be seen that the variety of independent data that can in principal be used in analyzing free-neutron-beta-decay experiments is sufficiently wide. The amount of these data is such that a detailed analysis makes it possible not only to confirm the validity of the two-parameter Standard Model in different ways but also to perform, on this basis, an investigation of the applicability range of some hypotheses beyond the Standard Model. This emphasizes a special role of neutron experiments. It is main objective of our study to perform of such an analysis.

The ensuing exposition is organized as follows. In Section 2, we present the current status of the Standard Model. After that, we investigate the boundaries of admissible deviations from the Standard Model within the aforementioned hypotheses: the hypothesis of right-handed currents (Section 3) and leptoquark hypothesis (Section 4). In the Conclusion (Section 5), we summarize the results of our analysis from the viewpoint of prospects for further neutron investigations. Here, in particular, we would like to attract the attention of researchers to the need for addressing the second mode of neutron decay—that is, the need for launching experiments devoted to radiative beta decay, which have never been performed.

2. ASSESSING REALIZATION OF THE STANDARD MODEL

Let us discuss basic experimental facts used to confirm that the Standard Model is realized in beta decay. We note that, while, in the period of consolidation of the Standard Model, relevant investigations were planned in such a way as to demonstrate the validity of basic principles underlying this model and were therefore full-scale, presently—when there is no doubt about its validity at the dominant-contribution level—the focus of attention is often on proving the consistency of the standard two-component form of the weak-interaction Hamiltonian. Historically, two alternative approaches to analysis were used in studies devoted to beta decay: before the late 1980s, great emphasis was placed on data concerning 0^+–0^+ nuclear transitions, along with neutron data; from the early 1990s, however, the priority in analysis has been given to neutron data, whereas nuclear data were only invoked to check the results. The latter version of analysis seems preferable because, in the former, it is tacitly assumed that the vector constant of weak interaction takes the same value in nuclear and in elementary beta decay, but this follows only from the additional use of the conservation of the vector current (CVC hypothesis, which requires confirmation itself).

We begin by giving an account of the approach relying on information about 0–0 nuclear transitions. Allowed 0^+–0^+ transitions in isotopic triplets of nuclei present a very convenient object for a precision investigation of beta decay; for this reason, experiments in this field reached a high level of precision earlier than other relevant experiments. Two properties of 0–0 transitions set them apart from others: (i) only the Fermi (S and V) versions of interaction are realized in them; (ii) nuclear matrix elements for such beta transitions between the neighboring components of isotopic triplets have the simple form

$$M_F^2 = T(T+1) - T_z(T_z+1), \qquad (12)$$

where T and $T_z = (N - Z)/2$ are, respectively, the total isospin and its projection in the final state of a given beta transition. In particular, $M_F^2 = 2$ for the group of the transitions in question with $T = 1$ and $T_z = 0$. An analysis of specific experimental data involves introducing corrections of the Coulomb and the nuclear type, these corrections being dependent on the structure of the chosen nucleus [41–43]. Presently, such experiments have been performed for the beta transitions in

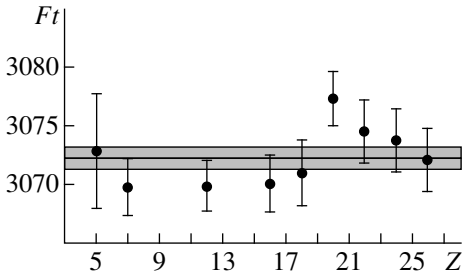

Fig. 1. Experimental values of the quantities (Ft) versus the nuclear charge Z and their mean value $\overline{Ft}$ (hatched band) with the uncertainty value adopted in the present analysis (borrowed from [43]).

the following nine nuclei: ^{10}C, ^{14}O, ^{26m}Al, ^{34}Cl, ^{38m}K, ^{42}Sc, ^{46}V, ^{50}Mn, and ^{54}Co. An analysis of the experimental data for these nuclei leads to the following results [43].

Let us introduce quantities (Ft) that are directly related to the fundamental weak-interaction constant $G_{V0\text{–}0}$ and which already include the calculated Coulomb corrections δ_{Coul} and the calculated structural corrections δ_R, which depend on a specific nucleus. These quantities and the vector constant of weak interaction for 0–0 transitions are related to the experimental values (ft) as follows:

$$\begin{aligned}(Ft) &= K\ln 2/(2G_{V\beta}^2) = (ft)(1+\delta_R)(1-\delta_C),\\ K &= 2\pi^3\hbar^7 c^6/(m_e c^2)^5\\ &= 8120.271(12)\times 10^{-10}\ \text{GeV}^{-4}\ \text{s}.\end{aligned} \tag{13}$$

The results of the calculations for (Ft) are displayed in Fig. 1 [43]. It can be seen from this figure that the experimental values are concentrated around some mean value $\overline{Ft}$. Concurrently, it turns out that the statistical scatter is less than the uncertainties in the theoretical corrections. According to those experimental data, the mean values of Ft and $G_{V0\text{–}0}$ are the following:

$$\begin{aligned}\overline{Ft} &= 3072.3\pm 0.9\ (\text{stat.})\pm 1.1\ (\text{syst.}),\\ \overline{G}_{V0\text{–}0} &= 1.4173(11)\times 10^{-62}\ \text{J m}^3.\end{aligned} \tag{14}$$

The quantity $\overline{G}_{V0\text{–}0}$ can be compared with the muon-decay constant $G_{\mu e}$; their ratio, taken with allowance for the internal radiative corrections Δ_R in the decays of the muon and the neutron [11, 13, 43], determines the element V_{ud} of the Kobayashi–Maskawa matrix [that this matrix element enters into the unitarity relation (11) makes it possible to check independently the value $G_{V0\text{–}0}$]:

$$\begin{aligned}V_{ud}^2 &= K\ln 2/(2G_{V\beta}^2)(1+\Delta_R)\overline{Ft},\\ \Delta_R &= 0.0240(8),\quad |V_{ud}| = 0.9740(5),\\ |V_{us}| &= 0.2196(23),\quad |V_{ub}| = 0.0032(8),\\ V_{ud}^2 + V_{us}^2 + V_{ub}^2 &= 0.9968(14).\end{aligned} \tag{15}$$

It can be seen from the unitarity relation that, by and large, the constant $G_{V0\text{–}0}$ as determined from the up-to-date data on 0–0 transitions agrees with data on elementary particles, but the possibility of nonstandard contributions cannot be ruled out completely at a level of 2.5σ. If we disregard this discrepancy, assuming the strict conservation of the vector current in accordance with the CVC hypothesis, data on 0–0 transitions determine the weak-interaction constant $G_{V\beta}$.

Given the constant $G_{V\beta}$, a full description of neutron beta decay within the Standard Model requires fixing the second fundamental parameter of the theory, the constant λ. For this, we can invoke data from one additional experiment. This can be either measurement of the neutron lifetime or measurement of any of the neutron correlation parameters (a, A, and B). Within the Standard Model, these parameters are given by

$$\begin{aligned}(f_n\tau_n) &= K/(G_{V\beta}^2)(1+3\lambda^2)^{-1},\\ a &= (1-\lambda^2)/(1+3\lambda^2),\ A = -2\lambda(1+\lambda)/(1+3\lambda^2),\\ B &= -2\lambda(1-\lambda)/(1+3\lambda^2),\ f_n = 1.71465(14).\end{aligned} \tag{16}$$

In the last study of Towner and Hardy [43], the value of f_n was refined, $f_n = 1.71489(2)$; however, we will use the commonly accepted value. It is obvious that, for analysis, it is convenient to use those parameters that are characterized by the highest experimental accuracy achieved so far and by the highest sensitivity to variations in λ. Detailed surveys of the current experimental situation concerning the measurements of the above parameters are given in [8–10]. In the present article, we restrict ourselves to brief comments on those experiments, paying special attention to the points that are of importance for our analysis.

At present, the measurements of the neutron lifetime are characterized by the highest relative accuracy. Such measurements have been conducted many times, with an ever improved accuracy, since the early 1950s [44, 45], but the most impressive advances were made in the late 1980s, when the experimental errors reached the level below 10 s and when the modern methods for the storage of ultracold neutrons began to be developed. Presently, seven experiments of this class have been performed [46–52]. According to the procedures used, they can be partitioned into two groups: beam experiments [46, 51] and experiments with ultracold neutrons [47–50, 52]. In the majority of the experiments from the second group, the simplest properties of ultracold-neutron interaction with the surface of the neutron-containing vessel were assumed a priori, which made it possible to extrapolate the resulting data to the limit where the escape of ultracold neutrons from the vessel due to surface effects can be disregarded. In recent years, however, several independent groups discovered

a new mechanism of such effects, which was neglected in the above studies (see, for example, [52]). This casts some doubt on the values presented previously for systematic effects. This criticism does not refer only to the results reported in [50, 52], where the flux of neutrons leaving the vessel was monitored from outside independently. For this reason, our further analysis relies on the results from [52]; in support of this choice, we also recall that, owing to the high accuracy of those results, their contribution to the world-average value (weighted mean over all data) of the neutron lifetime is dominant at present. The list of experiments that measured the neutron lifetime and which achieved accuracy higher than 10 s is displayed in Table 1. For the world-average value of the neutron lifetime and for the constant λ obtained from it by using data on 0^+–0^+ nuclear transitions, the results of these experiments yield

$$\tau_n = 885.7 \pm 1.0 \text{ s}, \quad \lambda = -1.2675(10). \qquad (17)$$

Let us briefly comment on the results obtained by studying the correlation between the neutron spin and the electron momentum (spin–electron correlation) in neutron decay. Only two experiments of this type had been performed before the mid-1990s [53–55]. The mean value of the parameter A as extracted from those experiments differed significantly from the value obtained by rescaling the neutron lifetime into this correlation through the constant λ. An analysis of this situation, which is known as the experimental neutron anomaly [20], revealed that it was necessary to perform additional experiments of this type. This was recently done by two independent methods [56, 57]. (We restricted our analysis to the results obtained prior to 1998 and did not include, at this stage, the results reported in [58].) However, the results of these new experiments, which removed, by and large, the above anomaly, still lead to ambiguous conclusions, because the extremes of the experimental values from [55] and [57] differ by more than three experimental errors (see Table 2). If we nevertheless assume that this discrepancy is of a purely statistical origin, the mean experimental value of the parameter A (corrections apart) and the value of λ extracted from it are

$$A = -0.1161 \pm 0.0007, \quad \lambda = -1.2664(19). \qquad (18)$$

We note that, among the neutron correlation parameters, A is characterized by the highest sensitivity to variations in the constant λ. The parameter specifying this sensitivity is $dA/d\lambda = 0.38$.

The high accuracy of the results of new measurements of the parameter of the spin–electron correlation in neutron decay made it possible, in the early 1990s, to propose and implement an alternative method for determining the parameters of weak interaction within the Standard Model. This method is based on the analysis of purely neutron results without resort to data on 0^+–0^+ nuclear transitions [8]. Indeed, a set of data on the neutron lifetime, which is determined by two independent basic weak-interaction constants $G_{V\beta}$ and $G_{A\beta} = \lambda G_{V\beta}$, and data on the spin–electron correlation, which is dependent on the ratio of these constants, makes it possible to deduce their experimental values directly without invoking data on nuclear transitions. These values can then be used to check the results if we additionally assume fulfillment of the CVC hypothesis (conservation of weak vector current), which was in fact assumed to be valid in analyzing data on 0^+–0^+ nuclear transition.

In a specific implementation of this method for data analysis, two bands of the values of $G_{V\beta}$ and $G_{A\beta}$ that are allowed by experimental data on $f_n\tau_n$ and on the ratio $G_{A\beta}/G_{V\beta}$ as rescaled from the values of the correlation parameter A in accordance with (16) are constructed in the plane spanned by these variables. The intersection of these bands determines the region of allowed values of the fundamental constants $G_{V\beta}$ and $G_{A\beta}$ according to data on neutron decay that are treated

Table 1. Display of experiments that measured the neutron lifetime

Year	Institute	Procedure	τ_n, s	References
1988	Kurchatov Institute	*n* beam	891 ± 9	[46]
1989	Bonn–ILL	Ultracold neutrons	877 ± 10	[47]
1989	ILL–Sussex Univ.–Rhode Island Univ.	Ultracold neutrons	887.6 ± 3	[48]
1992	PNPI–JINR	Ultracold neutrons	888.4 ± 4.3	[49]
1993	Kurchatov Institute–ILL	Ultracold neutrons	882.6 ± 2.7	[50]
1996	Sussex Univ.–ILL	*n* beam	889.2 ± 4.8	[51]
1997	Kurchatov Institute–ILL	Ultracold neutrons	885.4 ± 1.3	[52]

Table 2. Display of experiments that measured the spin--electron correlation

Year	Institute	Procedure	A	References
1986	ILL	PERKEO-I	−0.1146 ± 19	[53]
1991	PNPI–Kurchatov Institute	*ep* coincidences	−0.1116 (first publication)	[54]
			−0.1135 ± 14 (correction and addendum)	[55]
1995	ILL	drift chamber	−0.1160 ± 15	[56]
1996	ILL	PERKEO-II	−0.1190 ± 13	[57]

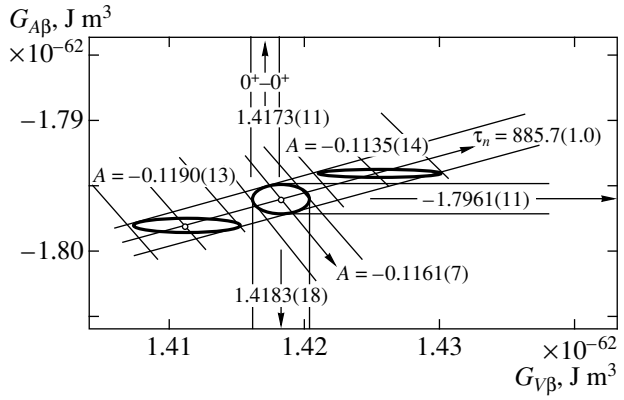

Fig. 2. Regions of allowed values of the beta-decay constants $G_{V\beta}$ and $G_{A\beta}$ as obtained from a global analysis of data on the neutron lifetime (world-average value) and data on the coefficient A of the spin–electron correlation from [55] [A = –0.1135(14)] and [57] [A = –0.1190(13)], as well as from the weighted mean value $\bar{A}$ = –0.1161(7) (see Table 2) at the same neutron-lifetime value.

on the basis of the basis of the Standard Model. Figure 2 shows three such regions corresponding to the world-average value of the neutron lifetime from (17) at three values of the parameter A: the average value from (18) and two extreme experimental values obtained in [55] and in [57], respectively. In addition, this figure displays the values of the constant G_{V0-0} according to data on 0^+–0^+ nuclear transitions and the values of the analogous constant that were extracted from data on elementary-particle decays by using the sum rule (11) for the Kobayashi–Maskawa matrix element. From Fig. 2, it can be seen that the world-average value of the parameter A leads to the region of $G_{V\beta}$ values that is virtually coincident with the region of the allowed values of G_{V0-0}. However, the result of a global analysis of data on the neutron lifetime and data from [55] differs considerably from the G_{V0-0} value as obtained from data on 0–0 transitions. A similar discrepancy, but in the region of smaller values of $G_{V\beta}$, is observed when the results from [57] are included in the analysis. By and large, the above analysis confirms the agreement of modern data with the Standard Model, but it indicates that new precision measurements of the parameter A are required for removing the existing discrepancies. {We recall that such experiments are being performed at the Laue–Langevin Institute (Grenoble) [58] and are planned in Los Alamos at a higher level of precision [59].}

Experiments to measure correlations of the spin–neutrino type are much more difficult in implementation than experiments studying the spin–electron correlation. This is the reason why only in recent years were experiments of the former type performed at a precision level [60, 61]. The accuracy achieved there made it possible to obtain the following independent estimate of λ (we emphasize that the uncertainty is large in that case):

$$B = +0.9820 \pm 0.0040, \quad \lambda = -1.3388(479). \quad (19)$$

In relation to the other correlation parameters, the quantity B is less sensitive to variations in the constant λ. The parameter determining this sensitivity is $dB/d\lambda = 0.084$, which is much less than the above value of $dA/d\lambda$.

Finally, experimental data on the electron–neutrino correlation in free-neutron decay can also be used for the purposes of independent analysis. We have already indicated that, for the first time, such experiments were successfully performed by an ITEP group with the participation of Vladimirsky in the 1960s [3–5]. Unfortunately, their implementation proved to be extremely difficult, and only one such experiment has been performed so far at a level of precision better than 10% [62]. It should be emphasized that this experiment dates as far back as the 1970s. Since it was naturally based on the facilities and procedures of that time, it is highly desirable to repeat it at a new level. The value of the parameter a as determined by employing the data from that experiment and the corresponding value of λ are

$$a = -0.1017 \pm 0.0051, \quad \lambda = -1.2591(168). \quad (20)$$

We would also like to indicate the sensitivity of this experiment to variations in the constant λ. The parameter specifying this sensitivity has a value close to the corresponding value for A: $da/d\lambda = 0.30$.

In order to determine the weak-interaction constants from experimental data on the beta decay of the free neutron, we have so far analyzed data of independent experiments, paying no attention to the interplay of the different experimental parameters. However, such an analysis can be performed with allowance for this interplay in accordance with equations (16) [63]. Assuming independent Gaussian distributions in each of the above-type experiments, we can determine the most probable value of the constant λ ($\bar{\lambda}$) that is consistent with data from the entire set of neutron experiments; by using this value, we can then again construct the expected, most probable, values of the neutron parameters. Such an analysis was performed in [63]. The results are

$$\bar{\lambda} = -1.2673(10), \quad \tau_n = 885.9 \text{ s},$$
$$a = -0.1042, \quad A = -0.1165, \quad B = 0.9877. \quad (21)$$

From a comparison of these results with experimental values of the corresponding parameters, it follows that almost all of them are consistent with experimental data within one standard deviation. The greatest discrepancy of 1.5σ is observed for the parameter B. This highlights once again the need for independent experiments for verifying its experimental value.

The results for $\bar{\lambda}$ can in principle be used again in an independent analysis of neutron data to extract the values of $G_{V\beta}$ and $G_{A\beta}$ by the method described above (see Fig. 2). Such an analysis was recently performed by Towner and Hardy in the report presented at the

symposium WEIN-98 [43]. They used the above data on the neutron lifetime and on the coefficient A and invoked additional data on A from a new experiment performed at the Laue–Langevin Institute [58]. These new data on A [$A = -0.1187(8)$] shift the mean value $\bar{A}$ to the region of larger absolute values and correspond to the mean value of $\bar{\lambda} = -1.2735(21)$. Let us now determine the value of the matrix element V_{ud} by combining this extreme value and the data on the neutron lifetime and calculate its contribution to the sum rule in (11). The results are [43]

$$\begin{aligned} |V_{ud}| &= 0.9714(15), \\ V_{ud}^2 + V_{us}^2 + V_{ub}^2 &= 0.9919(30). \end{aligned} \tag{22}$$

Thus, the inclusion of new data on A leads to the further violation of the sum rule for the Kobayashi–Maskawa matrix up to a level of three standard deviations. This conclusion should be taken to be preliminary. It obviously requires confirmation—for example, in the experiments planned in Los Alamos.

Thus, we see that, by and large, the Standard Model describes well the entire set of current data on neutron decay. Within this description, further experiments are required, however, for confirming the self-consistency of these data and their consistency with independent experiments studying 0–0 transitions and strange-particle decays at a precision level. On the other hand, the above data leave room for deviations from the Standard Model at a level of 1%. This enables us to consider now the problem of quantitatively estimating the possibility for such violations under specific assumptions about their form prescribed by the hypothesis under investigation.

3. ESTIMATES FOR THE HYPOTHESIS OF RIGHT-HANDED CURRENTS

Let us investigate constraints imposed by available neutron data on the possible admixture of the contributions from right-handed lepton currents to the Standard Model. According to modern theoretical concepts, the right-handed neutrinos exist in the schemes where heavy right-handed W_R bosons are introduced along with the standard left-handed W_L bosons. The simplest model featuring right-handed currents, the so-called explicitly symmetric model [17, 18], corresponds to $SU(2)_L \times SU(2)_R \times U(1)$ symmetry. In this model, two additional parameters—the mass of the right-handed boson (it is the ratio η of the squared masses of the left- and right-handed bosons that is actually used) and the angle of mixing between the left- and right-handed bosons, ξ—are introduced along with the parameters of the Standard Model. In this scheme, the general Hamiltonian of the weak nucleon–lepton interaction is given by

$$H_{RC} = [aJ_{L\mu}j_L^\mu + bJ_{R\mu}j_R^\mu + cJ_{L\mu}j_R^\mu + dJ_{R\mu}j_L^\mu];$$

$$\begin{aligned} (j_L)_\mu &= (\overline{\Psi}_e\gamma_\mu(1+\gamma_5)\Psi_{\nu e}), \\ (j_R)_\mu &= (\overline{\Psi}_e\gamma_\mu(1-\gamma_5)\Psi_{\nu e}), \\ (J_L)_\mu &= (\overline{\Psi}_p\gamma_\mu(1-\lambda_N\gamma_5)\Psi_n), \\ (J_R)_\mu &= (\overline{\Psi}_p\gamma_\mu(1+\lambda_N\gamma_5)\Psi_n). \end{aligned} \tag{23}$$

We note that the universality of the bare axial-current constant λ_N, which can a priori be different from the well-known experimental value λ, is assumed here. In the explicitly symmetric model conserving CP invariance, the constants a, b, c, and d of the Hamiltonian H_{RC} are related to the basic parameters of the model by the equations

$$\begin{aligned} a &= (g^2/8)\cos\theta_C((\cos\xi)^2/m_1^2 + (\sin\xi)^2/m_2^2), \\ b &= (g^2/8)\cos\theta_C((\sin\xi)^2/m_1^2 + (\cos\xi)^2/m_2^2), \\ c &= d = (g^2/8)\cos\theta_C\sin\xi\cos\xi(1/m_2^2 - 1/m_1^2), \end{aligned} \tag{24}$$

where g is the coupling constant for the basic interaction of leptons and quarks with W bosons, while $\cos\theta_C$ is the cosine of the Cabibbo angle. Exchange weak interaction is mediated by the physical bosons W_1 and W_2, which are represented by mixed states of masses m_1 and m_2, the mixing of the left- and right-handed bosons that results in the formation of the W_1 and W_2 bosons being specified by the scheme

$$\begin{aligned} W_1 &= W_L\cos\xi + W_R\sin\xi, \\ W_2 &= W_R\cos\xi - W_L\sin\xi. \end{aligned} \tag{25}$$

The parameters a, b, c, and d and the phenomenological constants of the Hamiltonian in (1) are related by the equations

$$\begin{aligned} (G_{F\beta}/\sqrt{2})C_V &= a + b + c + d \\ &= (g^2/8)\cos\theta_C[(1-\sin2\xi)/m_1^2 + (1+\sin2\xi)/m_2^2], \\ (G_{F\beta}/\sqrt{2})C_V' &= a - b - c + d \\ &= (g^2/8)\cos\theta_C\cos2\xi[1/m_1^2 - 1/m_2^2], \\ (G_{F\beta}/\sqrt{2})C_A &= \lambda_N(a + b - c - d) \\ &= (g^2/8)\cos\theta_C[(1+\sin2\xi)/m_1^2 + (1-\sin2\xi)/m_2^2], \\ (G_{F\beta}/\sqrt{2})C_A' &= (G_{F\beta}/\sqrt{2})C_V'\lambda_N = \lambda(a - b + c - d) \\ &= (g^2/8)\cos\theta_C\cos2\xi\cdot\lambda[1/m_1^2 - 1/m_2^2], \\ (G_{V\beta}/\sqrt{2}) &= (g^2/8)\cos\theta_C/m_1^2. \end{aligned} \tag{26}$$

(In the scheme featuring right-handed currents, it is assumed that $G_{F\beta} = G_{V\beta}$.) It should be noted that, in the specific model being considered, there is the additional

condition $c = d$, whence it follows that $C_A' = C_V'\lambda_N$. The Standard Model is obtained in the limit where $\xi \longrightarrow 0$ and $m_2 \longrightarrow \infty$. It should be emphasized that, in the scheme involving right-handed currents, the universal constant $G_{V\beta}$ is determined as the coupling constant for W_1-boson weak interaction, so that $C_V \longrightarrow 1$ only if the right-handed currents are suppressed.

In general, the Hamiltonian of the model being investigated depends on four parameters—$G_{V\beta}$, λ_N, ξ, and $\eta = m_1^2/m_2^2$—which must be determined from experimental data. For this reason, a full analysis requires at least four independent experiments: of these, one specifies the absolute scale—that is, the constant $G_{V\beta}$—while the three others determine the relative quantities. Our objective is to obtain experimental constraints on these parameters by using data on neutron beta decay and, if those are insufficient, by invoking supplementary data, thereby estimating the possible contribution of right-handed currents to the effective weak-interaction Hamiltonian. Here, we deliberately restrict ourselves to the simplest version of the model featuring right-handed currents since, in more complicated versions, the number of model parameters is greater, so that the resulting constraints become less reliable.

Let us establish relations between the experimental characteristics of neutron beta decay and the aforementioned four parameters. We begin by discussing relative measurements that determine the right-handed-current parameters proper, postponing the estimation of the absolute value of the constant $G_{V\beta}$ to the end of the section.

Let us first consider data on the neutron lifetime. In the explicitly symmetric model involving right-handed currents, the ratio of the quantity $(Ft)_{0-0}$ for Fermi 0–0 transitions to $f_n\tau_n$ including the neutron lifetime is determined by the relation

$$\begin{aligned} 2(Ft)_{0-0}\ln 2/(f_n\tau_n) &= 1 + 3\lambda^2 \\ &= 1 + 3(|C_A|^2 + |C_A'|^2)/(|C_V|^2 + |C_V'|^2) \\ &= 1 + 3\lambda_N^2[(1+\eta^2) + (1-\eta^2)\sin 2\xi]/[(1+\eta^2) \\ &\quad -(1-\eta^2)\sin 2\xi]. \end{aligned} \tag{27}$$

(Here and below, we first present the general expression for the relevant quantity and then its representation within the explicitly symmetric model.) It can be seen that, in the scheme featuring right-handed currents, the above ratio, which is determined by the experimental constant λ, depends on the bare coupling constant λ_N for the axial-vector interaction and on the model parameters η and ξ in a complicated way; it should be borne in mind here that the bare constant can differ significantly from the relevant experimental value. In the absence of right-handed currents, these constants coincide ($\lambda = \lambda_N$). By assuming that the weighted mean of the experimental value λ is $\bar{\lambda} = -1.2673(10)$, we find a first equation relating the parameters of the right-handed currents:

$$\begin{aligned} \lambda^2 &= \lambda_N^2[1 + \eta^2 + (1-\eta^2)\sin 2\xi]/[1+\eta^2 \\ &\quad -(1-\eta^2)\sin 2\xi] = (1.2673(10))^2 = 1.6060(25). \end{aligned} \tag{28}$$

In contrast to other correlation experiments, measurement of the electron–neutron correlation in neutron decay furnishes no new information in relation to the neutron lifetime. In order to demonstrate this explicitly, we note that, with allowance for right-handed currents, the correlation coefficient a has the form

$$\begin{aligned} a &= (|C_V|^2 + |C_V'|^2 - |C_A|^2 - |C_A'|^2)/(|C_V|^2 \\ &\quad + |C_V'|^2 + 3|C_A|^2 + 3|C_A'|^2) = (1-\lambda^2)/(1+3\lambda^2), \end{aligned} \tag{29}$$

where λ^2 is determined by equation (28), as before. This situation arises when we assume that the W boson is a vector particle, in which case only the vector and axial-vector versions contribute to the weak-interaction Hamiltonian. It will be seen below that the discrepancy of 0.5σ between data on the electron–neutrino correlation and the mean neutron lifetime—previously, we revealed this discrepancy in analyzing the Standard Model—may suggest leptoquark-mechanism-induced violation of this aspect of the Standard Model. In this case, the electron–neutrino correlation provides new information. In analyzing the hypothesis of right-handed currents, experiments studying this correlation can at best serve as a test of data on the lifetime—unfortunately, the accuracy of the former is presently much poorer than the accuracy of the latter.

Let us analyze the experiments devoted to correlations of the spin–electron and spin–neutrino types. Upon taking into account right-handed currents, the relevant coefficients take the form

$$\begin{aligned} A &= \frac{-4\,\mathrm{Re}(C_A C_A'^*) - 2\,\mathrm{Re}(C_V C_A'^* + C_V' C_A^*)}{|C_V|^2 + |C_V'|^2 + 3|C_A|^2 + 3|C_A'|^2} \\ &= \frac{-2(1-\eta)\cos 2\xi}{1+\eta^2-(1-\eta^2)\sin 2\xi} \\ &\quad \times \frac{(1+\eta)(\lambda_N^2 + \lambda_N) + (1-\eta)\sin 2\xi \cdot \lambda_N^2}{1+3\lambda^2}, \\ B &= \frac{4\,\mathrm{Re}(C_A C_A'^*) - 2\,\mathrm{Re}(C_V C_A'^* + C_V' C_A^*)}{|C_V|^2 + |C_V'|^2 + 3|C_A|^2 + 3|C_A'|^2} \\ &= \frac{2(1-\eta)\cos 2\xi}{1+\eta^2-(1-\eta^2)\sin 2\xi} \end{aligned} \tag{30}$$

$$\times\frac{(1+\eta)(\lambda_N^2-\lambda_N)+(1-\eta)\sin 2\xi\cdot\lambda_N^2}{1+3\lambda^2}.$$

In the ensuing analysis, we use both of these relations, taking the current experimental values of $A = -0.1161(7)$ and $B = +0.9820(40)$ for the correlation coefficients.

In analyzing the hypothesis of right-handed currents, we will need, in addition to data from correlation experiments for neutron beta decay, data extracted from polarization experiments. The polarizations of the electron and the neutrino originating from neutron beta decay are determined by the experimental parameter

$$H_n = \frac{6\,\mathrm{Re}(C_AC_A'^*)+2\,\mathrm{Re}(C_VC_V'^*)}{|C_V|^2+|C_V'|^2+3|C_A|^2+3|C_A'|^2}$$
$$=\frac{(1-\eta)\cos 2\xi}{1+\eta^2-(1-\eta^2)\sin 2\xi} \qquad (31)$$
$$\times\frac{(1+\eta)(1+3\lambda_N^2)+(1-\eta)\sin 2\xi(3\lambda_N^2-1)}{1+3\lambda^2},$$

which takes the value of $H_n = 1$ when there are no right-handed currents. It is interesting to note that, within the explicitly symmetric model featuring right-handed currents, there exists a correlation between the parameters A, B, H_n, and λ_N:

$$(A+B)/2+\lambda_N H_n+(1-3\lambda_N^2)(B-A)/(4\lambda_N)=0. \qquad (32)$$

Experimental constraints on H_n could be deduced from direct measurements of the polarization of the electron from neutron beta decay. Unfortunately, no such experiments have been performed so far; for estimates, we can therefore use only indirect data that make it possible to extract the parameter H_n for neutrino polarization from experiments aimed at determining the cross section for inverse-beta decay on a proton for reactor antineutrinos. Indeed, it was first indicated in [64] that the experimental cross section σ is approximately related to H_n by the equation

$$\sigma = \sigma_0(1+H_n^2)/2, \qquad (33)$$

where σ_0 is the cross section in the Standard Model (that is, without right-handed currents) as determined, for example, from the neutron lifetime by using the quantity λ. According to the latest data from reactor experiments measuring the cross section for antineutrino–proton interactions, H_n is estimated as [65]

$$H_n \geq 0.96 \ (67\%\ \text{C. L.}). \qquad (34)$$

Unfortunately, this estimate is not optimal—because of the large error, it does not lead to constraints on the right-handed-current parameters better than a few percent; for this reason, we will not use it in the ensuing analysis. From the viewpoint of our purposes, data on the cross sections are disadvantageous in that the parameter H_n appears in the experimental quantity quadratically, whence it follows that, in order to obtain the value of H_n with a precision higher than 1%, it is necessary to measure the cross section with an experimental uncertainty that is an order of magnitude less than that in the best currently available cross-section measurements, where this uncertainty is between 2 and 3%. In the experiments being discussed, so high a precision is not attainable at present. This makes us seek an alternative in polarization experiments on nuclei where some parameter similar to H_n would enter into the measured quantity linearly.

As such an alternative, we invoke data on the polarization of positrons from nuclear beta transitions. Specifically, we make use of precision measurements of the longitudinal polarization of positrons from purely Fermi and purely Gamow–Teller nuclear transitions, where the polarization coefficients are independent of nuclear matrix elements. Indeed, the polarization of decay electrons (positrons) that originate from Fermi 0^+–0^+ transitions occurring in the presence of right-handed currents is determined by the quantity

$$H_\mathrm{F} = \mp\frac{2\,\mathrm{Re}(C_VC_V'^*)}{|C_V|^2+|C_V'|^2}$$
$$=\mp\frac{(1-\eta)\cos 2\xi(1+\eta-(1-\eta)\sin 2\xi)}{1+\eta^2-(1-\eta^2)\sin 2\xi}. \qquad (35)$$

The analogous quantity for Gamow–Teller transitions has the form

$$H_\mathrm{GT} = \mp\frac{2\,\mathrm{Re}(C_AC_A'^*)}{|C_A|^2+|C_A'|^2}$$
$$=\mp\frac{(1-\eta)\cos 2\xi(1+\eta+(1-\eta)\sin 2\xi)}{1+\eta^2+(1-\eta^2)\sin 2\xi}. \qquad (36)$$

In a number of studies, the ratio of positron polarizations in Fermi and Gamow–Teller beta transitions for close pairs of nuclei was measured to a high precision. By way of example, we indicate that such measurements were performed in [66] for $^{14}\mathrm{O} \longrightarrow {}^{14}\mathrm{N}/{}^{10}\mathrm{C} \longrightarrow {}^{10}\mathrm{B}$ and in [67] for $^{26m}\mathrm{Al} \longrightarrow {}^{26}\mathrm{Mg}/{}^{30}\mathrm{P} \longrightarrow {}^{30}\mathrm{Si}$. From (35) and (36), it follows that this ratio can be written as

$$P = \frac{H_\mathrm{F}}{H_\mathrm{GT}}$$
$$=\frac{(1+\eta-(1-\eta)\sin 2\xi)(1+\eta^2+(1-\eta^2)\sin 2\xi)}{(1+\eta+(1-\eta)\sin 2\xi)(1+\eta^2-(1-\eta^2)\sin 2\xi)} \qquad (37)$$
$$=\frac{\lambda^2(1+\eta-(1-\eta)\sin 2\xi)}{\lambda_N^2(1+\eta+(1-\eta)\sin 2\xi)}.$$

The experimental values obtained for P in [66, 67] and the mean value of this quantity are

$$\begin{aligned} H_F/H_{GT} &= 1.003(4)\ [66], \\ H_F/H_{GT} &= 0.9996(37)\ [67], \\ \overline{(H_F/H_{GT})} &= \bar{P} = 1.0012(27). \end{aligned} \tag{38}$$

In our analysis, we will use the last value.

Thus, we have specified the range of experimental data that will be used to extract the parameters λ_N, ξ, and η, which characterize right-handed currents. Proceeding to analyze them directly, we note that, from the previous experience, it follows that the approximations $\eta^2 \ll 1$, $\sin 2\xi \approx 2\xi$, and $\cos 2\xi \approx 1$ are quite legitimate. In this case, the set of equations for determining the parameters of right-handed currents in terms of the experimental characteristics has the form

$$\begin{aligned} \lambda^2 &= \lambda_N^2(1+2\xi)/(1-2\xi), \\ (1+3\lambda^2)A &= 2\lambda(-1-\lambda_N(1+X)), \\ (1+3\lambda^2)B &= 2\lambda(-1+\lambda_N(1+X)), \\ \lambda^2/(P\lambda_N^2) &= (1+X)/(1-X) \\ (X &= 2\xi(1-\eta)/(1+\eta)). \end{aligned} \tag{39}$$

Since $\eta \ll 1$, the signs of X and ξ coincide, and two types of solutions are possible:

$$\begin{aligned} &\xi \geq 0, \quad X \geq 0, \quad \lambda_N^2 \leq \lambda^2; \\ &\xi \leq 0, \quad X \leq 0, \quad \lambda_N^2 \geq \lambda^2. \end{aligned} \tag{40}$$

Hence, $|\lambda_N|$ is always less than the experimental value $|\lambda|$ at positive mixing angles and is greater than it at negative mixing angles (the equality of these two quantities corresponds to the absence of right-handed currents). At small mixing angles, the difference $\lambda_N - \lambda$ is proportional to the mixing angle ξ.

The set of equations (39) includes four equations for three unknowns, but it can easily be shown that there is the relation

$$(1+3\lambda^2)(A+B) = -4\lambda. \tag{41}$$

It will be seen below that this relation plays an important role in a specific analysis. The inclusion of relation (41) makes it possible to confine our consideration in the following to a set of three equations. It is convenient to recast these three equations into the form

$$\begin{aligned} \lambda^2 &= \lambda_N^2(1+2\xi)/(1-2\xi), \\ (B-A)/(B+A) &= -\lambda_N(1+X), \\ \lambda^2/(P\lambda_N^2) &= (1+X)/(1-X). \end{aligned} \tag{42}$$

By performing a global analysis of this set of equations with allowance for the scatter of experimental characteristics, it is possible to determine, within fixed errors, the region of values of the right-handed-current parameters λ_N, ξ, and η that is compatible with modern experimental data. For example, it can be constructed by performing a step-by-step sampling of triples of these parameters and by selecting those for which the values of λ, $(B-A)/(B+A)$, and P determined by (42) are compatible with data within the chosen error corridors. This would yield a three-dimensional region in the space of the above parameters that is analogous to that obtained previously by one of the present authors (Yu.V. Gaponov) in [68], but which is reduced somewhat by taking into account more recent data. However, we take another way, using the scheme adopted in the literature. We begin by making an important comment that establishes the relationship between the two approaches in question.

In all studies published so far that are devoted to the problem of right-handed currents (with the exception of [68]), the authors generally restricted themselves to constructing the experimentally allowed region of two parameters, ξ and η, and to estimating, on this basis, the lower limit on the admissible mass of the right-handed boson, paying no attention to estimates of the parameter λ_N. This situation is natural if one uses only part of data determining the total set of the parameters of right-handed currents—for example, if an analysis employs only data on the neutron lifetime and the correlation coefficient B or A (or both of these coefficients), or if one assumes a priori that $\lambda_N = \lambda$. In principle, relations (42) make it possible to eliminate the parameter λ_N in such a way that only the unknown parameters ξ and η will appear in the reduced set of equations. We then obtain

$$\begin{aligned} (B-A)/((B+A)\lambda) &= \sqrt{(1+2\xi)/(1-2\xi)}(1+X), \\ (1+2\xi)/((1-2\xi)P) &= (1+X)/(1-X), \\ X &= 2\xi(1-\eta)/(1+\eta). \end{aligned} \tag{43}$$

This set of equations, together with the additional condition (41), is usually investigated in the literature devoted to evaluating the hypothesis of right-handed currents in neutron and nuclear beta decay [9, 11, 19–22]. It was emphasized above, however, that, in a full pattern that is described by the Hamiltonian in (23), the contribution of right-handed currents depends on all three parameters. Restricting our consideration to two of them, we actually pay no attention to the quantity λ_N, an analog of the axial-vector constant in the case of right-handed currents. However, this elimination of the bare constant from the analysis can hardly be justified. For this reason, we deem it necessary to present the results of a full analysis including constraints on λ_N, which have not yet been considered in the literature. It is obvious that our results for the parameters ξ and η do not differ from the most recent bounds of these parameters (see, for example, [69]). For this reason, we merely present the resulting bounds of ξ and η, restricting ourselves to a brief discussion on them supplemented with the relevant references. At the same time,

we quote the result of our analysis concerning essentially new information about the possible value of the bare coupling constant for the axial-vector weak interaction, a quantity that we believe to be of paramount importance for theoretical constructions, but which has not yet been analyzed.

With allowance for the most recent data on neutron decay and data from nuclear polarization experiments, the admissible region of the right-handed-current parameters ξ and η at a 90% C.L. was presented by Deutsch at the Symposium WEIN-98 in Santa Fe [69]. This region is demonstrated in Fig. 3. As can be seen, it includes the origin of coordinates corresponding to the Standard Model, so that there is no reliable evidence for the existence of right-handed currents. The maximum values allowed by experiments for the mixing parameter ξ occur near $\eta \approx 0$ and, at a C.L. of 1.5σ, fall within the interval

$$-0.037 \le \xi \le +0.035. \tag{44}$$

For the parameter η, which determines the mass of the right-handed boson, the maximal value is achieved at $\xi = 0$, amounting to $\eta \approx 0.067$; for the lower limit on the mass of the right-handed boson, this yields

$$M_R \ge 310 \text{ GeV}. \tag{45}$$

By using the first relation from (42), we can now estimate the values of the parameter λ_N that are consistent with data in the allowed region of the other parameters. At a 90% C.L., this result is

$$-1.335 \le \lambda_N \le -1.175 \tag{46}$$

at an experimental value of $\bar{\lambda} = -1.2673(10)$. Thus, we conclude that, in the case of right-handed admixtures, the bare constant for the ratio of the vector and axial-vector versions of weak interaction can differ noticeably (by 5–7%) from the experimental value even at moderately small mixing angles ($\xi \approx 0.035$). The allowed values of λ_N for smaller ξ can also be derived from the first relation in (42) by using the fact that the difference $|\lambda - \lambda_N|$ in the allowed region is proportional to $|\xi|$.

It should be noted here that, in the calculation of the admissible upper bound on η, an important role is played by relation (41), which must be satisfied in the Standard Model as well and which includes only experimental data, not involving the parameters of right-handed currents, since this relation, which must be met for data sets subjected to analysis, significantly restricts the allowed region of these parameters.

Thus, we have determined the region of values admissible for the relative parameters of right-handed currents. Let us now consider the parameter $G_{V\beta}$; in the case of right-handed currents, it specifies their absolute scale. Let us estimate it by using data on 0–0 transitions. With allowance for right-handed currents, the ratio of the values of $(Ft)_{0-0}$ in the Standard Model and in the scheme involving right-handed currents, $(Ft)_{St}/(Ft)_R$, is given by

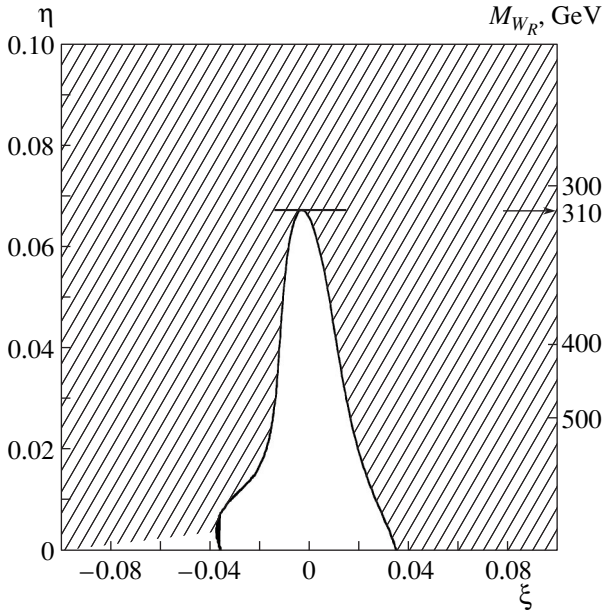

Fig. 3. Region of allowed values of the right-handed-current parameters ξ and η at a 90% C.L. (unhatched). Plotted along the right ordinate are the corresponding values of the mass of the right-handed W_R boson (borrowed from [69]).

$$\begin{aligned}(Ft)_{St}/(Ft)_R &= (|C_V^2| + |C_V'|^2)/2 \\ &= (|a+d|^2 + |b+c|^2)/G_{V\beta} \approx 1 + 2\xi.\end{aligned} \tag{47}$$

Hence, a comparison of the experimental value of this quantity with the value expected in the Standard Model will give a direct estimate of the parameter ξ. If we adopt the validity of the CVC hypothesis and of the unitarity condition for the elements of the Kobayashi–Maskawa matrix, we can estimate these matrix elements with the aid of data on strange-particle decays. In this case, the deviation of the value of $(Ft)_R$ from the that in the Standard Model would be associated with the violation of the sum rules (11) for the matrix elements. An analysis of the possible sum-rule violation was recently performed by Towner. If his result is interpreted as the contribution of right-handed currents, there arises an independent estimate of the mixing angle for right-handed currents [43]:

$$\xi \approx 0.0015(7). \tag{48}$$

This result, which corresponds to a deviation from zero at a level of two standard deviations, is compatible with the results of the above analysis. The estimate in (48) is one order of magnitude more stringent than that in (44), but it introduces the CVC hypothesis in the analysis and unfortunately does not rely on neutron data.

It is useful to compare the constraints on the parameters ξ and η that were obtained from data on neutron

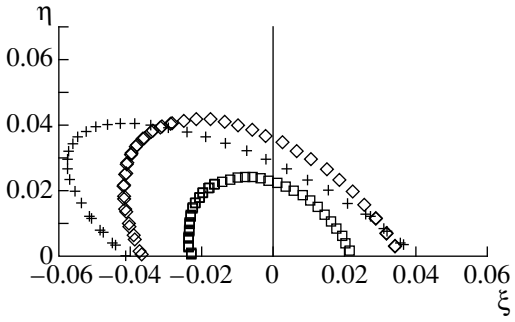

Fig. 4. Region of allowed values of the right-handed-current parameters ξ and η (internal regions of semiellipses) as obtained from data on μ–*e* decay on the basis of constraints on the Michel coefficients $P_\mu\xi\delta/\rho$ (diamonds) and ρ (crosses) [70], as well as from the possible measurement of the longitudinal polarization of electrons in neutron decay to within 0.1% (squares) [71].

beta decay with the corresponding constraints on the right-handed currents from the analysis of data on μ–*e* decay [70]. Experiments of the latter type measure the polarization of decay positrons. These measurements make it possible to estimate the Michel coefficients ρ and $P_\mu\xi\delta/\rho$, which are presently measured at a precision of 0.3% (Fig. 4). The resulting constraints on the parameters of the right-handed currents, $-0.04 \le \xi \le +0.04$ and $\eta \le 0.04$, do not contradict the constraints obtained from neutron data for the mixing angle [see (44)] and are somewhat more stringent than those for the ratio of the squared masses [see (45)], but they are by and large at the same level of precision. At present, a new series of μ–*e* experiments is under preparation that are expected to improve the accuracy in the limits on the various Michel parameters by more than one order of magnitude [69]. The results of these experiments must strengthen the constraints on the parameters of right-handed currents. However, it should be emphasized here that, in principle, the contributions of the right-handed currents to the purely leptonic decay of the muon and those to the hadron–lepton decay of the neutron can differ, although they are interrelated in the simplest models involving right-handed W_R bosons.

In comparing experiments studying neutron and muon decays, there arise the interesting question of what the fundamental distinction between these types of experiments is for the analysis of the right-handed-current hypothesis and the question of whether it is possible to obtain, from data on beta decay, constraints analogous to those coming from muon-decay data [71]. It appears that this difference is a direct consequence of the fact that muon experiments study the polarization of decay electrons (positrons), whereas such purposes have not yet been pursued in neutron experiments. At the same time, such experiments in a direct implementation or in its modified version aimed at measuring the degree of polarization of bremsstrahlung photons in radiative neutron decay or in beta transitions between the mirror pairs of nuclei would be extremely interesting, because the constraints that they can set on the right-handed currents differ qualitatively from those that exist at present. Predictions of such experiments at the required level of precision and the corresponding constraints for the case of a neutron are displayed in Fig. 4 [71], along with the constraints from μ–*e* decay at a 0.1% precision of electron-polarization measurements.

4. ESTIMATING SCALAR AND TENSOR CONTRIBUTIONS

Along with the hypothesis of right-handed currents, the possibility of violation of the Standard Model due to the leptoquark-interaction mechanism, which modifies the standard Hamiltonian by generating corrections associated with the scalar and tensor versions of interaction, is being actively discussed at present. The general theory of leptoquark contributions was given, for example, in [23–28]. Within a phenomenological description of the effective weak-interaction Hamiltonian (1), whose dominant part corresponds to the standard theory, there can exist two types of such models: (i) that in which scalar and tensor corrections involve the left-handed (standard) neutrino [condition (7)] and (ii) that in which the relevant corrections contain terms featuring the right-handed neutrino. The latter are mixed-type models, where the vector and axial-vector terms of the Hamiltonian describe the physical branch of the process with the emission of neutrinos having left-handed helicity and where the scalar and tensor terms are responsible for the emission of neutrinos having right-handed helicity [condition (9)]. The entire set of experiments devoted to neutron beta decay that have been performed by now makes it possible to obtain specific constraints on the structure of such models involving four phenomenological parameters. A more complicated case where leptoquark corrections involve the right-handed neutrino both in the vector and axial-vector parts and in the tensor and scalar parts [relation (8)] can be interpreted as a modified version in which the model involving right-handed currents (Section 3) is supplemented with corrections of the second type. In this case, the total number of phenomenological parameters is as great as eight. Since neutron experiments of only four or five types have been implemented so far, a precision analysis of such models on the basis of purely neutron data is impossible at present; for this reason, we will not discuss this point any more.

The question of whether the scalar or the tensor contributions (or both of them) can appear in the Hamiltonian of beta decay has a long history. Since the studies performed in the 1950s, it has been well known that precision constraints on these corrections can be obtained from the estimates of the Fierz terms, which are proportional to the parameter *b* in the electron spectrum of allowed beta transitions [equation (10)]. In the general case of the phenomenological Hamiltonian (1),

the parameters b for Fermi and Gamow–Teller transitions are given by [2, 34]

$$\begin{aligned} b_{\mathrm{F}} &= \mathrm{Re}(C_S C_V^* + C_S' C_V'^*)/|C_{\mathrm{F}}|^2, \\ b_{\mathrm{GT}} &= \mathrm{Re}(C_T C_A^* + C_T' C_A'^*)/|G_{\mathrm{GT}}|^2, \\ |C_{\mathrm{F}}|^2 &= |C_S|^2 + |C_S'|^2 + |C_V|^2 + |C_V'|^2, \\ |C_{\mathrm{GT}}|^2 &= |C_T|^2 + |C_T'|^2 + |C_A|^2 + |C_A'|^2. \end{aligned} \tag{49}$$

It was emphasized above that, in the absence of right-handed currents, we can make two basic assumptions concerning the physical pattern of additional scalar and tensor contributions. Assuming that these contributions are associated with the left-handed neutrino and that *CP* invariance is conserved and using equation (7), we obtain

$$\begin{aligned} b_{\mathrm{F}} &= C_S C_V/|C_{\mathrm{F}}|^2, \\ b_{\mathrm{GT}} &= C_T C_A/|C_{\mathrm{GT}}|^2, \\ |C_{\mathrm{F}}|^2 &= |C_S|^2 + |C_V|^2, \\ |C_{\mathrm{GT}}|^2 &= |C_T|^2 + |C_A|^2. \end{aligned} \tag{50}$$

These relations make it possible to estimate directly the admixture of the scalar version. But if we assume that the scalar and tensor contributions are associated with the right-handed neutrino, then the use of (9) enables us to demonstrate that, irrespective of the C_S and C_T values, the Fierz parameters vanish automatically; that is,

$$b_{\mathrm{F}} = b_{\mathrm{GT}} = 0. \tag{51}$$

We emphasize the special character of this case, which will be considered below at some length.

We are now going to derive a quantitative estimate associated with the contributions of left-handed neutrinos. Since no special estimates for the possible value of the Fierz term have been obtained for neutron beta decay, they will be deduced here from data on nuclear 0^+–0^+ transitions and from data on purely Gamow–Teller transitions. The first estimates of this kind were obtained in [43], where they were established by using admissible deviations of the shape of spectra for these transitions from the Fermi shape owing to additional terms of the E_e^{-1} type. We note that the inclusion of such terms shifts somewhat the adopted values of $\overline{Ft}$ for 0–0 transitions and affects the sum rule for the elements of the Kobayashi–Maskawa matrix. The estimates of Towner yield

$$\begin{aligned} &|b_{\mathrm{F}}| \le 0.0077(90\%\ \mathrm{C.L.}), \\ &\overline{Ft} = 3066.4 \pm 3.1, \quad |V_{ud}| = 0.9749(6), \\ &V_{ud}^2 + V_{us}^2 + V_{ub}^2 = 0.9986(16), \end{aligned} \tag{52}$$

whence, for the additional scalar contributions featuring left–handed neutrinos [see equation (7)], we obtain

$$\begin{aligned} |b_{\mathrm{F}}| &= |C_S||C_V|/(|C_S|^2 + |C_V|^2) \le 0.0077, \\ &|C_S|/|C_V| \le 0.0077(90\%\ \mathrm{C.L.}). \end{aligned} \tag{53}$$

We note that, in relation to the data from the Standard Model, where the sum rule for the elements of the Kobayashi–Maskawa matrix deviates somewhat from the rigorous unitarity condition [see equation (11)], allowances for the possible scalar contributions reduce the amount of violation of this condition.

The estimates of the Fierz terms in nuclear Gamow–Teller beta transitions from [9, 27] lead to

$$b_{\mathrm{GT}} = -0.0056(51). \tag{54}$$

For additional tensor contributions involving left-handed neutrinos [see equation (7)], we obtain

$$\begin{aligned} b_{\mathrm{GT}} &= C_T C_A/(|C_T|^2 + |C_A|^2) = -0.0056(51), \\ &C_T/|C_A| \approx -0.0056(51). \end{aligned} \tag{55}$$

Thus, the constraints on the Fierz terms allow us to obtain precision estimates for scalar and tensor contributions featuring left-handed neutrinos. Here, however, no attention is given to the case where the additional terms in the Hamiltonian describe a process that involves the emission of neutrinos having right-handed helicity.

Let us dwell at some length on this case, which is of interest from the viewpoint of new physics possibly involving heavy leptoquark bosons [40]. Physically, it corresponds to the production of left-handed neutrinos (right-handed antineutrinos) in the *V, A* interaction modes and the production of right-handed neutrinos (left-handed antineutrinos) in the *S, T* modes. The main feature of this case is that, owing to the special condition (9), the constraints on these contributions are the weakest, which was demonstrated for the first time within the phenomenological approach by one of the present authors (Yu.V. Gaponov) in the review article [34], published as far back as the early 1960s. Later, this case was analyzed is a series of studies performed by the second author (Yu.A. Mostovoy) [35–37], who proposed an original analytic method valid under the assumption of *CP* conservation. Within this method, admissible scalar and tensor contributions to neutron decay were constrained in [37] on the basis of experimental data available at that time.

In this section, we develop this method and extend our analysis to a more general case where the *CP*-conservation hypothesis is not introduced from outset.

By taking into account relation (9), the expression for the experimental parameters in terms of the constants of Hamiltonian (1) can be represented, in this case, as

$$f_n \tau_n (|G_{\mathrm{F}}|^2 + 3|G_{\mathrm{GT}}|^2) = K,$$

$$
\begin{aligned}
a(|C_F|^2 + 3|C_{GT}|^2) &= |C_V|^2 + |C_T|^2 - |C_S|^2 - |C_A|^2,\\
A(|C_F|^2 + 3|C_{GT}|^2) &= -2\,\mathrm{Re}(C_V C_A^* + C_S C_T^*)\\
&\quad - 2\,\mathrm{Re}(C_T C_T^* + C_A C_A^*),\\
B(|C_F|^2 + 3|C_{GT}|^2) &= -2\,\mathrm{Re}(C_V C_A^* - C_S C_T^*)\\
&\quad - 2\,\mathrm{Re}(C_T C_T^* - C_A C_A^*),\\
|G_F|^2 &= G_{F\beta}^2 |C_F|^2 = G_{F\beta}^2(|C_S|^2 + |C_V|^2),\\
|G_{GT}|^2 &= G_{F\beta}^2 |C_{GT}|^2 = G_{F\beta}^2(|C_T|^2 + |C_A|^2).
\end{aligned}
\tag{56}
$$

(Here, we use the constant $G_{F\beta}$ as a normalization factor, so that $C_V = 1$ in the limit $|C_S| \longrightarrow 0$.)

By applying the analytic approach developed in [37] and considering that, in general case, the constants C_i are complex-valued, we derive relations between the Hamiltonian parameters and the experimental coefficients τ_n, a, A, and B. From (56), we can easily obtain (as before, we assume that $G_{F\beta} = G_{V\beta}$)

$$
\begin{aligned}
(1 + A)N &= (C_S - C_T)(C_S - C_T)^*\\
&\quad + (C_V - C_A)(C_V - C_A)^*,\\
(B + a)N &= -(C_S - C_T)(C_S - C_T)^*\\
&\quad + (C_V - C_A)(C_V - C_A)^*,\\
(1 - A)N &= (C_S + C_T)(C_S + C_T)^*\\
&\quad + (C_V + C_A)(C_V + C_A)^* + 4|C_T|^2 + 4|C_A|^2,\\
(B - a)N &= (C_S + C_T)(C_S + C_T)^*\\
&\quad - (C_V + C_A)(C_V + C_A)^* - 4|C_T|^2 + 4|C_A|^2,\\
N &= (|C_S|^2 + |C_V|^2) + 3(|C_T|^2 + |C_A|^2)\\
&= K/(G_{F\beta}^2(f_n\tau_n)).
\end{aligned}
\tag{57}
$$

From (57), we can deduce two pairs of equations:

$$
\begin{aligned}
(1 + A + B + a)N/2 &= |C_V - C_A|^2,\\
(1 + A - B - a)N/2 &= |C_S - C_T|^2;\\
(1 - A - B + a)N/2 &= |C_V + C_A|^2 + 4|C_T|^2,\\
(1 - A + B - a)N/2 &= |C_S + C_T|^2 + 4|C_A|^2.
\end{aligned}
\tag{58}
$$

From the second and the third equation in (58), it follows that

$$
(1 + A) \geq (B + a), \quad (1 - A) \geq (B - a). \tag{59}
$$

These inequalities are very important because, within the theoretical scheme being investigated, the experimental parameters A, B, and a must satisfy them.

For the case of real-valued C_i, an analytic solution to equations (58) was found in [37]. It can easily be seen that, in this case, equations (58) determine completely C_i. However, this is not so if C_i can take complex values. We must then additionally include two experimental parameters in our analysis that emerge in studying triple correlations in allowed beta transitions. These are the well-known parameter D, which characterizes the electron–neutrino correlation in the beta decay of polarized neutrons (or in allowed nuclear beta transitions)—it was first estimated in [72] and was measured at a precision level in two independent experiments reported in [73] and in [74] (see Table 3)—and the parameter E, which is used to describe a J_1–e–J_2 correlation (a correlation between the electron momentum and the final-nucleus polarization J_2 in the decay of nuclei whose polarization is J_1—see [34]). The parameters D and E are defined by the relations

$$
\begin{aligned}
&D(|C_F|^2 + 3|C_{GT}|^2)\\
&= 2\,\mathrm{Im}(-C_V C_A^* - C_V' C_A'^* + C_S C_T^* + C_S' C_T'^*),\\
&E(|C_F|^2 + 3|C_{GT}|^2)\\
&= 2\,\mathrm{Im}(C_V C_A'^* + C_V' C_A^* - C_S C_T'^* - C_S' C_T^*),
\end{aligned}
\tag{60}
$$

whence we obtain two additional constraints:

$$
\begin{aligned}
i(D + E)N &= (C_S - C_T)(C_S + C_T)^*\\
&\quad - (C_S + C_T)(C_S - C_T)^*,\\
i(-D + E)N &= (C_V - C_A)(C_V + C_A)^*\\
&\quad - (C_V + C_A)(C_V - C_A)^*.
\end{aligned}
\tag{61}
$$

It follows from the first pair of equations in (58) that the absolute values of the differences of C_i for the V, A and S, T versions can be determined as simple combinations of the experimental parameters. By analogy with [37], it is therefore convenient to perform the ensuing analysis in terms of the differences

$$
\begin{aligned}
C_V - C_A &= N^{1/2}\nu = \sqrt{N}|\nu|e^{i\theta_\nu},\\
|\nu|^2 &= (1 + A + B + a)/2,\\
C_S - C_T &= N^{1/2}u = \sqrt{N}|u|e^{i\theta_u},\\
|u|^2 &= (1 + A - B - a)/2.
\end{aligned}
\tag{62}
$$

For the sums of these coefficients, we introduce the notation

$$
\begin{aligned}
C_V + C_A &= N^{1/2}x = \sqrt{N}|x|e^{i\theta_x},\\
C_S + C_T &= N^{1/2}y = \sqrt{N}|y|e^{i\theta_y}.
\end{aligned}
\tag{63}
$$

Further, we can construct a set of equations for x and y.

The result is

$$\begin{aligned}
|x|^2 + |x-\nu|^2 + |\nu|^2 + |y|^2 + |y-u|^2 + |u|^2 &= 2,\\
|x|^2 - |x-\nu|^2 + |\nu|^2 - |y|^2 + |y-u|^2 - |u|^2 &= 2a,\\
(-D+E)/2 &= \mathrm{Im}\,\nu\,\mathrm{Re}\,x - \mathrm{Im}\,x\,\mathrm{Re}\,\nu\\
&= |\nu||x|\sin(\theta_\nu - \theta_x),\\
(D+E)/2 &= \mathrm{Im}\,u\,\mathrm{Re}\,y - \mathrm{Im}\,y\,\mathrm{Re}\,u\\
&= |u||y|\sin(\theta_u - \theta_y).
\end{aligned} \tag{64}$$

By using this set of equations, we can find that the phases are related as

$$\begin{aligned}
\tan(\theta_\nu - \theta_x) &= (E-D)/(|x|^2 + |y|^2 + A + a),\\
\tan(\theta_u - \theta_y) &= (E+D)/(|x|^2 + |y|^2 + A - a).
\end{aligned} \tag{65}$$

By eliminating the dependence on the difference of the angles from (64), we obtain a set of equations for the absolute values $|x|$ and $|y|$:

$$\begin{aligned}
(|x|^2 + |y|^2 + A)^2 + a^2 + D^2 + E^2 &= 2|x|^2|\nu|^2 + 2|y|^2|u|^2,\\
|x|^2(|\nu|^2 - a) - |y|^2(|u|^2 + a) &= Aa - DE.
\end{aligned} \tag{66}$$

We note that, when the parameters D and E vanish and when x, y, u, and ν are real, the set of equations (66) reduces to that studied in [37].

After straightforward but cumbersome transformations, we can find that $|x|^2$ and $|y|^2$ satisfy the equations (which involve the parameters $|u|$ and $|\nu|$)

$$\begin{aligned}
&|x|^4(|u|^2 + |\nu|^2)^2 - 2|x|^2[2|\nu|^2(|u|^2 + a)^2\\
&- (|u|^2 + |\nu|^2)(A|u|^2 + a(|u|^2 + a) + DE)]\\
&+ (A|u|^2 + a(|u|^2 + a) + DE)^2\\
&+ (|u|^2 + a)^2(D-E)^2 = 0,\\
&|y|^4(|u|^2 + |\nu|^2)^2 - 2|y|^2[2|u|^2(|\nu|^2 - a)^2\\
&- (|u|^2 + |\nu|^2)(A|\nu|^2 - a(|\nu|^2 - a) - DE)]\\
&+ (A|\nu|^2 - a(|\nu|^2 - a) - DE)^2\\
&+ (|\nu|^2 - a)^2(D+E)^2 = 0.
\end{aligned} \tag{67}$$

Solutions to these equations can be represented in the compact form

$$\begin{aligned}
|x|^2(|u|^2 + |\nu|^2)^2 &= [|\nu|(|u|^2 + a) \pm \sqrt{\Delta}/(2|\nu|)]^2\\
&+ (D-E)^2(|u|^2 + |\nu|^2)^2/(4|\nu|^2),\\
|y|^2(|u|^2 + |\nu|^2)^2 &= [|u|(|\nu|^2 - a) \pm \sqrt{\Delta}/(2|u|)]^2\\
&+ (D+E)^2(|u|^2 + |\nu|^2)^2/(4|u|^2),
\end{aligned} \tag{68}$$

Table 3. Display of experiments that measured the spin–electron–neutrino correlation

Year	Institute (State)	Procedure	D	References
1976	ILL (USA–France)	double facility	−0.0011(17)	[73]
1978	Kurchatov Institute (Russia)	double facility	+0.0022(30)	[74]

$$\begin{aligned}
\Delta &= 4|u|^2|\nu|^2(|u|^2|\nu|^2 - a|u|^2\\
&+ a|\nu|^2 - a^2 - A(|u|^2 + |\nu|^2))\\
&- 2DE(|\nu|^4 - |u|^4) - (D^2 + E^2)(|u|^2 + |\nu|^2)^2.
\end{aligned}$$

For the coefficients C_i in the Hamiltonian, we obtain

$$\begin{aligned}
2C_V &= \sqrt{N}(|\nu| + |x|e^{i(\theta_x - \theta_\nu)})e^{i\theta_\nu},\\
2C_A &= \sqrt{N}(-|\nu| + |x|e^{i(\theta_x - \theta_\nu)})e^{i\theta_\nu},\\
2C_S &= \sqrt{N}(|u| + |y|e^{i(\theta_y - \theta_u)})e^{i\theta_u},\\
2C_T &= \sqrt{N}(-|u| + |y|e^{i(\theta_y - \theta_u)})e^{i\theta_u}.
\end{aligned} \tag{69}$$

Here, the relative phase of the pair of the V, A versions and the pair of the S, T versions are not fixed. Substituting the quantities $|x|$, $|y|$, $|u|$, and $|\nu|$ as expressed in terms of the experimental parameters into (69), we eventually find that the absolute values of these coefficients are given by

$$\begin{aligned}
8|C_V|^2 &= N/(4(1+A)^2) \times [\sqrt{1 + A + B + a}\\
&\times (3 + 3A - B + a) \pm \sqrt{4\Delta/(1 + A + B + a)}]^2\\
&+ N(D-E)^2/(1 + A + B + a),\\
8|C_A|^2 &= N/(4(1+A)^2) \times [\sqrt{1 + A + B + a}\\
&\times (1 + A + B - a) \mp \sqrt{4\Delta/(1 + A + B + a)}]^2\\
&+ N(D-E)^2/(1 + A + B + a),\\
8|C_S|^2 &= N/(4(1+A)^2) \times [\sqrt{1 + A - B - a}\\
&\times (3 + 3A + B - a) \pm \sqrt{4\Delta/(1 + A - B - a)}]^2\\
&+ N(D+E)^2/(1 + A - B - a),\\
8|C_T|^2 &= N/(4(1+A)^2) \times [\sqrt{1 + A - B - a}\\
&\times (1 + A - B + a) \mp \sqrt{4\Delta/(1 + A - B - a)}]^2\\
&+ N(D+E)^2/(1 + A - B - a),\\
4\Delta &= [(1+A)^2 - (B+a)^2]
\end{aligned} \tag{70}$$

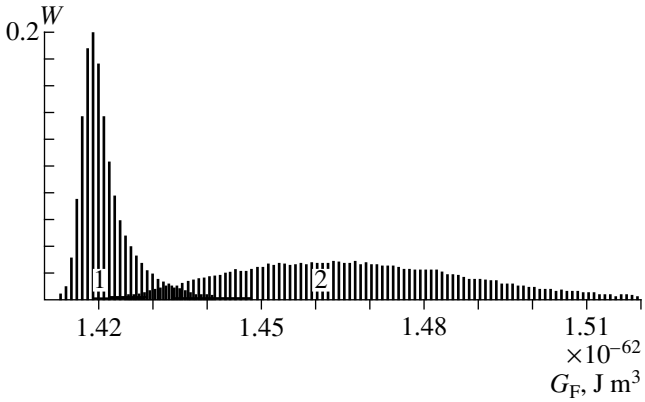

Fig. 5. Probability-density distribution $W = dn_i/\sum n_i$ for specific values of G_F over small intervals for two sets of solutions to the basic set of equations (70) (illustration of the arguments behind the choice between these solutions that is made for the present analysis and which leads to the value of G_F close to the independent estimate on the basis of data on 0–0 transitions).

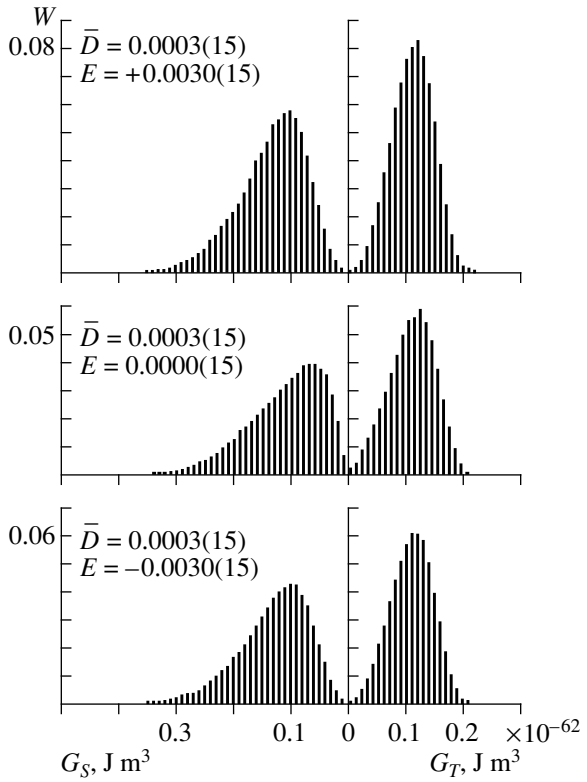

Fig. 6. Probability-density distribution $W = dn_i/\sum n_1$ for the expected values of the scalar-interaction constant $G_S = G_{V\beta}|C_S|$ and the tensor-interaction constant $G_T = G_{V\beta}|C_T|$ in the Hamiltonian of beta decay over small intervals at the mean value of the experimental correlation coefficient, $\bar{D}$ = 0.0003(15), and the values of the coefficient E that are chosen by convention [E = 0, ±0.0030(15)]. The number of solutions dn_i is normalized to $\sum n_1$ [that is, to the total number of events subjected to a Monte Carlo simulation for the tensor version of interaction at E = +0.0030(15)].

$$\times[(1-A)^2-(B-a)^2-4A^2]$$
$$-8DE(1+A)(B+a)-4(D^2+E^2)(1+A)^2,$$
$$N = K/(G_{V\beta}^2(f_n\tau_n)).$$

By way of example, we indicate that, at $E = D = 0$, the above expressions reduce to those presented in [37]. It should be emphasized that, if we require that the absolute values of $|C_V|$, $|C_A|$, $|C_S|$, and $|C_T|$ be real, this imposes some additional constraints on the experimental parameters,

$$1 + A + B + a \geq 0, \quad (1 + A) \geq (B + a), \quad \Delta \geq 0, \quad (71)$$

and the requirement that all values of the squares of the coefficients C_i determined by formulas (70) be positive. Within the theoretical scheme under investigation and at known values of the correlation coefficients a, A, B, and D, this leads to constraints on the experimental values of the correlation parameter E, which are presented below.

We solved the set of equations (70) by the Monte Carlo method for the experimental coefficients chosen to be

$$\tau = 885.7(9)\ \text{s}, \quad A = -0.1161(7),$$
$$B = +0.9820(40), \quad a = -0.1017(51), \quad (72)$$
$$D = -0.0003(15).$$

Within this method, we sampled 100000 combinations for a normal distribution of experimental data with quoted errors. As a result, we obtained a set of values for the Hamiltonian parameters $|C_A|$, $|C_V|$, $|C_S|$, and $|C_T|$, as well as of $|C_F|$ and $|C_{GT}|$, which determines the probability density for specific values of a given parameter within some range. The set of the allowed combinations of the signs of square roots appearing in (70) leads to two possible sets of solutions for the absolute values of these parameters. Bearing in mind that the expected value $|G_F| = G_{V\beta}|C_F|$ must be close to the independent estimate that was established on the basis of data on nuclear 0^+–0^+ transitions and data on the strange decays of elementary particles and must be consistent with the unitarity condition for the elements of the Kobayashi–Maskawa matrix, we can restrict our consideration to one set of solutions:

$$G_F \simeq G_{V0-0} = 1.4173 \times 10^{-62}\ \text{J m}^3. \quad (73)$$

To illustrate the selection criterion used, two spectra of G_F values associated with two sets of solutions are displayed in Fig. 5. Figures 6 and 7 present the calculated probability densities for the values of the parameters $G_S = G_{V\beta}|C_S|$ and $G_T = G_{V\beta}|C_T|$ at various values of the coefficients D and E. For D, we chose the mean value of $\bar{D}$ = 0.0003(15) (Fig. 6) or the value of D = 0.0022(30) (Fig. 7) from [74]. Since the coefficient E has not yet been measured experimentally, the results in Fig. 6 are given for some possible values of this param-

eter, its sign and absolute value both being varied around the mean value of the experimental coefficient D with an error at a level of the mean error in D. The behavior of the solution for the scalar contribution in response to the reversal of the sign of E is illustrated in Fig. 7 for the case of nonzero D. The most important result of this analysis is that a nonzero value of the constant C_T (appearing in the Hamiltonian), which has a virtually stable value at a level of 6% of λ for all cases investigated here, cannot be ruled out by current experimental data. Specifically, our result is

$$G_T = G_{V\beta}C_T \approx 0.12(4) \times 10^{-62}\ \text{J m}^3,$$
$$|C_T|/C_{\text{GT}} \approx |C_T|/|\lambda| = 0.065(22). \quad (74)$$

As to the constant C_S, its value depends pronouncedly on the unknown experimental coefficient E of triple correlation. This constant is minimal when the coefficients D and E are both close to zero, the deviation of the latter from zero being due, in this case, to the statistical scatter introduced for these coefficients. At nonzero E, the constant $G_S = G_{V\beta}|C_S|$ grows, approaching $G_S \approx (0.10\text{–}0.14) \times 10^{-62}$ J m^3, its specific value being dictated by the relative sign of D and E. On the whole, the situation concerning the possible scalar contribution is, however, more uncertain, especially as the statistical scatter for it is greater than that for the tensor contribution by a factor of 2 to 3.

In what is concerned with the results presented in Figs. 5–7, it is reasonable to make the following comment on the method for calculating the probability density for specific values of the constants G_i within the Monte Carlo procedure. For the basic parameters of the problem, we employed the currently adopted data on the neutron lifetime and the correlation coefficients a, A, and B with their experimental uncertainties, so that they were assigned various values in the sampling process that correspond to a Gaussian distribution for each of them. In doing this, we determined the values of $G_i = G_{V\beta}|C_i|$ by formula (70) and, for them, constructed the probability distribution for specific values of this quantity in some range—that is, the probability density $W_i = dn_i/(\sum n_i)$, where dn_i is the number of relevant solutions falling within a small range, while $\sum n_i$ is the total number of solutions for the quantity in question. It should be noted that, by virtue of conditions (71), the total number of solutions for the scalar and tensor versions does not always coincide with the total number of events in the simulation. By way of example, we indicate that, for the quantity G_F (Fig. 5), the area under the probability-distribution curve is equal to unity and has a Gaussian shape, while, for $|G_T|$ and $|G_S|$, this may not be so. For such distributions, we normalized dn_i to the total number of solutions for the case where this number was maximal and obeyed a distribution close to a Gaussian one. This corresponds to the distribution for the tensor version in the upper panels in Figs. 6 and 7 (denoted by $\sum n_1$). The resulting graphs of the probability-density distributions for the Hamiltonian parameters make it possible to determine their expected value and the statistical error and to reveal cases where the reduction of the probability distribution occurs owing to the additional conditions (71).

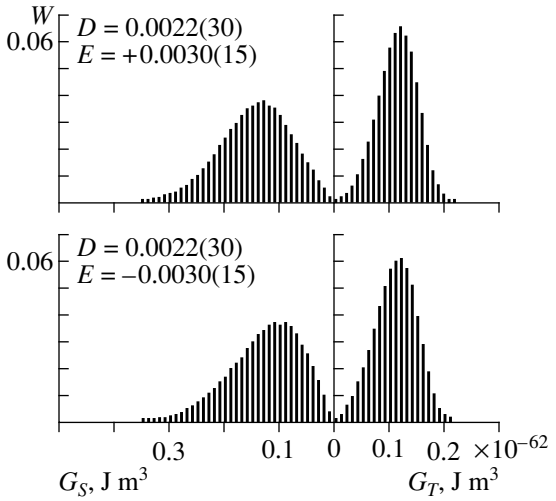

Fig. 7. As in Fig. 6, but at $D = 0.0022(30)$ [74] and $E = \pm 0.0030(15)$.

Thus, it follows from the above analysis that, within the hypothesis of additional tensor and scalar contributions that admits the production of right-handed neutrinos, available experimental data on neutron decay do not rule out the existence of tensor contributions at a level of 6% of the axial-vector contribution. This evinces the need for remeasuring the coefficient of the electron–neutrino correlation and of the triple correlation of the J_1–e–J_2 type (that is, a correlation between the electron momentum and the final-nucleus polarization J_2 in the decay of nuclei with polarization J_1) in order to estimate the possible scalar contribution. Unfortunately, a direct implementation of such an experiment for neutron beta decay is hardly possible. Measurement of the transverse polarization of electrons from polarized-neutron decay could be another possible method for experimentally estimating the coefficient E in neutron decay, but it would be rather hard to perform such a subtle experiment in the current situation where the polarization of electrons from neutron decay has not yet been measured.

5. PROSPECTS FOR NEUTRON EXPERIMENTS

A thorough experimental investigation of free-neutron decay—presently, a prominent line in beta-decay studies, which was initiated by experiments performed at ITEP with a direct participation of Vladimirsky—is now gaining new momentum after a few decades of a latent development. Novel methods in dealing with ultracold neutrons and improvements in the technique

of polarized beams give sufficient grounds to believe that further advances will soon be made in the entire variety of such experiments approaching now a precision level of a few tenths of a percent or even higher. So high a precision and a comparatively simple theoretical interpretation of results render neutron decay very appealing from the viewpoint of searches for nonstandard physics (physics beyond the Standard Model of weak interaction). As has been shown above, a precision analysis of neutron experiments demonstrates that, at the current level of accuracies, a dominant contribution to the process is determined by the Standard Model. Within the classical two-parameter Hamiltonian of weak interaction, free-neutron decay can be described at present to within a few percent, which makes it possible to study, within low-energy physics, the contributions of virtual processes involving a W_L boson of mass 80 GeV, a circumstance that evinces a very interesting potential of neutron physics in this respect. For further advancements along these lines, it is necessary, however, to implement, at the same level of precision, some other experiments—above all, those that measure a spin–electron correlation in the decays of polarized neutrons (that is, the coefficient A). In experiments of this type, data presented by different groups are still inconsistent.

At the same time, going beyond the standard form of weak interaction opens new fields for neutron studies. So far, attention has been given here primarily to searches for contributions from right-handed currents. Of particular interest within these lines are new independent experiments studying a spin–neutrino correlation in the decays of polarized neutrons. In particular, a version of experiments with polarized neutrons that measures directly the combination $(B - A)/(B + A)$ of the correlation coefficients that enter into the formulas used in the analysis for the presence of right-handed currents [see equations (42)] may prove to be of importance. This modification of the experimental setting is advantageous in that it enables measurement of the above ratio in one experiment at the same facility and in that the sensitivity to the absolute polarization of the neutron beam is low in this case. Yet another new way in the same direction may consist in directly measuring the polarization of electrons in free-neutron decay at a precision level of a few tenths of a percent. We emphasize once again that such experiments have not yet been performed in neutron decay. However, the character of information to be extracted from them would be analogous to that from μ–e decay and would lead to constraints of a qualitatively new type in relation to those that already exist [71]. Moreover, an implementation of such an experiment in polarized-neutron beams for measuring the triple J–e–σ correlation and the transverse polarization of electrons in polarized-neutron decay would make it possible to determine, for the first time, the extremely important coefficient E, which leads to *CP* violation (the important role of this coefficient in searches for scalar and tensor contributions in the case of *CP* violation was highlighted in Section 4). Measurements of the polarization of photons accompanying electron emission in the radiative mode of neutron beta decay—interest in this mode was provoked in recent years by the studies of one of the present authors (Yu.V. Gaponov) and R.U. Khafizov [75]—could be an analog to the measurement of electron polarization.

Searches for effects beyond the Standard Model that are associated with leptoquark degrees of freedom represent another important line of such investigations. Here, it seems necessary to perform, at the present-day methodological level, a precision measurement of the electron–neutrino correlation in free-neutron decay (a remake of the ITEP experiments of the 1960s). Such experiments exhibit the highest sensitivity to anomalous contributions of the scalar and tensor types—in particular, to a special version of leptoquark contributions where the emission of right-handed neutrinos is associated with these contributions [40]. That the present-day accuracy of these experiments is insufficient complicates considerably the analysis of the possible presence of such contributions, so that advances in this direction would be highly desirable. In the above discussion, we have presented a direct analytic method for analyzing these contributions that requires performing at least three independent precision measurements of the correlation type (five such experiments in the case where the analysis is performed with allowance for *CP* violation). This analysis has revealed the possible existence of tensor contributions at a level of 6%. In order to test these results, it is necessary to perform precision experiments measuring both the e–ν correlation and the two correlations in polarized-neutron decay. This highlights once again the need for performing further studies in these important realms.

Yet another possibility for developing studies of free-neutron decay is also worthy of note. The radiative mode of neutron beta decay—for photons with energies in excess of 50 keV, its probability must be between 0.1 and 0.2% of the total decay probability [75]—has not yet been observed experimentally. A direct observation of this mode of neutron decay would be of interest both from the viewpoint of experimentally testing the magnitude of radiative corrections in determining the true coupling constant $G_{V\beta}$ and comparing it with the muon-decay constant and the Kobayashi–Maskawa unitarity condition and from the viewpoint of developing new experimental procedures for studying neutron decay. To explain this point in greater detail, we note that, in observing the radiative mode of neutron beta decay, there does indeed arise the possibility of studying radically new correlation and polarization features, additionally including the momentum or the polarization of the emitted photon. It should be emphasized that the radiative-decay process can be observed both in the region of hard emitted photons with energies of a few keV and in the case of detection of light photons, a region where procedures for measuring light polarization are totally different. The observation of the radia-

tive mode of neutron beta decay is topical now; as far as we know, it is planned by a number of experimental groups.

The process of neutron beta decay has always been very appealing for fundamental investigations into the physics of weak interactions. The work along these lines will continue to be among investigations that are, because of the relative simplicity of the object under study, of paramount importance for obtaining deeper insights into the basic laws of physics. It is a pleasure for us to remind the reader that V.V. Vladimirsky, who celebrates the 85th anniversary of his birth this summer, was among those who initiated the first steps along these lines. On behalf of the physicists from the Kurchatov Institute, we wish him good health and many years of creative activity.

ACKNOWLEDGMENTS

We are grateful to the Editorial Board of the journal *Yadernaya Fizika* (presently known in the English-speaking world as *Physics of Atomic Nuclei*), who proposed that we write this review article. We are also indebted to B.G. Yerozolimsky, who actively stimulated the research described in Section 4 of this article. The kind permission of Professor J. Deutsch (Belgium) and Professor I.S. Towner (Canada–USA) to use their results illustratively in our article is gratefully acknowledged.

This work was supported by the Russian Foundation for Basic Research (project nos. 98-02-17706 and 97-02-16536).

REFERENCES

1. T. D. Lee and C. N. Yang, Phys. Rev. **104**, 254 (1956).
2. *Weak Interactions: The Latest Investigations of Beta Decay*, Ed. by A. I. Alikhanov (Fizmatgiz, Moscow, 1960).
3. Yu. V. Trebukhovskiĭ, V. V. Vladimirskiĭ, V. A. Ergakov, and V. K. Grigor'ev, Zh. Éksp. Teor. Fiz. **36**, 1314 (1959) [Sov. Phys. JETP **9**, 931 (1959)].
4. V. B. Berestesky, B. L. Joffe, A. P. Rudik, and K. A. Ter-Martirosyan, Nucl. Phys. **5**, 464 (1958).
5. V. V. Vladimirskiĭ, V. K. Grigor'ev, V. A. Ergakov, *et al.*, Izv. Akad. Nauk SSSR, Ser. Fiz. **25**, 1121 (1961).
6. V. K. Grigor'ev, A. P. Grishin, V. V. Vladimirskiĭ, *et al.*, Yad. Fiz. **6**, 329 (1967) [Sov. J. Nucl. Phys. **6**, 239 (1967)].
7. S. L. Glashow, Nucl. Phys. **22**, 579 (1961); S. Weinberg, Phys. Rev. Lett. **19**, 1264 (1967); A. Salam, in *Elementary Particle Theory*, Ed. by N. Svartholm (Almquist and Wiksell, Stockholm, 1968), p. 367.
8. K. Schreckenbach and W. Mampe, J. Phys. G **18**, 1 (1992).
9. J. Deutsch and P. Quin, in *Precision Tests of the Standard Electroweak Model*, Ed. by P. Langacker (World Sci., Singapore, 1995), p. 706.
10. Yu. A. Mostovoĭ *et al.*, Usp. Fiz. Nauk **166**, 987 (1996) [Phys. Usp. **39**, 925 (1996)].
11. *Precision Tests of the Standard Electroweak Model*, Ed. by P. Langacker (World Sci., Singapore, 1995).
12. D. H. Wilkinson, Nucl. Phys. A **377**, 474 (1982).
13. W. J. Marciano and A. Sirlin, Phys. Rev. Lett. **56**, 22 (1986).
14. D. H. Wilkinson, Nucl. Phys. A **511**, 301 (1990).
15. R. P. Feynman and M. Gell-Mann, Phys. Rev. **109**, 193 (1958).
16. Yu. A. Mostovoy, Yad. Fiz. **61**, 1418 (1998) [Phys. At. Nucl. **61**, 1316 (1998)].
17. J. C. Pati and A. Salam, Phys. Rev. D **10**, 275 (1974); R. N. Mohapatra and J. C. Pati, Phys. Rev. D **11**, 566, 2558 (1975).
18. G. Senjanovic and R. N. Mohapatra, Phys. Rev. D **12**, 1502 (1975).
19. P. Herczeg, in *Fundamental Symmetries in Nuclei and Particles* (World Sci., Singapore, 1990), p. 46.
20. Yu. V. Gaponov, P. E. Spivak, and N. B. Shul'gina, Yad. Fiz. **52**, 1653 (1990) [Sov. J. Nucl. Phys. **52**, 1042 (1990)]; Phys. Lett. B **253**, 283 (1991).
21. A. S. Carnoy *et al.*, Phys. Rev. Lett. **65**, 3249 (1990); J. Phys. G **18**, 823 (1992).
22. Yu. V. Gaponov, in *Proceedings of the III International Conference WEIN-92, Dubna, 1992* (World Sci., Singapore, 1993), p. 87.
23. R. N. Mohapatra *et al.*, Phys. Lett. B **145**, 433 (1984).
24. W. Buchmuller *et al.*, Phys. Lett. B **191**, 442 (1987).
25. S. Davidson *et al.*, Z. Phys. C **61**, 613 (1994).
26. M. Leurer, Phys. Rev. D **50**, 536 (1994).
27. P. Herczeg, in *Proceedings of the III International Conference WEIN-92, Dubna, 1992* (World Sci., Singapore, 1993), p. 262.
28. P. Quin, J. Deutsch *et al.*, in *Proceedings of the 14th International Conference on Particles and Nuclei, Williamsburg, 1996*, p. 555.
29. J. Govaerts, in *Proceedings of the International Europhysical Conference on High Energy Physics, Jerusalem, 1997* (in press).
30. P. Quin and T. A. Girard, Phys. Lett. B **229**, 29 (1989).
31. M. Allet *et al.*, Phys. Lett. B **383**, 139 (1996).
32. N. Severijns *et al.*, Phys. Rev. Lett. **70**, 4047 (1993); Erratum: **73**, 611 (1994).
33. J. Govaerts, Nucl. Instrum. Methods Phys. Res. A **402**, 303 (1998).
34. Yu. V. Gaponov, Usp. Fiz. Nauk **102**, 211 (1970) [Sov. Phys. Usp. **13**, 647 (1970)].
35. Yu. A. Mostovoĭ and A. I. Frank, Pis'ma Zh. Éksp. Teor. Fiz. **24**, 38 (1976) [JETP Lett. **24**, 43 (1976)].
36. Yu. A. Mostovoĭ, Pis'ma Zh. Éksp. Teor. Fiz. **37**, 162 (1983) [JETP Lett. **37**, 196 (1983)].
37. B. G. Erozolimskiĭ and Yu. A. Mostovoĭ, Yad. Fiz. **53**, 418 (1991) [Sov. J. Nucl. Phys. **53**, 260 (1991)].
38. B. G. Yerozolimsky, in *Proceedings of the International Workshop on Particle Physics with Slow Neutrons, ILL, Grenoble, France, 1998*; Nucl. Instrum. Methods Phys. Res. A **440** (2000) (in press).

39. Yu. A. Mostovoĭ, Yu. V. Gaponov, and B. G. Yerozolimsky, in *Proceedings of the II International Conference NANP-99, 1999*; Yad. Fiz. **63**, 1268 (2000) [Phys. At. Nucl. **63**, 1193 (2000)].
40. Yu. V. Gaponov, Yad. Fiz. **62**, 1281 (1999) [Phys. At. Nucl. **62**, 1206 (1999)]; Yu. V. Gaponov, in *Proceedings of the II International Conference NANP-99, 1999*; Yad. Fiz. **63**, 1274 (2000) [Phys. At. Nucl. **63**, 1200 (2000)].
41. J. C. Hardy, I. S. Towner, *et al.*, Nucl. Phys. A **509**, 429 (1990).
42. I. S. Towner *et al.*, in *Proceedings of the IV International Symposium WEIN-95, Osaka, Japan, 1995* (World Sci., Singapore, 1995), p. 313.
43. I. S. Towner and J. C. Hardy, in *Proceedings of the International Symposium WEIN-98, Santa Fe, USA, 1998* (World Sci., Singapore, 1999), p. 338.
44. B. G. Erozolimsky, Usp. Fiz. Nauk **116**, 145 (1975) [Sov. Phys. Usp. **18**, 377 (1975)].
45. B. G. Yerozolimsky, in *Collected Works* (Nauka, Leningrad, 1988), p. 3.
46. P. E. Spivak, Zh. Éksp. Teor. Fiz. **94** (9), 1 (1988) [Sov. Phys. JETP **67**, 1735 (1988)].
47. F. Anton, W. Paul, W. Mampe, *et al.*, Nucl. Instrum. Methods Phys. Res. A **284**, 101 (1989).
48. W. Mampe, P. Aregon, J. C. Bates, *et al.*, Nucl. Instrum. Methods Phys. Res. A **284**, 111 (1989).
49. V. V. Nesvizhevskiĭ, A. P. Serebrov, *et al.*, Zh. Éksp. Teor. Fiz. **102**, 740 (1992) [Sov. Phys. JETP **75**, 405 (1992)].
50. L. N. Bondarenko, V. Mampe, and V. I. Morozov, Pis'ma Zh. Éksp. Teor. Fiz. **57**, 82 (1993) [JETP Lett. **57**, 88 (1993)].
51. J. Byrne, P. Dawber, *et al.*, Europhys. Lett. **33**, 187 (1996).
52. S. S. Arzumanov *et al.*, in *Proceedings of the International Workshop on Particle Physics with Slow Neutrons, ILL, Grenoble, France, 1998*; Nucl. Instrum. Methods Phys. Res. A **440**, 511 (2000).
53. P. Bopp, D. Dubbers, R. Horing, *et al.*, Phys. Rev. Lett. **56**, 919 (1986).
54. B. G. Erozolimskii, I. A. Kuznetsov, I. V. Stepanenko, *et al.*, Phys. Lett. B **263**, 33 (1991).
55. B. G. Yerozolimsky *et al.*, Phys. Lett. B **412**, 240 (1997).
56. H. Abele *et al.*, Phys. Lett. B **407**, 202 (1997).
57. K. P. Schreckenbach *et al.*, Phys. Lett. B **349**, 427 (1995).
58. J. Reich, H. Abele, S. Baessler, *et al.*, in *Proceedings of the ISINN-5, Dubna, 1997*, p. 40.
59. L. Beck, Paper presented at International Symposium WEIN-98, Santa Fe, USA, 1998.
60. I. A. Kuznetsov *et al.*, Phys. Rev. Lett. **75**, 794 (1995); A. P. Serebrov *et al.*, Zh. Éksp. Teor. Fiz. **113**, 1963 (1998) [JETP **86**, 1074 (1998)].
61. D. Dubbers, W. Mampe, and J. Donner, Europhys. Lett. **11**, 195 (1990).
62. C. Stratova, R. Dobrozemsky, *et al.*, Phys. Rev. D **18**, 3978 (1978).
63. Yu. A. Mostovoi, Yad. Fiz. **59**, 1013 (1996) [Phys. At. Nucl. **59**, 968 (1996)]; Yu. A. Mostovoy, Preprint No. IAE-6040/2 (Kurchatov Institute of Atomic Energy, Moscow, 1997).
64. E. Kh. Akhmetov, A. A. Borovoĭ, Yu. V. Gaponov, and A. N. Kheruvimov, Pis'ma Zh. Éksp. Teor. Fiz. **46**, 258 (1987) [JETP Lett. **46**, 325 (1987)].
65. V. N. Vyrodov, Yu. V. Kozlov, V. P. Martem'yanov, *et al.*, Pis'ma Zh. Éksp. Teor. Fiz. **61**, 161 (1995) [JETP Lett. **61**, 163 (1995)].
66. V. A. Wicher *et al.*, Phys. Rev. Lett. **58**, 1821 (1987).
67. A. S. Carnoy *et al.*, Phys. Rev. Lett. **65**, 3249 (1990).
68. Yu. V. Gaponov and N. B. Shul'gina, Yad. Fiz. **49**, 1359 (1989) [Sov. J. Nucl. Phys. **49**, 845 (1989)].
69. J. Deutsch, in *Proceedings of the International Symposium WEIN-98, Santa Fe, USA, 1998* (World Sci., Singapore, 1999), p. 325.
70. M. A. B. Beg *et al.*, Phys. Rev. Lett. **38**, 1252 (1977).
71. Yu. V. Gaponov and R. U. Khafizov, Yad. Fiz. **57**, 34 (1994) [Phys. At. Nucl. **57**, 31 (1994)].
72. B. G. Erozolimsky, L. N. Bondarenko, Yu. A. Mostovoy, *et al.*, Phys. Lett. B **27**, 557 (1968).
73. R. Steinberg, B. Vignon, *et al.*, Phys. Rev. D **13**, 2469 (1976).
74. B. G. Erozolimskiĭ, Yu. A. Mostovoĭ, V. P. Fedunin, *et al.*, Yad. Fiz. **28**, 98 (1978) [Sov. J. Nucl. Phys. **28**, 48 (1978)].
75. Yu. V. Gaponov and R. U. Khafizov, Yad. Fiz. **59**, 1270 (1996) [Phys. At. Nucl. **59**, 1213 (1996)]; Yu. V. Gaponov and R. U. Khafizov, Phys. Lett. B **379**, 7 (1996).

Translated by A. Isaakyan

Physics of Atomic Nuclei, Vol. 63, No. 8, 2000, pp. 1377–1386. Translated from Yadernaya Fizika, Vol. 63, No. 8, 2000, pp. 1454–1464.

ON THE 85th ANNIVERSARY OF V.V. VLADIMIRSKY

Approximation of the Microscopic Effective Pairing Interaction by the Off-Shell *T* Matrix for Free Nucleon–Nucleon Scattering

M. Baldo[1)], U. Lombardo[1), 2)], É. E. Saperstein, and M. V. Zverev

Russian Research Centre Kurchatov Institute, pl. Kurchatova 1, Moscow, 123182 Russia

Received January 20, 2000

Abstract—The effective pairing interaction in the $^1S_0$ channel as calculated microscopically within the Brueckner method for a planar slab of nuclear matter by using the separable version of the Paris nucleon–nucleon potential is investigated. The effective interaction is determined for the model space including all negative-energy single-particle states. An analysis is performed for two values of the chemical potential, $\mu = -8$ and -4 MeV. It is shown that, to a high precision, the effective interaction can be approximated by the off-shell *T* matrix for free nucleon–nucleon interaction, the *T* matrix in question being taken at a negative value of the total energy of two nucleons $E = 2\mu$. © *2000 MAIK "Nauka/Interperiodica".*

1. INTRODUCTION

In [1, 2], a method was proposed for numerically solving the Bethe–Goldstone equation in nonhomogeneous nuclear systems for separable interaction without recourse to any form of local approximation. With the aid of this method, an effective pairing interaction $\mathcal{V}^p_{\text{eff}}$ was found in the $^1S_0$ channel for semi-infinite nuclear matter placed in the one-dimensional Woods–Saxon potential well $V(x)$. The model space was taken there in a form conventional for nuclear physics, so that it included all negative-energy single-particle states. The specific calculations were performed for the separable 3×3 form [3, 4] of the Paris potential [5]. In that case, the effective interaction $\mathcal{V}^p_{\text{eff}}$ is also a 3×3 matrix, whose coefficients $\Lambda_{ij}(X, X')$ depend on the center-of-mass (c.m.) coordinates of two nucleons prior to and after the interaction event. A determination of $\mathcal{V}^p_{\text{eff}}$ was reduced to solving a set of six one-dimensional integral equations for the coefficients $\Lambda_{ij}(X, X')$ (the matrix Λ_{ij} is symmetric; hence, only six coefficients are independent). In principle, it is not hard to solve this set of equations, but the main computational difficulty consists in calculating their kernels, which represent the convolution of the two-particle propagator B_{ij} with the form factors g_i and g_j of the nucleon–nucleon potential (for the sake of brevity, we will refer to it as merely the propagator). In order to determine such propagators, it is necessary to calculate a large number of multidimensional integrals, but this consumes a lot of machine time even if sufficiently fast computers are used. A solution to the equation for the effective interaction is represented in the form of some large matrices, which is not convenient for practical applications.

In order to simplify the calculation of the propagator B_{ij}, a version of the local approximation was proposed in [2]. This method, which was dubbed a local-potential approximation (LPA), consists in the following. At a fixed mean value $X_0 = (X + X')/2$ of the c.m. coordinates of the interacting nucleons, the exact value of $B_{ij}(X_0, t)$ ($t = X - X'$) in the nonhomogeneous system under study is replaced by the approximate value $B^{\text{LPA}}_{ij}(X_0, t)$ that coincides with the corresponding value for infinite nuclear matter placed in the potential well $V_0 = V(X_0)$. The LPA and the standard local-density approximation (LDA) are virtually equivalent within nuclear matter, but they differ substantially in the surface region, where there is no direct local relation between the density and the potential. In the surface region, the LDA is inapplicable almost completely, if for no other reason than the violation of the Pomeranchuk stability condition [6]; at the same time, the accuracy of the LPA in semi-infinite nuclear matter is at a level of a few percent even at the point where the potential $V(x)$ decreases at a maximum rate [1]. In practice, an LPA calculation at a fixed value of the chemical potential μ is performed in the following way. First, a fixed step δV in the magnitude of the potential-well depth is specified, and a set of two-particle propagators $B_{\text{inf}}([V_m], t)$ for infinite nuclear matter in the potential $V_m = \delta V(m - 1)$ is computed. For each point X of the nonhomogeneous system being considered, the propagator $B^{\text{LPA}}(X, t)$ is found after that by interpolating $B_{\text{inf}}([V_m], t)$ corresponding to the V_m values closest to $V(X)$. The kernels obtained in this way for the integral equations describing the components $\Lambda_{ij}(X, X')$ of the effective interaction—and, hence, the effective interaction itself—retain information about the geometry of the problem. The use of the LPA simplifies con-

[1)] Istituto Nazionale di Fisica Nucleare, Sezione di Catania, 57 Corso Italia, I-95129 Catania, Italy.

[2)] Università di Catania, Dipartimento di Fisica, 57 Corso Italia, I-95129 Catania, Italy.

siderably the determination of the effective interaction in relation to the method for constructing a precise solution, but the computational scheme is very involved even in this case.

In this study, we use the LPA to calculate $\mathcal{V}_{\text{eff}}^{\text{LPA}}$ for the case of planar-slab geometry and find that there is yet another approximation for the effective interaction, a very simple one indeed. It turns out that, to a high precision, $\mathcal{V}_{\text{eff}}^{\text{LPA}}$ coincides with the off-shell T matrix for free nucleon–nucleon scattering at the total energy E of two nucleons that is equal to 2μ (recall that is a negative value). Even within the LPA, the computation of this quantity is much simpler than the calculation of the effective interaction.

The ensuing exposition is organized as follows. In Section 2, we present general formulas relating the effective interaction $\mathcal{V}_{\text{eff}}^{p}$ to the T matrix. In Section 3, we develop a simple and highly accurate method for calculating the T matrix in the coordinate representation. In Section 4, we give an account of the results obtained by calculating the effective interaction $\mathcal{V}_{\text{eff}}^{p}$ and analyze the possibility of approximating it by the T matrix. The results are summarized and discussed in Section 5.

2. GENERAL RELATIONS FOR $\mathcal{V}_{\text{eff}}^{p}$

Following [1, 2], we employ the pairing-gap equation in the form

$$\Delta = \mathcal{V} A^{s} \Delta, \tag{1}$$

which is commonly accepted in many-body theory [6, 7] and which involves explicitly the two-particle propagator $A^s = GG^s$ in a superfluid system (G and G^s are single-particle Green's functions for, respectively, a normal and a superfluid system). In Bethe–Brueckner theory, the interaction block $\mathcal{V}$ irreducible in the particle–particle channel is approximated by the free nucleon–nucleon potential. As usual, an effective interaction is introduced via partitioning the full Hilbert space into the model subspace S_0 and the complementary subspace S'. As a result, the two-particle propagator A^s can be represented as the sum $A^s = A_0^s + A'$. In the second term on the right-hand side, we suppress the subscript s, because it is assumed that the effects of superfluidity can be disregarded in the subspace S'.

In the model space, equation (1) can be represented as

$$\Delta = \mathcal{V}_{\text{eff}}^{p} A_0^{s} \Delta, \tag{2}$$

where $\mathcal{V}_{\text{eff}}^{p}$ obeys the equation

$$\mathcal{V}_{\text{eff}}^{p} = \mathcal{V} + \mathcal{V} A' \mathcal{V}_{\text{eff}}^{p}. \tag{3}$$

It was noted above that, in [2], the model subspace S_0 includes all two-particle states (λ, λ') whose energies $(\varepsilon_\lambda, \varepsilon_{\lambda'})$ are both negative. In this case, the complementary subspace S' includes not only two-particle states characterized by two positive energies but also states for which one of the energy values (ε_λ or $\varepsilon_{\lambda'}$) is positive, while the other is negative (but it is higher than the chemical potential μ).

We consider a planar nuclear-matter slab of thickness $2L$ placed in the one-dimensional Woods–Saxon potential well $V(x)$ symmetric with respect to the point $x = 0$:

$$V(x) = \frac{V_0}{1 + \exp((x - L)/d) + \exp(-(x + L)/d)}. \tag{4}$$

The parameter values—the depth of $V_0 = 50$ MeV, the diffuseness of $d = 0.65$ fm, and the slab half-width of $L = 8$ fm—are taken to be close to the corresponding values for heavy nuclei. In the case of planar-slab geometry, all relations for the effective interaction are similar to those that are known for the semi-infinite system. For this reason, we present here only those that are necessary for understanding the computational scheme, referring the reader to [1, 2] for details. The separable form [3, 4] of the Paris potential is given by

$$\mathcal{V}(\mathbf{k}, \mathbf{k}') = \sum_{ij} \lambda_{ij} g_i(k^2) g_i(k'^2), \tag{5}$$

where $\mathbf{k}$ ($\mathbf{k}'$) is the relative momentum of the nucleons prior to (after) the scattering event. This form was tested earlier in the calculations within Brueckner theory for infinite [8, 9] and semi-infinite [1, 2] nuclear matter. In expansion (5), the original normalization from [3, 4] was modified in a such a way that the condition $g_i(0) = 1$ is satisfied. The absolute values of the coefficients λ_{ij} then furnish direct information about the strength of the corresponding components of the nucleon–nucleon interaction. These values (in MeV fm^3 units) are $\lambda_{11} = -3659$, $\lambda_{12} = 2169$, $\lambda_{22} = -1485$, $\lambda_{13} = -23.6$, $\lambda_{23} = 57.6$, and $\lambda_{33} = 17.2$. As can be seen, the last three components, which carry the subscript $j = 3$, are approximately two orders of magnitude smaller than the first three components, which feature only the subscripts $j = 1, 2$. The small components are operative only at high momenta, since the form factor $g_3(k)$ increases with increasing k, in contrast to the form factors $g_1(k)$ and $g_2(k)$, which decrease fast (see Fig. 1). But at momentum values around $k \simeq 1.5$ fm^{-1}, which are important in the pairing problem, the contribution of the small component does not exceed 10% of the contribution of the dominant components. Because of this, only the three large components can be taken into consideration in the ensuing qualitative analysis of the effective interaction. Of course, the calculations include all the terms.

The effective interaction for the nucleon–nucleon potential (5) also has a separable form. In the notation

adopted in [2], it is given by

$$\mathcal{V}^{p}_{\text{eff}}(k_\perp^2, k_\perp'^2; x_1, x_2, x_3, x_4; E) = \sum_{ij} \Lambda_{ij}(X_{12}, X_{34}; E) g_i(k_\perp^2, x_{12}) g_j(k_\perp'^2, x_{34}). \quad (6)$$

Here, we have introduced the c.m. coordinates and the relative coordinates in the x direction [$X_{12} = (x_1 + x_2)/2$, $x_{12} = x_1 - x_2$, and so on]; $\mathbf{k}_\perp$ is the two-dimensional momentum vector in the plane orthogonal to the x axis; and $g_i(k_\perp^2, x)$ is determined by the inverse Fourier transformation of the form factor $g_i(k_\perp^2 + k_x^2)$ with respect to the variable k_x.

The coefficients Λ_{ij} in this expansion obey the set of integral equations

$$\Lambda_{ij}(X_{12}, X_{34}; E) = \lambda_{ij}\delta(X_{12} - X_{34}) + \sum_{lm} \lambda_{il} \int dX_{56} B_{lm}(X_{12}, X_{56}; E) \Lambda_{mj}(X_{56}, X_{34}; E), \quad (7)$$

where the quantities B_{lm} are determined by the convolutions of the propagator A' with two form factors:

$$B_{lm}(X_{12}, X_{34}; E) = \sum_{nn'}{}' \int \frac{d^2\mathbf{k}_\perp}{(2\pi)^2} \frac{G^l_{nn'}(k_\perp^2, X_{12}) G^{m*}_{n'n}(k_\perp^2, X_{34})}{E - \varepsilon_\lambda - \varepsilon_{\lambda'}}, \quad (8)$$

$$G^l_{nn'}(k_\perp^2, X_{12}) = \int dx_{12} g_l(k_\perp^2, x_{12}) y_n(X_{12} + x_{12}/2) y_{n'}(X_{12} - x_{12}/2). \quad (9)$$

Here, $\lambda = (n, \mathbf{k}_\perp)$; $\varepsilon_\lambda = \varepsilon_n + k_\perp^2/2m$; and ε_n and y_n are, respectively, the eigenenergies and the wave functions for the one-dimensional Schrödinger equation with the potential (4). The primed sum in (8) is taken over those λ, λ' states that are not included in the model subspace. Hence, summation over n and n' actually includes summation over discrete states and integration over the continuous spectrum with the obvious substitution $\sum_n \longrightarrow \int dp_x/2\pi$. If, we set $\varepsilon_n < \varepsilon_{n'}$ (accordingly, $\varepsilon_\lambda < \varepsilon_{\lambda'}$) in (8), for the sake of convenience, multiplying the result by a factor of 2, summation over n and n' and integration with respect to $\mathbf{k}_\perp$ will be constrained by the conditions $\varepsilon_\lambda > \mu$ and $\varepsilon_{\lambda'} > 0$.

As is well known, the strong repulsion core of the nucleon–nucleon interaction (in particular, this characterizes the Paris potential) leads to a very slow convergence of the integrals with respect to the momenta in (8). In order to improve convergence, it is convenient to renormalize equation (3) by expressing the effective interaction in terms of the off-shell T matrix for free nucleon–nucleon scattering at energy $E = 2\mu$:

$$T(E) = \mathcal{V} + \mathcal{V} A^0(E) T(E). \quad (10)$$

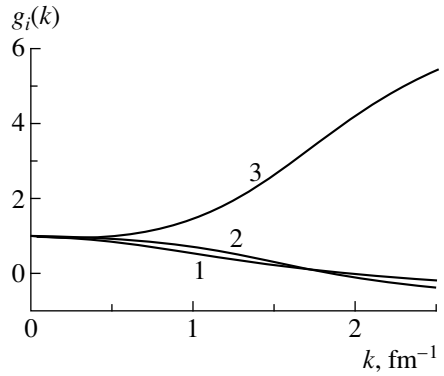

Fig. 1. Form factors $g_i(k)$. Figures on the curves correspond to the form-factor indices.

Here, $A^0(E)$ is the propagator for two free nucleons with total energy E.

Obviously, the T matrix admits a separable expansion of the form (6) with the coefficients $T_{ij}(t; E)$ depending only on the difference $t = X - X'$. These coefficients obey an equation that coincides in form with (7), but which differs from it by the substitutions $\Lambda \longrightarrow T$ and $B(X, X'; E) \longrightarrow B^0(t; E)$:

$$T_{ij}(t; E) = \lambda_{ij}\delta(t) + \sum_{lm} \lambda_{il} \int dt' B^0_{lm}(t - t'; E) T_{mj}(t'; E). \quad (11)$$

In a compact form, the renormalized equation for the effective interaction can be represented as

$$\Lambda_{ij} = T_{ij} + \sum_{lm} T_{il}(B_{lm} - B^0_{lm}) \Lambda_{mj}. \quad (12)$$

The difference kernel of this equation possesses a much better convergence than that in the original equation (7). The problem of slow convergence reappears now in the equation for the T matrix, but it can be solved there much more simply. Let us explain this point in some detail. First, we are dealing in that equation with the vector $T_{ij}(t)$, which is one-dimensional in the coordinate space, instead of the two-dimensional matrix $\Lambda_{ij}(X, X')$. Second, the law of momentum conservation in the case of free scattering simplifies significantly the problem, enabling us to find $T_{ij}(t)$ by means of the inverse Fourier transformation of the T matrix $T(P_x)$ calculated in the momentum representation.

As will be demonstrated below, the difference $(B_{lm} - B^0_{lm})$ in equation (12) for dominant lm components is small, so that its solution differs insignificantly from the free off-shell T matrix. Therefore, this quantity appears to be of paramount importance for the theory of pairing in nuclear systems. For this reason, we describe in detail a method for calculating it in the coordinate representation.

3. CALCULATION OF THE OFF-SHELL *T* MATRIX FOR FREE NUCLEON–NUCLEON SCATTERING

The off-shell T matrix taken at negative energy $E = 2\mu$ can easily be determined in the momentum representation by solving the algebraic set of equations

$$T_{ij}(P_x; E) = \lambda_{ij} + \sum_{lm} \lambda_{il} B^0_{lm}(P_x; E) T_{mj}(P_x; E), \quad (13)$$

where

$$B^0_{lm}(P_x; E) = \int \frac{d^3k}{(2\pi)^3} \frac{g_l(k^2) g_m(k^2)}{E - P_x^2/4m - k^2/m}. \quad (14)$$

The scattering matrix in the coordinate representation, $T_{ij}(t)$, can be expressed in terms of $T_{ij}(P_x)$ by means of the inverse Fourier transformation

$$T_{ij}(t; E) = \int_{-\infty}^{\infty} \frac{dP_x}{2\pi} T_{ij}(P_x; E) \exp(-iP_x t). \quad (15)$$

The form factors g_i in the integral in (14) are rational functions of k^2 [3, 4]—specifically, they are combinations of the Fourier transforms $1/(k^2 + \beta^2)$ of some Yukawa functions and their derivatives for various mass values β_{in} ($n = 1, \ldots, 4$). This integral can be calculated analytically, but this calculation is very cumbersome because there are very many individual terms in the integrand (about 70 for each lm). It is much more convenient to calculate it numerically, in which case the cutoff parameter of $k_c = 60$ fm^{-1} [a value that is chosen in accordance with the cutoff parameter in (8)] ensures a precision higher than 1%.

Upon isolating the constant λ_{ij}, the Fourier integral in (15) was computed in [2] by means of a direct integration along the real axis P_x. This method provides accurate results at small t; for t in excess of 2 to 3 fm, the integrand involves the quickly oscillating factor $\exp(-iP_x t)$ multiplied by the slowly decreasing function $(T_{ij}(P_x^2) - \lambda_{ij}) \simeq 1/P_x^2$; as a result, the integral in (15) becomes poorly convergent. In order to achieve a sufficient precision at t values between 4 and 5 fm, a huge cutoff-momentum value of $P_x^c = 3000$ fm^{-1} had to be used in [2] at a very small step of integration. But even at so large a cutoff parameter, the behavior of $T_{ij}(t)$ for $t > 5$ fm proves to be incorrect—there arise spurious aperiodic oscillations.

An attempt can be made to improve the convergence of the integral in (15) by isolating the asymptotic term in the T matrix. In order to establish the asymptotic form, we will first consider the free propagator B^0. It can easily be seen that, for $P_x \longrightarrow \infty$, the asymptotic behavior in question is given by

$$B^0_{lm}(P_x) \longrightarrow -b_{lm}/P_x^2, \quad (16)$$

where

$$b_{lm} = 4m \int \frac{d^3p}{(2\pi)^3} g_l(p^2) g_m(p^2). \quad (17)$$

In order to regularize the asymptotic term at the point $P_x = 0$, we redefine it as

$$B^a_{lm} = -\frac{b_{lm}}{P_x^2 + \gamma^2}, \quad (18)$$

where γ is an arbitrary constant. We then have

$$B^0_{lm} = B^a_{lm} + B'_{lm}. \quad (19)$$

The inverse Fourier transformation of expression (18) can be performed straightforwardly. The result is

$$B^a_{lm}(t) = -\frac{b_{lm}}{2\gamma} \exp(-\gamma|t|). \quad (20)$$

Upon the subtraction of the asymptotic term, the propagator assumes the form

$$B'_{lm}(P_x) = -4m \int \frac{d^3p}{(2\pi)^3} g_l(p^2) g_m(p^2) \times \left[\frac{1}{P_x^2 + 4p^2 + \gamma_0^2} - \frac{1}{P_x^2 + \gamma^2} \right], \quad (21)$$

where $\gamma_0^2 = -8m\mu$. This difference converges for $P_x \longrightarrow \infty$ faster than B^0_{lm} (namely, $B'_{lm} \simeq 1/P_x^4$).

Let us now address directly the T matrix. It can be seen from (13) that, for $P_x \longrightarrow \infty$, it involves the constant λ_{ij} corresponding to a delta function in the x space. It is reasonable to subtract it from the outset and to analyze the quantity

$$\delta T_{ij}(P_x; E) = T_{ij}(P_x; E) - \lambda_{ij}. \quad (22)$$

It can easily be seen from (11) that, for $P_x \longrightarrow \infty$, we have

$$\delta T_{ij}(P_x) \longrightarrow \delta T^a_{ij}(P_x) = -\frac{\alpha_{ij}}{P_x^2 + \gamma^2}, \quad (23)$$

where

$$\alpha_{ij} = \sum_{lm} \lambda_{il} b^0_{lm} \lambda_{mj}. \quad (24)$$

We again obtain

$$\delta T_{ij} = \delta T^a_{ij} + \delta T'_{ij}, \quad (25)$$

where

$$\delta T^a_{ij}(t) = -\frac{\alpha_{ij}}{2\gamma} \exp(-\gamma|t|). \quad (26)$$

For $P_x \longrightarrow \infty$, the convergence of $\delta T'_{ij}$ is again much faster than the convergence of δT_{ij} ($1/P_x^4$ instead of

$1/P_x^2$). In this case, the calculation of the integral in (15) along the real axis P_x with the same cutoff parameter and the same step of integration as previously leads to a correct behavior of $\delta T'_{ij}(X)$ at $X \simeq 5$ fm, but unphysical oscillations again arise from $X \simeq 6$ fm. In order to get rid of them completely, it would be better, in accordance with the general prescription for integrating quickly oscillating functions [10], to go over to integration in the complex plane of P_x in (15).

In modifying the integration contour to arrive at a form convenient for the calculations, we must take into consideration the singularities of the integrand. As was indicated above, the form factors $g_i(k^2)$ in the integral in (14) are rational functions of k^2; therefore, the entire integrand is also a rational function of k^2. We will show that, in this case, the free propagator $B^0_{ij}(P_x; E)$ at negative energy E has no singularities other than two cuts going along the imaginary axis symmetrically with respect to the origin and issuing from the branching points $P_x = \pm i\gamma_0$, where $\gamma_0 = \sqrt{-8m\mu}$. For this purpose, we first consider the explicit form of one of the typical terms in the sum that arises upon substituting into (14) the rational form factors [3, 4]

$$I_1 = \int_0^\infty k^2 dk \frac{1}{k^2+\alpha^2}\frac{1}{k^2+\beta_1^2}\frac{1}{k^2+\beta_2^2}, \qquad (27)$$

where

$$\alpha^2 = (P_x^2 + \gamma_0^2)/4, \qquad (28)$$

while β_1 and β_2 are the masses of the corresponding form-factor terms. Expression (27) emerges from those form-factor terms that are Fourier transforms of the Yukawa functions.

Upon some simple algebra, we obtain

$$I_1 = \frac{\pi}{2(\beta_1+\beta_2)}\frac{1}{(\alpha+\beta_1)(\alpha+\beta_2)}. \qquad (29)$$

By α, we mean here the arithmetic value of the square root of expression (28). It can be seen that the above branching points are the only singularities of expression (29) considered as a function of the complex variable P_x.

Let us now consider the term that is next in the order of complexity and which arises upon taking the derivative of the Fourier transform of the Yukawa function in one of the form factors:

$$I_2 = \int_0^\infty k^2 dk \frac{1}{k^2+\alpha^2}\frac{k^2}{(k^2+\beta_1^2)^2}\frac{1}{k^2+\beta_2^2}. \qquad (30)$$

This integral can easily be expressed in terms of the integral in (27) as

$$I_2 = I_1 + \frac{\beta_1}{2}\frac{\partial I_1}{\partial \beta_1}. \qquad (31)$$

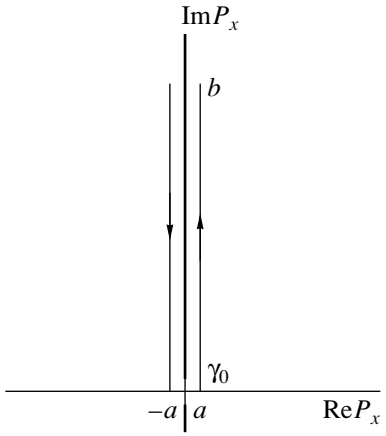

Fig. 2. Contour of integration in the complex plane of P_x for the inverse Fourier transformation (15).

From here, it becomes clear what is to be done to construct the algorithm for determining other terms in the integral in (14), which involve higher derivatives of the Yukawa function. It can also be seen that, in just the same way as the integral in (31), these terms do not have singularities other than those of expression (29). Thus, we have shown that the two cuts going along the imaginary axis symmetrically with respect to the origin (see Fig. 2) exhaust the list of singularities of the functions $B^0_{lm}(P_x; E < 0)$ in the complex plane of P_x. It is convenient to deform the integration contour in such a way that it embraces the upper cut (in Fig. 2, $b \longrightarrow \infty$). The convergence of the integral in the parameter b is much faster than the convergence in the parameter P_x^c in the case of integration along the real axis. In practice, we have used the contour depicted in Fig. 2 with the following values of the parameters: $a = 2$ fm^{-1} and $b = 130$ fm^{-1}. In this case, it lies sufficiently far off the cut, and the integral in (15) is calculated numerically with without any difficulties; this leads to a nearly precise exponentially decaying result at any t values of interest. As can be seen from (13), the singularities of the propagator B^0 are present in the T matrix. Apart from this, the T matrix can develop new poles on the imaginary axis that correspond to a real or a virtual level. In the case of the $S = 0$ singlet channel being considered, this level is virtual, and the relevant poles occur on the cuts. In order to calculate the T matrix, we can therefore use the same contour as that for the propagator B^0.

4. RESULTS OF THE CALCULATIONS: COMPARISON OF $\mathcal{V}^p_{\text{eff}}$ WITH THE T MATRIX

Although all equations of Section 2 for planar-slab geometry coincide formally with the equations for the semi-infinite system, mirror symmetry in the x direction results in some obvious simplifications in the former case. First, the eigenfunctions y_n in the potential

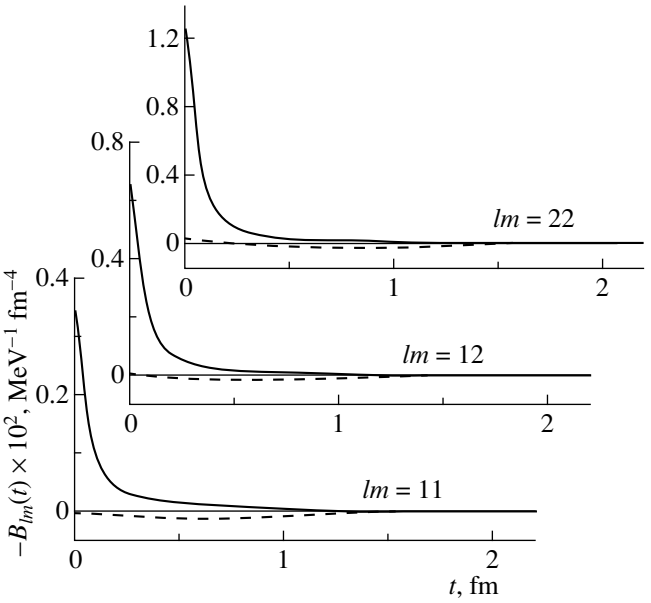

Fig. 3. Calculated dominant components of (solid curves) the free propagator B^0_{lm} taken with the inverted sign and of (dashed curves) the difference ($B^{\inf}_{lm}[V = 50\ \text{MeV}] - B^0_{lm}$) as functions of the relative coordinate $t = X - X'$ at $\mu = -8$ MeV.

(4) are characterized by parity [there are even (y^+_n) and odd (y^-_n) functions]. The full propagator $A^s = GG^s$ in equation (1) is the sum $A^s = A^s_{\text{even}} + A^s_{\text{odd}}$ of the components preserving and reversing parity (that is, the even and the odd component—A^s_{even} and A^s_{odd}, respectively). The same is true for the kernels of equation (7). As a result, all equations can be reduced to the form that involves only positive x. They are presented in the Appendix.

Instead of a direct evaluation of the propagator in (12) for the system being considered, we calculate it within the LPA. The scheme of this calculation was briefly described in the Introduction. In practice, we changed the potential-well depth from zero to 50 MeV with a step of $\delta V = 2$ MeV. At a fixed value of the chemical potential μ, we first computed a set of two-particle propagators $B_{\inf}([V_m], t; E = 2\mu)$ for infinite nuclear matter in the potential $V_m = \delta V(m-1)$. This calculation was performed on a fixed mesh of values $t_k = h(k-1)$ with $h = 0.1$ fm and $k = 1, \ldots, 61$ (for $t > 6$ fm, all the propagators being investigated are negligibly small). It is obvious that the free propagator $B^0(t)$ coincides with $B_{\inf}([V_{m=1}], t; E = 2\mu)$. After that, we fixed a mesh of X_k values with a step h in the range $(0, L + a)$. The parameter a must be taken to be sufficiently large (in the present calculation, we used the value of $a = 6$ fm). On this mesh, we constructed the matrix $B^{\text{LPA}}(X_i, X_k)$ for the nonhomogeneous system under consideration. It was calculated in the following way. At fixed X_i and X_k [$X = (X_i + X_k)/2$, $t = X_i - X_k$], we computed the potential-well depth by using equation (4) and determined the required LPA by performing a linear interpolation between two neighboring values $B_{\inf}([V_m], t; E)$ and $B_{\inf}([V_{m+1}], t; E)$ so that the condition $V_m < V(X) < V_{m+1}$ was satisfied. In order to calculate the kernel for equation (13), the difference of the resulting propagator $B^{\text{LPA}}(X_i, X_k; E)$ and the free propagator B^0 was integrated with the free T matrix; after that, this equation was solved by the same method as that used for semi-infinite nuclear matter [1, 2].

Let us first consider the value of $\mu = -8$ MeV, which characterizes beta-stable nuclei and analyze the differences ($B^{\inf}_{lm}(V_0) - B^0_{lm}$) for three dominant lm components at the maximal potential-well depth of $V = V_0 = 50$ MeV. They are displayed in Fig. 3, along with the free propagator B^0_{lm}. As can be seen, all propagators B^0_{lm} have a sharp maximum at small t; in this region, each difference is considerably smaller than the corresponding free propagator. The propagators under consideration differ significantly only in that region of t where they are both small. For smaller values of V, the differences ($B - B^0$) are obviously still smaller. In order to analyze the reason behind this smallness, we break down the sum in (8) into two parts. In the first, we include terms corresponding to such states λ and λ' whose energies ε_λ and $\varepsilon_{\lambda'}$ are both positive; in the second, we include terms for which one of these energies is positive, while the other is negative (but it is higher than μ). Each part of the sum is then compared with the corresponding sum in the free propagator. Within the LPA, it is easy to draw such a comparison because, in this case, expression (8) is very similar to the corresponding sum for B^0_{lm}. The functions y_n can then indeed be replaced by plane waves in the constant potential $V_0 = V(X)$. Let us now compare directly each term in the first part of the sum in (8) for $B^{\inf}_{lm}$ with that term in B^0_{lm} which has the same denominator. It can easily be seen that the numerator of the propagator in nuclear matter is smaller than that of the free propagator because it involves the matrix element of the form factor at higher momentum values of $q = \sqrt{k^2 + 2mV_0}$ in a medium instead of k in the free case. The form factors $g_i(k^2)$ for $i = 1, 2$, which are of interest for the present purposes, decrease with increasing k (see Fig. 1), so that the first part of $B^{\inf}_{lm}$ is smaller in absolute value than B^0_{lm}. We note that it is this part of the propagator B_{lm} that was calculated in [1], where it was shown that the difference under investigation amounts to 20–30% of B^0_{lm}. The second part of the sum has no analog in the free propagator. At first glance, it must be much smaller than the first part because of a substantial reduction of the phase

space. However, its contribution is considerably enhanced owing to small values of the energy denominators. As a result, the absolute value of this part of $B^{\inf}_{lm}$ proves to be on the same order of magnitude as the difference of the first part and B^{0}_{lm}. This means that the full propagator $B^{\inf}_{lm}([V_0], t)$ in nuclear matter and the free propagator $B^{0}_{lm}(t)$ at small t (that is, in the region where both of them are large) appear to be very close to each other.

The dominant components of the effective interaction $\overset{\circ}{V}{}^{\inf}_{\text{eff}}(X = 0, t)$ inside the slab are displayed in Fig. 4, along with the corresponding components of the free T matrix. Of course, we eliminated here the delta-function terms $\lambda_{ij}\delta(t)$ from both amplitudes [see equations (7) and (11)]. Here, the situation for various ij is similar to that for the corresponding components of the propagator—that is, they are very close to each other at small t, where the quantities under investigation are both large. In order to draw a more detailed quantitative comparison between the "precise" effective interaction (that is, that which was calculated within the LPA) and the free T matrix, the zeroth moments of their individual components—these zeroth moments measure the corresponding mean intensities—are depicted in Figs. 5 and 6. For the effective interaction, they are defined as

$$\bar{\Lambda}_{ij}(X) = \int dt \Lambda_{ij}(X - t/2, X + t/2). \qquad (32)$$

Obviously, the analogous moments of the T matrix are independent of X:

$$\bar{T}_{ij} = \int dt T_{ij}(t). \qquad (33)$$

Figure 5 demonstrates that, for dominant components, the zeroth moments of the effective interaction [equation (32)] are very close to those of the T matrix [equation (33). The analogous comparison for the small component is illustrated in Fig. 6. Here, the distinction between the effective interaction and the T matrix is much greater, but it should be recalled that, in absolute values, these components are much smaller than those that are shown in Fig. 5. In the calculation of the gap Δ, a role more important than that of the individual components Λ_{ij} is played by their combinations that appear in the interaction averaged near the Fermi surface [2]. For this interaction, we have

$$\overline{\overset{\circ}{V}}{}^{\text{F}}_{\text{eff}}(X) = \sum_{ij} \bar{\Lambda}_{ij}(X) g_i(k_{\text{F}}^2(X)) g_j(k_{\text{F}}^2(X)), \qquad (34)$$

where we have introduced the local Fermi momentum that is defined as $k_{\text{F}}(X) = \sqrt{2m(\mu - V(X))}$ for $\mu - V(X) > 0$ and which otherwise takes zero value. The interaction in (34) is displayed in Fig. 7, along with the corresponding local form of the T matrix,

$$\bar{T}^{\text{F}}(X) = \sum_{ij} \bar{T}_{ij} g_i(k_{\text{F}}^2(X)) g_j(k_{\text{F}}^2(X)). \qquad (35)$$

It can be seen that these mean values differ more pronouncedly than the dominant components shown in Fig. 5. This is due to the effect of the small components. As was indicated above, the third form factor $g_3(k)$, in contrast to the first two, grows with increasing momentum (see Fig. 1) and, at momentum values about the Fermi momentum of $k_{\text{F}} \simeq 1.4$ fm^{-1}, exceeds them nearly by an order of magnitude. Although the constant λ_{13}, for example, is less than the constant λ_{11} by two orders

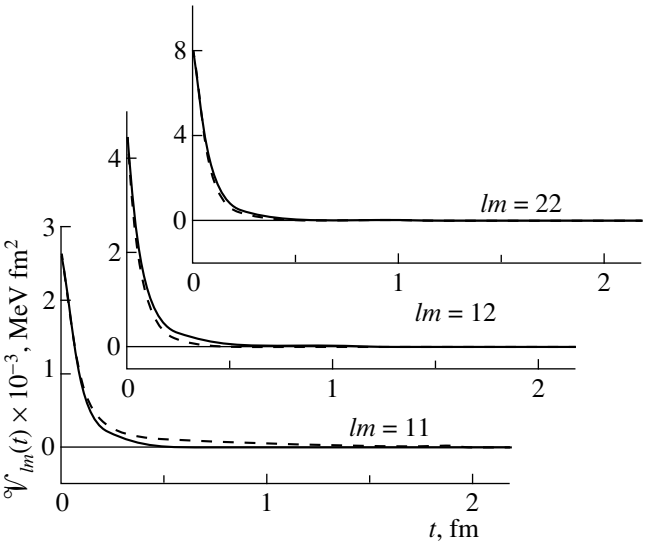

Fig. 4. Calculated dominant components of (solid curves) the effective interaction $\overset{\circ}{V}{}^{\inf}_{\text{eff}}$ [V = 50 MeV] and (dashed curves) the free T matrix as functions of the relative coordinate $t = X - X'$ at $\mu = -8$ MeV. The sign was reversed for lm = 11 and 22.

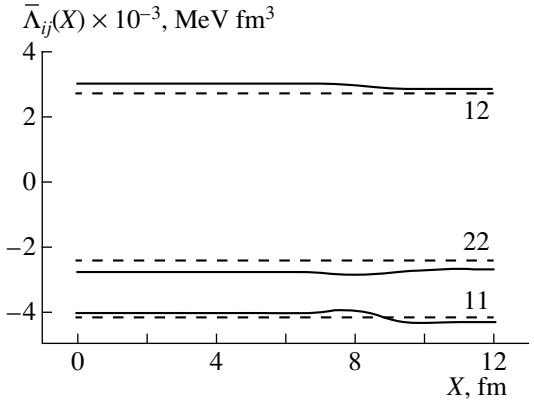

Fig. 5. Zero moments of the dominant components of (solid curves) the effective interaction $\bar{\Lambda}_{ij}(X)$ and (dashed curves) the free T matrix ($\bar{T}_{ij}$) at $\mu = -8$ MeV.

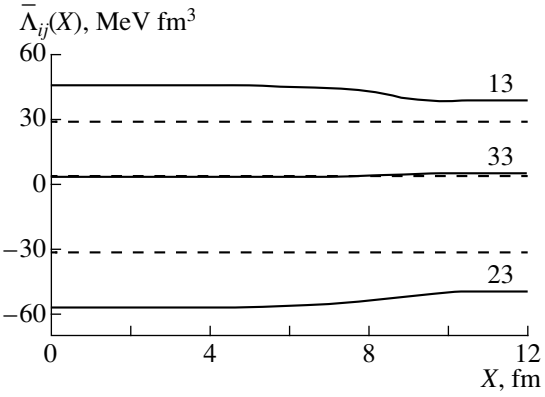

Fig. 6. As in Fig. 5, but for the small components with ij = 13, 23, and 33.

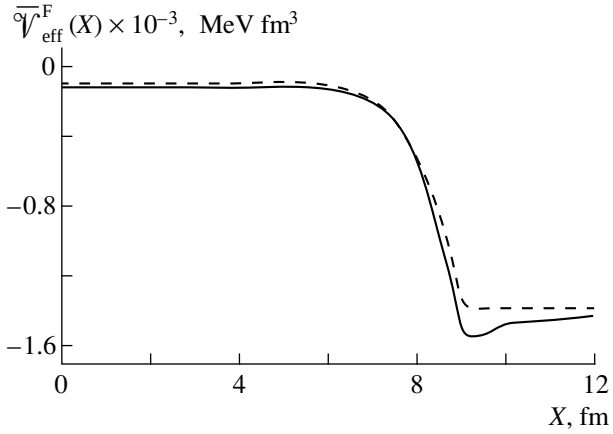

Fig. 7. Averaged effective interaction $\bar{\mathcal{V}}^{\mathrm{F}}_{\mathrm{eff}}(X)$ at the Fermi surface (solid curves) and similar averaged value $\bar{T}^{\mathrm{F}}_{\mathrm{eff}}(X)$ of the T matrix (dashed curves) at $\mu = -8$ MeV.

of magnitude, the contribution of the 13 component to the sums in (34) and (35) will therefore be about 10%, so that this contribution must be taken into account. The same is true for the remaining small components. However, the relevant average values at the Fermi surface are also rather close to one another. Indeed, the maximal difference of about 15% between two curves is achieved within the slab, where the average values being considered are one order of magnitude less than their maximal values (in modulus) attained at the surface. But in the surface region, this difference is as small as some 5%. In the case of the application of the effective interaction that we obtained to calculations for finite nuclei, the matrix elements of this interaction between the states lying near the Fermi surface will of course be determined primarily by the surface layer. The point is that, while, in planar geometry, a tenfold excess of the surface value of the interaction over its volume value is compensated to a considerable extent by the smallness of the surface-to-volume ratio, in the case of spherical geometry, the contribution of the surface is enhanced by the factor r^2, which appears in the volume element in the integrand of the matrix element. Therefore, the difference between the effective pairing interaction and the free T matrix must inevitably be less than 10% for the matrix elements in question.

In order to assess the extent to which the resulting proximity of the effective pairing interaction to the free off-shell T matrix is universal, we performed anew all the calculations for the smaller (in modulus) chemical-potential value of $\mu = -4$ MeV, which is peculiar to nuclei lying away from the beta-stability region. A comparison of the individual components of the averaged and the free propagator, as well as of the effective interaction and the T matrix, is illustrated in Figs. 8–11. We can see that, qualitatively, the situation is close to that which we observed at $\mu = -8$ MeV. Thus, the approximation of $\mathcal{V}^{p}_{\mathrm{eff}}$ by the free off-shell T matrix

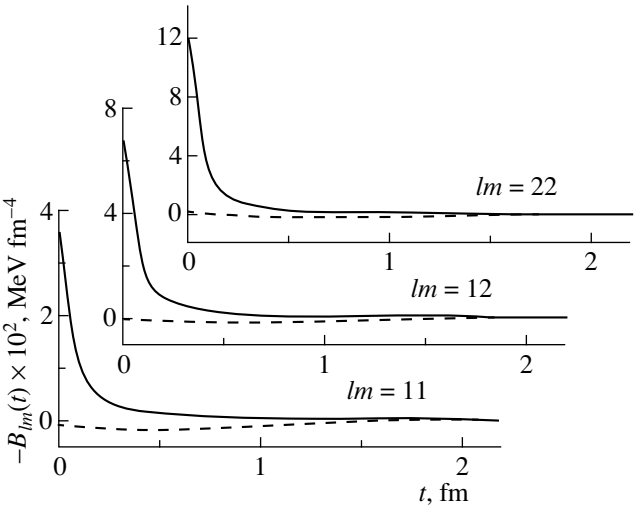

Fig. 8. As in Fig. 3, but for $\mu = -4$ MeV.

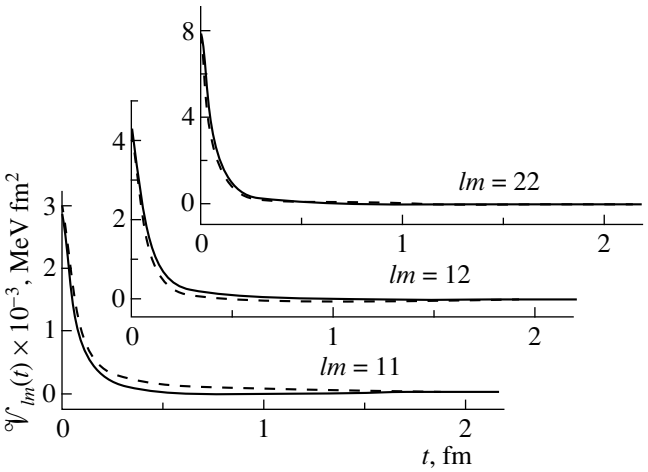

Fig. 9. As in Fig. 4, but for $\mu = -4$ MeV.

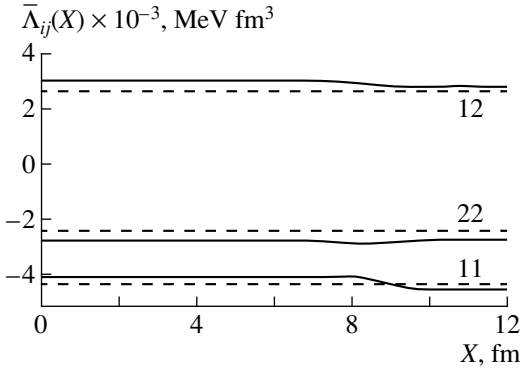

Fig. 10. As in Fig. 5, but for μ = –4 MeV.

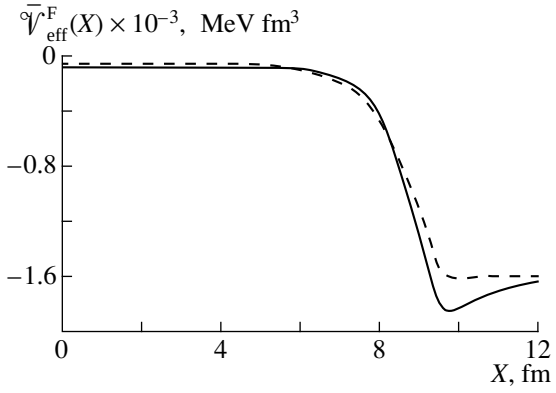

Fig. 11. As in Fig. 7, but for μ = –4 MeV.

remains quite accurate even upon the reduction of the absolute value of the chemical potential.

5. CONCLUSION

The microscopic effective pairing interaction for the slab of nuclear matter placed in the Woods–Saxon potential well has been calculated within Brueckner theory by using the separable 3 × 3 version of the Paris potential. The effective interaction has been determined for the model subspace including all negative-energy single-particle states. The calculations have been performed within the local-potential approximation, whose accuracy for semi-infinite nuclear matter was earlier demonstrated in [2]. The results of the calculations have been presented for two values of the chemical potential, the value of μ = –8 MeV characteristic of stable atomic nuclei and the value of μ = –4 MeV mimicking the approach to the nucleon drip line. It was shown that, in both cases, the effective interaction agrees, to within 10%, with the off-shell T matrix for free nucleon–nucleon scattering at the total energy of two nucleons that is equal to $E = 2\mu$ (recall that this is a negative value). We have constructed a simple and efficient method for calculating the T matrix in the coordinate representation. This method is based on calculating the inverse Fourier integral in the complex plane of the total two-nucleon momentum. The above approximation is convenient for calculating the superfluidity features of atomic nuclei, including those that occur far off the beta-stability region.

ACKNOWLEDGMENTS

We are grateful to P. Schuck for stimulating discussions. É.E. Saperstein and M.V. Zverev gratefully acknowledge the hospitality extended to them at Istituto Nazionale di Fisica Nucleare, Sezione di Catania (Catania), and Dipartimento di Fisica di Universitá di Catania. É.E. Saperstein is grateful to the Ministry for Foreign Affairs of Italy and the Landau Network–Centro Volta Cultural Center for support during the autumn of 1999. M.V. Zverev is indebted to Nguyen Van Giai for the hospitality extended to him at the Nuclear Physics Institute (Orsay).

This work was supported in part by the Russian Ministry for Higher Education (grant no. 97-0-6.1-7) and by the Russian Foundation for Basic Research (project nos. 00-02-17319 and 00-15-96590).

APPENDIX

Simplified Form of the Gap Equation in the Case of Planar-Slab Geometry

In the case of the separable interaction being considered, the gap Δ has also the separable form [1, 2]

$$\Delta(\mathbf{k}_\perp, x_1, x_2) = \sum_i \Delta_i(X) g_i(k_\perp^2, x). \qquad \text{(A.1)}$$

The gap equation (2) written for the component Δ_i has the form

$$\Delta_i(X) = \sum_{jl} \int_{-\infty}^{\infty} dX_1 \int_{-\infty}^{\infty} dX_2 \Lambda_{ij}(X, X_1) B^0_{jl}(X_1, X_2) \Delta_l(X_2). \qquad \text{(A.2)}$$

The superscript "0" on the two-particle propagator $B^0_{jl}(X_1, X_2)$ in (A.2) means that it is calculated in the model subspace S_0. For a planar slab symmetric with respect to the plane $x = 0$, the components $\Delta_i(X)$ are obviously even functions of X. Therefore, equation (A.2) can be simplified by reducing it to the form involving only integrals over positive X. Specifically, we arrive at

$$\Delta_i(X) = \sum_{jl} \int_0^{\infty} dX_1 \int_0^{\infty} dX_2 \Lambda^+_{ij}(X, X_1) B^{0+}_{jl}(X_1, X_2) \Delta_l(X_2), \qquad \text{(A.3)}$$

where

$$\Lambda^{+}_{ij}(X_1, X_2) = \Lambda_{ij}(X_1, X_2) + \Lambda_{ij}(X_1, -X_2), \quad \text{(A.4)}$$

$$B^{0+}_{jl}(X_1, X_2) = B^{0}_{jl}(X_1, X_2) + B^{0}_{jl}(X_1, -X_2). \quad \text{(A.5)}$$

By analogy with (A.5), we further introduce the symmetrized two-particle propagator $B^{+}_{jl}(X_1, X_2)$ for the complementary subspace S'. It obviously satisfies the identities

$$B^{+}_{jl}(X_1, X_2) = B^{+}_{jl}(X_1, -X_2) = B^{+}_{jl}(-X_1, X_2). \quad \text{(A.6)}$$

By using (A.6), we can easily reduce equation (7) to the form

$$\Lambda^{+}_{ij}(X, X') = \lambda_{ij}\delta(X - X') + \lambda_{ij}\delta(X + X') + \sum_{lm}\lambda_{il}\int_0^\infty dX_1 B^{+}_{lm}(X, X_1)\Lambda^{+}_{mj}(X_1, X'). \quad \text{(A.7)}$$

A solution to equation (A.7) can be considered to be defined only for $X, X' \geq 0$; hence, the second nonhomogeneous term in this equation is nonzero only at $X = X' = 0$.

In the same way, we transform the renormalized equation (10). The result is

$$\Lambda^{+}_{ij}(X, X') = T^{+}_{ij}(X, X') + \sum_{lm}\int_0^\infty dX_1 \int_0^\infty dX_2 T^{+}_{il}(X, X_1)B^{+}_{lm}(X_1, X_2)\Lambda^{+}_{mj}(X_2, X'), \quad \text{(A.8)}$$

where

$$T^{+}_{ij}(X, X') = T_{ij}(|X - X'|) + T_{ij}(X + X'). \quad \text{(A.9)}$$

REFERENCES

1. M. Baldo, U. Lombardo, E. E. Saperstein, and M. V. Zverev, Yad. Fiz. **58**, 1572 (1995) [Phys. At. Nucl. **58**, 1483 (1995)]; Yad. Fiz. **60**, 1206 (1997) [Phys. At. Nucl. **60**, 1081 (1997)].
2. M. Baldo, U. Lombardo, E. E. Saperstein, and M. V. Zverev, Nucl. Phys. A **628**, 503 (1998).
3. J. Haidenbauer and W. Plessas, Phys. Rev. C **30**, 1822 (1984).
4. J. Haidenbauer and W. Plessas, Phys. Rev. C **32**, 1424 (1985).
5. M. Lacombe, B. Loiseaux, J. M. Richard, *et al.*, Phys. Rev. C **21**, 861 (1980).
6. A. B. Migdal, *Theory of Finite Fermi Systems and Applications to Atomic Nuclei* (Nauka, Moscow, 1983, 2nd ed.; Interscience, New York, 1967).
7. P. Ring and P. Schuck, *The Nuclear Many-Body Problem* (Springer-Verlag, Berlin, 1980).
8. M. Baldo, J. Cugnon, A. Lejeune, and U. Lombardo, Nucl. Phys. A **515**, 409 (1990).
9. M. Baldo, I. Bombaci, G. Giansiracusa, and U. Lombardo, Nucl. Phys. A **545**, 741 (1992).
10. A. B. Migdal and V. P. Kraĭnov, *Approximation Methods in Quantum Mechanics* (Nauka, Moscow, 1966; Benjamin, New York, 1969).

Translated by A. Isaakyan

Physics of Atomic Nuclei, Vol. 63, No. 8, 2000, pp. 1387–1390. Translated from Yadernaya Fizika, Vol. 63, No. 8, 2000, pp. 1465–1468.

ON THE 85th ANNIVERSARY OF V.V. VLADIMIRSKY

Parity Violation in Neutron Scattering on Lead Isotopes

G. A. Lobov

Institute of Theoretical and Experimental Physics, Bol'shaya Cheremushkinskaya ul. 25 Moscow, 117259 Russia

Received December 2, 1999

Abstract—On the basis of an analysis of experimental data, it is shown that a subthreshold (negative) *p*-wave resonance can exist in the ^{204}Pb isotope at $E_p = -16$ eV. The presence of this resonance may explain unexpectedly large values observed experimentally for the *P*-odd angle of the rotation of the spin of transversely polarized neutrons about their momentum that are scattered on a natural mixture of lead isotopes. No available data are at odds with the existence of the $E_p = -16$ eV subthreshold resonance in ^{204}Pb. © *2000 MAIK "Nauka/Interperiodica".*

1. INTRODUCTION

Parity-violation effects in neutron scattering on nuclei provide a rare example of physical phenomena whose theory was developed [1] long before their experimental discovery [2] (see also [3]). In this theory, *P*-odd effects in complex nuclei are considerably enhanced owing to a dynamical enhancement of level mixing in compound nuclei and to special features of scattering kinematics. The enhancement of parity nonconservation in neutron scattering near *p*-wave resonances in compound nuclei was predicted theoretically for the first time in [1]. Resonance states in compound nuclei have a complicated multiparticle structure involving products of a large number N of the wave functions of excited particles and holes. In the statistical model of the nucleus, typical values of N are determined by the strength of strong nucleon–nucleon interaction. If we denote by ω the scale of this interaction (spacing between single-particle energy levels) and by D the spacing between the energy levels of the compound nucleus, then an order-of-magnitude estimate for N can be represented as

$$N \sim \omega/D. \tag{1}$$

This estimate can be obtained, for example, within the black-nucleus model. The quantity D decreases exponentially with increasing number of excited particles (increasing mass number A of the nucleus):

$$\text{for } A \sim 100, \quad D \sim 1\text{–}10 \text{ eV},$$

$$\text{for } A \sim 240, \quad D \sim 1 \text{ eV}.$$

Bearing in mind that the typical spacing between single-particle energy levels is $\omega \sim 1$ MeV, we then obtain

$$N \sim 10^5\text{–}10^6.$$

Let us consider low-energy neutron scattering on nuclei via a compound-nucleus state for the case where *P*-odd effects are enhanced. When the neutron energy is closer to *p*- than to *s*-wave resonances in compound nuclei, *P*-odd effects are enhanced [4]. The enhancement factor for single-particle *P*-odd effects estimated at $F = 10^{-5}(m_\pi/m)^2 \sim 10^{-7}$ (m_π and m are, respectively, the pion and the nucleon mass) is determined by N values as given by (1) and is equal to

$$\sqrt{N} \sim 10^2\text{–}10^3. \tag{2}$$

In polarized-neutron scattering on nuclei, there are two parity-violating effects: the cross-section asymmetry A_n in the scattering of longitudinally polarized neutrons on nuclei and the angle φ of the rotation of the spin of neutrons transversely polarized to their momentum. These quantities are both determined by the interference of the *P*-even and the *P*-odd Breit–Wigner scattering amplitude. The *P*-even amplitude describes neutron scattering from an initial *p*-wave state into the same final *p*-wave state through a resonance *p*-wave state of the compound nucleus. The *P*-odd amplitude describes neutron scattering from an initial *s*-wave state into a final *p*-wave state. The transition from the *s*- to the *p*-wave state is induced by weak nucleon–nucleon interaction in the compound nucleus. The expressions for A_n and φ are given by

$$A_n = -2\sqrt{\Gamma_s(E)/\Gamma_p(E)}\langle P|V^{sp}|S\rangle/E_s, \tag{3}$$

$$\varphi = \{2\sqrt{2}\pi n/\sqrt{mE}\}\{\langle P|V^{sp}|S\rangle/E_sE_p\} \times \sqrt{\Gamma_s(E)/\Gamma_p(E)}. \tag{4}$$

In expressions (3) and (4), E is the neutron energy; E_s and E_p are the energies of, respectively, the *s*- and the *p*-wave resonance in the compound nucleus; n is the number of nuclei in 1 cm^3 of the target; $\langle P|V^{sp}|S\rangle$ is the matrix element of the weak-interaction operator between the single-particle states of the compound nucleus; and $\Gamma_s(E)$ and $\Gamma_p(E)$ are the quantities obtained by rescaling the partial neutron widths of the *s*- and *p*-wave resonances to the neutron energy E as

$$\Gamma_l(E) = \Gamma_l^0(E/E_l)^{l+1/2}, \tag{5}$$

where l is the orbital angular momentum of the neutrons. In order to avoid encumbering the presentation, expressions (3) and (4) were written in the approximation $E \ll E_{s,p}$, which is usually valid for thermal and cold neutrons. The neutron-spin-rotation angle (4) (in radians) refers to a unit length of the target. From expressions (3)–(5), it follows that

$$A_n(E) \propto 1/\sqrt{E}, \tag{6}$$

$$\varphi(E) = \text{const}. \tag{7}$$

From (3)–(5), it additionally follows that the cross-section asymmetry A_n in neutron scattering has, in contrast to the spin-rotation angle φ, an extra [in relation to (2)] enhancement factor (which is especially pronounced in the ^{139}La nucleus)

$$\sqrt{\Gamma_s/\Gamma_p} \sim (pR)^{-1} \sim 10^1\text{–}10^3,$$

where p is the neutron momentum, while R is the nuclear radius. For the weak-interaction matrix element appearing in (3) and (4), we can use the phenomenological expression

$$\langle P|V^{\text{sp}}|S\rangle = 2 \times 10^{-4}\sqrt{\overline{D}}\ (\text{eV}), \tag{8}$$

where $\overline{D}$ is the mean spacing between the resonances in a specific compound nucleus. In deriving expression (8), it is advisable to make use of the fact that the weak-interaction matrix elements are formally similar to the partial widths with respect to electromagnetic transitions (giant resonance of the $M0$ type) between the compound-nucleus states. The phenomenological expression (8) describes quite accurately parity-nonconservation effects for all nuclei where the effects in question were observed experimentally.

2. PROBLEM OF *P*-ODD EFFECTS IN LEAD ISOTOPES

Natural lead is a mixture of four isotopes with mass numbers of 204, 207, 206, and 208, their fractions being 1.43, 24.15, 22.4, and 52.4%, respectively. The ^{208}Pb isotope is a doubly magic nucleus—that is, a nucleus having magic numbers of both protons and neutrons. For this reason, the level density is not great in all four isotopes. Moreover, it is well known that, for these isotopes, compound nuclei have no appropriate low-energy s- and p-wave resonance states that could be responsible for parity-nonconservation effects in neutron scattering. Nevertheless, experiments revealed a comparatively large value for the angle (4) of the rotation of the spin of transversely polarized neutrons about their momentum:

$$\varphi = (2.24 \pm 0.33) \times 10^{-6}\ [5] \tag{9}$$

$$\varphi = (3.53 \pm 0.79) \times 10^{-6}\ [6]. \tag{10}$$

A direct measurement of the angle φ for a lead target enriched in ^{207}Pb to 87% resulted in

$$\varphi < 4.3 \times 10^{-6} \tag{11}$$

at a 90% C.L. [6]. Once the last experimental result had appeared, it became clear that, in contrast to the statement of the authors of the so-called valence model [7], the rotation angles (9) and (10) in natural lead are not associated with the ^{207}Pb isotope. If, in the experiments reported in [5, 6], this isotope had been responsible for the neutron-spin rotation in natural lead, then the effect in the target enriched in ^{207}Pb to 87% would have exceeded the values in (9) and (10) approximately by a factor of four, amounting to 10^{-5}. In contrast to the model featuring the weak-interaction-induced mixing of opposite-parity compound-nucleus states, the valence model aims at explaining P-odd effects by the interference of the p-wave resonance in the compound nucleus with the s-wave potential scattering. The experimental constraint in (11) seems to disprove the valence model of P-odd effects.

For lead isotopes, present-day experimental data [8] show no evidence for s- and p-wave resonances that could explain the P-odd values in (9) and (10) by the mixing of compound-nucleus states. This is not so only for the ^{204}Pb isotope, which has a broad subthreshold s-wave resonance at –2.98 keV and the nearest p-wave resonance at 0.48 keV, their widths being, respectively, $\Gamma_s^0 = 72$ eV and $\Gamma_p^0 = 3 \times 10^{-3}$ eV. For these resonance features, known from experiments, the value of the P-odd angle (4) is $\varphi \approx 5 \times 10^{-9}$, which is much smaller than the observed values from (9) and (10). Those experimental values can be explained under the assumption that there exists an as-yet-unobserved neutron p-wave resonance that has a width of $\Gamma_p^0 \approx 3 \times 10^{-3}$ eV, typical of ^{204}Pb, and which is mixed, by weak interaction, with the aforementioned broad s-wave resonance. With allowance for the abundance of ^{204}Pb in natural mixtures, expression (4), together with the experimental values from (9) or (10), then yields an equation for determining the energy E_p of the resonance in question. Solving this equation, we obtain

$$E_p \approx -16\ \text{eV}. \tag{12}$$

Thus, the hypothetical p-wave resonance is subthreshold, in the same way as the s-wave resonance. Our result agrees with data of experimentalists from the Joint Institute for Nuclear Research (JINR, Dubna) [9], who were unable to find any p-wave resonance in a natural mixture of lead isotopes at energies in the energy region $E_p \approx 0$–100 eV. I do not think that the existence of a subthreshold neutron resonance in ^{204}Pb at the energy quoted in (12) is unnatural. First, its existence naturally breaks the hierarchy of many known subthreshold s-wave resonances. Second, there are no obvious reasons for subthreshold p-wave resonances to

be strongly forbidden, and it should be borne in mind that everything is allowed, unless it is forbidden.

A measurement of the spin-rotation angle for the scattering of transversely polarized neutrons on a sample enriched in the ^{204}Pb isotope could be a test of the existence of a *p*-wave resonance at the energy presented in (12). By way of example, we indicate that, for a sample 1.5 cm long and enrichment of 36.6%, the spin-rotation-angle value rescaled from (9) or (10) is

$$\varphi \approx 8 \times 10^{-5}. \quad (13)$$

The expected value in (13) corresponds to the conditions of the experiments that are being currently performed at the reactor of the Berlin Neutron Scattering Center (BENSC).

3. OTHER EFFECTS IN NEUTRON SCATTERING ON ^{204}Pb NUCLEI

In this section, we will study the contribution of the subthreshold *p*-wave resonance in ^{204}Pb to effects other than those considered in the preceding section.

For the case of thermal neutrons, the contribution of this *p*-wave resonance to the cross section for $n\gamma$ scattering is

$$\sigma_{n\gamma} = \pi\Gamma_p(E)\Gamma_\gamma/2mE \times E_p^2 = 22\ \text{mb} \times \Gamma_\gamma, \quad (14)$$

where Γ_γ is the radiative width of the *p*-wave resonance. Assuming a realistic value in the region $\Gamma_\gamma \ll 0.1$ eV, we find that the cross section in (14) is much smaller than 2 mb, a value well below the experimental error in determining the total cross section for radiative-thermal-neutron capture by ^{204}Pb nuclei (661 ± 70 mb). Thus, the contribution of the *p*-wave resonance in question to the cross section (14) is negligibly small.

The cross-section asymmetry (3) and the spin-rotation angle (4) are proportional, respectively, to the imaginary and to the real part of the difference of the Breit–Wigner scattering amplitudes corresponding to opposite neutron helicities [4]. This difference of the amplitudes is an analytic function that has no singularities in the upper complex half-plane of the neutron energy. By virtue of this, the quantities in (3) and (4) are related by the equation

$$\varphi = n\{(E - E_p)/\Gamma_p\}\Delta\sigma, \quad (15)$$

where n is the number of nuclei in 1 cm^3 of the target, Γ_p is the total width of the *p*-wave resonance, and

$$\Delta\sigma = 2A_n(E)\sigma_0. \quad (16)$$

Here, σ_0 is the total cross section for neutron absorption at a specific energy E [10]. The cross-section asymmetry in the scattering of longitudinally polarized thermal neutrons on a natural mixture of lead isotopes was studied by Abov *et al*. [11], who found that

$$A_n = (-0.7 \pm 0.8) \times 10^{-6}. \quad (17)$$

Substituting the experimental values of φ from (9) and (10), which correspond to the neutron energy of $E = 1.75 \times 10^{-3}$ eV ($\lambda = 6.8$ Å); the values of $\sigma_0 = 2.25$ b and $\Gamma_p = 3 \times 10^{-3}$ eV; the abundance of ^{204}Pb in a natural mixture of isotopes (1.43%); and the *p*-resonance position at $E_p = -16$ eV into relations (15) and (16) and solving them for A_n, we obtain

$$A_n = 2 \times 10^{-7}. \quad (18)$$

This result is close to the single-particle value. By rescaling the value in (18) to the thermal point (E = 0.025 eV, which corresponds to $\lambda = 1.8$ Å) with σ_0 = 0.65 b at this neutron energy, we obtain

$$A_n = 10^{-9}. \quad (19)$$

Thus, the assumption that there exists a subthreshold *p*-wave resonance in ^{204}Pb does not contradict available experimental data.

4. CONCLUSION

Unexpectedly large experimental values in (9) and (10) for the angle of the rotation of the spin of transversely polarized neutrons about their momentum that are scattered on a natural mixture of lead isotopes have given impetus to searches for reasons behind this phenomenon. An analysis of experimental data has led to the conclusion that the effect may be due to the existence of an as-yet-unobserved subthreshold (negative) *p*-wave resonance in ^{204}Pb. This resonance, whose features naturally follow from (9) and (10), makes a negligibly small contribution to the total cross section for the radiative capture of thermal neutrons, and its existence does not contradict available experimental data.

ACKNOWLEDGMENTS

I am indebted to Yu.G. Abov, O.N. Ermakov, I.L. Karpikhin, P.A. Krupchitskiĭ, and L.B. Pikel'ner for numerous discussions on relevant experimental data and for valuable advice.

This work was supported by the Russian Foundation for Basic Research (project no. 97-02-16184).

Note added. The width of the negative *p*-wave neutron resonance can be estimated by using the relevant strength function and the mean spacing between the *p*-wave neutron resonances [8, 9]. The result proves to be 0.03 eV, which is one order of magnitude greater than the value used in the present study. A *p*-wave resonance of width 0.03 eV corresponds to an energy of –29 eV. Thus, the occurrence of a *p*-wave resonance in the energy range –(16–29) eV seems to be admissible theoretically.

REFERENCES

1. V. A. Karmanov and G. A. Lobov, Pis'ma Zh. Éksp. Teor. Fiz. **10**, 332 (1969) [JETP Lett. **10**, 212 (1969)];

G. A. Lobov, Izv. Akad. Nauk SSSR, Ser. Fiz. **34**, 1141 (1970).

2. E. A. Kolomensky *et al.*, Phys. Lett. B **107**, 272 (1981); V. P. Alfimenkov *et al.*, Pis'ma Zh. Éksp. Teor. Fiz. **34**, 308 (1981) [JETP Lett. **34**, 295 (1981)].
3. V. P. Alfimenkov, Usp. Fiz. Nauk **144**, 361 (1984) [Sov. Phys. Usp. **27**, 797 (1984)]; S. J. Seestrom, in *Time Reversal Invariance and Parity Violation in Neutron Reactions*, Ed. by C. R. Could *et al.* (World Sci., Singapore, 1993).
4. G. A. Lobov, Preprint No. 20, ITÉF (Institute of Theoretical and Experimental Physics, Moscow, 1982); Preprint No. 45, ITÉF (Institute of Theoretical and Experimental Physics, Moscow, 1981); Yad. Fiz. **35**, 1408 (1982) [Sov. J. Nucl. Phys. **35**, 822 (1982)].
5. B. R. Heckel *et al.*, Phys. Lett. B **119**, 298 (1982).
6. V. P. Bolotsky *et al.*, Yad. Fiz. **59**, 1873 (1996) [Phys. At. Nucl. **59**, 1808 (1996)].
7. D. F. Zaretskiĭ and V. K. Sirotkin, Yad. Fiz. **45**, 1302 (1987) [Sov. J. Nucl. Phys. **45**, 808 (1987)].
8. S. Mughabghab *et al.*, *Neutron Cross Sections* (Academic, New York, 1984), vol. 1.
9. L. B. Pikel'ner, private communication.
10. P. A. Krupchitsky, *Fundamental Research with Polarized Slow Neutrons* (Énergoatomizdat, Moscow, 1985; Springer-Verlag, New York, 1987).
11. Yu. G. Abov *et al.*, Yad. Fiz. **40**, 1585 (1984) [Sov. J. Nucl. Phys. **40**, 1006 (1984)].

Translated by M. Kobrinsky

Physics of Atomic Nuclei, Vol. 63, No. 8, 2000, pp. 1391–1394. Translated from Yadernaya Fizika, Vol. 63, No. 8, 2000, pp. 1469–1473.

ON THE 85th ANNIVERSARY OF V.V. VLADIMIRSKY

Investigation of the Diffractive Reaction $p + N \longrightarrow [\Sigma^+ K^0] + N$ at the Proton Energy of $E_p = 70$ GeV and Observation of the Decay Process $X(2000) \longrightarrow \Sigma^+ K^0$

D. V. Vavilov[1)], V. A. Viktorov[1)], S. V. Golovkin[1)], A. P. Kozhevnikov[1)], V. Z. Kolganov[2)], V. P. Kubarovsky[1)], V. F. Kurshetsov[1)], L. G. Landsberg[1)], G. S. Lomkatsi[2)], V. V. Molchanov[1)], V. A. Mukhin[1)], A. F. Nilov[2)], S. V. Petrenko[1)], and V. T. Smolyankin[2)]

SPHINX Collaboration (IHEP–ITEP)

Received September 28, 1999

Abstract—The diffractive reaction $p + N \longrightarrow [\Sigma^+ K^0] + N$ induced by 70-GeV protons is investigated at the SPHINX facility. The measured mass spectrum of the $\Sigma^+ K^0$ system originating from this reaction shows a resonance structure with a mass of $M = 1995 \pm 18$ MeV and a width of $\Gamma = 90 \pm 32$ MeV. The cross section for the formation of this structure is found to be $\sigma = 182 \pm 38$ nb per target nucleon. These data comply well with the results that we obtained previously in studying the reaction $p + N \longrightarrow [\Sigma^0 K^+] + N$, where we observed the formation of the $X(2000) \longrightarrow \Sigma^0 K^+$ state, a candidate for an exotic baryon with hidden strangeness. The measured ratio R of the two branching fractions, $R = \mathrm{Br}[X(2000) \longrightarrow \Sigma^+ K^0]/\mathrm{Br}[X(2000) \longrightarrow \Sigma^0 K^+] = 1.91 \pm 0.38$, is consistent with the value of $R = 2$ expected for an isospin-1/2 baryon. © *2000 MAIK "Nauka/Interperiodica".*

1. INTRODUCTION

The experiments of the SPHINX collaboration have been implementing a broad program of searches for exotic hadronic states in diffractive proton-induced reactions and in transitions characterized by high momentum transfers. The major results of these investigations have been reported in [1–11] and summarized in the review articles [12–15].

The SPHINX facility used in the measurements being discussed included a wide-aperture magnetic spectrometer equipped with proportional and drift chambers, drift tubes, and scintillation hodoscopes; a γ spectrometer composed of lead-glass counters; and a system of Cherenkov detectors, including a RICH device, for identifying charged secondaries. For further details on the apparatus, the reader is referred to [1, 10] (the latter reference describes the partially upgraded apparatus with a new γ spectrometer ensuring a more efficient detection of the decay processes $\Lambda \longrightarrow p\pi^-$ and $\Sigma^0 \longrightarrow \Lambda\gamma$). Some $(2–4) \times 10^6$ 70-GeV protons were delivered to the apparatus per accelerator cycle.

Reported in [4–7, 10, 11] are our previous investigations of the diffractive reaction

$$\begin{array}{l} p + N \longrightarrow [\Sigma^0 K^+] + N, \\ \qquad\quad \hookrightarrow \Lambda\gamma \\ \qquad\quad\quad \hookrightarrow p\pi^- \end{array} \qquad (1)$$

where N denotes either a nucleon or a carbon nucleus as a discrete unit (for a coherent process). The effective-mass spectrum of the $\Sigma^0 K^+$ system originating from this reaction is dominated by a resonance enhancement with a mass of $M = 1986 \pm 6$ MeV and a width of $\Gamma = 98 \pm 20$ MeV. The statistical significance of the enhancement, referred to as $X(2000)$, exceeds ten standard deviations. The product of the formation cross section and the relevant branching fraction was estimated as

$$\begin{aligned} \sigma &= [p + N \longrightarrow X(2000) + N] \\ &\times \mathrm{Br}[X(2000) \longrightarrow \Sigma^0 K^+] = 95 \pm 20 \text{ nb/nucleon}. \end{aligned} \qquad (2)$$

Apart from having a relatively small width, the $X(2000)$ state is anomalous in that it predominantly decays through channels involving the emission of strange particles: specifically, we found that

$$\begin{aligned} R &= \mathrm{Br}[X(2000) \longrightarrow \Sigma K] \\ &\times (\mathrm{Br}[X(2000) \longrightarrow \Delta(1232)\pi;\ p\pi\pi] \geq 1)^{-1}; \end{aligned} \qquad (3)$$

recall that, for ordinary three-quark isobars, this ratio does not exceed a few percent [15, 16]. On this basis,

[1)] Institute for High Energy Physics, Protvino, Moscow oblast, 142284 Russia.

[2)] Institute of Theoretical and Experimental Physics, Bol'shaya Cheremushkinskaya 25, Moscow, 117259 Russia.

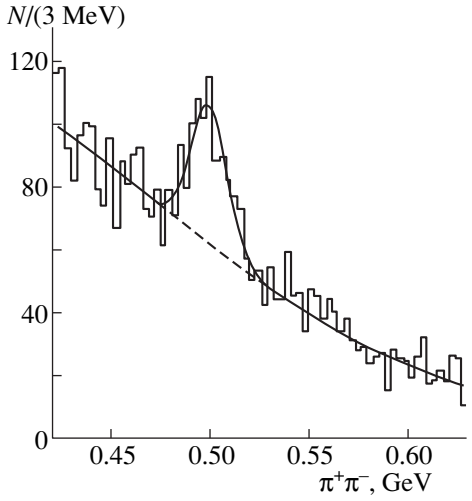

Fig. 1. Effective-mass spectrum of the $\pi^+\pi^-$ system for events selected to isolate reaction (4) (see main body of the text). We can see here a distinct peak due to the decay $K_S^0 \longrightarrow \pi^+\pi^-$.

we tentatively interpret the $X(2000)$ state as an exotic pentaquark baryon with hidden strangeness ($|uud\bar{s}s\rangle$).

In the near-threshold region, the mass spectrum of the Σ^0K^+ system emitted in the coherent reaction (1) shows yet another enhancement at $M = 1807 \pm 7$ MeV, $X(1810)$, its width being $\Gamma = 62 \pm 19$ MeV. That this state is formed at very low transverse momenta ($P_T^2 < 0.01$ GeV^2) may suggest the Coulomb production mechanism [11, 17].

The present article reports on our first results for the diffractive reaction

$$\begin{array}{l} p + N \longrightarrow [\Sigma^+K^0] + N, \\ \qquad\qquad\quad \big\lfloor\!\!\rightarrow \pi^+\pi^- \\ \qquad\quad \big\lfloor\!\!\rightarrow p\pi^0 \\ \qquad\qquad\quad \big\lfloor\!\!\rightarrow 2\gamma \end{array} \qquad (4)$$

which features a Σ^0K^+ system in an isospin state different from that in reaction (1). Analyzed are the same data as in our latest investigation of reaction (1) with the partially upgraded apparatus (see [10, 11]).

2. INVESTIGATION OF THE REACTION $p + N \longrightarrow [\Sigma^+K^0] + N$

Among all final states of the transition

$$\begin{array}{l} p + N \longrightarrow p\pi^+\pi^-\pi^0 + N, \\ \qquad\qquad\quad \big\lfloor\!\!\rightarrow 2\gamma \end{array} \qquad (5)$$

we sought events of reaction (4), which features two unstable particles. For this, we adopted a special procedure consisting of the following successive stages:

(i) Events involving three charged secondaries in the final state and two photon showers detected by the γ spectrometer were selected. It was required that the three charged secondaries be identified as p, π^+, and π^- by the system of Cherenkov counters and that the measured energy of each photon exceed a lower threshold of 1 GeV; the latter was necessary for the soft background in the γ spectrometer to be suppressed.

(ii) The position of the primary vertex was determined for a first approximation as a fitted point of intersection of all three charged tracks, which was then used to reconstruct the photon 3-momenta. The effective mass of two photons was required to lie within the π^0 window $110 < M_{\gamma\gamma} < 160$ MeV. In choosing the width of the π^0 window, it was considered that the final-state π^0 meson originates from the secondary vertex of the decay $\Sigma^+ \longrightarrow p\pi^0$ rather than from the primary vertex, whereby $M_{\gamma\gamma}$ is effectively reduced by a value not greater than some 10 MeV.

(iii) The estimate of the π^0 momentum was refined by kinematically constraining the two photons to correspond to the decay $\pi^0 \longrightarrow \gamma\gamma$.

(iv) A selected event was required to satisfy the elasticity condition $65 < E_p + E_{\pi^+} + E_{\pi^-} + E_{\pi^0} < 75$ GeV.

(v) The point of intersection of the trajectories of the final-state π^+ and π^- mesons and their total momentum (referred to by convention as the K^0-meson momentum) were found. The longitudinal coordinate of this secondary decay vertex, $Z1$, was determined.

(vi) Likewise, the vertex of Σ^+ decay was found as the point of intersection of the trajectories of the final-state proton and π^0 meson, and the momentum of the Σ^+ candidate was estimated as the sum of their momenta.

(vii) The momenta of the proton and the π^0 meson were refined by refitting the trajectories of these particles to the estimated vertex of Σ^+-hyperon decay.

(viii) The position of the primary vertex was determined more precisely by intersecting the refined Σ^+ trajectory with the K^0 and the primary-proton trajectory. The longitudinal coordinate of the primary vertex estimated in this way was denoted by Z.

(ix) We further studied the effective mass distribution of the $\pi^+\pi^-$ system versus $d = (Z1 - Z)/((D(Z1) + D(Z))^{1/2}$, where $D(Z)$ and $D(Z1)$ are the uncertainties in determining the coordinates Z and $Z1$, respectively. The condition $d > 0$ selects the K_S^0-decay vertex downstream of the primary vertex; a further increase in the lower cut on d improves the purity of the selected event sample, but this is accompanied by a reduction of relevant statistics. Our analysis revealed that the condition $d > 1.0$ is optimal. For this selection, Fig. 1 shows the effective-mass distribution of the $\pi^+\pi^-$ system; there, we can see a prominent peak associated with the K^0 meson: in the mass window 0.486–0.510 GeV, there

is a signal of some 271 events above a smooth background.

(x) For events that contained K^0 candidates selected in the way outlined above, we then plotted the effective-mass spectrum of the $p\pi^0$ system (see Fig. 2). That this spectrum features a distinct signal due to the decay process $\Sigma^+ \longrightarrow p\pi^0$ makes it possible to isolate reliably reaction (4). In the mass window 1.174–1.204 GeV, there are 194 events above a smooth background, with the signal-to-background ratio being close to four.

We can conclude that the above procedure has enabled us to isolate reliably reaction (4), which features two unstable secondaries, and to analyze its kinematics.

Figure 3 displays the effective-mass spectrum of the Σ^+K^0 system for events of reaction (4) that were selected from the Σ^+-hyperon mass window in Fig. 2. Despite comparatively low statistics, we can state that, qualitatively, this distribution is consistent with the analogous data obtained in previous SPHINX experiments for reaction (1) [10, 11]. The Σ^+K^0 spectrum in Fig. 3 shows two resonance enhancements whose parameters are

$$M = 1812 \pm 7 \text{ MeV}, \quad \Gamma = 41 \pm 30 \text{ MeV}, \quad N = 26 \pm 13;$$

$$M = 1995 \pm 18 \text{ MeV}, \quad \Gamma = 90 \pm 32 \text{ MeV}, \quad N = 68 \pm 12.$$

The first enhancement, which needs to be confirmed at a higher level of statistics (which are being collected at present), is not discussed here (see [11]). The parameters of the second enhancement suggest that it arises from Σ^+K^0 decays of the baryon state $X(2000)$, which we detected earlier in the Σ^+K^0 decay channel.

In order to compare quantitatively the results of the present study with those for reaction (1), we estimated the detection efficiency for events of reaction (4), taking into account the above selection criteria (see Fig. 4). In determining the cross section for $X(2000)$ formation, information about statistics and the efficiency was supplemented with the following inputs:

(a) The total number of primary protons delivered to the target was 4.3×10^{10}.

(b) Under the assumption that, for one CH_2 molecule, the effective number of nucleons was $2 + A^{2/3} = 7.24$, the effective thickness of the polyethylene target was estimated at 3.46×10^{24} nucleon/cm^2.

(c) The $\Sigma^+ \longrightarrow p\pi^0$ branching fraction was set to 51.6%.

(d) Fifty percent of all K^0 mesons were assumed to be emitted in the form of K_S^0.

(e) The $K_S^0 \longrightarrow \pi^+\pi^-$ branching fraction was set to 68.6%.

Taking all the above into account, we estimated the product of the cross section for the formation of $X(2000)$ in reaction (4) and the corresponding branching ratio at

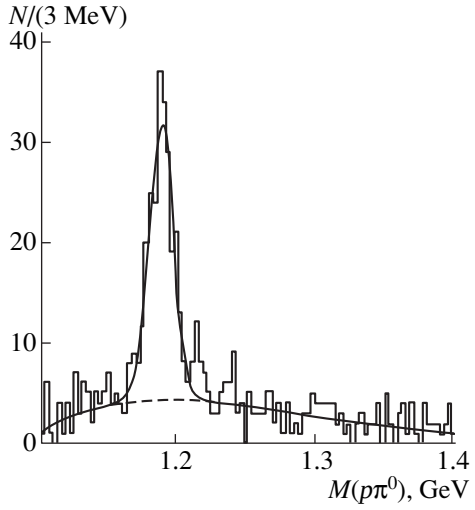

Fig. 2. Effective-mass distribution of the $p\pi^0$ system for events selected in the K_S^0 window (see Fig. 1). That this distribution features a distinct peak due to the decay $\Sigma^+ \longrightarrow p\pi^0$ allowed us to select events of reaction (4).

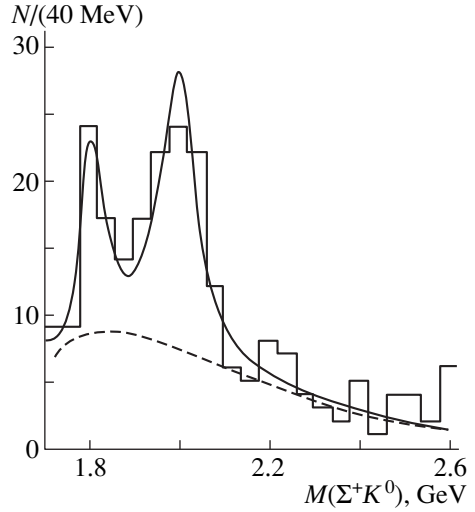

Fig. 3. Effective-mass distribution of the Σ^+K^0 system emitted in reaction (4). The solid curve represents the results of a fit in terms of two Breit–Wigner distributions and a regular polynomial background illustrated by the dashed curve (in all, ten adjustable parameters were used). The fitted parameter values are quoted in the main body of the text.

$$\sigma[p + N \longrightarrow X(2000) + N]\text{Br}[X(2000) \longrightarrow \Sigma^+K^0] = 182 \pm 32 \text{ nb/nucleon}. \quad (6)$$

Dividing this by the analogous estimate for reaction (2) from [11], we obtain

$$R = \text{Br}[X(2000) \longrightarrow \Sigma^+K^0] \times (\text{Br}[X(2000) \longrightarrow \Sigma^0K^+])^{-1} = 1.91 \pm 0.38. \quad (7)$$

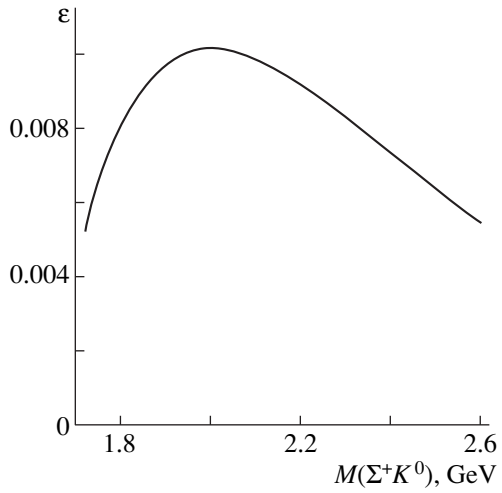

Fig. 4. Estimated detection efficiency for reaction (4) as a function of the effective mass of the Σ^+K^0 system.

We also have

$$\sigma[p + N \longrightarrow X(2000) + N]\mathrm{Br}[X(2000) \longrightarrow \Sigma K^+] = 277 \pm 72 \text{ nb/nucleon}. \quad (8)$$

Only statistical errors are quoted in the above results. The systematic uncertainties in estimating the detection efficiency, the absolute normalization, and the A dependence are about ±20 and ±15% for, respectively, the absolute cross section and the ratio of the branching fractions.

Since the $X(2000)^+$ baryon is formed via the diffractive dissociation of a proton, its isospin must be 1/2. The expected value of the ratio of the branching fractions must then be

$$R(X^+_{I=1/2}) = 2.$$

This agrees well with the experimental value in (7).

3. CONCLUSION

In summary, we have isolated, for the first time, the diffractive reaction (4) and observed the formation of the $X(2000)^+$ state decaying into Σ^+K^0; originally, the SPHINX collaboration detected this state in its decay through another isotopic channel, $X(2000)^+ \longrightarrow \Sigma^0K^+$. The results of the new measurements comply well with previous data on process (1) (see [11]), independently confirming the existence of the $X(2000)$ state, which is interpreted as a candidate for an exotic pentaquark baryon with hidden strangeness.

Preliminary results of the present experiment were reported at a symposium in Tbilisi [18].

The analysis of reaction (4) will benefit from a tenfold increase in statistics that is foreseen in the near future.

ACKNOWLEDGMENTS

It is a pleasure and honor for us to contribute to the issue of *Yadernaya Fizika* (Physics of Atomic Nuclei) that is dedicated to the 85th anniversary of Prof. Vasiliĭ V. Vladimirsky, with whom many of us have collaborated for years in various realms of science. Our research work benefited much from Prof. Vladimirsky's keen perception of physical phenomena; many of our investigations were based on his ideas, and many were completed owing to his participation. We wish Prof. Vladimirsky long years of creative activity.

This work was supported in part by the Russian Foundation for Basic Research (project no. 99-02-18251).

REFERENCES

1. SPHINX Collab. (D. V. Vavilov *et al.*), Yad. Fiz. **57**, 241 (1994) [Phys. At. Nucl. **57**, 227 (1994)]; M. Ya. Balatz *et al.*, Z. Phys. C **61**, 220 (1994).
2. M. Ya. Balatz *et al.*, Z. Phys. C **61**, 399 (1994).
3. SPHINX Collab. (D. V. Vavilov *et al.*), Yad. Fiz. **57**, 253 (1994) [Phys. At. Nucl. **57**, 238 (1994)].
4. SPHINX Collab. (D. V. Vavilov *et al.*), Yad. Fiz. **57**, 1449 (1994) [Phys. At. Nucl. **57**, 1376 (1994)].
5. SPHINX Collab. (D. V. Vavilov *et al.*), Yad. Fiz. **58**, 1426 (1995) [Phys. At. Nucl. **58**, 1342 (1995)].
6. SPHINX Collab. (S. V. Golovkin *et al.*), Z. Phys. C **68**, 585 (1995).
7. SPHINX Collab. (S. V. Golovkin *et al.*), Yad. Fiz. **59**, 1395 (1996) [Phys. At. Nucl. **59**, 1336 (1996)].
8. S. V. Golovkin *et al.*, Z. Phys. A **359**, 327 (1997).
9. S. V. Golovkin *et al.*, Z. Phys. A **359**, 435 (1997).
10. SPHINX Collab. (V. A. Bezzubov *et al.*), Yad. Fiz. **59**, 2199 (1996) [Phys. At. Nucl. **59**, 2117 (1996)].
11. S. V. Golovkin *et al.*, Eur. Phys. J. A **5**, 409 (1999).
12. L. G. Landsberg, Usp. Fiz. Nauk **164**, 1129 (1994) [Phys. Usp. **37**, 1043 (1994)].
13. V. F. Kurshetsov and L. G. Landsberg, Yad. Fiz. **57**, 2030 (1994) [Phys. At. Nucl. **57**, 1954 (1994)].
14. L. G. Landsberg, Yad. Fiz. **60**, 1541 (1997) [Phys. At. Nucl. **60**, 1397 (1997)]; in *Proceedings of the Seventh International Conference on Hadron Spectroscopy, Hadron 97, Upton, New York, 1997*, Ed. by S. U. Chang and H. J. Willutzki, p. 725.
15. L. G. Landsberg, Yad. Fiz. **62**, 2167 (1999) [Phys. At. Nucl. **62**, 1999 (1999)].
16. C. Caso *et al.*, (PDG), Eur. Phys. J. C **3**, 1 (1998).
17. D. V. Vavilov *et al.*, Yad. Fiz. **62**, 501 (1999) [Phys. At. Nucl. **62**, 459 (1999)].
18. G. S. Lomkatsi, Paper Presented at the Symposium on Modern Trends in Particle Physics, Dedicated to the Anniversary of G. Chikovani, Tbilisi, Georgia, Sept. 1998.

Translated by A. Asratyan

Physics of Atomic Nuclei, Vol. 63, No. 8, 2000, pp. 1395–1409. Translated from Yadernaya Fizika, Vol. 63, No. 8, 2000, pp. 1474–1488.

ON THE 85th ANNIVERSARY OF V.V. VLADIMIRSKY

Electromagnetic Form Factors for Nucleons and Pions at Positive and Negative q^2 in the Model of Quark–Gluon Strings

A. B. Kaidalov, L. A. Kondratyuk, and D. V. Tchekin[1)]

Institute of Theoretical and Experimental Physics, Bol'shaya Cheremushkinskaya ul. 25, Moscow, 117259 Russia

Received December 30, 1999

Abstract—The electromagnetic form factors for pions and nucleons are considered within the model of quark–gluon strings, where the momentum-transfer dependence of hadronic form factors is determined by the intercepts of the corresponding Regge trajectories and by the Sudakov form factor. Analytic expressions found for form factors in the timelike region admit an analytic continuation to the spacelike region. The resulting form factors for pions and nucleons comply well with experimental data both for positive and for negative values of the squared momentum transfer q^2. It is shown that the distinctions between the absolute values of the pion and nucleon form factors $F_\pi(q^2)$, $G_m(q^2)$, and $F_2(q^2)$ at positive values of q^2 and those at negative values of this variable are associated with the analytic properties of the double-logarithmic term in the exponent of the Sudakov form factor. The spin structure of the amplitudes for quark transitions into hadrons that is proposed in the present study makes it possible to describe fairly well available experimental data on the Pauli form factor F_2 and on the ratio G_e/G_m. © *2000 MAIK "Nauka/Interperiodica".*

1. INTRODUCTION

It is well known that, at high momentum transfers ($|q^2| \gg M^2$, where M is nucleon mass), the charge and the magnetic form factor for nucleons can be closely approximated by the dipole formula $|G_{e,m}(q^2)| \sim 1/|q^2|^2$ (for an overview, see [1]). For the Pauli form factors, this dependence becomes $|F_1(q^2)| \sim 1/|q^2|^2$ and $|F_2(q^2)| \sim 1/|q^2|^3$. The experimental data from [2, 3] also indicate that, at high $|q^2|$, the absolute value of the nucleon form factor $G_m(q^2)$ in the timelike region is approximately twice as great as that in the spacelike region—specifically, we have $|G_m(q^2)| \sim c_1/|q^2|^2$ for $q^2 > 0$ and $|G_m(q^2)| \sim c_2/|q^2|^2$ for $q^2 < 0$ with $c_1 \simeq 2c_2$ (see, for example, the review article of Gauzzi [3] and references therein).

Available experimental data on the pion form factor can be similarly described by the power-law expression $F_\pi(q^2) \sim c_\pi/q^2$. In all probability, the absolute value of the pion form factor, $|F_\pi(q^2)|$, is also greater in the timelike region than in the spacelike region, their ratio being again equal to two (see [3]).

As to theoretical studies, they agree in that, at asymptotically high momentum transfers, a correct description of the form factors in question is provided by the hard-scattering model, which is based on the assumption that soft and hard contributions factorize (see, for example, [4] and references therein). Nonetheless, there is the question of whether it is possible to apply this approach (which relies on perturbative QCD) in the region $q^2 \leq 30$ GeV^2) (see, for example, [5–8]), where experimental data are available. In the past few years, the hard-scattering model has been modified to take into account the $\mathbf{k}_\perp$ dependence of the hadron wave function and to include various parametrizations of the Sudakov form factor [9–12]. Within this modified approach, it is possible to perform a self-consistent calculation of perturbative contributions to the form factors even at comparatively low squares of the momentum transfers (between about 2 and 3 GeV^2). Among other things, such calculations revealed that, in this region, the perturbative contribution to the form factors is overly small to describe experimental data [13–15]. An analysis of the latest studies devoted to computing electromagnetic form factors on the basis of perturbative QCD showed (see, for example, the survey of Jain *et al.* [16]) that the absolute form-factor values cannot be predicted by calculations in the leading order in the strong-interaction coupling constant α_s. This result implies that nonperturbative (soft) contributions are of importance in calculating form factors.

A nonperturbative approach to describing hadronic form factors at finite q^2 on the basis of the model of quark–gluon strings (QGS model, also known as QGSM) [17] was proposed in [18]. Previously, the QGSM was used to describe soft hadron interactions at high energies [19, 20]. The QGSM is based on the ideas of a topological $1/N$ expansion [21–24] and on the color-tube model [25–28]. The QGSM can be considered as a microscopic model describing Regge phenomenology in terms of quark degrees of freedom; with the aid of this model, it proves to be possible to establish links between many soft hadronic reactions. Within the QGSM, the q^2 dependence of hadronic form factors is determined by [18] the intercepts of the Regge trajectories of mesons and baryons and by the Sudakov form factor.

[1)] Moscow Institute for Physics and Technology, Institutskiĭ proezd 9, Dolgoprudnyĭ, Moscow oblast, 141700 Russia.

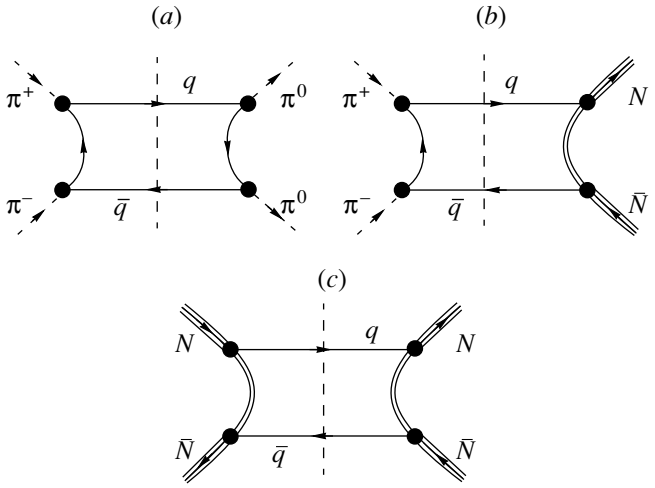

Fig. 1. Planar diagrams corresponding to the binary reactions (*a*) $\pi^+\pi^- \longrightarrow \pi^0\pi^0$, (*b*) $\pi\bar{\pi} \longrightarrow N\bar{N}$, and (*c*) $N\bar{N} \longrightarrow N\bar{N}$.

In the present study, it is shown that, within the QGSM, the distinction between the absolute values of hadronic form factors at positive q^2 and those at negative values of this variable is naturally explained by the analytic dependence of the Sudakov form factor on q^2. The model is generalized to take into account spin variables. This is done by introducing the amplitudes for quark transitions into hadrons, $T^{q\bar{q}\to h\bar{h}}$, and for hadron transitions into quarks, $T^{h\bar{h}\to q\bar{q}}$. Previously, spin effects within the QGSM were discussed in [18, 29]. The method proposed here differs substantially from the approach used in [29]. The introduction of spin variables makes it possible to separate the nucleon form factors F_1 and F_2 and to prove that, at high q^2, the pion form factor is additionally suppressed within the QGSM because of helicity conservation.

Relevant formulas are derived in the timelike region. Since the results are obtained in the form of analytic expressions, our formulas for the form factors in question can be continued analytically to the spacelike region. In the model used here, the distinction between the absolute values of the form factors at positive q^2 and those at negative q^2 are explained by the analytic dependence of the double-logarithmic term in the exponent of the Sudakov form factor.

The ensuing exposition is organized as follows. In Section 2, we present the fundamentals of the QGSM. We consider the amplitudes for the transitions of a quark–antiquark pair into a nucleon–antinucleon pair, $A^{q\bar{q}\to N\bar{N}}(s,t)$, and into a $\pi^+\pi^-$ pair, $A^{q\bar{q}\to\pi^+\pi^-}(s,t)$, and find the asymptotic behavior of these amplitudes for large s and finite t. For the transitions $\gamma \longrightarrow N\bar{N}$ and $\gamma \longrightarrow \pi^+\pi^-$, the matrix elements, which are defined as the convolution of the amplitudes for the transitions $\gamma \longrightarrow q\bar{q}$ and $q\bar{q} \longrightarrow h\bar{h}$ in the momentum representation or as the product of these amplitudes in the impact-parameter representation, are obtained analytically for $|s| \gg M^2$ and $|t| \le M^2$. In Section 3, we determine the spin structure of the amplitudes $T^{q\bar{q}\to N\bar{N}}$ and $T^{q\bar{q}\to\pi^+\pi^-}$ and derive expressions for the pion form factor $F_\pi(s)$, as well as for the nucleon charge and magnetic form factors [$G_e(s)$ and $G_m(s)$, respectively]. In Section 4, we consider the suppression of the amplitudes for the transitions $\gamma \longrightarrow N\bar{N}$ and $\gamma \longrightarrow \pi^+\pi^-$ that is described by the Sudakov form factor. In Section 5, we present numerical results for the form factors $G_m(s)$, $G_e(s)$, and $F_\pi(s)$ and compare these results with experimental data. A brief summary of the results obtained in this study is given in Section 6.

2. MODEL OF QUARK–GLUON STRINGS: AMPLITUDE FOR THE TRANSITION $q\bar{q} \longrightarrow h\bar{h}$ IN THE LIMIT OF LARGE s AND FINITE t

Let us consider the binary reactions $\pi^+\pi^- \longrightarrow \pi^0\pi^0$, $\pi^+\pi^- \longrightarrow N\bar{N}$, and $p\bar{p} \longrightarrow N\bar{N}$. At large values of s and finite values of t, these reactions can be described in terms of planar diagrams featuring t-channel valence-quark exchanges. In the diagrams presented in Fig. 1, single and double solid lines represent valence quarks and diquarks, respectively; no exchanges of soft gluons are shown there. In accordance with the topological $1/N_f$ expansion [18, 22], these planar diagrams are dominant at $N_f \gg 1$ and $N_c/N_f \sim 1$. In the case of nucleonic and pionic reactions, the main contribution comes from the exchanges of light u, d, and s quarks, and the expansion parameter is not very small: $1/N_f = 1/3$. Nonetheless, it is $1/N_f^2 \approx 1/10$, rather than $1/N_f$ [22], that appears to be an actual expansion parameter for the amplitudes of exclusive reactions featuring specific quantum numbers in the t channel. With each planar diagram of the topological expansion, we can associate a spacetime pattern formulated in terms of the string model or a color-tube model [17].

By way of example, we will consider the spacetime pattern of the binary reaction $\pi^+\pi^- \longrightarrow \pi^0\pi^0$ (see Fig. 1*a*). At a high c.m. energy $\sqrt{s}$, the reaction occurs if, in each pion, there arises a rare quark configuration such that one quark (antiquark), which plays the role of a spectator, carries almost the entire hadron momentum, while the valence antiquark (quark) in this system is slow. In this configuration, the difference of the rapidities y between the active and the spectator quark (between the quark and the antiquark) in each hadron is

$$y_q - y_{\bar{q}} \simeq \frac{1}{2}\ln\left(\frac{s}{s_0}\right), \qquad (1)$$

where $s_0 \sim 1$ GeV^2.

After that, two slow valence partons—the quark and the antiquark—from each pion (π^+ and π^-) annihilate, whereas the fast spectator quark and antiquark continue moving. As the fast quarks move apart, a gluon string is stretched between them. The string in question may rupture, whereby a two-particle hadronic state is formed via the process in which the generation of a quark–antiquark pair $q\bar{q}$ from a vacuum is followed by the recombination of the quarks from this pair with the corresponding spectator quarks. In the specific case being considered, this leads to the formation of a $\pi^0\pi^0$ system. The same spacetime pattern describes the process depicted in Fig. 1*b*. The only difference is that the rupture of the string leads, in the latter case, to the production of a diquark–antidiquark pair from a vacuum with the subsequent formation of a nucleon–antinucleon system in the final state.

In perfect analogy with the above, the diagram in Fig. 1*c* describes the process where a valence diquark (qq) and a valence antidiquark ($\overline{qq}$) annihilate, which results in the formation of a quark–gluon string in the intermediate state. The string then ruptures, producing a quark–antidiquark pair in the final state. The primary $q\bar{q}$ [or $(qq)(\overline{qq})$] structures annihilate if the rapidity difference between the valence quark q and the valence antiquark $\bar{q}$ [or between (qq) and $(\overline{qq})$] is small, $y_i \approx 0$ (either of the two interacting partons is nearly at rest in the c.m. frame), and if the relative impact parameter $|\mathbf{b}_\perp - \mathbf{b}_{0\perp}|$ is less than the interaction range. The probability of finding a valence quark with a rapidity y_q and with an impact parameter $\mathbf{b}_\perp$ in a hadron has the form [18]

$$w(y_q - y_0, \mathbf{b}_\perp - \mathbf{b}_{0\perp}) = \frac{c}{4\pi R^2(s)} \exp\left[-\beta(y_q - y_0) - \frac{(\mathbf{b}_\perp - \mathbf{b}_{0\perp})^2}{4R^2(s)}\right], \quad (2)$$

where $R^2(s)$ is the square of the effective range of interaction, y_0 is the hadron rapidity in the reaction c.m. frame, $\mathbf{b}_\perp$ is the coordinate of the valence quark in the impact-parameter representation, and β is a parameter. As was shown in [18], the parameters β and $R^2(s)$, which determine the density of quark distribution in a hadron, can be expressed in terms of the phenomenological parameters of the Regge trajectory $\alpha_R(t)$ that makes the dominant contribution to a given planar diagram. Specifically, the parameter β is related to the intercept of the Regge trajectory as $\beta = 1 - \alpha_R(0)$, while $R^2(s) = R_0^2 + \alpha'(y_q - y_0)$, where $\alpha' = \alpha'_R(0)$ is the slope of the dominant Regge trajectory.

For an $ab \longrightarrow cd$ binary reaction involving the formation of a quark–gluon string (or a color tube) in the intermediate state, the above spacetime pattern leads to the factorization of the amplitudes in the s channel. Since the product color tube does not preserve information about the properties of the initial state, the probability of the formation of an arbitrary state depends neither on the type of the annihilated quarks nor on the structure of the initial state; it is determined exclusively by the type of quarks produced upon the rupture of the string.

Generalizing the approach developed in [19, 20], we introduce the amplitudes $\tilde{T}^{ab\to q\bar{q}}(s, \mathbf{b}_\perp)$ and $\tilde{T}^{q\bar{q}\to cd}(s, \mathbf{b}_\perp)$ that describe, respectively, the formation and the rupture of a quark–gluon tube. For an $ab \longrightarrow cd$ binary reaction, the amplitude that corresponds to the diagram in Fig. 1*a*, 1*b*, or 1*c* can be represented as the product of the amplitudes in the impact-parameter representation,

$$\tilde{A}^{ab\to cd}(s, \mathbf{b}_\perp) = \frac{i}{2s}\tilde{T}^{ab\to q\bar{q}}(s, \mathbf{b}_\perp)\tilde{T}^{q\bar{q}\to cd}(s, \mathbf{b}_\perp), \quad (3)$$

or as the convolution of the two amplitudes in the momentum representation,

$$A^{ab\to cd}(s, \mathbf{q}_\perp) = \frac{i}{(8\pi^2 s)}\int d^2\mathbf{k}_\perp T^{ab\to q\bar{q}}(s, \mathbf{k}_\perp)T^{q\bar{q}\to cd}(s, \mathbf{q}_\perp - \mathbf{k}_\perp). \quad (4)$$

Let us now find the parameters appearing in the amplitudes $T^{\pi^+\pi^-\to q\bar{q}}(s, \mathbf{k}_\perp)$ and $T^{q\bar{q}\to N\bar{N}}(s, \mathbf{k}_\perp)$ at asymptotically large values of s. This corresponds to the Regge parametrization of the amplitudes $A^{\pi^+\pi^-\to\pi^0\pi^0}$, $A^{\pi\bar{\pi}\to N\bar{N}}$, and $A^{N\bar{N}\to N\bar{N}}$; that is,

$$\begin{aligned} A^{\pi^+\pi^-\to\pi^0\pi^0}(s, t) &= N_M\left(-\frac{s}{s_0}\right)^{\alpha_M(t)}\exp(R_{0M}^2 t), \\ A^{\pi\bar{\pi}\to N\bar{N}}(s, t) &= N_B\left(-\frac{s}{s_0}\right)^{\alpha_B(t)}\exp(R_{0B}^2 t), \\ A^{N\bar{N}\to N\bar{N}}(s, t) &= N_D\left(-\frac{s}{s_0}\right)^{\alpha_D(t)}\exp(R_{0D}^2 t), \end{aligned} \quad (5)$$

where $\alpha_M(t)$, $\alpha_B(t)$, and $\alpha_D(t)$ are the dominant meson, baryon, and quark–diquark Regge trajectories, respectively, while N_M, N_B, and N_D are the corresponding normalization constants. For the dominant Regge poles, we have

$$\begin{aligned} \alpha_M(0) \simeq 0.5, \quad \alpha_B(0) \simeq -0.5, \\ \alpha_D(0) \simeq 2\alpha_B(0) - \alpha_M(0) \simeq -1.5. \end{aligned} \quad (6)$$

For the case of light constituent quarks, the relevant slopes of the Regge trajectories are

$$\alpha'_M(0) \simeq \alpha'_B(0) \simeq \alpha'_D(0) \simeq 1.0 \text{ GeV}^{-2}. \quad (7)$$

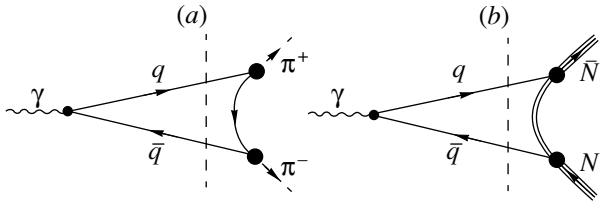

Fig. 2. Planar diagrams corresponding to the processes (a) $\gamma \longrightarrow \pi^+\pi^-$ and (b) $\gamma \longrightarrow N\bar{N}$.

Taking into account the factorization equations (3) and (4), we can represent the amplitudes $\tilde{T}^{q\bar{q}\to\pi\bar{\pi}}(s, \mathbf{b}_\perp)$ and $\tilde{T}^{q\bar{q}\to N\bar{N}}(s, \mathbf{b}_\perp)$ as

$$\tilde{T}^{q\bar{q}\to\pi\bar{\pi}}(s, \mathbf{b}_\perp) = N_M^{1/2}\frac{1}{2\sqrt{\pi}R_M(s)}\left(-\frac{s}{s_0}\right)^{(\alpha_M(0)+1)/2}\exp\left(-\frac{\mathbf{b}_\perp^2}{8R_M^2(s)}\right),$$
$$\tilde{T}^{q\bar{q}\to N\bar{N}}(s, \mathbf{b}_\perp) = N_D^{1/2}\frac{1}{2\sqrt{\pi}R_D(s)}\left(-\frac{s}{s_0}\right)^{(\alpha_D(0)+1)/2}\exp\left(-\frac{\mathbf{b}_\perp^2}{8R_D^2(s)}\right), \quad (8)$$

where the quantities $R_M(s)$ and $R_D(s)$ defined by the relations

$$R_M^2(s) = R_{0M}^2 + \alpha_M'(0)\ln\left(-\frac{s}{s_0}\right),$$
$$R_D^2(s) = R_{0D}^2 + \alpha_D'(0)\ln\left(-\frac{s}{s_0}\right) \quad (9)$$

have the meaning of the effective ranges of interaction.

Substituting the amplitudes specified by equations (8) into (3), we obtain

$$\tilde{A}^{\pi\bar{\pi}\to N\bar{N}}(s, \mathbf{b}_\perp) = (N_M N_D)^{1/2}\frac{1}{4\pi R_D(s)R_M(s)} \times\left(-\frac{s}{s_0}\right)^{\frac{1}{2}(\alpha_D(0)+\alpha_M(0))}\exp\left[-\mathbf{b}_\perp^2\left(\frac{1}{8R_M^2(s)}+\frac{1}{8R_D^2(s)}\right)\right]. \quad (10)$$

For the equalities in (5) and (10) to be consistent, it is necessary to require that the parameters of the Regge trajectories [18] and the normalization constants satisfy the relations

$$2\frac{1}{R_B^2(s)} = \frac{1}{R_M^2(s)} + \frac{1}{R_D^2(s)},$$
$$2\alpha(0)_B = \alpha_D(0) + \alpha_M(0), \quad (11)$$

$$(N_M N_D)^{1/2}\frac{1}{R_D(s)R_M(s)} = N_B\frac{1}{R_B^2(s)}. \quad (12)$$

Assuming that only light u, d, and s quarks participate in the above reactions, we arrive at [18]

$$\alpha_M'(0) = \alpha_B'(0) = \alpha_D'(0) \equiv \alpha'(0),$$
$$R_{0M}^2(0) = R_{0B}^2(0) = R_{0D}^2(0) \equiv R_0^2(0), \quad (13)$$
$$(N_M N_D)^{1/2} = N_B.$$

In this case, relations (11) and (12) hold for all values of s. Otherwise, these relations are satisfied at sufficiently large values of s (see also [18]).

Within this approach, we can also consider the reaction of electron–positron annihilation into hadrons (see Fig. 2). In the case of $\gamma \longrightarrow N\bar{N}$ (Fig. 2*b*), a virtual photon produces a quark–antiquark pair. As the components of the pair move apart, a color tube is stretched between the fast quarks. The rupture of the tube with the formation of a final-state hadron pair is governed by the same mechanism as that in the processes illustrated in Fig. 2*b*. The string ruptures, generating a diquark–antidiquark pair, which subsequently forms a final nucleon–antinucleon state via the interaction with spectator quarks. The corresponding transition form factors can be expressed in terms of the amplitudes $T^{\gamma\to q\bar{q}}(s, \mathbf{b}_\perp)$ and $\tilde{T}^{q\bar{q}\to N\bar{N}}(s, \mathbf{b}_\perp)$ as

$$A^{\gamma\to N\bar{N}}(s) = \frac{i}{2s}T^{\gamma\to q\bar{q}}(s)\tilde{T}^{q\bar{q}\to N\bar{N}}(s, \mathbf{b}_\perp = 0). \quad (14)$$

Thus, we find that, at large s, the nucleon form factors are given by

$$|G_{m,e}(s)| \sim |s|^{-1}\left|\tilde{T}^{q\bar{q}\to N\bar{N}}(s, \mathbf{b}_\perp = 0)\right| \sim \frac{1}{R_D(s)}|s|^{(\alpha_D(0)-1)/2}. \quad (15)$$

In the case where a $\pi^+\pi^-$ pair is formed in the final state (see Fig. 2*a*), the relevant expressions for the amplitudes and for the form factor can be represented as

$$A^{\gamma\to\pi\bar{\pi}}(s) = \frac{i}{2s}T^{\gamma\to q\bar{q}}(s)\tilde{T}^{q\bar{q}\to\pi\bar{\pi}}(s, \mathbf{b}_\perp = 0), \quad (16)$$

$$|F_\pi(s)| \sim |s|^{-1}\left|\tilde{T}^{q\bar{q}\to\pi\bar{\pi}}(s, \mathbf{b}_\perp = 0)\right| \sim \frac{1}{R_M(s)}|s|^{(\alpha_M(0)-1)/2}. \quad (17)$$

Taking into account the intercept values specified by (6), we find that the asymptotic behavior of the form factors is described by the expressions

$$F_\pi(s) \sim |s/s_0|^{-1/4},$$
$$|G_{m,e}(s)| \sim |s/s_0|^{-5/4}.$$

This asymptotic behavior of the form factors differs from that which is predicted by the quark-counting

rules [30] and from that which follows from the calculations based on perturbative QCD [4]. Moreover, the asymptotic behavior that we obtained is at odds with experimental data on the pion and nucleon form factors, which vary, in experiments, in inverse proportion to the total c.m. energy and its square, respectively; that is, $F_\pi(s) \sim s^{-1}$ and $G_{m,e}(s) \sim s^{-2}$. The reason behind this discrepancy is that we took no account of the suppression of the amplitudes that is due to the Sudakov form factor. In Sections 3 and 4, it will be shown that, as soon as the Sudakov form factor is included in our theoretical scheme, a correct q^2 dependence of the hadron form factors is recovered both in the time- and in the spacelike region; moreover, the ratios of the absolute values of the form factors at positive and negative values of $q^2 \equiv s$ take proper values thereupon. Prior to proceeding to derive the expression for the Sudakov form factor, we will consider the spin structure of the amplitudes for quark transitions into hadrons in order to be able to take into account spin effects in various hadronic reactions and to separate the form factors G_e and G_m. It will also be shown that helicity conservation leads to an additional suppression of the pion form factor in proportion to $1/\sqrt{s}$ at large s.

3. SPIN STRUCTURE OF AMPLITUDES AND DETERMINATION OF FORM FACTORS

Let us begin by introducing the required notation. The pion and nucleon form factors are defined as

$$A_\mu^{\gamma\to\pi^+\pi^-}(q^2) = F_\pi(q^2)(p_h - p_{\bar h})_\mu, \tag{18}$$

$$\begin{aligned} A_\mu^{\gamma\to N\bar N}(q^2) &= \bar u_{\lambda_N}\Big[G_m(q^2)\gamma_\mu + 2M\Big(G_e(q^2) \\ &\quad - G_m(q^2)\Big)\frac{(p_h - p_{\bar h})_\mu}{(p_h - p_{\bar h})^2}\Big]v_{\lambda_{\bar N}} \\ &= \bar u_{\lambda_N}\Big[F_1(q^2)\gamma_\mu - \frac{\kappa_p F_2(q^2)}{2M_h}\sigma_{\mu\nu}q_\nu\Big]v_{\lambda_{\bar N}}, \end{aligned} \tag{19}$$

where p_h and $p_{\bar h}$ are the 4-momenta of final-state hadrons, while $\kappa_p = \mu_p - 1$, $\mu_p = 2.793$ being the proton magnetic moment.

Let us now proceed to construct the spin structure of the amplitudes $T^{q\bar q\to\pi\bar\pi}$ and $T^{q\bar q\to N\bar N}$. We define the invariants s and t in the standard way as

$$\begin{aligned} s &= (p_q + p_{\bar q})^2 = (p_h + p_{\bar h})^2, \\ t &= (p_q - p_h)^2 = (p_{\bar q} - p_{\bar h})^2 \end{aligned} \tag{20}$$

and introduce the relative momenta $p_\mu = \frac{1}{2}(p_{q\mu} - p_{\bar q\mu})$, $P_\mu = \frac{1}{2}(p_{h\mu} - p_{\bar h\mu})$, and $k_\mu = P_\mu - p_\mu$, where $p_{q\mu}$ and k_μ are the 4-momenta of, respectively, the fast quark and the slow antiquark (or diquark).

In the region of large s and finite t, we have $\{\mathbf{P}^2, \mathbf{p}^2\} \gg \{M^2, m^2\}$, where m is the light-quark mass and $\mathbf{P} = \{\mathbf{P}_\perp = 0, P_z\}$. For the variables introduced immediately above, we have

$$\begin{aligned} k_z &= P_z - p_z \approx \frac{\sqrt{s}}{2} - \frac{M^2}{\sqrt{s}} \\ &\quad - \left(\frac{\sqrt{s}}{2} - \frac{m^2 + \mathbf{k}_\perp^2}{\sqrt{s}}\right) \sim \left(\frac{M^2}{\sqrt{s}} - \frac{m^2 + \mathbf{k}_\perp^2}{\sqrt{s}}\right). \end{aligned} \tag{21}$$

As can be seen from (21), the component k_z is asymptotically small in relation to $|\mathbf{k}_\perp|$: $k_z = O(1/s)$.

Let us now consider the pion form factor. The amplitude $T^{q\bar q\to\pi\bar\pi}$ can be expressed in terms of two invariant amplitudes $\tilde B_1$ and $\tilde B_2$ as

$$\begin{aligned} &T^{q\bar q\to\pi\bar\pi}_{\lambda_q\lambda_{\bar q}}(s, \mathbf{k}_\perp^2) \\ &= (\chi^*_{\lambda_{\bar q}}\sigma_i\chi_{\lambda_q})[\tilde B_1(s, \mathbf{k}_\perp^2)P_i + \tilde B_2(s, \mathbf{k}_\perp^2)p_i]. \end{aligned} \tag{22}$$

We assume that the amplitudes $\tilde B_1$ and $\tilde B_2$ are characterized by the same asymptotic behavior. Their s dependence can then be represented as

$$\begin{aligned} &\tilde B_{\{1,2\}}(s, t) \\ &= \beta^0_{\{1,2\}}\left(-\frac{s}{s_0}\right)^{\alpha_M(0)/2}\frac{1}{R_M(s)}\exp\left[\frac{1}{2}R_M^2(s)t\right]. \end{aligned} \tag{23}$$

We note that, in contrast to the expressions in (8), these amplitudes feature no extra power of $s^{1/2}$, which has been taken into account in the momenta $|\mathbf{P}|, |\mathbf{p}| \sim s^{1/2}$.

It is convenient to recast expression (22) into the form

$$\begin{aligned} &T^{q\bar q\to\pi\bar\pi}_{\lambda_q\lambda_{\bar q}}(s, \mathbf{k}_\perp^2) \\ &= (\chi^*_{\lambda_{\bar q}}\sigma_i\chi_{\lambda_q})[B_1(s, \mathbf{k}_\perp^2)P_i + B_2(s, \mathbf{k}_\perp^2)k_i]. \end{aligned} \tag{24}$$

Since $|\mathbf{k}_\perp|/|\mathbf{P}| \sim s^{-1/2}$, the contribution of the second term from (24) to the form factors features a small parameter and can therefore be disregarded, as will be seen from the formulas given below.

The amplitude $A_\mu^{\gamma\to\pi^+\pi^-}$ can be written as the convolution of the quark-current amplitude and the amplitude

for the quark transition into pions [see equations (8)]:

$$A_\mu^{\gamma\to\pi^+\pi^-}(s) = \frac{i}{(8\pi^2 s)}\int d^2\mathbf{k}_\perp T_\mu^{\gamma\to q\bar q}(s,\mathbf{k}_\perp^2)T^{q\bar q\to\pi\bar\pi}(s,\mathbf{k}_\perp^2). \quad (25)$$

The quark-current operator $A_i^{\gamma\to q\bar q} = \bar u(p_q,\lambda_q)\times\gamma_i v(p_{\bar q},\lambda_{\bar q})$ as expressed in terms of two-component spinors in the c.m. frame, where $\mathbf{p}_q = -\mathbf{p}_{\bar q} = \mathbf{p}$, has the form

$$A_i^{\gamma\to q\bar q} = 2(\varepsilon+m)^{-1}\chi^*_{\lambda_q}[\varepsilon(\varepsilon+m)\sigma_i - p_i(\mathbf{p}\cdot\boldsymbol{\sigma})]\chi_{\lambda_{\bar q}}, \quad (26)$$

where ε is the total quark energy. For convenience of the ensuing transformations, we break down the quark-current operator into the transverse and longitudinal components as

$$A_i^{\gamma\to\pi^+\pi^-} = 2\left[\varepsilon\left(\delta_{ij}-\frac{p_ip_j}{\mathbf{p}^2}\right)+m\frac{p_ip_j}{\mathbf{p}^2}\right](\chi^*_{\lambda_q}\sigma_j\chi_{\lambda_{\bar q}}). \quad (27)$$

In taking into account spin variables in (25), the transition amplitude $A^{\gamma\to\pi^+\pi^-}$ can be represented as

$$A_i^{\gamma\to\pi^+\pi^-}(s) = \frac{i}{(8\pi^2 s)}\int d^2\mathbf{k}_\perp\cdot 2\,\mathrm{tr}[\sigma_j\sigma_l]$$

$$\times\left[\left(\varepsilon-(\varepsilon-m)\frac{\mathbf{k}_\perp^2}{2\mathbf{p}^2}\right)\delta_{ij}^\perp+\left(m+(\varepsilon-m)\frac{\mathbf{k}_\perp^2}{\mathbf{p}^2}\right)\frac{P_iP_j}{\mathbf{P}^2}\right] \quad (28)$$

$$\times[B_1(s,\mathbf{k}_\perp^2)P_l + B_2(s,\mathbf{k}_\perp^2)k_l],$$

where $\delta_{ij}^\perp = \delta_{ij} - P_iP_j/\mathbf{P}^2$. It can easily be shown that, with respect to $B_2(s,\mathbf{k}_\perp^2)$, the relative contribution of the term proportional to $B_1(s,\mathbf{k}_\perp^2)$ is of order $(m^2+\mathbf{k}_\perp^2)/s$. Therefore, we obtain

$$A_i^{\gamma\to\pi^+\pi^-}(s) = \frac{i}{(8\pi^2 s)}\int d^2\mathbf{k}_\perp\cdot 2\left[m+(\varepsilon-m)\frac{\mathbf{k}_\perp^2}{\mathbf{p}^2}\right]B_1(s,\mathbf{k}_\perp^2)P_i \quad (29)$$

$$\approx\frac{i}{(8\pi^2 s)}\int d^2\mathbf{k}_\perp\cdot 2mB_1(s,\mathbf{k}_\perp^2)P_i,$$

where, in the last expression, we have discarded all preasymptotic terms of orders $s^{-1/2}$, s^{-1}, etc.

Here, it is important to note that the transverse and the longitudinal components of the $\gamma\longrightarrow q\bar q$ quark current behave differently at large s:

$$A_\perp^{\gamma\to q\bar q}\sim\varepsilon\boldsymbol{\sigma}_\perp\sim s^{1/2}\boldsymbol{\sigma}_\perp,$$
$$A_z^{\gamma\to q\bar q}\sim m\sigma_z. \quad (30)$$

The above smallness of the longitudinal component is due to helicity conservation. This component vanishes in the limit $m\longrightarrow 0$.

In the case of the transition $\gamma\longrightarrow\pi^+\pi^-$, only the longitudinal component is operative at large s, while the transverse component does not contribute in this limit. This is the reason why the pion form factor involves an additional suppression in proportion to $s^{-1/2}$ in relation to the estimate in (17), which was presented in the preceding section and which was obtained without allowing for spin effects. We note that this behavior of the pion form factor was predicted in [31] on the basis of the parton model. No such suppression is expected for the transitions $\gamma\longrightarrow\pi\rho$ and $\gamma\longrightarrow\pi\omega$. It follows that the QGSM predicts that the form-factor ratios $F_{\pi\pi}/F_{\pi\rho}$ and $F_{\pi\pi}/F_{\pi\omega}$ must decrease in proportion to $1/\sqrt{s}$. The situation is different in perturbative QCD (pQCD), where the helicity of quarks must be conserved, which would yield $(F_{\pi\pi}/F_{\pi\rho})_{\mathrm{pQCD}} \sim (F_{\pi\pi}/F_{\pi\omega})_{\mathrm{pQCD}} \sim s$. Thus, we can see that the QGSM predictions for $\gamma\longrightarrow\pi\pi$ and $\gamma\longrightarrow\pi\rho(\omega)$ form factors at large s differ drastically from the corresponding predictions of perturbative QCD. We note that, in the case of nucleons, where both contributions, $A_\perp$ and A_z, are operative, there arises no additional suppression of the magnetic form factor [see equation (38)].

We will now show that, of the two invariant amplitudes defined above, $B_1(s,\mathbf{k}_\perp^2)$ and $B_2(s,\mathbf{k}_\perp^2)$, it is the amplitude $B_1(s,\mathbf{k}_\perp^2)$ that makes the main contribution to the planar pion diagram; that is,

$$A^{\pi\bar\pi\to\pi\bar\pi}(s,\mathbf{q}_\perp^2) = \frac{i}{(8\pi^2 s)}\sum_{\lambda_q\lambda_{\bar q}}\int d^2\mathbf{k}_\perp(\chi^*_{\lambda_q}\sigma_i\chi_{\lambda_{\bar q}})(\chi^*_{\lambda_{\bar q}}\sigma_j\chi_{\lambda_q})$$

$$\times[B_1^*(s,\mathbf{k}_\perp^2)P_i + B_2^*(s,\mathbf{k}_\perp^2)k_i]$$

$$\times[B_1(s,(\mathbf{q}-\mathbf{k})_\perp^2)P_j + B_2(s,(\mathbf{q}-\mathbf{k})_\perp^2)k_j]$$

$$= \frac{i}{(8\pi^2 s)}\int d^2\mathbf{k}_\perp[B_1^*(s,\mathbf{k}_\perp^2)P_i + B_2^*(s,\mathbf{k}_\perp^2)k_i] \quad (31)$$

$$\times[B_1(s,(\mathbf{q}-\mathbf{k})_\perp^2)P_i + B_2(s,(\mathbf{q}-\mathbf{k})_\perp^2)k_i]$$

$$= \frac{i}{(8\pi^2 s)}\int d^2\mathbf{k}_\perp B_1^*(s,\mathbf{k}_\perp^2)B_1(s,(\mathbf{q}-\mathbf{k})_\perp^2)s + O\left(\frac{\mathbf{k}_\perp^2}{s},\frac{m_q^2}{s}\right).$$

Since $B_1\sim(-s/s_0)^{\alpha_M(0)/2}$, equation (31) yields a correct s dependence for the amplitude being considered:

$A^{\pi\bar{\pi}\to\pi\bar{\pi}} \sim (-s/s_0)^{\alpha_M(0)}$. Equation (31) can be used to fix the normalization of the amplitude $B_1(s, \mathbf{k}_\perp^2)$.

Thus, the pion form factor F_π is directly expressed in terms of the amplitude $B_1(s, \mathbf{k}_\perp^2)$ as

$$F_\pi(s) \simeq m\frac{i}{(8\pi^2 s)}\int d^2\mathbf{k}_\perp B_1(s, \mathbf{k}_\perp^2) = \frac{N_\pi}{R_M(s)}\left(-\frac{s}{s_0}\right)^{\alpha_M(0)/2-1}, \quad (32)$$

where N_π is a normalization factor, which is taken here to be a free parameter.

Let us now proceed to consider the nucleon form factor. The spin structure of the amplitude for the transition $q\bar{q} \longrightarrow N\bar{N}$ can generally be represented in the form

$$T^{q\bar{q}\to N\bar{N}}(s, \mathbf{k}_\perp) = \chi^*_{\lambda_N}\chi^{(c)*}_{\lambda_{\bar{N}}}\hat{U}_{(\lambda_N\lambda_{\bar{N}};\,\lambda_q\lambda_{\bar{q}})}\chi_{\lambda_q}\chi^{(c)}_{\lambda_{\bar{q}}}, \quad \chi^{(c)}_\lambda = i\sigma_y\chi^{*(T)}_\lambda, \quad (33)$$

where $\hat{U}$ is a spin operator that acts on the spin variables of the nucleons and quarks involved and which can be expressed in terms of eight invariant amplitudes as

$$\begin{aligned}\hat{U} &= D_1(s, \mathbf{q}_\perp)1\cdot 1 + D_2(s, \mathbf{k}_\perp)(\boldsymbol{\sigma}\cdot\mathbf{n})\cdot 1\\ &+ D_3(s, \mathbf{k}_\perp)1\cdot(\boldsymbol{\sigma}'\cdot\mathbf{n}) + D_4(s, \mathbf{k}_\perp)\sigma_x\cdot\sigma'_x\\ &+ D_5(s, \mathbf{k}_\perp)\sigma_y\cdot\sigma'_y + D_6(s, \mathbf{k}_\perp)\sigma_z\cdot\sigma'_z\\ &+ D_7(s, \mathbf{k}_\perp)\sigma_x\cdot\sigma'_z + D_8(s, \mathbf{k}_\perp)\sigma_z\cdot\sigma'_x,\end{aligned} \quad (34)$$

where the matrices σ_i and σ'_i act on the spin variables of the nucleon and the quark (antinucleon and antiquark), respectively, while the unit vector $\mathbf{n}$ is defined as

$$\mathbf{n} = \frac{\mathbf{P}\times\mathbf{p}}{|\mathbf{P}\times\mathbf{p}|}. \quad (35)$$

Let us first consider the case where none of the amplitudes $D_i(s, \mathbf{k}_\perp)$ is suppressed and where all of them have the same asymptotic behavior

$$D_i(s, t) = \gamma_i^0\left(-\frac{s}{s_0}\right)^{(\alpha_D(0)+1)/2}\frac{1}{R_D(s)}\exp\left[\frac{1}{2}R_D(s)^2 t\right]. \quad (36)$$

In taking into account spin variables, the amplitude for the transition $\gamma \longrightarrow N\bar{N}$ will then assume the form

$$\begin{aligned}A_i^{\gamma\to N\bar{N}}(s) &= \frac{i}{(8\pi^2 s)}\\ &\times\int d^2\mathbf{k}_\perp T_i^{\gamma\to q\bar{q}}(s, \mathbf{k}_\perp)T^{q\bar{q}\to N\bar{N}}(s, \mathbf{k}_\perp)\\ &= \frac{i}{(8\pi^2 s)}\sum_{\lambda_q\lambda_{\bar{q}}}\int d^2\mathbf{k}_\perp\times 2\left[\left(\varepsilon - (\varepsilon - m)\frac{\mathbf{k}_\perp^2}{2\mathbf{p}^2}\right)\delta_{ij}^\perp\right.\\ &\left.+\left(m + (\varepsilon - m)\frac{\mathbf{k}_\perp^2}{\mathbf{p}^2}\right)\frac{P_iP_j}{\mathbf{P}^2}\right]\\ &\times(\chi^*_{\lambda_q}\sigma_j\chi^{(c)}_{\lambda_{\bar{q}}})\chi^*_{\lambda_N}\chi^{(c)*}_{\lambda_{\bar{q}}}\hat{U}_{(\lambda_N\lambda_{\bar{N}};\,\lambda_q\lambda_{\bar{q}})}\chi_{\lambda_q}\chi^{(c)}_{\lambda_{\bar{N}}}\\ &= 2\left[\varepsilon G_m\delta_{ij}^\perp + MG_e\frac{P_iP_j}{\mathbf{P}^2}\right](\chi^*_{\lambda_N}\sigma_j\chi^{(c)}_{\lambda_{\bar{N}}}).\end{aligned} \quad (37)$$

Let us now present expressions for the longitudinal and transverse components of the matrix elements of the relevant current. It can be seen from (37) that, here, the Sachs form factors are separated—that is, G_e contributes only to the longitudinal current component, while G_m contributes only to the transverse component. From (30), it follows that the leading terms in the asymptotic expression for the quark current are independent of $\mathbf{k}_\perp$. Considering that, upon integration with respect to this two-dimensional vector, terms that are not invariant under rotations about the z axis must vanish, we can represent the transverse and the longitudinal component of the current operator as

$$\begin{aligned}A_\perp^{\gamma\to N\bar{N}} &= \frac{i}{(8\pi^2 s)}\sum_{\lambda_q\lambda_{\bar{q}}}\sum_l\int d^2\mathbf{k}_\perp D_l(s, \mathbf{k}_\perp^2)\\ &\times(2\varepsilon)\chi^*_{\lambda_N}\sigma_{n_l}\chi^{(c)*}_{\lambda_{\bar{q}}}(\chi^*_{\lambda_q}\boldsymbol{\sigma}_\perp\chi^{(c)}_{\lambda_{\bar{q}}})\chi_{\lambda_q}\sigma_{n_l}\chi^{(c)}_{\lambda_{\bar{N}}}\\ &= 2\varepsilon G_m(\chi^*_{\lambda_N}\boldsymbol{\sigma}_\perp\chi^{(c)}_{\lambda_{\bar{N}}}),\end{aligned} \quad (38)$$

$$\begin{aligned}A_z^{\gamma\to N\bar{N}} &= \frac{i}{(8\pi^2 s)}\sum_{\lambda_q\lambda_{\bar{q}}}\sum_l\int d^2\mathbf{k}_\perp D_l(s, \mathbf{k}_\perp^2)\\ &\times 2m\chi^*_{\lambda_N}\sigma_{n_l}\chi^{(c)*}_{\lambda_{\bar{q}}}(\chi^*_{\lambda_q}\sigma_z\chi^{(c)}_{\lambda_{\bar{q}}})\chi_{\lambda_{\bar{q}}}\sigma_{n_l}\chi^{(c)}_{\lambda_{\bar{N}}}\\ &= 2MG_e(\chi^*_{\lambda_N}\sigma_z\chi^{(c)}_{\lambda_{\bar{N}}}),\end{aligned}$$

where $l = 1, 4, 5$, and 6. As a result, the form factors G_e and G_m will be expressed in terms of different linear combinations of the amplitudes D_1, D_4, D_5, and D_6. If all these amplitudes have the same asymptotic behavior, the form factors G_e and G_m will also have the same asymptotic behavior:

$$G_m(s), G_e(s) \sim \left(-\frac{s}{s_0}\right)^{(\alpha_D(0)-1)/2}. \quad (39)$$

However, the ratio G_e/G_m may depend on the choice of specific model for the invariant amplitudes.

Equations (38) also guarantee that the Pauli form factor F_2 has an additional degree of suppression, s^{-1}, in

relation to G_m and G_e. This suppression is of a purely kinematical origin and follows from the definition of F_2:

$$F_2(s) = \left(\frac{q^2}{4M^2} - 1\right)^{-1} [G_e(s) - G_m(s)], \qquad F_2(s) \sim \left(-\frac{s}{s_0}\right)^{\alpha_D(0)/2 - 1.5}. \tag{40}$$

Since specific relations between the amplitudes D_1, D_4, D_5, and D_6 are not known, we will perform our calculations for two simple cases: (i) the case where the amplitude D_1, which preserves the helicity of the particles participating in the reaction, is dominant [model (i)] and (ii) the case where the amplitude $T^{q\bar{q} \to N\bar{N}}$ can be described in terms of t-channel scalar-diquark exchange [model (ii)].

In case (i), we have

$$T^{q\bar{q} \to N\bar{N}}_{\lambda_N \lambda_{\bar{N}} \lambda_q \lambda_{\bar{q}}} \longrightarrow D_1(s, \mathbf{k}_\perp) 1 \cdot 1 \equiv D_1(s, \mathbf{k}_\perp) \delta_{\lambda_N \lambda_q} \delta_{\lambda_{\bar{N}} \lambda_{\bar{q}}}, \tag{41}$$

and the expression for the amplitude $A_i^{\gamma \to N\bar{N}}$ is simplified significantly to become

$$A_i^{\gamma \to N\bar{N}}(s) = \frac{i}{(8\pi^2 s)} \int d^2\mathbf{k}_\perp D_1(s, \mathbf{k}_\perp) (\chi^*_{\lambda_N} \sigma_j \chi^{(c)}_{\lambda_{\bar{N}}}) \times 2 \left[\left(\varepsilon - (\varepsilon - m) \frac{\mathbf{k}_\perp^2}{2\mathbf{p}^2} \right) \delta_{ij}^\perp + \left(m + (\varepsilon - m) \frac{\mathbf{k}_\perp^2}{\mathbf{p}^2} \right) \frac{P_i P_j}{\mathbf{P}^2} \right]. \tag{42}$$

In the leading order in s, we can disregard terms proportional to $\mathbf{k}_\perp^2/\mathbf{p}^2$ and represent the amplitude $A_i^{\gamma \to N\bar{N}}$ in the form

$$A_i^{\gamma \to N\bar{N}}(s) = \frac{i}{(8\pi^2 s)} \times \int d^2\mathbf{k}_\perp D_1(s, \mathbf{k}_\perp) (\chi^*_{\lambda_N} \sigma_j \chi^{(c)}_{\lambda_{\bar{N}}}) \times 2 \left[\varepsilon \delta_{ij}^\perp + m \frac{P_i P_j}{\mathbf{P}^2} \right]. \tag{43}$$

For the Sachs form factors, it follows from the above that

$$G_m(s) = \frac{i}{(8\pi^2 s)} \int d^2\mathbf{k}_\perp D_1(s, \mathbf{k}_\perp) = \frac{C}{R_D(s)} \left(-\frac{s}{s_0}\right)^{(\alpha_D(0) - 1)/2}, \qquad G_e(s) = \frac{m}{M} \frac{i}{(8\pi^2 s)} \int d^2\mathbf{k}_\perp D_1(s, \mathbf{k}_\perp) = \frac{m}{M} \frac{C}{R_D(s)} \left(-\frac{s}{s_0}\right)^{(\alpha_D(0) - 1)/2}, \tag{44}$$

where C is a normalization constant.

The Pauli form factor F_2 is directly expressed in terms of G_m and G_e as [see equation (40)]

$$F_2(s) = -\left(\frac{s}{4M^2} - 1\right)^{-1} \left(1 - \frac{m}{M}\right) \frac{C}{R_D(s)} \left(-\frac{s}{s_0}\right)^{(\alpha_D(0) - 3)/2}. \tag{45}$$

From expressions (33) and (34), it follows that the above parametrization corresponds to the correct Regge behavior of the amplitude $T^{N\bar{N} \to N\bar{N}}$. In the specific case where the invariant amplitude $D_1(s, \mathbf{k}_\perp)$ is dominant, $T^{N\bar{N} \to N\bar{N}}$ is expressed directly in terms of the square of this amplitude as

$$T^{N\bar{N} \to N\bar{N}}(s, \mathbf{q}_\perp) = \frac{i}{(8\pi^2 s)} \int d^2\mathbf{k}_\perp D_1^*(s, \mathbf{k}_\perp) D_1(s, \mathbf{q}_\perp - \mathbf{k}_\perp), \tag{46}$$

whence it follows that

$$T^{N\bar{N} \to N\bar{N}}(s, \mathbf{q}_\perp) \sim \left(-\frac{s}{s_0}\right)^{\alpha_D(-\mathbf{q}_\perp^2)} \tag{47}$$

[compare with equation (5)].

In case (ii), the amplitude for the transition $q\bar{q} \longrightarrow N\bar{N}$ can be expressed, in a covariant way, in terms of the quark and nucleon Dirac spinors:

$$T^{q\bar{q} \to N\bar{N}}(\lambda_q \lambda_{\bar{q}} \lambda_N \lambda_{\bar{N}}) = (\bar{u}_N^{\lambda_N} u_q^{\lambda_q}) \cdot (\bar{u}_{\bar{N}}^{\lambda_{\bar{N}}} u_{\bar{q}}^{\lambda_{\bar{q}}}). \tag{48}$$

In this case, the expression for the nucleon current $A^{\gamma \to N\bar{N}}$ can be recast into the form

$$A^{\gamma \to N\bar{N}} = \int d^2\mathbf{k}_\perp A(s, -\mathbf{k}_\perp^2) ([(M + m)^2 + \mathbf{k}_\perp^2] \gamma_\mu - 2(M + m) k_\mu + 2 k_\mu k_\nu \gamma_\nu) = G_m \gamma_\mu + 2M(G_e - G_m) \frac{P_\mu}{\mathbf{P}^2}. \tag{49}$$

The Sachs form factors $G_e(s)$ and $G_m(s)$ can easily be found from this expression if we consider, in just the same way as in the case of the pion current, that $\mathbf{k}_\perp^2$ has the meaning of the square of the diquark momentum within the nucleon. This quantity is not related directly to the parametrization of the amplitude for quark transitions into hadrons; therefore, it is not related to the exponent in the $q\bar{q} \longrightarrow h\bar{h}$ amplitude. For a first approximation, we can replace $\mathbf{k}_\perp^2$ by the effective mean value $\langle \mathbf{k}_\perp^2 \rangle$ as determined from the momentum distribution of the diquark in the wave function.

For the Sachs form factors, we then obtain

$$G_m = (M+m)^2 \frac{\tilde{C}}{R_D(s)}\left(-\frac{s}{s_0}\right)^{(\alpha_D(0)-1)/2},$$

$$G_e - G_m = \left[\left(1+\frac{m}{M}\right)(m^2 - M^2 + \langle \mathbf{k}_\perp^2\rangle) + \langle \mathbf{k}_\perp^2\rangle\right] \times \frac{\tilde{C}}{R_D(s)}\left(-\frac{s}{s_0}\right)^{(\alpha_D(0)-1)/2}, \quad (50)$$

where $\tilde{C}$ is a normalization constant, which does not coincide in general with the normalization constant C in (44).

We note that, in the limit $\langle \mathbf{k}_\perp^2\rangle = 0$, expressions (50) for G_m and G_e coincide with the results presented in (44). Indeed, we can see that, in the case of identical s dependences, the ratio G_e/G_m at $\langle \mathbf{k}_\perp^2\rangle = 0$ is

$$\frac{G_e}{G_m} = \frac{m}{M}. \quad (51)$$

The nucleon form factors (32), (44), and (50) were obtained for positive values of $q^2 = s$. Nonetheless, the formulas for them can be continued analytically to the spacelike region; hence, these form factors are defined over the entire complex plane of the variable q^2. That the form factors have no cuts at negative s corresponds to the presence of the factor $(-s/s_0)$ in all the expressions for the hadronic form factors.

4. SUDAKOV FORM FACTOR

For a collinear quark configuration, which leads to the production of a two-particle hadronic state, to be formed, it is necessary that no hard gluon be emitted at the initial stage of the motion of the quarks in opposite directions. If this condition is not satisfied—that is, if a hard gluon with a momentum $|\mathbf{k}_\perp| > R^{-1}$ is emitted at the initial state—the $q\bar{q}$ configuration ceases to be collinear, and a hard gluon generates the development of a hadronic string in addition to the $h\bar{h}$ system. A separation of a collinear configuration $q\bar{q}$ from the entire spectrum of quark momenta leads to an additional suppression of the amplitude, and this suppression is described by the Sudakov form factor. The Sudakov form factor is associated with the initial stage of electron–positron annihilation into hadrons, a stage that proceeds at small distances and which is described by perturbative QCD.

In the double-logarithmic approximation (DLA), the Sudakov form factor can be represented as (for various parametrizations of the Sudakov form factor and for its role in jet-formation processes, see [32] and references therein)

$$S^{(0)}(s) = C_1 \exp\left[-\frac{\alpha_s^{\text{eff}}}{2\pi} C_F \ln^2\left(-\frac{s}{\omega_{\max}^2}\right)\right], \quad (52)$$

where $\omega_{\max}$ stands for the maximal value of the emitted-gluon energy (transverse momentum) at which collinearity of the quark–antiquark state is not violated. The quantities α_s^{eff} and $\omega_{\max}$ are introduced in (52) as free phenomenological parameters. In the following, we will vary them within limits that are consistent both with known theoretical considerations and with experimental data.

Here, it is important to note that the absolute value of the Sudakov form factor specified by expression (52) takes different values at positive and negative values of s. This is associated with the analytic properties of the double-logarithmic term in the exponent in the expression for the Sudakov form factor. Specifically, we have

$$r_{\text{TS}}^{(0)} = \frac{|S^{(0)}(s)|}{|S^{(0)}(-s)|} \simeq \exp\left[C_F \frac{\alpha_s^{\text{eff}}}{2}\pi\right]. \quad (53)$$

At $\alpha_s^{\text{eff}} \simeq 0.4$, the ratio in (53) takes the value of $r_{\text{TS}}^{(0)} \simeq 2$.

In the double-logarithmic approximation, the quantity α_s is treated as a constant. This approximation seems appropriate at not very large s such that characteristic transverse momenta of emitted gluons are $\langle \mathbf{k}_\perp^2\rangle \sim 1$ GeV^2 ($\langle \mathbf{k}_\perp^2\rangle \ll s$); in this region, $\alpha_s(\mathbf{k}_\perp^2)$ can be reasonably approximated by a constant, $\alpha_s^{\text{eff}} \approx 0.4$–0.5 [33, 34].

At very large s, however, it is necessary to take into account the logarithmic dependence of α_s on s. In this case, it is convenient to recast the expression for the Sudakov form factor into the form

$$S^{(1)}(s) \sim \exp\left[-\frac{C_F}{2\pi}\ln\left(-\frac{s}{\mu_1^2}\right)\int_{\mu_2^2}^{s}\frac{d\mu^2}{\mu^2}\alpha_s(\mu^2)\right], \quad (54)$$

where the first logarithm $\ln(s/\mu_1^2)$ corresponds to integration with respect to the longitudinal momentum (energy), while the second logarithm $\ln(s/\mu_2^2)$ corresponds to integration with respect to the transverse momentum. If the loop expression for $\alpha_s(q^2)$ is chosen in the form

$$\alpha_s(\mu^2) = 4\pi\left[\beta_0 \ln\left(-\frac{\mu^2}{\Lambda^2}\right)\right]^{-1}, \quad (55)$$

where

$$\beta_0 = \frac{11}{3}N_c - \frac{2}{3}N_f = 9, \quad (56)$$

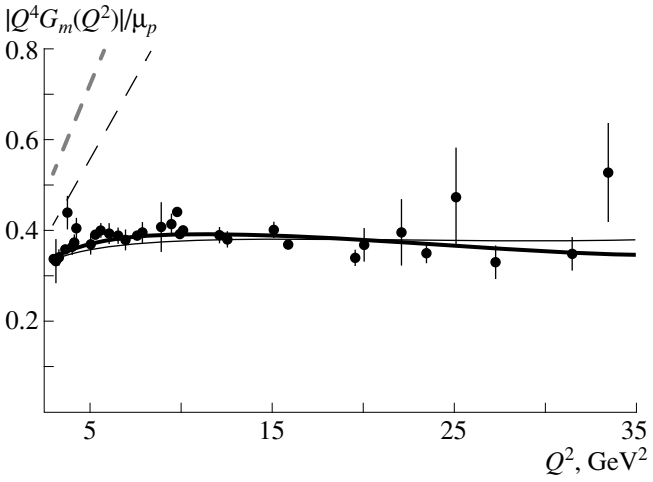

Fig. 3. Proton magnetic form factor $G_m(Q^2)$ in the spacelike region as a function of $Q^2 = -q^2$: (thick and thin solid curves) results obtained with allowance for the Sudakov form factor parametrized according to (52) and (57), respectively, and (thick and thin dashed curves) results of the QGSM calculations without the Sudakov form factor. The dashed curves were obtained by dividing the results corresponding to the solid curves by the relevant Sudakov form factor. Experimental data were borrowed from [36].

the Sudakov form factor becomes [35]

$$S^{(1)}(s) = C_2 \exp\left[-\frac{2C_F}{\beta_0}\ln\left(-\frac{s}{\mu_1^2}\right)\ln\left(\frac{\alpha_s(\mu_2^2)}{\alpha_s(s)}\right)\right]. \quad (57)$$

The choice of sign in front of s is determined by the analytic properties of the form factors. In the following, the constants μ_1 and μ_2 in (57) are assumed to be free parameters.

The ratio of the absolute value of the Sudakov form factor $S^{(1)}(s)$ in the timelike region to its absolute value in the spacelike region then proves to be less than the analogous ratio following from (52). Nonetheless, the phenomenological parameters appearing in the formula in question can be chosen in such a way that the ratio will take values close to two in the region 5–15 GeV^2. At asymptotically large values of s, the ratio $r_{\mathrm{TS}}^{(1)}$ assumes the form

$$r_{\mathrm{TS}}^{(1)}\big|_{s\to\infty} = \exp\left[\frac{2C_F}{\beta_0}\frac{\pi^2}{\ln s}\right] \quad (58)$$

[compare with equation (53)]. From (58), it can be seen, however, that, with increasing s, the ratio $r_{\mathrm{TS}}^{(1)}$ tends slowly to unity; as a result, the effect that is determined by the Sudakov form factor disappears at very large values of $\ln s$.

Upon taking into account the Sudakov form factor given by (57), the effective rate of decrease in hadronic form factors is determined according to

$$G_{e,m} \sim \left(\frac{s}{s_0}\right)^{(\alpha_D(0)-1)/2} S^{(1)}(s) \sim \left(-\frac{s}{s_0}\right)^{\xi_N(s)},$$

$$F_\pi \sim \left(\frac{s}{s_0}\right)^{(\alpha_M(0)-2)/2} S^{(1)}(s) \sim \left(-\frac{s}{s_0}\right)^{\xi_\pi(s)},$$

where $\xi_N(s) = -(2C_F/\beta_0)\ln[\ln(-s)] + (\alpha_D(0)-1)/2$ for the nucleon form factors and $\xi_\pi(s) = -(2C_F/\beta_0)\ln[\ln(-s)] + (\alpha_M(0)-2)/2$ for the pion form factor.

Thus, the hadronic form factors as calculated on the basis of the QGSM decrease faster than any finite power of s. At very large s, the dominant contribution is therefore proportional to $\alpha_s(s)/s$ for the pion form factor and to $\alpha_s^2(s)/s^2$ for the nucleon form factor. However, the exponent $\xi_{N,\pi}(s)$ of the nonperturbative contribution decreases slowly with increasing s—this decrease is determined by the logarithmic term $\ln[\ln(-s)]$—so that the scale $\tilde{s}$ at which the nonperturbative contribution becomes commensurate with the perturbative contribution is far beyond the experimentally accessible region of s ($\tilde{s} > 10^2$ GeV^2).

Actually, the nonperturbative contribution is dominant at currently accessible values of $s \simeq 30$–50 GeV^2. Here, the gluon virtuality is relatively low ($\mu^2 \sim 1$ GeV$^2 \ll s$), falling within the region where $\alpha_s(\mu^2)$ is frozen [33] (nearly independent of the virtuality μ^2).

Thus, the behavior of the hadronic form factors as functions of s has a clear physical interpretation in this region: the probability of the formation of a two-particle hadronic state in virtual-photon annihilation involves two suppression factors. Of these, the first is due to the quenching of the formation of a quark–antiquark pair (prohibition of hard-gluon emission) at the first stage of the process. This suppression factor can be calculated by perturbative QCD and is determined by the Sudakov form factor. The second, small, suppression factor is associated with the probability of the formation of a two-particle hadronic state in the hadronization of the quark–antiquark system via the rupture of the string. This suppression factor is determined by large-distance physics and is expressed in terms of the intercepts of the relevant Regge trajectories.

5. NUMERICAL RESULTS AND THEIR COMPARISON WITH EXPERIMENTAL DATA

In Figs. 3–8, the results of our calculations for the hadronic form factors $G_m(q^2)$, $G_e(q^2)$, $F_2(q^2)$, and $F_\pi(q^2)$ are presented along with available experimental data in the time- and spacelike regions of the variable q^2.

In the calculations, the parameters m and $\langle \mathbf{k}_\perp^2 \rangle$ were set to $m = 0.22$ GeV and $\langle \mathbf{k}_\perp^2 \rangle = 0.2$ GeV^2. The parameter R_0 was taken to be $R_0^2 = 3$ GeV^2.

We have used both parametrizations of the Sudakov form factor: (a) $S^{(0)}(q^2)$ (52) in the double-logarithmic approximation with frozen α_s^{eff} and (b) $S^{(1)}(q^2)$ (57) in the one-loop approximation with the running coupling constant $\alpha_s(\mu^2)$ (55).

In the case of nucleon transitions, the best description of experimental data was achieved when the parameters $\omega_{\max}^2$ and α_s^{eff} appearing in expression (52) for $S^{(0)}(q^2)$ were set to $\omega_{\max}^2 = 0.35$ GeV^2 and $\alpha_s^{\text{eff}} = 0.45$. For the Sudakov form factor (57) involving the running coupling constant $\alpha_s(\mu^2)$, the parameters μ_1, μ_2, and Λ_{QCD} appearing in the expression for this form factor were chosen to be $\mu_1 = 1.3$ GeV, $\mu_2 = 0.6$ GeV, and $\Lambda_{\text{QCD}} = 0.4$ GeV.

Figure 3 shows the results of the calculations for the proton magnetic form factor in the spacelike region ($Q^2 = -q^2 = -s$). The solid curves were calculated by taking into account the Sudakov form factor according to (thick solid curve) (52) [model (a)] and (thin solid curve) (57) [model (b)]. For either model, the common normalization factor C was determined from the best fit to experimental data. Each model reproduces faithfully the experimental dependence of the magnetic form factor G_m on Q^2. The dashed curves represent results of the calculations without the Sudakov form factor on the basis of (thick solid curve) model (a) and (thin solid curve) model (b). It can be seen that the inclusion of the Sudakov form factor is of crucial importance for describing the Q^2 dependence of G_m. By way of example, we indicate that, at $Q^2 = 5$ GeV^2, the solid and the dashed curve as obtained on the basis of model (a) differ by a factor of about two. A similar situation is observed in model (b), where the corresponding curves differ by about 1.5 at the same point $Q^2 = 5$ GeV^2.

Figure 4 shows the proton magnetic form factor in the timelike region. The solid curves, which were calculated with allowance for the Sudakov form factor, reproduce the q^2 dependence of the form factor $q^4G_m(q^2)$. Quantitatively, model (a) agrees well with experimental data (thick solid curve), whereas model (b) yields results that fall short of those in model (a) by a factor of about 1.5. It is important to note that the same value was used for the normalization factor both in the spacelike and in the timelike region. The dashed curves represent the results of the QGSM calculation taking no account of the Sudakov form factor. They correspond to the form factor $q^4G_m(q^2)$, which grows with increasing q^2. The values at $q^2 = 5$ GeV^2 on these curves are less than those on the corresponding solid curves by a factor of about 1.2 to 1.5.

In Section 3, we have considered two versions of parametrization of the spin structure of the amplitude $T_i^{q\bar{q}\to N\bar{N}}$. For the proton magnetic form factor, the results of our calculations proved to be insensitive to the choice of spin structure. By fixing the spin depen-

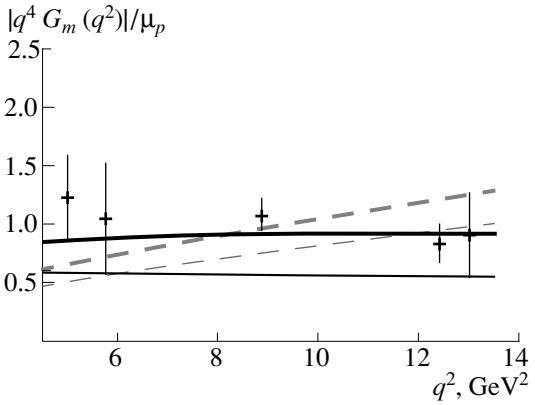

Fig. 4. Proton magnetic form factor $G_m(q^2)$ in the timelike region as a function of q^2. The notation for the curves is identical to that in Fig. 3. Experimental data were borrowed from [37, 38].

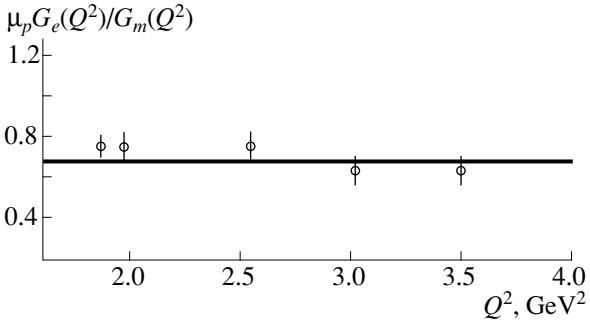

Fig. 5. Ratio $\mu_p G_e(Q^2)/G_m(Q^2)$ of the Sachs form factors for the proton in the timelike region as a function of $Q^2 = -q^2$. The spin amplitude is parametrized according to (1), the quark mass being set to $m = 0.22$ GeV. Experimental data were borrowed from [39].

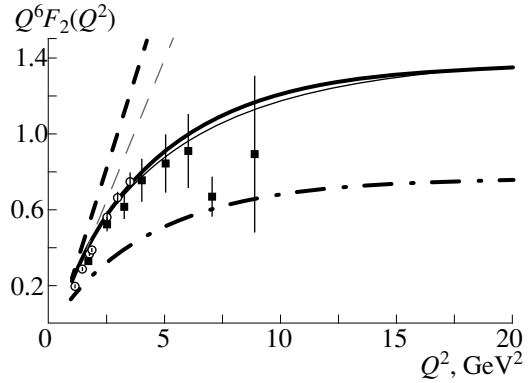

Fig. 6. Pauli form factor $F_2(Q^2)$ for the proton in the spacelike region as a function of $Q^2 = -q^2$. The solid curves correspond to model (i) for the spin structure of the amplitude $A^{q\bar{q}\to N\bar{N}}$, the thick and thin curves representing results obtained with the Sudakov form factor parametrized according to (52) and (57), respectively. The dashed curves illustrate the results of the calculations without the Sudakov form factor. The dash-dotted curve lying below the experimental points corresponds to the model (ii) of the spin structure and to the parametrization (52) of the Sudakov form factor. The parameters m and $\langle \mathbf{k}_\perp^2 \rangle$ were set to $m = 0.22$ GeV and $\langle \mathbf{k}_\perp^2 \rangle = 0.2$ GeV^2. Experimental data were borrowed from [39, 40].

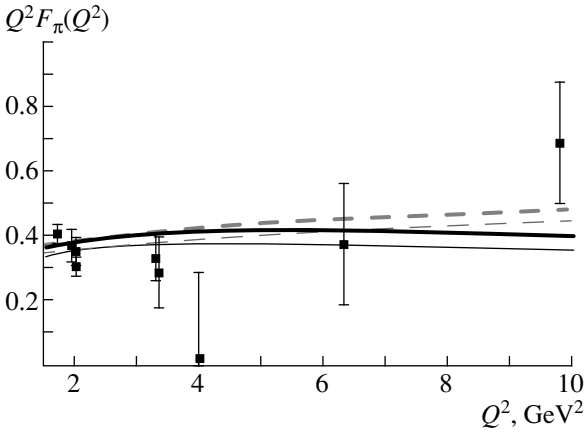

Fig. 7. Pion form factor $F_\pi(Q^2)$ in the spacelike region as a function of $Q^2 = -q^2$. The notation for the curves is identical to that in Fig. 3. Experimental data were borrowed from [41].

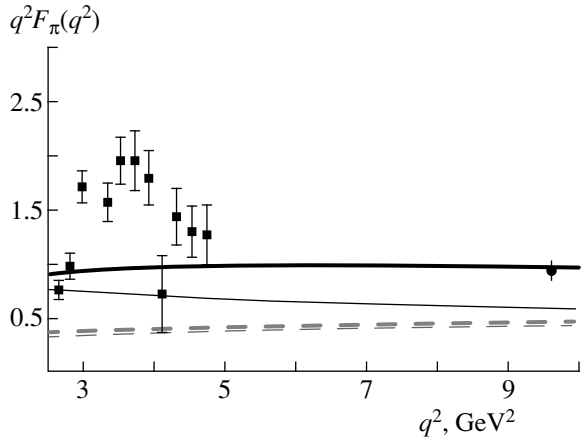

Fig. 8. Pion form factor $F_\pi(q^2)$ in the timelike region as a function of q^2. The notation for the curves is identical to that in Fig. 3. Experimental data were borrowed from [42, 43].

dence, we were able, however, to distinguish between the Sachs form factors $G_e(q^2)$ and $G_m(q^2)$ and to determine thereby the Pauli form factor $F_2(q^2)$. From a comparison of expressions (45) and (50), it can be seen that the difference of $G_e(q^2)$ and $G_m(q^2)$ and, hence, the Pauli form factor depend on m^2, M^2, and $\langle \mathbf{k}_\perp^2 \rangle$ [model (ii)] or only on the ratio m/M [model (i)]. Thus, we see that, if we choose the normalization of G_m, the choice of the spin structure is dictated by the ratio of the form factors G_e and G_m that follows from experimental data.

In Fig. 5, the ratio $\mu_p \dfrac{G_e}{G_m}$ of the nucleon form factors is displayed for spacelike $q^2 = -Q^2$ values. This ratio changes slowly in the range Q^2 = 0.5–0.35 GeV^2, approaching a value of about 0.6–0.7. For the ratio G_e/G_m, we accordingly expect $G_e/G_m \approx 0.2$–0.25. In the spin models considered here, the ratio G_e/G_m is independent of q^2 (see Section 3):

$$\frac{G_e}{G_m} = \frac{m}{M} \quad \text{for model (i)},$$
$$\frac{G_e}{G_m} = \frac{m}{M} + \frac{\langle \mathbf{k}_\perp^2 \rangle}{(m+M)^2}\left(2 + \frac{m}{M}\right) \quad \text{for model (ii)}. \tag{59}$$

The experimental value of the ratio G_e/G_m is reproduced within model (i) at the natural quark-mass value of m = 0.22 GeV. Experimental data on the Pauli form factor F_2 [40] correspond to a somewhat greater ratio of $\mu_p G_e/G_m \approx 0.7$–$0.75$. Nonetheless, model (i) describes well available data within the errors (at m = 0.22 GeV).

For the ratio G_e/G_m, model (ii) predicts a greater value than model (i) [see equation (59)]. In order to describe experimental data on the Pauli form factor F_2 (or on the ratio G_e/G_m), the quantities m and $\langle \mathbf{k}_\perp^2 \rangle$ must be set to $m \simeq 0$ and $\langle \mathbf{k}_\perp^2 \rangle = 0.15$ GeV^2, but this set of values does not appear to be a natural option. It should be noted that, at $\langle \mathbf{k}_\perp^2 \rangle = 0$ (the longitudinal momentum of the quark is aligned with the nucleon momentum), model (ii) involving scalar-diquark exchange corresponds to helicity conservation and to the formulas of model (i).

Figure 6 presents the Pauli form factor $F_2(Q^2)$ as calculated for two parametrizations of the Sudakov form factor. The thick and the thin solid curve represent the results of the calculations based on model (a) and model (b), respectively. The form factor F_2 corresponding to the spin structure associated with scalar-diquark exchange is depicted by the dash-dotted curve. For this curve, the Sudakov form factor was taken in the approximation of a constant α_s^{eff} [model (a)]. It can be seen that, even at sufficiently small $\langle \mathbf{k}_\perp^2 \rangle$, the absolute value of the Pauli form factor cannot be reproduced within this model.

Thus, the QGSM reproduces faithfully experimental data on the nucleon form factors at positive and negative values of q^2. Either parametrization of the Sudakov form factor describes well the experimental dependences at negative q^2, the necessary absolute normalization of the form factor $G_m(q^2)$ in the timelike region being achieved in model (a). We can also conclude that model (i), which assumes the dominance of the amplitude $D_1(s, \mathbf{k}_\perp^2)$, reproduces closely spin effects even at moderate values of Q^2. Within model (ii), experimental data can be described only at unnaturally small values of the parameters m and $\langle \mathbf{k}_\perp^2 \rangle$.

The degree of decrease in the Sachs form factors for the nucleons, $|q^2|^{-2}$, is determined by (A) the power-law decrease in the absolute value of the amplitude for

quark transitions into nucleons $(q^2)^{-1}|T^{q\bar{q}\to N\bar{N}}(q^2)| \sim |q^2|^{-(1-2\alpha_B(0)+\alpha_M(0))/2} \sim |q^2|^{-5/4}$ and (B) the decrease in the Sudakov form factor, which varies as $|S(q^2)| \sim |q^2|^{-3/4}$ in the region 10 GeV^2 < $|q^2|$ < 30 GeV^2 for the nucleons (in the region of a few tens of GeV^2 under consideration, either parametrization of the Sudakov form factor, $S^{(0)}$ and $S^{(1)}$, yields approximately the same power-law dependence, $|q^2|^{-3/4}$).

Since the behavior of the Sachs form factors G_m and G_e is determined by the asymptotic factor $(q^2/s_0)^{(\alpha_D(0)+1)/2}$ in the amplitude $T^{q\bar{q}\to N\bar{N}}$, the Pauli form factor $(Q^2)^3F_2$ grows approximately in direct proportion to Q^2 in the region of small Q^2, approaching a constant at greater values of Q^2. In order to take this effect into account, the preasymptotic factor $(q^2/4M^2 - 1)^{-1}$, which determines a linear growth of $(Q^2)^3F_2(Q^2)$ in the range $Q^2 \approx$ 2–5 GeV^2, is retained in expression (40) for $F_2(Q^2)$.

The behavior of the pion form factor $F_\pi(q^2)$ differs somewhat from the behavior of the nucleon form factors. Since a pair of pseudoscalar particles is formed by a virtual photon in the reaction $\gamma \longrightarrow \pi^+\pi^-$, the two product pions can be formed only in a state whose relative orbital angular momentum is $l = 1$. In this case, the main contribution comes from the amplitude $A_z^{\gamma\to q\bar{q}}$ associated with the transition suppressed by the helicity-conservation condition, whereby there arises an additional suppression of the pion form factor in proportion to $|q^2|^{-1/2}$ [see equation (32)].

The absolute value of the amplitude for quark transitions into hadrons—it is determined by the meson Regge trajectory $\alpha_M(t)$—depends on q^2 as $|A^{q\bar{q}\to\pi^+\pi^-}(q^2)| \sim |q^2|^{(\alpha_M(0)-1)/2} = |q^2|^{-1/4}$.

The parameters of the Sudakov form factor in models (a) and (b) were determined by fitting experimental data on the pion form factor. The results are

$$\alpha_s^{\text{eff}} = 0.45, \quad \omega_{\max}^2 = 2.5 \text{ GeV}^2;$$

$$\Lambda_{\text{QCD}} = 0.5 \text{ GeV}, \quad \mu_1 = 1.5 \text{ GeV}, \quad \mu_2 = 1.5 \text{ GeV}.$$

This choice of parameter values makes it possible to describe the behavior of the pion form factor, $q^2F_\pi(q^2) \sim (q^2)^0$, in the region where we have experimental data at our disposal. Here, model (a), where the ratio r_{TS} (53) is determined by the choice of α_s^{eff} exclusively, reproduces correctly the absolute value of the pion form factor in the timelike region.

Figure 7 displays the results of the calculations for the pion form factor in the spacelike region. The thick (thin) solid curve corresponds to the choice of the Sudakov form factor in model (a) [model (b)]. The dashed curve represents the results of the calculations taking no account of the Sudakov form factor in either model [(a) and (b)]. It shows a slowly ascending behavior of $F_\pi(Q^2)Q^2$ in the region of Q^2 values being considered.

Figure 8 presents the graphs of the pion form factor in the timelike region. The solid curves correspond to models (a) and (b) for the parametrization of the Sudakov form factors. The thick and the thin dashed curve depict the results of the calculations without the Sudakov form factor that were performed on the basis of model (a) and model (b), respectively. In just the same way as in the spacelike region, the function $q^2F_\pi(q^2)$ is approximately constant in the region where experimental data are available. For model (a), the ratio of the absolute value of the pion form factor in the timelike region to that in the spacelike region is $|F_\pi(q^2)|/|F_\pi(-q^2)| \approx 2.5$ at $q^2 \approx 10$ GeV^2, as in the case of the nucleon form factors, and is determined by the analytic properties of the Sudakov form factor. In the timelike region, model (b) fails to reproduce the absolute value of the pion form factor. The results of the calculations that take no account of the Sudakov form factor fall significantly short of experimental values.

We note that, within perturbative QCD, the distinctions between the meson form factors at positive and negative values of the variable q^2 were discussed in [44] with allowance for Sudakov effects. In the model adopted in [44], however, the deviation of $|F_\pi(q^2)|/|F_\pi(-q^2)|$ from unity is due to the singularities of the hard-rescattering amplitudes rather than to the Sudakov form factor. A similar result is obtained within the model that was proposed in [45] and which employs the pion form factor based on a phenomenological parametrization of the imaginary part: there, the ratio $|F_\pi(q^2)|/|F_\pi(-q^2)|$ proves to be determined by the energy dependence of the imaginary part of $F_\pi(q^2)$. In our model, such corrections must show a power-law decrease in proportion to M^2/q^2 and must be small even at q^2 = 10–20 GeV^2 if the mass M is chosen to be between 1 and 2 GeV. If, on the other hand, the Sudakov effect is important, the ratios $r_{\text{TS}}^\pi = |F_\pi(q^2)|/|F_\pi(-q^2)|$ and $r_{\text{TS}}^N = |G_m(q^2)|/|G_m(-q^2)|$ will decrease rather slowly with increasing q^2 [see equations (53) and (58)]. By way of example, we indicate that, in model (i), $r_{\text{TS}}^{(0)}$ is independent of q^2 ($r_{\text{TS}}^{(0)} = 2.5$). Within model (ii), $r_{\text{TS}}^{(1)}$ is about 1.8 at q^2 = 5 GeV^2 and decreases to about 1.35 at q^2 = 100 GeV^2. Thus, a variation of r_{TS} for the nucleons and for the pion at large q^2 would be of crucial importance for resolving the fundamental question of whether the behavior of the hadronic form factors in the region $q^2 \sim$ 10–50 GeV^2 is governed by perturbative or nonperturbative QCD dynamics. It would be interesting to test experimentally our result predicting, within the present model, that

$q^2F_\pi(q^2)$ must decrease with increasing q^2 both for $q^2 > 0$ and for $q^2 < 0$.

6. CONCLUSION

An analysis of the pion and nucleon form factors in the space- and timelike regions has been performed on the basis of the QGSM. Spin effects have been introduced by specifying appropriately the amplitudes $T^{q\bar{q}\to h\bar{h}}$ for quark transitions into hadrons. By taking into account the spin structure of these amplitudes, it has become possible to describe spin effects in binary hadronic reactions and in hadronic form factors. The approximate asymptotic forms $G_{m,e} \sim (q^2)^{-2}$ and $F_\pi \sim (q^2)^{-1}$ extracted for the nucleon and pion form factors from experimental data for $q^2 \le 100$ GeV^2 have been reproduced here within the QGSM owing to the Regge behavior of the amplitudes for quark transitions into hadrons and the Sudakov form factor. The inclusion of spin variables has enabled us to separate the nucleon form factors $G_e(q^2)$ and $G_m(q^2)$ and to calculate the Pauli form factor $F_2(q^2)$. For the pion form factor, it has been shown that, because of approximate helicity conservation in the transition $\gamma \longrightarrow q\bar{q}$, the form factor $F_\pi(q^2)$ is additionally suppressed in proportion to $(q^2)^{-1/2}$. In contrast to what is obtained within perturbative QCD predicting a linear growth of the ratios $F_{\pi\pi}(q^2)/F_{\pi\omega}(q^2)$ and $F_{\pi\pi}(q^2)/F_{\pi\rho}(q^2)$ with increasing q^2, it has been found on the basis of the QGSM that these ratios decrease in proportion to $1/\sqrt{q^2}$. The expressions obtained within this model for the form factors in question are analytic in the complex plane of the variable q^2 and can be continued analytically from the timelike region to the region of negative q^2 values. That the absolute values of the hadronic form factors at positive q^2 differ from those at negative values of this variable is associated primarily with the analytic properties of the double-logarithmic term in the exponent of the Sudakov form factor. The presence of the Sudakov form factor results in that the hadronic form factors as obtained on the basis of the QGSM decrease exponentially at very large q^2. However, this decrease is very slow in the q^2 region accessible to current experiments. For this reason, the nonperturbative contributions that emerge in the form factors within the QGSM may prove to be dominant up to $q^2 \sim 10^2$ GeV^2.

ACKNOWLEDGMENTS

We are grateful to R. Baldini, K.G. Boreskov, B.V. Geshkenbein, O.V. Kancheli, and Yu.A. Simonov for stimulating discussions.

This work was supported in part by the International Association for the Promotion of Cooperation with Scientists from the Independent States of the Former Soviet Union (grant no. INTAS-99-1692), by the Russian Foundation for Basic Research (project no. 98-02-17463), and by NATO (grant no. OUTR.LG.971390).

REFERENCES

1. G. Sterman and P. Stoler, Annu. Rev. Nucl. Part. Sci. **47**, 193 (1997).
2. R. Baldini *et al.*, Phys. Lett. B **444**, 111 (1998).
3. P. Gauzzi, Yad. Fiz. **59**, 1441 (1996) [Phys. At. Nucl. **59**, 1382 (1996)].
4. G. P. Lepage and S. J. Brodsky, Phys. Rev. D **22**, 2157 (1980).
5. B. L. Ioffe and A. V. Smilga, Nucl. Phys. B **216**, 373 (1983).
6. N. Isgur and C. H. Llewellyn Smith, Phys. Lett. B **217**, 535 (1989); Phys. Rev. Lett. **52**, 1080 (1984).
7. A. V. Radyushkin, Nucl. Phys. A **532**, 141 (1991).
8. I. G. Aznaurian, A. S. Bagdasarian, S. V. Esaibegian, and N. L. Ter-Isaakian, Yad. Fiz. **55**, 1979 (1992) [Sov. J. Nucl. Phys. **55**, 1099 (1992)].
9. J. Botts and G. Sterman, Nucl. Phys. B **325**, 62 (1989).
10. H. Li and G. Sterman, Nucl. Phys. B **381**, 129 (1992).
11. H. Li, Phys. Rev. D **48**, 4243 (1993).
12. R. Jakob and P. Kroll, Phys. Lett. B **315**, 463 (1993); Erratum: **319**, 545 (1993).
13. J. Bolz, R. Jakob, P. Kroll, *et al.*, Phys. Lett. B **342**, 345 (1995).
14. T. Hyer, Phys. Rev. D **47**, 3875 (1993).
15. P. Kroll, Preprint WU-B-94-17 (Wuppertal Univ., 1994), p. 18; P. Kroll, T. Pilsner, M. Schurmann, and W. Schweiger, Phys. Lett. B **316**, 546 (1993); P. Kroll *et al.*, Phys. Lett. B **316**, 109 (1993).
16. P. Jain, B. Kundu, H. Li, *et al.*, Paper presented at the Workshop on the Structure of the Nucleon, NUCLEON 99, Frascati, Italy, 1999; hep-ph/9907388.
17. A. B. Kaidalov, in *Proceedings of the International Conference: QCD at 200 TeV*, Ed. by L. Ciafarelli and Yu. L. Dokshitzer (Plenum, New York, 1992), p. 1.
18. A. B. Kaĭdalov, Pis'ma Zh. Éksp. Teor. Fiz. **32**, 494 (1980) [JETP Lett. **32**, 474 (1980)].
19. A. B. Kaĭdalov, Yad. Fiz. **33**, 1369 (1981) [Sov. J. Nucl. Phys. **33**, 733 (1981)].
20. A. B. Kaidalov, Z. Phys. C **12**, 63 (1982).
21. G. 't Hooft, Nucl. Phys. B **72**, 461 (1974); **75**, 461 (1974).
22. G. Veneziano, Nucl. Phys. B **74**, 365 (1974); **117**, 519 (1976).
23. Chan Hong Mo *et al.*, Nucl. Phys. B **86**, 479 (1975); **92**, 13 (1975).
24. G. F. Chew and C. Rosenzweig, Nucl. Phys. B **104**, 290 (1976); Phys. Rep. **41**, 263 (1978).
25. A. Casher, J. Kogut, and L. Susskind, Phys. Rev. Lett. **31**, 792 (1973).
26. X. Artru and G. Mennessier, Nucl. Phys. B **70**, 93 (1974).
27. A. Casher, H. Neuberger, and S. Nussinov, Phys. Rev. D **20**, 179 (1979).

28. E. G. Gurvich, Phys. Lett. B **87**, 386 (1979); Pis'ma Zh. Éksp. Teor. Fiz. **32**, 491 (1980) [JETP Lett. **32**, 471 (1980)].
29. A. A. Grigorian, N. Y. Ivanov, and A. B. Kaĭdalov, Yad. Fiz. **36**, 1490 (1982) [Sov. J. Nucl. Phys. **36**, 867 (1982)].
30. S. J. Brodsky and G. R. Farrar, Phys. Rev. Lett. **31**, 1153 (1973); Phys. Rev. D **11**, 1309 (1975); V. A. Matveev, R. M. Muradian, and A. N. Tavkhelidze, Lett. Nuovo Cimento **7**, 719 (1973).
31. F. Ravndal, Phys. Lett. B **47**, 67 (1973).
32. Yu. L. Dokshitzer and S. I. Troyan, in *Leningrad-84-922, Leningrad Institute of Nuclear Physics, 1984*; in *Proceedings of the XIV Winter School of Leningrad Institute of Nuclear Physics, 1979.*
33. A. M. Badalian and Yu. A. Simonov, Yad. Fiz. **60**, 714 (1997) [Phys. At. Nucl. **60**, 630 (1997)].
34. Yu. L. Dokshitzer, G. Marchesini, and B. R. Webber, Nucl. Phys. B **469**, 93 (1996).
35. G. Sterman and S. Weinberg, Phys. Rev. Lett. **39**, 1436 (1977).
36. R. G. Arnold *et al.*, Phys. Rev. Lett. **57**, 174 (1986).
37. T. Armstrong *et al.*, Phys. Rev. Lett. **70**, 1212 (1993).
38. D. Bisello *et al.*, Nucl. Phys. B **411**, 3 (1994).
39. M. K. Jones *et al.*, nucl-ex/9910005; Phys. Rev. Lett. **84**, 1398 (2000).
40. P. Bosted *et al.*, Phys. Rev. Lett. **68**, 3841 (1992).
41. C. J. Bebek *et al.*, Phys. Rev. D **13**, 25 (1976).
42. D. Bisello *et al.*, Phys. Lett. B **220**, 321 (1989).
43. J. Milana, S. Nussinov, and M. G. Olsson, Phys. Rev. Lett. **71**, 2533 (1993).
44. T. Gousset and B. Pire, Phys. Rev. D **51**, 15 (1995).
45. B. V. Geshkenbein, hep-ph/9806418.

Translated by A. Isaakyan

Physics of Atomic Nuclei, Vol. 63, No. 8, 2000, pp. 1410–1427. From Yadernaya Fizika, Vol. 63, No. 8, 2000, pp. 1489–1506.

ON THE 85th ANNIVERSARY OF V.V. VLADIMIRSKY

Two-Pion Spectra for the Reaction $\pi^- p \longrightarrow \pi^0\pi^0 n$ at a Pion Momentum of 38 GeV/c and Combined Analysis of GAMS, Crystal Barrel, and BNL Data*

V. V. Anisovich, A. A. Kondashov[1)], Yu. D. Prokoshkin[†], S. A. Sadovsky[1)], and A. V. Sarantsev

Petersburg Nuclear Physics Institute, Russian Academy of Sciences, Gatchina, 188350 Russia

Received October 18, 1999

Abstract—We perform a K-matrix analysis of $IJ^{PC} = 00^{++}$, 10^{++}, 02^{++}, and 12^{++} meson partial waves using GAMS data on $\pi^- p \longrightarrow \pi^0\pi^0 n$, $\eta\eta n$, $\eta\eta' n$ that are supplemented with BNL data on $\pi^- p \longrightarrow K\bar{K}n$ and Crystal Barrel data on $p\bar{p}$ (at rest) $\longrightarrow \pi^0\pi^0\pi^0$, $\pi^0\eta\eta$, $\pi^0\pi^0\eta$. The positions of the amplitude poles (physical resonances) are determined, together with the positions of the K-matrix poles (bare states) and the values of bare-state couplings to two-meson channels. The nonet classification of the bare states found in the present analysis is discussed. © *2000 MAIK "Nauka/Interperiodica".*

1. INTRODUCTION

In this article, we complete the K-matrix analysis of GAMS data on the reactions $\pi^- p \longrightarrow \pi^0\pi^0 n$ [1], $\eta\eta n$ [2], and $\eta\eta' n$ [3] that was begun by the papers [4–6]. A K-matrix analysis furnishes rich information about meson states, thereby helping classify $q\bar{q}$ states and facilitating searches for exotic mesons. In order to reconstruct the K-matrix amplitude, it is necessary, however, to study the complete set of open channels with sufficiently high statistics. This is the reason why we are going to extend our fit to data on $\pi^- p \longrightarrow K\bar{K}n$ [7] and $p\bar{p}$ (at rest) $\longrightarrow \pi^0\pi^0\pi^0$, $\pi^0\eta\eta$, $\pi^0\pi^0\eta$ [8].

We note that K-matrix poles, which are the subject of the present consideration, differ from the amplitude poles in two respects:

(i) States corresponding to the K-matrix poles involve no components featuring real mesons that are inherent in resonances. The absence of a real-meson cloud allows one to refer to these states by convention as bare ones [5, 6].

(ii) Owing to *bare state* $\longrightarrow$ *real mesons* $\longrightarrow$ *bare state* transitions, the observed resonances appear to be mixtures of bare states. For quark systematics, bare states are therefore primary objects rather than resonances.

The *bare state* $\longrightarrow$ *real mesons* coupling constants are responsible not only for the mixing of states but also for resonance decays; the relations between the couplings allow one to reconstruct the quark–gluon content of bare states [9, 10].

Our article is organized as follows.

In Section 2, we introduce a set of formulas that are used in our data fit. We present the S- and D-wave K-matrix amplitudes for the on-mass-shell reactions $\pi\pi \longrightarrow \pi\pi$, $K\bar{K}$, $\eta\eta$, and $\eta\eta'$, along with those for an off-mass-shell pion in the initial state: $\pi\pi(t)$ with $t \neq m_\pi^2$. The K-matrix formulas for the final-state interaction in the three-meson-production process, $p\bar{p} \longrightarrow$ *three mesons*, are also displayed.

In Section 3, we write down the couplings for *bare state* $\longrightarrow$ *two pseudoscalars* transitions, with the quark-combinatorics constraints imposed both for $q\bar{q}$ states (isoscalar and isovector) and for the glueball. The reconstruction of the couplings in the fit allows us to determine the quark content of isoscalar states and to find a candidate for the glueball.

Mesons that belong to the same $q\bar{q}$ nonet have approximately equal masses; they also have approximately equal decay couplings. In addition, the flavor wave functions for the isoscalars of the same nonet are orthogonal. In Section 4, we present the results of the fit with the imposed nonet-classification constraints. A fit to the 00^{++} wave confirms the result of [6], while, for the 02^{++}, 10^{++}, and 12^{++} waves, the K-matrix representation of the amplitudes in the mass region below 1900 MeV is implemented for the first time. The reconstructed bare states, together with those found in the $K\pi$ S-wave K-matrix analysis [11], allow us to construct the $1^3P_0 q\bar{q}$ and $1^3P_2 q\bar{q}$ nonets unambiguously; for the $2^3P_0 q\bar{q}$ nonet, two versions are possible that differ in the mass of the lightest scalar–isoscalar state.

---

† Deceased.

* This article was submitted by the authors in English.

1) Institute for High Energy Physics, Protvino, Moscow oblast, 142284 Russia.

The origin of the lightest scalars, $f_0(980)$ and $a_0(980)$, is crucial for the nonet classification. These states are located near the $K\bar{K}$ threshold and give rise to the question of whether these states are hadronic $K\bar{K}$ molecules. In Section 5, we present arguments based on direct GAMS measurements and on the results of the performed *K*-matrix fit that the bare states from which $f_0(980)$ and $a_0(980)$ originate have a $q\bar{q}$ nature.

A short summary is given in Section 6.

2. EXPERIMENTAL DATA AND *K*-MATRIX AMPLITUDE

Here, we briefly introduce the fitted data and present the *K*-matrix formulas used in our data analysis.

2.1. Experimental Data

A simultaneous analysis of the meson spectra in the $IJ^{PC} = 00^{++}$, 10^{++}, 02^{++}, and 12^{++} channels is performed on the basis of the following data set:

(i) GAMS data on *S*-wave two-meson production in the reactions $\pi p \longrightarrow \pi^0\pi^0 n$, $\eta\eta n$, and $\eta\eta' n$ at low nucleon momentum transfers, $|t| < 0.2$ (GeV/c)^2 [1–3];

(ii) GAMS data on the *S*-wave $\pi\pi$ production in the reaction $\pi p \longrightarrow \pi^0\pi^0 n$ at high momentum transfers, $0.30 < |t| < 1.0$ (GeV/c)^2 [1].

(iii) GAMS data on *D*-wave $\pi\pi$ production in the reaction $\pi p \longrightarrow \pi^0\pi^0 n$ at small and large $|t|$, $0 < |t| < 0.5$ (GeV/c)^2 [3];

(iv)) BNL data on $\pi p^- \longrightarrow K\bar{K} n$ [7];

(v) Crystal Barrel data on $p\bar{p}$ (at rest) $\longrightarrow \pi^0\pi^0\pi^0$, $\pi^0\pi^0\eta$, $\pi^0\eta\eta$ [8].

2.2. K-Matrix Amplitude and Analyticity

The *K*-matrix technique is used to describe the two-meson coupled channels:

$$A = K(I - i\hat{\rho}K)^{-1}. \quad (1)$$

Here, K is an $n \times n$ matrix, n being the number of channels under consideration, while I is an identity matrix. The phase-space matrix is diagonal: $\hat{\rho}_{ab} = \delta_{ab}\rho_a$. The phase-space factor ρ_a is responsible for the threshold singularities of the amplitude: for the amplitude to be analytic in the physical region under consideration, we use an analytic continuation for ρ_a below threshold. For example, the $\eta\eta$ phase-space factor $\rho_a = (1 - 4m_\eta^2/s)^{1/2}$ is equal to $i(4m_\eta^2/s - 1)^{1/2}$ below the $\eta\eta$ threshold (s is two-meson invariant energy squared). The phase-space factors that we use lead to spurious kinematical singularities at $s = 0$ (in all factors) and at $s = (m_{\eta'} - m_\eta)^2$ (in the $\eta\eta'$ space factor), but these spurious singularities, which are peculiar to the *K*-matrix approach are too far from the investigated physical region.

For the multimeson phase space in the isoscalar sector, we use the four-pion phase space defined as either $\rho\rho$ or $\sigma\sigma$ phase space, where σ denotes the *S*-wave $\pi\pi$ amplitude below 1.2 GeV. The result is virtually independent of whether we use the $\rho\rho$ or $\sigma\sigma$ state to describe the multimeson channel: below, we present formulas and parameter values obtained for the $\rho\rho$ case, for which fitted expressions are less cumbersome. The multimeson phase space in the $I = 1$ sector is taken in a form that, in its low-energy part, simulates the $a_0\rho$ phase space.

2.3. Isoscalar–Scalar, 00^{++}, Partial Wave

For the *S*-wave interaction in the isoscalar sector, we use a parametrization similar to that in [6]:

$$K_{ab}^{00}(s) = \left(\sum_\alpha \frac{g_a^{(\alpha)} g_b^{(\alpha)}}{M_\alpha^2 - s} + f_{ab}\frac{1\ \text{GeV}^2 + s_0}{s + s_0}\right)\frac{s - m_\pi^2/2}{s}. \quad (2)$$

Here, K_{ab}^{IJ} is a 5×5 matrix ($a, b = 1, \ldots, 5$), with the following notation for meson states: $1 = \pi\pi$, $2 = K\bar{K}$, $3 = \eta\eta$, $4 = \eta\eta'$, and 5 = multimeson states (four-pion state mainly at $\sqrt{s} < 1.6$ GeV). The quantity $g_a^{(\alpha)}$ is the constant of coupling of the bare state α to the meson channel; the parameters f_{ab} and s_0 describe the smooth part of the *K*-matrix elements ($s_0 > 1.5$ GeV^2). We use the factor $(s - m_\pi^2/2)/s$ to suppress the effect of the spurious kinematical singularity at $s = 0$ in the amplitude near the $\pi\pi$ threshold.

The phase-space matrix elements are given by

$$\rho_a(s) = \sqrt{\frac{s - 4m_a^2}{s}}, \quad a = 1, 2, 3, \quad (3)$$

where $m_1 = m_\pi$, $m_2 = m_K$, $m_3 = m_\eta$, and

$$\rho_4(s) = \begin{cases} \rho_{41} & \text{at } s > (m_\eta - m_{\eta'})^2 \\ \rho_{42} & \text{at } s < (m_\eta - m_{\eta'})^2, \end{cases}$$

$$\rho_{41} = \sqrt{\left[1 - \frac{(m_\eta + m_{\eta'})^2}{s}\right]\left[1 - \frac{(m_\eta - m_{\eta'})^2}{s}\right]}, \quad (4)$$

$$\rho_{42} = 0.$$

The multimeson phase-space factor is defined as

$$\rho_5(s) = \begin{cases} \rho_{51} & \text{at } s < 1\ \text{GeV}^2 \\ \rho_{52} & \text{at } s > 1\ \text{GeV}^2, \end{cases}$$

$$\rho_{51} = \rho_0 \int \frac{ds_1}{\pi} \int \frac{ds_2}{\pi} \times M^2 \Gamma(s_1)\Gamma(s_2)\sqrt{(s+s_1-s_2)^2 - 4ss_1} \times s^{-1}[(M^2-s_1)^2 + M^2\Gamma^2(s_1)]^{-1} \times [(M^2-s_2)^2 + M^2\Gamma^2(s_2)]^{-1}, \quad \rho_{52} = 1. \tag{5}$$

Here, s_1 and s_2 are the two-pion energies squared, M is ρ-meson mass, and $\Gamma(s)$ is its energy-dependent width, $\Gamma(s) = \gamma\rho_1^3(s)$. The factor ρ_0 ensures the continuity of $\rho_5(s)$ at $s = 1$ GeV^2.

The following formulas describe the amplitudes of ππ, ηη, and ηη' production via *t*-channel pion exchange:

$$A_{\pi N \to Nb} = N(\bar{\Psi}_N \gamma_5 \Psi_N) F_N(t) D(t) \tilde{K}_{\pi\pi(t),a} (1 - i\rho K)^{-1}_{ab}, \quad b = \pi\pi, \eta\eta, \eta\eta',$$
$$\tilde{K}_{\pi\pi(t),a} = \left(\sum_\alpha \frac{\tilde{g}^{(\alpha)}(t) g_a^{(\alpha)}}{M_\alpha^2 - s} + \tilde{f}_a(t) \frac{1\ \text{GeV}^2 + s_0}{s + s_0} \right) \times (s - m_\pi^2/2)/s. \tag{6}$$

Here, N is a normalization factor; $F_N(t)$ is the nucleon form factor, and $D(t)$ is the pion propagator,

$$F_N(t) = \left[\frac{\tilde{\Lambda} - m_\pi^2}{\tilde{\Lambda} - t} \right]^4, \quad D(t) = (m_\pi^2 - t)^{-1};$$
$$\tilde{g}^{(\alpha)}(t) = g_1^{(\alpha)} + \left(1 - \frac{t}{m_\pi^2}\right)\left(\Lambda_g - \frac{t}{m_\pi^2}\right) g'^{(\alpha)}, \quad \tilde{f}_a(t) = f_{1a} + \left(1 - \frac{t}{m_\pi^2}\right)\left(\Lambda_f - \frac{t}{m_\pi^2}\right) f'_a, \tag{7}$$

where Λ's, g', and f' are the fitted parameter values.

2.4. Isoscalar–Tensor, 02^{++}, Partial Wave

The *D*-wave interaction in the isoscalar sector is parametrized by a 4×4 *K* matrix, where 1 = ππ, 2 = $K\bar{K}$, 3 = ηη, and 4 = multimeson states:

$$K_{ab}^{02}(s) = D_a(s) \left(\sum_\alpha \frac{g_a^{(\alpha)} g_b^{(\alpha)}}{M_\alpha^2 - s} + f_{ab} \frac{1\ \text{GeV}^2 + s_2}{s + s_2} \right) D_b(s). \tag{8}$$

The factor $D_a(s)$ stands for the *D*-wave centrifugal barrier. We take this factor in the form

$$D_a(s) = \frac{k_a^2}{k_a^2 + 3/r_a^2}, \quad a = 1, 2, \tag{9}$$

where $k_a = \sqrt{s/4 - m_a^2}$ is the momentum of the decaying meson in the resonance c.m. frame. For multimeson decay, the factor $D_4(s)$ is set to 1. The phase-space factors used are identical to those for the isoscalar *S*-wave channel.

2.5. Isovector–Scalar, 10^{++}, and Isovector–Tensor, 12^{++}, Partial Waves

For the amplitude in the isovector–scalar and isovector–tensor channels, we use a 4×4 *K* matrix with 1 = πη, 2 = $K\bar{K}$, 3 = πη', and 4 = multimeson states:

$$K_{ab}^{1J}(s) = D_a(s) \left(\sum_\alpha \frac{g_a^{(\alpha)} g_b^{(\alpha)}}{M_\alpha^2 - s} + f_{ab} \frac{1.5\ \text{GeV}^2 + s_1}{s + s_1} \right) D_b(s). \tag{10}$$

Here, $J = 0, 2$; for the 10^{++} amplitude and for the *D*-wave partial amplitude, the factor $D_a(s)$ is, respectively, set to unity and taken in the form

$$D_a(s) = \frac{k_a^2}{k_a^2 + 3/r_3^2}, \quad a = 1, 2, 3, \quad D_4(s) = 1. \tag{11}$$

The elements of the phase-space matrix in the isovector sector are defined as

$$\rho_1(s) = \begin{cases} \rho_{11} & \text{at } s > (m_\eta - m_\pi)^2 \\ \rho_{12} & \text{at } s < (m_\eta - m_\pi)^2, \end{cases}$$
$$\rho_{11} = \sqrt{\left[1 - \frac{(m_\eta + m_\pi)^2}{s}\right]\left[1 - \frac{(m_\eta - m_\pi)^2}{s}\right]}, \quad \rho_{12} = 0, \tag{12}$$

$$\rho_2(s) = \sqrt{\frac{s - 4m_K^2}{s}}, \tag{13}$$

$$\rho_3(s) = \begin{cases} \rho_{31} & \text{at } s > (m_{\eta'} - m_\pi)^2 \\ \rho_{32} & \text{at } s < (m_{\eta'} - m_\pi)^2, \end{cases}$$
$$\rho_{31} = \sqrt{\left[1 - \frac{(m_{\eta'} + m_\pi)^2}{s}\right]\left[1 - \frac{(m_{\eta'} - m_\pi)^2}{s}\right]}, \quad \rho_{32} = 0. \tag{14}$$

The multimeson phase-space factor $\rho_4(s)$ is taken in a form that simulates the ρa_0 phase-space factor below

$s = 2.25\ \text{GeV}^2$:

$$\rho_4(s) = \begin{cases} \rho_{41} & \text{at } (m_\eta + 3m_\pi)^2 < s < 2.25\ \text{GeV}^2 \\ \rho_{42} & \text{at } s > 2.25\ \text{GeV}^2 \\ \rho_{43} & \text{at } s < (m_\eta + 3m_\pi)^2, \end{cases}$$

$$\rho_{41} = \left[\frac{1 - (m_\eta + 3m_\pi)^2/s}{1 - (m_\eta + 3m_\pi)^2/2.25\ \text{GeV}^2}\right]^{5/2}, \quad (15)$$

$$\rho_{42} = 1,$$

$$\rho_{43} = 0.$$

2.6. Amplitudes of Three-Meson Production

The $p\bar{p}$ (at rest) $\longrightarrow \pi^0\pi^0\pi^0, \pi^0\eta\eta$ amplitudes corresponding to the production of the two-meson isoscalar states are given by

$$A_{p\bar{p} \to \text{three mesons}} = A_1(23) + A_2(13) + A_3(12),$$

where the amplitude $A_k(ij)$ stands for diagrams with particle interaction in intermediate states and the last interaction involving particles i and j, with particle k being a spectator. As in [5, 6], we assume that $p\bar{p}$ annihilates at rest from the $^1S_0$ level. For the two-particle interaction block, we use the form

$$A_1(23) = \sum_{J=0,2} X_J(23)\tilde{K}^{0J}_{p\bar{p}\pi,a}(s_{23})[1 - i\hat{\rho}K^{0J}(s_{23})]^{-1}_{ab}, \quad (16)$$

where $b = \pi^0\pi^0$ stands for $\pi^0\pi^0\pi^0$ production and $b = \eta\eta$ for $\pi^0\eta\eta$. The centrifugal-barrier factor X_J is equal to unity for the production of the S-wave resonance. For the production of a D-wave resonance, this factor is

$$X_2(23) = \frac{1}{2}(3\cos^2\Theta_{12} - 1)\frac{p_1^2}{p_1^2 + 3/R^2}, \quad (17)$$

where Θ_{12} is the angle between particles 1 and 2 in the rest frame of particles 2 and 3, p_1 is the momentum of particle 1 in this frame, and R is the annihilation radius. The $\tilde{K}$ matrices that describe the prompt resonance production in $p\bar{p}$ annihilation are given by

$$\tilde{K}^{00}_{p\bar{p}\pi,a}(s_{ij}) = \left(\sum_\alpha \frac{\Lambda^{(\alpha)}_{p\bar{p}\pi}[00]g^{(\alpha)}_a}{M^2_\alpha - s_{ij}} + \phi_{p\bar{p}\pi,a}[00]\frac{1\ \text{GeV}^2 + s_0}{s_{ij} + s_0}\right) \times\left(\frac{s_{ij} - m_\pi^2/2}{s_{ij}}\right), \quad (18)$$

$$\tilde{K}^{02}_{p\bar{p}\pi,a}(s_{ij}) = \left(\sum_\alpha \frac{\Lambda^{(\alpha)}_{p\bar{p}\pi}[02]g^{(\alpha)}_a}{M^2_\alpha - s_{ij}} + \phi_{p\bar{p}\pi,a}[02]\frac{1\ \text{GeV}^2 + s_0}{s_{ij} + s_0}\right)D_a(s_{ij}). \quad (19)$$

The $\pi\pi\pi$-production amplitude is described by (16)–(19) completely because of the amplitude symmetry under the rotation of pion indices i, j, and k.

That piece of the amplitude $p\bar{p}$ (at rest) $\longrightarrow \eta\pi^0\pi^0$ which corresponds to the production of isoscalar resonances reads

$$A_1(23) = \sum_{J=0,2} X_J(23)\tilde{K}^{0J}_{p\bar{p}\eta,a}(s_{23})[1 - i\hat{\rho}K^{0J}(s_{23})]^{-1}_{ab}, \quad (20)$$

$$b = \pi^0\pi^0,$$

where

$$\tilde{K}^{00}_{p\bar{p}\eta,a}(s_{ij}) = \left(\sum_\alpha \frac{\Lambda^{(\alpha)}_{p\bar{p}\eta}[00]g^{(\alpha)}_a}{M^2_\alpha - s_{ij}} + \phi_{p\bar{p}\eta,a}[00]\frac{1\ \text{GeV}^2 + s_0}{s_{ij} + s_0}\right)\left(\frac{s_{ij} - m_\pi^2/2}{s_{ij}}\right). \quad (21)$$

The parameters $\Lambda^\alpha_{p\bar{p}\pi}[0J]$ and $\phi_{p\bar{p}\pi}[0J]$ (or $\Lambda^\alpha_{p\bar{p}\eta}[0J]$ and $\phi_{p\bar{p}\eta}[0J]$) can be complex-valued and have different phases because of three-particle interactions.

That part of the amplitude which corresponds to the production of isovector resonances in the reaction $p\bar{p}$ (at rest) $\longrightarrow \eta\eta\pi^0$ is written as $A_1(23) + A_2(13)$ and

$$A_2(13) = \sum_{J=0,2} X_J(13)\tilde{K}^{1J}_{p\bar{p}\eta,a}(s_{13})[1 - i\hat{\rho}K^{1J}(s_{13})]^{-1}_{ab}, \quad (22)$$

$$b = \eta\pi^0,$$

where

$$\tilde{K}^{1J}_{p\bar{p}\eta,a}(s_{ij}) = \left(\sum_\alpha \frac{\Lambda^{(\alpha)}_{p\bar{p}\eta}[1J]g^{(\alpha)}_a}{M^2_\alpha - s_{ij}} + \phi_{p\bar{p}\eta,a}[1J]\frac{1\ \text{GeV}^2 + s_1}{s_{ij} + s_1}\right)D_a(s_{ij}). \quad (23)$$

The amplitude of isovector-resonance production in the reaction $p\bar{p}$ (at rest) $\longrightarrow \pi^0\pi^0\eta$ has the form $A_1(23) + A_2(13)$ and

$$A_2(13) = \sum_{J=0,1,2} X_J(13)\tilde{K}^{1J}_{p\bar{p}\pi,a}(s_{13})[1 - i\hat{\rho}K^{1J}(s_{13})]^{-1}_{ab}, \quad (24)$$

$$b = \eta\pi^0,$$

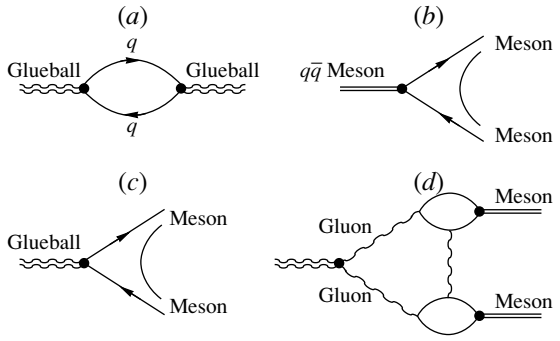

Fig. 1. (*a*) Quark–antiquark loop diagram determining the glueball width; (*b*) diagrams for the decay of a $q\bar{q}$ meson; and (*c*) and (*d*) diagrams for the decay of a glueball into two $q\bar{q}$-meson states.

where $\tilde{K}^{1J}_{p\bar{p}\pi,a}$ is given by (23) with the substitutions $\Lambda^{(\alpha)}_{p\bar{p}\eta}[1J] \longrightarrow \Lambda^{(\alpha)}_{p\bar{p}\pi}[1J]$ and $\phi_{p\bar{p}\eta,a}[1J] \longrightarrow \phi_{p\bar{p}\pi,a}[1J]$.

3. QUARK-COMBINATORICS RULES FOR DECAY COUPLINGS AND THE $q\bar{q}$ CONTENT OF MESONS

The decay couplings of the $q\bar{q}$ mesons and of the glueball to a pair of mesons are determined by the diagrams with $q\bar{q}$ pairs produced by gluons. Figures 1*b* and 1*c* provide an example of diagrams that contribute to the leading terms in the $1/N$ expansion [12] ($N = N_c = N_f$, where N_c and N_f are numbers of colors and flavors, respectively), and Fig. 1*d* exemplifies diagrams for the next-to-leading contribution. The production of soft $q\bar{q}$ pairs by gluons violates flavor symmetry, the corresponding ratios of the production probabilities being

$$u\bar{u} : d\bar{d} : s\bar{s} = 1 : 1 : \lambda, \qquad (25)$$

where $\lambda = 0.4$–0.8 [13]. In our fit, we fix $\lambda = 0.6$.

We have calculated the ratios of the decay coupling constants on the basis of quark-combinatorics rules previously proposed for high-energy hadron production [14] and then extended to hadronic J/ψ decays [15]. For the glueball and for isoscalar–scalar $q\bar{q}$ mesons, the calculations of the decay coupling constants were performed in [5, 9, 10]. The decay couplings for isoscalar and isovector mesons are given in Tables 1 and 2.

Isoscalar-meson decay couplings depend on the nonstrange–strange component ratio of the decaying meson as given by the mixing angle Φ:

$$\psi^{\text{flavor}}_{\text{decaying meson}} = n\bar{n}\cos\Phi + s\bar{s}\sin\Phi, \qquad (26)$$

where $n\bar{n} = (u\bar{u} + d\bar{d})/\sqrt{2}$. This allows us to reconstruct Φ and, at the same time, to determine the decay couplings.

The glueball decay couplings obey the same ratios as the couplings of isoscalar–scalar $q\bar{q}$ mesons with the mixing angle

$$\Phi = \Phi_{\text{glueball}}, \quad \tan\Phi_{\text{glueball}} = \sqrt{\lambda/2}. \qquad (27)$$

It follows from the two-stage decay of the glueball [10] (see Fig. 1*c*) that an intermediate $q\bar{q}$ state in the glue-

Table 1. Coupling constants given by quark combinatorics for a $q\bar{q}$-meson decaying into a pair of pseudoscalar mesons in the leading order of the $1/N_c$ expansion and for glueball decay in the next-to-leading order of the $1/N_c$ expansion (Φ is the mixing angle for $n\bar{n}$ and $s\bar{s}$ states, and Θ is the mixing angle for η–η' mesons: $\eta = n\bar{n}\cos\Theta - s\bar{s}\sin\Theta$ and $\eta' = n\bar{n}\sin\Theta + s\bar{s}\cos\Theta$; glueball decay couplings in the leading order of $1/N_c$ expansion are obtained by the replacements $g/\sqrt{2}\cos\Phi \longrightarrow G^L$ and $g/\sin\Phi \longrightarrow \sqrt{\lambda}\,G^L$.)

Channel	The $q\bar{q}$-meson decay couplings in the leading order of $1/N_c$ expansion	Glueball decay couplings in the next-to-leading terms of $1/N_c$ expansion	Identity factor in phase space
$\pi^0\pi^0$	$g\cos\Phi/\sqrt{2}$	0	1/2
$\pi^+\pi^-$	$g\cos\Phi/\sqrt{2}$	0	1
K^+K^-	$g(\sqrt{2}\sin\Phi + \sqrt{\lambda}\cos\Phi)/\sqrt{8}$	0	1
K^0K^0	$g(\sqrt{2}\sin\Phi + \sqrt{\lambda}\cos\Phi)/\sqrt{8}$	0	1
$\eta\eta$	$g(\cos^2\Theta\cos\Phi/\sqrt{2} + \sqrt{\lambda}\sin\Phi\sin^2\Theta)$	$2g_G(\cos\Theta - \sqrt{\frac{\lambda}{2}}\sin\Theta)^2$	1/2
$\eta\eta'$	$g\sin\Theta\cos\Theta(\cos\Phi/\sqrt{2} - \sqrt{\lambda}\sin\Phi)$	$2g_G(\cos\Theta - \sqrt{\frac{\lambda}{2}}\sin\Theta)(\sin\Theta + \sqrt{\frac{\lambda}{2}}\cos\Theta)$	1
$\eta'\eta'$	$g(\sin^2\Theta\cos\Phi/\sqrt{2} + \sqrt{\lambda}\sin\Phi\cos^2\Theta)$	$2g_G(\sin\Theta + \sqrt{\frac{\lambda}{2}}\cos\Theta)^2$	1/2

ball decay is a mixture of $n\bar{n}$ and $s\bar{s}$ quarks produced in the proportion given by (25). We fix $\Phi_{\text{glueball}} = 25^\circ \pm 5^\circ$.

The coincidence of the glueball decay couplings with those for the $q\bar{q}$ meson at $\Phi = \Phi_{\text{glueball}}$ indicates that there is no simple signature for a determination of a glueball state: in seeking a glueball, it is necessary to perform a full $q\bar{q}$ classification of mesons; thus, the existence of a state extraneous to the $q\bar{q}$ classification is an indication of exoticism.

The normalization in Table 1 is done in such a way that, for glueball decay, the sum of couplings squared over all channels is proportional to the probability of quark-pair production [$(2 + \lambda)^2$—see (25)]. Thus, we have

$$\sum_{\text{channels}} G^2(c)I(c) = \frac{1}{2}G^2(2+\lambda)^2,$$
$$\sum_{\text{channels}} g_G^2(c)I(c) = \frac{1}{2}g_G^2(2+\lambda)^2, \quad (28)$$

where $I(c)$ is an identity factor and $c = \pi^0\pi^0$, $\pi^+\pi^-$, K^+K^-, and so on (see Table 1). With this normalization, we have $g_G/G \simeq 1/N_c$. Experience gained in quark–gluon diagram calculations teaches us that the factor $1/N_c$ actually leads to a suppression on the order of 1/10—in the fitting procedure, we impose the constraint $|g_G/G| < 1/3$.

The nonet classification of isoscalar mesons is based on the following two constraints:

(i) The difference of the angles between isoscalar nonet partners must be 90°. For this value, the corridor ±5° is allowed in our analysis:

$$\Phi(1) - \Phi(2) = 90^\circ \pm 5^\circ. \quad (29)$$

(ii) The coupling constants g from Tables 1 and 2 must be roughly equal to each other for all nonet partners:

$$g[f_J(1)] \simeq g[f_J(2)] \simeq g[a_J] \simeq g[K_J]. \quad (30)$$

The conventional quark model requires exact coincidence of the couplings g, but the energy dependence of the loop diagram in Fig. 1*a*, $B(s)$, may violate this coupling-constant balance because of the mass splitting within a nonet. The K-matrix coupling constant involves an additional s-dependent factor in relation to the coupling in the N/D amplitude [10]: $g^2(K) = g^2(N/D)/[1 + B'(s)]$. The factor $[1 + B'(s)]^{-1}$ mostly affects the low-s region because of the threshold and left-hand singularities of the partial amplitude. Therefore, the coupling-constant equality is mostly violated for the lightest 00^{++} nonet, 1^3P_0 $q\bar{q}$. We allow for the members of this nonet, $1 \le g[f_0[(1)]/g[f_0(2)] \le 1.5$. For the members of the 2^3P_0 $q\bar{q}$ nonet, we assume the equality of the two-meson couplings both for isoscalar and for isovector mesons. The equality of coupling constants is also imposed for tensor resonances.

Table 2. Coupling constants given by quark combinatorics for scalar mesons K_0^- and a_0^- decaying into two pseudoscalar mesons in the leading order of the $1/N_c$ expansion

Channel	The $s\bar{u}$-meson decay couplings	Channel	The $d\bar{u}$-meson decay couplings
$\bar{K}^0\pi^-$	$g\left(-\frac{1}{2}\right)$	$\eta\pi^-$	$g\frac{1}{\sqrt{2}}\cos\Theta$
$K^-\pi^0$	$g\frac{1}{\sqrt{8}}$	$\eta'\pi^-$	$g\frac{1}{\sqrt{2}}\sin\Theta$
$K^-\eta$	$g\frac{1}{\sqrt{8}}(\cos\Theta - \sqrt{2\lambda}\sin\Theta)$	K^0K^-	$g\frac{\sqrt{\lambda}}{2}$
$K^-\eta'$	$g\frac{1}{\sqrt{8}}(\sin\Theta + \sqrt{2\lambda}\cos\Theta)$	–	–

4. DESCRIPTION OF DATA AND THE RESULTS

Our K-matrix fit provides a good description of data (see Figs. 2–6). The χ^2 values for the fit are given in Table 3, while the parameters of the fit are presented in Tables 4–7. Below, we highlight the main results of this fit.

4.1. $IJ^{PC} = 00^{++}$ Wave

The present fit confirms the results obtained in the previous analysis of the 00^{++} wave [4–6]. Five K-matrix poles are needed for describing the 00^{++} wave in the mass region below 2000 MeV (a four-pole amplitude fails to describe well the data set under consideration). Accordingly, we have found five bare states:

$$f_0^{\text{bare}}(720 \pm 100),$$
$$\psi^{\text{flavor}} = (0.45 \pm 0.1)n\bar{n} - (0.89 \pm 0.05)s\bar{s},$$
$$f_0^{\text{bare}}(1230 \pm 50),$$
$$\psi^{\text{flavor}} = (0.9^{+0.05}_{-0.2})n\bar{n} + (0.45^{+0.3}_{-0.1})s\bar{s},$$
$$f_0^{\text{bare}}(1260 \pm 30),$$
$$\psi^{\text{flavor}} = (0.93^{+0.02}_{-0.1})n\bar{n} + (0.37^{+0.2}_{-0.06})s\bar{s}, \quad (31)$$
$$f_0^{\text{bare}}(1600 \pm 50),$$
$$\psi^{\text{flavor}} = (0.95 \pm 0.05)n\bar{n} + (0.3^{+014}_{-0.4})s\bar{s},$$
$$f_0^{\text{bare}}(1810 \pm 30),$$
$$\psi^{\text{flavor}} = \begin{cases} (0.10 \pm 0.05)n\bar{n} + (0.995^{+0.005}_{-0.015})s\bar{s} \text{ (Solution I)} \\ (0.67 \pm 0.08)n\bar{n} - (0.74 \pm 0.08)s\bar{s} \text{ (Solution II)}. \end{cases}$$

Table 3. χ^2 values for the *K*-matrix solutions

	Solution I	Solution II-1	Solution II-2	Number of points
Crystal Barrel data [8]				
$p\bar{p} \longrightarrow \pi^0\pi^0\pi^0$	1.52	1.41	1.42	1338
$p\bar{p} \longrightarrow \pi^0\eta\eta$	1.57	1.60	1.59	1798
$p\bar{p} \longrightarrow \pi^0\pi^0\eta$	1.38	1.43	1.43	1738
$\pi^+\pi^- \longrightarrow \pi^0\pi^0$				
S-wave GAMS data [1]	1.47	1.71	1.59	70
D-wave GAMS data [1]	1.63	2.16	2.14	56
SD correlation function [1]	1.82	2.26	2.12	47
t-Dependent GAMS data [1]				
$0 < \|t\| < 0.20$	3.03	3.42	3.37	21
$0.30 < \|t\| < 1.00$	2.64	3.25	2.98	38
$0.35 < \|t\| < 1.00$	1.30	1.55	1.44	38
$0.40 < \|t\| < 1.00$	2.75	2.48	2.79	38
$0.45 < \|t\| < 1.00$	1.92	1.49	1.67	38
$0.50 < \|t\| < 1.00$	2.29	1.85	2.04	38
GAMS data [2, 3]				
$\pi\pi \longrightarrow \eta\eta$	0.70	0.97	0.87	16
$\pi\pi \longrightarrow \eta\eta'$	0.49	0.65	0.64	8
$\pi\pi \longrightarrow K\bar{K}$				
BNL data [7]	0.88	0.77	0.97	35

Note: $|t|$ is given in $(\mathrm{GeV}/c)^2$ units.

The experimental data used in the fit do not fix unambiguously the flavor wave function of $f_0^{\mathrm{bare}}(1810 \pm 30)$—two solutions are found for it.

The scattering amplitude has five poles in the complex plane of energy; four of them correspond to relatively narrow resonances, while the fifth resonance is very broad:

$$\begin{aligned} f_0(980) &\longrightarrow (1015 \pm 15) - i(43 \pm 8)\ \mathrm{MeV}, \\ f_0(1300) &\longrightarrow (1300 \pm 20) - i(120 \pm 20)\ \mathrm{MeV}, \\ f_0(1500) &\longrightarrow (1499 \pm 8) - i(65 \pm 10)\ \mathrm{MeV}, \\ f_0(1530) &\longrightarrow (1530^{+90}_{-250}) - i(560 \pm 140)\ \mathrm{MeV}, \\ f_0(1780) &\longrightarrow \begin{cases} (1780 \pm 30) - i(140 \pm 20)\ \mathrm{MeV\ (Solution\ I)} \\ (1780 \pm 50) - i(220 \pm 50)\ \mathrm{MeV\ (Solution\ II)}. \end{cases} \end{aligned} \tag{32}$$

The broad resonance is crucial for describing the 00^{++} wave, because it is responsible for large interference effects that are seen in various reactions—namely, the resonance $f_0(980)$ manifests itself as a dip in the *S*-wave $\pi\pi \longrightarrow \pi\pi$ spectrum (Fig. 2*a*) and as a sharp peak in the $\pi\pi(t) \longrightarrow \pi\pi$ spectra at large $|t|$ (Fig. 3). The resonance $f_0(1300)$ is seen in the $\pi\pi(t) \longrightarrow \pi\pi$ spectra at large $|t|$ as a well-shaped bump (Fig. 3); in the $\pi\pi \longrightarrow \pi\pi$ and $\pi\pi \longrightarrow K\bar{K}$ spectra, it reveals itself as a shoulder (Figs. 2 and 5). The resonance $f_0(1500)$ is seen as a dip in the $\pi\pi \longrightarrow \pi\pi$ and $\pi\pi \longrightarrow \eta\eta$ spectra (Figs. 2, 5) and as a peak in the $p\bar{p}$ (at rest) $\longrightarrow \pi^0\pi^0\pi^0$ reaction (Fig. 6). In all these manifestations of $f_0(980)$, $f_0(1300)$, and $f_0(1500)$, their interference with $f_0(1530^{+90}_{-250})$ plays a decisive role. In the case of large interference effects, it is useful to display the amplitude on an Argand plot. Argand plots for the amplitudes $\pi\pi \longrightarrow \pi\pi$, $\pi\pi \longrightarrow \eta\eta$, $\pi\pi \longrightarrow K\bar{K}$, $\pi\pi \longrightarrow \eta\eta'$ and $\pi\pi(t) \longrightarrow \pi\pi$ are shown in Figs. 7 and 8.

Four bare states in (31) can be naturally classified as nonet partners to the $q\bar{q}$ multiplets 1^3P_0 and 2^3P_0. The fifth bare state is superfluous for the $q\bar{q}$ classification, so that it is a good candidate for the lightest scalar glueball. Equation (31) gives two versions for the glueball: either it is a bare state with a mass near 1250 MeV, or it is located near 1600 MeV. Having imposed the constraints in (29) and (30), we accordingly found the fol-

Table 4. Masses, coupling constants (in GeV), and mixing angles (in deg) for the f_0^{bare} resonances for solution I (the errors reflect the boundaries for a satisfactory description of the data; II sheet is for the $\pi\pi$ and 4π cuts; IV sheet is for the $\pi\pi$, 4π, $K\bar{K}$, and $\eta\eta$ cuts; V sheet is for the $\pi\pi$, 4π, $K\bar{K}$, $\eta\eta$, and $\eta\eta'$ cuts)

	Solution I-1				
	$\alpha = 1$	$\alpha = 2$	$\alpha = 3$	$\alpha = 4$	$\alpha = 5$
M	$0.651^{+0.120}_{-0.030}$	$1.247^{+0.150}_{-0.030}$	$1.253^{+0.015}_{-0.045}$	$1.684^{+0.010}_{-0.045}$	$1.792^{+0.040}_{-0.040}$
$g^{(\alpha)}$	$1.318^{+0.100}_{-0.100}$	$0.597^{+0.050}_{-0.100}$	$0.879^{+0.080}_{-0.050}$	$0.702^{+0.020}_{-0.060}$	$0.702^{+0.020}_{-0.060}$
g_G	0	$-0.135^{+0.050}_{-0.050}$	0	0	0
$g_5^{(\alpha)}$	0	$0.944^{+0.100}_{-0.150}$	0	$0.898^{+0.070}_{-0.150}$	$0.302^{+0.150}_{-0.070}$
Φ_α	$-(71.5^{+3}_{-15})$	21.5^{+8}_{-8}	14.1^{+10}_{-5}	-6.0^{+10}_{-10}	89^{+5}_{-15}
	$\alpha = \pi\pi$	$\alpha = K\bar{K}$	$\alpha = \eta\eta$	$\alpha = \eta\eta'$	$\alpha = 4\pi$
f_{1a}	$0.455^{+0.100}_{-0.100}$	$0.061^{+0.100}_{-0.100}$	$0.501^{+0.100}_{-0.100}$	$0.448^{+0.100}_{-0.100}$	$-0.129^{+0.060}_{-0.060}$
$f_{ba} = 0, \quad b = 2, 3, 4, 5,$ $g_3^{(1)} = -0.259^{+0.045}_{-0.045}, \quad g_4^{(1)} = -0.275^{+0.100}_{-0.100}, \quad s_0 = 3.25^{+\infty}_{-1.0}$					
	Pole position				
II sheet	$1.006^{+0.008}_{-0.008}$ $-i(0.048^{+0.008}_{-0.008})$				
IV sheet		$1.303^{+0.010}_{-0.020}$ $-i(0.138^{+0.115}_{-0.025})$	$1.496^{+0.008}_{-0.004}$ $-i(0.059^{+0.005}_{-0.005})$	$1.670^{+0.100}_{-0.150}$ $-i(0.760^{+0.080}_{-0.170})$	
V sheet					$1.775^{+0.015}_{-0.015}$ $-i(0.056^{+0.015}_{-0.010})$

lowing versions of the nonet classification. For solution I,

I. $f_0^{\text{bare}}(720)$ and $f_0^{\text{bare}}(1260)$ are 1^3P_0 nonet partners,

$f_0^{\text{bare}}(1600)$ and $f_0^{\text{bare}}(1810)$ are 2^3P_0 nonet partners,

$f_0^{\text{bare}}(1230)$ is a glueball.

Within solution II, two versions describe well the data set:

II-1. $f_0^{\text{bare}}(720)$ and $f_0^{\text{bare}}(1260)$ are 1^3P_0 nonet partners,

$f_0^{\text{bare}}(1600)$ and $f_0^{\text{bare}}(1810)$ are 2^3P_0 nonet partners,

$f_0^{\text{bare}}(1230)$ is a glueball;

II-2. $f_0^{\text{bare}}(720)$ and $f_0^{\text{bare}}(1260)$ are 1^3P_0 nonet partners,

$f_0^{\text{bare}}(1230)$ and $f_0^{\text{bare}}(1810)$ are 2^3P_0 nonet partners,

$f_0^{\text{bare}}(1600)$ is a glueball.

Tables 4 and 5 present parameters corresponding to these three versions.

Lattice calculations for the gluodynamics glueball [16] yield the mass of the lightest scalar state in the range 1550–1750 MeV, which is equivalent to version II-2. However, it should be emphasized that the state $f_0^{\text{bare}}(1600)$ cannot be identified as a pure gluodynamics glueball because f_0^{bare}'s contains the $q\bar{q}$ components associated with the real parts of the loop transition diagrams: this problem is discussed in detail in [10, 17, 18]. An extraction of the $q\bar{q}$ component from $f_0^{\text{bare}}(1600)$ leads to a mass shift for the state, but it is not large according to [10, 18]: $f_0^{\text{bare}}(1600) \longrightarrow f_0^{\text{pure gluball}}(1633)$.

4.2. $IJ^{PC} = 10^{++}$ Wave

Two isovector–scalar resonances are well seen in $p\bar{p}$ annihilation into three mesons [5, 6, 8, 19, 20]. The lightest one is the well-known $a_0(980)$, while the

Table 5. Masses, coupling constants (in GeV), and mixing angles (in deg) for the f_0^{bare} resonances for solutions II-1 and II-2

	Solution II-1				
	$\alpha = 1$	$\alpha = 2$	$\alpha = 3$	$\alpha = 4$	$\alpha = 5$
M	$0.651^{+0.120}_{-0.030}$	$1.246^{+0.150}_{-0.035}$	$1.263^{+0.015}_{-0.045}$	$1.595^{+0.030}_{-0.040}$	$1.832^{+0.030}_{-0.050}$
$g^{(\alpha)}$	$1.385^{+0.100}_{-0.100}$	$0.375^{+0.070}_{-0.050}$	$0.923^{+0.080}_{-0.050}$	$0.424^{+0.050}_{-0.050}$	$0.424^{+0.070}_{-0.050}$
g_G	0	$-0.017^{+0.050}_{-0.050}$	0	0	0
$g_5^{(\alpha)}$	0	$0.705^{+0.100}_{-0.100}$	0	$0.552^{+0.070}_{-0.070}$	$-0.557^{+0.070}_{-0.070}$
Φ_α	$-(70.1^{+3}_{-15})$	30.0^{+8}_{-8}	18.3^{+8}_{-5}	20.6^{+8}_{-15}	-64.4^{+10}_{-10}
	$\alpha = \pi\pi$	$\alpha = K\bar{K}$	$\alpha = \eta\eta$	$\alpha = \eta\eta'$	$\alpha = 4\pi$
f_{1a}	$0.440^{+0.100}_{-0.100}$	$-0.064^{+0.100}_{-0.100}$	$0.387^{+0.100}_{-0.100}$	$0.419^{+0.100}_{-0.100}$	$-0.165^{+0.060}_{-0.060}$
$f_{ba} = 0, \quad b = 2, 3, 4, 5,$					
$g_3^{(1)} = -0.239^{+0.045}_{-0.045}, \quad g_4^{(1)} = -0.284^{+0.100}_{-0.100}, \quad s_0 = 3.28^{+\infty}_{-1.0}$					
	Pole position				
II sheet	$1.017^{+0.008}_{-0.008}$ $-i(0.049^{+0.008}_{-0.008})$				
IV sheet		$1.311^{+0.010}_{-0.020}$ $-i(0.117^{+0.015}_{-0.025})$	$1.500^{+0.004}_{-0.006}$ $-i(0.063^{+0.003}_{-0.006})$	$1.470^{+0.150}_{-0.100}$ $-i(0.545^{+0.080}_{-0.080})$	
V sheet					$1.814^{+0.015}_{-0.015}$ $-i(0.082^{+0.025}_{-0.010})$
	Solution II-2				
	$\alpha = 1$	$\alpha = 2$	$\alpha = 3$	$\alpha = 4$	$\alpha = 5$
M	$0.651^{+0.120}_{-0.030}$	$1.219^{+0.150}_{-0.030}$	$1.267^{+0.015}_{-0.045}$	$1.584^{+0.010}_{-0.045}$	$1.817^{+0.040}_{-0.040}$
$g^{(\alpha)}$	$1.351^{+0.100}_{-0.100}$	$0.435^{+0.070}_{-0.050}$	$0.901^{+0.080}_{-0.050}$	$0.433^{+0.050}_{-0.050}$	$0.435^{+0.070}_{-0.050}$
g_G	0	0	0	$-0.005^{+0.050}_{-0.050}$	0
$g_5^{(\alpha)}$	0	$0.719^{+0.100}_{-0.100}$	0	$0.542^{+0.070}_{-0.070}$	$-0.512^{+0.070}_{-0.070}$
Φ_α	$-(69.5^{+3}_{-15})$	40.7^{+8}_{-8}	19.6^{+10}_{-5}	20.0^{+8}_{-15}	-54^{+10}_{-10}
	$\alpha = \pi\pi$	$\alpha = K\bar{K}$	$\alpha = \eta\eta$	$\alpha = \eta\eta'$	$\alpha = 4\pi$
f_{1a}	$0.459^{+0.100}_{-0.100}$	$0.046^{+0.100}_{-0.100}$	$0.405^{+0.100}_{-0.100}$	$0.420^{+0.100}_{-0.100}$	$-0.214^{+0.060}_{-0.060}$
$f_{ba} = 0, \quad b = 2, 3, 4, 5,$					
$g_3^{(1)} = -0.241^{+0.045}_{-0.045}, \quad g_4^{(1)} = -0.273^{+0.100}_{-0.100}, \quad s_0 = 3.05^{+\infty}_{-1.0}$					
	Pole position				
II sheet	$1.020^{+0.008}_{-0.008}$ $-i(0.048^{+0.008}_{-0.008})$				
IV sheet		$1.304^{+0.010}_{-0.020}$ $-i(0.118^{+0.015}_{-0.025})$	$1.505^{+0.004}_{-0.008}$ $-i(0.063^{+0.003}_{-0.006})$	$1.420^{+0.150}_{-0.070}$ $-i(0.540^{+0.080}_{-0.080})$	
V sheet					$1.809^{+0.015}_{-0.015}$ $-i(0.080^{+0.025}_{-0.010})$

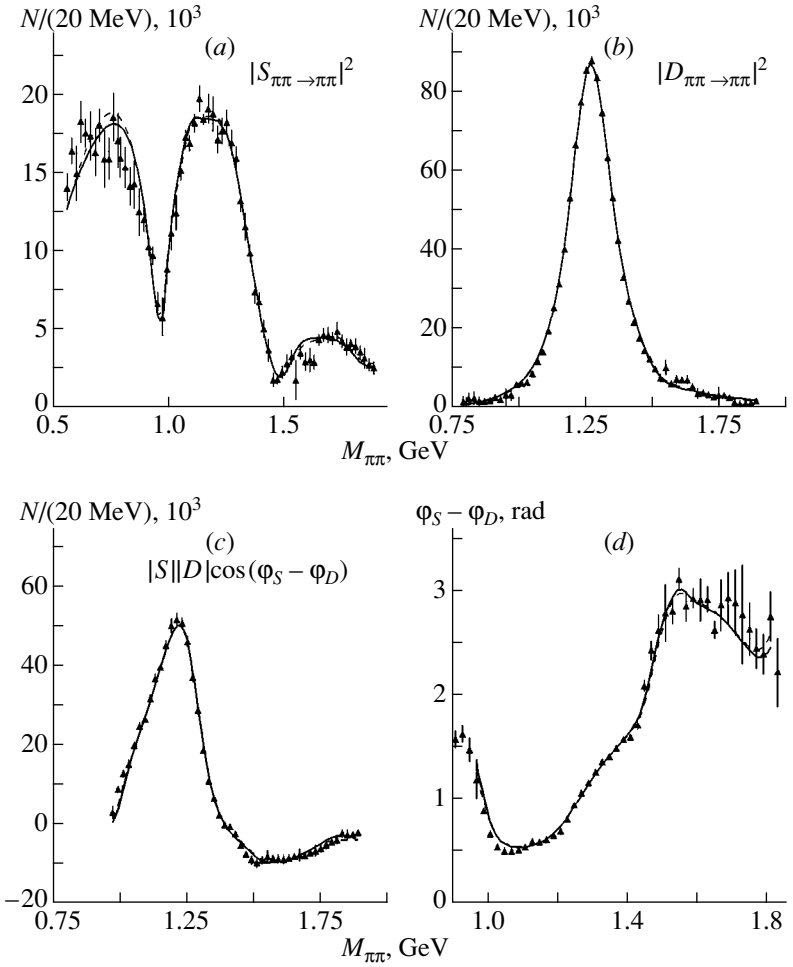

Fig. 2. (*a*) Squared modulus of the $\pi\pi \longrightarrow \pi\pi$ *S*-wave amplitude [1], (*b*) squared modulus of the *D*-wave amplitude, (*c*) SD correlation function, and (*d*) phase difference between the *S* and the *D* wave. Relevant events were collected at squared momentum transfers of $|t| < 0.20$ (GeV/*c*)^2 [1]. The solid and the dashed curve correspond, respectively, to solution II-2 and to solution I.

next resonance is the newly discovered resonance $a_0(1450)$ having a mass of 1450 ± 40 MeV and a width of $\Gamma = 270 \pm 40$ MeV, as is given by the Particle Data Group [21]. We note that, in fitting the latest high-statistics Crystal Barrel data on the basis of the *T*-matrix method used for this wave [6, 19, 20], the mass of this resonance appeared to be slightly higher: 1520 ± 40 MeV. A similar result is obtained in the present *K*-matrix approach.

In order to describe the isovector–isoscalar scattering amplitude, we use a two-pole 4×4 *K* matrix featuring two-meson coupling constants given in Table 2.

At the first stage of the fit, the coupling of the lightest a_0 state was allowed to vary in the interval bounded by $g[f_0^{\text{bare}}(720)]$ and $g[f_0^{\text{bare}}(1260)]$. In all versions of the fit, the two-meson coupling constant for the lightest state, $g[a_0^{\text{bare}}(\text{lightest state})]$, appeared to be very close to the coupling constant $g[f_0^{\text{bare}}(1260)]$: in the final fit, we set these couplings to each other in line with the constraint in (30). The two-meson coupling for the next isovector–scalar state is set to the couplings of the 2^3P_0 isoscalar–scalar states.

The fit gives two solutions for the 10^{++} wave that virtually coincide in terms related to the resonance–bare-state sector and differ in background terms. The parameters for the 10^{++} wave and the pole position are given in Table 6. For the resonance positions and for the bare states, we have, respectively,

$$\begin{aligned} a_0(980) &\longrightarrow (988 \pm 6) - i(46 \pm 10)\ \text{MeV}, \\ a_0(1450) &\longrightarrow (1535 \pm 30) - i(146 \pm 20)\ \text{MeV}, \end{aligned} \tag{33}$$

and

$$a_0^{\text{bare}}(964 \pm 16), \quad a_0^{\text{bare}}(1670 \pm 80). \tag{34}$$

But these two solutions lead to different predictions for the scattering amplitudes: for the first solution (without *K*-matrix background terms), the $\pi\eta \longrightarrow \pi\eta$ scattering

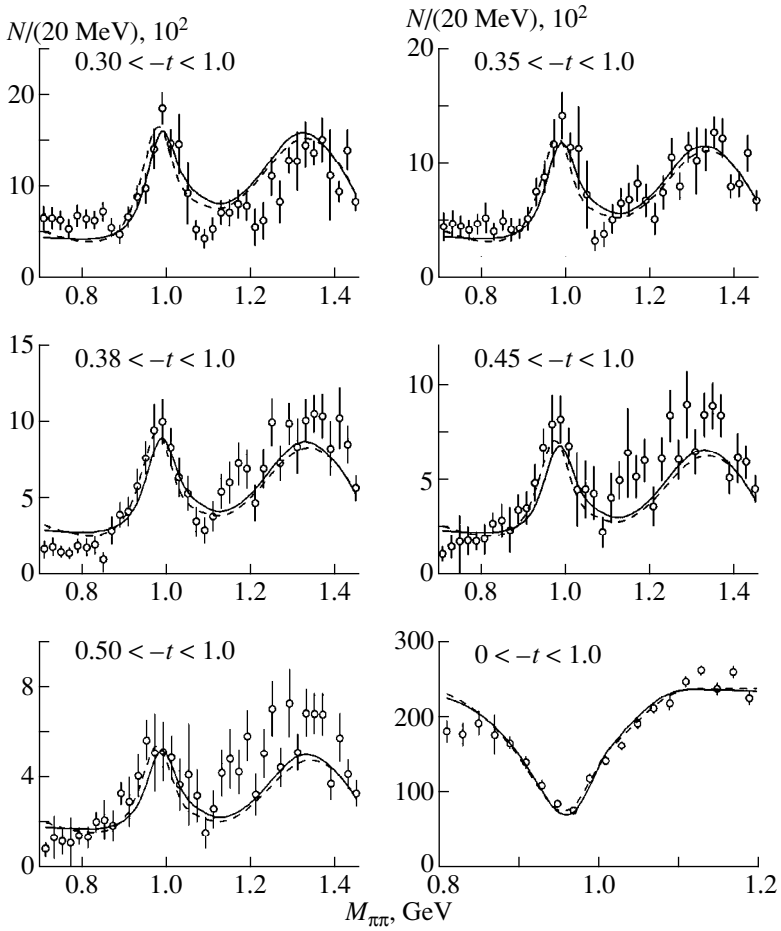

Fig. 3. Event numbers versus the invariant mass of the $\pi\pi$ system in the S wave for various t intervals in the reaction $\pi^- p \longrightarrow \pi^0\pi^0 n$ [1] [t is given in $(\mathrm{GeV}/c)^2$ units]. Solid and dashed curves correspond, respectively, to solution II-2 and to solution I.

amplitude squared (see Fig. 9) has a dip in the $a_0(1450)$ region because of the destructive interference of the resonance with the background; for the second solution (with the K-matrix background terms), a dip appears at 1100 MeV. In the present fit, information about the isovector–scalar wave comes only from Crystal Barrel data. Since these data are highly sensitive to the pole structure, they provide poor information about K-matrix background terms: this is a source of ambiguities in our K-matrix solution. We emphasize, however, that the description of other partial waves is virtually independent of the solution type (first or second one) used: the variation in the parameter values is within the quoted errors.

4.3. $IJ^{PC} = 12^{++}$ Wave

In just the same way as in the isovector–scalar case, a 4×4 two-pole K matrix is used to describe the 12^{++} wave. The coupling constants for bare states and the poles of the scattering amplitude are given in Table 7. We have determined two bare states:

$$a_2^{\text{bare}}(1314 \pm 7), \quad a_2^{\text{bare}}(1670 \pm 75). \tag{35}$$

The poles of the amplitude are found at

$$\begin{aligned} a_2(1320) &\longrightarrow (1309 \pm 6) - i(58 \pm 6)\ \text{MeV}, \\ a_2(1640) &\longrightarrow (1640 \pm 50) - i(122 \pm 18)\ \text{MeV}. \end{aligned} \tag{36}$$

The lightest state is the well-known $a_2(1320)$ resonance; according to [21], it has a mass of 1318 ± 1 MeV and a width of $\Gamma = 107 \pm 5$ MeV.

In fitting Crystal Barrel data on the reaction $p\bar{p}$ (at rest) $\longrightarrow \eta\pi\pi$, the Dalitz plot description is considerably improved in this region upon introducing an isovector–tensor resonance that has a mass in the range 1600–1700 MeV.

4.4. $IJ^{PC} = 02^{++}$ Wave

The two lightest isoscalar–tensor states, $f_2(1270)$ and $f_2'(1525)$, are well known: they are members of the nonet $1^3P_2 q\bar{q}$. Crystal Barrel data suggest the existence of the resonance $f_2(1565)$, which helps describe the $p\bar{p} \longrightarrow \pi^0\pi^0\pi^0$ Dalitz plot in the region of large

Table 6. Masses and coupling constants (in GeV) for the a_0 resonances (the asterisk denotes that the parameter is fixed)

	a_0 resonances without K-matrix background term			
	solution I-1		solution II-1,2	
	$\alpha = 1$	$\alpha = 2$	$\alpha = 1$	$\alpha = 2$
M	$0.963^{+0.015}_{-0.015}$	$1.630^{+0.100}_{-0.040}$	$0.965^{+0.015}_{-0.015}$	$1.654^{+0.100}_{-0.040}$
$g^{(\alpha)}$	$0.879^{+0.100}_{-0.100}$	0.702*	$0.901^{+0.100}_{-0.100}$	0.435*
$g_4^{(\alpha)}$	$0.598^{+0.150}_{-0.050}$	$0.511^{+0.060}_{-0.060}$	$0.689^{+0.150}_{-0.050}$	$0.687^{+0.080}_{-0.080}$
Pole position				
II sheet	$0.987^{+0.005}_{-0.005}$		$0.989^{+0.005}_{-0.005}$	
	$-i(0.045^{+0.005}_{-0.005})$		$-i(0.048^{+0.010}_{-0.010})$	
III sheet	$0.964^{+0.015}_{-0.015}$	$1.558^{+0.025}_{-0.025}$	$0.965^{+0.015}_{-0.015}$	$1.571^{+0.025}_{-0.025}$
	$-i(0.070^{+0.010}_{-0.010})$	$-i(0.141^{+0.015}_{-0.015})$	$-i(0.073^{+0.010}_{-0.010})$	$-i(0.151^{+0.015}_{-0.015})$
	a_0 resonances with K-matrix background term			
	solution I-1		solution II-1,2	
	$\alpha = 1$	$\alpha = 2$	$\alpha = 1$	$\alpha = 2$
M	$0.944^{+0.015}_{-0.015}$	$1.624^{+0.100}_{-0.030}$	$0.939^{+0.015}_{-0.015}$	$1.640^{+0.100}_{-0.040}$
$g^{(\alpha)}$	$0.879^{+0.100}_{-0.100}$	0.702*	$0.901^{+0.100}_{-0.100}$	0.435*
$g_4^{(\alpha)}$	$0.651^{+0.100}_{-0.080}$	$0.519^{+0.060}_{-0.060}$	$0.653^{+0.150}_{-0.050}$	$0.687^{+0.080}_{-0.080}$
	$f_{11} = 0.529^{+0.100}_{-0.100}$	$s_0 = 1.0^{+2.0}_{-0.3}$	$f_{11} = 0.731^{+0.100}_{-0.100}$	$s_0 = 1.9^{+2.0}_{-0.8}$
Pole position				
II sheet	$0.990^{+0.005}_{-0.005}$		$0.993^{+0.005}_{-0.005}$	
	$-i(0.039^{+0.005}_{-0.005})$		$-i(0.042^{+0.010}_{-0.010})$	
III sheet	$0.965^{+0.015}_{-0.015}$	$1.559^{+0.025}_{-0.025}$	$0.965^{+0.015}_{-0.015}$	$1.575^{+0.025}_{-0.025}$
	$-i(0.063^{+0.010}_{-0.010})$	$-i(0.145^{+0.015}_{-0.015})$	$-i(0.068^{+0.010}_{-0.010})$	$-i(0.153^{+0.015}_{-0.015})$

two-pion masses [8, 17, 20]. Because of this, we also begin our analysis by introducing a three-pole K-matrix amplitude. Upon imposing the nonet constraints on the 1^3P_2 states [see (28) and (29)], we find, however, that the couplings of the third state prove to be negligibly small. Although the description of the reaction $p\bar{p} \longrightarrow \eta\eta\pi^0$ becomes slightly poorer under the imposed constraints (about 0.1 per degree of freedom for χ^2), the description of the reaction $p\bar{p} \longrightarrow \pi^0\pi^0\pi^0$ {where $f_2(1560)$ is seen according to [8, 17, 20]} leads to an improvement of 0.07 in χ^2, yielding virtually the same total χ^2.

The resonance $f_2(1560)$ is not seen in GAMS data; this gives a strong constraint on the partial width with respect to the resonance decay into the $\pi\pi$ channel: it must be less than 20 MeV.

In our final fit, we have used the two-pole K-matrix amplitude with the nonet constraints; the parameters for this fit are presented in Table 7.

The K-matrix fit gives the following bare isoscalar–tensor states, the members of the $^3P_2$ nonet:

$$f_2^{\text{bare}}(1235 \pm 10), \quad f_2^{\text{bare}}(1530 \pm 10), \quad \Phi[f_2^{\text{bare}}(1530)] = 86^\circ \pm 5^\circ. \tag{37}$$

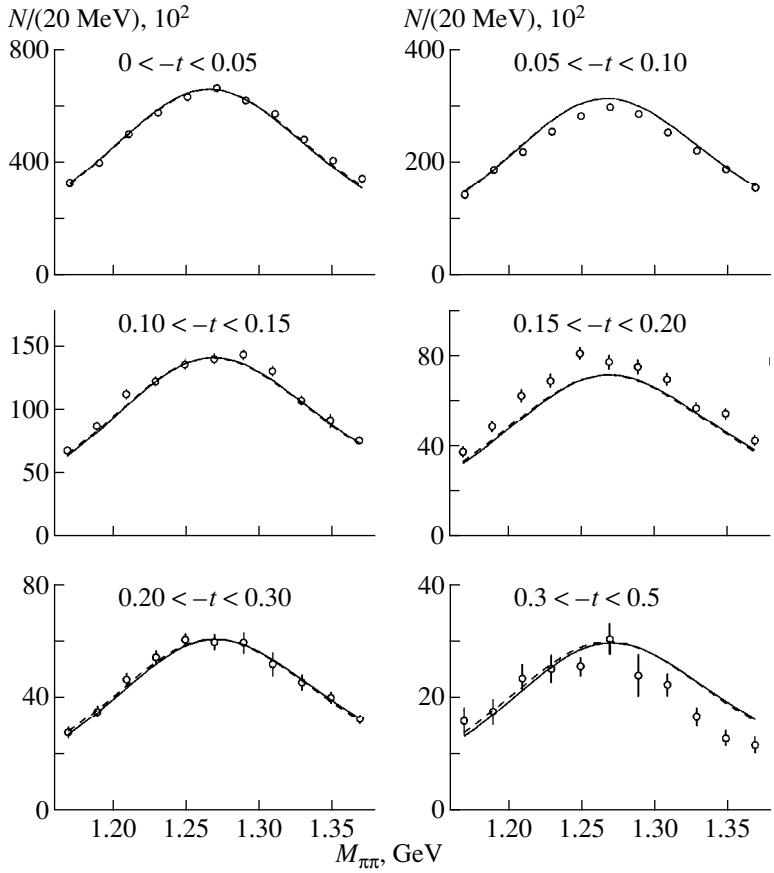

Fig. 4. Event numbers versus the invariant mass of the $\pi\pi$ system in the D wave for various t intervals in the reaction $\pi^- p \longrightarrow \pi^0\pi^0 n$ [1] [t is given in $(\mathrm{GeV}/c)^2$ units]. The solid and dashed curves correspond, respectively, to solution II-2 and to solution I.

The K-matrix 0^{2++} amplitude has poles at the complex mass values

$$f_2(1270) \longrightarrow (1262 \pm 6) - i(90 \pm 7)\ \mathrm{MeV},$$
$$f_2'(1525) \longrightarrow (1518 \pm 9) - i(71 \pm 10)\ \mathrm{MeV}. \quad (38)$$

These values should be compared with the masses and half-widths presented by the Particle Data Group [21], which are, respectively, 1275 ± 5, 92.5 ± 10 MeV and 1525 ± 5, 38 ± 5 MeV. The width of $f_2'(1525)$ found in our fit appears to be much larger than that given by the Particle Data Group. It is quite possible that, in fitting the present data set, we cannot resolve a possible D-wave double-pole structure in the region around 1530 MeV caused by the $f_2'(1525)$ and the $f_2(1560)$ resonance, for they are located near the edge of the phase space for Crystal Barrel data, while GAMS data give a constraint only on the couplings to the $\pi\pi$ channel. We believe that additional information from Crystal Barrel data on $KK\pi$ production, together with GAMS [22] and VES data [23] on $\omega\omega$ production, will clarify this point.

4.5. Nonet Classification

The results of the above analysis, together with the results of the K-matrix analysis of the $K\pi$ S wave [11], allow us to construct uniquely the lightest scalar $q\bar{q}$ nonet as

$$1^3P_0\colon\ f_0^{\mathrm{bare}}(720 \pm 100),$$
$$f_0^{\mathrm{bare}}(1260 \pm 30),$$
$$a_0^{\mathrm{bare}}(960 \pm 30), \quad (39)$$
$$K_0^{\mathrm{bare}}(1220^{+50}_{-150}),$$
$$\Phi[f_0^{\mathrm{bare}}(720)] = -70^{\circ\,+5^\circ}_{-16^\circ}.$$

The lightest scalar, $f_0^{\mathrm{bare}}(720 \pm 100)$, is dominantly a $s\bar{s}$ state with a mixing angle close to the ideal octet one, $\Phi_{\mathrm{ideal\ octet}} = -55^\circ$. The situation with the lightest scalar nonet is similar to that with the lightest pseudoscalar nonet, where the mixing angle for the η meson is also close to $\Phi_{\mathrm{ideal\ octet}}$: this definitively indicates the degeneracy of the lightest 0^{++} and 0^{-+} states.

Table 7. Masses and coupling constants (in GeV) for the f_2 and a_2 resonances

	f_2 resonances			
	solution I-1		solution II-1,2	
	$\alpha = 1$	$\alpha = 2$	$\alpha = 1$	$\alpha = 2$
M	$1.236^{+0.010}_{-0.010}$	$1.530^{+0.010}_{-0.010}$	$1.233^{+0.010}_{-0.005}$	$1.529^{+0.010}_{-0.010}$
$g^{(\alpha)}$	$1.342^{+0.100}_{-0.100}$	$1.342^{+0.100}_{-0.100}$	$1.038^{+0.100}_{-0.100}$	$1.038^{+0.100}_{-0.100}$
Φ_α	$-(8.4^{+2.0}_{-3.0})$	$86.6^{+2.5}_{-4.5}$	$-(8.8^{+2.0}_{-3.0})$	$86.2^{+2.5}_{-4.5}$
$g_{4\pi}^{(\alpha)}$	$0.318^{+0.020}_{-0.020}$	$0.448^{+0.020}_{-0.020}$	$0.318^{+0.020}_{-0.020}$	$0.472^{+0.020}_{-0.020}$
	$\alpha = \pi\pi$	$\alpha = \eta\eta$	$\alpha = \pi\pi$	$\alpha = \eta\eta$
f_{1a}	$0.742^{+0.050}_{-0.250}$	$-(1.01^{+0.050}_{-0.500})$	$0.287^{+0.070}_{-0.070}$	$-0.143^{+0.100}_{-0.100}$
r_a	$1.997^{+0.150}_{-0.150}$	$1.077^{+0.050}_{-0.500}$	$2.474^{+0.150}_{-0.150}$	$1.295^{+0.150}_{-0.150}$
	$f_{13} = 0.684 \pm 0.100$		$f_{13} = 0.578 \pm 0.100$	
	$f_{ba} = 0$, $b = 2, 3$; $s_0 = 5.0$			
Pole position	$1.262^{+0.005}_{-0.005}$	$1.514^{+0.010}_{-0.006}$	$1.261^{+0.005}_{-0.005}$	$1.522^{+0.005}_{-0.010}$
	$-i(0.092^{+0.005}_{-0.005})$	$-i(0.066^{+0.008}_{-0.005})$	$-i(0.089^{+0.005}_{-0.005})$	$-i(0.076^{+0.005}_{-0.007})$
	a_2 resonances			
	solution I-1		solution II-1,2	
	$\alpha = 1$	$\alpha = 2$	$\alpha = 1$	$\alpha = 2$
M	$1.316^{+0.005}_{-0.005}$	$1.645^{+0.050}_{-0.050}$	$1.312^{+0.005}_{-0.005}$	$1.695^{+0.050}_{-0.080}$
$g^{(\alpha)}$	$1.080^{+0.100}_{-0.100}$	$0.270^{+0.100}_{-0.100}$	$1.300^{+0.100}_{-0.100}$	$0.325^{+0.100}_{-0.100}$
$g_4^{(\alpha)}$	$0.381^{+0.050}_{-0.050}$	$0.597^{+0.050}_{-0.050}$	$0.426^{+0.050}_{-0.050}$	$0.617^{+0.050}_{-0.050}$
	$r_1 = 1.845^{+0.150}_{-0.150}$		$r_1 = 2.406^{+0.150}_{-0.150}$	
Pole position	$1.309^{+0.005}_{-0.005}$	$1.615^{+0.030}_{-0.030}$	$1.308^{+0.005}_{-0.005}$	$1.667^{+0.030}_{-0.030}$
	$-i(0.058^{+0.005}_{-0.005})$	$-i(0.121^{+0.015}_{-0.015})$	$-i(0.059^{+0.005}_{-0.005})$	$-i(0.123^{+0.015}_{-0.015})$

The multiplet of the lightest tensor states appears as

$$1^3P_2\colon\ f_2^{\text{bare}}(1240 \pm 10),$$
$$f_2^{\text{bare}}(1522 \pm 10),$$
$$a_2^{\text{bare}}(1311 \pm 3), \qquad (40)$$
$$K_2^*(1430),$$
$$\Phi[f_2^{\text{bare}}(1240)] = -10^\circ \pm 3^\circ.$$

The K-matrix analysis of the πK D wave has not yet been performed: the $(J = 2)\pi K$ resonance with a mass of 1431 ± 3 MeV is reported in [24]; we have used this resonance to complete the multiplet in (40).

Our analysis leads to two versions for the $2^3P_0 q\bar{q}$ nonet:

The first version gives

$$2^3P_0\colon\ f_0^{\text{bare}}(1600 \pm 50),$$
$$f_0^{\text{bare}}(1810 \pm 30),$$
$$a_0^{\text{bare}}(1650 \pm 50), \qquad (41)$$
$$K_0^{\text{bare}}(1885^{+50}_{-100}),$$
$$\Phi[f_0^{\text{bare}}(1810)] = 84^\circ \pm 5^\circ.$$

The state $K_0^{\text{bare}}(1885^{+50}_{-150})$ is fixed by the analysis [11]

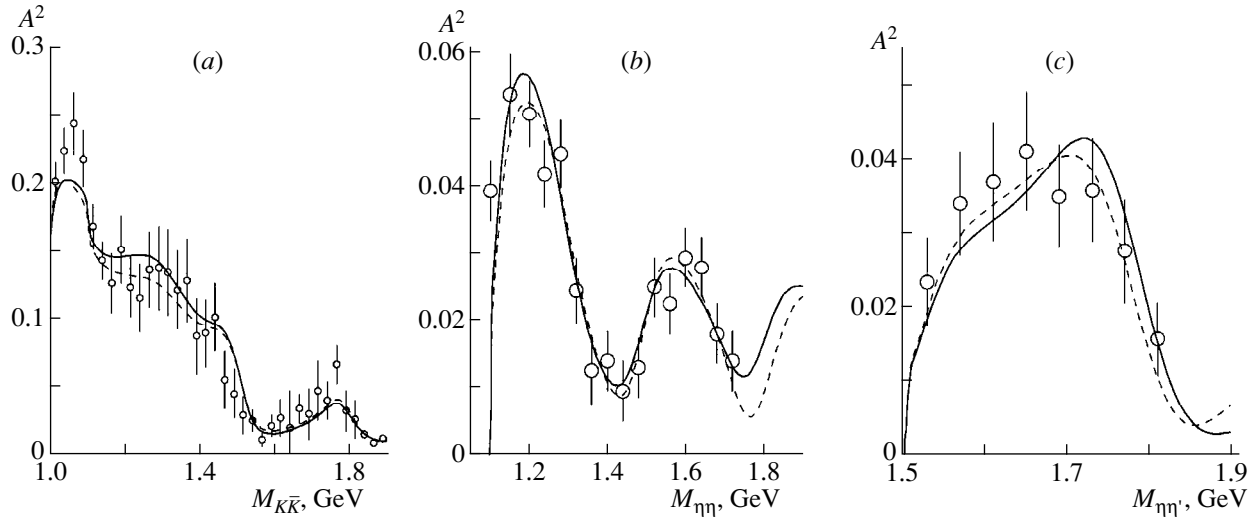

Fig. 5. *S*-wave amplitudes squared for the transitions (*a*) $\pi\pi \longrightarrow K\bar{K}$ [7], (*b*) $\pi\pi \longrightarrow \eta\eta$ [2], and (*c*) $\pi\pi \longrightarrow \eta\eta'$ [3]. Solid and dashed curves correspond, respectively, to solution II-2 and to solution I.

of the $K\pi$ *S* wave. In this version, the lightest glueball state is $f_0^{\text{bare}}(1230^{+150}_{-30})$. In the second version, the lightest glueball state is identified as $f_0^{\text{bare}}(1600)$, namely,

$$
\begin{aligned}
&2^3P_0\text{: } f_0^{\text{bare}}(1230^{+150}_{-30}),\\
&f_0^{\text{bare}}(1810 \pm 30),\\
&a_0^{\text{bare}}(1650 \pm 50),\\
&K_0^{\text{bare}}(1885^{+50}_{-100}),\\
&\Phi[f_0^{\text{bare}}(1810)] = 44^\circ \pm 10^\circ.
\end{aligned}
\tag{42}
$$

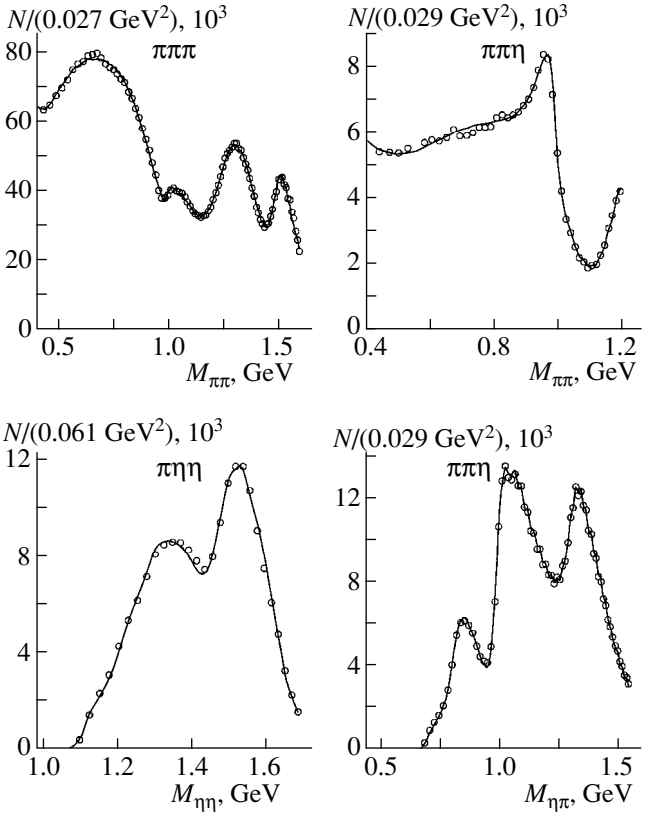

Fig. 6. Mass projections of the Dalitz plot onto the two-meson invariant mass for Crystal Barrel data. The curves correspond to solution II-2.

5. RESONANCE $f_0(980)$: IS IT A $K\bar{K}$ MOLECULE?

We begin by discussing the origin of $f_0(980)$. GAMS data on $f_0(980)$ production at high $|t|$ (see Fig. 3) directly demonstrate that this resonance has a hard component, while the location of the pole near the $K\bar{K}$ threshold definitively indicates that its kaon component is long-range. The presence of a long-range component gives rise to a discussion on the molecular structure of this state [25]. The problem to discuss is how substantial these components are in the formation of the resonance. We bear in mind that the short-range component (with $r < 1$ fm) is the subject of quark–gluon considerations and quark systematics.

The resonance $f_0(980)$ corresponds to the two poles located at (in MeV units)

$$M = 1015 - i46 \text{ (II sheet, under } \pi\pi \text{ cut)},$$

$$M = 936 - i238 \text{ (III sheet, under } \pi\pi \text{ and } K\bar{K} \text{ cuts)}.$$

The second pole appears owing to the well-known double-pole structure caused by the $K\bar{K}$ threshold (see, for example, [26]), while the first pole at $M = 1015 - i46$ MeV generates the leading irregularities in $\pi\pi$ spectra.

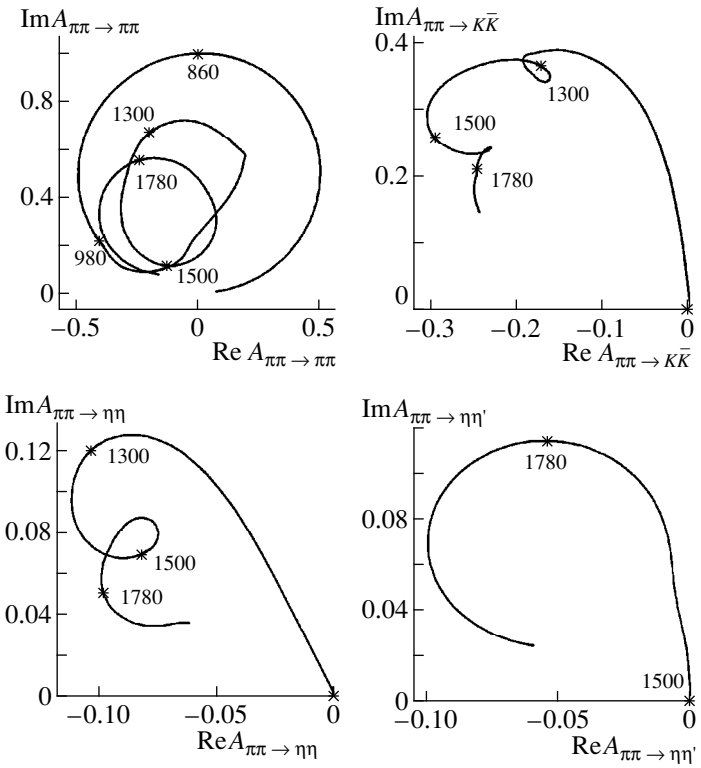

Fig. 7. Argand plots for the *S*-wave scattering amplitudes in solution II-2: (*a*) $\pi\pi \longrightarrow \pi\pi$, (*b*) $\pi\pi \longrightarrow K\bar{K}$, (*c*) $\pi\pi \longrightarrow \eta\eta$, and (*d*) $\pi\pi \longrightarrow \eta\eta'$.

The reconstructed *K*-matrix amplitude allows one to see the role of the $K\bar{K}$ component in the formation of $f_0(980)$, thereby clarifying the question of whether this resonance is a descendant of a $q\bar{q}$ state or it is a molecular-type system. To this end, we switch off $f_0(980)$-decay processes (transitions into $\pi\pi$ and $K\bar{K}$) and look at the dynamics of pole positions with a gradual onset of couplings. In order to simulate a gradual evolution of the couplings, we made the following substitution in the *K*-matrix 0^{++} amplitude:

$$g_a^{(\alpha)} \longrightarrow \xi g_a^{(\alpha)}. \qquad (43)$$

Here, the parameter ξ was constrained to change in the interval

$$0 < \xi \le 1. \qquad (44)$$

For $\xi \longrightarrow 0$, the decay channels are switched off and we return to a bare state, while, at $\xi = 1$, the real case is recovered.

For $\xi \longrightarrow 0$, the masses of the lightest scalar bare states are 650 and 1260 MeV (the positions of the *K*-matrix poles). With increasing ξ, the trajectories of the states are shown in Fig. 10.

The crucial point is what component, $\pi\pi$ or $K\bar{K}$, is responsible predominantly for the mass shift from 650 MeV to 1020 – *i*48 MeV. We can clarify this point

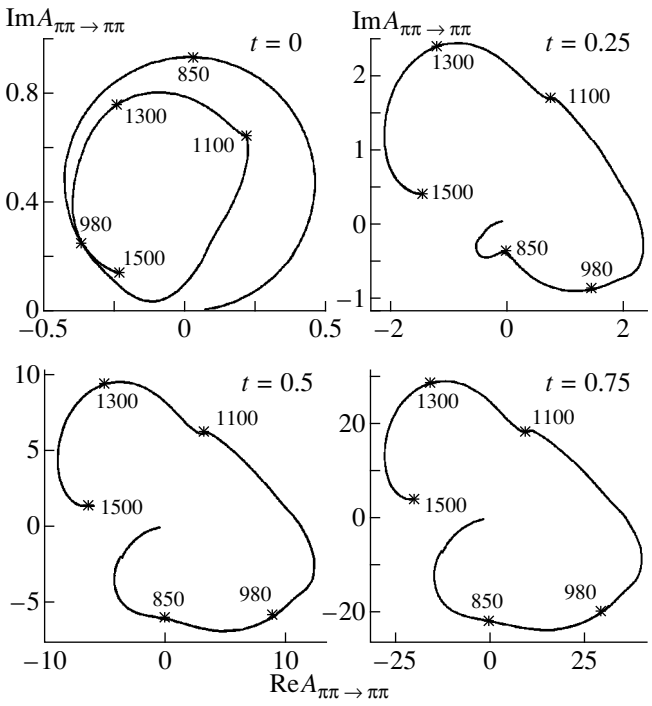

Fig. 8. Argand plots for the $\pi\pi(t) \longrightarrow \pi\pi$ *S*-wave scattering amplitudes at various values of t [t is given in $(\mathrm{GeV}/c)^2$ units].

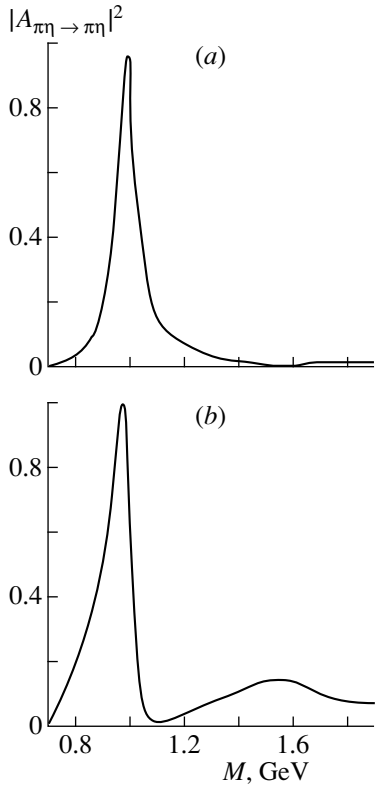

Fig. 9. Squared *S*-wave $\pi\eta \longrightarrow \pi\eta$ scattering amplitude: solutions (*a*) I and (*b*) II for the $\pi\eta \longrightarrow \pi\eta$ scattering amplitude.

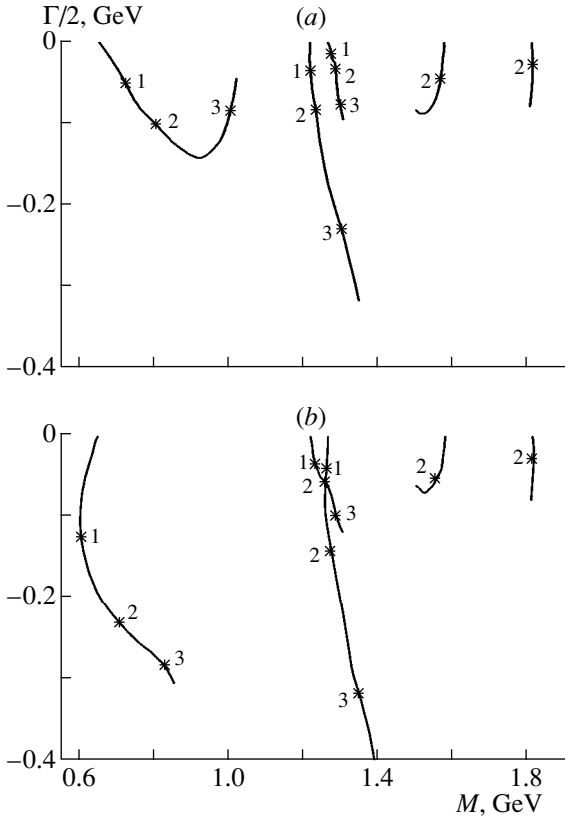

Fig. 10. Positions of the poles of the 00^{++} amplitude in the complex plane of $\sqrt{s}$ ($M = \mathrm{Re}\sqrt{s}$, $-\Gamma/2 = \mathrm{Im}\sqrt{s}$) after the substitution $g_a^\alpha \longrightarrow \xi g_a^\alpha$: (*a*) on the sheet under the $\pi\pi$ cut and (*b*) on the sheet under the $\pi\pi$ and $K\bar{K}$ cuts. The case of $\xi \longrightarrow 0$ gives the positions of the bare-state masses; $\xi = 1$ corresponds to the real case. The points (1), (2), and (3) correspond to $\xi = 0.4$, $\xi = 0.6$, and $\xi = 0.9$, respectively.

by switching off the $K\bar{K}$ component and by leaving $\pi\pi$ unchanged, and vice versa. In the first case, the mass of $f_0(980)$ state is

$$M(\text{without } K\bar{K}) = 974 - i115 \text{ MeV}. \quad (45)$$

One sees that the mass shift

$$\delta_{K\bar{K}} = M(\xi = 1) - M(\text{without } K\bar{K}) = 41 + i67 \text{ MeV} \quad (46)$$

is not large: the $K\bar{K}$ component which is responsible for the value of δ does not play an important role in the formation of the $f_0(980)$ mass. In the second case, where the $\pi\pi$ component is switched off, we obtain the state that is the nearest to the $K\bar{K}$ threshold and which is located at

$$M(\text{without } \pi\pi) = 810 - i10 \text{ MeV}. \quad (47)$$

Thus, the mass shift is

$$\delta_{\pi\pi} = M(\xi = 1) - M(\text{without } \pi\pi) = 205 + i36 \text{ MeV}, \quad (48)$$

which is much greater than $\delta_{K\bar{K}}$. The transition into real pions,

$$f_0^{\text{bare}}(720) \longrightarrow \pi\pi, \quad (49)$$

is mainly in charge of the mixing of the lightest scalar $q\bar{q}$ state with other scalars, thus shifting its mass by chance to the region of the next threshold, $K\bar{K}$. The $K\bar{K}$ component of $f_0(980)$ is of the molecule type: relative kaon momenta are small; therefore, the relative separations are large. We emphasize once again, however, that the two-kaon component does not play a crucial role in the formation of the $f_0(980)$ mass.

6. CONCLUSION

We have performed a *K*-matrix analysis of GAMS *S*- and *D*-wave $\pi^0\pi^0$, $\eta\eta$, and $\eta\eta'$ data, together with data obtained by BNL and Crystal Barrel collaboration. The partial-wave amplitudes for the 00^{++}, 02^{++}, 10^{++}, and 12^{++} states have been investigated in the mass region up to 2000 MeV, and the poles of these amplitudes have been found (see Tables 4–7). The pole terms of the *K* matrix have been reconstructed; that is, the

00^{++}, 02^{++}, 10^{++}, and 12^{++} bare states have been found. The quark content of these bare states has been determined on the basis of the relations between the decay coupling constants: this has enabled us to reconstruct the 1^3P_0, 2^3P_0, and 1^3P_2 quark nonets. Our analysis has confirmed the result that was presented in [6] and which is based on the *K*-matrix analysis of the only 00^{++} wave: in the region 1200–1600 MeV, there exists a scalar–isoscalar state that is extraneous to the $q\bar{q}$ systematics. This state is a good candidate for the lightest scalar glueball.

Our analysis has revealed degeneracy of the lightest 00^{++} and 00^{-+} states.

ACKNOWLEDGMENTS

We are grateful to D.V. Bugg, S.S. Gershtein, A.K. Likhoded, L. Montanet, and B.S. Zou for stimulating discussions and to the Crystal Barrel collaboration for providing us with their data.

The work of V.V. Anisovich and A.V. Sadovsky was supported in part by the Russian Foundation for Basic Research (RFBR), project no. 96-02-17934, and by INTAS–RFBR, project no. 95-0267.

REFERENCES

1. D. Alde *et al.*, Z. Phys. C **66**, 375 (1995); A. A. Kondashov *et al.*, in *Proceedings of the 27th International Conference on High Energy Physics, Glasgow*, 1994, p. 1407; Yu. D. Prokoshkin *et al.*, Phys. Dokl. **342**, 473 (1995); A. A. Kondashov, Preprint No. IHEP 95-137 (Institute for High Energy Physics, Protvino, 1995).
2. F. Binon *et al.*, Nuovo Cimento A **78**, 313 (1983).
3. F. Binon *et al.*, Nuovo Cimento A **80**, 363 (1984).
4. V. V. Anisovich, A. A. Kondashov, Yu. D. Prokoshkin, *et al.*, Phys. Lett. B **355**, 363 (1995).
5. V. V. Anisovich and A. V. Sarantsev, Phys. Lett. B **382**, 429 (1996).
6. V. V. Anisovich, Yu. D. Prokoshkin, and A. V. Sarantsev, Phys. Lett. B **389**, 388 (1996).
7. S. J. Lindenbaum and R. S. Longacre, Phys. Lett. B **274**, 492 (1992); A. Etkin *et al.*, Phys. Rev. D **25**, 1786 (1982).
8. V. V. Anisovich *et al.*, Phys. Lett. B **323**, 233 (1994); C. Amsler *et al.*, Phys. Lett. B **342**, 433 (1995); **355**, 425 (1995).
9. S. S. Gershtein, A. K. Likhoded, and Yu. D. Prokoshkin, Z. Phys. C **24**, 305 (1984); C. Amsler and F. E. Close, Phys. Rev. D **53**, 295 (1996); Phys. Lett. B **353**, 385 (1995); V. V. Anisovich, Phys. Lett. B **364**, 195 (1995).
10. A. V. Anisovich, V. V. Anisovich, and A. V. Sarantsev, Z. Phys. A **359**, 173 (1997).
11. A. V. Anisovich and A. V. Sarantsev, Phys. Lett. B **413**, 137 (1997).
12. G. 't Hooft, Nucl. Phys. B **72**, 161 (1974); G. Veneziano, Nucl. Phys. B **117**, 519 (1976).
13. V. V. Anisovich, M. G. Huber, M. N. Kobrinsky, and B. Ch. Metch, Phys. Rev. D **42**, 3045 (1990); K. Peters and E. Klempt, Phys. Lett. B **352**, 467 (1995); V. V. Anisovich, Phys. Lett. B **364**, 195 (1995); B. S. Zou, private communication.
14. V. V. Anisovich and V. M. Shekhter, Nucl. Phys. B **55**, 455 (1973); J. D. Bjorken and G. E. Farrar, Phys. Rev. D **9**, 1449 (1974).
15. M. A. Voloshin, Yu. P. Nikitin, and P. I. Porfirov, Yad. Fiz. **35**, 1006 (1982) [Sov. J. Nucl. Phys. **35**, 586 (1982)].
16. G. S. Bali *et al.*, Phys. Lett. B **309**, 378 (1993); J. Sexton, A. Vaccarino, and D. Weingarten, Phys. Rev. Lett. **75**, 4563 (1995); F. E. Close and M. J. Teper, Preprint No. RAL-96-040 (1996); C. J. Morningstar and M. Peardon, hep-lat/9704011.
17. A. V. Anisovich, V. V. Anisovich, Yu. D. Prokoshkin, and A. V. Sarantsev, Z. Phys. A **357**, 123 (1997).
18. A. V. Anisovich, V. V. Anisovich, and A. V. Sarantsev, Phys. Lett. B **395**, 123 (1997).
19. D. V. Bugg, V. V. Anisovich, A. V. Sarantsev, and B. S. Zou, Phys. Rev. D **50**, 4412 (1994).
20. D. V. Bugg, A. V. Sarantsev, and B. S. Zou, Nucl. Phys. B **471**, 59 (1996).
21. Particle Data Group (R. M. Barnet *et al.*), Phys. Rev. D **54**, 1 (1996).
22. D. Alde *et al.*, Phys. Lett. B **241**, 600 (1990).
23. G. M. Beladidze *et al.*, Z. Phys. C **54**, 367 (1992).
24. D. Aston *et al.*, Nucl. Phys. B **296**, 493 (1988).
25. J. Weinstein and N. Isgur, Phys. Rev. D **27**, 588 (1983); **41**, 2236 (1990); D. Lohse *et al.*, Nucl. Phys. B **516**, 513 (1996); G. Janssen *et al.*, Phys. Rev. D **52**, 2690 (1995).
26. W. Flatté, Phys. Lett. B **63**, 224 (1976).

Physics of Atomic Nuclei, Vol. 63, No. 8, 2000, pp. 1428–1447. From Yadernaya Fizika, Vol. 63, No. 8, 2000, pp. 1507–1526.

ON THE 85th ANNIVERSARY OF V.V. VLADIMIRSKY

Glueball Spectrum and Pomeron in the Wilson Loop Approach*

A. B. Kaidalov and Yu. A. Simonov

Institute of Theoretical and Experimental Physics, Bol'shaya Cheremushkinskaya ul. 25, Moscow, 117259 Russia

Received November 12, 1999

Abstract—Using a nonperturbative method based on the asymptotic behavior of Wilson loops, we calculate the masses of glueballs and the corresponding Regge trajectories. The only input is the string tension fixed by the meson Regge slope, while perturbative contributions to spin splittings are defined by standard α_s values. The masses of the lowest glueball states are in a perfect agreement with lattice results. The leading glueball trajectory, which is associated with the Pomeron is discussed in detail, and its mixing with f and f' trajectories is taken into account. © *2000 MAIK "Nauka/Interperiodica".*

1. INTRODUCTION

The problem of the existence of glueballs is one of the most interesting in QCD. Lattice calculations give definitive predictions for the spectrum of such states [1–4], but experimental evidence is not conclusive [5, 6]. Mixing between gluons and $q\bar{q}$ pairs complicates the separation of glueballs. A theoretical study of glueballs within QCD was initiated in [7–10] and is closely related to the problem of the Pomeron—that is, the leading Regge pole, which determines the asymptotic behavior of scattering amplitudes at very high energies. It is usually assumed that the Pomeron in QCD is mostly a gluonic object [11], and glueball resonances with vacuum quantum numbers and spins belong to this trajectory. Another interesting hypothetical Regge singularity is the "odderon," which has negative signature and C parity and can be constructed from at least three gluons. Most studies of the Pomeron and odderon singularities within QCD are based on perturbation theory [12].

In this study, we will address both the problem of spectra of glueballs and the problem of the Pomeron (odderon) singularity using the method of Wilson loop path integrals that was developed in [13–15]. The method is based on the assumption of the area law for Wilson loops at large distances in QCD, which is equivalent to the condition of quark and gluon confinement. It was first applied to calculating the spectra of $q\bar{q}$ states in [16], of baryons in [17], and of glueballs in [18]. In those calculations, the rotation of the string between quarks or gluons was not taken into account with the result that there arose some distortion in the mass spectra—in particular, the Regge slope was $1/8\sigma$ instead of the string slope of $1/2\pi\sigma$, where σ is the string tension. In the present study, we will use a more accurate computational method for glueballs that was developed in [14, 15] for $q\bar{q}$ states and which yields a correct Regge slope (see [19] for numerical data and discussion). We also study in detail possible corrections to large-distance string dynamics due to small-distance perturbative gluon exchanges (PGE) and demonstrate that their effect on the mass spectrum of glueball states is rather small and can be computed as a correction. This is in contrast to the glueball spectrum in [8], where PGE in the form of the adjoint Coulomb potential was assumed, as in many other papers on the subject. Instead, we argue below that PGE sums up to another series, the BFKL ladder [12], where loop corrections strongly suppress the final results, so that PGE can be disregarded for a first approximation. Our predictions for the masses of the lowest spin-averaged glueball states in $\sqrt{\sigma}$ units are in a perfect agreement with results of recent lattice calculations [1–3]. In addition, spin–orbit and spin–spin interactions are also calculated and found to comply well with lattice data.

The leading glueball Regge trajectory is calculated in the positive-t region and is extrapolated to the scattering region of $t \le 0$. The importance of mixing among this trajectory and $q\bar{q}$ trajectories (f, f') is emphasized; a calculation of these mixing effects yields the leading Pomeron trajectory with $\alpha_{\mathbf{P}}(0) > 1$ ($\alpha_{\mathbf{P}}(0) = 1.1$–$1.2$) in accord with experimental observations [20]. An interesting pattern of three colliding vacuum trajectories in the region $t > 0$ is observed, which can be important for the decay properties of resonances occurring on these trajectories.

The present article is organized as follows. Field operators creating glueball states in the general case and in the background-field method are introduced in Section 2 and presented in Appendix 1. The general formalism of the Wilson loop path integrals and the resulting relativistic Hamiltonian are discussed in Section 2 and in Appendix 2. The spectrum of spin-averaged glueball states that follows from this Hamiltonian is obtained in Section 2 and is compared with the corresponding lattice results. The spin splittings of glueball masses from both nonperturbative and perturbative

* This article was submitted by the authors in English.

parts are considered in Section 3 and in Appendices 3 and 4. The resulting glueball spectrum is compared in Section 3 with the results of lattice calculations. The PGE effect on the glueball masses and Regge trajectories is discussed in Section 4. It is indicated that small distances have only a slight effect on the glueball spectrum. Three-gluon glueballs are considered in Section 5. It is shown that the lowest $3g$ states have a rather large mass of $M_{3g} \approx 3.4$ GeV. The relation between the glueball Regge trajectories and the vacuum Pomeron trajectory is discussed in Section 6. In that section and in Appendix 5, the effects of mixing between gluonic and $q\bar{q}$ Regge trajectories are investigated.

The possible implications and improvements of our results are discussed in Section 7.

2. GENERAL FORMALISM

Following [13, 21], we break down gluonic fields A_μ into a nonperturbative background B_μ and perturbative gluons a_μ, $A_\mu = B_\mu + a_\mu$,[1)] and consider two-gluon glueballs described by the Green's functions

$$G_{\mu\nu,\,\mu'\nu'}(x, y|x', y') = \langle \Psi^{(\mathrm{in})}(x, y)\Psi^{(\mathrm{out})}(x', y')\rangle_{a,\,B} = \langle \Gamma^{(\mathrm{in})}G_{\mu\mu'}(x, x')G_{\nu\nu'}(y, y')\Gamma^{(\mathrm{out})}\rangle_B + \text{perm.} \quad (1)$$

Here, $\Psi^{(\mathrm{in})}$ ($\Psi^{(\mathrm{out})}$) are glueball operators in the initial (final) state made of gluon fields a_μ and B_μ (see Appendix 1 for the explicit form of $\Psi^{(\mathrm{in}),\,(\mathrm{out})}$ in the lowest states); and $G_{\mu\mu'}$ is the gluon Green's function of the field a_μ in the background field B_μ, namely,

$$G_{\mu\nu}(x, y) = \langle x|(-\hat{D}^2\delta_{\mu\nu} - 2ig\hat{F}_{\mu\nu})^{-1}|y\rangle_B, \quad (2)$$

where $\hat{D}_\mu = \partial_\mu - ig\hat{B}_\mu$, $\hat{F}_{\mu\nu}$ is the strength of the field $\hat{B}_\mu$ in the adjoint representation, and averaging over the background fields B_μ is denoted by angular brackets (there, the subscript B will be omitted in the following).

Referring the reader for details of the derivation to [13, 18, 21] and to Appendix 2, we can write the path integral for (1) in the form

$$G_{\mu\nu,\,\mu'\nu'}(x, y|x', y') = \mathrm{const}\times\int_0^\infty ds\int_0^\infty ds' DzDz' e^{-K-K'}\langle \Gamma^{(\mathrm{in})}W_F\Gamma^{(\mathrm{out})}\rangle, \quad (3)$$

where

$$K = \frac{1}{4}\int_0^s (dz/d\tau)^2 d\tau;$$

K' is the same with primed z, τ, and s; and

$$\langle W_F\rangle = \mathrm{tr}\,P_B P_F \times\left\langle \exp\left\{ig\int_C B_\mu du_\mu + 2ig\int_0^s \hat{F}d\tau + 2ig\int_0^{s'}\hat{F}d\tau'\right\}\right\rangle. \quad (4)$$

Here, P_B and P_F are ordering operators for the color matrices B_μ and $\hat{F}$, respectively. It will be seen in Section 3 that terms involving $\hat{F}$ generate a spin-dependent contribution of nonperturbative background, which is calculable and small; for this reason, we will treat those terms perturbatively.

Neglecting $\hat{F}$'s for a first approximation and omitting, for the sake of simplicity, the projection operators $\Gamma^{(\mathrm{in})}$ and $\Gamma^{(\mathrm{out})}$, which do not affect the form of the resulting Hamiltonian, one arrives at the Wilson loop in the adjoint representation, for which one can use the minimal-area law confirmed by numerous lattice data [22] at least up to the distance on the order of 1 fm,

$$\langle W_{\mathrm{adj}}\rangle = Z\exp(-\sigma_{\mathrm{adj}}S_{\min}), \quad (5)$$

where we have included in Z self-energy and nonasymptotic corrections, since (5) is valid for large loops of size R, $T \gg T_g$, where T_g is the gluon correlation length.

Note that we could treat (4) by the field-correlation-function method [13, 23], retaining only the lowest (Gaussian) correlation function $\langle F(x)F(y)\rangle$. In this case, the leading term will again have the form (5); we will use this method to evaluate the contribution of the gluon spin terms $\hat{F}$ in (4); the result in (5) is more general, since σ_{adj} in (5) contains the contribution of all correlation functions and is not associated with the Gaussian approximation.

Applying now the general method of [14] to the Green's function (3), one introduces an auxiliary (einbein) function $\mu(t)$ of the real time t instead of the proper time s and τ, via relation $d\tau = dt/2\mu(t)$, and auxiliary einbein function $\nu(\beta, t)$ to get rid of the square-root Nambu–Goto form for $S_{\min}$ in (5). As a result, one defines the Hamiltonian H through the equality $G \sim \exp(-TH)$, where T is the evolution parameter, taken here to be the center-of-mass time T, $0 \le t \le T$.

The resulting relativistic Hamiltonian for two spin-

[1)] Note that the background formalism exploiting the 't Hooft identity [21] allows us to avoid the double-counting problem, and the principle of the above partition is immaterial here, provided that the background B_μ is characterized by the input string tension σ and that the perturbation is in the known α_s constant.

Table 1. Effective-mass eigenvalues $\mu_0(n, L)$ (in GeV for $\sigma_{fund} = 0.18$ GeV^2) obtained from (8) {$\mu_0 = \sqrt{\sigma_{adj}}\,(a(n)/3)^{3/4}$ is the upper entry, and eigenvalues of reduced equation [$a(n)$] is the lower entry}

L \ n	0	1	2	3
0	0.528	0.803	1.005	1.174
	2.3381	4.0879	5.520	6.786
1	0.693	0.917		
	3.3613	4.8845		
2	0.826	1.020		
	4.2482	5.6297		

Table 2. Eigenvalues (in GeV) of relativistic Hamiltonian for $L = 0$

n	0	1	2	3	4	5
M_n	2.01	2.99	3.75	4.37	4.92	5.41

less gluons takes the form [14]

$$H_0 = \frac{p_r^2}{\mu(t)} + \mu(t) + \frac{L(L+1)}{r^2\left[\mu + 2\int_0^1 \left(\beta - \frac{1}{2}\right)^2 \nu d\beta\right]} + \int_0^1 \frac{\sigma_{adj}^2 d\beta}{2\nu(\beta, t)} r^2 + \frac{1}{2}\int_0^1 \nu(\beta, t) d\beta. \quad (6)$$

Here, $\mu(t)$ and $\nu(\beta, t)$ are positive auxiliary functions that are to be found from the extremum condition [14]. Their extremal values are equal to the effective gluon energy $\langle\mu\rangle$ and the energy density of the adjoint string $\langle\nu\rangle$, respectively.

For the case of $L = 0$, the extremization with respect to μ and ν yields the simple result [14]

$$H_0 = 2\sqrt{p_r^2} + \sigma_{adj} r, \quad (7)$$

which coincides with the Hamiltonian of the relativistic potential model. The approximation made in [16–18] corresponds to the replacement of the operators $\mu(\tau)$ and $\nu(\tau, \beta)$ (which are expressed in terms of the operators p and r by means of extremization) by c numbers to be found from extremization of eigenvalues of H_0. This yields another form, used in [18],

$$H_0' = \frac{\mathbf{p}^2}{\mu_0} + \mu_0 + \sigma_{adj} r; \quad (8)$$

as can be seen from Table 3 of [19], the eigenvalues of (8) are about 5% higher than those of H_0. The value of σ_{adj} in (8) can be found from the string tension of the $q\bar{q}$ system, since the Casimir scaling found on a lattice [22] predicts that

$$\sigma_{adj} = \frac{C_2(adj)}{C_2(fund)}\sigma_{fund} = \frac{9}{4}\sigma_{fund}. \quad (9)$$

For light quarks, the value of σ_{fund} is found from the slope of meson Regge trajectories and is given by

$$\sigma_{fund} = \frac{1}{2\pi\alpha'} \approx 0.18 \text{ GeV}^2, \quad (10)$$

whence we obtain

$$\sigma_{adj} \approx 0.40 \text{ GeV}^2. \quad (11)$$

In what follows, the parameter μ and its optimal value μ_0, which appears in (8), play a very important role. The way in which they enter into spin corrections in Section 3 and into magnetic moments shows that μ_0 plays the role of an effective (constituent) gluon mass (or constituent quark mass in the equation for the $q\bar{q}$ system).

In contrast to potential models, where the constituent gluon and quark mass is introduced as a fixed input parameter in addition to the parameters of the potential, our approach involves calculating μ_0 from the extremum of the eigenvalue of (8); this yields

$$\mu_0(n) = \sqrt{\sigma}\left(\frac{a(n)}{3}\right)^{3/4}, \quad M_0(n) = 4\mu_0(n),$$

where $\sigma = \sigma_{adj}$ for gluons and $\sigma = \sigma_{fund}$ for massless quarks and where $a(n)$ is the eigenvalue for the reduced equation $d^2\psi/d\rho^2 + (a(n) - \rho - L(L+1)/\rho^2)\psi = 0$. The first few values of $a(n)$ and $\mu_0(n)$ are given in Table 1; they will be used in Section 3.

We note that our lowest "constituent gluon mass," $\mu_0(n = L = 0) = 0.528$ GeV (for $\sigma_{fund} = 0.18$ GeV^2), is not far from the values introduced in the potential models, the drastic difference being that μ_0 depends on n and L and grows for higher states; it is calculable in our case.

The eigenvalues of H_0 (7) for $L = 0$ and $n = 0, 1, 2, \ldots$ are given in Table 2 for $\sigma_{adj} = \frac{9}{4}\sigma_{fund} = \frac{9}{4} \times 0.18$ GeV^2. The mass spectrum for $L > 0$ is given by the eigenvalues of H_0 (6) and was studied in [14]. Within a 5% accuracy of the Wentzel–Kramers–Brillouin approximation, one can exploit much simpler expressions from [19], which predict for $L > 0$ the eigenvalues shown in Table 3. An independent numerical estimation of the rotating string spectrum from [24] yields similar eigenvalues.

From Tables 1–3 and from [24], one can see that the mass spectra of the Hamiltonian in (6) are described to a high precision by the very simple formula

$$\frac{M^2}{2\pi\sigma} = L + 2n_r + c_1, \quad (12)$$

where L is the orbital angular momentum, n_r is the radial quantum number, and $c_1 \approx 1.55$ is a constant. It describes an infinite set of linear Regge trajectories shifted by $2n_r$ from the leading one ($n_r = 0$). At this stage, the only difference between light quarks and gluons is the value of σ, which determines the mass scale.

Thus, the lowest glueball state with $L = 0$ and $n_r = 0$ according to Table 2 and equation (12) has $M^2 = 4.04\ \text{GeV}^2$.

This corresponds to a degenerate 0^{++} and a 2^{++} state:

$$M = 2.01\ \text{GeV}. \tag{13}$$

In order to compare our results with the corresponding lattice calculations from [1–4], it is convenient to consider the quantity $\overline{M}/\sqrt{\sigma_{\text{fund}}}$, which is not sensitive to the choice of the string tension σ_{fund}.[2)] From these data, we find that, for the $L = 0$, $n_r = 0$ states, the value of the spin-averaged mass

$$\frac{\overline{M}}{\sqrt{\sigma_{\text{fund}}}} = \frac{M(0^{++}) + 2M(2^{++})}{3}\frac{1}{\sqrt{\sigma_{\text{fund}}}} \tag{14}$$

is equal to 4.61 ± 0.1, which is to be compared with our prediction $\overline{M}^{(\text{theor})}(L = 0, n_r = 0)/\sqrt{\sigma_{\text{fund}}} = 4.68$.

For a radially excited state, our theory predicts

$$\frac{\overline{M}^{(\text{theor})}}{\sqrt{\sigma_{\text{fund}}}}(L = 0, n_r = 1) = 7.0. \tag{15}$$

For this quantity, lattice data from [1] yield

$$\frac{\overline{M}^{(\text{lat})}}{\sqrt{\sigma_{\text{fund}}}}(L = 0, n_r = 1) = 6.56 \pm 0.55. \tag{16}$$

For the $L = 1$, $S = 1$ states, one can define a spin-averaged mass in a similar way:

$$\frac{\overline{M}}{\sqrt{\sigma_{\text{fund}}}} = \frac{M(0^{-+}) + 2M(2^{-+})}{3}\frac{1}{\sqrt{\sigma_{\text{fund}}}}; \tag{17}$$

lattice data [1–4] yield

$$\frac{\overline{M}^{(\text{lat})}}{\sqrt{\sigma_{\text{fund}}}}(L = 1, n_r = 0) = 6.11 \pm 0.38, \tag{18}$$

which is in reasonable agreement with our prediction,

$$\frac{\overline{M}^{(\text{theor})}}{\sqrt{\sigma_{\text{fund}}}}(L = 1, n_r = 0) = 6.0. \tag{19}$$

[2)]Note that the value $\sigma_{\text{fund}} \simeq 0.23\ \text{GeV}^2$ used in lattice calculations differs by about 20% from the "experimental" value (10).

Table 3. Eigenvalues (in GeV) of rotating-string Hamiltonian (6) for $L > 0$

n \ L	1	2	3	4	5
0	2.65	3.13	3.53	3.88	4.206
1	3.645	4.03	4.366	4.67	4.95
2	4.40	4.737	5.04	5.31	5.56
3	5.02	5.34	5.62	5.87	6.10
4	5.58	5.87	6.13	6.37	6.59
5	6.09	6.36	6.60	6.82	7.03

Table 4. Spin-averaged glueball masses $M_G/\sqrt{\sigma_{\text{fund}}}$

	Quantum numbers	Our study	Lattice data	
			[3]	[1]
2-gluon states	$L = 0$, $n_r = 0$	4.68	4.66 ± 0.14	4.53 ± 0.23
	$L = 1$, $n_r = 0$	6.0	6.36 ± 0.6	6.1 ± 0.38
	$L = 0$, $n_r = 1$	7.0	6.68 ± 0.6	6.56 ± 0.55
	$L = 2$, $n_r = 0$	7.0	$9.0 \pm 0.7(3^{++})$	$7.7 \pm 0.4(3^{++})$
	$L = 1$, $n_r = 1$	8.0		7.94 ± 0.48
3-gluon state	$K = 0$	7.61		8.19 ± 0.48

For $L = 2$, $n_r = 0$ and $L = 1$, $n_r = 1$, we have the following values of the spin-averaged mass:

$$\begin{aligned}\frac{\overline{M}^{(\text{theor})}(L = 0, n_r = 0)}{\sqrt{\sigma_{\text{fund}}}} &= 7.0,\\ \frac{\overline{M}^{(\text{theor})}}{\sqrt{\sigma_{\text{fund}}}}(L = 1, n_r = 1) &= 8.0.\end{aligned} \tag{20}$$

Lattice data from [1] yield, respectively, 7.7 ± 0.4 and 7.94 ± 0.48. Note that, in the first multiplet, lattice data exist only for 3^{++}. An overall comparison of the spin-averaged masses computed here and on a lattice is illustrated in Table 4.

Thus, we arrive at the conclusion that the spin-averaged masses obtained from a purely confining force with relativistic kinematics for valence gluons are in accord with lattice data. This implies that the PGE shifts of glueball masses in lattice calculations are small.

3. SPIN SPLITTINGS OF GLUEBALL MASSES

Here, we will treat spin effects in a perturbative way; a glance at our predictions in Table 5 and at the lattice results given in Table 6 tells us that, in glueball states apart from 2^{++}–0^{++}, the spin splittings are less

Table 5. Masses of glueballs with $L = 0, 1, 2$ and $n = 0, 1$ (for $\sigma_{fund} = 0.18$ GeV^2)

J^{PC}	n	M, GeV	J^{PC}	n	M, GeV
0^{++}	0	1.4	2^{++}	0	3.13, 3.11
	1	2.4	0^{++}	0	3.06
2^{++}	0	2.3	1^{++}	0	3.07
	1	3.3	3^{++}	0	3.14
0^{-+}	0	2.52	4^{++}	0	3.16
	1	3.55	3^{--}	0	3.51
2^{-+}	0	2.70	2^{--}	0	3.23
	1	3.7	1^{--}	0	3.04

Table 6. Comparison of predicted glueball masses with lattice data (for $\sigma_{fund} = 0.228$ GeV^2)

J^{PC}	M, GeV		
	our study	lattice data	
		[1]	[3]
0^{++}	1.58	1.73 ± 0.13	1.74 ± 0.05
$0^{++}*$	2.71	2.67 ± 0.31	3.14 ± 0.10
2^{++}	2.59	2.40 ± 0.15	2.47 ± 0.08
$2^{++}*$	3.73	3.29 ± 0.16	3.21 ± 0.35
0^{-+}	2.56	2.59 ± 0.17	2.37 ± 0.27
$0^{-+}*$	3.77	3.64 ± 0.24	
2^{-+}	3.03	3.1 ± 0.18	3.37 ± 0.31
$2^{-+}*$	4.15	3.89 ± 0.23	
3^{++}	3.58	3.69 ± 0.22	4.3 ± 0.34
1^{--}	3.49	3.85 ± 0.24	
2^{--}	3.71	3.93 ± 0.23	
3^{--}	4.03	4.13 ± 0.29	

than 10–15% of the total mass; hence, a perturbative treatment is justified to this level of accuracy.

Before proceeding to actual calculations of spin splittings, it is necessary to choose between two possible strategies (and corresponding physical mechanisms) for treating gluon polarizations. In the first approach, one insists on the transversality condition and on the resulting two-gluon polarizations as for a free gluon [7].

In the second approach, it is assumed that the gluon acquires a nonzero mass owing to the adjacent string, in a way similar to that in the case of $W^{\pm}$ and Z^0, where mass is created by the Higgs condensate. In this case, one has three massive-gluon polarizations, and the spin-coupling scheme for two gluons can be taken to be the LS one with the characteristic J^{PC} pattern of lowest levels, which is observed in lattice calculations [1–4].

Therefore, we choose the second approach and consider the gluon-spin operator $\mathbf{S}^{(i)}$, $i = 1, 2$; the total-spin operator $\mathbf{S} = \mathbf{S}^{(1)} + \mathbf{S}^{(2)}$; the orbital angular momentum $\mathbf{L}$; and the total angular momentum $\mathbf{J} = \mathbf{L} + \mathbf{S}$; each level (mass) is assigned not only the conserved values of J^{PC} but also the values of L and S (which in some cases may have an admixture of $L' = L \pm 2$ and $S' = S \pm 2$, but this admixture is generally small).

A detailed discussion of gluon-mass generation in the context of gauge invariance and symmetry breaking (as in the electroweak case) is postponed to a separate publication.

The two-gluon mass operator can be written as

$$M = M_0(n, L) + \mathbf{S} \cdot \mathbf{L} M_{SL} + \mathbf{S}^{(1)} \cdot \mathbf{S}^{(2)} M_{SS} + M_T, \quad (21)$$

where M_0 is the eigenvalue of the Hamiltonian $H \equiv H_0 + \Delta H_{pert}$, and H_0 is given in (7) [or its approximation in (8)], while ΔH_{pert} is due to perturbative gluon exchanges and is discussed in the next section.

To obtain the other three terms in (21), one should consider averaging of the operators $\hat{F}$ in the exponent of (4) and take into account the relation

$$-2i\hat{F}_{\mu\nu} = 2(\mathbf{S}^{(1)} \cdot \mathbf{B}^{(1)} + \tilde{\mathbf{S}}^{(1)} \cdot \mathbf{E}^{(1)})_{\mu\nu} \quad (22)$$

and a similar relation for the term in the integral $\int \hat{F} d\tau'$, with the substitution $1 \longrightarrow 2$ for indices. Here, gluon-spin operators are introduced, for example,

$$(S_m^{(1)})_{ik} = -ie_{mik}, \quad i, k = 1, 2, 3,$$
$$(\tilde{S}_m^{(1)})_{i4} = -i\delta_{im}. \quad (23)$$

Two remarks are in order here: (i) the gluon spin appears via the integral $\int 2(\mathbf{S} \cdot \mathbf{B}) d\tau' = \int [(\mathbf{S} \cdot \mathbf{B})/\mu(t)] dt$, where $\mu(t)$ and its extremal value μ_0 are the same as those in, respectively, (6) and (8) (for details, see Appendix 2); (ii) the main part of the Hamiltonian, H_0, is diagonal in the spin indices i and k, while the spin-dependent part (22) is treated as a perturbation, so that the admixture of the fourth polarization due to $\tilde{S}$ in (23) does not appear in the lowest order.

The detailed derivation of spin-dependent terms is performed in Appendix 3; here, we only quote the results. Since the structure of the term $\hat{F}$ in (4) due to (22) is identical to that in the heavy-quark case with the replacement of the heavy-quark mass by the effective gluon parameter μ_0 [see (8)], one can use the spin analysis of heavy quarkonia from [25] to represent the spin-dependent part of the Hamiltonian in a form similar to that of Eichten and Feinberg [26]; that is,

$$\Delta H_S = \frac{\mathbf{S} \cdot \mathbf{L}}{\mu_0^2}\left(\frac{1}{r}\frac{dV_1}{dr} + \frac{1}{r}\frac{dV_2}{dr}\right) + \frac{\mathbf{S}^{(1)} \cdot \mathbf{S}^{(2)}}{3\mu_0^2} V_4(r)$$
$$+ \frac{1}{3\mu_0^2}(3(\mathbf{S}^{(1)} \cdot \mathbf{n})(\mathbf{S}^{(2)} \cdot \mathbf{n}) - \mathbf{S}^{(1)} \cdot \mathbf{S}^{(2)}) V_3(r) + \Delta V, \quad (24)$$

where ΔV contains higher cumulant contributions, which can be estimated at about 10% of the main term in (24) and which will be neglected in what follows. Note that the spin of the gluon is twice as large as that of the quark; therefore, the spin–orbit (spin–spin) term for glueballs is effectively greater than those for the quarkonium case by a factor of 2 (4).

The functions $V_i(r)$ differ from those for heavy quarkonia [25] only in that the Casimir operators make them greater by a factor of 9/4; the corresponding expressions for $V_i(r)$ in terms of the correlation functions $D(x)$ and $D_1(x)$ [23] are given in Appendix 3. Both D and D_1 were measured on a lattice [27], and D_1 was found to be much smaller than D. Therefore, one can neglect the nonperturbative part of $V_3(r)$; that of V_4 also proves to be small numerically, $M_{SS}^{(\mathrm{nonpert})} < 30$ MeV, and we will also neglect it.

The only sizable spin-dependent nonperturbative contribution comes from the term dV_1/dr (Thomas precession) and can be written at large distances as

$$\Delta H_{\mathrm{Thom}} = -\frac{\sigma_{\mathrm{adj}}}{r}\frac{\mathbf{S}\cdot\mathbf{L}}{2\mu_0^2}. \tag{25}$$

We now come to the point of perturbative contributions to spin splittings. The simplest way to calculate those to order α_s (and this procedure is true for quarkonia) is to represent perturbative gluon exchanges by the same Eichten–Feinberg formulas (24), where only perturbative contributions to the correlation functions D and D_1 in (A.3.8)–(A.3.11) must be retained in $V_i(r)$; to order α_s, one then obtains

$$\frac{1}{r}\frac{dV_1^{(\mathrm{pert})}}{dr} = 0, \quad \frac{dV_2^{(\mathrm{pert})}}{dr} = \frac{C_2(\mathrm{adj})\alpha_s}{r^2}, \tag{26}$$

$$V_3^{(\mathrm{pert})} = \frac{3C_2(\mathrm{adj})\alpha_s}{r^3}, \tag{27}$$

$$V_4^{(\mathrm{pert})} = 8\pi C_2(\mathrm{adj})\alpha_s\delta^{(3)}(r). \tag{28}$$

However, this procedure must be corrected for glueballs since (i) valence and exchanged gluons are identical and (ii) there is a four-gluon vertex in addition. The corresponding calculations performed in [28] showed that corrections amount to multiplication in (26) by the factor of 3/4 and in (28) by the factor of 5/8.

With allowance for these corrections, the corresponding matrix elements in (21) are given by

$$M_{SL}^{(\mathrm{pert})} = \frac{3C_2(\mathrm{adj})}{4\mu_0^2}\left\langle\frac{\alpha_s}{r^3}\right\rangle, \tag{29}$$

$$M_{SS}^{(\mathrm{pert})} = \frac{5\pi C_2(\mathrm{adj})}{3\mu_0^2}\langle\alpha_s\delta^{(3)}(r)\rangle, \tag{30}$$

$$M_T^{(\mathrm{pert})} = \frac{C_2(\mathrm{adj})}{\mu_0^2}\left\langle\frac{\alpha_s}{r^3}[3(\mathbf{S}^{(1)}\cdot\mathbf{n})(\mathbf{S}^{(2)}\cdot\mathbf{n}) - \mathbf{S}^{(1)}\cdot\mathbf{S}^{(2)}]\right\rangle. \tag{31}$$

From (30), one can see that M_{SS} can be written as

$$M_{SS} = \frac{5\alpha_s}{4\mu_0^2}|R(0)|^2. \tag{32}$$

To make simple estimates, we will neglect, first, the interaction due to PGE between valence gluons. Indeed, we show in the next section that this interaction cannot be written as a Coulomb potential between adjoint charges, and comparison with perturbative BFKL Pomeron theory [12] shows that it is much weaker than the Coulomb potential. Neglecting this interaction altogether, one gets a lower bound on spin-dependent effects, since all matrix elements like $\langle\delta^{(3)}(r)\rangle$, $\langle 1/r\rangle$, and $\langle 1/r^3\rangle$ are enhanced by attractive Coulomb interaction.

For a purely linear potential, one has a simple relation independent of the radial quantum number n [29],

$$|\Psi(0)|^2 = \frac{|R(0)|^2}{4\pi} = \frac{\mu_0\langle V'(r)\rangle}{4\pi} = \frac{\mu_0\sigma_{\mathrm{adj}}}{4\pi}. \tag{33}$$

Using (33) and $M_0 = 4\mu_0$ and taking M_0 from Table 1, one obtains

$$M_{SS} = \frac{5\alpha_s\sigma_{\mathrm{adj}}}{M_0}; \tag{34}$$

for $n_r = 0$, 1 and $\alpha_s = 0.3$, the spin–spin splitting is

$$\begin{aligned} M_{SS}(n_r = 0) &= 0.3\ \mathrm{GeV}, \\ M_{SS}(n_r = 1) &= 0.20\ \mathrm{GeV}. \end{aligned} \tag{35}$$

For $M(0^{++})$ and $M(2^{++})$, one has the values given in Table 5 for $\sigma_{\mathrm{fund}} = 0.18$ GeV^2 and, for the sake of comparison with lattice calculations, in Table 6 for $\sigma_{\mathrm{fund}} = 0.228$ GeV^2 and $\alpha_s = 0.3$.

For $L > 0$, it is necessary to compute the spin corrections M_{SL} and M_T. First of all, the situation can be simplified by using the equation {it is derived in the same way as that followed in [29] to derive (33); for details, see Appendix 4}

$$L(L+1)\left\langle\frac{1}{r^3}\right\rangle = \frac{\mu_0}{2}\langle V'(r)\rangle. \tag{36}$$

For $V(r) = \sigma_{\mathrm{adj}}r$, both $M_{SL}^{(\mathrm{pert})}$ and $M_T^{(\mathrm{pert})}$ can easily be calculated; the results are listed in Table 7.

The nonperturbative part of spin splittings is due to the Thomas term, $(dV_1/dr + dV_2/dr)$, and is calculated numerically by using the exponential form of D and D_1 found on a lattice [27] (for details see [25]).

The resulting values for ΔM_{Thom} are given in Table 7. Combining all corrections and values of M_0 from

Table 7. Spin–orbit and tensor corrections (in GeV) to two-gluon glueball masses (upper entires are for $n = 0$ and lower entries are for $n = 1$; $\sigma_{\text{fund}} = 0.18$ GeV^2)

J^{PC}	$L = S = 1$		$L = S = 2$				
	0^{-+}	2^{-+}	0^{++}	1^{++}	2^{++}	3^{++}	4^{++}
$M_{SL}^{(\text{pert})} \cdot \mathbf{S} \cdot \mathbf{L}$	−0.197	−0.0985	−0.1656	−0.138	−0.083	0	0.110
	−0.148	0.074	−0.128	−0.107	−0.064	0	0.085
$M_T^{(\text{pert})}$	−0.263	0.0263	−0.072	−0.036	0.015	0.041	0.020
	−0.198	−0.02	−0.056	−0.028	0.0116	0.032	0.0155
$\Delta M_{\text{tot}}^{(\text{pert})}$	−0.46	0.072	−0.238	−0.174	−0.068	0.041	0.13
	−0.347	0.054	−0.185	−0.135	−0.053	0.032	0.101
$\Delta M_{\text{Thom}} \cdot \mathbf{S} \cdot \mathbf{L}$	0.082	−0.041	0.216	0.18	0.108	0	−0.144
	0.05	−0.025	0.138	0.115	0.07	0	−0.092
ΔM_{tot}	−0.38	0.031	−0.022	0.006	0.04	0.041	−0.014
	−0.3	0.029	−0.047	−0.02	0.017	0.032	0.009
$\langle S_{12} \rangle$	–2	–1/5	–2	–1	3/7	8/7	–4/7
$\langle \mathbf{L} \cdot \mathbf{S} \rangle$	–2	+1	–6	–5	–3	0	4

Tables 2 and 3, one obtains the glueball masses shown in Table 5 for $\sigma_{\text{fund}} = 0.18$ GeV^2 and compared with lattice data in Table 6 for $\sigma_{\text{fund}} = 0.228$ GeV^2.

One can see from Table 6 that the calculated spin splittings of the lowest levels are in good agreement with lattice data. This is another phenomenological manifestation of PGE suppression in the glueball system; indeed, had we taken PGE in the adjoint Coulomb form with $\alpha_s = 0.3$, we would have obtained a threefold increase in the spin splittings [18].

A general feature of the spin-dependent contribution ΔH_S is that it dies out very fast with growing orbital or radial quantum number, which can be seen in the appearance of the factor μ_0^2 in the denominator of (29)–(31).

From (8), one can indeed deduce that $M_0 \approx 4\mu_0$; therefore, we have $\Delta H_S \sim [1/M^2(n, L)]\langle O(1/r)\rangle$, where O stands for terms like const $\cdot$ $1/r$ or const' $\cdot$ $1/r^3$ (from perturbation theory). Hence, spin splittings of the radial recurrence of 0^{++}, 2^{++} or 0^{-+}, 2^{-+} states are expected to be smaller than the corresponding ground states. This feature is also well supported by the lattice data in Table 5.

4. PERTURBATIVE GLUON LADDERS AND GLUEBALLS

In many analytic calculations of glueball masses, it is postulated that there is a Coulomb-type interaction between valence gluons, which differs from the $q\bar{q}$ case by the Casimir factor, $C_2(\text{adj}) = 3$ instead of $C_2(\text{fund}) = 4/3$. Before going into the details of the question of how the PGEs give rise to the Coulomb kernel, we first assume here that this is indeed the case and correspondingly calculate the eigenvalues of the Hamiltonian

$$H = H_0' - \frac{C_2(\text{adj})\alpha_s}{r}, \tag{37}$$

where H_0' is given in (8). The resulting masses are listed in Table 8 (the first three lines) for $\alpha_s = 0$, 0.2, 0.3, 0.39.

One can see a drastic decrease in the mass due to the Coulomb attraction, especially for $L = 0$. For a conservative value of $\alpha_s = 0.3$, this mass drops down by 0.5 GeV.

This is much larger than in the $q\bar{q}$ case [13, 19], evidently owing to a large Casimir factor.

Other characteristics of the Coulomb shift, which are useful for a comparison with the perturbative Pomeron approach [12], are the Regge slope $\alpha_G'(0)$ and the Regge intercept $\alpha_G(0)$ of the glueball trajectory drawn as a straight line through the $L = 0(2^{++})$ and $L = 0(4^{++})$ glueballs.[3)] These values are given in the last two rows of Table 8 and show a drastic increase of $\Delta\alpha_G(0) \approx 0.64$ at $\alpha_s = 0.3$ in the intercept owing to Coulomb interaction.

This will be compared later in this section with a similar large shift of the perturbative Pomeron trajectory $\Delta\alpha_{\mathbf{P}}(0)$ in the lowest $O(\alpha_s)$ approximation [12] and with much smaller value of $\Delta\alpha_{\mathbf{P}}(0)$ in the next (one-loop) approximation [30]. This comparison casts more

[3)] This discussion is rather qualitative. Indeed, Coulomb interaction modifies linearity of nonperturbative glueball trajectories.

doubt on the validity of the assumption that the adjoint Coulomb interaction is present in the form (37).

A similar conclusion can be deduced from spin-averaged eigenvalues. For the Hamiltonian in (37), the eigenvalues are given in Table 8.

One can see that, for $L = 0$, both $\alpha_s = 0.3$ and 0.39 strongly contradict the data; this shows that the perturbative gluon ladder strongly differs from the adjoint Coulomb interaction; moreover, the overall agreement of our results for M_0 (where no Coulomb interaction is present) with spin-averaged lattice masses tells one that PGE is strongly reduced on a lattice.

To study this point in detail, one should consider the set of perturbative gluon exchanges and compare them with the BFKL diagrams describing the perturbative Pomeron [12].

First of all, one should inquire into the mechanism that produces color Coulomb interaction, and it is instructive to compare quark–antiquark and gluon–gluon systems from this point of view. For both systems, there are diagrams of gluon exchanges of order g^2; in addition, the gluon–gluon system is characterized by the presence of a contact-interaction diagram that is of the same order and which affects the hyperfine splitting [28].

The main point is whether and how these diagrams are summed up to produce the color Coulomb kernel in the exponent appearing in the Green's function of the system. For the $q\bar{q}$ system (spin degrees of freedom are neglected for simplicity of comparison), one has the exact Feynman–Schwinger representation (FSR)

$$G_{q\bar{q}} = \int ds d\bar{s} Dz D\bar{z} e^{-K-\bar{K}} \langle W(C_{z\bar{z}}) \rangle, \qquad (38)$$

where the Wilson loop is along the paths z and $\bar{z}$ integrated in (38). One can use a cluster expansion for purely perturbative gluons in $W(C)$ as was done, for example, in [13, 21],

$$\langle W(C) \rangle = \exp\left[-C_2 \frac{g^2}{2} \int\int_{C\,C} \frac{dz_\mu d\bar{z}_\mu}{(z-\bar{z})^2} + O(g^4) \right]. \qquad (39)$$

For straight-line trajectories $z(\tau)$ and $\bar{z}(\tau')$ (for example, for static quarks), the integral in the exponent in (39) readily yields the color Coulomb potential, $\langle W \rangle \sim \exp[(C_2 \alpha_s / r) t]$.

For light quarks, one can consider the integral in the exponent in (39) as the full-fledged relativistic Coulomb kernel. It is legitimate to retain this kernel, which is an $O(g^2)$ quantity, in the exponent and neglect $O(g^4)$ terms, provided that the Coulomb kernel yields some amplification. This is indeed true in the nonrelativistic region, where the Coulomb correction is of order α_s/u, $u \ll 1$, or at small distances (high energies), where this kernel yields double-logarithmic terms [31]. Let us now consider the gg system (the same is true a fortiori for the three-gluon system).

Table 8. Effect of the inclusion of Coulomb interactions on glueball masses (in GeV) and Regge parameters, $M(\alpha_s, L = 0, 1, 2)$, $\sigma_{\text{fund}} = 0.18\ \text{GeV}^2$

	$\alpha_s = 0$	0.2	0.3	0.39
$M_0(L = 0)$	2.11	1.776	1.587	1.390
$M_0(L = 1)$	2.77	2.56	2.45	2.36
$M_0(L = 2)$	3.30	3.14	3.05	2.97
$\alpha'_G(0)$	0.31	0.298	0.294	0.290
$\alpha_G(0)$	0.617	1.06	1.259	1.44

In (3), we have derived the gg Green's function for valence perturbative gluons in the nonperturbative background. A similarity of the forms in (3) and in (38) is only superficial, since the Wilson loop in (38) contains both perturbative and nonperturbative contributions, and one may argue that perturbative exchanges dominate at small distances and, hence, exponentiate as in (39), eventually arriving at the color Coulomb kernel.

In contrast to that, in (3), $\langle W_F \rangle$ contains only the nonperturbative fields B_μ, yielding a confining string between gluons, but no perturbative exchanges at all. Within background perturbation theory, the perturbative vertices $O(a^3)$ and $O(a^4)$ enter into the interaction Lagrangian, and there is a priori no guarantee that gluon exchanges produced by these vertices exponentiate to give a color Coulomb kernel. (Note that there is a difference between gluon exchanges and spin-dependent vertices considered in the preceding section, since the latter are taken as a perturbation in the lowest order, and there is no need for them to exponentiate to the Coulomb ladder.)

Having all this in mind, we proceed to consider the subset of graphs that are summed up in the BFKL approach [12] and distinguished by the principle of leading diagrams in high-energy scattering, or in another setting, by the summation of ladders for the leading Regge trajectory in the t channel. Since these ladders are dominant perturbative series (see [12]) for the Pomeron trajectory, we can consider the same contribution in our circumstances—in order to calculate glueball masses—extending, in this way, a BFKL-type analysis from Pomeron-generating glueballs (4^{++}, 2^{++}, etc.) to all others and bearing in mind that this may give only an order of magnitude estimate.

Thus, we now aim at estimating the contribution of the BFKL diagrams to the glueball masses (perturbative mass shift) and at comparing it with the usual color Coulomb contribution.

In order to estimate effects of small-distance contributions, we analyze these effects on gluonic Regge trajectories not from the glueball mass spectra at positive t, but for $t = 0$. Extensive calculations of the gluonic-Pomeron-trajectory intercept were performed in the leading-logarithm approximation [12], and α_s correc-

tions were calculated in [30]. It was shown that the leading Regge singularity corresponds to the sum of ladder-type diagrams, where exchanged gluons are Reggeized. In the leading approximation, the intercept of this singularity is [12]

$$\alpha_{\mathbf{P}}(0) = 1 + \alpha_s \frac{4N_c}{\pi} \ln 2. \quad (40)$$

The shift from the noninteracting-gluon point $\alpha_{\mathbf{P}}(0) = 1$ is equal to $\Delta = \alpha_{\mathbf{P}}(0) - 1 \approx 0.5$ for $\alpha_s \approx 0.2$. This rather large a shift is strongly reduced by α_s corrections [30]:

$$\Delta = \alpha_s \frac{12}{\pi} \ln 2 \times (1 - C\alpha_s). \quad (41)$$

The coefficient C is rather large (about 6.5), and the α_s correction strongly reduces Δ. Its value depends on the renormalization scheme and on the scale for α_s. In the "physical" (BLM) scheme, Δ values fall within the region 0.15–0.17 [30]. In this approximation, the leading gluonic singularity is a Regge pole, and we can estimate the mass shift for the lowest glueball state by using this result and by assuming that the slope $\alpha'_{\mathbf{P}} = 1/2\pi\sigma_{\text{adj}} \approx 0.4\ \text{GeV}^{-2}$ (11) will not be strongly modified by perturbative effects. Thus, one can expect that the characteristic shift due to perturbative effects in $\overline{M}^2$ ($L = 0$, $n_r = 0$) is $\delta\overline{M}^2 \approx \Delta/\alpha'_{\mathbf{P}} \approx 0.38$–$0.48\ \text{GeV}^2$. The corresponding shift in $\overline{M}$ ($L = 0$, $n_r = 0$) is $\delta\overline{M} \approx \delta\overline{M}^2/2\overline{M} \approx 0.1$ GeV. This shift should be compared with a much larger mass shift from the pure Coulomb interaction given in Table 8. Thus, the $O(\alpha_s)$ correction to the BFKL ladder gives a strong suppression of PGE series and may be a possible explanation why Coulomb-like attraction is seen neither in spin-averaged masses $\overline{M}(L, n_r)$ nor in spin splittings. It should be noted that this is only a rough estimate of the perturbative effects because higher orders of perturbation theory can modify this result.

5. THREE-GLUON GLUEBALLS

The three-gluon system can be considered in the same way as this was done for the two-gluon glueballs. The $3g$ Green's function $G^{(3g)}$ is obtained as the background-averaged product of three one-gluon Green's functions, in full analogy with (1). Assuming the large-N_c limit for the sake of simplicity and neglecting spin splittings and projection operators, one arrives at the path integral [compare with (3)]

$$G^{(3g)} = \text{const} \times \prod_{i=1}^{3} \int_0^\infty ds_i Dz^{(i)} e^{-K_i - \sigma S_i}, \quad (42)$$

where $\sigma \equiv \sigma_{\text{fund}}$, since every gluon is connected by a fundamental string with each of its neighbors.

Using, as before, the method from [13, 14] and the three-body treatment from [17], one obtains, omitting spin-dependent terms, the following Hamiltonian {we assume a symmetric solution with equal $\mu_i(\tau) \equiv \mu(\tau)$, $i = 1, 2, 3$ [no orbital excitations was assumed as in (8)}:

$$H^{(3g)} = \frac{\mathbf{p}_\eta^2 + \mathbf{p}_\xi^2}{2\mu} + \frac{3\mu}{2} + \sigma \sum_{i<j=1}^{3} r_{ij}. \quad (43)$$

Here, $r_{ij} = |\mathbf{r}_i - \mathbf{r}_j|$, $\mathbf{r}_i$ being the spatial coordinate of the ith gluon, while $\boldsymbol{\xi}$, $\mathbf{p}_\xi$, and $\boldsymbol{\eta}$, $\mathbf{p}_\eta$ are defined as

$$\boldsymbol{\xi} = \sqrt{\frac{3}{2}}\left(\frac{\mathbf{r}_1 + \mathbf{r}_2}{2} - \mathbf{r}_3\right), \quad \mathbf{p}_\xi = \frac{1}{i}\frac{\partial}{\partial\boldsymbol{\xi}},$$
$$\boldsymbol{\eta} = \frac{\mathbf{r}_1 - \mathbf{r}_2}{\sqrt{2}}, \quad \mathbf{p}_\eta = \frac{1}{i}\frac{\partial}{\partial\boldsymbol{\eta}}. \quad (44)$$

To simplify the treatment further, we will consider μ as a constant to be found from the extremum of eigenvalues, as in (8), which provided, in that case, a 5% increase in eigenvalues (see Table 3 of [19]), and we expect this in the case being considered as well.

In order to find the eigenvalues of $H^{(3g)}$, one can use the hyperspherical method introduced in [32] and applied to the $3q$ system in [17]. Defining the hyperradius ρ as $\rho^2 = \boldsymbol{\eta}^2 + \boldsymbol{\xi}^2$, one obtains a one-dimensional equation for the eigenfunction $\chi_n^K(\rho) \equiv \chi(\rho)$ (K is the grand orbital, $K = 0, 1, 2, \ldots$, and n is radial quantum number),

$$-\frac{1}{2\mu}\chi'' + U_{\text{eff}}(\rho)\chi(\rho) = M\chi(\rho), \quad (45)$$

where

$$U_{\text{eff}}(\rho) = \frac{1}{2\mu\rho^2}\left(K^2 + 4K + \frac{15}{4}\right) + \frac{32\sqrt{2}}{5\pi}\rho\sigma. \quad (46)$$

A solution to equation (45) is expressed in terms of generalized Airy functions.

A reliable (within a few percent accuracy) estimate of M is obtained by replacing $U_{\text{eff}}(\rho)$ by the oscillator well, with the center at the minimum of $U_{\text{eff}}(\rho)$, $\rho = \rho_0$, and frequency ω_0 expressed in terms of $U''_{\text{eff}}(\rho_0)$. At $K = 0$, we have

$$\rho_0 = \left(\frac{75\pi}{128\sqrt{2}\mu\sigma}\right)^{1/3}, \quad \omega_0 = \left(\frac{45}{4\mu^2\rho_0^4}\right)^{1/2}. \quad (47)$$

In this way, we obtain

$$M(\mu) = \frac{3\mu}{2} + 36\left(\frac{\sigma^2}{45\mu\pi^2}\right)^{1/3} + \frac{\omega_0}{2}, \quad (48)$$

and the minimization of $M(\mu)$ with respect to μ yields

$$\mu_0 \cong (1.6)^{1/4}\left(\frac{8\sigma}{3\pi}\right)^{1/2},$$
$$M(\mu_0) = 6\mu_0 + \frac{\omega_0}{2} = 6\mu_0 + \left(\frac{8}{5}\right)^{3/4}\left(\frac{3\sigma}{\pi}\right)^{1/2}. \quad (49)$$

For $\sigma = 0.18$ GeV^2, we obtain $\omega_0 = 1.18$ GeV and $\mu_0 = 0.44$ GeV; hence, the minimal eigenvalue is

$$M_0 = 3.23 \text{ GeV}. \quad (50)$$

This spin-averaged value is presented in Table 4. Radial excitations are given by the approximate equation

$$M_n = 6\mu_0 + \frac{\omega_0}{2} + n\omega_0, \quad n = 0, 1, 2\ldots. \quad (51)$$

Orbital excitations yield an increase in mass of

$$\Delta M^K \sim \frac{K^2 + 4K}{2\mu\rho_0^2}, \quad (52)$$

which, for the lowest excitation, yields

$$\Delta M^{K=1} \sim 1 \text{ GeV}, \quad (53)$$

which is almost identical to the mass shift for the radial excitation.

The Coulomb shift (if the Coulomb interaction existed between gluons) would be enormous: $\Delta M_{\text{Coul}} = -1.3$ GeV. Here, one can use, however, the same arguments as for two-gluon glueballs and discard the color Coulomb interaction between gluons altogether.

Finally, we address the question of quantum numbers and spin splittings for the $3g$ states. According to (27), perturbative hyperfine interaction is given by matrix elements

$$\Delta M_{SS} = \sum_{i>j}\left\langle \mathbf{S}_i\cdot\mathbf{S}_j\frac{5\pi C_2(\text{fund})}{3\mu_0^2}\alpha_s\delta^{(3)}(\mathbf{r}_{ij})\right\rangle. \quad (54)$$

We note that, in the large-N_c limit, gluon lines are replaced by double-fundamental lines and planar gluon exchanges occur with a fundamental charge; hence, the fundamental Casimir operator appears in (54).

For the $K = 0$ state, the wave function depends only on the hyperradius ρ, and we have

$$\langle\delta^{(3)}(\mathbf{r}_{ij})\rangle = \left\langle\frac{\sqrt{2}}{\pi^2\rho^3}\right\rangle. \quad (55)$$

Now, for $K = 0$ state, all internal angular momenta are zero, and we can express $\langle\mathbf{S}_i\cdot\mathbf{S}_j\rangle$ in terms of the total angular momentum J as

$$\langle\mathbf{S}_i\cdot\mathbf{S}_j\rangle = \frac{J(J+1)-6}{6}. \quad (56)$$

As a result, we find that, for $\alpha_s = 0.3$ and $\sigma = 0.18$ GeV^2, ΔM_{SS} is

$$\Delta M_{SS} \cong \frac{5\sqrt{2}C_2(\text{fund})\alpha_s}{\pi\mu_0^2\rho_0^3}\langle\mathbf{S}_i\cdot\mathbf{S}_j\rangle \approx 0.644\mu_0\frac{J(J+1)-6}{6}. \quad (57)$$

Hence, the candidate for the $J^{PC} = 3^{--}$ odderon state is shifted by 0.28 GeV upward, while 1^{--} is shifted by 0.189 GeV downward with respect to the result in (50). The resulting values of the glueball masses are listed in Tables 5 and 6.

6. GLUEBALL REGGE TRAJECTORIES AND POMERON

The leading Regge trajectory [with the largest intercept $\alpha_{\mathbf{P}}(0)$] is usually referred to as the Pomeron trajectory. It plays a special role in the Reggeon approach to high-energy hadronic interactions. The parameters of the Pomeron trajectory and especially its intercept play a fundamental role for asymptotic behavior of diffractive processes. We have already touched upon the Pomeron intercept problem in Section 4, where the perturbative, small-distance, contribution has been discussed. We will now consider this problem in more detail, taking into account both nonperturbative and perturbative contributions to Pomeron dynamics.

For the leading glueball trajectory ($n_r = 0$), the large-distance nonperturbative contribution gives, according to (12),

$$\alpha_{\mathbf{P}}(t) = -c_1 + \alpha'_{\mathbf{P}}t, \quad (58)$$

where $\alpha'_{\mathbf{P}} = 1/2\pi\sigma_{\text{adj}}$.

Taking into account the spins of "constituent" gluons, but neglecting small nonperturbative spin effects, we find for the intercept of the leading trajectory that

$$\alpha_{\mathbf{P}}(0) = -c_1 + 2, \quad (59)$$

which leads to $\alpha_{\mathbf{P}}(0) \approx 0.5$, and this value is substantially below the value found from the analysis of high-energy interactions, $\alpha_{\mathbf{P}}(0) = 1.1$–$1.2$ [20].

The perturbative (BFKL) contribution leads to an increase of 0.2 in the Pomeron intercept, as was explained in Section 4. The resulting value of $\alpha_{\mathbf{P}}(0) \approx 0.7$ is still far from the experimental value.

There are other nonperturbative sources that can lead to an increase in the Pomeron intercept. In our opinion, one of the most important ones is quark–gluon mixing or the inclusion of quark loops in the gluon "medium." In the $1/N_c$ expansion, the effect is proportional to N_f/N_c, where N_f is the number of light flavors, and this mixing is known to be of importance (at least in the small-t region).

In the leading approximation of the $1/N_c$ expansion, there are three Regge trajectories—planar $q\bar{q}$ trajecto-

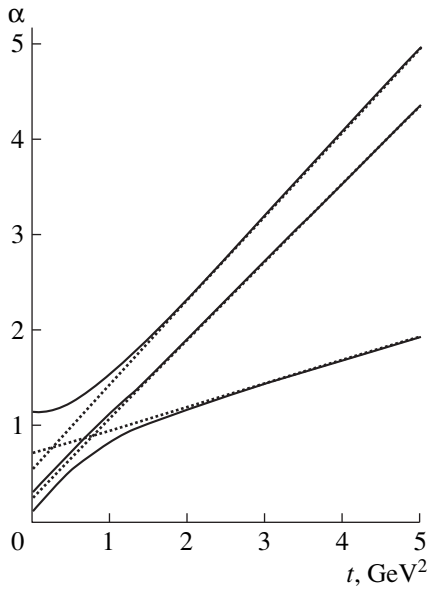

Fig. 1. Glueball, f, and f' Regge trajectories as functions of the t-channel energy squared t (in GeV^2). Dotted curves represent the bare trajectories, while the solid curves are the trajectories with the coupling $g_{ik}(t)$ taken into account in the form (A.5.7), with parameters $k = 1$ and $\lambda^2 = 2/3$ GeV^2.

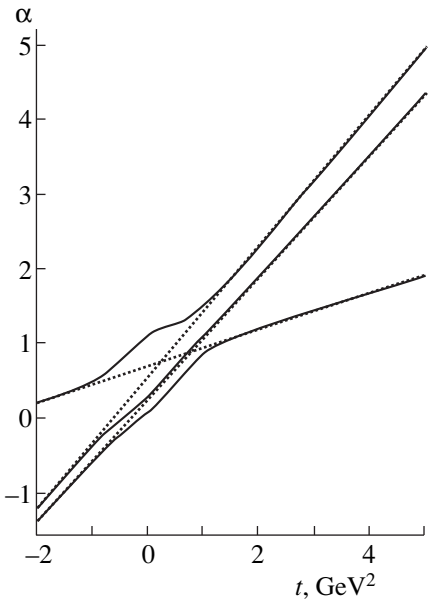

Fig. 2. As in Fig. 1, but for the coupling parameters $k = 2$ and $\lambda^2 = 2/3$ GeV^2.

ries [$f^{(0)}$ made of $u\bar{u}$ and $d\bar{d}$ quarks and $f'^{(0)}$ made of $s\bar{s}$ quarks) and purely gluonic trajectory, G. The transitions between quarks and gluons—their contributions are of order $1/N_c$—will lead to the mixing of all these trajectories. For want of calculations of these effects in QCD, we will consider them in a semiphenomenological manner. From the mixing of two trajectories 1 and 2 with the transition constant g_{12}, it is easy to obtain the following values for new trajectories (see, for example, [33]):

$$\alpha_\pm(t) = \frac{1}{2}[\alpha_1(t) + \alpha_2(t) \pm \sqrt{(\alpha_1(t) - \alpha_2(t))^2 + 4g_{12}^2(t)}]. \quad (60)$$

We note that, for the realistic case of G, f, and f' trajectories (Fig. 1), all three trajectories before mixing are close to one another in the small-t region. The trajectory of gluonium intersects the planar f and f' trajectories in the positive-t region ($t < 1$ GeV^2). In this region, mixing between trajectories plays an important role even for small coupling matrix $g_{ik}(t)$.

The dual-unitarization scheme [34–36] leads to the conclusion that the quantity g_{12}^2 decreases fast as t increases in the positive-t region. This means that, at large positive t, $\alpha_\pm(t)$ coincide with the trajectories α_1 and α_2, as this happens in (60) for $g_{12}^2 \ll |\alpha_1 - \alpha_2|$:

$$\alpha_+ \approx \alpha_1 + \frac{g_{12}^2}{\alpha_1 - \alpha_2}, \quad \alpha_- \approx \alpha_2 + \frac{g_{12}^2}{\alpha_2 - \alpha_1}. \quad (61)$$

This phenomenon is referred to as asymptotic planarity [36]. We note that mixing effects will be small in the large-t region even if the couplings have weak t dependence because the differences between planar and gluonic trajectories increase in proportion to t at large t.

For weak mixing between trajectories ($g_{ik}^2 \ll |\alpha_i^{(0)} - \alpha_k^{(0)}|$), relations (61) can be generalized as

$$\alpha_i \approx \alpha_i^{(0)} + \sum_k \frac{g_{ik}^2}{\alpha_i^{(0)} - \alpha_k^{(0)}}. \quad (62)$$

For $g_{ik}^2 \sim 0.1$, typical resulting trajectories are shown in Figs. 1 and 2 by solid lines (for details, see Appendix 5). The Pomeron trajectory is shifted to the values $\alpha_{\mathbf{P}}(0) \geq 1$. For $t > 1$ GeV^2, the Pomeron trajectory is very close to the planar f trajectory.

The position of the second vacuum trajectory for $t \leq 0$ is close to α_f, while, for $t > 1$ GeV^2, it is close to $\alpha_{f'}$. The third vacuum trajectory is below $\alpha_{f'}$ for $t \leq 0$; at $t > 1$ GeV^2, it is close to α_G. Owing to asymptotic planarity, mixing effects are not very important for the properties of physical particles on these trajectories, since all resonances are in the region $t > 1.5$ GeV^2. On the other hand, they are important for understanding $SU(3)$-breaking effects for the Pomeron-exchange amplitudes for $t \leq 0$.

At the end of this section, we consider the "odderon"—the leading Regge trajectory with negative signature and C parity. The mass of the lowest $3g$ glueball with spin–parity 3^{--} corresponding to this trajectory has been estimated in the preceding section and found

to be large ($\approx$3.51 GeV for $\sigma_{\text{fund}} = 0.18$ GeV^2), in accord with lattice data. The slope α'_{3g} of this trajectory must be equal to that of the gg trajectory;[4] thus, the intercept of the nonperturbative glueball "odderon" is very low: $\alpha_{3g}(0) \approx -1.5$. Mixing with $q\bar{q}$ trajectories (ω, φ) is much smaller than in the Pomeron case since there is no intersection of the odderon and (ω, φ) trajectories in the small-t region; therefore, the gluonic "odderon" is immaterial for high-energy phenomenology (at least, in the small-t region).

7. DISCUSSION AND CONCLUSIONS

The basic results of this study can be separated into two groups. In the first part, we have calculated the $2g$ and $3g$ glueball spectrum analytically and compared the resulting masses with lattice data, finding very good agreement. In the second part, the glueball Regge trajectories have been obtained, and their correspondence with the Pomeron and odderon has been discussed.

In what is concerned with the glueball spectrum, the spin-averaged results of Section 3 calculated for all states of $2g$ and $3g$ glueballs yield very good agreement between our results and spin-averaged lattice masses. We emphasize that our spectrum, in contrast to the majority of the existing theoretical models, contains no fitting parameters, and all masses are expressed in terms of the string tension σ, as this is done on a lattice as well.

This coincidence and the obvious smallness of the PGE interaction, which would have been very strong if it had been the adjoint Coulomb interaction due to the Casimir factor of three, have called for a more detailed investigation into the question of whether Coulomb interaction is indeed appropriate in the systems of valence gluons. The analysis performed in Section 4 has led us to the conclusion that the situation in the system of valence gluons is completely different from that in the system of valence quarks and that the perturbative gluon exchanges do not exponentiate into the Coulomb kernel for $2g$ and $3g$ systems, in contrast to what occurs in the $q\bar{q}$ and $3q$ systems.

This observation explains qualitatively the absence of strong Coulomb downward shifts of glueball masses and moderate spin splittings in lattice calculations. To make a quantitative estimate, we have considered the BFKL perturbative series for the Pomeron [12], including one-loop correction [30]. This series is not a Coulomb ladder, and, with allowance for corrections of next-to-leading order, it leads to a mass shift that is approximately three to four times smaller than that for the Coulomb interaction.

In contrast to Coulomb interaction, the spin splittings of glueball masses are obtained from the first perturbative correction calculated with nonperturbative wave functions. There is good agreement for spin splittings (within a few tens of MeV) between our calculations and lattice data, as is shown in Table 6.

The agreement implies that the main ingredient of glueball dynamics is the adjoint string (or two fundamental strings) occurring between gluons in the two-gluon glueballs and the triangle construction of fundamental strings in the $3g$ glueballs. String dynamics reveals that the glueball masses lie on the corresponding straight-line Regge trajectories having the Regge slope equal to 4/9 of that for meson trajectories. In other respects, the glueball trajectories are similar to the $q\bar{q}$ trajectories for massless quarks [13–16, 19, 24]: they are straight to a high precision and have daughter recurrences that are associated with radial excitations and which are also approximately straight lines.

In the last part of the article, we have used our knowledge of the glueball Regge trajectories for investigating the Pomeron singularity. The Pomeron, which yields an asymptotically dominant contribution at high energies, is of course a complicated object, which has some features associating it with the dominant glueball trajectory. First of all, Pomeron exchange has a cylindrical topology (which is supported by the multiplicity analysis [37]) similar to that of glueball amplitude—this becomes obvious when one replaces the adjoint string by the double-fundamental string.

The idea of the Pomeron as a two-gluon exchange amplitude has a long history [11] and was exploited in perturbative [12], nonperturbative [18], and hybrid [38] approaches. The purely perturbative approach has some difficulties of internal consistency both because of slow convergence of perturbative series [30] and because of sensitivity to large-distance contributions [39]. The latter suggests that nonperturbative effects may play a very important role in Pomeron dynamics, and our study demonstrates this. The character of nonperturbative trajectories is linear owing to string dynamics and to the absence of a mass-dimension parameter other than the string tension. Perturbative singularities in the j plane are not always poles and are certainly not linear trajectories.

Our discussion in the preceding sections has arrived at the conclusion that perturbative effects shift only slightly nonperturbative trajectories (increase of about 0.2 in the Regge intercept).

With all that, we have arrived at the Regge intercept of 0.7 for the leading Regge trajectory. This value differs considerably from the experimental Pomeron intercept of 1.07–1.2. And here comes an interesting observation made earlier in a slightly different context [33]: owing to the different slopes of the meson and glueball trajectories, they must intersect in the region $t < 1$ GeV^2. We have taken this fact into account in the three-pole model, where the constants of coupling

[4] The situation is analogous here to the case of $q\bar{q}$ (meson) and qqq (baryon) Regge trajectories, where the baryon trajectory displays the quark–diquark structure and, hence, the meson Regge slope [17].

between the *f*, *f*', and *G* channels are introduced phenomenologically.

The results shown in Fig. 1 demonstrate a dramatic change in the course of trajectories: the largest intercept increases by 0.5, reaching the physically reasonable value of 1.2.[5)]

Both nonperturbative (string dynamics, quark loops) and perturbative effects are important for obtaining $\alpha_{\mathbf{P}}(0) > 1$. It is impossible to separate "soft" and "hard" Pomerons, as is sometimes done in phenomenological studies of the high-energy interactions of hadrons and in the small-*x* physics of deep-inelastic scattering.

In the theory of a supercritical Pomeron with $\Delta \equiv \alpha_{\mathbf{P}}(0) - 1 > 0$, the corresponding multi-Pomeron exchanges are important at very high energies. They allow one to obtain scattering amplitudes that satisfy the condition of *s*-channel unitarity and the Froissart bound for the total interaction cross sections as $s \longrightarrow \infty$. From the viewpoint of $1/N_c$ expansion, multi-Pomeron exchanges contribute in the order $(1/N_c^2)^{2n}$, where *n* is the number of exchanged Pomerons, but they have a faster increase with energy ($\sim(s/s_0)^{n\Delta}$) than the pole term and must be resummed. This can be done by using Gribov's Reggeon diagram technique [40]. In practical applications of Reggeon theory to describing high-energy hadronic interactions, multi-Pomeron exchanges are of importance for a simultaneous description of the total interaction cross sections and multiparticle production (for an overview, see [41]).

Looking back to the structure of vacuum trajectories, we found that each of three new trajectories $\alpha_i(t)$ is now a mixture of *G*, *f*, and *f*', and only asymptotically at large *t* do they tend to the original trajectories. As can be seen from Fig. 1, the leading trajectory (with the largest intercept), which must be associated with the Pomeron, asymptotically tends to *f*; the second trajectory at positive *t* is close to *f*'; and the third trajectory asymptotically (at large *t*) coincides with *G*, while, at $t = 0$, it is below the first two trajectories. Thus, a rearrangement takes place: the *G* trajectory is shifted downward, while the *f* trajectory is lifted up and becomes the Pomeron.

One of immediate consequences of this rearrangement is a special pattern of the Pomeron couplings, which can be measured experimentally. While the *G* trajectory was flavor-blind, one can now calculate, owing to mixing, the couplings of the Pomeron to light quarks (via *f*), to strange quarks (via *f*'), and symmetrically to all flavors (via *G*).

[5)]We discuss here the "bare" Pomeron intercept, which is greater than the "effective" Pomeron intercept usually extracted from data on high-energy scattering. As was discussed in [41], the bare Pomeron characteristics are measured in small-*x* deep-inelastic-scattering experiments, which yield an intercept value around 1.2.

Mixing between gluons and $q\bar{q}$ pairs has another important aspect—it leads not only to shifts of $\mathrm{Re}\,\alpha_i(t)$ but also to the appearance of $\mathrm{Im}\,\alpha_G(t)$ and, as a consequence, to nonzero widths of resonances on glueball trajectories. They must be of the same size as the mass shift due to the mixing; therefore, they are expected to be not too large, $\Gamma_G \sim 100$ MeV.

The present study can be improved in several aspects. First, perturbative contributions to the glueball trajectory, including spin-dependent terms, must be studied more systematically. Second, analytic calculations of $g_{ik}(t)$ are necessary to make our theory complete. Finally, a detailed analysis of experimental implications of our results is needed. It is planned for a separate publication.

ACKNOWLEDGMENTS

The work of A.B. Kaidalov was supported in part by the Russian Foundation for Basic Research (project no. 98-02-17463) and by NATO (grant no. OUTR.LG 971390).

APPENDIX 1

Creation Operators for Glueball States

In this Appendix (see also Tables 9 and 10), we consider the operators $\Psi_k^{(\mathrm{in})}$ and $\Psi_k^{(\mathrm{out})}$ in (1), (A.2.16), and (A.2.17). These operators specify glueball states and their quantum numbers J^{PC}. One may consider local $\Psi(x, x)$ or nonlocal operators $\Psi(x, y)$ for two-gluon glueballs and corresponding operators for many-gluon glueballs, $\Psi(x^{(1)}, \ldots, x^{(n)})$. For the sake of simplicity, we list below only local versions, since nonlocal ones can be constructed with the aid of the parallel transporters $\Phi(x, y)$, as this is done in (A.2.16) and (A.2.17).

First, one can construct Ψ_k in a general form, not assuming separation of A_μ into background and valence parts, in just the same way as was done on a lattice. One then has the vectors $\mathbf{E}_a$ and $\mathbf{D}_a$; the pseudovector $\mathbf{B}_a$; and the color tensors δ_{ab}, f_{abc}, and d_{abc}. It is also necessary to consider that, under charge conjugation *C*, the following transformations hold:

$$CA_\mu C^{-1} \equiv A_\mu^C = -A_\mu^T,$$
$$CF_{\mu\nu}C^{-1} = -F_{\mu\nu}^T, \quad CD_\mu C^{-1} = -D_\mu^T. \tag{A.1.1}$$

Hence, one obtains the following list of states for the two-gluon glueballs (containing two field operators) and, due to Bose statistics, symmetry with respect to exchange of all coordinates of two gluons. We also list the dimensions of the corresponding operator in the first columns of Tables 9 and 10.

In the background perturbation theory (BPT), $\Psi^{(\mathrm{in})}$ and $\Psi^{(\mathrm{out})}$ can be constructed from the special components of the gluonic field a_i, $i = 1, 2, 3$, since the fourth

Table 9. Two-gluon glueball operators

Dimension	J^{PC}	$\Psi^{(in)}$, $\Psi^{(out)}$	$\Psi^{(in),(out)}$ in BPT
4	0^{++}	$\mathrm{tr}(E_iE_i)$	$\mathrm{tr}(a_ia_i)$
4	2^{++}	$\mathrm{symm}_{(ik)}\mathrm{tr}(E_iE_k)$	$\mathrm{symm}_{(ik)}\mathrm{tr}(a_ia_k)$
4	0^{-+}	$\mathrm{tr}(E_iB_i)$	$\mathrm{tr}(a_i(\mathbf{D}\times\mathbf{a})_i)$
4	1^{-+}	$\mathrm{tr}(\mathbf{E}\times\mathbf{B})$	$\mathrm{tr}(\mathbf{a}\times(\mathbf{D}\times\mathbf{a}))$
4	2^{-+}	$\mathrm{symm}_{(ik)}\mathrm{tr}(E_iB_k)$	$\mathrm{symm}_{(ik)}\mathrm{tr}(a_i(\mathbf{D}\times\mathbf{a})_k)$
4	0^{++}	$\mathrm{tr}(B_iB_i)$	$\mathrm{tr}((\mathbf{D}\times\mathbf{a})\cdot(\mathbf{D}\times\mathbf{a}))$
4	2^{++}	$\mathrm{symm}_{(ik)}\mathrm{tr}(B_iB_k)$	$\mathrm{symm}_{(ik)}\mathrm{tr}((\mathbf{D}\times\mathbf{a})_i\cdot(\mathbf{D}\times\mathbf{a})_k)$
6	3^{++}	$\mathrm{symm}_{(klm)}\mathrm{tr}(D_4E_kD_lB_m + D_4B_mD_lE_k)$	$\mathrm{symm}_{(ikl)}\mathrm{tr}((\mathbf{D}\times\mathbf{a})_iD_ka_l)$
6	4^{++}	$\mathrm{symm}_{(iklm)}\mathrm{tr}(D_iE_kD_lE_m)$	$\mathrm{symm}_{(iklm)}\mathrm{tr}(D_ia_kD_la_m)$

Table 10. Three-gluon glueball operators

Dimension	J^{PC}	$\Psi^{(in)}$, $\Psi^{(out)}$	$\Psi^{(in),(out)}$ in BPT	L
6	1^{+-}	$\mathrm{tr}(\{E_k, E_l\}B_l)$	$\mathrm{tr}(\{a_ka_l\}(\mathbf{D}\times\mathbf{a})_l)$	1
6	3^{+-}	$\mathrm{symm}_{(klm)}\mathrm{tr}(\{E_k, E_l\}B_m)$	$\mathrm{symm}_{(klm)}\mathrm{tr}(\{a_k, a_l\}(\mathbf{D}\times\mathbf{a})_m)$	1
6	2^{+-}	$\mathrm{symm}_{(kn)}e_{nlm}\mathrm{tr}(\{E_k, E_l\}B_m)$	$\mathrm{symm}_{(kn)}e_{nlm}\mathrm{tr}(\{a_k, a_l\}(\mathbf{D}\times\mathbf{a})_m)$	1
6	1^{--}	$\mathrm{tr}(E_iE_kE_k)$	$\mathrm{tr}(a_ia_ka_k)$	0
6	3^{--}	$\mathrm{symm}_{(klm)}\mathrm{tr}(E_kE_lE_m)$	$\mathrm{symm}_{(klm)}\mathrm{tr}(a_ka_la_m)$	0

component a_4 can be expressed in terms of the background gauge condition $D_\mu a_\mu = 0$. Note that a_i transforms homogeneously [see equation (A.2.4) of Appendix 2]; therefore, one obtains gauge-invariant combinations for $\Psi^{(in)}$ and $\Psi^{(out)}$, replacing E_i in the third columns of Tables 9 and 10 by a_i, whereas J^{PC} does not change. In the same way, B_k is replaced by $(\mathbf{D}\times\mathbf{a})_k$, and one obtains the fourth columns of Tables 9 and 10. The dimension of BPT operators is given in the fifth column, and the orbital-angular-momentum values can be found in the last column.

For the three-gluon glueballs, the corresponding entries are given in Table 10. One should notice that the C parity of all listed states is negative here. Again, the dimensions of BPT operators is given in the last column.

As can be seen from the results of our calculations in Tables 4–6, the glueball spectrum is in good agreement with the hierarchy associated with increasing orbital angular momentum L or increasing BPT dimension (they differ by two units for two-gluon glueballs). The same ordering persists in lattice data. The masses of three-gluon glueball are typically shifted by 1.5–2 GeV (an exception of 1^{+-} and 3^{+-} states in lattice data waits for explanation). Note the absence of $J = 1^{++}$ states in the lattice spectrum. From Table 9, one can see the only candidate, 1^{-+}, but the corresponding local operator is proportional to the energy–momentum tensor and, by the arguments of [42], the residue of this state must vanish.

In Tables 9 and 10, we have used the notation

$$\mathrm{symm}_{(ik)}T_{ik} = T_{ik} + T_{ki} - \frac{2}{3}\delta_{ik}T_{ll}.$$

Symmetrization of the higher operators T_{ikl} and T_{iklm} is performed in a usual way to construct irreducible $O(3)$ tensors.

APPENDIX 2

Glueball Green's Function and Hamiltonian in the Background Formalism

In what follows, the Euclidean spacetime is used.

The total gluonic field A_μ is split into a nonperturbative background B_μ and a valence (perturbative) gluon field a_μ,

$$A_\mu = B_\mu + a_\mu. \tag{A.2.1}$$

The QCD partition function $Z(J)$,

$$Z(J) = \frac{1}{N}\int \exp[-S_E(A) + \int J_\mu(x)A_\mu(x)d^4x]DAD\psi D\bar{\psi}, \tag{A.2.2}$$

where S_E is the Euclidean action functional, can be rewritten by using the 't Hooft identity as

$$Z(J) = \frac{1}{N'}\int DB\eta(B)\exp\Big(\int JBd^4x\Big) \times \int DaD\psi D\bar{\psi}\exp[-S_E(B+a) + \int Jad^4x]. \tag{A.2.3}$$

Here, $\eta(B)$ is (an arbitrary) weight of integration over background fields B_μ; its exact form is of no interest to us, since the overall effect of background fields will enter into our results via the string tension σ and (in some corrections) as a nonperturbative field correlation function $\langle F(x)F(y)\rangle$. The two quantities are considered as inputs.

In what follows, we will expand (A.2.4) in powers of ga_μ as this is usually done in background perturbation theory [21, 43]. In the lowest order of $1/N_c$ expansion, quarks are decoupled from gluons, and we will neglect coupling to quarks till the last two sections of our article.

It is convenient to prescribe the gauge transformations

$$a_\mu \longrightarrow U^+ a_\mu U, \tag{A.2.4}$$

$$B_\mu \longrightarrow U\left(B_\mu + \frac{i}{g}\partial_\mu\right)U \tag{A.2.5}$$

and to impose on a_μ the background gauge condition

$$D_\mu a_\mu^a = \partial_\mu a_\mu^a + g f^{abc} B_\mu^b a_\mu^c = 0. \tag{A.2.6}$$

In this case, ghost fields have to be introduced, and one can write the resulting partition function as

$$Z(J) = \frac{1}{N'}\int DB\eta(B)\exp\left(\int J_\mu B_\mu d^4x\right)Z(J, B), \tag{A.2.7}$$

where

$$Z(J, B) = \int Da \det\left(\frac{\delta G^a}{\delta\omega^b}\right) \times \exp\left(\int d^4x\left[L(a) - \frac{1}{2}(G^a)^2 + J_\mu^a a_\mu^a\right]\right), \tag{A.2.8}$$

with

$$L(a) = L_0 + L_1(a) + L_2(a) + L_{\rm int}(a),$$

$$L_2(a) = \frac{1}{2}a_\nu(\hat{D}_\lambda^2\delta_{\mu\nu} - \hat{D}_\mu\hat{D}_\nu + ig\hat{F}_{\mu\nu})a_\mu$$

$$= \frac{1}{2}a_\nu^c[D_\lambda^{ca}D_\lambda^{ad}\delta_{\mu\nu} - D_\mu^{ca}D_\nu^{ad} - g f^{cad}F_{\mu\nu}^a]a_\mu^d, \tag{A.2.9}$$

$$D_\lambda^{ca} = \partial_\lambda\delta_{ca} + g f^{cda}B_\lambda^d \equiv \hat{D}_\lambda,$$

$$L_0 = -\frac{1}{4}(F_{\mu\nu}^a(B))^2, \quad L_1 = a_\nu^c D_\mu^{ca}(B)F_{\mu\nu}^a,$$

$$L_{\rm int} = -\frac{1}{2}(D_\mu(B)a_\nu - D_\nu(B)a_\mu)^a g f^{abc}a_\mu^b a_\nu^c - \frac{1}{4}g^2 f^{abc}a_\mu^b a_\nu^c f^{aef}a_\mu^e a_\nu^f. \tag{A.2.10}$$

The background gauge condition is written as

$$G^a = \partial_\mu a_\mu^a + g f^{abc}B_\mu^b a_\mu^c = (D_\mu a_\mu)^a, \tag{A.2.11}$$

and the ghost vertex [21, 43] is found from $\frac{\delta G^a}{\delta\omega^b}(D_\mu(B)D_\mu(B + a))_{ab}$ to be

$$L_{\rm ghost} = -\theta_a^+(D_\mu(B)D_\mu(B + a))_{ab}\theta_b. \tag{A.2.12}$$

The linear part of the Lagrangian, L_1, vanishes if B_μ satisfies classical equations of motion.

We can now identify the a_μ propagator from the quadratic terms in Lagrangian $L_2(a) - \frac{1}{2\xi}(G^a)^2$:

$$G_{\mu\nu}^{ab} = \left[\hat{D}_\lambda^2\delta_{\mu\nu} - \hat{D}_\mu\hat{D}_\nu + ig\hat{F}_{\mu\nu} + \frac{1}{\xi}\hat{D}_\nu\hat{D}_\mu\right]_{ab}^{-1}. \tag{A.2.13}$$

It will be convenient sometimes to choose $\xi = 1$ and end up with the well-known form of propagator in—what one would call—the background Feynman gauge:

$$G_{\mu\nu}^{ab} = [\hat{D}_\lambda^2\delta_{\mu\nu} + 2ig\hat{F}_{\mu\nu}]_{ab}^{-1}. \tag{A.2.14}$$

We are interested in the glueball Green's function and must therefore define first the initial- and final-state vectors of glueballs, consisting of n_i valence gluons in the initial and of n_f gluons in the final state. The following general nonlocal state vectors can be used for k gluons:

$$\Psi_k(x^{(0)}, \ldots, x^{(k-1)}) = {\rm tr}[f_0(a(x^{(0)}))\phi(x^{(0)}, x^{(1)})f_1(a(x^{(1)})), \ldots \ldots, f_{k-1}(a(x^{(k-1)}))\phi(x^{(k-1)}, x^{(0)})]. \tag{A.2.15}$$

Here,

$$\phi(x, y) = P\exp\left(ig\int_y^x B_\mu(z)dz_\mu\right)$$

is a parallel transporter; all a_μ are in the fundamental representation; and $f(a)$ is a polynomial in a_μ, which may contain derivatives in the form of $D_\mu \equiv \partial_\mu - igB_\mu$.

According to (A.2.4) and (A.2.5), Ψ_k are color singlets. One can also have a local form of Ψ_k, taking all $x^{(i)}$ at one point. The exact form of Ψ_k is given in Appendix 1.

As will be seen below, the state in (A.2.15) will evolve as a closed fundamental string with k gluons "sitting" on the string when all f_i are linear (and more gluons when some f_i have larger power). This form of initial and final states is convenient for multigluon glueballs and is used for three-gluon glueballs in Section 5.

Another form of Ψ_k (equivalence to the preceding one in the limit $N_c \longrightarrow \infty$) is obtained when one takes the adjoint string. By way of example, we indicate that, for two-gluon glueballs, the corresponding state vector then has the form

$$\hat{\Psi}_2(x^{(1)}, x^{(2)}) = \hat{\mathrm{tr}}[\hat{a}_\mu(x^{(1)}\hat{\phi}(x^{(1)}, x^{(2)})\hat{a}_\nu(x^{(2)})]. \quad \text{(A.2.16)}$$

Here, hats denote the adjoint representation. For two-gluon glueballs, we use (A.2.17) for the initial and final states, and the corresponding Green's function describes the evolution of the open adjoint string with adjoint charges (gluons) at the ends.

It can be calculated by using (A.2.4) in the form given by equation (1) in the main body of the text, where we neglect terms $L_1(a)$ and $L_{\mathrm{int}}(a)$ (the first gives an insignificant correction discussed in [21], while L_{int} contains higher powers of ga_μ and will be used to calculate perturbative corrections to the Green's function).

The next step is the FSR [13, 14] for the gluon Green's function (A.2.15), which allows us to exponentiate B_μ and $\hat{F}_{\mu\nu}$ as

$$G_{\mu\nu}(x, y) = \mathrm{const} \cdot \int_{-\infty}^{\infty} dsDze^{-K}P_BP_F \times \exp\left[ig\int_y^x \hat{B}_\mu dz_\mu + 2ig\int_0^s \hat{F}(z(\tau))d\tau\right]. \quad \text{(A.2.17)}$$

Substituting (A.2.17) into (1) and using the fact that ordering inversion for one of the gluons yields ($-\hat{B}_\mu^T$, $-\hat{F}^T$) instead of $\hat{B}_\mu$ and $\hat{F}$ leads to equations (3) and (4) of the main body of the text.

Equation (3) [(4)] is another form of equation (1), [(2)] and involves no approximations [with the exception of the omission of L_1 and L_{int}, which was discussed above and which was used in writing (1) and (2)].

Another important step made first in [13, 16] and developed in [14, 15] consists in introducing the auxiliary function $\mu(\tau)$, which may be called the einbein and which plays a crucial role of effective gluon mass in the whole formalism. This is done rigorously and without introducing arbitrary fitting parameters, in contrast to usual potential models.

Defining

$$2\mu(t) = dt/d\tau, \quad t \equiv z_4, \quad \text{(A.2.18)}$$

where τ or s is the Schwinger proper time, and t is the Euclidean time at any point of trajectory $z_\mu(\tau)$, one can identically rewrite FSR (3) as

$$G_{\mu\nu,\,\mu'\nu'}(x, y|x', y') = \mathrm{const} \cdot \int D\mu(t)D\mu(t')Dz_iDz_k'e^{-K-K'}\langle W_F\rangle, \quad \text{(A.2.19)}$$

where Dz_i (or Dz_k') is three-dimensional path integrals over the trajectories $z_i(t)$ [or $z_k'(t')$], $i, k = 1, 2, 3$, and $D\mu(t)$ is the one-dimensional path integral over the functions $\mu(t)$. The kinetic terms K and K' can be expressed in terms of $\mu(t)$, for example,

$$K = \int_0^T \frac{\mu(t)}{2}[(\dot{z}_i(t))^2 + 1]dt, \quad T = x_4 - y_4, \quad \text{(A.2.20)}$$

where an overdot denotes a time derivative. The form (A.2.20) resembles a nonrelativistic kinetic energy, but it is an exact relativistic form. In the case of a massive relativistic particle with mass m, the corresponding term in the action functional, K_m, has the form

$$K_m = \int_0^T \left(\frac{m^2}{2\mu(t)} + \frac{\mu(t)}{2}[(\dot{z}_i(t))^2 + 1]\right)dt. \quad \text{(A.2.21)}$$

Introducing the momentum $p_i = \partial K_m/\partial \dot{z}_i(t)$, one would obtain, after extremization with respect to $\mu(t)$, the usual result for the Hamiltonian:

$$H_0 = \sqrt{p_i^2 + m^2}. \quad \text{(A.2.22)}$$

In case of zero mass, $m = 0$, one would obtain, from (A.2.21), the free Hamiltonian $\sqrt{\mathbf{p}^2}$ for a free gluon without spin.

The nonperturbative interaction in the two-gluon system is given by (4), where the term $\int B_\mu dz_\mu$ generates the adjoint string [see equation (5)]; upon introducing another einbein function $\nu(t)$, as was done in [14], one obtains the Hamiltonian given by (6). The latter describes the straight-line adjoint string that connects two gluons and which can rotate and change its length.

The contribution of nonperturbative spin terms is considered in Appendix 3.

APPENDIX 3

Nonperturbative Spin-Splitting Terms

Introducing the spin matrix of the gluon as in (22) and using (A.2.18), one can rewrite the terms $\hat{F}$ in the exponential on the right-hand side of (4) as

$$2g\int (SF(t))\frac{dt}{2\mu(t)} - 2g\int (S'F(t'))\frac{dt'}{2\mu(t')}, \quad \text{(A.3.1)}$$

where $(SF) \equiv S_iB_i + \tilde{S}_iE_i \equiv S_{\mu\nu}F_{\mu\nu}$. Note that the contribution of the second (primed) gluon to (A.3.1) has an opposite sign in relation to that of the first gluon. This is a consequence of the fact that color and time ordering of operators B and F, on one hand, and B' and F', on the other hand, are opposite in the closed loop W_F. One must therefore use, in W_F, the transposed operators for the second (or the first) gluon and write $B'^T = -B'$.

To calculate the average of the exponential in (4), one can use the following trick: by using the non-Abe-

lian Stokes theorem and cluster expansion in the Gaussian approximation, one rewrites Wilson loop integral as

$$\langle W_{\rm adj}\rangle = \mathrm{tr}\,P_F\left\langle \exp\left\{ig\int_s F_{\mu\nu}(u)d\sigma_{\mu\nu}(u)\right\}\right\rangle = \exp\left[-\frac{g^2}{2}\iint_{s\,s}\langle F_{\mu\nu}F_{\lambda\sigma}\rangle d\sigma_{\mu\nu}d\sigma_{\lambda\sigma}\right]. \quad \text{(A.3.2)}$$

Expression (4) can then be recast into the form

$$\langle W_F\rangle = \mathrm{tr}\exp\left[-2i\int_0^T\frac{dt}{2\mu(t)}S_{\mu\nu}\frac{\delta}{\delta\sigma_{\mu\nu}(u)} + 2i\int_0^T\frac{dt'}{2\mu(t')}S'_{\mu\nu}\frac{\delta}{\delta\sigma_{\mu\nu}(u)}\right]\langle W_{\rm adj}\rangle. \quad \text{(A.3.3)}$$

Evaluating derivatives, one arrives at the expression, based on the Gaussian approximation,

$$\langle W_F\rangle = \mathrm{tr}\exp\left\{-\frac{g^2}{2}\iint\left[d\sigma_{\mu\nu}(u) - 2iS_{\mu\nu}\frac{dt}{2\mu(t)}\right] \times\left[d\sigma_{\lambda\sigma}(u') + 2iS'_{\lambda\sigma}\frac{dt'}{2\mu(t')}\right]\langle F_{\mu\nu}(u)F_{\lambda\sigma}(u')\rangle\right\}. \quad \text{(A.3.4)}$$

We can supplement the exponent in (A.3.2) with all higher correlation functions in spin-independent terms, thereby recovering the area law (5) with exact $\sigma_{\rm adj}$ (that is, beyond the Gaussian approximation). For spin-dependent terms, higher correlation functions bring about higher powers of S and S'.

Since spin-dependent terms are relatively small corrections, it is legitimate to retain the lowest (Gaussian) approximation for them and write

$$\langle W_F\rangle \approx Z\,\mathrm{tr}\exp(-\sigma_{\rm adj}S_{\rm min})\exp(N_1 + N_2 + N_{12}), \quad \text{(A.3.5)}$$

where the notation used is

$$N_1 = ig^2\iint d\sigma_{\lambda\sigma}(u)S_{\mu\nu}\frac{dt}{2\mu(t)}\langle F_{\mu\nu}(u)F_{\lambda\sigma}(\omega(t))\rangle, \quad \text{(A.3.6)}$$

$$N_{12} = 2g^2\iint\frac{dt}{2\mu(t)}\frac{dt'}{2\mu(t')}S_{\mu\nu}S'_{\lambda\sigma}\langle F_{\mu\nu}(u(t))F_{\lambda\sigma}(u'(t'))\rangle. \quad \text{(A.3.7)}$$

Here, N_2 is obtained from N_1 by means of the substitution $t \longrightarrow t'$.

The transformations in (A.3.6) and (A.3.7) into the spin–orbit, spin–spin, and tensor terms in (24) are identical to those in the corresponding heavy-quarkonium expressions given in [25], which are similar to (A.3.6) and (A.3.7) modulo numerical coefficients and different gluon spin factors.

The field correlation functions $\langle FF\rangle$ appear in the final expression via the potentials $V_i(r)$ (i = 1, 2, 3, 4), which are identical to those for heavy quarkonia and which are given in [25], with the substitution $C_2(\mathrm{fund}) \longrightarrow C_2(\mathrm{adj})$. If one introduces two scalar functions D and D_1, as in [23], one can write

$$\frac{1}{R}\frac{dV_1}{dR} = -\int_{-\infty}^{\infty}d\nu\int_0^R\frac{d\lambda}{R}\left(1-\frac{\lambda}{R}\right)D(\lambda,\nu), \quad \text{(A.3.8)}$$

$$\frac{1}{R}\frac{dV_2}{dR} = \int_{-\infty}^{\infty}d\nu\int_0^R\frac{\lambda d\lambda}{R^2}\left[D(\lambda,\nu) + D_1(\lambda,\nu) + \lambda^2\frac{\partial D_1}{\partial\lambda^2}\right], \quad \text{(A.3.9)}$$

$$V_3 = -\int_{-\infty}^{\infty}d\nu R^2\frac{\partial D_1(R,\nu)}{\partial R^2}, \quad \text{(A.3.10)}$$

$$V_4 = \int_{-\infty}^{\infty}d\nu\left[3D(R,\nu) + 3D_1(R,\nu) + R^2\frac{\partial D_1}{\partial R^2}\right]. \quad \text{(A.3.11)}$$

Note that $D = \dfrac{C_2(\mathrm{adj})}{C_2(\mathrm{fund})}D^{\rm fund}$ and that the same relation holds for D_1, where $D^{\rm fund}$ and $D_1^{\rm fund}$ refer to the fundamental representation. The normalization of D can be obtained from the relation

$$\sigma_{\rm adj}^{(2)} = \frac{1}{2}\int d^2xD(x), \quad \text{(A.3.12)}$$

where the superscript (2) on $\sigma_{\rm adj}$ denotes the lowest (quadratic) correlation-function contribution to the string tension. As one can argue, the accuracy of this quadratic approximation is around 10% [23].

Taking asymptotically large R in (A.3.8) and using (A.3.12), one obtains the asymptotic expression in (25), given in the main body of the text.

To evaluate the nonperturbative spin–orbit splitting, we must estimate the matrix element $\langle V_1' + V_2'\rangle$—that is, some integrals with D and D_1. The latter have been measured on a lattice [27] and found to be of an exponential form,

$$D(x) = D(0)\exp(-x\delta), \quad D_1(x) \ll D(x), \quad \text{(A.3.13)}$$

with $\delta \approx 1$ GeV. To estimate $\langle V_1' + V_2'\rangle$, we neglect D_1 and calculate

$$\langle V_1' + V_2'\rangle = \frac{2\sigma_{\rm adj}}{\pi}\left(2\left[-J_1(x) + \frac{2-x^2K_2(x)}{x}\right] + J_2(x)\right), \quad \text{(A.3.14)}$$

where $J_n(x)$ and $K_n(x)$ are Bessel and Macdonald functions, respectively, and where $x = \delta r$.

From (A.3.14), one can see that asymptotic behavior in (25) is obtained only for $r > 7\delta^{-1} \sim 1.5$ fm. Therefore, the average of ΔH_{Thom} with the square of the glueball eigenfunction is considerably reduced in relation to the average of the asymptotic expression in (25), and the resulting nonperturbative spin–orbit term given in Table 7 is smaller than the corresponding perturbative term; therefore, the ordering of the levels is due to the perturbative part of the spin-dependent forces.

APPENDIX 4

Derivation of the Relation for the Matrix Element $\langle r^{-3}\rangle$

Writing the solution to the Hamiltonian H_0' [see equation (8)] in the form

$$\psi_n(r) = \frac{y_n(r)}{r}Y_{lm}, \quad y_n(r) \sim r^{l+1}, \quad r \longrightarrow 0, \quad \text{(A.4.1)}$$

we arrive at the equation

$$y_n'' = \left[2\tilde{\mu}(V(r) - E_n) + \frac{L(L+1)}{r^2}\right]y_n(r). \quad \text{(A.4.2)}$$

We will use the procedure proposed in the second reference quoted in [29]. Multiplying both sides of (A.4.2) by $y_n'(r)/4\pi r^2$ and performing three-dimensional integration with respect to d^3r, we obtain

$$\int d^3r\frac{y_n''y_n'}{4\pi r^2} = -\frac{1}{2}[y_n'(0)]^2$$

$$= \int_0^\infty dr\left[2\tilde{\mu}(V(r) - E_n) + \frac{L(L+1)}{r^2}\right]\frac{y_n^2(r)}{2} \quad \text{(A.4.3)}$$

$$= -\frac{1}{2}\int_0^\infty y_n^2(r)dr\left[2\tilde{\mu}V'(r) - 2\frac{L(L+1)}{r^3}\right].$$

Taking into account (A.4.1), we have two results:

for $L = 0$, we obtain the well-known relation [29]

$$|\psi_n(0)|^2 = \frac{\tilde{\mu}}{2\pi}\langle V'(r)\rangle; \quad \text{(A.4.4)}$$

for $L > 0$, we have

$$L(L+1)\left\langle\frac{1}{r^3}\right\rangle = \tilde{\mu}\langle V'(r)\rangle. \quad \text{(A.4.5)}$$

In our case specified by (8), $\mu_0 = 2\tilde{\mu}$ and $V'(r) = \sigma_{\text{adj}}$. Note that the left-hand sides in (A.4.4) and in (A.4.5) are both independent of the radial quantum number n.

APPENDIX 5

Mixing of Glueball and f and f' Trajectories

We can begin by considering the amplitude of the scattering of hadron a on hadron b in the Regge pole approximation. We have

$$T^{(ab)} = \sum_{i,k} g_i^{(aa)}T_{ik}g_k^{(bb)}, \quad \text{(A.5.1)}$$

where $i, k = 1, 2, 3$ refer to the bare Regge trajectories

$$j = \bar{\alpha}_i(t), \quad i = 1, 2, 3, \quad \text{(A.5.2)}$$

while the matrix T_{ik} has the form

$$T_{ik} = (j - \hat{\alpha}t - \hat{g}(t))_{ik}^{-1}. \quad \text{(A.5.3)}$$

Here, we have used the notation

$$(\hat{\alpha}(t))_{ik} = \bar{\alpha}_i(t)\delta_{ik},$$
$$(\hat{g}(t))_{ik} = g_{ik}(t), \quad g_{ll} = 0. \quad \text{(A.5.4)}$$

The nondiagonal matrix $\hat{g}(t)$ describes the mixing of Regge trajectories. In what follows, we consider three bare trajectories. In particular, $\bar{\alpha}_1(t)$ is the glueball trajectory calculated in Section 6. We approximate it in the region $0 \le t \le 6$ GeV^2 by the linear form

$$\bar{\alpha}_1(t) = \bar{\alpha}_1(0) + \bar{\alpha}_1'(0)t = 0.7 + 0.246t, \quad \text{(A.5.5)}$$

where the value for $\bar{\alpha}_1'(0)$ is chosen in such a way as to reproduce the first glueball 2^{++} state at $M = 2.3$ GeV (Table 5).

The bare f and f' trajectories are denoted by $\bar{\alpha}_2(t)$ and $\bar{\alpha}_3(t)$, respectively, and are taken in the form

$$\bar{\alpha}_2(t) = 0.55 + 0.89t, \quad \bar{\alpha}_3(t) = 0.25 + 0.83t. \quad \text{(A.5.6)}$$

The mixing matrix $g_{ik}(t)$ is not known theoretically; as was discussed in Section 6, the condition of planarity [34–36] requires that $g_{ik}(t)$ fall off at large positive t. Therefore, we assume that it has the form

$$g_{ik}(t) = \frac{g_{ik}^{(0)}}{1 + (t/\lambda^2)^k}. \quad \text{(A.5.7)}$$

For explicit calculations in the region $t > 0$, we set $k = 1$ and $\lambda^2 = 2/3$ GeV^2.

To find the shifted Regge poles in T, one can rewrite (A.5.3) as

$$T_{ik} = \frac{t_{ik}}{\det(j - \hat{\alpha}(t) - \hat{g}(t))}, \quad \text{(A.5.8)}$$

where t_{ik} are minors of $\hat{T}$. The roots of the determinant

in (A.5.8) are given by the cubic equation

$$j^3 - j^2\sum \bar{\alpha}_i + j\left(\sum_{i\neq k}\bar{\alpha}_i\bar{\alpha}_k - g_{ik}^2\right) - \bar{\alpha}_1\bar{\alpha}_2\bar{\alpha}_3 + \sum_{i\neq k\neq l} g_{ik}^2\bar{\alpha}_l - 2g_{12}g_{13}g_{23} = 0. \quad \text{(A.5.9)}$$

We denote the three roots of (A.5.9) by

$$j = \alpha_i(t), \quad i = 1, 2, 3. \quad \text{(A.5.10)}$$

Let us start with $t = 0$. We assume the values in (A.5.5) and (A.5.6) for $\bar{\alpha}_i(0)$ and the following values for $g_{ik}^{(0)}$:[6)]

$$(g_{12}^{(0)})^2 = 0.16, \quad (g_{13}^{(0)})^2 = 0.08, \quad (g_{23}^{(0)})^2 = 0.01. \quad \text{(A.5.11)}$$

The intercepts of the mixed trajectories are then obtained to be

$$\alpha(0) = 1.2, \quad \alpha_2(0) = 0.225, \quad \alpha_3(0) = 0.075. \quad \text{(A.5.12)}$$

Thus, we have derived a realistic Pomeron intercept corresponding to the bare Pomeron intercept observed in deep-inelastic scattering at small x [20]. Note, however, that the theoretical uncertainty in $g_{ik}^{(0)}$ and in the Pomeron intercept are larger (~0.1).

The resulting trajectories are depicted in Fig. 1.

From a comparison with the bare trajectories $\bar{\alpha}_i(t)$ in Fig. 1, one can see that the role and ordering of trajectories are changed in relation to the bare ones when one goes over from the large-t to the small-t region. This property is very general and is not associated with a particular choice of $g_{ik}(t)$.

It is also of interest to define the coupling of new Regge poles to the hadrons a and b and to probe, in this way, the quark and gluon contents of the poles. To this end, we express the matrix T_{ik} as

$$T_{ik} = O_{in}\lambda_n O_{nk}^{+}, \quad \text{(A.5.13)}$$

where the diagonal matrix $\hat{\lambda}$ is

$$\hat{\lambda} = \begin{pmatrix} \frac{1}{j-\alpha_1(t)} & 0 & 0 \\ 0 & \frac{1}{j-\alpha_2(t)} & 0 \\ 0 & 0 & \frac{1}{j-\alpha_3(t)} \end{pmatrix}, \quad \text{(A.5.14)}$$

and find the matrix elements O_{ik} from the set of equations

$$(\alpha_k - \bar{\alpha}_1)O_{1k} + g_{12}O_{2k} + g_{13}O_{3k} = 0, \quad \text{(A.5.15)}$$

$$g_{12}O_{1k} + (\alpha_k - \bar{\alpha}_2)O_{2k} + g_{23}O_{3k} = 0, \quad \text{(A.5.16)}$$

$$g_{13}O_{1k} + g_{23}O_{2k} + (\alpha_k - \bar{\alpha}_3)O_{3k} = 0. \quad \text{(A.5.17)}$$

Equations (A.5.15)–(A.5.17) for $k = 1, 2, 3$ and the normalization condition

$$|O_{k1}|^2 + |O_{k2}|^2 + |O_{k3}|^2 = 1 \quad \text{(A.5.18)}$$

define O_{ik} apart from a common phase.

Physically, $|O_{ki}|^2 = |O_{ik}|^2$ gives the probability of finding the original pole $\bar{\alpha}_i$ in the new pole k.

Since the original indices i refer to the glueball trajectory ($i = 1$), the $u\bar{u} + d\bar{d}$ trajectory ($i = 2$), and the $s\bar{s}$ trajectory ($i = 3$), one can define, in this way, the percentage of the corresponding components in the new trajectory.

[6)]The value of $g_{12}^{(0)}$ can be estimated from the model of f dominance and experimental data on residues of the Pomeron and f poles, $g_{12}^{(0)} = 0.3$–0.5. The $g_{13}^{(0)}$ coupling is approximately $\sim 0.5 g_{12}^{(0)}$ and $g_{23}^{(0)} \approx g_{12}^{(0)} g_{13}^{(0)}$.

REFERENCES

1. C. Morningstar and M. Peardon, Nucl. Phys. B (Proc. Suppl.) **63**, 22 (1998); Phys. Rev. D **60**, 034509 (1999).
2. UK QCD Collab. (G. S. Bali *et al.*), Phys. Lett. B **309**, 318 (1993); G. S. Bali, hep-lat/9901023; G. S. Bali *et al.*, Nucl. Phys. B (Proc. Suppl.) **63**, 209 (1998).
3. M. Teper, hep-th/9812187.
4. A. Vaccarino and D. Weingarten, hep-lat/9910007.
5. K. Peters, in *Hadron Spectroscopy*, Ed. by S.-U. Chung and H. J. Willutzki, AIP Conf. Proc. **432**, 669 (1998).
6. *Proceedings of the V Biennial Conference on Low-Energy Antiproton Physics, Villasimius, 1998*, Ed. by C. Cicalo, A. De Falco, G. Puddu, and S. Serci (North-Holland, Amsterdam, 1999).
7. H. Fritzsch and P. Minkowski, Nuovo Cimento A **30**, 393 (1975); H. Fritzsch and M. Gell-Mann, in *Proceedings of the 16th International Conference on High-Energy Physics, FNAL, 1972*, Vol. 2, p. 135.
8. R. L. Jaffe and K. Johnson, Phys. Lett. B **60**, 201 (1976).
9. P. Hasenfrantz and J. Kuti, Phys. Rep. **40**, 75 (1978).
10. D. Robson, Nucl. Phys. B **130**, 328 (1977); J. M. Cornwall and A. Soni, Phys. Lett. B **120**, 431 (1983).
11. F. E. Low, Phys. Rev. D **12**, 163 (1975); S. Nussinov, Phys. Rev. Lett. **34**, 1286 (1975).

12. V. S. Fadin, E. A. Kuraev, and L. N. Lipatov, Zh. Éksp. Teor. Fiz. **71**, 840 (1976) [Sov. Phys. JETP **44**, 443 (1976)]; **72**, 377 (1977) [**45**, 199 (1977)]; Ya. Ya. Balitskiĭ and L. N. Lipatov, Yad. Fiz. **28**, 1597 (1978) [Sov. J. Nucl. Phys. **28**, 822 (1978)]; L. N. Lipatov, Nucl. Phys. B **365**, 614 (1991); Zh. Éksp. Teor. Fiz. **90**, 1536 (1986) [Sov. Phys. JETP **63**, 904 (1986)].
13. Yu. A. Simonov, Nucl. Phys. B **307**, 512 (1988); Yad. Fiz. **54**, 192 (1991) [Sov. J. Nucl. Phys. **54**, 115 (1991)].
14. A. Yu. Dubin, A. B. Kaidalov, and Yu. A. Simonov, Phys. Lett. B **323**, 41 (1994); Yad. Fiz. **56** (12), 213 (1993) [Phys. At. Nucl. **56**, 1745 (1993)].
15. A. Yu. Dubin, A. B. Kaidalov, and Yu. A. Simonov, Phys. Lett. B **343**, 360 (1995); Yad. Fiz. **58**, 348 (1995) [Phys. At. Nucl. **58**, 300 (1995)].
16. Yu. A. Simonov, Phys. Lett. B **226**, 151 (1989); Z. Phys. C **53**, 419 (1992).
17. Yu. A. Simonov, Phys. Lett. B **228**, 413 (1989); M. Fabre de la Ripelle and Yu. A. Simonov, Ann. Phys. **212**, 235 (1991).
18. Yu. A. Simonov, Phys. Lett. B **249**, 514 (1990); Preprint No. TPI-MINN-90/19-T.
19. V. L. Morgunov, A. V. Nefediev, and Yu. A. Simonov, Phys. Lett. B **459**, 653 (1999); hep-ph/9906318.
20. A. Donnachi and P. V. Landshoff, Nucl. Phys. B **244**, 332 (1984); A. B. Kaĭdalov, L. A. Ponomarev, and K. A. Ter-Martirosyan, Yad. Fiz. **44**, 722 (1986) [Sov. J. Nucl. Phys. **44**, 468 (1986)].
21. Yu. A. Simonov, in *Lecture Notes in Physics* (1996), Vol. 479, p. 139.
22. I. J. Ford, R. H. Dalitz, and J. Hoek, Phys. Lett. B **208**, 286 (1988); N. A. Campbell, I. H. Jorysz, and C. Michael, Phys. Lett. B **167**, 91 (1986); S. Deldar, hep-lat/9809137; G. S. Bali, hep-lat/9908021.
23. H. G. Dosch, Phys. Lett. B **190**, 177 (1987); H. G. Dosch and Yu. A. Simonov, Phys. Lett. B **205**, 339 (1988); For a review see Yu. A. Simonov, Usp. Fiz. Nauk **166**, 337 (1996) [Phys. Usp. **39**, 313 (1996)].
24. Dan La Course and M. G. Olsson, Phys. Rev. D **39**, 2751 (1989); M. G. Olsson, Nuovo Cimento A **107**, 2541 (1994).
25. Yu. A. Simonov, Nucl. Phys. B **324**, 67 (1989); A. M. Badalian and Yu. A. Simonov, Yad. Fiz. **59**, 2247 (1996) [Phys. At. Nucl. **59**, 2164 (1996)].
26. E. Eichten and F. L. Feinberg, Phys. Rev. D **23**, 2724 (1981).
27. A. Di Giacomo and H. Panagopoulos, Phys. Lett. B **285**, 133 (1992); A. Di Giacomo, E. Meggiolaro, and H. Panagopoulos, Nucl. Phys. B **483**, 371 (1997); Nucl. Phys. B (Proc. Suppl.) **A54**, 343 (1997).
28. T. Barnes, Z. Phys. C **10**, 275 (1981); T. Barnes, F. E. Close, and S. Monaghan, Phys. Lett. B **110**, 159 (1982); Nucl. Phys. B **198**, 380 (1982).
29. E. Eichten *et al.*, Phys. Rev. D **17**, 3090 (1978); W. Lucha, F. Schoeberl, and D. Gromes, Phys. Rep. **200**, 127 (1991).
30. V. S. Fadin and L. N. Lipatov, Phys. Lett. B **429**, 127 (1998); M. Ciafaloni and G. Camici, Phys. Lett. B **430**, 349 (1998); S. J. Brodsky *et al.*, Pis'ma Zh. Éksp. Teor. Fiz. **70**, 225 (1999) [JETP Lett. **70**, 155 (1999)].
31. Yu. A. Simonov, Phys. Lett. B (in press).
32. Yu. A. Simonov, Yad. Fiz. **3**, 630 (1966) [Sov. J. Nucl. Phys. **3**, 461 (1966)]; A. M. Badalian and Yu. A. Simonov, Yad. Fiz. **3**, 1032 (1966) [Sov. J. Nucl. Phys. **3**, 755 (1966)]; **5**, 88 (1967) [**5**, 60 (1967)]; F. Calogero and Yu. A. Simonov, Phys. Rev. **169**, 789 (1968).
33. G. Veneziano, Nucl. Phys. B **108**, 285 (1976).
34. G. Veneziano, Phys. Lett. B **43**, 413 (1973); Nucl. Phys. B **74**, 365 (1974).
35. Chan Hong-Mo and J. Paton, Phys. Lett. B **46**, 228 (1973); Chan Hong-Mo, J. Paton, and Tseri Sheund Tsum, Nucl. Phys. B **86**, 479 (1975).
36. G. F. Chew and C. Rosenzweig, Phys. Lett. B **58**, 93 (1975); Phys. Rev. D **12**, 907 (1975); Nucl. Phys. B **104**, 296 (1976).
37. A. Capella *et al.*, Phys. Rep. **236**, 225 (1994).
38. P. V. Landshoff, hep-ph/9907392; J. R. Cudell, A. Donnachie, and P. V. Landshoff, Phys. Lett. B **448**, 281 (1999).
39. L. P. A. Haakman, O. V. Kancheli, and J. H. Koch, Nucl. Phys. B **518**, 275 (1998).
40. V. N. Gribov, Zh. Éksp. Teor. Fiz. **53**, 654 (1967) [Sov. Phys. JETP **26**, 414 (1967)].
41. A. B. Kaidalov, Surv. High Energy Phys. **13**, 265 (1999).
42. R. L. Jaffe, K. Johnson, and Z. Ryzak, Ann. Phys. **168**, 344 (1986).
43. B. S. DeWitt, Phys. Rev. **162**, 1195, 1239 (1967); J. Honerkamp, Nucl. Phys. B **48**, 269 (1972); G. 't Hooft, Nucl. Phys. B **62**, 44 (1973); Lectures at Karpacz, Acta Univ. Wratislaviensis **368**, 345 (1976); L. F. Abbot, Nucl. Phys. B **185**, 189 (1981).

Physics of Atomic Nuclei, Vol. 63, No. 8, 2000, pp. 1448–1454. From Yadernaya Fizika, Vol. 63, No. 8, 2000, pp. 1527–1533.

ON THE 85th ANNIVERSARY OF V.V. VLADIMIRSKY

Correlation Function for Topological Charge Densities within the Instanton Model in QCD*

B. L. Ioffe and A. V. Samsonov*****

Institute of Theoretical and Experimental Physics, Bol'shaya Cheremushkinskaya ul. 25, Moscow, 117259 Russia

Received June 9, 1999; in final form, November 15, 1999

Abstract—The QCD sum rule for the correlation of topological charge densities $\chi(Q^2)$ and for the longitudinal part of the correlation function for singlet axial currents (the latter is related to the former) is considered within the instanton model. The constant $f_{\eta'}$ of η'-meson coupling to the singlet axial current is determined. Its value appears to be in good agreement with that determined recently from the relation between the proton-spin fraction Σ carried by *u*, *d*, and *s* quarks and the derivative of the QCD topological susceptibility $\chi'(0)$. On the basis of the same sum rule, the η–η' mixing angle θ_8 is found within the model employing two mixing angles. The value of θ_8 coincides with that in effective chiral theory. The correlation function for topological charge densities $\chi(Q^2)$ at large Q^2 is calculated. It is shown that the Q^2 dependence at high Q^2 matches well with that at low Q^2, the latter being determined by the known values $\chi'(0)$ and by the contributions of the π and η mesons.

1. INTRODUCTION

In [1], the vacuum expectation value of the singlet axial current f_0^2 induced by an external singlet axial field A_μ was found to be

$$\langle 0|j_{\mu 5}|0\rangle_A = 3f_0^2 A_\mu, \tag{1}$$

where $j_{\mu 5}$ is the singlet quark current

$$j_{\mu 5}(x) = \sum_q \bar{q}(x)\gamma_\mu\gamma_5 q(x), \quad q = u, d, s. \tag{2}$$

The term

$$\Delta L = j_{\mu 5}A_\mu \tag{3}$$

was added to the QCD Lagrangian, where A_μ is a singlet axial field that is constant in space and time, and the limit of weak A_μ field was considered. In the limit of massless *u*, *d*, and *s* quarks, it was found that [1, 2]

$$f_0^2 = (2.8 \pm 0.7) \times 10^{-2}\ \text{GeV}^2. \tag{4}$$

In order to derive this result, a QCD sum rule in the external field A_μ was formulated in such a way that it determines the proton-spin fraction Σ carried by *u*, *d*, and *s* quarks. The quantity Σ is related to the proton matrix element of the current $j_{\mu 5}$ by the equation

$$2ms_\mu\Sigma = \langle p, s|j_{\mu 5}|p, s\rangle, \tag{5}$$

where s_μ is the proton-spin 4-vector and *m* is the proton mass. The sum rule for Σ depends substantially on f_0^2, and the numerical result in (4) comes out in two ways, producing the same value: (i) from the requirement that the phenomenological side of the sum rule and its side calculated within QCD as functions of the Borel parameter M^2 be consistent and (ii) from the use of the experimental value for Σ (Σ = 0.3 ± 0.1).

It was shown in [1] that, in the limit of massless *u*, *d*, and *s* quarks, f_0^2 is related to the first derivative $\chi'(0)$ of the correlation function for the topological charge densities $Q_5(x)$:

$$\chi(q^2) = i\int d^4x e^{iqx}\langle 0|T\{Q_5(x), Q_5(0)\}|0\rangle, \tag{6}$$

$$Q_5(x) = \frac{\alpha_s}{8\pi}G^n_{\mu\nu}(x)\tilde{G}^n_{\mu\nu}(x). \tag{7}$$

Here, $G^n_{\mu\nu}(x)$ is gluonic field strength, while $\tilde{G}^n_{\mu\nu}(x)$ is its dual, $\tilde{G}^n_{\mu\nu} = (1/2)\varepsilon_{\mu\nu\lambda\sigma}G^n_{\lambda\sigma}$,

$$f_0^2 = 12\chi'(0). \tag{8}$$

As follows from (4),

$$\chi'(0) = (2.3 \pm 0.6) \times 10^{-3}\ \text{GeV}^2. \tag{9}$$

Let us recall the derivation of (8). Using (3), we can write

$$\langle 0|j_{\mu 5}|0\rangle_A = \lim_{q\to 0} i\int d^4x e^{iqx}\langle 0|T\{j_{\nu 5}(x), j_{\mu 5}(0)\}|0\rangle A_\nu \equiv \lim_{q\to 0} P_{\mu\nu}(q)A_\nu. \tag{10}$$

* This article was submitted by authors in English.

** e-mail: ioffe@vitep5.itep.ru

*** e-mail: sams@heron.itep.ru

The general structure of $P_{\mu\nu}(q)$ is

$$P_{\mu\nu}(q) = -P_L(q^2)\delta_{\mu\nu} + P_T(q^2)(-\delta_{\mu\nu}q^2 + q_\mu q_\nu). \quad (11)$$

Because of an anomaly, there are no massless states in the spectrum of the singlet polarization operator $P_{\mu\nu}$ even for massless quarks. The quantity $P_{T,L}(q^2)$ does not have kinematical singularities at $q^2 = 0$ either. Therefore, the nonvanishing value $P_{\mu\nu}(0)$ comes entirely from $P_L(q^2)$. Multiplying $P_{\mu\nu}(q)$ by $q_\mu q_\nu$ and using the anomaly condition

$$\partial_\mu j_{\mu 5}(x) = 2N_f Q_5(x) + 2i\sum_q m_q \bar{q}(x)\gamma_5 q(x) \quad (12)$$

(N_f is the number of flavors, $N_f = 3$), in the limit of massless quarks we obtain

$$q_\mu q_\nu P_{\mu\nu}(q) = -P_L(q^2)q^2 = 36\chi(q^2). \quad (13)$$

As is known from [3], $\chi(0) = 0$ if there is at least one massless quark. The relation (8) then follows directly from (1), (10), (11), and (13). According to (1), we also have

$$f_0^2 = -(1/3)P_L(0). \quad (14)$$

An attempt at determining f_0^2 directly by constructing a special QCD sum rule was made in [4]. However, this attempt failed: it was found that the operator product expansion (OPE) used in the sum rule does not converge—the higher order terms of OPE that were not taken into account must be of importance.

In the present paper, we use the instanton model [5] (for review, see [6]) to calculate these higher order terms. The idea that instantons make the main contribution to the longitudinal part $P_L(q^2)$ of the correlation function for the singlet axial current $P_{\mu\nu}(q)$ at intermediate values of $|q^2| \sim 1$ GeV^2 is not original—it was proposed as far back as 1979 [7, 8]. In [7], it was argued that the appearance of η and η' mesons as almost pure octet and singlet states in $SU(3)$ flavor symmetry—that is, the large mixing of $\bar{u}u + \bar{d}d$ and $\bar{s}s$ in this channel—cannot be described by perturbative QCD and can be attributed only to a dominant instanton contribution. We construct a sum rule for a direct determination of f_0^2. At standard values for the parameters of the instanton model, the f_0^2 value found from this sum rule is in good agreement with (4).

For massless quarks, the phenomenological side of the sum rule is saturated by η'-meson contribution (plus contributions of excited states, approximated by a continuum). The strange-quark mass m_s can also be taken into account in the sum rule. In this case, the η-meson contribution also comes into play, and the η–η' mixing angle can be found from the analysis. In the model of two mixing angles [9], the value of the maximal angle θ_8 is determined and appears to be in good agreement with the values found from chiral theory and phenomenology [9–11].

Within the same instanton model, the q^2 dependence of the correlation function for the topological charge density $\chi(Q^2)$ is determined at spacelike $Q^2 = -q^2 > 0$. At intermediate $Q^2 \sim 1$ GeV^2, it matches well with the low-Q^2 form of $\chi(Q^2)$ found in [12] on the basis of (9) and the contributions of the Goldstone bosons π^0 and η.

2. SUM RULE

Strictly speaking, the quantity f_0^2 given by (1) is defined as the nonperturbative part of the vacuum expectation value $\langle 0|j_{\mu 5}|0\rangle_A$ induced by the external field A_μ, with perturbative contribution being subtracted. The numerical value (4) corresponds precisely to this definition. The reason for this definition is that, in the sum rule for Σ, from which the value f_0^2 in (4) was determined, all perturbative contributions were taken into account explicitly, with exception of the nonperturbative part of $\langle 0|j_{\mu 5}|0\rangle_A$, which was parametrized by unknown constant f_0^2. Similarly, $\chi(q^2)$ in (6) and (8) has the meaning of the nonperturbative part of the correlation function for the topological charge densities. This definition is physically reasonable, since the perturbative part of (6) is badly divergent—it depends substantially on the renormalization scheme and therefore has no physical meaning. The same statement applies to the perturbative contribution to f_0^2. This distinction between the perturbative and nonperturbative contributions allows one to avoid any uncertainties in the sum rule for the physically measurable quantity Σ.

The idea of determining f_0^2 or the quantity $P_L(0)$, which is proportional to f_0^2, was put forth in [4]. We can briefly summarize it as follows.

The imaginary part of $P_L(q^2)$ is represented by the contribution of the lowest resonance (η' meson) and that of a continuum:

$$\mathrm{Im}\,P_L(q^2) = 3\pi\tilde{f}_{\eta'}^2 m_{\eta'}^2 \delta(q^2 - m_{\eta'}^2) + \beta(q^2)\theta(q^2 - s_0). \quad (15)$$

Here, $\tilde{f}_{\eta'}$ is the coupling of the η' meson to the singlet axial current

$$\langle 0|j_{\mu 5}|\eta'\rangle = i\sqrt{3}\tilde{f}_{\eta'}q_\mu \quad (16)$$

in the limit of massless u, d, and s quarks (q_μ is η' meson momentum). The second term on the right-hand side of (15) represents the contribution of a continuum, and s_0 is the continuum threshold. The continuum contribution corresponds to the gluonic bare loop in the

correlation function (6) and is given by

$$\beta(q^2) = \frac{9\alpha_s^2}{8\pi^3}q^2. \quad (17)$$

In order to derive the nonperturbative part of $\mathrm{Im}P_L$, we should subtract the perturbative part, equal to $\beta(q^2)$ from (15). This yields

$$\mathrm{Im}\,P_L(q^2)_{\mathrm{nonp}} = 3\pi\tilde{f}^2_{\eta'}m^2_{\eta'}\delta(q^2-m^2_{\eta'}) - \beta(q^2)\theta(s_0-q^2). \quad (18)$$

As was shown in [4], the nonperturbative part of $P_L(0)$ is given by

$$P_L(0)_{\mathrm{nonp}} = -3\tilde{f}^2_{\eta'} + \frac{1}{\pi}\int_0^{s_0}\frac{\beta(s)}{s}ds. \quad (19)$$

Therefore, the problem reduces to determining the coupling constant $\tilde{f}^2_{\eta'}$. This can be done by standard technique of the QCD sum rule. Let us write OPE for $P_L(Q^2) = (36/Q^2)\chi(Q^2)$ at high Q^2 and use the instanton liquid approximation to calculate the instanton contribution. (The instanton contribution was not taken into account in [4].) The OPE for $P_L(Q^2)$ has the form [8]

$$-P_L(Q^2) = \frac{9\alpha_s^2}{8\pi^4}Q^2\ln\frac{Q^2}{\mu^2} + \frac{9\alpha_s}{4\pi}\frac{1}{Q^2}\left\langle 0\left|\frac{\alpha_s}{\pi}G^2\right|0\right\rangle + \frac{9\alpha_s^2}{2\pi^2}\frac{1}{Q^4}gf^{abc}\langle 0|G^a_{\mu\alpha}G^b_{\alpha\beta}G^c_{\beta\mu}|0\rangle + \frac{9\alpha_s^3}{2\pi Q^6}f^{abc}f^{ade} \times\langle 0|G^b_{\mu\nu}G^c_{\alpha\beta}G^d_{\mu\nu}G^e_{\alpha\beta} + 10G^b_{\mu\alpha}G^c_{\alpha\nu}G^d_{\mu\beta}G^e_{\beta\nu}|0\rangle + 18Q^2\int d\rho n(\rho)\rho^4K_2^2(Q\rho). \quad (20)$$

We retain only contributions of operators having dimensions not lower than eight. The first term on the right-hand side of (20) is the bare-loop contribution, while the last one is the contribution of instantons plus anti-instantons [7, 8]; $K_2(x)$ is a Macdonald function, ρ is the instanton size, and $n(\rho)$ is the instanton density. For $n(\rho)$, we use the Shuryak model [5, 6] of instanton density:

$$n(\rho) = n_0\delta(\rho-\rho_c). \quad (21)$$

As was demonstrated by Schäfer and Shuryak [6], this model describes well many hadronic correlation functions in QCD. For the parameters in (21), we choose numerical values of $n_0 = 0.75\times10^{-3}$ GeV^4, $\rho_c = 1.5$ GeV^{-1}, which lie within the ranges allowed by these models. At this n_0, the standard value of gluonic condensate,

$$\left\langle 0\left|\frac{\alpha_s}{\pi}G^2\right|0\right\rangle = 0.012\ \mathrm{GeV}^4, \quad (22)$$

may be attributed entirely to instantons. In order to estimate gluonic condensate of dimension eight, we assume the factorization hypothesis—the saturation by vacuum intermediate states. We then have [8]

$$f^{abc}f^{ade}\langle 0|G^b_{\mu\nu}G^c_{\alpha\beta}G^d_{\mu\nu}G^e_{\alpha\beta} + 10G^b_{\mu\alpha}G^c_{\alpha\nu}G^d_{\mu\beta}G^e_{\beta\nu}|0\rangle = \frac{15}{16}\langle 0|G^n_{\mu\nu}G^n_{\mu\nu}|0\rangle^2. \quad (23)$$

It should be noted that the calculation of the same term within the instanton model would give quite a different result,

$$(2^{11}\times3\pi/7)n_0\rho_c^{-4}, \quad (24)$$

which is one order of magnitude greater than that in (23) at the accepted values of the model parameters. This comes an no surprise. For the gluonic condensate with k gluonic fields, we would indeed have, on a dimensional basis,

$$\langle 0|G^k|0\rangle \sim \int n(\rho)\frac{1}{\rho^{2k-4}}d\rho, \quad (25)$$

and the integral in equation (25) diverges at sufficiently high k for any physical $n(\rho)$. Therefore, one can hope that the instanton model overestimates the gluonic condensate of dimension eight and accept the estimate in (23), which is based on factorization hypothesis. This estimate is supported by the analysis of the sum rules for heavy quarkonia that was performed with allowance for dimension-8 operators [13] and which employed the factorization hypothesis. Much greater values of gluonic condensates of dimension eight would contradict the analysis in [13]. Of course, values that are two or even three times as great as those in (23) cannot be ruled out, but, fortunately, the contribution of these condensates to the sum rule is small, and even a threefold increase in it would not affect the result significantly. For the gluonic condensate of dimension six, there is no independent estimate other than that given by the instanton model [8]:

$$\frac{g^3}{12\pi^2}f^{abc}\langle 0|G^a_{\mu\nu}G^b_{\nu\alpha}G^c_{\alpha\mu}|0\rangle = \frac{4}{5}\frac{1}{\rho_c^2}\left\langle 0\left|\frac{\alpha_s}{\pi}G^2\right|0\right\rangle. \quad (26)$$

The phenomenological representation of $P_L(Q^2)$ follows from (15). By equating the phenomenological and QCD representations, we arrive at the required sum rule. Applying the Borel transformation to both sides of this sum rule, we obtain

$$3\tilde{f}^2_{\eta'}m^2_{\eta'}e^{-m^2_{\eta'}/M^2} = \frac{9\alpha_s^2}{8\pi^4}M^4E_1\left(\frac{s_0}{M^2}\right) + \frac{9\alpha_s}{4\pi}\left\langle 0\left|\frac{\alpha_s}{\pi}G^2\right|0\right\rangle\left(1+\frac{\varepsilon}{M^2}\right) + \frac{135}{64}\frac{\pi\alpha_s}{M^4}\left\langle 0\left|\frac{\alpha_s}{\pi}G^2\right|0\right\rangle^2 + 18n_0\rho_c^4\mathcal{B}_{M^2}Q^2K_2^2(Q\rho_c), \quad (27)$$

$$E_1(x) = 1 - (1 + x)e^{-x}, \tag{28}$$

where $\mathcal{B}_{M^2}$ stands for a Borel transform. In (27), ε corresponds to contribution of dimension-6 gluonic condensate. The instanton-model estimate (26) gives $\varepsilon = 2.2$ GeV^2. Since we hope that the instanton model overestimates the gluonic condensate of dimension six as well, we set $\varepsilon = 1$ GeV^2 and include the possible uncertainty in the error. The Borel transformation of the Macdonald function can be performed using its asymptotic expansion. This yields (see [14])

$$\begin{aligned} &18 n_0 \rho_c^4 \mathcal{B}_{M^2} Q^2 K_2^2(Q\rho_c) \\ &\approx 9 n_0 M^3 \rho_c^3 \sqrt{\pi} e^{-M^2\rho_c^2}\left(M^2\rho_c^2 + \frac{13}{4} + \frac{165}{32}\frac{1}{M^2\rho_c^2}\right). \end{aligned} \tag{29}$$

In our M^2 domain, the next terms of the expansion are small. In order to verify this fact, we carried out a numerical calculation using the integral representation of the Macdonald function.

The results of the calculation of $\tilde{f}^2_{\eta'}$ according to the sum rule (27) are plotted in Fig. 1. (We set $\Lambda_{\rm QCD} = 200$ MeV; α_s was calculated in the leading order.) The standard procedure for estimating the M^2 interval where the sum rule is reliable (the requirement that highest order terms of OPE be small) cannot be applied here because the instanton contribution is dominant—it saturates about 75–80% of the total result. Therefore, we have to invoke physical arguments. We assume that the continuum threshold $s_0 = 2.5$ GeV^2 is close to the position of the second resonance with η' quantum numbers, $\eta'(1440)$ [probably, $\eta(1295)$ belongs to the octet], and require that the continuum contribution to the bare loop not exceed ~50%. For the lower boundary of the M^2 interval, we choose the M^2 value where the M^2 dependence begins to rise steeply. These requirements result in $1.2 \lesssim M^2 \lesssim 1.6$ GeV^2. In this interval, the M^2 dependence is not strong, and we have the estimate $\tilde{f}^2_{\eta'} \approx (2.4 \pm 0.6) \times 10^{-2}$ GeV^2. (The error includes a 15% possible variation of ρ_c.) The contribution of the second term to the right-hand side of (19) is negligible. From (14) and (8), we finally obtain

$$f_0^2 = (2.4 \pm 0.6) \times 10^{-2}\ \text{GeV}^2, \tag{30}$$

$$\chi'(0) = (2.0 \pm 0.5) \times 10^{-3}\ \text{GeV}^2, \tag{31}$$

in good agreement with (4) and with the value of $\chi'(0) = (2.3 \pm 0.6) \times 10^{-3}$ GeV^2 found in [1].

3. INCLUSION OF THE STRANGE-QUARK MASS: η'–η MIXING ANGLE

Let us consider the polarization operator $P_L(q^2)$ with allowance for the strange quark mass m_s and determine the coupling constant $f_{\eta'}$ for physical η'. The u- and d-quark masses are chosen to be zero as before. Using the definition of $P_{\mu\nu}(q)$ and (12), we have

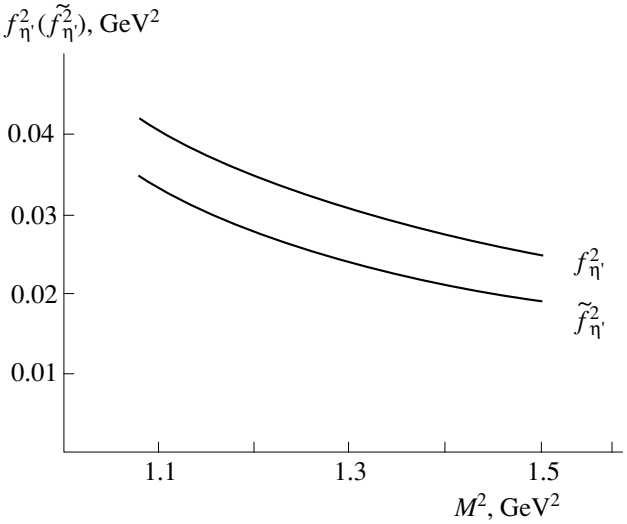

Fig. 1. Functions $\tilde{f}^2_{\eta'}(M^2)$ and $f^2_{\eta'}(M^2)$ determined by (27) and (41), respectively. In (41), $\theta_1 = 0$.

$$\begin{aligned} -P_L(q^2)q^2 &= q_\mu q_\nu P_{\mu\nu}(q) \\ &= i\int d^4x e^{iqx}\langle 0|T\{2N_f Q_5(x), 2N_f Q_5(0)\} \\ &\quad + T\{2N_f Q_5(x), 2im_s\bar{s}(0)\gamma_5 s(0)\} \\ &\quad + T\{2im_s\bar{s}(x)\gamma_5 s(x), 2N_f Q_5(0)\} \\ &\quad - 4m_s^2 T\{\bar{s}(x)\gamma_5 s(x), \bar{s}(0)\gamma_5 s(0)\}|0\rangle \\ &\quad + 4m_s\langle 0|\bar{s}(0)s(0)|0\rangle. \end{aligned} \tag{32}$$

The last term in (32) is caused by the equal-time commutator. We further perform the OPE on the right-hand side of (32). In relation to (20), there then appear three additional terms: the equal-time commutator term; the term that is proportional to m_s^2 and which corresponds to the bare loop of strange quarks; and the term that arises from the second and third terms in (32) and which is proportional to the quark–gluon condensate [15]:

$$-g\langle 0|\bar{s}\sigma_{\mu\nu}(\lambda^n/2)G^n_{\mu\nu}s|0\rangle = m_0^2\langle 0|\bar{s}s|0\rangle. \tag{33}$$

Here, $m_0^2 = 0.8$ GeV^2 was determined in [16]. After the Borel transformation, the right-hand side of the sum rule becomes

$$\begin{aligned} &R(M^2) - 4m_s\langle 0|\bar{s}s|0\rangle + \frac{3m_s^2}{2\pi^2}M^2 E_0\left(\frac{s_0}{M^2}\right)L^{-8/9} \\ &\quad - 6\alpha_s\frac{m_s m_0^2}{\pi M^2}\langle 0|\bar{s}s|0\rangle, \end{aligned} \tag{34}$$

where $R(M^2)$ is the right-hand side of (27),

$$E_0(x) = 1 - e^{-x} \tag{35}$$

$$L = \ln(M^2/\Lambda^2)/\ln(\mu^2/\Lambda^2). \tag{36}$$

The factor $L^{-8/9}$ takes into account the quark mass anomalous dimension.

It is also useful to consider the correlation function $P_{\mu\nu}(q)$ in the case where one of the currents is still $j_{\mu 5}(x)$, but where the other is the that of u and d quarks: $\bar{u}\gamma_\mu\gamma_5 u + \bar{d}\gamma_\mu\gamma_5 d$. In this case, the right-hand side of the sum rule is given by

$$\frac{2}{3}R(M^2) - 2\alpha_s\frac{m_s m_0^2}{\pi M^2}\langle 0|\bar{s}s|0\rangle. \tag{37}$$

In the phenomenology (left-hand side of the sum rule), η' and η mesons contribute, and it is necessary to take into account their mixing. We adopt the two-mixing-angles model [9], which is based on low-energy effective chiral theory and which describes the experimental data better [9, 10] than the single-mixing-angle model. In this model, the couplings of η and η' mesons, f_η and $f_{\eta'}$, to octet and singlet axial currents are related to the couplings of the fictitious octet and singlet pseudoscalar states, f_8 and f_1, by the equations

$$\begin{aligned} f_\eta^8 &= f_8\cos\theta_8, \quad f_\eta^1 = -f_1\sin\theta_1, \\ f_{\eta'}^8 &= f_8\sin\theta_8, \quad f_{\eta'}^1 = f_1\cos\theta_1. \end{aligned} \tag{38}$$

The η'- and η-meson contributions to $P_L(q^2)$ can easily be calculated within this model. It is convenient to present them separately for the cases where one of the currents is $\bar{s}\gamma_\mu\gamma_5 s$ or $\bar{u}\gamma_\mu\gamma_5 u + \bar{d}\gamma_\mu\gamma_5 d$ (The other is always $j_{\mu 5}$). Instead of the left-hand side of (27), we now have

$$\begin{aligned} &m_{\eta'}^2 e^{-m_{\eta'}^2/M^2} f_1^2[\cos^2\theta_1 - \sqrt{2}(f_8/f_1)\sin\theta_8\cos\theta_1] \\ &+ m_\eta^2 e^{-m_\eta^2/M^2} f_1^2[\sin^2\theta_1 + \sqrt{2}(f_8/f_1)\sin\theta_1\cos\theta_8] \end{aligned} \tag{39}$$

for the $\bar{s}\gamma_\mu\gamma_5 s$ current and

$$\begin{aligned} &m_{\eta'}^2 e^{-m_{\eta'}^2/M^2} f_1^2[2\cos^2\theta_1 + \sqrt{2}(f_8/f_1)\sin\theta_8\cos\theta_1] \\ &+ m_\eta^2 e^{-m_\eta^2/M^2} f_1^2[2\sin^2\theta_1 - \sqrt{2}(f_8/f_1)\cos\theta_8\sin\theta_1] \end{aligned} \tag{40}$$

for the $\bar{u}\gamma_\mu\gamma_5 u + \bar{d}\gamma_\mu\gamma_5 d$ current.

Taking the sum of (39) and (40), setting $\theta_1 = \theta_8 = 0$, and equating it to (34) at $m_s = 0$, we obtain the preceding result with $f_1 = f_0$. At nonzero, m_s the mixing angles must be taken into account; for the sum of (39) and (40), we then obtain

$$\begin{aligned} &3m_{\eta'}^2 f_1^2 e^{-m_{\eta'}^2/M^2}\left[\cos^2\theta_1 + \frac{m_\eta^2}{m_{\eta'}^2}e^{(m_{\eta'}^2 - m_\eta^2)/M^2}\sin^2\theta_1\right] \\ &= R(M^2) - 4m_s\langle 0|\bar{s}s|0\rangle + \frac{3m_s^2}{2\pi^2}M^2E_0\left(\frac{s_0}{M^2}\right)L^{-8/9} \\ &\quad - 6\alpha_s\frac{m_s m_0^2}{\pi M^2}\langle 0|\bar{s}s|0\rangle. \end{aligned} \tag{41}$$

Let us now take the difference of (39) and one-half of (40). The corresponding sum rule is

$$\begin{aligned} &-\frac{3}{\sqrt{2}}m_{\eta'}^2 e^{-m_{\eta'}^2/M^2} f_1 f_8\left[\sin\theta_8\cos\theta_1\right. \\ &\left. - \frac{m_\eta^2}{m_{\eta'}^2}e^{(m_{\eta'}^2 - m_\eta^2)/M^2}\cos\theta_8\sin\theta_1\right] = -4m_s\langle 0|\bar{s}s|0\rangle \\ &+ \frac{3m_s^2}{2\pi^2}M^2E_0\left(\frac{s_0}{M^2}\right)L^{-8/9} - 3\alpha_s\frac{m_s m_0^2}{\pi M^2}\langle 0|\bar{s}s|0\rangle. \end{aligned} \tag{42}$$

The theoretical value of θ_1 found in [9–11] is small: $\theta_1 = -(2.7\text{–}4)°$. (The phenomenological value [10, 11] is slightly higher: $\theta_1 = -9.2°$). To a high accuracy, we can therefore set $\theta_1 \approx 0$ in (41) and (42). Equation (41) then determines $f_1^2 \approx f_{\eta'}^2$. The quantity f_1^2 as a function of M^2 is presented in Fig. 1. (We used here the numerical values of $\langle 0|\bar{s}s|0\rangle = -1.11 \times 10^{-2}$ GeV^3 and m_s(1 GeV) = 150 MeV.) From the curve in Fig. 1, we derive the estimate

$$\begin{aligned} f_{\eta'}^2 &= (3.2 \pm 0.6) \times 10^{-2}\ \text{GeV}^2, \\ f_{\eta'} &= 178 \pm 17\ \text{MeV}. \end{aligned} \tag{43}$$

The ratio of (42) and (41) gives the mixing angle θ_8. In the limit $\theta_1 \approx 0°$ and at $f_8/f_1 = 1.12$ [9–11], it is given by

$$\theta_8 = -(17.0 \pm 5.0)°. \tag{44}$$

Upon taking into account the value of $\theta_1 = -2.7°$, θ_8 becomes

$$\theta_8 = -(18.8 \pm 5.0)°. \tag{45}$$

The values of $f_{\eta'}$ and θ_8 agree with those found in [9–11] from the low-energy effective theory or phenomenology. They are, respectively,

$$\begin{aligned} &\text{theory:}\quad f_{\eta'} = 151\ \text{MeV}, \quad \theta_8 = -21°; \\ &\text{phenomenology:}\quad f_{\eta'} = 153\ \text{MeV}, \quad \theta_8 = -21°. \end{aligned} \tag{46}$$

4. Q^2 DEPENDENCE OF $\chi(Q^2)$

Using OPE for $P_L(Q^2)$ [(20) and (13)], we can find the Q^2 dependence of $\chi(Q^2)$ at high Q^2. Since the perturbative part must be subtracted an accordance with the definition of $\chi(Q^2)$, the first term on the right-hand side of (20) is omitted, and we have

$$\chi(Q^2) = -\frac{\alpha_s}{16\pi}\left\langle 0\left|\frac{\alpha_s}{\pi}G^2\right|0\right\rangle\left(1+\frac{\varepsilon}{Q^2}\right) - \frac{15}{128}\pi\alpha_s\frac{1}{Q^4}\left\langle 0\left|\frac{\alpha_s}{\pi}G^2\right|0\right\rangle^2 - \frac{1}{2}n_0Q^4\rho_c^4K_2^2(Q\rho_c), \quad (47)$$

where ε parametrizes the gluonic-condensate contribution of dimension [see (27)] and where equation (23) has been used. The quantity $\chi(Q^2)$ (47) is plotted in Fig. 2. It is instructive to compare $\chi(Q^2)$ at large Q^2 with $\chi(Q^2)$ at low Q^2 found in [12],

$$\chi(Q^2) = \chi(0) - \chi'(0)Q^2 - \frac{1}{8}f_\pi^2Q^2\left[\left(\frac{m_u-m_d}{m_u+m_d}\right)^2\frac{m_\pi^2}{Q^2+m_\pi^2}+\frac{1}{3}\frac{m_\eta^2}{Q^2+m_\eta^2}\right], \quad (48)$$

where

$$\chi(0) = \frac{m_um_d}{m_u+m_d}\langle 0|\bar{u}u|0\rangle \quad (49)$$

and where the last term represents the contributions of π^0 and η mesons. The curve representing the low-Q^2 behavior of $\chi(Q^2)$ (48) is also plotted in Fig. 2; for $\chi'(0)$, we chose the value was found in [1]: $\chi'(0) = 2.3\times10^{-3}$ GeV^2. As can be seen from Fig. 2, the two curves match quite well in the range $Q^2 \approx 0.4$–1 GeV^2.

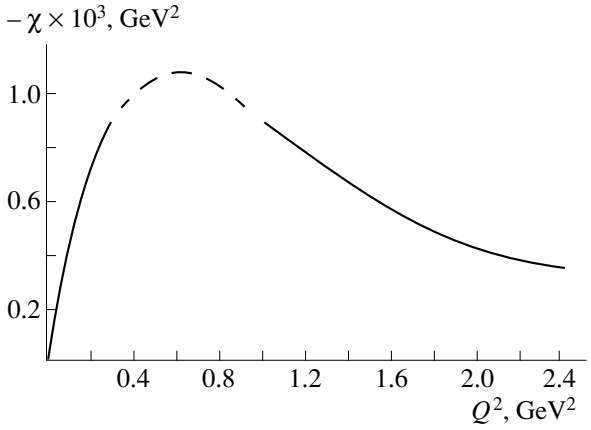

Fig. 2. Function $\chi(Q^2)$ at [equations (48)] low and [equation (47)] high Q^2 (solid lines). The dashed line represents the possible matching of the two branches of the curve.

5. DISCUSSION AND COMPARISON WITH THE RESULTS OF OTHER STUDIES

As was mentioned in the Introduction, instantons are the most plausible QCD objects for describing physical η' channels or, what is equivalent, the longitudinal part of the singlet-axial-vector-current correlation function. The results of the calculations of the correlation function for the flavor-singlet pseudoscalar current $j_5 = \bar{q}\gamma_5 q$ that were performed by Shuryak and Verbaarschot [17] and by Schäfer [18] within various instanton models are in good agreement with a phenomenological coordinate dependence up to distances of $x \sim 0.3$ fm (sometimes, even up to larger distances). Therefore, we could expect that the instanton model is suitable for considering the problem in question. Here, we have used the simplest version of the instanton model—the instanton liquid approximation with the instanton density given by the Shuryak model (21). For this reason, the accuracy of our results is only modest.

Since the main contribution (about 80%) to the sum rules that were used to determine f_0^2 and $f_{\eta'}^2$ comes from the instanton term, the main uncertainty is caused by the instanton parameters n_0 and ρ_c. These parameters were taken from the best fit (performed by Schäfer and Shuryak [6]) to various hadronic correlation functions, as well as to some other QCD objects, like the gluonic condensate. Possible uncertainties are included in the errors. The errors in determining the mixing angle θ_8 are smaller because instantons do not contribute to the right-hand side of (42). If f_1 and f_8 are set to their phenomenological values of $f_1 = 1.28f_\pi$ and $f_8 = 1.15f_\pi$ [9–11], instead of $f_1 = f_{\eta'}$ found from the sum rule, the use of equation (42) (at $\theta_1 = -2.7°$) yields

$$\theta_8 = -(26.5\pm3.5)°. \quad (50)$$

The value obtained above for $f_{\eta'}$ [see (43)] is slightly higher than the low-energy result (46); bearing in mind the uncertainties, we can consider, however, the agreement to be satisfactory.

In our calculation, we have taken no account of α_s corrections, which are of importance for the first term on the right-hand side of (27) [19], but this term contributes only 5% to the total result. The α_s corrections to gluonic-condensate contributions are masked by uncertainties in higher order gluonic condensates. Among terms proportional to m_s and m_s^2, α_s corrections appear only as corrections to the two last terms in (34), not to the main term $-4m_s\langle 0|\bar{s}s|0\rangle$, which is proportional to m_s. These corrections are not so great as to affect the value of the mixing angle. To the term proportional to m_s^2, there are also instanton corrections on the same order of magnitude. Allowances for all these corrections to the terms proportional to m_s^2 is the subject of a further study. We believe that, upon their inclusion, the value of the mixing angle will still be within the limits adopted above for errors.

The slopes of the left- and right-hand sides of (41) in M^2 are different: positive on the left-hand side and negative on the right-hand side. For this reason, it is impossible to determine $m^2_{\eta'}$ through the derivative of (41) with respect to M^2, as this was done sometimes in the QCD sum-rule approach: the sum rule is satisfactory, but its derivative is not.

The problem of determining $\chi'(0)$ or $f_{\eta'}$ within the standard approach of QCD sum rules without allowing for instantons was studied in [19]. The result obtained there for $\chi'(0)$ or $f^2_{\eta'}$ is smaller than ours (by a factor of 3 to 4). The basic difference from the calculations presented here (apart from the instanton contribution) is that the authors of [19] chose much larger values for the continuum and for the effective Borel parameter: $s_0 = 6$ GeV^2 and $M^2 \sim 3$–4 GeV^2. Therefore, the model of the hadronic spectrum in $J^{PC} = 0^{-+}$ flavor-singlet channel with a gap between the η'-meson mass and 2.5 GeV was accepted in [19]. However, there are at least three resonances with η' quantum numbers between the η'-meson mass and 2.5 GeV. For this reason, that model is not acceptable physically. The other drawback of the sum rule used in [19] {equation (D.11) from [19], which is similar to (41), but which features no η–η' mixing} is that the main contribution to the sum rule comes from the terms proportional to m_s and m_s^2. These terms saturate 60% of the final result, and $SU(3)$ flavor symmetry is badly violated in the sum rule [19], in contradiction to experimental data. Moreover, if η–η' mixing were introduced (this was not done in [19]), one could calculate the η–η' mixing angle, representing the phenomenological side of the sum rule by (39) and (40). The result for the mixing angle θ_8 would then be $\theta_8 \approx 45°$; that is, η' is not mainly flavor-singlet, and η is not mainly octet—in evident contradiction to experimental data.

In summary, we have shown that, in even the simplest version, the instanton model describes reasonably well the properties of the correlation function for the topological density—that is, the value of $\chi'(0)$, $\chi(Q^2)$ at high Q^2, the values of the η' coupling constant, and the η'–η mixing angle.

ACKNOWLEDGMENTS

This work was supported in part by the Russian Foundation for Basic Research (project no. 97-02-16131).

One of the authors (B.I.) has known V.V. Vladimirsky since 1950. Throughout these years B.I. was strongly impressed by his ingenious activity in such dissimilar fields as accelerator design, nuclear engineering, experimental and theoretical nuclear physics, and experimental and theoretical particle physics. We wish V.V. good health and many years of creative activity.

REFERENCES

1. B. L. Ioffe and A. G. Oganesian, Phys. Rev. D **57**, R6590 (1998).
2. B. L. Ioffe, in *Lectures at St. Petersburg Winter School on Theoretical Physics, 1998*; Preprint No. 7-98, ITÉF (Institute of Theoretical and Experimental Physics, 1998); Surv. High Energy Phys. (in press).
3. R. J. Crewther, Phys. Lett. B **70**, 349 (1977).
4. B. L. Ioffe and A. Yu. Khodzhamirian, Yad. Fiz. **55**, 3045 (1992) [Sov. J. Nucl. Phys. **55**, 1701 (1992)].
5. E. V. Shuryak, Nucl. Phys. B **203**, 93 (1982); **214**, 237 (1983).
6. T. Schäfer and E. V. Shuryak, Rev. Mod. Phys. **70**, 323 (1998).
7. B. V. Geshkenbein and B. L. Ioffe, Nucl. Phys. B **166**, 340 (1980).
8. V. A. Novikov, M. A. Shifman, A. I. Vainshtein, and V. I. Zakharov, Phys. Lett. B **86**, 347 (1979).
9. H. Leutwyler, Nucl. Phys. B (Proc. Suppl.) **64**, 223 (1998); R. Kaiser and H. Leutwyler, hep-ph/9806336.
10. Th. Feldmann, P. Kroll, and B. Stech, Phys. Rev. D **58**, 114006 (1998).
11. Th. Feldmann, P. Kroll, and B. Stech, hep-ph/9812269.
12. B. L. Ioffe, Preprint FZ-IKP(TH)-1998-28; hep-ph/9811217; Yad. Fiz. **62**, 2226 (1999) [Phys. At. Nucl. **62**, 2052 (1999)].
13. R. J. Reinders, H. R. Rubinstein, and H. Yazaki, Phys. Lett. B. **138**, 425 (1984).
14. V. A. Novikov, M. A. Shifman, A. I. Vainshtein, and V. I. Zakharov, Nucl. Phys. B **191**, 301 (1981).
15. B. L. Ioffe, Nucl. Phys. B **188**, 317 (1981); **191**, 591 (1981).
16. V. M. Belyaev and B. L. Ioffe, Zh. Éksp. Teor. Fiz. **83**, 876 (1982) [Sov. Phys. JETP **56**, 493 (1982)].
17. E. V. Shuryak and J. J. M. Verbaarschot, Nucl. Phys. B **410**, 37, 55 (1993).
18. T. Schäfer, Phys. Lett. B **389**, 445 (1996).
19. S. Narison, G. M. Shore, and G. Veneziano, Preprint CERN-TH/98-385; hep-ph/9812333.

Physics of Atomic Nuclei, Vol. 63, No. 8, 2000, pp. 1455–1462. Translated from Yadernaya Fizika, Vol. 63, No. 8, 2000, pp. 1534–1542.

ON THE 85th ANNIVERSARY OF V.V. VLADIMIRSKY

Calculation of One-Loop Corrections to the QCD Lagrangian for a Constant Chromomagnetic Condensate

V. V. Vladimirsky and D. V. Peregudov[1)]

Institute of Theoretical and Experimental Physics, Bol'shaya Cheremushkinskaya ul. 25, Moscow, 117259 Russia

Received July 19, 1999; in final form, November 30, 1999

Abstract—Within the theory of *SU*(2) and *SU*(3) Yang–Mills gauge fields, the effective Lagrangian is derived with allowance for the modification in the gluon and quark spectra that arises in a constant magnetic field with constant potentials. © *2000 MAIK "Nauka/Interperiodica".*

1. INTRODUCTION

Many models have been proposed to describe the vacuum state of a gluon field (see [1–38]). However, attention given to the simplest possibility—that is, to the model featuring a semiclassical field that is constant in time and space—has been insufficient in our opinion. We mean here coordinate- and time-independent solutions to the Yang–Mills equation with a constant right-hand side—for example, those of the type

$$V_\mu^a(x) = V\delta_\mu^a, \tag{1}$$

where V is a constant having dimensions of mass; $\mu = 0, \ldots, 3$; and $a = 1, \ldots, 8$. This solution is known in the literature (see [12, 20–22]) as a non-Abelian condensate. It satisfies the classical Yang–Mills equation with external current $J_\mu^a = 2g^2V\delta_\mu^a$. Within a theory exhibiting a spontaneous breakdown of trivial-vacuum stability, such a condensate can be generated by quantum corrections to the Yang–Mills Lagrangian at $J_\mu^a = 0$. In the present study, we do not study the conditions under which a condensate may arise; instead, we focus on deriving the one-loop effective Lagrangian in a given field. Our calculations are performed in the background-field gauge. Since the results presented in the literature for *SU*(2) theory are not always consistent and since the effective Lagrangian has not yet been calculated for the more realistic *SU*(3) case, we pursue our goal, invoking two different approaches: that which relies on evaluating determinants and that which involves determining the trace of the matrix logarithm (the results proved to be coincident). In calculating $L_{\text{eff}}^{(1)}$, we ignore the tachyon part of the gluon spectrum, assuming that quantum corrections are controlled by the logarithmically divergent contribution from the ultraviolet part of the spectrum [19], in which case they are not sensitive to the region of low momenta.

2. ORIGINAL LAGRANGIAN

The gauge-field Lagrangian $L = L_{\text{YM}} + L_{\text{GF}} + L_{\text{FP}} + J_\mu^a V_\mu^a + L_q$ includes the conventional Yang–Mills Lagrangian

$$L_{\text{YM}} = -\frac{1}{4}F_{\mu\nu}^a F_{\mu\nu}^a, \tag{2}$$

where

$$F_{\mu\nu}^a = \partial_\mu V_\nu^a - \partial_\nu V_\mu^a + gc^{abc}V_\mu^b V_\nu^c; \tag{3}$$

the gauge-fixing L_{GF} term; the Faddeev–Popov ghost Lagrangian L_{FP}; the term responsible for coupling to external currents J_μ^a; and the quark Lagrangian L_q. We seek solutions close to a constant classical field: $V_\mu^a \longrightarrow V_\mu^a + v_\mu^a$. For the Lagrangian of quantum fluctuations v_μ^a, we choose the background-field gauge, setting

$$L_{\text{GF}} = -\frac{1}{2}(\partial_\mu v_\mu^a + gc^{abc}V_\mu^b v_\mu^c)^2 = -\frac{1}{2}(\nabla_\mu^{ac}v_\mu^c)^2, \tag{4}$$

where V_μ^b is a constant. With the aid of the vector operator $\nabla_\mu^{ac} = \partial_\mu\delta^{ac} + gc^{abc}V_\mu^b$, the linearized equations of motion for small deviations v_ν^c from the constant field V_ν^c can be conveniently represented as

$$-M_{\mu\nu}^{ad}v_\nu^d = (\delta_{\mu\nu}\nabla_\lambda^{ac}\nabla_\lambda^{cd} + 2gc^{abd}F_{\mu\nu}^b)v_\nu^d = -j_\mu^a, \tag{5}$$

where j_μ^a stands for small external currents and $F_{\mu\nu}^b = gc^{bcd}V_\mu^c V_\nu^d$.

[1)]Schmidt Joint Institute of Physics of the Earth, Russian Academy of Sciences, ul. Bol'shaya Gruzinskaya 10, Moscow, 123810 Russia.

Equations (5) are valid for any background field—in particular, they remain in force for arbitrary constant fields generated by constant currents. The matrix $M^{ad}_{\mu\nu} = M^{da}_{\nu\mu}$ involves the term $\delta_{\mu\nu}\nabla^{ac}_{\lambda}\nabla^{cd}_{\lambda}$, which is symmetric under the permutations $\mu\nu \longrightarrow \nu\mu$ or $ad \longrightarrow da$, and the term $2gc^{abd}F^{b}_{\mu\nu}$, which is antisymmetric under these permutations. Hence, the spectrum of the matrix $M^{ad}_{\mu\nu}$ depends not only on the invariant $F^2 = F^a_{\mu\nu}F^a_{\mu\nu}$, but also on $V^a_\mu V^a_\mu$. However, the final result contains only F^2.

The translation invariance of the linearized equations (5) enables us to represent quantum fluctuations as the sum of plane waves $\exp(-ip_\mu x_\mu) = \exp(-i\omega x_0 + i\mathbf{k}\cdot\mathbf{x})$. The eigenvalues of the momentum $p_\mu \equiv (\omega, \mathbf{k})$ are determined by the matrix $M^{ad}_{\mu\nu}$, with the sum of the squared momentum eigenvalues, $\sum_s p^{(s)}_\mu p^{(s)}_\mu$, being controlled by the trace of this matrix (to be more specific, by the trace of the first term $\delta_{\mu\nu}\nabla^{ac}_{\lambda}\nabla^{cd}_{\lambda}$ in $M^{ad}_{\mu\nu}$, since the second term involves no diagonal elements).

3. CALCULATING ONE-LOOP CORRECTIONS TO THE YANG–MILLS LAGRANGIAN

In the constant-background-field gauge, the contribution of the time component of fluctuations cancels half the ghost contribution. The quantity $L^{(1)}$ is calculated by the formula

$$L^{(1)} = \pm\frac{1}{2}\int\frac{d^4p}{(2\pi)^4}\ln\frac{\mathrm{Det}\,M}{\mathrm{Det}\,M^{(0)}}, \qquad (6)$$

a minus (plus) sign being taken for the spacelike (timelike) components (the matrix in question involves no mixed elements).

The matrix $M \equiv M^{ad}_{\mu\nu}$ appears in the linearized equation of motion $Mv = -j$ and has the form $M = -\nabla^2 - 2gF$, while the matrix $M^{(0)}$ is given by the simple expression $M^{(0)} = -\partial^2_\mu$.

3.1. Within $SU(2)$ theory, M has dimensions of 12×12 and admits a partial diagonalization. The time sector (3×3) is diagonalized completely by choosing a basis formed by amplitudes featuring isospin projections of 0 and ±1 onto the momentum direction. The spatial sector (9×9) can be simplified by using a basis constructed in terms of the amplitudes characterized by the combined-spin projections of ±2 (two singlets), ±1 (two doublets), and 0 (triplet) (by the combined spin, we mean the vector sum $\mathbf{s} + \mathbf{j}$, where $\mathbf{j}$ is the ordinary spin and $\mathbf{s}$ is the isospin). We consider the constant-field condensate

$$V^a_\mu = V\delta^a_\mu, \qquad (7)$$

where V is a constant. It can also be written in the form $V^1_1 = V^2_2 = V^3_3 = V$, with the remaining components being equal to zero.

All calculations are performed in the Euclidean metric, where the squared four-momentum is $p^2 = k^2 + \omega^2$, k and ω being, respectively, the absolute value of the 3-momentum and the frequency. In integrating, with respect to angles, power series in terms of p and k, we make use of the relations $\langle k^2p^{-2}\rangle = 3/4$, $\langle k^4p^{-4}\rangle = 5/8$, $\langle\omega^2p^{-2}\rangle = 1/4$, and $\langle\omega^4p^{-4}\rangle = 1/8$. In performing integration with respect to the radial momentum component, we set $d^4p = \pi^2p^2dp^2$. The logarithm of the determinant of the matrix M can be replaced by the sum of logarithms of the determinants of separate blocks, which appear to be polynomials in p^2 and k. The calculations are simplified by combining blocks characterized by spin projections that are equal in absolute value, but which are opposite in sign. In this case, only even powers of k survive, so that a smaller number of terms must be taken into account in the expansion being considered. The determinants represent products of the eigenvalues λ_i; therefore, only the products $\prod_i \lambda_i$ are needed to calculate $L^{(1)}$, solving the characteristic equations being unnecessary. The computational technique will be demonstrated by considering the example of the product of the blocks characterized by the combined-spin projections of ±1. We have

$$\mathrm{Det}(\pm) = \begin{vmatrix} p^2 + 2 \pm 2k & -2 \\ -2 & p^2 + 2 \end{vmatrix}. \qquad (8)$$

Here, the momentum is taken to be a dimensionless variable that is obtained upon the substitution $p^2 \longrightarrow p^2/g^2V^2$. Further, we consider the product $p^8 + 8p^6 - 4k^2p^4 + 16\omega^2p^2 - 16k^2$ of the determinants for the matrix $M^{(0)}$. Dividing this product by p^8 and taking the logarithm of the quotient, we arrive at

$$\ln(1 + (8 - 4k^2p^{-2})p^{-2} + 16\omega^2p^{-6} - 16k^2p^{-8}). \qquad (9)$$

Expanding the logarithm in a power series in terms of p^{-2}, we obtain

$$\begin{aligned}&(8 - 4k^2p^{-2})p^{-2} + 16(\omega^2p^{-2})p^{-4}\\ &-\frac{1}{2}(64 - 64k^2p^{-2} + 16k^4p^{-4})p^{-4} + \ldots.\end{aligned} \qquad (10)$$

Here, the first term leads to a quadratic divergence, which is discarded. We retain only terms of order p^{-4}, which lead to a logarithmic divergence. Integration with respect to the angles of a four-dimensional sphere with allowance for the common sign yields the total prelogarithmic factor of $\gamma = -[4 - (1/2)(64 - 48 + 10)] = +9$. The contributions of the remaining blocks are calculated in a similar way. For $SU(2)$ theory, the numerical factors for all the blocks are presented in Table 1. In this

table, m is the combined-spin projection, n is the number of the amplitudes in a block, γ is a numerical factor, and Det is a characteristic polynomial. We display spacelike amplitudes in the first three rows, timelike amplitudes in the two rows that follow, and the sum in the last row.

Summing the numerical factors for all the blocks and recovering the dimensional form, we find in the $SU(2)$ case that

$$L^{(1)} = -\frac{11g^4V^4}{16\pi^2}\ln\frac{V^2}{\mu^2} = -\frac{11g^2H^2}{48\pi^2}\ln\frac{H}{\mu^2}, \qquad (11)$$

where μ is the normalization point and $H^2 = \frac{1}{2}F^2$ is the square of the constant-chromomagnetic-field strength. This result is half as great as that obtained in [22], but it coincides with the result obtained in [1–3] for the case of a constant Abelian field.

3.2. Going over to $SU(3)$ theory, we first consider the case of a conventional condensate as given by (7) (below, it is denoted by N_s). This condensate corresponds to the mapping of the rotation group onto the $SU(2)$ group that appears to be a subgroup of the color group and which is spanned by the generators T_1, T_2, and T_3. Within this subgroup, all features of the gluon spectrum and the contributions of individual sectors to the effective Lagrangian replicate exactly the pattern of $SU(2)$ theory. Five generators of the $SU(3)$ group beyond the subgroup form a coset involving 20 amplitudes. The corresponding 20×20 matrix can be partitioned into blocks according to the values of the combined spin

$$\mathbf{S} = \mathbf{j} + \mathbf{s} \qquad (12)$$

and of its projection m onto the momentum direction. The amplitudes associated with the isospin-singlet generator T_8 do not interact with the condensate and do not therefore contribute to $L^{(1)}$. The generators T_4, T_5, T_6, and T_7 corresponding to the isospin of 1/2 give rise to 2×4 $S = 3/2$ amplitudes and 2×2 $S = 1/2$ amplitudes in spatial components; they also generate 2×2 $S = 1/2$ amplitudes in time components. The combined-spin projection onto the momentum direction,

$$m = (\mathbf{S}\cdot\mathbf{k})/|\mathbf{k}|, \qquad (13)$$

is unaffected by any term of the matrix M, while the square of combined spin, $(\mathbf{S})^2 = S(S+1)$, is conserved by any term, with exception of $V_\mu\partial_\mu$. In order to establish the relation between the matrix $M^{ad}_{\mu\nu}$ and the quantum numbers S and m, we write this matrix in the expanded form

$$M^{ad}_{\mu\nu} = \delta_{\mu\nu}(\partial_\lambda\partial_\lambda\delta^{ad} + 2V\partial_i c^{aid} + V^2 c^{aic}c^{cid}) + 2V^2 c^{abd}c^{b\mu\nu}. \qquad (14)$$

Table 1

m	n	γ	Det
±2	2	5	$p^4 - 4k^2$
±1	4	9	$p^8 + 8p^6 - 4k^2p^4 + 16\omega^2p^2 - 16k^2$
0	3	7	$p^6 + 10p^4 - 4k^2p^2 + 24p^2 - 8k^2$
±1	2	3	$p^4 + 4\omega^2 + 4$
0	1	–2	$p^2 + 2$
	12	22	

In the last term, which is proportional to $F^b_{\mu\nu}$, the factor $c^{b\mu\nu}$ vanishes if at least one of the subscripts μ or ν is zero. The terms involving V^2 can easily be expressed in terms of the spin variables as

$$c^{aic}c^{cid} = s(s+1), \qquad (15)$$

$$2c^{abd}c^{bij} = -2(\mathbf{j}\cdot\mathbf{s}) = j(j+1) + s(s+1) - S(S+1). \qquad (16)$$

The operator $2V\partial_i c^{aid}$ is proportional to the isospin projection onto the direction associated with the momentum; it does not conserve the total combined spin, but conserves its projection onto the momentum direction. In order to employ the amplitudes characterized by specific quantum numbers S and m as a basis, it is necessary to introduce the subspace of amplitudes associated with all those values of S that are compatible with a given value of m and to go over, by using conventional rules for the composition of angular momenta, to the helicity amplitudes characterized by specific values of the projections of $\mathbf{j}$ and $\mathbf{s}$ onto the quantization axis. By applying this technique to amplitudes associated with the generators $T_4, \ldots, T_7$, we obtain following results.

For the $m = \pm 3/2$ sector, the characteristic polynomial is $\mathrm{Det} = p^2 \pm k - 1/4$ and the resulting contribution is $\gamma = 3/4$. The $S = 3/2$ amplitudes are unstable even at $k = 0$, which results in the existence of tachyons for $k^2 < V^2$.

For the $m = \pm 1/2$ spacelike amplitudes, the characteristic polynomial is

$$\mathrm{Det} = \begin{vmatrix} p^2 \pm k/3 - 1/4 & \mp 2\sqrt{2}k/3 \\ \mp 2\sqrt{2}k/3 & p^2 \mp k/3 - 11/4 \end{vmatrix} = p^4 + \frac{5}{2}p^2 - k^2 \pm k - 11/16 \qquad (17)$$

and the resulting contribution is $\gamma = 9/2$.

For the sector of $m = \pm 1/2$ timelike amplitudes, we have $\mathrm{Det} = p^2 \pm k + 3/4$ and $\gamma = 1/4$.

Upon summation, the result must be doubled since each sector makes a double contribution: $\sum\gamma = 11$. The total contribution of the generators T_4, T_5, T_6, and T_7 amounts to half the contribution of the generators T_1,

Table 2

j	m	n	γ	Det
1	±3	2	9/4	$p^2 + 1/2 \pm 2k$
1	±2	4	–15/16	$p^4 + \frac{5}{2}p^2 + 2k^2 + 1 \pm k(3p^2 + 7/2)$
1	±1	6	21/16	$p^6 + \frac{11}{2}p^4 + 2p^2k^2 + \frac{17}{2}p^2 + 3k^2 + 3 \pm k(3p^4 + 10p^2 + 27/4)$
1	0	3	63/16	$p^6 + \frac{11}{2}p^4 - p^2k^2 + \frac{17}{2}p^2 - \frac{3}{2}k^2 + 3$
0	±2	2	7/4	$p^2 + 3/2 \pm 2k$
0	±1	2	–5/16	$p^2 + 3/2 \pm k$
0	0	1	–9/8	$p^2 + 3/2$
		20	55/8	

T_2, and T_3 spanning the subgroup. For the N_s case within $SU(3)$ theory, we eventually obtain

$$L^{(1)} = -\frac{33}{32\pi^2}g^4V^4\ln\frac{V^2}{\mu^2} = -\frac{11g^2H^2}{32\pi^2}\ln\frac{H}{\mu^2}. \quad (18)$$

3.3. There is another version of the $SU(3)$ condensate, N_w. It corresponds to the mapping of the rotation group onto an $SU(2)$ subgroup spanned by three $SU(3)$ generators associated with the structure constants equal to ±1/2—for example, T_2, T_7, and T_5. In this case, the remaining five generators (T_1, T_3, T_4, T_6, and T_8) form a quintet that corresponds to the formal-isospin value of 2. This partition of eight $SU(3)$ generators (8 = 3 + 5) is used to describe quadrupole deformations of nuclei. In order to assign the triplet of the subgroup generators an isospin of 1 and the remaining generators an isospin of 2, the common normalization of the generators must be doubled. We choose the direction of T_2 for the quantization axis in the group space and introduce the operators $T_{s\mu}$ characterized by specific values of the isospin and of its projection: $T_{11} = (-\lambda_7 + i\lambda_5)/\sqrt{2}$, $T_{10} = \lambda_2$, $T_{1-1} = (\lambda_7 + i\lambda_5)/\sqrt{2}$, $T_{22} = (-\lambda_3 - i\lambda_1)/\sqrt{2}$, $T_{21} = (\lambda_4 + i\lambda_6)/\sqrt{2}$, $T_{20} = +\lambda_8$, $T_{2-1} = (-\lambda_4 + i\lambda_6)/\sqrt{2}$, and $T_{2-2} = (-\lambda_3 + i\lambda_1)/\sqrt{2}$. On the right-hand sides of these equalities, we use the conventional notation for the Gell-Mann matrices, but we imply the matrices of the adjoint representation, which obey the same commutation relations. These operators satisfy the standard commutation relations

$$[T_{1\nu}, T_{s\mu}] = \sqrt{s(s+1)}C^{s\mu+\nu}_{s\mu 1\nu}T_{s\mu+\nu}. \quad (19)$$

The introduction of the basis $T_{s\mu}$ and the use of the combined spin (12) simplify considerably the diagonalization of the matrix $M^{ad}_{\mu\nu}$.

The classification of 12 $s = 1$ amplitudes coincides with that presented in subsection 3.1 for the amplitudes in $SU(2)$ theory. The set of 20 $s = 2$ amplitudes can be partitioned into the $m = \pm 3, \pm 2, \pm 1$, and 0 blocks of the spacelike sector, which have dimensions 2×2, 4×4, 6×6, and 3×3, respectively, and $m = \pm 2, \pm 1$, and 0 blocks of the timelike sector, which have dimensions 2×2, 2×2, and 1×1, respectively. The operator $2V\delta_{\mu\nu}\partial_i c^{aId}$ [see equation (14)] is diagonal within the basis of amplitudes characterized by a specific value μ of the projection of the isospin **s** onto the momentum direction **k** ($\mu = (\mathbf{k}\cdot\mathbf{s})/|k|$) and is equal to $kV\mu$. Here, $I = I(i)$ is an integer-valued function of the index i; it takes the values of 2, 5, and 7 at $i = 1$, 2, and 3, respectively. The operators quadratic in V are diagonal at a specific value of the combined spin S and are independent of the combined-spin projection m. Taking into account the change in the normalization of the generators, we must use the following relations for the N_w condensate instead of (15) and (16):

$$c^{aic}c^{cid} = \frac{1}{4}s(s+1), \quad (20)$$

$$2c^{abc}c^{bij} = \frac{1}{4}(j(j+1) + s(s+1) - S(S+1)). \quad (21)$$

For N_w, the contribution of 12 $s = 1$ amplitudes associated with the $SU(2)$ subgroup amounts to one-sixteenth of that obtained in $SU(2)$ theory: $\sum\gamma = 11/8$. The results for 20 $s = 2$ amplitudes are displayed in Table 2.

In this table, the expressions for the determinants involve the dimensionless momenta obtained upon the substitutions $p \longrightarrow p/gV$ and $k \longrightarrow k/gV$. Summing the contributions from the $s = 1$ [($SU(2)$ subgroup] and $s = 2$ sectors, we arrive at $\sum\gamma = 33/4$ and

$$L^{(1)} = -\frac{33}{128\pi^2}g^4V^4\ln\frac{V^2}{\mu^2} = -\frac{11}{32\pi^2}g^2H^2\ln\frac{H}{\mu^2}. \quad (22)$$

The ratio of the contribution from the amplitudes associated with the subgroup to that from the remaining amplitudes is 2 : 1 for N_s and 1 : 5 for N_w. Despite such large differences, the expressions for $L^{(1)}(H)$ are identical in the two cases.

4. QUARK CONTRIBUTION TO THE ONE-LOOP CORRECTION TO THE LAGRANGIAN

Quarks interacting with the condensate are treated as fermions in the fundamental representation of the color group. The quantity $L_q^{(1)}$ is determined by an integral of the logarithm of the determinant with respect to momenta:

$$L_q^{(1)} = \int\frac{d^4p}{(2\pi)^4}\ln\frac{\mathrm{Det}\,M_q}{\mathrm{Det}\,M_q^{(0)}}. \quad (23)$$

Here, M_q ($M_q^{(0)}$) is the matrix for the Dirac equations featuring a (no) field. Within $SU(2)$ and $SU(3)$ theories, the dimensions of these matrices are, respectively, 8×8 and 12×12. Specifically, we have

$$M_q = i\gamma_\mu \nabla_\mu^{\alpha\beta} - m\delta^{\alpha\beta}, \quad (24)$$

$$i\nabla_\mu^{\alpha\beta} = p_\mu \delta^{\alpha\beta} - W_\mu^{\alpha\beta}, \quad (25)$$

$$W_\mu^{\alpha\beta} = gV_\mu^b \lambda_b^{\alpha\beta}/2, \quad (26)$$

where α and β (a and b) are the color indices in the fundamental (adjoint) representation, while λ_b is a Gell-Mann matrix [within $SU(2)$ theory, it corresponds to the ordinary isospin matrices $\tau_b^{\alpha\beta}$].

In order to evaluate the determinants, it is convenient to go over to a second-order equation in terms of momenta by means of multiplication by the projection operator selecting solutions with $p_0 > 0$. Since the logarithmically divergent part of the integral in (23) is controlled by high momenta, we can disregard the mass m.

If $V_0^b = 0$ and $V_i^b = V\delta_i^b$, the square of the matrix M_q is given by

$$M_q^2 = p^2 - \gamma_i\gamma_j(p_i W_j + p_j W_i - W_i W_j). \quad (27)$$

First, we perform our calculations within $SU(2)$ theory. Using the relation $\gamma_i\gamma_j = -(\delta_{ij} + i\varepsilon_{ijk}\sigma_k)$, $\tau_i\tau_j = \delta_{ij} + i\varepsilon_{ijk}\tau_k$, and $2\sigma_k\tau_k = 4(S(S+1) - 3/2)$, we obtain

$$M_q^2 = p^2 + Vp_i\tau_i - \frac{1}{4}V^2(9 - 4S(S+1)), \quad (28)$$

where $p^2 = p_\mu p_\mu$ and S is the combined spin, so that $S(S+1) = (\sigma_k + \tau_k)^2/4$. Further, we go over to the Euclidean metric, $p^2 = \omega^2 + k^2$, and break down the determinant into two blocks associated with $S_z = \pm 1$ and $S_z = 0$ (the direction of the spatial component of the momentum $p_i = k_i$ is chosen for the quantization axis). For the first block, the result obtained after the Wick rotation is

$$\mathrm{Det}(1) = (p^2 + 1/4)^2 - k^2 \quad (29)$$

with $\tau_i = \pm 1$. Within the second block, the operator τ_i permutes the functions associated with $S = 1$ and $S = 0$, and we have

$$\mathrm{Det}(2) = \begin{vmatrix} p^2 + 1/4 & k \\ k & p^2 + 9/4 \end{vmatrix} = p^4 + \frac{5}{2}p^2 - k^2 + 9/16. \quad (30)$$

In either case, the determinants of $M_q^{(0)}$ are equal to p^4. The quark spectra are free from the tachyon part.

By using the same procedure as in the preceding section to calculate the momentum integral in (23), we find that Det(1) does not contribute and that the contribution of the second determinant is $\sum\gamma = 1$. For the effective Lagrangian, we obtain

$$L_q^{(1)} = N_q \frac{g^4 V^4}{16\pi^2} \ln\frac{V^2}{\mu^2}, \quad (31)$$

where N_q is the number of quark types.

Within $SU(3)$ theory, there are two modifications of the gluon condensate. For the first one, denoted below by N_s, the rotation group $O(3)$ is projected onto ordinary $SU(2)$ subgroup of the color group; the generators of this subgroup can be chosen to be $\lambda_1/2$, $\lambda_2/2$, and $\lambda_3/2$. For the second type of condensate (we denote it by N_w), the doubled operators λ_2, λ_7, and $-\lambda_5$, which would have, in the case of a conventional normalization, the structure constants of $\pm 1/2$ (not ± 1, as in the preceding version), are taken for the generators of the subgroup.

We begin by considering the first possibility, in which case we arrive at a result nearly identical to the preceding one. For the $SU(3)$ case, the result obtained instead of (28) in the Euclidean metric is

$$M_q^2 = p^2 + Vk_i\lambda_i + \frac{1}{4}V^2(2 + \delta_{ij}d_{ijk}\lambda_k - \varepsilon_{ijk}c^{ijl}\sigma_k\lambda_l). \quad (32)$$

The operator $\varepsilon_{ijk}c^{ijl}$ is equal to $2\delta_{kl}$ for N_s and half as great as that for N_w.

In the N_s case, the operator $2 + d_{iik}\lambda_k$ is equal to the tripled projection operator diag(1, 1, 0). Hence, the third component of the fundamental $SU(3)$ representation is inoperative completely, and the correction to the Lagrangian is given by (31).

In the N_w case, all three quark colors must be taken into account. The constant-potential components are

$$V_1 = V\lambda_2/2, \quad V_2 = V\lambda_7/2, \quad V_3 = -V\lambda_5/2. \quad (33)$$

In a condensed notation, we have $V_i = V\lambda_I/2$, where λ_I takes the form of λ_2, λ_7, and $-\lambda_5$ for $i = 1$, 2, and 3, respectively. In this case, we can easily show that $d_{IIk}\lambda_k = 0$. A partial diagonalization of the relevant matrix is accomplished by partitioning the amplitude according to the values of the combined-spin projection onto the momentum direction,

$$m = (\sigma_i/2 + \lambda_i)k_i/k, \quad (34)$$

m taking the values of $\pm 3/2$ and $\pm 1/2$.

In calculating the product $\sigma_k\lambda_k$, it is convenient to use the quark basis

$$a_+ = \frac{1}{\sqrt{2}}\begin{pmatrix} 1 \\ i \\ 0 \end{pmatrix}, \quad a_0 = \begin{pmatrix} 0 \\ 0 \\ 1 \end{pmatrix}, \quad a_- = \frac{1}{\sqrt{2}}\begin{pmatrix} 1 \\ -i \\ 0 \end{pmatrix}, \quad (35)$$

in which the matrix λ_2 acts as a diagonal operator:

$$\lambda_2 a_+ = a_+, \quad \lambda_2 a_0 = 0, \quad \lambda_2 a_- = -a_-. \tag{36}$$

The $m = 1/2$ amplitudes

$$\begin{aligned} A_3 &= (a_+ b_- + \sqrt{2} a_0 b_+)/\sqrt{3}, \\ A_1 &= (\sqrt{2} a_+ b_- - a_0 b_+)/\sqrt{3} \end{aligned} \tag{37}$$

are associated with the combined-spin values of 3/2 and 1/2, with the projection of the combined spin being +1/2 in either case (b_+ and b_- are the eigenvectors of the ordinary spin, $\sigma_i b_\pm = \pm b_\pm$).

With the aid of the identity $S(S+1) = 3/4 + 2 + \sigma_k \lambda_k$, we obtain $\sigma_i \lambda_I = -2$ and 1 for A_1 and A_3, respectively. It is obvious that $m = \pm 3/2$ for the $S = 3/2$ amplitudes. We also have $k_i \lambda_I = \pm k$ for $S = 3/2$ and $m = \pm 3/2$. When $m = \pm 1/2$, there is a nondiagonal operator in the basis formed by A_3 and A_1:

$$k_i \lambda_I = \frac{k}{3} \begin{pmatrix} 1 & \pm\sqrt{2} \\ \pm\sqrt{2} & 2 \end{pmatrix}. \tag{38}$$

The characteristic polynomial for the $m = \pm 3/2$ sector coincides with the right-hand side of (29). This sector does not contribute to $L^{(1)}$. In the $m = \pm 1/2$ case, we obtain

$$\begin{aligned} \mathrm{Det} &= \begin{vmatrix} p^2 + 1/4 \pm k/3 & \pm\sqrt{2}/3 \\ \pm\sqrt{2}/3 & p^2 + 1 \pm 2k/3 \end{vmatrix} \\ &= p^4 + \frac{9}{4} p^2 + 1/4 \pm k(p^2 + 1/2). \end{aligned} \tag{39}$$

In summary, $\sum \gamma = 1/4$, and the final result is

$$L_q^{(1)} = \frac{N_q}{64\pi^2} g^4 V^4 \ln \frac{V^2}{\mu^2} = \frac{N_q}{48\pi^2} g^2 H^2 \ln \frac{H}{\mu^2}. \tag{40}$$

5. CALCULATION OF THE LOGARITHMICALLY DIVERGENT PART OF THE ONE-LOOP EFFECTIVE LAGRANGIAN WITHIN ARBITRARY GAUGE THEORY FOR AN ARBITRARY CONSTANT BACKGROUND FIELD

The calculations presented in preceding sections can be considerably generalized and extended if we focus on the divergent part of the effective Lagrangian. It turned out that this divergent part can be calculated in a compact form within an arbitrary gauge theory and for an arbitrary background field. We begin by introducing the convenient notation

$$(\hat{A})_{ab} = g(T_c)_{ab} A_c \tag{41}$$

for the contraction of a group vector with the group generators (here, g stands for the coupling constant). In the adjoint representation, we have $(T_c)_{ab} = c_{acb}$. In the following, we everywhere suppress group indices on the quantities involved, retaining only Lorentz indices. The covariant derivative can then be written in the form $\nabla = \partial + \hat{V}$. For the constant field V, the Jacobi identity yields

$$\hat{F}_{\mu\nu} = \widehat{\hat{V}_\mu V_\nu} = \hat{V}_\mu \hat{V}_\nu - \hat{V}_\nu \hat{V}_\mu. \tag{42}$$

As in preceding sections, we will employ here the cutoff regularization, denoting the cutoff momentum by Λ.

The one-loop Lagrangian is given by

$$\begin{aligned} L^{(1)} &= \ln[\mathrm{Det}^{-1/2}(G/G_0)\mathrm{Det}(D/D_0)\mathrm{Det}^N(S/S_0)] \\ &= -\frac{1}{2}\ln\mathrm{Det}(G/G_0) + \ln\mathrm{Det}(D/D_0) + N\ln\mathrm{Det}(S/S_0). \end{aligned} \tag{43}$$

Here, G, D, and S are the quadratic-form operators defined for gluons, ghosts, and fermions, respectively; they are obtained upon a shift by the background field in the Lagrangian. This means that G and S coincide with the matrices M and M_q from the preceding sections, but they are written in a new notation:

$$G_{\mu\nu} = \nabla^2 \delta_{\mu\nu} + 2\hat{F}_{\mu\nu}, \tag{44}$$

$$D = \nabla^2, \quad S = \gamma\nabla - m. \tag{45}$$

In (43), we have also denoted by G_0, D_0, and S_0 the values of G, D, and S, respectively, at zero background field and by N the number of flavors. In the following, we disregard fermion masses. In the momentum representation, we have $\partial \longrightarrow ip$; introducing a unit vector n directed along the momentum vector, we obtain

$$(G/G_0)_{\mu\nu} = \delta_{\mu\nu} - \frac{2in\hat{V}\delta_{\mu\nu}}{p} - \frac{\hat{V}^2\delta_{\mu\nu} + 2\hat{F}_{\mu\nu}}{p^2}, \tag{46}$$

$$\begin{aligned} D/D_0 &= 1 - \frac{2in\hat{V}}{p} - \frac{\hat{V}^2}{p^2}, \\ S/S_0 &= 1 - \frac{(\gamma\hat{V})(\gamma n)}{p}. \end{aligned} \tag{47}$$

Since the divergence in the momentum integral stems exclusively from the upper limit, it can be isolated in the following way. We break down the integration interval $[0, \Lambda]$ in the regularized integral into the intervals $[0, V]$ and $[V, \Lambda]$, where V is the value of any component of the background potential. Only the second integral diverges upon the removal of regularization; therefore, it is sufficient to restrict our consideration to this integral. Using the identity $\ln\mathrm{Det}A = \mathrm{tr}\ln A$ and expanding the matrix logarithm into a power series as

$$\ln(1-A) = -A - \frac{1}{2}A^2 - \frac{1}{3}A^3 - \frac{1}{4}A^4 + \ldots, \tag{48}$$

we can isolate terms proportional to $1/p^4$, which lead to a logarithmic divergence:

$$\int_V^\Lambda \frac{d^4p}{(2\pi)^4}\frac{A(n)}{p^4} = \frac{1}{8\pi^2}\langle A(n)\rangle \ln\frac{\Lambda}{V}. \quad (49)$$

(The averaging denoted by angular brackets is performed over the directions of the vector n.) We further consider the contributions of gluons, ghosts, and fermions separately.

The gluon contribution is given by

$$\left\langle \mathrm{tr}\left[-\frac{1}{2}(\hat{V}^2\delta_{\mu\nu} + 2\hat{F}_{\mu\nu})(\hat{V}^2\delta_{\mu\nu} + 2\hat{F}_{\nu\mu}) - 4\hat{V}^2(2in\hat{V})^2 - (2in\hat{V})^4\right]\right\rangle. \quad (50)$$

The mean values of the products of two and four vectors can be determined by the formulas

$$\langle n_\alpha n_\beta\rangle = \frac{1}{4}\delta_{\alpha\beta},$$
$$\langle n_\alpha n_\beta n_\mu n_\nu\rangle = \frac{1}{24}(\delta_{\alpha\beta}\delta_{\mu\nu} + \delta_{\alpha\mu}\delta_{\beta\nu} + \delta_{\alpha\nu}\delta_{\beta\mu}). \quad (51)$$

Upon performing all contractions and taking into account the factor of 1/2 in (43), we obtain $(5/6)\mathrm{tr}(\hat{F}_{\mu\nu}\hat{F}_{\mu\nu})$. For the ghost contribution, we similarly arrive at [taking into account the factor of –1 in (43)] $(1/12)\mathrm{tr}(\hat{F}_{\mu\nu}\hat{F}_{\mu\nu})$. Thus, the logarithmically divergent part of the effective Lagrangian within a fermion-free theory has the form

$$L^{(1)} = -\frac{1}{8\pi^2}\frac{11}{12}\mathrm{tr}(\hat{F}_{\mu\nu}\hat{F}_{\mu\nu})\ln\frac{\Lambda}{V}. \quad (52)$$

The fermion contribution can be represented in the form $-(1/4)\mathrm{tr}[(\gamma\hat{V})(\gamma n)]^4$. We assume that, in the Euclidean case, $\gamma_4 = i\gamma_0$; therefore, $\gamma_\mu\gamma_\nu + \gamma_\nu\gamma_\mu = -2\delta_{\mu\nu}$. Using the formula for the average of the product of four vectors n and the well-known properties of the Dirac matrices and taking into account the factor $-N$ in (43), we obtain the fermion contribution in the form $(N/3)\mathrm{tr}(\hat{F}_{\mu\nu}, \hat{F}_{\mu\nu})$, where the trace is calculated in that representation to which the fermions belong.

For any compact group and in any representation, we have

$$\mathrm{tr}(T_aT_b) \sim \delta_{ab}. \quad (53)$$

Therefore, only the product $F_{\mu\nu}F_{\mu\nu}$ appears in all relevant expressions. This is a nontrivial fact, since we might have expected the emergence of the combinations $\mathrm{tr}(\hat{V}_\mu\hat{V}_\mu\hat{V}_\nu\hat{V}_\nu)$ and $\mathrm{tr}(\hat{V}_\mu\hat{V}_\nu\hat{V}_\mu\hat{V}_\nu)$, which appear in intermediate calculations; however, only their difference, as expressed in terms of $F_{\mu\nu}F_{\mu\nu}$, enters into the eventual result.

In the presence of fermions, the final expression for the logarithmically divergent part of the effective Lagrangian is given by

$$L^{(1)} = -\frac{1}{8\pi^2}\left(\frac{11}{12}A + \frac{N}{3}B\right)F_{\mu\nu}F_{\mu\nu}\ln\frac{\Lambda}{V}, \quad (54)$$

where A and B are factors entering into (53) in the adjoint representation and in the representation to which the fermions belong.

For example, $A = -2$ and $B = 1/2$ for the $SU(2)$ group and fermions in the fundamental representation, and $A = -3$ and $B = 1/2$ for the $SU(3)$ case and fermions in the fundamental representation.

Two important comments are in order here. It can easily be seen that the effective Lagrangian involves not only logarithmically divergent but also quadratically divergent terms. In order to eliminate them, we need gluon-mass counterterms, which break gauge invariance. In fact, gauge invariance is not broken: noninvariant gluon-mass counterterms are required only because of noninvariance of intermediate cutoff regularization. Had an invariant regularization procedure (for example, dimensional regularization) been employed, noninvariant counterterms would not have been necessary.

If the background field features only one dimensional parameter, it is meaningless to calculate the finite part of the effective Lagrangian. Its background-field dependence is obvious from dimensional considerations, while the coefficient is absorbed upon renormalization. For the background field of this type, the divergent part computed above represents the full one-loop contribution.

The coefficient in (54) is exactly equal to the one-loop beta function. To the best of our knowledge, 't Hooft [39] was the first to derive this result within the background-field method. By no means is this coincidence accidental since it is necessary to evaluate the same diagrams in deriving the beta function and the effective Lagrangian.

6. CONCLUSION

Calculation of quantum corrections to the Lagrangian is one of the most straightforward and conventional methods for studying the vacuum state in field theory [40]. The problem can be broken into two parts: (i) First, the trivial (perturbative) vacuum $|0\rangle$ is analyzed for stability. (ii) If this vacuum is found to be unstable, the second step consists in addressing the problem of establishing the stable vacuum state $|\mathrm{vac}\rangle$ for the system in question. Within the Yang–Mills theory, the eventual solution to these problems has yet to be obtained, so that it is worthwhile to explain in some detail what advances have been made owing to the above calculations. We begin by discussing methodological questions. Within the background-field method, both the classical (background) and the quantum (fluctuations) part are traditionally considered by

means of perturbation theory [32]. A condensate (if any) cannot be treated as a small perturbation. In view of this, a procedure employing a complicated propagator that includes background-field effects in zero approximation seems preferable. Coleman and Weinberg [34] proposed such a procedure for a scalar field (ϕ^4 theory). In the present study, this procedure has been implemented for a more complicated gauge-field theory in the one-loop approximation. The interaction of fluctuations with the background field have been taken into account nonperturbatively; perturbation theory has been employed only to describe the interaction between various degrees of freedom of quantum fluctuations.

Addressing the problem of stability of the trivial vacuum $|0\rangle$, we would like to recall that Kabo and Shabad [21] obtained an incorrect sign of the one-loop effective Lagrangian and, on this basis, concluded erroneously that the vacuum state $|0\rangle$ cannot become unstable. Our calculations correct this result, which is probably due to an inappropriate choice of the quantization scheme. Although the region of the possible instability of $|0\rangle$ is beyond the validity limits of perturbation theory, a nonperturbative character of the calculation of the one-loop contribution to $L^{(1)}$ has enabled us to conclude that the stability of the trivial vacuum can in principle be violated.

Of course, it is hardly correct to consider the physical vacuum $|\mathrm{vac}\rangle$ of the Yang–Mills field merely as a shifted field $V^a_\mu + v^a_\mu$ with fixed V^a_μ. It is rather an ensemble—that is, a set of solutions compatible with the requirement of minimum energy. The results presented above indicate that, most likely, the degree of degeneracy of such a vacuum is higher than that which might have been expected in advance. This is because the expression obtained for $L^{(1)}$ is insensitive to condensate parameters of secondary importance: to a logarithmic accuracy, $L^{(1)}$ depends only on F^2, the relevant expressions for the Abelian and the non-Abelian condensate configurations being identical. That $L^{(1)}$ is independent of other field invariants of the same dimension is due not only to the symmetry of Yang–Mills theory but also to the appropriate choice of gauge. However, investigation of the gauge dependence of the one-loop Lagrangian is beyond the scope of the present study.

REFERENCES

1. G. K. Savvidi, Phys. Lett. B **71**, 133 (1977).
2. S. G. Matinyan and G. K. Savvidi, Nucl. Phys. B **143**, 539 (1978).
3. I. A. Batalin, S. G. Matinyan, and G. K. Savvidi, Yad. Fiz. **26**, 407 (1977) [Sov. J. Nucl. Phys. **26**, 214 (1977)].
4. V. V. Vladimirskii, Yad. Fiz. **58**, 107 (1995) [Phys. At. Nucl. **58**, 101 (1995)].
5. V. V. Vladimirsky, Yad. Fiz. **59**, 2063 (1996) [Phys. At. Nucl. **59**, 1988 (1996)].
6. V. V. Vladimirsky, Yad. Fiz. **61**, 573 (1998) [Phys. At. Nucl. **61**, 508 (1998)].
7. H. Pagels amd E. Tomboulis, Nucl. Phys. B **143**, 485 (1978).
8. N. K. Nielsen and P. Olesen, Nucl. Phys. B **144**, 376 (1978).
9. N. K. Nielsen and P. Olesen, Phys. Lett. B **79**, 304 (1978).
10. J. Ambjorn, N. K. Nielsen, and P. Olesen, Nucl. Phys. B **152**, 75 (1979).
11. N. K. Nielsen and P. Olesen, Nucl. Phys. B **160**, 380 (1979).
12. L. S. Brown and W. I. Wiesberger, Nucl. Phys. B **157**, 285 (1979).
13. H. B. Nielsen and M. Ninomiya, Nucl. Phys. B **156**, 1 (1979).
14. J. Ambjorn and P. Olesen, Nucl. Phys. B **170**, 60, 265 (1980).
15. H. Leutwyler, Nucl. Phys. B **179**, 129 (1981).
16. M. Ninomiya and N. Sakai, Nucl. Phys. B **190**, 316 (1981).
17. A. I. Mil'shtein and Yu. F. Pinelis, Phys. Lett. B **137**, 233 (1984).
18. A. V. Yung, Yad. Fiz. **41**, 1324 (1985) [Sov. J. Nucl. Phys. **41**, 842 (1985)].
19. L. Maiani *et al.*, Nucl. Phys. B **273**, 275 (1986).
20. A. S. Vshivtsev and D. V. Peregudov, Teor. Mat. Fiz. **104**, 435 (1995).
21. A. Kabo and A. E. Shabad, Tr. Fiz. Inst. Akad. Nauk SSSR **192**, 153 (1988).
22. R. Parthasarathy, M. Singer, and K. S. Viswanathan, Can. J. Phys. **61**, 1442 (1983).
23. D. Kay, Phys. Rev. D **28**, 1562 (1983).
24. S. Huang and A. R. Levi, Phys. Rev. D **49**, 6849 (1994).
25. A. I. Mil'shtein and Yu. F. Pinelis, Z. Phys. C **27**, 461 (1985).
26. V. E. Rochev, J. Phys. A **31**, 409 (1998).
27. A. S. Vshivtsev and D. V. Peregudov, Izv. Vyssh. Uchebn. Zaved., Fiz., No. 7, 18 (1997).
28. R. Anishetty, Phys. Lett. B **108**, 295 (1982).
29. M. Reuter and C. Wetterich, Phys. Rev. D **56**, 7893 (1997).
30. G. V. Efimov and S. N. Nedelko, Eur. Phys. J. C **1**, 343 (1998).
31. A. V. Averin, A. V. Borisov, and V. Ch. Zhukovskii, Z. Phys. C **48**, 457 (1990).
32. L. F. Abbott, Nucl. Phys. B **185**, 189 (1981).
33. A. Rebhan, Z. Phys. C **30**, 309 (1986).
34. S. Coleman and E. Weinberg, Phys. Rev. D **7**, 1888 (1973).
35. Yu. A. Simonov, Usp. Fiz. Nauk **166**, 337 (1996) [Phys. Usp. **39**, 313 (1996)].
36. C. D. Roberts and A. G. Williams, Prog. Part. Nucl. Phys. **33**, 477 (1994).
37. A. Hadice, Int. J. Mod. Phys. A **6**, 3321 (1991).
38. P. A. Kovalenko and L. V. Laperashvili, Yad. Fiz. **62**, 1857 (1999) [Phys. At. Nucl. **62**, 1729 (1999)].
39. G. 't Hooft, Nucl. Phys. B **62**, 444 (1973).
40. W. Heisenberg and H. Euler, Z. Phys. **98**, 714 (1936); V. F. Weisskopf, K. Mat. Fys. Medd. Dan. Vidensk. Selsk. **14**, 1 (1936).

Translated by O. Chernavskaya

Physics of Atomic Nuclei, Vol. 63, No. 8, 2000, pp. 1463–1476. From Yadernaya Fizika, Vol. 63, No. 8, 2000, pp. 1543–1556.

ON THE 85th ANNIVERSARY OF V.V. VLADIMIRSKY

Nuclear-Medium Modification of the $\rho^0(1S)$ and $\rho'(2S)$ Mesons in Coherent Photo- and Electroproduction: Coupled-Channel Analysis*

N. N. Nikolaev[1)], J. Speth[1)], and B. G. Zakharov[2)]

Received October 1, 1999

Abstract—We study medium modifications of the dilepton e^+e^- and $\mu^+\mu^-$ mass spectra in coherent photo- and electroproduction of $\rho^0(1S)$- and $\rho'(2S)$-meson resonances on nuclear targets. The analysis is performed within the coupled $\rho^0(1S)$, $\rho'(2S)$, … channel formalism, where nuclear modifications derive from off-diagonal rescatterings. We find that the effect of off-diagonal rescatterings on the shape of the dilepton-mass spectrum in the $\rho^0(1S)$-meson mass region is only marginal, but it is very important in the $\rho'(2S)$ mass region. The main off-diagonal contribution in the $\rho'(2S)$ mass region comes from the sequential mechanism $\gamma^* \longrightarrow \rho^0(1S) \longrightarrow \rho'(2S)$, which dominates $\rho'(2S)$ production for heavy nuclei. Our results also show that, in the $\rho'(2S)$ mass region, there is a considerable interference of the Breit–Wigner tail of the amplitude for the decay $\rho^0(1S)$ to e^+e^- and $\mu^+\mu^-$ with the amplitude for the decay of $\rho'(2S)$ to e^+e^- and $\mu^+\mu^-$. © *2000 MAIK "Nauka/Interperiodica".*

1. INTRODUCTION

The in-medium modification of hadrons in cold nuclear matter and hot QCD medium has been under active investigation throughout the last years. In particular, there was considerable interest in medium effects for light vector mesons. In several papers, the masses of vector mesons at rest in nuclear matter were calculated within various approaches [1–7]. The in-medium effects for moving vector mesons were discussed in [8–12]. Recall that, in optics, medium effects are described by the refraction index, which is calculable for dilute media in terms of the photon–atom forward-scattering amplitude. An extension of this formalism to fast vector mesons with the wavelength $\lambda = 1/p$ much shorter than the separation of nucleons in nuclear matter gives the in-medium mass shift Δm_V and the collision broadening $\Delta\Gamma_V$ in the form ([8]; for relevant earlier work, see [13, 14])

$$\Delta m_V(E) = -2\pi\frac{n_A}{m_V}\mathrm{Re}\, f(E),$$
$$\Delta\Gamma_V(E) = \frac{n_A}{m_V}p\sigma(E), \quad (1)$$

where E and m_V are the meson energy and in-vacuum mass, respectively; $f(E)$ is vector-meson–nucleon forward-scattering amplitude; and n_A is the nuclear matter density. These formulas are quite general and must hold for any particle species in an infinite medium if inelastic rescatterings or coupled-channel effects can be neglected (see below). An experimental observation of the in-medium mass shift and collision broadening (1) would be very interesting. Potentially, it could furnish information about the *VN*-scattering amplitude, which cannot be measured directly.

For the mass shift and collision broadening (1) to be observed experimentally, the typical decay length $L_d \sim E/m_V\Gamma_V$ must be smaller than the nucleus radius R_A; that is, the momentum of the vector meson must be less than

$$p_\rho < 6\ \mathrm{GeV}, \quad p_\omega < 300\ \mathrm{MeV}, \quad p_\phi < 200\ \mathrm{MeV}, \quad (2)$$

for the ρ^0, ω^0, and ϕ^0 meson, respectively [8]. Thus, only for the ρ^0 meson[3)] is there a sufficiently broad energy interval where the relations (1) could be used.

The applicability limits (2) are purely kinematical ones: they do not take into account the possible interference of decays of a vector meson inside and outside the target nucleus and quantum effects in production of the vector mesons. Both effects were studied—and found to be important—in the recent [10] Glauber–Gribov multiple-scattering theory [15, 16] analysis of coherent ρ^0-meson photoproduction observed in e^+e^- and $\mu^+\mu^-$ dilepton modes or in both of them. The dilepton-mass spectrum was shown to have a two-component structure corresponding to the decays of ρ^0 mesons inside and outside the target nucleus. The inside component can be approximately described by the Breit–Wigner formula with the in-medium modified mass and width as predicted by (1). Since the nucleus has a finite size, this component with a broad width does not

* This article was submitted by the authors in English.

[1)]Institut für Kernphysik, Forschungszentrum Jülich, D-52425 Jülich, Germany.

[2)]Landau Institute for Theoretical Physics, Russian Academy of Sciences, ul. Kosygina 2, Moscow, 117334 Russia.

[3)]Hereafter, wherever appropriate, ρ^0 will stand for the ground state $\rho^0(1S)$ meson.

develop, however, a genuine pole in the complex plane of the invariant mass M of the lepton pair. The genuine pole in the complex plane of M comes only from ρ^0-meson decays in a vacuum, and this outside component can be described by the standard Breit–Wigner formula with the in-vacuum mass and width. Boreskov *et al.* [10] found that, even at a low energy of $E \sim 2$ GeV, such that $R_A/L_d \sim 2$ for heavy nuclei, the interference between the inside and outside components is substantial and produces a complex dilepton mass spectrum that cannot be described in terms of the Breit–Wigner formula with a definite mass and a definite width. By way of example, we indicate that, at $E = 2$ GeV, the dilepton mass spectrum was found to develop a minimum near the ρ^0-meson mass. An experimental observation of this phenomenon would be of great interest. On the theoretical side, this calls for a numerical analysis within tested models of photoproduction in order to find out how a model analysis of such data would allow one to distinguish the inside and outside components and extract the ρ^0-meson mass shift and collision broadening for the inside component.

In the present article, we study the coherent reaction $\gamma^*A \longrightarrow VA \longrightarrow e^+e^-A$, $\mu^+\mu^-A$, where γ^* is a real or a virtual photon and where the target nucleus remains in the ground state. We use the coupled-channel approach, extending the work performed in [10], where numerical calculations were performed without the off-diagonal rescatterings of ρ^0 mesons. The coupled-channel analysis presented here is based on our well-tested color dipole approach (see, for instance, [17] and references therein), which was earlier successfully used to analyze data on ρ^0 and J/ψ electroproduction on nuclear targets at high energies [18–20] and data on vector-meson production at HERA [17, 21, 22]. This analysis is of interest for two reasons. First, the inclusion of off-diagonal rescatterings allows one to check the accuracy of the one-channel approximation in the $\rho^0(1S)$-meson mass region $0.5 < M < 1$ GeV studied in [10]. On the other hand, in the coupled-channel approach, one can extend the mass region and investigate the medium effects for the $2S$ state $\rho'(2S)$, for which the sequential off-diagonal mechanism $\gamma^* \longrightarrow \rho^0(1S) \longrightarrow \rho'(2S)$ is potentially important. This extension to the $\rho'(2S)$ meson is of great interest in itself. The key feature of the photoproduction of the $2S$ vector mesons on a free nucleon is strong suppression due to the nodal structure of the wave function of the $2S$ state [18, 23]. In [24], it was shown that the node effect can lead to anomalous A and Q^2 dependences of $\rho'(2S)$ photo- and electroproduction. This effect may help resolve the long-standing problem of the D-wave versus $2S$-wave assignment for the $\rho'(1480)$ and $\rho'(1700)$ states. The strong suppression of the cross section for the $\rho'(2S)$ meson in relation to the $\rho^0(1S)$ meson renders the experimental study of this phenomenon a challenging task. In particular, the mass spectra of the final particles in the $\rho'(2S)$ mass region can be affected by the interference with the $\rho^0(1S)$-meson Breit–Wigner tail. Our color dipole coupled-channel approach describes very well the suppression of ψ' production in relation to J/ψ observed by the NMC [25, 26], E687 [27], and H1 [28] collaboration and provides a sound framework for understanding the prospects for the experimental study of the $\rho'(2S)$-meson production $\gamma^*A \longrightarrow \rho^0(1S)A$, $\rho'(2S)A \longrightarrow e^+e^-A$. In the numerical analysis reported here, we focus on the energy range of the forthcoming high-luminosity experiments at TJNAF.

The ensuing exposition is organized as follows. In Section 2, we give basic formulas of the coupled-channel approach to the coherent reaction $\gamma^*A \longrightarrow e^+e^-A$, $\mu^+\mu^-A$. In Section 3, we discuss evaluation of the diffraction-scattering matrix. The numerical results on the nuclear modifications of the in-nucleus decay component of the dilepton mass spectrum are presented in Section 4. The results are summarized in Section 5.

2. COUPLED-CHANNEL FORMALISM

The description of the coupled-channel formalism for the reaction $\gamma A \longrightarrow e^+e^-A$ can be found in [10] (see also our early study in [29]). For this reason, we discuss it here briefly and give only basic formulas that are necessary for understanding technical aspects of our approach.

Standard Glauber–Gribov multiple-scattering theory [15, 16] for the coherent interaction of a projectile of energy E with a nucleus is equivalent to solving the set of coupled-channel eikonal wave equations [11]

$$\left[-\frac{\partial^2}{\partial z^2} + \hat{m}^2 + \hat{U}(\mathbf{r})\right]_{ij} \Psi_j(\mathbf{r}) = E^2\Psi_i(\mathbf{r}). \qquad (3)$$

Here, the z axis is chosen along the photon momentum; Ψ_i is the wave function for the channel $|i\rangle$, which can be a hadronic resonance or the initial photon; and $\hat{m}^2$ is the diagonal mass operator with eigenvalues $m_{ij}^2 = (m_i^2 - im_i\Gamma_i)\delta_{ij}$, where m_i and Γ_i are the in-vacuum mass and width of the state $|i\rangle$. For the incident photon, $\Gamma_{\gamma^*} = 0$ and $m_{\gamma^*}^2 = -Q^2$, where Q^2 is the photon virtuality, and the optical potential $\hat{U}(\mathbf{r})$ in (3) is given by

$$U_{ij}(\mathbf{r}) = -4\pi\langle i|\hat{f}|j\rangle n_A(\mathbf{r}), \qquad (4)$$

where $n_A(\mathbf{r})$ is the nuclear number density and $\hat{f}$ is the forward-scattering matrix in the normalization

$$\mathrm{Im}\langle i|\hat{f}|i\rangle = \frac{p_i}{4\pi}\sigma_{\mathrm{tot}}(iN \longrightarrow iN).$$

The boundary condition on the front face of the nucleus, $z = -R_A$, is $|i\rangle = \delta_{i\gamma^*}$.

The probability amplitude for the coherent transition $\gamma^*A \longrightarrow e^+e^-A$ can be expressed in terms of the solution $\Psi_i(\mathbf{r})$ of (3) as [10]

$$T(E, M, \mathbf{p}_\perp) = N\sum_{i=h}\langle e^+e^-|t|i\rangle\int d^2\mathbf{b}\,dz\exp[-i(p_z z + \mathbf{p}_\perp\cdot\mathbf{b})]\Psi_i(\mathbf{r}), \quad (5)$$

where $\mathbf{r} = (\mathbf{b}, z)$; M is the invariant mass of the e^+e^- pair; p_z and $\mathbf{p}_\perp$ are its longitudinal and transverse momenta, respectively; $\langle e^+e^-|t|i\rangle$ is the probability amplitude for $i \longrightarrow e^+e^-$ transition; and N is a normalization factor, which is immaterial from the point of view of the shape of the e^+e^- mass spectrum. Summation in (5) is performed only over the hadronic states, which, in our case, are vector mesons $\rho^0(1S)$, $\rho'(2S)$, etc. For a heavy nucleus with a mass number $A \gg 1$ and at $E \gg M$, the nuclear recoil can be neglected, and the longitudinal momentum of the e^+e^- pair then becomes

$$p_z \approx E - \frac{Q^2 + M^2 + \mathbf{p}_\perp^2}{2E}. \quad (6)$$

In the coherent production $\mathbf{p}_\perp^2 \lesssim 1/R_A^2$ and in what follows, we focus on $\mathbf{p}_\perp = 0$ and suppress this argument. By virtue of (6), the p_z dependence of the spatial integral on the right-hand side of (5) then transforms directly into the M dependence of the amplitude $T(E, M, \mathbf{p}_\perp)$ and the nuclear modification of the e^+e^- spectrum.

At high energies, the solution to (3) for the hadronic sector—we need it for evaluating the amplitude in (5)—can be written in the form

$$\Psi_h(\mathbf{b}, z) = \langle h|\hat{S}(\mathbf{b}, z)|\gamma^*\rangle\exp(ip_{\gamma^*}z), \quad (7)$$

where the operator $\hat{S}$ is given by

$$\hat{S}(\mathbf{b}, z) = \hat{P}_z\exp\left\{-\frac{i}{2p_{\gamma^*}}\int_{-\infty}^{z}d\xi[\hat{m}^2 + Q^2 + \hat{U}(\mathbf{b}, \xi)]\right\}. \quad (8)$$

Here, $\hat{P}_z$ is the z-ordering operator, and the p_{γ^*} is the photon momentum. For numerical calculations, it is convenient to treat in (8) the off-diagonal part of the optical potential in the hadronic sector as a perturbation; the diagonal transitions are included to all orders. Following [29], one can then represent the matrix elements of the operator $\hat{S}(\mathbf{b}, z)$ in the form of the ν-fold off-diagonal rescattering series,

$$\langle h|\hat{S}(\mathbf{b}, z)|\gamma^*\rangle = \sum_{\nu=0}^{\infty}\langle h|\hat{S}^{(\nu)}(\mathbf{b}, z)|\gamma^*\rangle, \quad (9)$$

where

$$\langle h|\hat{S}^{(0)}(\mathbf{b}, z)|\gamma^*\rangle = -\frac{1}{2}\sigma_{h\gamma^*}\int_{-\infty}^{z}dz_1 n_A(\mathbf{b}, z_1) \times\exp\left[ik_{\gamma^*h}(z - z_1) - \frac{1}{2}t(\mathbf{b}, z, z_1)\sigma_{hh}\right], \quad (10)$$

$$\langle h|\hat{S}^{(\nu)}(\mathbf{b}, z)|\gamma^*\rangle = \left(-\frac{1}{2}\right)^{\nu+1}\sum_{i_1,\ldots,i_\nu}\sigma'_{hi_\nu}\sigma'_{i_\nu i_{\nu-1}}\cdots\sigma_{i_1\gamma^*}\exp(ik_{\gamma^*h}z) \times\int_{-\infty}^{z}dz_{\nu+1}n_A(\mathbf{b}, z_{\nu+1})\exp\left[ik_{hi_\nu}z_{\nu+1} - \frac{1}{2}t(\mathbf{b}, z, z_{\nu+1})\sigma_{hh}\right]\int_{-\infty}^{z_{\nu+1}}dz_\nu n_A(\mathbf{b}, z_\nu)\exp\left[ik_{i_\nu i_{\nu-1}}z_\nu - \frac{1}{2}t(\mathbf{b}, z_{\nu+1}, z_\nu)\sigma_{i_\nu i_\nu}\right]\cdots\int_{-\infty}^{z_2}dz_1 n_A(\mathbf{b}, z_1) \times\exp\left[ik_{i_1\gamma^*}z_1 - \frac{1}{2}t(\mathbf{b}, z_2, z_1)\sigma_{i_1 i_1}\right], \quad \nu \geq 1. \quad (11)$$

Here, $\sigma'_{ik} = \sigma_{ik} - \delta_{ik}\sigma_{ii}$, the matrix $\hat{\sigma}$ is related to the forward-diffraction-scattering matrix by the equation

$$\hat{f} = \frac{ip_{\gamma^*}}{4\pi}\hat{\sigma}, \quad (12)$$

$$t(\mathbf{b}, z_2, z_1) = \int_{z_1}^{z_2}dz n_A(\mathbf{b}, z) \quad (13)$$

is the partial optical thickness, and

$$k_{ij} = \frac{m_i^2 - im_i\Gamma_i - m_j^2 + im_j\Gamma_j}{2E}, \quad (14)$$

$$k_{h\gamma^*} = -k_{\gamma^*h} = \frac{m_i^2 - im_i\Gamma_i + Q^2}{2E}. \quad (15)$$

The exponential factor $\exp\left[ik_{\gamma^*h}(z - z_1) - \frac{1}{2}t(\mathbf{b}, z, z_1)\sigma_{ii}\right]$ in (10) and (11) sums elastic, diagonal, and iN rescatterings to all orders.

The real part of (15)—the longitudinal-momentum transfer in the $j \longrightarrow i$ transition—increases with the difference between m_i and m_j. Consequently, the oscillating exponential factors in (10) and (11) lead to the form-factor suppression of the contribution from heavy

intermediate resonance states and to the related form-factor suppression of heavy-mass production and of the coherent cross section at high Q^2 when the longitudinal-momentum transfer $k_{h\gamma^*}$ in the $\gamma^* \longrightarrow h$ transition becomes large. Precisely the same form-factor effect generates a strong dependence of the probability amplitude (5) on the e^+e^- mass, so that the shape of resonances would differ substantially from the standard Breit–Wigner shape.

Equation (5) quantifies the separation of the production amplitude $T(E, M)$ into the inside and outside components—beyond the target nucleus, the z dependence of the wave functions $\Psi_i(z, \mathbf{b})$ follows the in-vacuum decay law, while the corresponding outside contribution to $T(E, M)$ has the familiar form of the sum of Breit–Wigner amplitudes with residues proportional to $\Psi_i(z = +R_A, \mathbf{b})$. Nuclear effects can modify dramatically both the relative amplitude and the phase of these residues in relation to $\sigma_{h\gamma^*}$ for the free-nucleon case. As was explained in the Introduction, the inside contribution is a Fourier transform over the finite range $-R_A < z < R_A$ and could develop the Breit–Wigner form with the shifted mass and collision-broadened width only if $L_d \ll R_A$.

The first-order term (10) corresponds to the standard Glauber approximation, where the state $|h\rangle$ produced in the $\gamma^* \longrightarrow h$ transition then propagates through the nucleus without inelastic rescatterings. The correction from the off-diagonal rescatterings is given by (11) and is responsible for the color-transparency phenomenon in the electroproduction of vector mesons at high Q^2, where it changes drastically the cross section in relation to the Glauber model predictions. However, as will be seen from our results for $\gamma^*A \longrightarrow \rho'(2S)A$ reactions, the off-diagonal effects come into play even at moderate values of the photon virtuality $Q^2 \lesssim 1$ GeV^2. This is a consequence of strong suppression of the direct transition $\gamma^* \longrightarrow \rho'(2S)$. As a result, the sequential mechanism $\gamma^* \longrightarrow \rho^0(1S) \longrightarrow \rho'(2S)$, involving the off-diagonal $\rho^0(1S) \longrightarrow \rho'(2S)$ rescattering, becomes important even at $Q^2 = 0$.

3. CALCULATION OF THE FORWARD-DIFFRACTION MATRIX

As an input to the coupled-channel calculations, one needs the forward-diffraction matrix. At high energies, it can be written as the sum of the Pomeron and Reggeon contributions:

$$\hat{\sigma} = \hat{\sigma}_{\mathbf{P}} + \hat{\sigma}_R. \qquad (16)$$

At energies of $E \gtrsim 2$ GeV to be considered below, the main contribution to $\hat{\sigma}$ comes from Pomeron exchange. We evaluate Pomeron exchange within the dipole approach describing the resonances as nonrelativistic $q\bar{q}$ states. The Pomeron contribution to the diffraction matrix element σ_{ij} for hadronic states can then be written as

$$\langle i|\hat{\sigma}_{\mathbf{P}}|k\rangle = \int d^2\boldsymbol{\rho}\, dz\, \psi_i^*(\boldsymbol{\rho}, z)\sigma(\rho)\psi_k(\boldsymbol{\rho}, z), \qquad (17)$$

where $\boldsymbol{\rho}$ is the transverse size of the $q\bar{q}$ pair, $\psi_{i,k}(\boldsymbol{\rho}, z)$ are the wave functions describing the $q\bar{q}$ states, and $\sigma(\rho)$ is the cross section for the interaction of the $q\bar{q}$ pair with a nucleon.

We also need the excitation matrix elements $\langle i|\hat{\sigma}|\gamma^*\rangle$ for $\gamma^* \longrightarrow q\bar{q}$ excitation on a free nucleon; in the nonrelativistic approximation, this proceeds into $q\bar{q}$ states with the sum of the quark helicities that is equal to the photon helicity [23]. Using the corresponding perturbative light-cone wave function of the virtual photon [30], we have [23]

$$\langle i|\hat{\sigma}|\gamma^*\rangle = C\int d^2\boldsymbol{\rho}\,\psi_i^*(\boldsymbol{\rho}, z = 0)\sigma(\rho)K_0(\epsilon\rho), \qquad (18)$$

where $K_0(x)$ is a modified Bessel function and

$$\epsilon^2 = m_q^2 + Q^2/4, \qquad (19)$$

m_q being the quark mass. In the present article, we focus on the nuclear-modification of the shape of resonances, paying no special attention to the absolute value of the normalizing factor C in (18) [it is immaterial here and in (5) as well].

We use the oscillator wave functions for the $q\bar{q}$ states, which simplify considerably numerical calculations: because of azimuthal symmetry of $\sigma_{\mathbf{P}}(\rho)$, only the transverse excitations with zero azimuthal quantum number can be excited in the intermediate state for off-diagonal rescatterings. The excitation energy of the transverse $q\bar{q}$ oscillator is $2\hbar\omega$, where ω is the oscillator frequency. In our analysis, we set the quark mass to $m_q = m_\rho/2$ and the oscillator frequency to $\omega = (m_{\rho'} - m_{\rho^0})/2 \approx 0.35$ GeV, assuming 1480 MeV for the mass of the radial excitation of ρ^0 meson. For the widths of the first two excitations, we use the values of $\Gamma_{\rho^0} \approx 150$ MeV and $\Gamma_{\rho'} \approx 285$ MeV; following the string model [31], we assume $\Gamma_i \propto m_i$ for higher states. Our results are not sensitive to this assumption because the contribution of higher excitations proves to be very small.

Experimental data on the low-x structure function F_2 and on vector-meson electroproduction on a nucleon can be described by representing $\sigma(\rho)$ as a sum of the energy-dependent perturbative and energy-independent nonperturbative components [17, 22, 32]. Here, we focus on the energy region $E \lesssim 20$ GeV, where the energy dependence of the dipole cross section can be neglected for a first approximation. In the present analysis, we are sensitive to $\sigma(\rho)$ mostly in the nonperturbative region $\rho \gtrsim 0.5$ fm. Here, the gross features of

$\sigma(\rho)$ are well parametrized by the two-gluon exchange model of the Pomeron [33, 34]:

$$\sigma(\rho) = \frac{16\alpha_s^2}{3}\int d^2\mathbf{q}\frac{[1-\exp(i\mathbf{q}\cdot\boldsymbol{\rho})][1-G_2(\mathbf{q},-\mathbf{q})]}{(\mathbf{q}^2+\mu_g^2)^2}. \quad (20)$$

Here, $G_2(\mathbf{q}_1, \mathbf{q}_2) = \langle N|\exp(i\mathbf{q}_1\cdot\mathbf{r}_1 + i\mathbf{q}_2\cdot\mathbf{r}_2)|N\rangle$ is the two-quark form factor for the nucleon and $\mu_g = 0.3$ GeV is an infrared cutoff. It reproduces the color-transparency property $\sigma(\rho) \propto \rho^2$ at small ρ, whereby the point-like $q\bar{q}$ system, which can be represented as a superposition of an infinite set of the resonance states, propagates through a nucleus without interaction. In terms of resonance states, this color-transparency phenomenon is associated with the exact cancellation of the diagonal and off-diagonal amplitudes [35]. The coupling constant α_s was normalized in such a way that the Pomeron contribution to the $\rho^0 N$ total cross section is $\sigma_{\mathbf{P}}^{\text{tot}}(\rho^0 N) = \langle\rho^0|\hat{\sigma}_{\mathbf{P}}|\rho^0\rangle \approx 20$ mb. In this case, the two-gluon formula gives, at $\rho \gtrsim 0.5$ fm, the $\sigma(\rho)$ value that is close to the dipole cross section as extracted from the analysis of experimental data on vector-meson electroproduction [17]. Hereafter, we will consider real, $Q^2 = 0$, and virtual, $Q^2 = 1$ GeV^2, photoproduction. With our nonrelativistic wave functions, we obtain

$$R(2S/1S) = \frac{\langle\rho'(2S)|\hat{\sigma}|\gamma^*\rangle}{\langle\rho^0(1S)|\hat{\sigma}|\gamma^*\rangle} = \begin{cases}0.21, & Q^2 = 0,\\ 0.5, & Q^2 = 1\ \text{GeV}^2,\end{cases} \quad (21)$$

which is close to the predictions from [17] obtained for the relativized wave functions. At $\rho \lesssim 0.5$ fm, the present parametrization gives $\sigma(\rho)$ values somewhat larger than those from [17]. But because of the larger quark mass in the present nonrelativistic model for $q\bar{q}$ states, the resulting diffractive matrix proves to be close to that from [17]. At this point, it must be made clear that the two-gluon parametrization (20) of $\sigma(\rho)$ is oriented toward describing the combined nonperturbative + perturbative dipole cross section, and μ_g is a phenomenological parameter that must not be taken at face value. The analysis [32] of low-x HERA data on the proton structure function F_{2p} within the generalized BFKL equation [36] and the nonperturbative evaluation of the gluon correlation radius [37] yield clear-cut evidence for the infrared cutoff $\mu_g \sim 0.75$ GeV for the perturbative dipole cross section.

In our calculations, we take into account the first four transverse excitations. The Pomeron contribution to the diffraction matrix in terms of these transverse oscillator states obtained here from (17) for our parametrization (20) of $\sigma(\rho)$ is given by

$$\langle i|\hat{\sigma}_{\mathbf{P}}|k\rangle \approx \begin{pmatrix} 20 & -10.1 & -4.8 & 2.4\\ -10.1 & 30.2 & -8.0 & 5.2\\ -4.8 & -8.0 & 32.9 & 6.5\\ 2.4 & 5.2 & 6.5 & 34.1\end{pmatrix}. \quad (22)$$

Here, the matrix elements in (22) are in mb units, while i and k are the radial quantum numbers of the transverse oscillators (as was said above, Pomeron exchange does not change the longitudinal quantum number). The matrix in (22) shows clearly the decrease of the off-diagonal amplitudes with increasing difference between the initial and final radial quantum numbers, $|i-k|$, which derives from the oscillation of the resonance wave function and which, in conjunction with the form-factor effect, suppresses the contribution of higher excitations to the production-amplitude matrix element (11). Using the three-dimensional $\rho'(2S)$-meson wave function from (22), one obtains the value of $\sigma_{\mathbf{P}}^{\text{tot}}(\rho'(2S)N) = \langle\rho'(2S)|\hat{\sigma}_{\mathbf{P}}|\rho'(2S)\rangle \approx 27$ mb for the Pomeron contribution to the $\rho'(2S)N$ total cross section.

In parametrizing the Reggeon contribution to the diffraction matrix, we assume that secondary Reggeon exchanges can be treated in terms of scattering amplitudes for the quark (or antiquark) forming the $q\bar{q}$ state as predicted by the dual parton model [38] and the model of quark–gluon strings [39], which is based on the idea of a topological expansion [40]. In this case, one can neglect the Reggeon contribution to off-diagonal transitions, and, for all excited ρ' states, the Reggeon contribution to the amplitudes for diagonal $\rho' N$ scattering proves to be equal to the Reggeon contribution to the amplitude for $\rho^0(1S)N$ scattering. This amplitude is dominated by the contribution of the Regge pole P', which can be written in the Regge approach as

$$\langle\rho^0|\hat{\sigma}_R|\rho^0\rangle = r_{P'}\left(\frac{s}{s_0}\right)^{\alpha_{P'}-1}\left[1 + i\frac{1+\cos\pi\alpha_{P'}}{\sin\pi\alpha_{P'}}\right], \quad (23)$$

where $s = m_N^2 + 2Em_N$. In our analysis, we take the standard Reggeon intercept of $\alpha_{P'} = 0.5$. The residue $r_{P'}$ was adjusted to reproduce, at $E \sim 10$ GeV, the real part of the $\rho^0 N$-scattering amplitude extracted in [12] from experimental data on ρ^0-meson photoproduction by using the vector-dominance model. For $s_0 = 1$ GeV^2, this yields $r_{P'} \approx 15$ mb. A nonzero Re/Im ratio for the diffraction-scattering matrix leads to a mass shift for resonance states decaying inside the nucleus. For the ρ^0 meson in the energy region $E \sim 2$–20 GeV considered in the present article, this yields $\Delta m_{\rho^0} \sim 50$–$100$ MeV.

In order to evaluate the e^+e^- mass spectrum, we also need the transition amplitude $\langle e^+e^-|t|i\rangle$ which enters

into equation (5). Following [10], we neglect the possible smooth M dependence of this transition amplitude against that which comes from the spatial integral on the right-hand side of (5) and set $\langle e^+e^-|t|i\rangle \propto \psi_i(\mathbf{r}=0)$ as predicted by the nonrelativistic model of $q\bar{q}$ states. In the nonrelativistic approach, the D-wave $q\bar{q}$ state does not contribute to dilepton production. For this reason, the absence of splitting of the $2S$ and D states in the oscillator model is not very important from the point of view of the e^+e^- mass spectrum.

The applicability of the full-fledged coupled-channel formalism depends on two spacetime scales: the formation length L_f associated with the $i \longrightarrow k$ transitions,

$$L_f = \frac{1}{k_{ik}} = \frac{2E}{m_i^2 - m_k^2} \sim \frac{2E}{m_{\rho'}^2 - m_{\rho^0}^2} \approx 0.25\ \text{fm} \times \frac{E}{1\ \text{GeV}}, \quad (24)$$

and the coherence length

$$L_c = \frac{1}{k_{h\gamma^*}} = \frac{2E}{M^2 + Q^2} \approx 0.75\ \text{fm} \times \frac{E}{1\ \text{GeV}} \frac{m_{\rho^0}^2}{M^2 + Q^2} \quad (25)$$

associated with the transition $\gamma^* \longrightarrow i$. Strictly speaking, the evaluation of the diffraction matrix from equation (17) and of the excitation amplitudes from (18) in terms of the color dipole cross section is valid only if $L_f > R_N$ and $L_c > R_N$. For the region $Q^2 \lesssim 1$, which of interest to us GeV^2 and for $\rho^0(1S)$ and $\rho'(2S)$ mesons, the full-fledged coupled-channel effects develop only at $E \sim 5$–8 GeV. At lower energies, the only change is, however, the decoupling of higher excitations from the photon and of off-diagonal diffractive transitions to and from higher excitations, and we can extend the formalism even down to $E = 2$ GeV. At this energy, we have a single-channel problem with $\gamma^* \longrightarrow \rho^0$ excitation followed by diagonal $\rho^0 N$ scattering. In order to evaluate relevant diagonal elastic rescatterings, we only need the $\rho^0 N$ total cross section, and the color-dipole value of $\langle\rho^0|\hat{\sigma}_{\mathbf{B}}|\rho^0\rangle$ still does a good job for the almost energy-independent Pomeron contribution. Simultaneously, $\langle\rho^0|\hat{\sigma}|\gamma^*\rangle$ appears only as an overall normalization, and whether it is evaluated from (18) or within a different approach does not affect nuclear modifications of the e^+e^- mass spectrum.

4. NUMERICAL RESULTS

4.1. Input Parameters

We have performed our numerical calculations at energies of $E = 2$, 5, 10, and 20 GeV at $Q^2 = 0$ and 1 GeV^2 for the target nuclei ^{9}Be, ^{56}Fe, and ^{207}Pb. For the parametrization of the diffractive matrix and of the photon and vector-meson wave functions, the reader is referred to Section 3. For the nuclear matter density in the light target nucleus ^{9}Be, use was made of the oscillator shell model with the oscillator frequency adjusted in such a way as to reproduce the experimental value of the root-mean-square radius of the charge distribution, $\langle r^2\rangle_{^9\text{Be}}^{1/2} = 2.51$ fm [41]. For the target nucleus ^{56}Fe, we employed the parametrization of the nuclear density by the sum of Gaussian functions from [41]. For ^{207}Pb, we used the Wood–Saxon parametrization of the nuclear density with parameters borrowed from [41].

4.2. Basis of Vector-Meson States

As was stated above, we included four transverse resonance states in our numerical calculations. For the number of the off-diagonal rescatterings of the $q\bar{q}$ state, we take $\nu = 2$. We checked that, in our kinematical region, the contribution from higher excitations and higher order off-diagonal rescatterings can be safely neglected. Furthermore, the sum of the first two states and one off-diagonal rescattering of the $q\bar{q}$ state is sufficient for all practical purposes. Our principal interest is in the interplay of nuclear effects and the interference of $\rho^0(1S)$ and $\rho'(2S)$, and we did not include the numerically smaller contributions from the ω and ϕ mesons and their excitations. These long-lived resonances decay for the most part outside the target nucleus, and the nuclear effects do not modify considerably their shapes.

4.3. Presentation of the Results

Because of the aforementioned form-factor effect associated with the longitudinal-momentum transfer and the suppression of $\rho'(2S)$ production by the node effect, the amplitude in (5) decreases strongly with increasing e^+e^- mass. In order to facilitate the graphical presentation of the results, we use, as in [10], the scaled amplitude

$$T'(E, M) = M^2 T(E, M)/A. \quad (26)$$

Since expression (5) leads to the amplitude proportional to $\propto A$ in the absence of absorption effects, we also introduced the factor $1/A$ in (26). Our basic numerical results for the mass spectrum are shown in Figs. 1–6 in the form

$$|T'|^2 \propto \frac{M^4}{A^2} \frac{d\sigma}{dM^2 dp_\perp^2}\bigg|_{p_\perp = 0}.$$

We focus on the mass region $M < 1.75$ GeV and include the vector mesons $\rho^0(1S)$ and $\rho'(2S)$ as final states.

In order to see better the resonance behavior of production amplitudes, we also display the Argand plots for T' in Figs. 7–9.

We will now comment on the salient features of the Q^2, energy, and nuclear-target dependences of these mass spectra.

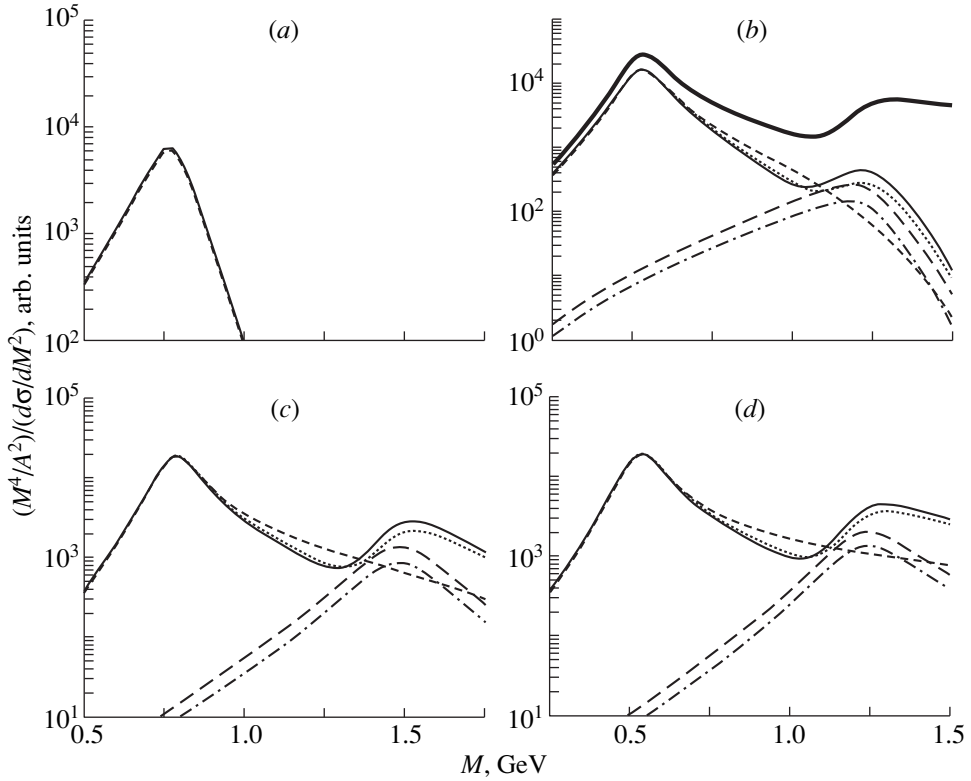

Fig. 1. Rescaled e^+e^-, $\mu^+\mu^-$ mass spectrum for coherent real photoproduction ($Q^2 = 0$) on a ^{9}Be nucleus for the incident-beam energies of E = (*a*) 2, (*b*) 5, (*c*) 10, and (*d*) 20 GeV. In Fig. 1*a*, the solid curve represents the prediction of the Glauber approximation with mass shift (10) from the Reggeon amplitude (23) included, and the dashed line shows the results obtained without the mass shift. In Fig. 1*b*, the thick solid curve represents the spectrum for the nucleon target, while all other curves illustrate results for the nuclear target: (thin solid curve) results of the full coupled-channel calculation [$\nu = 2$ in expansion (10)], (dotted curve) result from the diagonal approximation [$\nu = 0$ in expansion (10); $\rho^0(1S)$–$\rho'(2S)$ interference in e^+e^- or in $\mu^+\mu^-$ (or in both) decay channels is included), (short-dashed curve) pure ρ^0 signal in the coupled-channel calculation ($\nu = 2$), (long-dashed curve) $\rho'(2S)$ signal in the coupled-channel calculation ($\nu = 2$), and (dot-dashed curve) $\rho'(2S)$ signal in the diagonal approximation ($\nu = 2$). Figures 1*c* and 1*d* show the same data as Fig. 1*b*, but for E = 10 and 20 GeV, respectively, the mass spectrum for the free-nucleon target being omitted here.

4.4. Nucleon Target

The reference e^+e^- mass spectrum for the proton target and the photon energy E = 5 GeV are represented by thick solid curves in Figs. 1*b*–6*b*. In the approximation of the energy-independent dipole cross section $\sigma(\rho)$, it does not depend on the photon energy E. The mass spectrum exhibits the well separated $\rho^0(760)$ and $\rho'(1480)$ resonance peaks. Recall the factor M^4, which makes the $\rho'(2S)$ tail nearly flat at large M^2.

The suppression by the node effect is lifted with increasing Q^2 [see equation (21)], and a comparison of the mass spectra for real ($Q^2 = 0$) and virtual ($Q^2 = 1$ GeV^2) photoproduction shows clearly the predicted rise of the $\rho'(2S)/\rho^0(1S)$ ratio with increasing Q^2 [18, 23, 24]. This rise of the $\rho'(2S)$ signal with Q^2 is clearly seen from a comparison of the Argand diagrams in Figs. 7*a* and 7*b*.

4.5. Mass Shift versus Nuclear Form-Factor Effects: The ρ^0 Region at Low Energies

In Figs. 1*a*–6*a*, we show the mass spectrum for the low energy of E = 2 GeV, at which $\rho'(2S)$ production is negligible and the single-channel Glauber approximation (10) holds. The energy of E = 2 GeV is too low for ρ^0 to be expected to decay within the nucleus. Although this reasoning is correct, our results show that the effect of the mass shift (1) due to the real part of the amplitude for forward $\rho^0 N$ scattering proves to be marginal in the nuclear modification of the inside component of the production amplitude. The point is that the mass shift appears in the exponent of the integrand on the right-hand side of (10) via the extra phase

$$\phi = \frac{1}{2}t(\mathbf{b}, z, z_1)\,\mathrm{Im}\,\sigma_{hh} \approx \frac{1}{2}r_{\mathbf{P}'}n_A(z-z_1)\sqrt{\frac{s_0}{s}}(z-z_1), \quad (27)$$

which must be compared with the phase $k_{\gamma^* h}(z - z_1) = -(z - z_1)/L_c$ from the finite-coherence length. Obviously, the significance of the mass shift for the inside component of the dilepton-production amplitude is controlled by the parameter

$$\eta = \frac{1}{2}r_{\mathbf{P}'}n_A\sqrt{\frac{s_0}{s}}L_c \approx 0.1\frac{m_\rho^2}{M^2+Q^2}\sqrt{\frac{E}{1\ \mathrm{GeV}}}. \quad (28)$$

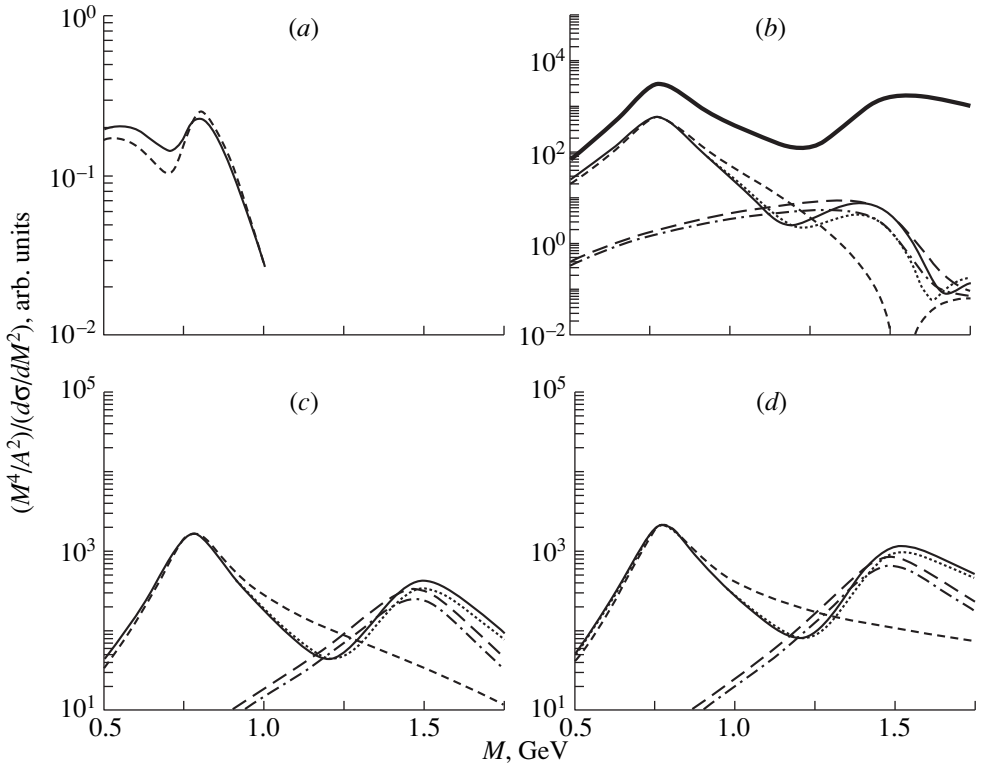

Fig. 2. As in Fig. 1, but for virtual photoproduction, $Q^2 = 1$ GeV^2.

In the numerical evaluation in (28), we used the standard parameters of $\rho^0 N$ interaction as quoted in Section 3 and a normal nuclear density. We see that the mass shift (1) amounts to the renormalization

$$k_{\gamma^* h} \longrightarrow k_{\gamma^* h}(1 - \eta). \tag{29}$$

At $E = 2$ GeV, we have $\eta \ll 1$. On the other hand, the coherence length (25) is very short,

$$L_c(E = 2\ \text{GeV}) = 1.5\ \text{fm} \times \frac{m_{\rho^0}^2}{M^2 + Q^2},$$

much smaller than nuclear radii for heavy nuclei; even for the light Be nucleus, it is commensurate with the nuclear radius. For this reason, nuclear effects are dominated by the attenuation of ρ^0 due to the diagonal $\rho^0 N \longrightarrow \rho^0 N$ transitions and, most significantly, by distortions due to nuclear form-factor effects.

The results for the mass spectrum are represented by solid curves in Figs. 1*a*–6*a*. For the Be target, the main effect is that the mass spectrum drops at $M \gtrsim 1$ GeV much faster than for the free-nucleon target. For the heavy Pb target, the form-factor oscillations lead to an effective splitting of the ρ^0 peak—the mass spectrum develops a minimum at $M \sim m_{\rho^0}$. At $Q^2 = 1$ GeV^2, the coherence length becomes still smaller, and the distortion of the e^+e^- mass spectrum by form-factor effects becomes much stronger, such that the dip at the ρ^0 mass evolves even for the Be target. The corresponding Argand diagrams in Figs. 8*a* and 9*a* span the mass range $0.5 < M < 1$ GeV and exhibit a structure more complex than a single resonance loop. Our findings for real photoproduction on Fe and Pb targets are similar to those obtained in [10] for the target mass number $A = 50$ and 200 in the approximation of a uniform nuclear density.

We note that nowhere does the splitting of the ρ^0 mass spectrum look like a superposition of two Breit–Wigner peaks with the in-vacuum ρ^0 mass and the in-medium mass shifted by ≈50 MeV, as quoted in Section 3. The weak impact of the in-medium shift (1) on the ρ^0 splitting is obvious from the dashed curves in Figs. 1*a*–6*a*, which show the mass spectrum obtained when the mass shift (1) is neglected—that is, by setting Re/Im = 0. The distortions of the mass spectrum change little; as a matter of fact, the splitting of the ρ^0 peak is even enhanced somewhat in conformity to the rescaling in (29). Despite the slow rise of the parameter η with energy, $\eta \ll 1$ in the range $E = 2$–20 GeV, which is of interest for experiments at the Jefferson laboratory. Furthermore, the contribution from the in-medium decays decreases at higher energies, and the overall effect of the mass shift becomes still weaker.

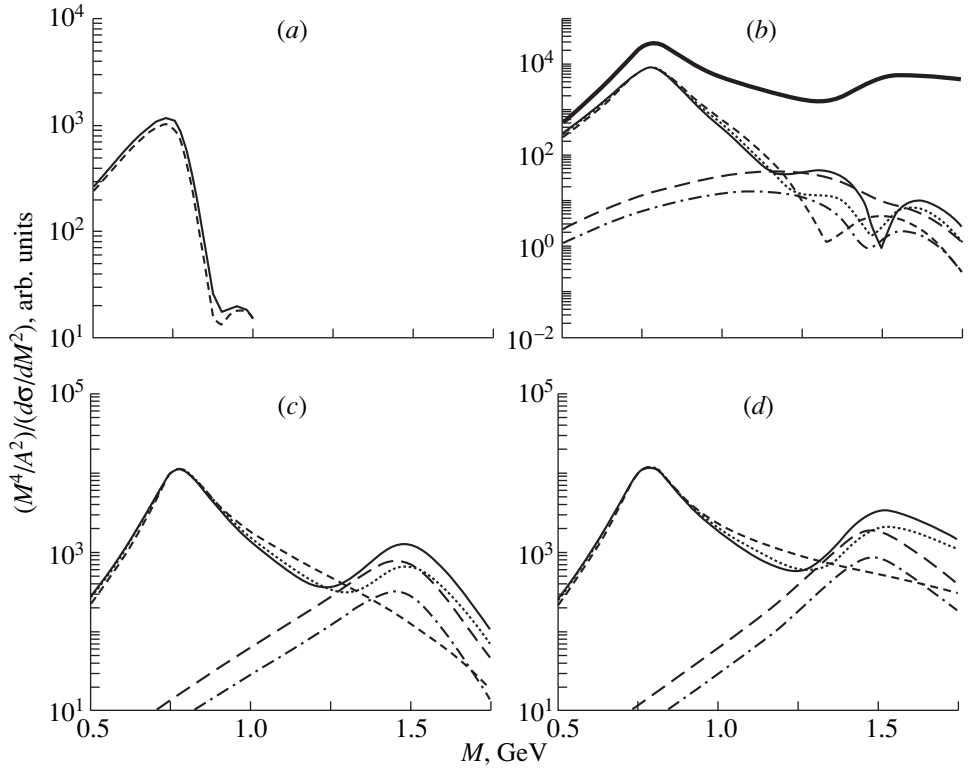

Fig. 3. As in Fig. 1, but for the target nucleus ^{56}Fe.

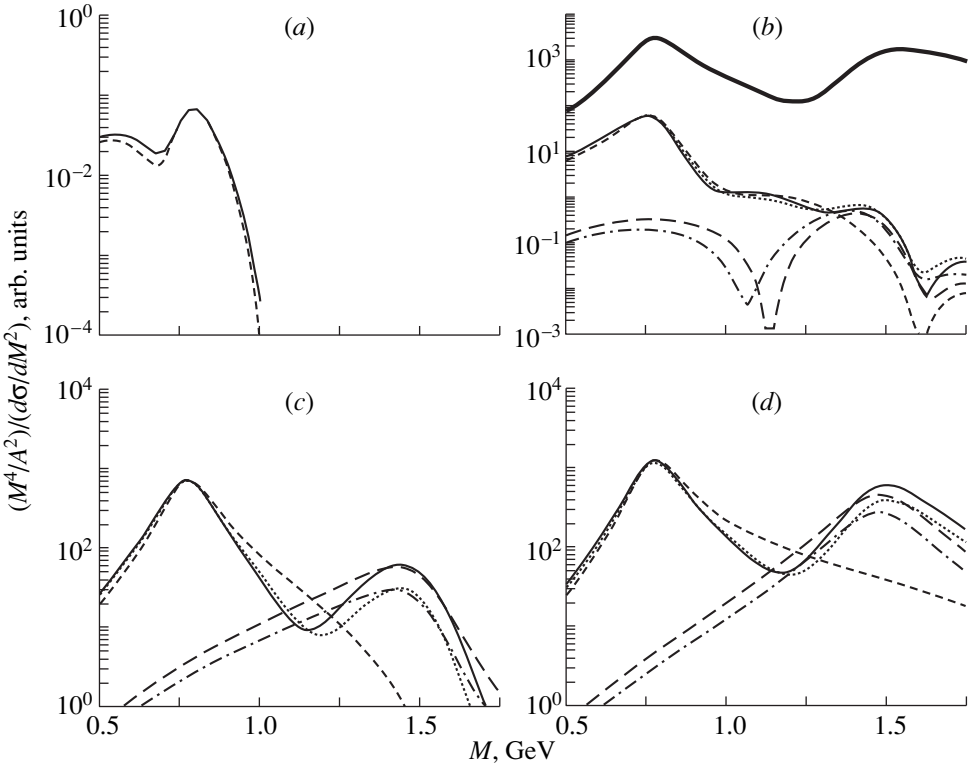

Fig. 4. As in Fig. 1, but for virtual photoproduction, $Q^2 = 1$ GeV^2, and the target nucleus ^{56}Fe.

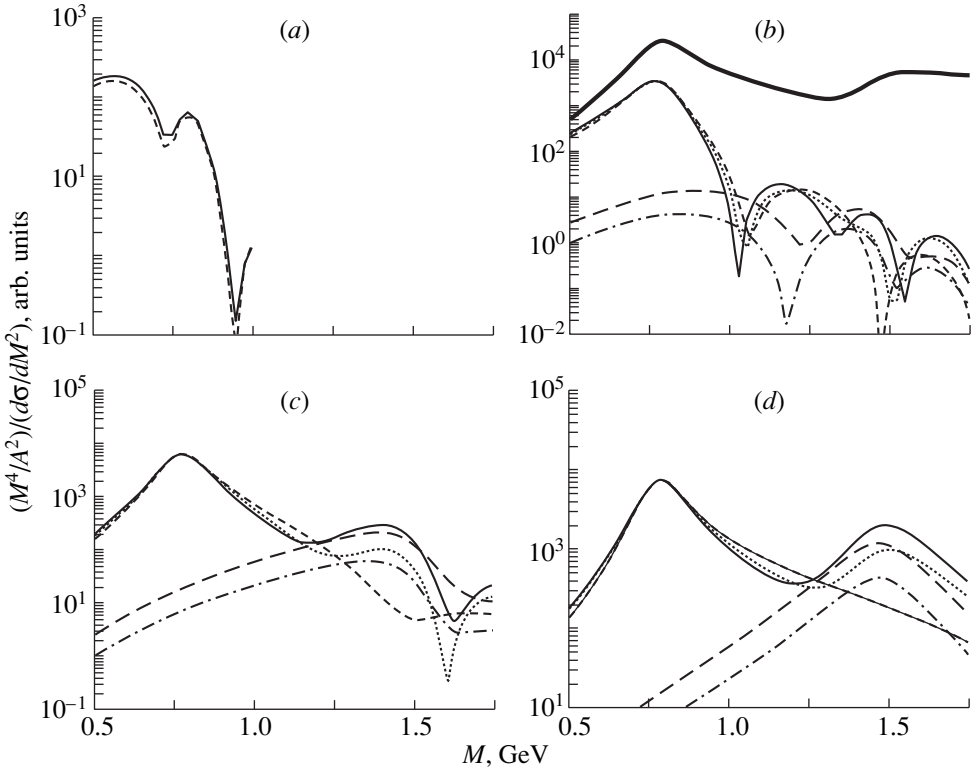

Fig. 5. As in Fig. 1, but for the target nucleus ^{207}Pb.

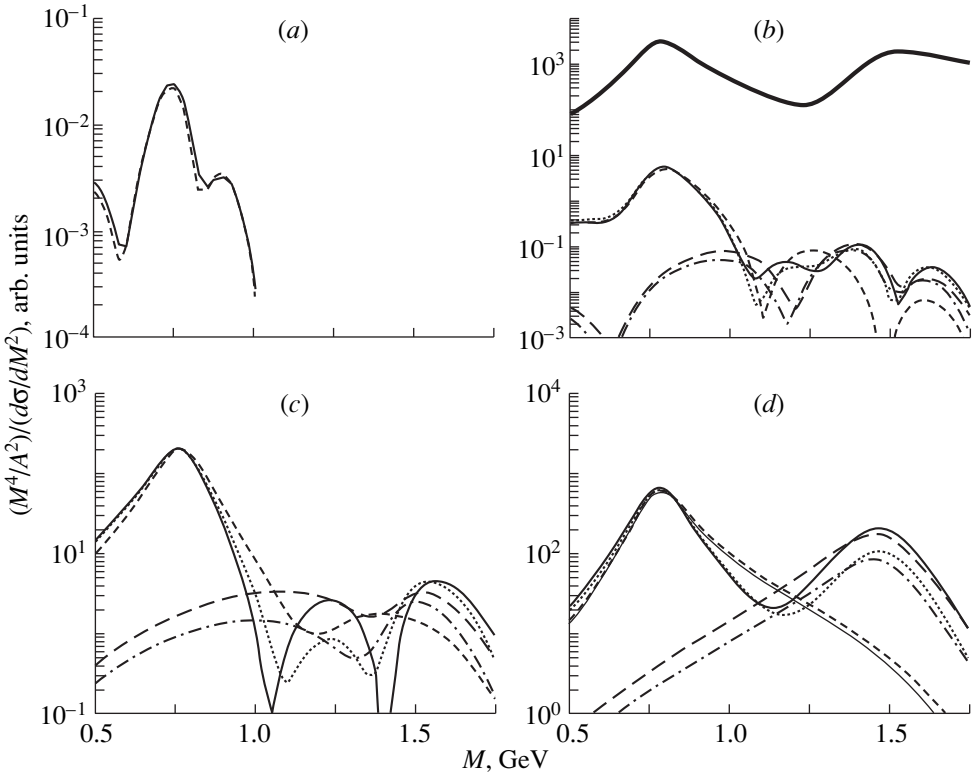

Fig. 6. As Fig. 1, but for virtual photoproduction, $Q^2 = 1$ GeV^2, and the target nucleus ^{207}Pb.

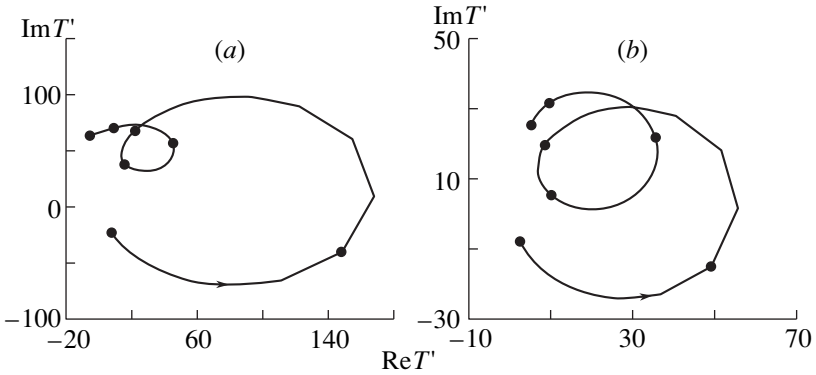

Fig. 7. Argand plots for the scaled amplitude $T' = M^2T(E, M)$ for (*a*) real ($Q^2 = 0$) and (*b*) virtual ($Q^2 = 1$ GeV^2) photoproduction on the free-nucleon target.

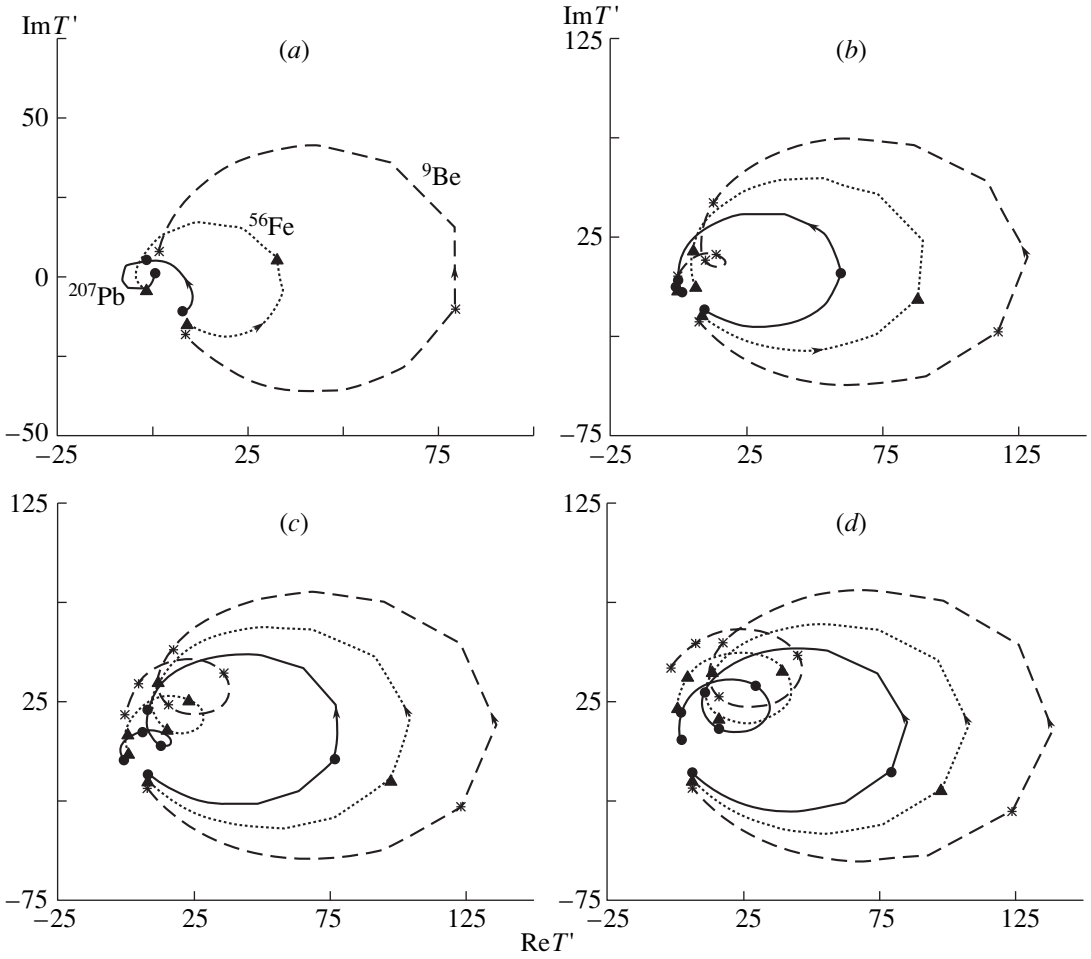

Fig. 8. Argand plots for the scaled amplitude (26) at $Q^2 = 0$. The solid, dotted, and dashed curves show the results for the target nuclei ^{207}Pb, ^{56}Fe, and ^{9}Be, respectively. The curves are given in arbitrary units. The mass intervals are 0.5–1 GeV for (*a*) $E = 2$ GeV, and 0.5–2 GeV for $E =$ (*b*) 5, (*c*) 10, and (*d*) 20 GeV. The spacing of mass points along the curves is 0.25 GeV. The arrows show the direction of the increasing mass.

4.6. Higher Energies: Opening of the ρ'(2S) Channel

The opening of the ρ'(2*S*) channel and coupled-channel effects are new feature of high-energy photoproduction. For the purposes of comparison, we show, by the thick solid curve in Figs. 1*b*–6*b*, the mass spectrum for the free-nucleon target. The full coupled-channel results for nuclear targets comprise attenuation; nuclear form-factor effects; the effects of $\rho^0(1S) \longleftrightarrow$

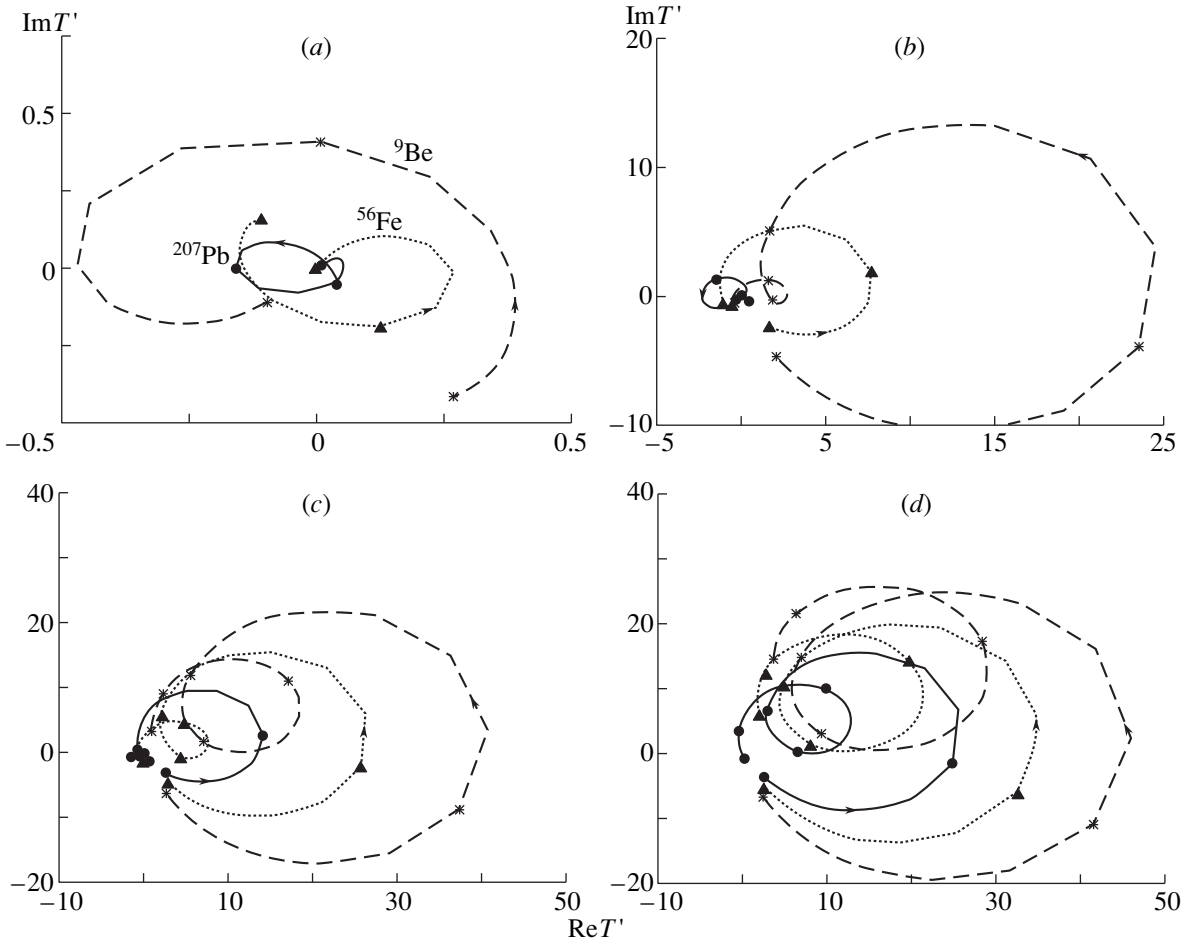

Fig. 9. As in Fig. 8, but for $Q^2 = 1$ GeV^2.

$\rho'(2S)$ transitions, including the multistep transitions; and the resonance mass shift due to Re/Im $\neq 0$. The relative importance of these effects depends on the mass region, energy, and the target mass number.

The importance of the off-diagonal transitions in the target nucleus can be judged from a comparison of the full coupled-channel results (thin solid curve) with those from the diagonal approximation (dotted curve), where off-diagonal rescatterings are switched off (that is, $\nu = 0$), and only the direct $\gamma^* \longrightarrow \rho^0(1S)$ and $\gamma^* \longrightarrow \rho'(2S)$ transitions followed by elastic $\rho^0 N$ and $\rho'(2S)N$ rescatterings are included. One can see that, in the ρ^0-meson mass region $0.5 < M \lesssim 1$ GeV, the effect of off-diagonal rescatterings for both values of Q^2 proves to be small. Indeed, the direct $\gamma^* \longrightarrow \rho^0(1S)$ transition is strong, whereas both transitions in the off-diagonal sequence $\gamma^* \longrightarrow \rho'(2S) \longrightarrow \rho^0(1S)$ are weak (see the description of diffraction matrix in Section 3). In our discussion of the off-diagonal effect, we will henceforth focus on the $\rho'(2S)$ contribution because the contribution of intermediate states heavier than the $\rho'(2S)$ meson is still smaller.

Our results for real photoproduction, $Q^2 = 0$, in the $\rho^0(1S)$ mass region for ^{56}Fe and ^{207}Pb targets are close to those from [10] obtained for real photons at the nucleus mass numbers $A = 50$ and 200 in the uniform-nuclear-density approximation.

At $Q^2 = 1$ GeV^2, the coherence length is also short at $E = 5$ GeV, and distortions of the shape of the e^+e^- mass spectrum in the $\rho^0(1S)$-meson mass region by the nuclear form factor as described in Subsection 4.5 persist for $E = 5$ GeV as well. The dominance of the form-factor effects is obvious from the fact that these distortions change insignificantly from the full coupled-channel to diagonal case.

At higher masses, the coupled-channel effects become more important. Here, the direct $\gamma^* \longrightarrow \rho'(2S)$ transition is weak, and there is a strong interference with the off-diagonal sequential transition $\gamma^* \longrightarrow \rho^0(1S) \longrightarrow \rho'(2S)$, which contains a comparably weak transition $\rho^0(1S) \longrightarrow \rho'(2S)$. For heavy target nuclei, the sequential mechanism $\gamma^* \longrightarrow \rho^0(1S) \longrightarrow \rho'(2S)$ is found to dominate over the direct mechanism $\gamma^* \longrightarrow \rho'(2S)$. This can be seen as follows. In Figs. 1–6, we show, by the short-dashed and long-dashed curves, the

pure $\rho^0(1S)$ and the $\rho'(2S)$ contributions evaluated in the full coupled-channel approach, $\nu = 2$. The dash-dotted curve represents the pure $\rho'(2S)$ contribution evaluated in the diagonal approximation, $\nu = 0$; in this approximation, the $\rho'(2S)$ signal is much weaker than in the coupled-channel case, where $\rho'(2S)$ is fed by sequential transitions. This is a very interesting example where $\rho'(2S)$ production on heavy nuclei opens the possibility for extracting the matrix element $\langle\rho'(2S)|\hat{\sigma}|\rho^0(1S)\rangle$ from the experimental data on the e^+e^- mass spectrum in the $\rho'(2S)$ mass region. Measurement of this matrix element could furnish unique information about the overlap of the $\rho^0(1S)$ and $\rho'(2S)$ wave functions.

The $\rho^0(1S)$–$\rho'(2S)$ interference is destructive at masses M below the $\rho'(2S)$ peak, but it becomes constructive at and above the $\rho'(2S)$ peak, reflecting the mass dependence of the relative phase of the $\rho^0(1S) \longrightarrow e^+e^-$ and $\rho'(2S) \longrightarrow e^+e^-$ Breit–Wigner amplitudes: (i) the mass spectrum develops a dip in between the $\rho^0(1S)$- and $\rho'(2S)$-resonance peaks, where the coupled-channel (thin solid) curve goes below the short-dashed curve for the pure $\rho^0(1S)$ contribution; (ii) at, and beyond, the $\rho'(2S)$ peak the coupled-channel (thin solid) curve goes well above the long-dashed curve for the pure $\rho'(2S)$ contribution. The latter evinces a substantial contribution from the large-mass tail of $\rho^0(1S)$ in the $\rho'(2S)$ region. Obviously, this prevents experimental extraction of the cross section for $\rho'(2S)$ production within a probabilistic approach where the interference with the Breit–Wigner tail of the $\rho^0(1S)$ meson is neglected.

4.7. Form-Factor Effects in the $\rho'(2S)$ Region

For moderate energies and heavier nuclei, and also for larger Q^2, we encounter the situation where the coherence length L_c for the $\rho'(2S)$ mass region becomes commensurate with or even smaller than the nuclear radius R_A. In this case, the $\rho'(2S)$ signal will be subjected to distortions by the form-factor effect in precisely the same manner as the ρ^0 signal at lower energies (see Subsection 4.5). By way of example, we indicate that, in real photoproduction of ^{56}Fe target at E = 5 GeV, the $\rho'(2S)$ peak splits into two bumps with a dip at $M \approx m_{\rho'}$ (see Fig. 3*b*). That this dip is associated with form factor effects is obvious from the shift of the dip toward smaller values of M and from the development of the secondary dip with increasing Q^2 (compare Figs. 3*b* and 4*b*). The results for the heavy target ^{207}Pb (see Figs. 5*b*–5*d*) show clearly how the dip–bump structure moves to higher masses M as the coherence length L_c increases with increasing energy E.

A comparison of the Argand diagram for the free-nucleon target (Fig. 7) with the analogous diagrams for nuclear targets (Figs. 8 and 9) shows that the resonance loop corresponding to the $\rho'(2S)$ meson becomes well pronounced only at $E \gtrsim 10$ GeV. Even in this energy region, however, the contribution to the amplitude from the Breit–Wigner tail of the $\rho^0(1S)$ meson cannot be neglected against that from the $\rho'(2S)$ meson.

5. CONCLUSIONS

We have performed a coupled-channel analysis of nuclear-medium modifications to the $\rho^0(1S)$ and $\rho'(2S)$ mesons in the coherent $\gamma^* \longrightarrow \rho^0(1S)A$, $\rho'(2S)A \longrightarrow e^+e^-A$ reactions in the kinematical region specified by the conditions $E \sim$ 2–20 GeV and $Q^2 \lesssim 1$ GeV^2. Our findings for the interplay of the inside and outside decays, in-medium modifications of the inside component, and the coupled-channel effects can be summarized as follows:

(i) In the $\rho^0(1S)$-meson mass region $0.5 \lesssim M \lesssim 1$ GeV, the effect of off-diagonal rescatterings is small. For heavy nuclei, our results in this mass region agree with those obtained in [10] within the one-channel approximation.

(ii) Off-diagonal rescatterings become important for $M \gtrsim 1$ GeV. The main off-diagonal contribution is the $\rho'(2S)$ production through the sequential mechanism $\gamma^* \longrightarrow \rho^0(1S) \longrightarrow \rho'(2S)$. This mechanism dominates the cross section for $\rho'(2S)$ production on heavy nuclei.

(iii) For energies not higher than 5 GeV, the shapes of the $\rho^0(1S)$ and $\rho'(2S)$ resonances are strongly affected by nuclear effects associated with the interference interplay of the resonance decays inside and outside the target nucleus and form-factor effects due to longitudinal-momentum transfer.

(iv) The $\rho'(2S)$ resonance is seen well only for $E \gtrsim 10$ GeV. Even at high energies, its shape is affected by the interference with the Breit–Wigner tail of the $\rho^0(1S)$ meson, which must be included properly in an analysis of experimental data on the e^+e^- mass spectrum in the $\rho'(2S)$ mass region.

In our analysis, we have focused on the dilepton decay mode. Obviously, very similar effects must be observed in measurements of $\rho^0(1S)$ and $\rho'(2S)$ production through the $\pi\pi$ decay mode. The major difference from the dilepton mode would come from the final-state interaction of the $\pi\pi$ system, which would reduce the relative contribution of the inside component in relation to that for the e^+e^- mode. For this reason, a comparison of the mass spectra for these two cases would be of great interest. It is especially interesting at low energies of $E \sim$ 2–5 GeV for heavy nuclei, where the inside component is sufficiently large for the e^+e^- decay mode and will be strongly suppressed by final-state absorption for the $\pi\pi$ mode. A comparative theoretical analysis of coherent $\rho^0(1S)$ and $\rho'(2S)$ photo- and electroproduction for the e^+e^- and $\pi\pi$ decay modes is now in progress.

ACKNOWLEDGMENTS

The work of B.G. Zakharov was supported in part by grant nos. INTAS 96-0597 and DFG 436RUS17/11/99.

REFERENCES

1. V. Bernard and U.-G. Meissner, Nucl. Phys. A **489**, 647 (1988).
2. A. Hosaka, Phys. Lett. B **244**, 363 (1990).
3. G. E. Brown and M. Rho, Phys. Rev. Lett. **66**, 2720 (1991).
4. T. Hatsuda and S. H. Lee, Phys. Rev. C **46**, R34 (1992).
5. M. Asakawa, C. M. Ko, P. Levai, and X. J. Qiu, Phys. Rev. C **46**, R1159 (1992).
6. Y. Koike, Phys. Rev. C **51**, 1488 (1995).
7. T. Hatsuda, S. H. Lee, and H. Shiomi, Phys. Rev. C **52**, 3364 (1995).
8. V. I. Eletsky and B. L. Ioffe, Phys. Rev. Lett. **78**, 1010 (1997).
9. V. I. Eletsky, B. L. Ioffe, and J. I. Kapusta, Eur. Phys. J. A **3**, 381 (1998);hep-ph/9907411.
10. K. G. Boreskov, L. A. Kondratyuk, M. I. Krivoruchenko, and J. H. Koch, Nucl. Phys. A **619**, 295 (1997).
11. Ye. S. Golubeva, L. A. Kondratyuk, and W. Cassing, Nucl. Phys. A **625**, 832 (1997).
12. L. A. Kondratyuk, A. Sibirtsev, W. Cassing, *et al.*, Phys. Rev. C **58**, 1078 (1998).
13. L. A. Kondratyuk, M. I. Krivoruchenko, N. Bianchi, *et al.*, Nucl. Phys. A **579**, 453 (1994).
14. D. V. Bugg, Nucl. Phys. B **88**, 381 (1975).
15. R. J. Glauber, in *Lectures in Theoretical Physics*, Ed. by W. Brittain and L. G. Dunham (Interscience, New York, 1959), Vol. 1; R. J. Glauber and G. Matthiae, Nucl. Phys. B **21**, 135 (1970).
16. V. N. Gribov, Zh. Éksp. Teor. Fiz. **56**, 892 (1969) [Sov. Phys. JETP **29**, 483 (1969)]; **57**, 1306 (1970) [**30**, 709 (1970)].
17. J. Nemchick, N. N. Nikolaev, E. Predazzi, and B. G. Zakharov, Z. Phys. C **75**, 71 (1997).
18. O. Benhar, B. Z. Kopeliovich, C. Mariotti, *et al.*, Phys. Rev. Lett. **69**, 1156 (1992).
19. B. Z. Kopeliovich, J. Nemchick, N. N. Nikolaev, and B. G. Zakharov, Phys. Lett. B **309**, 179 (1993).
20. B. Z. Kopeliovich, J. Nemchick, N. N. Nikolaev, and B. G. Zakharov, Phys. Lett. B **324**, 469 (1994).
21. J. Nemchick, N. N. Nikolaev, E. Predazzi, and B. G. Zakharov, Phys. Lett. B **374**, 199 (1996).
22. J. Nemchick, N. N. Nikolaev, E. Predazzi, *et al.*, Zh. Éksp. Teor. Fiz. **113**, 1930 (1998) [JETP **86**, 1054 (1998)].
23. B. Z. Kopeliovich and B. G. Zakharov, Phys. Rev. D **44**, 3466 (1991).
24. J. Nemchick, N. N. Nikolaev, and B. G. Zakharov, Phys. Lett. B **339**, 194 (1994).
25. NMC Collab. (M. Arneodo *et al.*), Phys. Lett. B **332**, 195 (1994).
26. NMC Collab. (P. Amaudruz *et al.*), Nucl. Phys. B **371**, 553 (1992).
27. E687 Collab. (P. L. Frabetti, *et al.*), Paper presented at the Europhysics Conference on High Energy Physics, Brussels, 1995.
28. H1 Collab. (C. Adloff *et al.*), Phys. Lett. B **421**, 385 (1998).
29. O. Benhar, S. Fantoni, N. N. Nikolaev, and B. G. Zakharov, Zh. Éksp. Teor. Fiz. **111**, 769 (1997) [JETP **84**, 421 (1997)].
30. N. N. Nikolaev and B. G. Zakharov, Z. Phys. C **49**, 607 (1991).
31. A. Casher, H. Neuberger, and S. Nussinov, Phys. Rev. D **20**, 179 (1979).
32. N. N. Nikolaev and B. G. Zakharov, Phys. Lett. B **327**, 149 (1994).
33. F. E. Low, Phys. Rev. D **12**, 163 (1975).
34. J. F. Gunion and D. E. Soper, Phys. Rev. D **15**, 2617 (1977).
35. N. N. Nikolaev, Comments Nucl. Part. Phys. **21**, 41 (1992).
36. N. N. Nikolaev, V. R. Zoller, and B. G. Zakharov, Phys. Lett. B **328**, 143 (1994).
37. E. Schuryak, Rev. Mod. Phys. **65**, 1 (1993).
38. A. Capella, U. Sukhatme, C.-I. Tan, and J. Tran Thanh Van, Phys. Lett. B **81**, 68 (1979); Phys. Rep. **236**, 225 (1994).
39. A. B. Kaidalov, Phys. Lett. B **116**, 459 (1982).
40. G. Veneziano, Phys. Lett. B **52**, 220 (1974); Nucl. Phys. B **74**, 365 (1974); **117**, 519 (1976).
41. H. de Vries, C. W. de Jaeger, and C. de Vries, At. Data Nucl. Data Tables **36**, 496 (1987).

Physics of Atomic Nuclei, Vol. 63, No. 8, 2000, pp. 1477–1488. Translated from Yadernaya Fizika, Vol. 63, No. 8, 2000, pp. 1557–1568.

ELEMENTARY PARTICLES AND FIELDS
Experiment

Electrons and Muons in Extensive Air Showers of Energies $E_0 \geq 3 \times 10^{17}$ eV: Yakutsk Array Data and QGSJET Model

A. V. Glushkov, M. I. Pravdin, I. E. Sleptsov, V. R. Sleptsova, and N. N. Kalmykov[1)]

Institute of Cosmophysical Research and Aeronomy, Yakutsk Research Center, Siberian Division, Russian Academy of Sciences, pr. Lenina 31, Yakutsk, 677891 Yakut Republic, Russia

Received March 31, 1999; in final form, November 1, 1999

Abstract—The results obtained from an analysis of the 1974–1998 Yakutsk array data on muons with threshold energy $E_\mu \approx 1.0 \times \sec\theta$ GeV and on all charged particles (electrons and muons) in extensive air showers (EAS) are reported and compared with the results of calculations based on the model of quark–gluon strings with jets. For energies of $E_0 \leq 3 \times 10^{18}$ eV and zenith angles of $\theta \leq 45°$, the results of the model calculations are consistent with the measured properties of the showers, while, for higher energy EASs, there are considerable discrepancies, which are probably due to the change in the development of the shower cascade in the region $E_0 \geq 3 \times 10^{18}$ eV.

1. INTRODUCTION

The lateral distribution functions (LDF) obtained from the Yakutsk array data for muons with threshold energy $E_\mu \approx 1.0 \times \sec\theta$ GeV and for all charged particles (electrons and muons) in extensive air showers (EAS) were reported in [1–4]. The LDF for either EAS component exhibited anomalous behavior for shower energies of $E_0 \geq (3\text{–}5) \times 10^{18}$ eV. According to the opinion put forth in [1–4], this behavior is associated with some new processes in the development of EASs at these energies.

In this connection, it is reasonable to analyze the Yakutsk array data within a model that would describe the development of EASs without coming in conflict with any of the observations for energies of $E_0 \leq (1\text{–}3) \times 10^{18}$ eV. The majority of studies devoted to calculating the properties of EASs have long since relied on the model of quark–gluon strings (commonly known as QGS model, or, merely, QGSM) [5]. Some features calculated on the basis of this model (see, for example, [6, 7]) are consistent with experimental data from [1, 2, 8] for $E_0 \leq (1\text{–}3) \times 10^{18}$ eV.

In this study, the Yakutsk array data on muons and all charged particles are compared with the results of the calculations based on the QGS model involving jets (QGSJET model) [9], which faithfully reproduces a vast variety of experimental data on EASs [10]. Moreover, the study of Erlykin and Wolfendale [11] revealed that the QGSJET model is the best one at energies around 10^6 GeV in the sense that the same estimates for the mass composition of cosmic rays are obtained near the cusp of the primary-energy spectrum when the model is employed to analyze different experimental features of EASs.

[1)]Institute of Nuclear Physics, Moscow State University, Vorob'evy gory, Moscow, 119899 Russia.

2. EXPERIMENTAL DATA

Subjected to analysis were data on showers with zenith angles $\theta \leq 60°$. In just the same way as in [3, 4], the LDFs for charged particles were constructed on the basis of data from only 13 stations located at the center of the array. Together with the central station, they form two subarrays, each consisting of six master triangles with a side of 500 m for one subarray (small master, SM) and a side of 1000 m for the other subarray (large master, LM). Each station included two scintillation detectors of size 2×2 m^2, which operated in the coincidence mode.

That the mean LDFs were constructed here by using showers selected at least by one of the aforementioned master triangles distinguishes the present analysis from those that were reported in [1, 2] and which took into account relevant events accumulated over the total area of the array. As a result, statistics were reduced by a factor of 1.5–3, but the data set selected in this way was free from showers recorded at the array boundaries, where the accuracy of the measurement was poorer than that in the more densely meshed central part of the array.

As in [12, 13], the energy of primary particles was estimated with the aid of the relations

$$E_0 = (4.8 \pm 1.6) \times 10^{17} (\rho_{s,600}(0°))^{1.0 \pm 0.02} \text{ [eV]}, \quad (1)$$

$$\rho_{s,600}(0°) = \rho_{s,600}(\theta) \exp((\sec\theta - 1) \times 1020/\lambda_\rho) \text{ [m}^{-2}\text{]}, \quad (2)$$

$$\lambda_\rho = (450 \pm 44) + (32 \pm 15) \log(\rho_{s,600}(0°)) \text{ [g/cm}^2\text{]}, \quad (3)$$

where $\rho_{s,600}(\theta)$ is the charged-particle density measured by scintillation detectors positioned on the

Earth's surface at the distance of $R = 600$ m from the shower axis. The axis coordinates and the density $\rho_{s,600}(\theta)$ were calculated with the aid of the Linsley formula [14]

$$f_s = N_s C_s r^{-a}(1+r)^{a-b_s}, \quad (4)$$

where $r = R/R_M$, R_M being the Mollier radius, which depends on the temperature T and pressure P as

$$R_M \approx (7.5\times 10^4/P)(T/273). \quad (5)$$

The R_M values were determined for each shower (according to the Yakutsk data $\langle R_M\rangle \approx 70$ m). The as-yet-undefined quantities in (4) are the following: C_s is a normalization constant; N_s is the total number of charged particles at the observation level; $a = 1$; and b_s is the parameter defined in [15] as

$$b_s = b_1 + b_2\cos\theta + b_3\log(\rho_{s,600}(\theta)), \quad (6)$$

where $b_1 = 1.38$, $b_2 = 2.16$, and $b_3 = 0.15$.

Our final analysis included showers for which the SM (LM) determined the coordinates of their axes to within 20–30 (50–60) m.

The entire set of showers was partitioned into groups with step values of $\Delta\cos\theta = 0.1$ and $\Delta\log E_0 = 0.2$. The showers were averaged within each of the groups. The individual densities in groups were normalized to the mean shower energy $\langle E_0\rangle$ and were averaged over the intervals of $\Delta\log R = 0.04$. The averaged charged-particle densities not less than 4 m^{-2} were calculated by the formula

$$\langle\rho_s(R_i)\rangle = \left(\sum_{n=1}^{N_1}\rho_n(R_i)\right)/N_1 \ [\text{particle/m}^2]. \quad (7)$$

In order to extend the range of R, especially for low E_0, we followed the procedure invented in [3, 4], determining the densities near the detector threshold by the method used for hodoscopes. The probability of the actuation of two detectors operating in the coincidence mode is

$$F = (1-\exp\{-\rho_s(R_i)S\})^2 = N_1/(N_1+N_0), \quad (8)$$

where N_1 and N_0 are the number of stations that were actuated or not actuated, respectively, in showers at distances from the axes between $\log R_i$ and $\log R_i + 0.04$, while $S = 2$ m^2 is the area of an individual detector. From equation (8), it follows that

$$\langle\rho_s(R_i)\rangle = \beta\frac{-\ln(1-\sqrt{F})}{S}. \quad (9)$$

The coefficient $\beta = \rho_s/\rho_{ch}$ considers that relation (9) is valid for charged particles and that expression (7) includes readings of the scintillation detectors. At distances of $R \approx 200$–1000 m, previous measurements at the Yakutsk array yielded the value of $\beta = 1.23 \pm 0.07$ in $E_0 \approx 10^{17}$–10^{19} eV showers [16].

The resulting LDFs for charged particles were approximated as

$$\rho_s(R) = f_s(1+R/2000)^{-g_s}, \quad (10)$$

where f_s corresponds (4) at $a = 1.3$. At a specific choice of values for the parameter g_s, the functions in (10) agree better with experimental values than the functions in (4), especially at large distances from the shower axis.

As in [1, 2], the averaged muon densities for $E_\mu \approx 1.0\times\sec\theta$ GeV were found from the relation

$$\langle\rho_\mu(R_i)\rangle = \left(\sum_{n=1}^{N_1}\rho_n(R_i)\right)/(N_1+N_0), \quad (11)$$

where N_1 and N_0 are the numbers of, respectively, nonzero and zero readings of the muon detectors in the interval between $\log R_i$ and $\log R_i + 0.04$. Zero readings correspond to cases where the detectors in the waiting mode recorded no muons. Such events are possible near the threshold densities. Their number depends on the effective detector areas varying from 8 to 36 m^2 in the case under consideration.

The LDFs for muons were approximated as

$$\rho_\mu(R) = f_\mu(1+R/2000)^{-g_\mu}, \quad (12)$$

where f_μ is given by the well-known Greisen relation [17]

$$f_\mu = N_\mu C_\mu r^{-0.75}(1+r)^{0.75-b_\mu}. \quad (13)$$

Here, $r = R/R_0$ with $R_0 = 280$ m, C_μ is a normalization constant, N_μ is the total number of muons at the observation level (1020 g/cm^2 for Yakutsk), and b_μ is a parameter.

The most appropriate values of the parameters (b_s, g_s) and (b_μ, g_μ) in (10) and (12), respectively, were determined from a least squares fit, their significance being assessed on the basis of a χ^2 test. The procedure for determining the LDFs for the two EAS components was verified by means of a mathematical simulation.

3. COMPUTATIONAL PROCEDURE

The LDFs presented here for charged particles and muons were calculated on the basis of the QGSJET model [9, 10] for primary protons and Fe nuclei. A feature peculiar to this model is that it takes into account a soft preevolution preceding hard parton scattering. Thus, a simulation of interactions of hadrons and nuclei with nuclei includes contributions both from soft parton cascades characterized by low transverse momenta,

$$Q_t^2 < Q_0^2$$

($Q_0 \approx 2$ GeV), and from semihard processes, where

$$Q_t^2 > Q_0^2.$$

In the energy range from the threshold energy $E_{thr} = E_0 \times 10^{-3}/A$, where A is the atomic number of a primary particle, to E_0, the development of the nuclear cascade was simulated by the Monte Carlo method; below E_{thr}, the cascade was estimated in terms of averaged quantities. The equations for the nuclear cascade were solved numerically to a precision of about 1%. The LDFs for electrons were calculated at the Mollier radius of R_M = 70 m to within 10%. The response of the scintillation detector was not calculated because of difficulties plaguing the theory of electron–photon cascades.

We also took into account the deflection of EAS electrons and muons by the Earth's magnetic field, whose effect is pronounced for all showers [7, 18], including the most intense ones [19]. In the Yakutsk region, the Earth's magnetic field has a strength of $|\mathbf{B}|$ = 0.6 G, an inclination of 76°, and a west declination of 19° from the northward direction.

The LDFs for muons were calculated with the threshold of $E_\mu = 1.0 \times \sec\theta$ GeV for distances from the shower axis in the range ΔR = 150–1500 m, while the LDFs for all charged particles were calculated for ΔR = 150–1000 m as the sum of the densities of electrons with energies $E_e \geq 0.5$ MeV and of muons with energies $E_\mu \geq 0.3$ GeV; that is, $\rho_{ch} = \rho_e(\geq 0.5\ \text{MeV}) + \rho_\mu(\geq 0.3\ \text{GeV})$.

The entire set of the data computed for the showers was partitioned into the same groups in E_0 and θ as those chosen in experimentally deducing the averaged LDFs. For each value of θ, the number of showers simulated in these groups varied from 3000 for E_0 in the range 10^{18}–$10^{18.2}$ eV to 200 for E_0 in the range $10^{19.6}$–$10^{19.8}$ eV. In just the same way as the experimental LDFs, the simulated ones were represented analytically by the functions in (10) and (12), with the most appropriate values of the parameters (b_s, g_s) and (b_μ, g_μ), respectively, being determined by the least squares method.

4. COMPARISON OF DATA FOR $E_0 < 3 \times 10^{18}$ eV

All the results presented below were obtained from an analysis of the averaged LDFs. Figure 1 shows the theoretical and experimental LDFs of all charged particles and of muons for $\langle E_0 \rangle = 2 \times 10^{18}$ eV. Their parameters are listed in Table 1.

The experimental and theoretical LDFs for either component in nearly vertical EASs are consistent in shape, but the calculation overestimates the density by a factor of about 1.4. A similar pattern is observed at other θ values that are not very large. Only for strongly inclined showers ($\theta \geq 45°$) do we see deviations from it: there, the experimental LDFs for charged particles are much steeper than the calculated LDFs, intersecting them at distances from the axis about 400 m (see Fig. 1*c*).

Our analysis revealed that, at all E_0 values and $\theta \leq 60°$, the calculated LDFs for muons are consistent with the approximation in (12) at $g_\mu = 6.5$ and that the same conclusion follows from our experimental data; it should be borne in mind, however, that, in [1, 2], our group used the approximation in (12) with $g_\mu = 1$. A possible reason behind so great a distinction between the g_μ values is that it is difficult to determine accu-

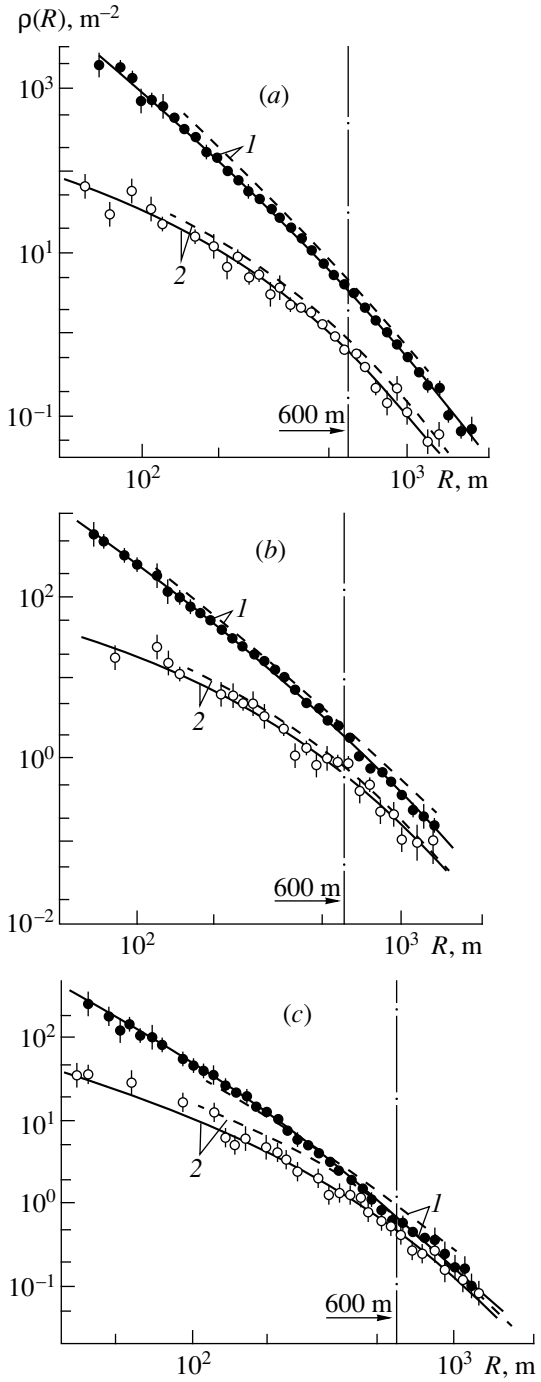

Fig. 1. Lateral distributions of (closed circles) all charged particles and (open circles) muons with threshold energy $E_\mu \approx 1.0 \times \sec\theta$ GeV for $E_0 = 2 \times 10^{18}$ eV showers at $\langle \cos\theta \rangle$ = (*a*) 0.98, (*b*) 0.78, and (*c*) 0.58. Curves *1* and *2* represent the approximations (10) and (12) of (solid curves) the experimental data and (dashed curves) the distributions calculated within the QGSJET model for primary protons with the parameters from Table 1.

Table 1. LDF parameters at $\langle E_0 \rangle = 10^{18.3}$ eV

Parameter \ $\langle\cos\theta\rangle$		0.98	0.78	0.58
$\langle b_s \rangle$	Exp.	3.50 ± 0.01	3.06 ± 0.01	2.28 ± 0.02
	Theor.	3.63 ± 0.01	3.00 ± 0.01	1.66 ± 0.01
g_s	Exp.	1	1	3
	Theor.	1	1	3
$\log\langle \rho_{s,600} \rangle$	Exp.	0.53 ± 0.01	0.27 ± 0.01	–0.19 ± 0.01
	Theor.	0.64 ± 0.01	0.36 ± 0.01	–0.05 ± 0.01
$\log\langle N_s \rangle$	Exp.	8.51 ± 0.01	7.93 ± 0.01	7.12 ± 0.02
	Theor.	8.73 ± 0.01	7.97 ± 0.01	7.00 ± 0.01
$\log\langle N_s(100–1000) \rangle$	Exp.	7.72 ± 0.01	7.30 ± 0.01	6.69 ± 0.02
	Theor.	7.88 ± 0.01	7.36 ± 0.01	6.70 ± 0.01
χ^2	Exp.	37(32)	29(29)	22(33)
	Theor.	5(4)	3(4)	6(4)
$\langle b_\mu \rangle$	Exp.	2.21 ± 0.04	1.39 ± 0.05	1.21 ± 0.06
	Theor.	2.08 ± 0.01	1.36 ± 0.01	1.09 ± 0.01
g_μ	Exp.	6.5	6.5	6.5
	Theor.	6.5	6.5	6.5
$\log\langle \rho_{\mu,600} \rangle$	Exp.	–0.19 ± 0.02	–0.15 ± 0.04	–0.29 ± 0.06
	Theor.	–0.07 ± 0.01	–0.10 ± 0.01	–0.15 ± 0.01
$\log\langle N_\mu \rangle$	Exp.	6.86 ± 0.04	6.72 ± 0.05	6.56 ± 0.06
	Theor.	6.95 ± 0.01	6.78 ± 0.01	6.68 ± 0.01
$\log\langle N_\mu(100–1000) \rangle$	Exp.	6.66 ± 0.02	6.57 ± 0.03	6.40 ± 0.03
	Theor.	6.76 ± 0.01	6.63 ± 0.01	6.53 ± 0.01
χ^2	Exp.	28(25)	15(20)	22(17)
	Theor.	5(9)	6(9)	12(9)

rately the muon densities on the periphery of showers near their detection threshold. In order to avoid misdetections, the range of R was reduced in [1, 2] by excluding the periphery; this led to the value of $g_\mu = 1$, but different versions were also possible.

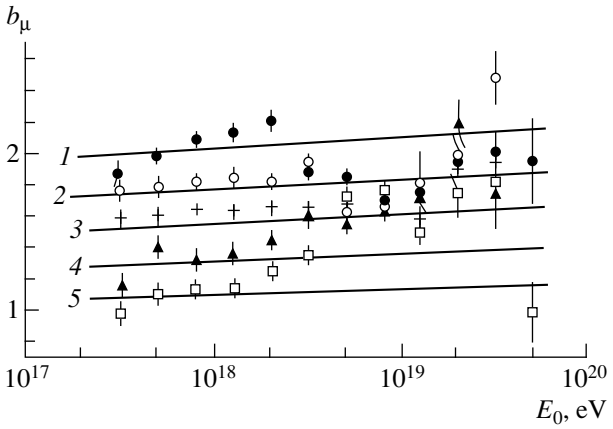

Fig. 2. Parameter b_μ as a function of E_0 for the lateral distributions (points) measured experimentally and (curves) calculated within the QGSJET model for proton-induced showers with $\langle\cos\theta\rangle$ = (closed circles, curve *1*) 0.98, (open circles, curve *2*) 0.88, (crosses, curve *3*) 0.78, (triangles, curve *4*) 0.68, and (squares, curve *5*) 0.58. The lateral distributions were approximated by the functions in (12) at $g_\mu = 6.5$.

Figure 2 shows b_μ values corresponding to the approximations given in (12) with $g_\mu = 6.5$ versus E_0 at various values of θ. The curves in the figure illustrate the behavior of the parameter b_μ from the QGSJET model for primary protons. The results of the calculations are compatible with the relation

$$b_\mu = 2.07 + 2.32(1 - \cos\theta) + 0.07(\log E_0 - 18). \quad (14)$$

Experimental data for $E_0 \le 2 \times 10^{18}$ eV suggest the value of $\partial b_\mu/\partial\cos\theta = 2.36 \pm 0.12$ in agreement with (14) within the measurement errors, but they imply the higher rate of the growth of the parameter $\partial b_\mu/\partial \log E_0$ with energy ($\partial b_\mu/\partial \log E_0 = 0.19 \pm 0.09$). The latter may be due to a change in the primary composition, from a mixture enriched at $E_0 \sim 10^{17}$ eV in heavy nuclei {Z = 10–30 nuclei constitute (63 ± 7)% [20]} to a lighter composition [8]. According to our estimates [21], the fraction of protons is about 80% ($\langle \ln A \rangle \approx 0.4$) at $E_0 \sim 10^{18}$ eV. By and large, the data here are in agreement with the theoretical results. At higher energies, the LDFs for muons will be considered below.

The LDF for charged particles is one of the important features of EASs because it is used to determine the axis coordinates; the density $\rho_{s,600}(\theta)$; and many other shower parameters, including the primary-particle

energy E_0. At a fixed value of g_s, the LDF shape is governed solely by the parameter b_s, which depends on E_0 and θ.

This is obvious from Fig. 3, which shows the b_s values calculated for primary protons and the experimental results for LDFs (10) at $g_s = 1$. For $\theta \le 45°$, the b_s values found from the theoretical LDFs can be approximated by the dependence

$$b_s = b_0 - b_1(\sec\theta - 1) + b_2(\log E_0 - 18), \qquad (15)$$

where $b_0 = 3.58 \pm 0.02$, $b_1 = 1.9 \pm 0.05$, and $b_2 = 0.14 \pm 0.01$. The experimental data at $E_0 \approx (3\text{–}30) \times 10^{17}$ eV and $\theta \le 45°$ are approximated by expression (15) with coefficients $b_0 = 3.45 \pm 0.03$, $b_1 = 1.9 \pm 0.11$, and $b_2 = 0.30 \pm 0.05$. In more inclined EASs ($\theta > 45°$), the experimental LDFs exhibit slighter dependence on the zenith angle: $b_1 = 1.05 \pm 0.13$.

In just the same way as for the parameter b_μ, the discrepancy between the theoretical and experimental results for the coefficient b_2, which characterizes the rate at which the LDF for charged particles becomes steeper with increasing E_0 is interpreted in terms of the additional change in the primary-particle composition: $b_2 \approx 0.14(1 + \partial \log A / \partial \log E_0)$. The LDF has a smaller slope for primary Fe nuclei than for primary protons. The superposition model yields $b_s(p) - b_s(\mathrm{Fe}) \approx 0.25$.

Let us consider the behavior of the densities $\rho_{\mu,600}(\theta)$ and $\rho_{s,600}(\theta)$. Figure 4 shows the density $\rho_{\mu,600}(\theta)$ as a function of E_0 at $\langle\cos\theta\rangle = 0.98$ and 0.58. Curves *1* and *5* represent the QGSJET results for primary protons and Fe nuclei. The model density for proton-induced vertical EASs can be approximated by the dependence

$$\rho_{\mu,600}(0°) = 0.45(E_0/10^{18})^{0.92 \pm 0.01}, \qquad (16)$$

whereas the experiment yields

$$\rho_{\mu,600}(0°) = (0.32 \pm 0.02)(E_0/10^{18})^{0.84 \pm 0.02}. \qquad (17)$$

In all probability, a slower growth of the experimental density $\rho_{\mu,600}(\theta)$ with E_0 for $E_0 \le 3 \times 10^{18}$ eV in relation to the dependence in (16) is caused by a transition from a heavy primary composition to a composition enriched in light nuclei and protons.

The zenith-angle dependence of $\rho_{\mu,600}(\theta)$ at $\langle E_0\rangle = 2 \times 10^{18}$ eV is depicted in Fig. 5*a*, whence we can see that the theoretical results and the experiment results both evince a slight change in this parameter for $\theta \le 60°$.

Figure 5*a* also displays the zenith-angle dependences of $\rho_{s,600}$ and $\rho_{e,600}$ (the latter is the electron density at a distance of 600 m from the shower axis). Experimentally, ρ_e was determined as the difference $\rho_e = \rho_s - d(\theta)\rho_\mu(E_\mu \ge 1.0 \times \sec\theta$ GeV). The factor $d(\theta) = 1.25$–1.4 was borrowed from the QGSJET calculations for a transition to the density of muons with threshold $E_\mu \ge 0.01$ GeV.

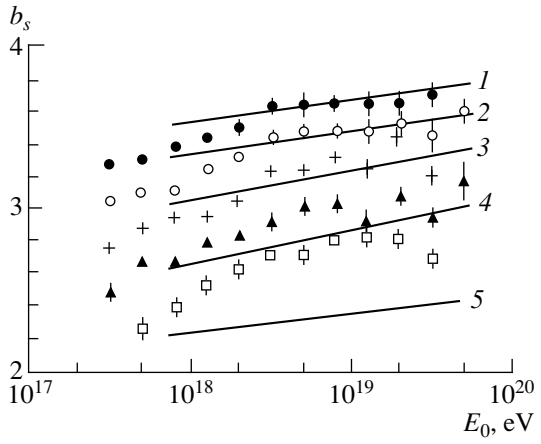

Fig. 3. As in Fig. 2, but for the parameter b_s. The lateral distributions were approximated by the function in (10) at $g_s = 1$.

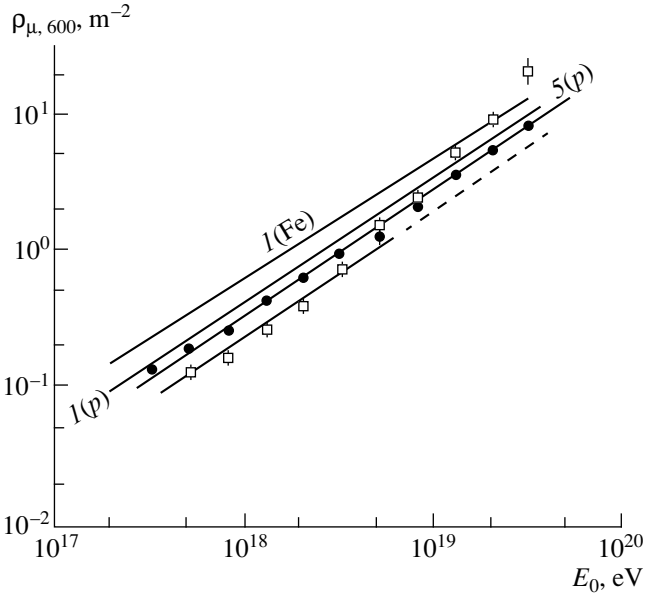

Fig. 4. Density $\rho_{\mu,600}(\theta)$ as a function of E_0 for the lateral distributions (points) measured experimentally and (curves) calculated within the QGSJET model for (*p*) primary protons and (Fe) primary Fe nuclei at $\langle\cos\theta\rangle =$ (closed circles, curve *1*) 0.98 and (squares, curve *5*) 0.58. The solid and dashed curves represent, respectively, an interpolation and an extrapolation of experimental data for $\langle\cos\theta\rangle = 0.58$.

The experimental values of the density $\rho_{s,600}(\theta)$ for $\theta \le 45°$ can be approximated as

$$\log(\rho_{s,600}(0°)) = \log(\rho_{s,600}(\theta)) + k_\theta(\sec\theta - 1) \qquad (18)$$

with $k_\theta = 1.02 \pm 0.08$. The results of the calculations are compatible with (18) at $k_\theta = 1.14 \pm 0.05$.

Figure 6 shows the densities $\rho_{s,600}(\theta)$ as functions of E_0 for $\langle\cos\theta\rangle = 0.98$, 0.78, and 0.58. Curves *1*, *3*, and *5* represent the results of the calculations for primary pro-

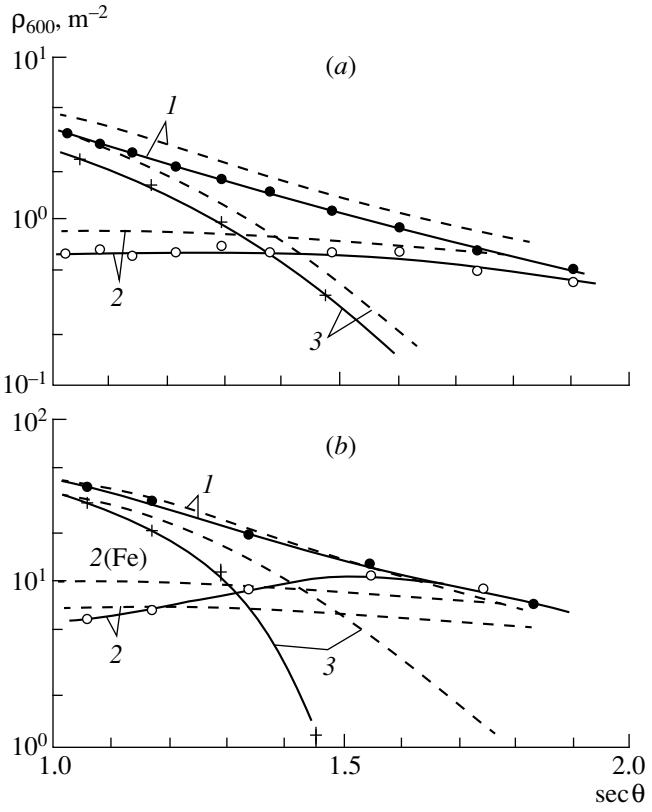

Fig. 5. Densities ρ_{600} of (*1*) all charged particles, (*2*) muons, and (*3*) electrons as functions of sec θ (θ is the zenith angle) at $E_0 = (a)\ 2 \times 10^{18}$ and $(b)\ 2 \times 10^{19}$ eV: (points) experimental data and (dashed curves) results of the QGSJET calculation for primary protons and (Fe) Fe nuclei.

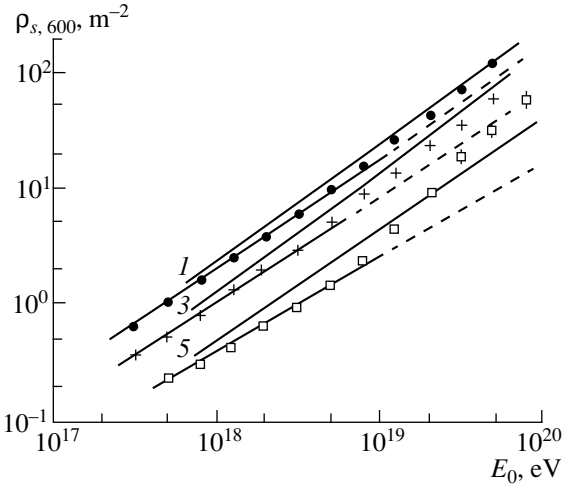

Fig. 6. Density $\rho_{s,\,600}(\theta)$ as a function of E_0. The solid and dashed curves represent, respectively, an interpolation and an extrapolation of experimental data (see main body of the text).

tons. At θ = 0°, these results comply with the relation

$$\rho_{ch,\,600}(0^\circ) = 2.4(E_0/10^{18})^{1.0 \pm 0.01}. \quad (19)$$

The $\rho_{s,\,600}$ values (like $\rho_{\mu,\,600}$ values) deduced from the experimental data are less than the theoretical results. For $E_0 \le 3 \times 10^{18}$ eV vertical showers, we have

$$\rho_{s,\,600}(0^\circ) = (2.0 \pm 0.3)(E_0/10^{18})^{0.94 \pm 0.02}. \quad (20)$$

The relations inverse to (17) and (16),

$$E_0 = 3.94 \times 10^{18}(\rho_{\mu,\,600}(0^\circ))^{1.19 \pm 0.02} \quad (21)$$

$$E_0 = 2.4 \times 10^{18}(\rho_{\mu,\,600}(0^\circ))^{1.08 \pm 0.01}, \quad (22)$$

are convenient for determining E_0 from $\rho_{\mu,\,600}(0^\circ)$. The estimates of energy that are obtained from these relations differ by a factor of about 1.4 near 10^{18} eV.

From (19) and (20), we similarly obtain the inverse relations

$$E_0 = (4.8 \pm 0.3) \times 10^{17}(\rho_{s,\,600}(0^\circ))^{1.06 \pm 0.03} \quad (23)$$

$$E_0 = 4.17 \times 10^{17}(\rho_{ch,\,600}(0^\circ))^{1.0 \pm 0.01}, \quad (24)$$

which also differ by a factor of about 1.2 near 10^{18} eV. The photon contribution disregarded in ρ_{ch} can increase the ratio of (23) and (24) up to 1.35–1.4.

Note that relations (23) and (1) involve different exponents. The exponent is equal to 1.06 ± 0.03 for $E_0 \le 3 \times 10^{18}$ eV and to 0.94 ± 0.03 for higher energies. This is because the above method was used to deduce $\rho_{s,\,600}(0^\circ)$ values in (23) from the averaged LDFs, whereas the preliminary processing of showers recorded by the Yakutsk array relied on the Linsley functions (4) with $a = 1$ and b_s as determined according to (6). The individual values $\rho_{s,\,600}(\theta)$ and E_0 in showers were found on the basis of the same functions.

The above data suggest the following. The LDF for either component measured in the experiment is ~1.4 times less than the corresponding QGSJET result for primary protons. This difference cannot be associated with a transition to a heavier primary-particle composition because this assumption would lead to a more glaring contradiction with the experimental data. If the results of the calculation are normalized to the experimental data, for example, by reducing the energy E_0 in the calculations by a factor of about 1.4 at a fixed density $\rho_{s,\,600}(0^\circ)$, the LDFs measured for EASs of energies $E_0 \le 3 \times 10^{18}$ eV and those expected on the basis of the QGSJET model will have similar shapes. In this case, the dynamical features of the measured LDFs are compatible with the hypothesis that the primary-particle composition becomes lighter with increasing E_0 with the result that the primary mixture proves to be dominated by protons at $E_0 \approx (1\text{–}2) \times 10^{18}$ eV.

5. COMPARISON OF DATA FOR $E_0 \ge 3 \times 10^{18}$ eV

As was indicated in [1–4] and as can be seen from Figs. 2–6, the development of $E_0 \ge (3\text{–}5) \times 10^{18}$ eV showers is somewhat different from the development of showers having lower energies. Figure 7 shows the experimental and theoretical LDFs for charged parti-

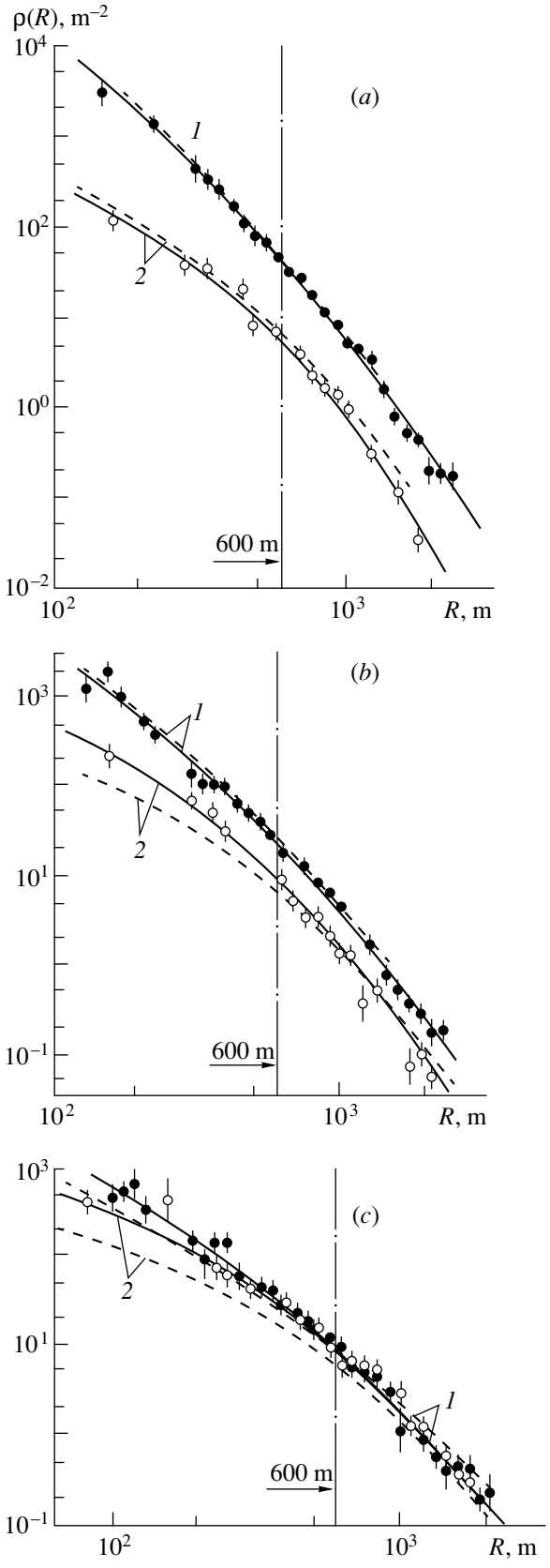

Fig. 7. As in Fig. 1, but for $E = 2 \times 10^{19}$ eV showers. The parameters of approximations are listed in Table 2.

cles and muons at $E_0 = 2 \times 10^{19}$ eV for three zenith angles whose mean cosines are $\langle \cos\theta \rangle = 0.98$, 0.78, and 0.58. The LDF parameters are listed in Table 2.

At first glance, it seems that, for $\theta \le 35$–$40°$ showers having such energies, the theory also exhibits some kind of agreement with the experiment data, especially for the LDFs for charged particles. The closed circles in Fig. 8 represent all values obtained by reducing the parameters b_s displayed in Fig. 3 to the vertical direction and averaging the results. For $E_0 > 2 \times 10^{18}$ eV, this parameter approaches the QGSJET theoretical dependence [curve *1*(*p*)] for primary protons.

A different pattern is observed in more inclined EASs. This is clearly seen from Fig. 7*c*, where the experimental LDFs for the two components agree for all $R > 100$ m. It follows that only muons with energies $E_\mu \ge 1.8$ GeV are detected in these showers at the above distances from the axis: there are no softer muons and, the more so, electrons, in contrast to what is observed in similar inclined EASs of energies $E_0 \le 3 \times 10^{18}$ eV (see Fig. 1*c*).

Figure 5*b* shows the densities $\rho_{s,\,600}(\theta)$, $\rho_{e,\,600}(\theta)$, and $\rho_{\mu,\,600}(\theta)$ in $E_0 = 2 \times 10^{19}$ eV showers as functions of the zenith angle. The experimental densities $\rho_{e,\,600}(\theta)$ were determined in the same way as those in Fig. 5*a*. Their behavior with increasing θ differs considerably from the model prediction: The experimental densities $\rho_{e,\,600}(\theta)$ decrease much faster, while the densities

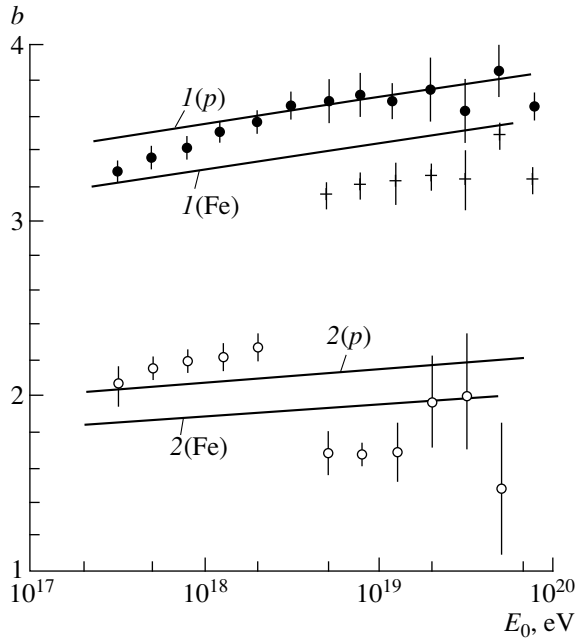

Fig. 8. E_0 dependences of the parameters (open circles) b_μ and (closed circles and crosses) b_s of the approximation (10) of lateral distributions in vertical EASs at $g_s = 1$ and 3.5, respectively. Curves represent the results of the QGSJET calculations for (*1*) all charged particles and (*2*) muons from showers induced by primary (*p*) protons and (Fe) Fe nuclei.

Table 2. LDF parameters at $\langle E_0 \rangle = 10^{19.3}$ eV

Parameter \ $\langle\cos\theta\rangle$		0.98	0.78	0.58
$\langle b_s \rangle$	Exp.	3.19 ± 0.04	2.67 ± 0.03	2.15 ± 0.04
	Theor.	3.76 ± 0.01	3.23 ± 0.01	1.91 ± 0.01
g_s	Exp.	3.5	3.5	3.5
	Theor.	1.0	1.0	3.0
$\log\langle \rho_{s,600} \rangle$	Exp.	1.63 ± 0.02	1.35 ± 0.02	0.95 ± 0.02
	Theor.	1.63 ± 0.01	1.39 ± 0.01	0.92 ± 0.01
$\log\langle N_s \rangle$	Exp.	9.62 ± 0.03	8.97 ± 0.04	8.23 ± 0.03
	Theor.	9.82 ± 0.01	9.17 ± 0.01	8.05 ± 0.01
$\log\langle N_s(100–1000) \rangle$	Exp.	8.86 ± 0.02	8.40 ± 0.02	7.82 ± 0.02
	Theor.	8.92 ± 0.01	8.48 ± 0.01	7.71 ± 0.01
χ^2	Exp.	17(18)	26(20)	32(24)
	Theor.	7(4)	3(4)	6(4)
$\langle b_\mu \rangle$	Exp.	1.92 ± 0.06	2.07 ± 0.08	1.32 ± 0.03
	Theor.	2.12 ± 0.01	1.39 ± 0.01	1.13 ± 0.02
g_μ	Exp.	8.0	8.0	6.5
	Theor.	6.5	6.5	6.5
$\log\langle \rho_{\mu,600} \rangle$	Exp.	0.74 ± 0.05	0.92 ± 0.05	0.98 ± 0.03
	Theor.	0.84 ± 0.01	0.82 ± 0.01	0.75 ± 0.01
$\log\langle N_\mu \rangle$	Exp.	7.82 ± 0.04	8.04 ± 0.07	7.85 ± 0.06
	Theor.	7.87 ± 0.01	7.69 ± 0.01	7.59 ± 0.01
$\log\langle N_\mu(100–1000) \rangle$	Exp.	7.62 ± 0.02	7.83 ± 0.04	7.69 ± 0.04
	Theor.	7.68 ± 0.01	7.54 ± 0.01	7.44 ± 0.01
χ^2	Exp.	10(12)	17(12)	17(15)
	Theor.	11(9)	6(9)	12(9)

$\rho_{\mu,600}(\theta)$, in contrast, increase, appearing to be in accord with $\rho_{s,600}(\theta)$ for $\theta > 45°$. The variations in the densities $\rho_{\mu,600}(\theta)$ go beyond the boundary of the region compatible with the change in the primary-particle composition from protons to Fe nuclei, the maximal excess over this boundary being twofold. A noticeable increase in the muon contribution is accompanied by a reduction of the number of electrons (Fig. 5*b*); that is, the muon-to-electron ratio in the total flux of charged particles changes. This affects considerably the measurement of particle densities by ground-based detectors whose energy absorption is high (for instance, by the water Cherenkov reservoirs in the Haverah Park Array).

For $E_0 \le 10^{18}$ eV showers, experimental data comply well with the approximation in (10) at $g_s = 1$. This can be seen from Fig. 9, where closed circles represent the ratio of the measured LDFs to their approximations given by (10) at $g_s = 1$ for $E_0 = 8 \times 10^{17}$ eV showers at $\langle\cos\theta\rangle = 0.98$, 0.78, and 0.58.

The observed pattern is strongly different for $E_0 > 3 \times 10^{18}$ eV. It was indicated in [3, 4] that, here, the measured LDFs cannot be approximated by expression (10) at $g_s = 1$ over the entire range of distances from the shower axis. In the region $R > 400$ m, the densities show much steeper variations. This is clearly seen from Fig. 9, where open circles represent the ratio of the LDFs measured in this energy region to the values extrapolated from the region $E_0 \le 10^{18}$ eV. The extrapolated LDFs were taken with the $\rho_{s,600}(\theta)$ values depicted by the dashed curves in Fig. 6, the parameters g_s being set to unity; as to the parameter b_s, it was chosen in accordance with Fig. 3 (for $E_0 \le 10^{18}$ eV):

$$b_s = 3.45 - 1.9(\sec\theta - 1) + 0.3(\log E_0 - 18). \quad (25)$$

In order to increase the statistical significance, all data for $E_0 \ge 3 \times 10^{18}$ eV were averaged and rescaled to $E_0 = 2 \times 10^{19}$ eV.

On the whole, the LDFs become more humpbacked. Analytically, they can be represented by the functions in (10) at $g_s = 3.5$ (dashed curves in Fig. 9). The corresponding averaged values of the parameters b_s in vertical showers are shown by the crosses in Fig. 8. They were obtained for all five intervals of zenith angles in just the same way as the values at $g_s = 3.5$.

Let us compare the above LDFs for charged particles with the LDFs measured at the Akeno Giant Air Shower Array (AGASA), which employs scintillation detectors similar to ours [22]. According to [23], the LDFs measured at that array can be approximated by the form

$$\rho_s(R) \sim (R/91.6)^{-1.2} \times (1 + R/91.6)^{1.2-\eta}(1 + (R/1000)^2)^{-0.6}, \quad (26)$$

which is similar to (10). For $E_0 \geq 2 \times 10^{18}$ eV showers with $\sec\theta \leq 1.7$, the parameter η in the exponent on the right-hand side of (26) can be represented as

$$\eta = \eta_0 - \eta_1(\sec\theta - 1) - \eta_2(\log s_{600} - 1), \quad (27)$$

where $\eta_0 = 4.02 \pm 0.18$, $\eta_1 = 1.87 \pm 0.64$, and $\eta_2 = 0.11 \pm 0.43$ [the parameter s_{600} is equivalent to $\rho_{s,600}(0°)$]. Since the quantity η_2 is much less than the measurement errors, the function in (26) with the parameter η of the simplified form

$$\eta = (3.97 \pm 0.13) - (1.79 \pm 0.64)(\sec\theta - 1) \quad (28)$$

was used for all EASs of extremely high energies.

The coefficients of $(\sec\theta - 1)$ in relations (15) and (28) agree well with each other, although the accuracy of (28) is very poor. Data represented by closed circles in Fig. 8 are also compatible with the conclusion that, for $E_0 \geq 2 \times 10^{18}$ eV, the LDF for charged particles is independent of the EAS energy because the parameter b_s can be taken to be invariable within the errors (along with the parameter η, it controls the LDF shape). However, this conclusion is erroneous because, as was mentioned above (Fig. 9), the shape of charged-particle LDF changes in this energy region.

6. PHENOMENOLOGY OF EAS DEVELOPMENT

The density $\rho_{s,600}(\theta)$ as a function of $\sec\theta$, where θ is the zenith angle, is shown in Fig. 10 for a wide interval of E_0 values. The dashed curves represent the above theoretical LDFs considered for primary protons. To make a comparison more convenient, all theoretical values of $\rho_{ch,600}(\theta)$ (dashed curves) were reduced by a factor of 1.4.

In the region $E_0 < (5–80) \times 10^{17}$ eV, the decrease in the theoretical density $\rho_{s,600}(\theta)$ agrees well with the experimental data up to zenith angles of about 60°. For $E_0 \geq 8 \times 10^{18}$ eV, the theoretical values fall somewhat short of the experimental densities $\rho_{s,600}(\theta)$ for extremely inclined EASs. As E_0 is increased further, this trend is enhanced and is manifested in less inclined showers. Finally, it appears in vertical EASs for $E_0 \geq (4–5) \times 10^{19}$ eV.

The LDF for muons suffers more considerable changes in the region $E_0 \geq 3 \times 10^{18}$ eV. The data presented in Figs. 2 and 4 indicate that, in inclined EASs, the LDF becomes much steeper and greater than that expected on the basis of an extrapolation from the region of lower E_0. From Figs. 1*c* and 7*c*, it can be seen the QGSJET model for primary protons predicts that, as E_0 is increased by one order of magnitude, the LDF for muons decreases by a factor of about 1.2; on the contrary, the experimental LDFs show a nearly twofold increase. In addition, the data for $E_0 \geq 3 \times 10^{18}$ eV in Fig. 2 suggest a slight zenith-angle dependence of the LDF shape, but this dependence is within the experimental errors.

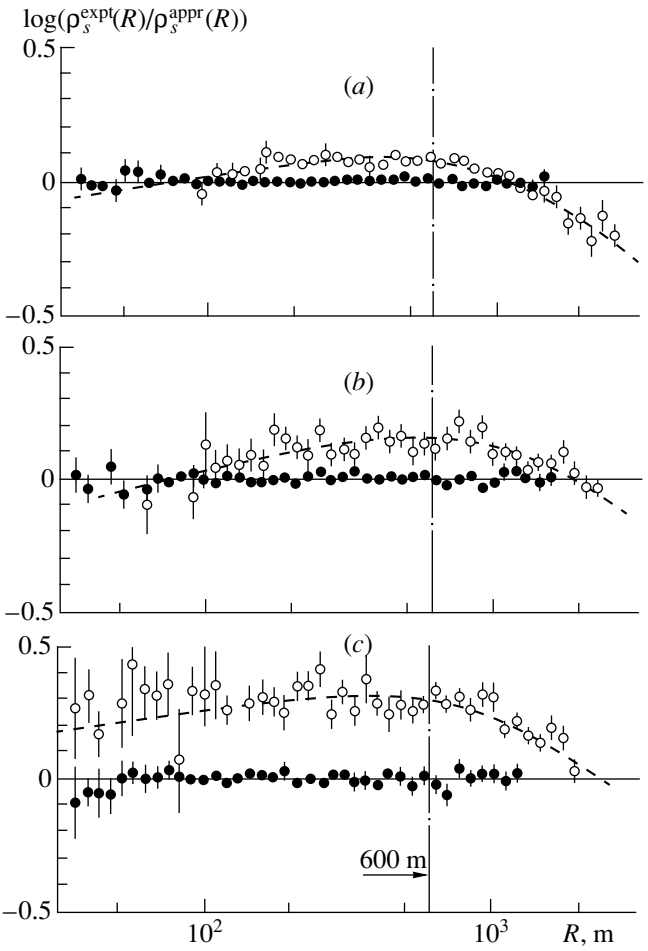

Fig. 9. Ratio of the lateral distribution functions measured for all charged particles in EASs of energies (closed circles) $E_0 = 8 \times 10^{17}$ eV and (open circles) $E_0 \geq 3 \times 10^{18}$ eV to the lateral distributions approximated by (10) with $g_s = 1$ and b_s taken from Fig. 3 for $\langle\cos\theta\rangle$ = (*a*) 0.98 (1207 showers), (*b*) 0.78 (788 showers), and (*c*) 0.58 (790 showers). The dashed curves represent the best fits in terms of expression (10) with $g_s = 3.5$ at $E_0 = 3.16 \times 10^{19}$ eV.

Open circles in Fig. 8 represent the averaged values of b_μ. For $E_0 < 2 \times 10^{18}$ eV showers, the b_μ values from Fig. 2 (for five angular intervals) were first rescaled to the vertical direction and were then averaged. For $E_0 \geq 3 \times 10^{18}$ eV, the experimental points from Fig. 2 were averaged directly.

Figure 11 displays the ratios of the muon densities measured in $\langle E_0\rangle = 2 \times 10^{19}$ eV EASs with $\langle\cos\theta\rangle$ =

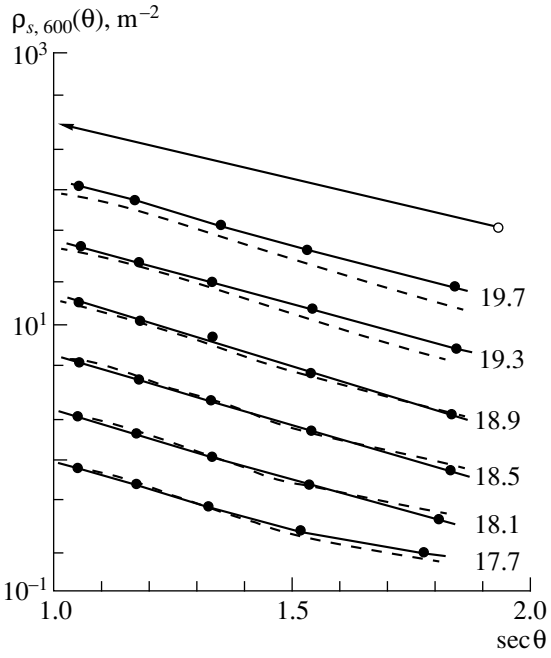

Fig. 10. Densities $\rho_{s,\,600}(\theta)$ as functions of $\sec\theta$ (θ is the zenith angle) for various E_0 values whose common logarithms are indicated on the curves: (closed circles) experimental data and (open circle) $\rho_{s,\,600}(58.7^\circ) = 54$ m^{-2}, the density of the most intense shower ($E_0 \approx 1.5 \times 10^{20}$ eV) detected at the Yakutsk array [24, 25]. The dashed curves represent the results of the QGSJET calculations for primary protons [calculated $\rho_{ch,\,600}(\theta)$ values were reduced by a factor of 1.4].

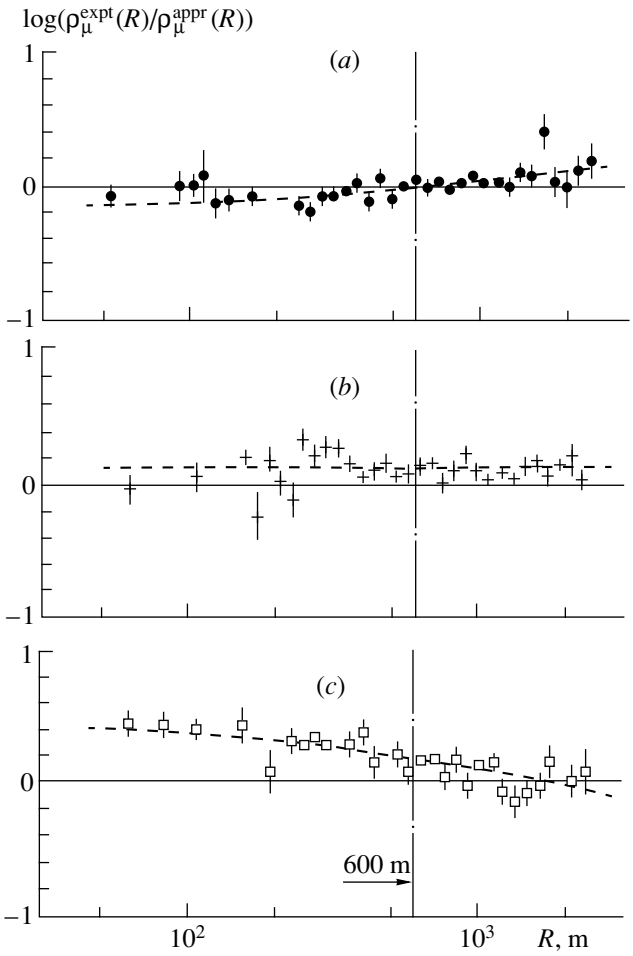

Fig. 11. Ratio of the lateral distribution of muons that was measured in the $\langle E_0\rangle = 2 \times 10^{19}$ eV EASs to the lateral distribution obtained by extrapolating approximation (12) from the energy region $E_0 < 2 \times 10^{18}$ eV with $g_\mu = 6.5$ and b_μ taken from Fig. 2 (points) at $\langle\cos\theta\rangle$ = (*a*) 0.98 (868 showers), (*b*) 0.78 (909 showers), and (*c*) 0.58 (335 showers). The dashed curves represent the best fits in terms of expression (12) at $E_0 = 2 \times 10^{19}$ eV.

0.98, 0.78, and 0.58 (points) to the LDF for muons that was approximated according to (12) and which was then extrapolated from the energy region $E_0 < 2 \times 10^{18}$ eV (horizontal zero line) at $g_\mu = 6.5$ and at b_μ values from Fig. 2. For $\langle E_0\rangle = 2 \times 10^{19}$ eV, the LDFs were obtained by averaging all data corresponding $E_0 \geq 3 \times 10^{18}$ eV. The LDF for muons becomes more gently sloping for nearly vertical EASs and steeper for the most inclined EASs.

For a wide interval of E_0, Fig. 12 shows the zenith-angle dependences of the density $\rho_{\mu,\,600}(\theta)$, which appear to be an additional characteristic of general changes in the LDFs for muons. The dashed curves depict the QGSJET results for primary protons, while the points represent the measured density. All the calculated values of $\rho_{\mu,\,600}(\theta)$ were reduced by a factor of 1.4 in order to eliminate the distinctions between the E_0 estimates obtained from the theoretical and experimental densities.

As in Fig. 10, the density $\rho_{s,\,600}(\theta)$ for $E_0 < 2 \times 10^{18}$ eV as obtained within the QGSJET model shows a descending angular dependence that complies with relevant experimental data. In the region of higher energies—especially at extremely high energies—the calculated values deviate considerably from experimental data. Experimental data suggest that, in inclined showers ($\theta > 35$–40°), the relative fraction of muons in the total flux of charged particles increases (Fig. 5*b*) at all distances R in excess of 100 m where the measurements were performed.

Open circles in Figs. 10 and 12 represent densities for the most intense shower detected at the Yakutsk array [$\rho_{s,\,600}(58.7^\circ) \approx \rho_{\mu,\,600}(58.7^\circ) = 54$ m^{-2}] [24, 25]. The arrow in Fig. 10 indicates the rescaling of this density to the vertical direction according to (3), with the absorption range being $\lambda_\rho = 530$ g/cm^2. For the energy of this shower, relation (1) and the QGSJET model yield the estimated values of $E_0 = 1.5 \times 10^{20}$ and 2.2×10^{20} eV, respectively.

From the above experimental data, it follows that the spatial structure of EASs changes at high ener-

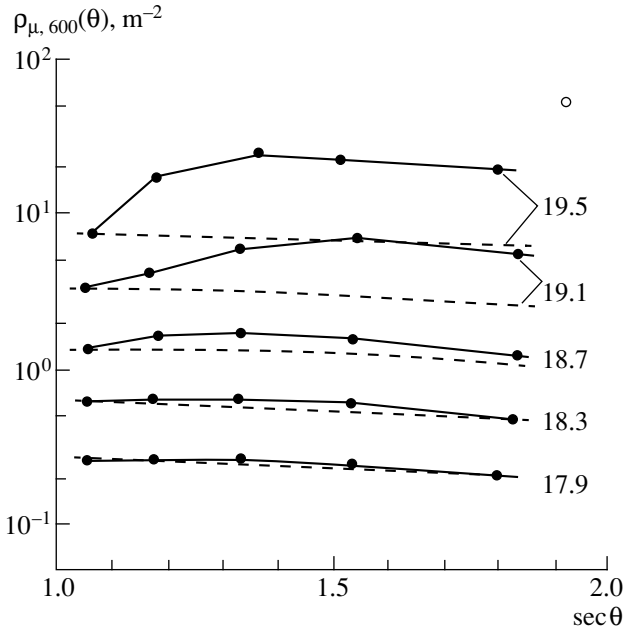

Fig. 12. As in Fig. 10, but for the density $\rho_{\mu,600}(\theta)$ [the calculated $\rho_{\mu,600}(\theta)$ values were reduced by a factor of 1.4].

gies—specifically, the shape of the LDFs for electrons and muons is modified considerably (Figs. 2 and 3). The resulting shape cannot be explained by a transition to a heavier primary composition up to that dominated by iron nuclei (see, for example, the behavior of the LDF for muons in Fig. 5*b*). Any extrapolations of not only the experimental but also the calculated dependences to the region of extremely high energies may result in large errors—in particular, errors in the estimates of the primary-particle energy. In this energy region, it is necessary to study further the LDFs for charged particles and muons at arrays including detectors spaced by distances not greater than 200–300 m.

7. CONCLUSION

The results of the present analysis can be summarized as follows. In the energy range $E_0 \approx (3\text{–}30) \times 10^{17}$ eV, the entire body of experimental data from the Yakutsk array for $\theta \le 45°$ can be described within the QGSJET model under specific assumptions. The observed 1.4-fold discrepancy between the estimates of E_0 and the distinctions between the shapes of LDFs for charged particles in showers with $\theta > 45°$ require additionally refining some parameters of the model and calculating the response of the scintillation detector.

At $E_0 \ge (3\text{–}5) \times 10^{18}$ eV, a shower develops in a different way. First, its lateral structure is changed (Figs. 9 and 11). Second, the fraction of muons increases noticeably in inclined showers with $\theta > 35°$–$40°$ (Fig. 5), the muon component undergoing more pronounced changes (Figs. 10 and 12). These changes cannot be explained within the QGSJET model for any primary-particle composition from that of protons to that of iron nuclei. Thus, they require invoking new mechanisms of the development of EASs at extremely high energies. It can be assumed that these mechanisms become operative above the energy threshold of $(2\text{–}3) \times 10^{18}$ eV, where some new processes of nuclear interactions may come into play.

We are going to continue a global investigation of the electron and muon EAS components at the Yakutsk array both by further accumulating shower statistics and by analyzing data collected to date in greater detail and within improved processing techniques. A theoretical analysis of the problems discussed above will also be continued.

ACKNOWLEDGMENTS

This work was supported by the Ministry of Sciences of Russian Federation (grant no. 01-30 for the Yakutsk multipurpose EAS array) and by the Russian Foundation for Basic Research (project no. 98-02-16964). The work of N. N. Kalmykov was supported by the Russian Foundation for Basic Research (project nos. 96-15-96783 and 99-02-16250).

REFERENCES

1. A. V. Glushkov *et al.*, Yad. Fiz. **58**, 1265 (1995) [Phys. At. Nucl. **58**, 1186 (1995)].
2. A. V. Glushkov *et al.*, Astropart. Phys. **4**, 1274 (1995).
3. A. V. Glushkov *et al.*, Izv. Akad. Nauk, Ser. Fiz. **61**, 516 (1997).
4. A. V. Glushkov *et al.*, in *Proceedings of the 25th International Cosmic Ray Conference*, 1997, Vol. 6, p. 233.
5. A. B. Kaĭdalov *et al.*, Yad. Fiz. **43**, 1282 (1986) [Sov. J. Nucl. Phys. **43**, 822 (1986)].
6. N. N. Kalmykov and S. S. Ostapchenko, Izv. Akad. Nauk, Ser. Fiz. **58**, 21 (1994).
7. A. M. Anokhina *et al.*, Yad. Fiz. **60**, 290 (1997) [Phys. At. Nucl. **60**, 230 (1997)].
8. B. N. Afanasiev *et al.*, in *Proceedings of the 25th International Cosmic Ray Conference*, 1997, Vol. 6, p. 229.
9. N. N. Kalmykov *et al.*, in *Proceedings of the 24th International Cosmic Ray Conference*, 1995, Vol. 1, p. 123.
10. N. N. Kalmykov *et al.*, Nucl. Phys. B (Proc. Suppl.) **52B**, 17 (1997).
11. A. D. Erlykin and A. W. Wolfendale, in *Proceedings of the 16th European Cosmic Ray Symposium, Alcala de Henares*, 1998, p. 269.
12. A. V. Glushkov *et al.*, Izv. Akad. Nauk, Ser. Fiz. **55**, 713 (1991).
13. N. N. Efimov *et al.*, in *Proceedings of the 22nd International Cosmic Ray Conference*, 1991, Vol. 4, p. 335.
14. J. Linsley *et al.*, J. Phys. Soc. Jpn. (Suppl. A-III) **17**, 91 (1962).
15. O. S. Diminshteĭn *et al.*, in *Collected Scientific Articles* (Yakutsk Branch, Siberian Division, USSR Acad. Sci., Yakutsk, 1983), p. 30.

16. S. N. Vernov *et al.*, Izv. Akad. Nauk SSSR, Ser. Fiz. **36**, 1705 (1972).
17. K. Greisen, Annu. Rev. Nucl. Sci. **10**, 63 (1960).
18. B. N. Afanasiev *et al.*, in *Proceedings of the ICRR International Symposium, Tokyo*, 1996, p. 412.
19. E. E. Antonov *et al.*, Pis'ma Zh. Éksp. Teor. Fiz. **68**, 177 (1998) [JETP Lett. **68**, 185 (1998)].
20. E. A. Vishnevskaya *et al.*, Yad. Fiz. **62**, 300 (1999) [Phys. At. Nucl. **62**, 265 (1999)].
21. A. V. Glushkov *et al.*, Izv. Akad. Nauk SSSR, Ser. Fiz. **50**, 2166 (1986).
22. N. Chiba *et al.*, Nucl. Instrum. Methods A **311**, 338 (1992).
23. S. Yashida *et al.*, J. Phys. G **20**, 651 (1994).
24. N. N. Efimov *et al.*, in *Proceedings of the ICRR International Symposium "Astrophysical Aspects of Most Energetic Cosmic Rays," Kofu*, 1990, p. 20.
25. A. V. Glushkov *et al.*, Izv. Akad. Nauk, Ser. Fiz. **55**, 717 (1991).

Translated by R. Tyapaev